VYSOKÁ ŠKOLA CHEMICKO-TECHNOLOGICKÁ V PRAZE

Fakulta chemické technologie

Ústav anorganické chemie

Habilitační práce

Anorganické materiály pro fotonické součástky

Autor: Ing. Pavla Nekvindová, Ph.D.

Praha: 2015

PROHLÁŠENÍ

Prohlašuji, že jsem tuto práci vypracovala samostatně. Veškeré literární prameny a informace, které jsem v práci využila, jsou uvedeny v seznamu použité literatury. Byla jsem seznámena s tím, že na moji práci se vztahují práva a povinnosti vyplývající ze zákona č. 121/2000 Sb.,o právu autorském, o právech souvisejících s právem autorským a o změně některých zákonů (autorský zákon). Souhlasím se zveřejněním své práce podle zákona č. 111/1998 Sb.,o vysokých školách, ve znění pozdějších předpisů.

V Praze dne 22. 9. 2015

Ráda bych poděkovala především paní doktorce Jarmile Špirkové za její rady, trpělivost a životní optimismus. Dále pak prof. Davidu Sedmidubskému za jeho cenné rady a připomínky k habilitační práci. V neposlední řadě bych chtěla poděkovat mým spolupracovníkům, kteří se podíleli na společných publikacích, a studentům, především doktorce Blance Švecové. I Ti všichni se mnou měli velkou trpělivost a mnohému mě naučili. Děkuji.

OBSAH

1. ÚVOD

Interakce světelného paprsku s pevnou látkou je jevem, který fascinoval a přitahoval lidstvo od samého počátku jeho bytí. Přes pocit bezpečí, krásu a vznešenost dokáže člověk v dnešní době využívat spojení světla a materiálu také k usnadnění jeho každodenního života. Přenos informace v komunikační technice pomocí laserových zdrojů produkujících monochromatické koherentní záření a skleněných optických vláken je bezesporu jedním z významných fenoménů současnosti. Navíc dnes lidé dokáží využívat optické záření nejen k přenosu informace, ale k mnoha dalším činnostem, např. optické biosenzory můžeme využít ke kontrole životního prostředí a lékařské diagnostice, vláknové lasery při lékařské diagnostice při operacích - např. operace očí, ale také v průmyslu pro gravírování, přesné řezání a sváření a povrchové úpravy materiálů. Na základě reakce fotonů s nanočásticemi pevných látek je dnes možná také detekce velmi nízkých koncentrací lehkých prvků.

Přitom na začátku přípravy každé fotonické součástky stojí otázka, z jakého materiálu ji vyrobíme, má daná sloučenina – pevná látka potřebnou vlastnost? Uvědomíme-li si, že světlo je proud fotonů a zároveň elektromagnetická vlna a že pevná látka je poměrně značný soubor částic (atomů, iontů nebo molekul), které podléhají zákonům kvantové mechaniky a termodynamiky, je třeba studovat a porozumět jevům probíhajícím na atomární úrovni hmoty. Právě tento kvantově mechanický přístup k řešení otázek o podstatě vlastností anorganických látek dokázal předpovědět existenci nových možností pro interakci světla s hmotou. Příkladem mohou být uměle připravené krystaly perovskitů, které mají zcela výjimečné a pestré vlastnosti, nebo i úžasná variabilita složení skla jako amorfního anorganického materiálu.

Klíčová je v tomto výzkumu otázka vztahů mezi složením a strukturou anorganických sloučenin, popř. také chováním „funkčních“ iontů - iontů nebo prvků pomocí, kterých byla sloučenina modifikována, a účelně pozměněnou vlastností materiálu. Stále více se projevuje význam poznání, jak lze účinně ovlivnit vlastnosti materiálu pro vytvoření fotonické součástky s předem přesně zadanými vlastnostmi. A právě zde je velké pole působnosti pro anorganického chemika, který dokáže využívat znalostí a studia vztahů mezi strukturními, vazebnými a fyzikálními parametry, které jsou obecně určené chemickým složením materiálů.

Myslím si, že se nám společně za posledních dvacet let podařilo vytvořit v naší laboratoři pracoviště, které právě sledování a interpretací uvedených vztahů umožňuje, úspěšně studuje a je v tom jedinečné.

Předkládaná habilitační práce se dělí na dvě základní části. První část obsahuje popis základních používaných jevů a pojmů společně s krátkými komentáři zdůrazňujícími nejdůležitější poznatky z původních publikovaných pracích. Práce samy jsou pak přiloženy v druhé části habilitační práce a popisují podrobně dané experimenty, použité metody, dosažené výsledky a patřičné závěry. Přikládané články jsou vždy dílem kolektivním, kdy se všichni uvedení autoři na publikaci podíleli svým dílem. Jsou také výsledkem dlouholetých a plodných spoluprací, za které jsem svým spoluautorům vděčná.

2. KOMENTÁŘ K PŘEDLOŽENÝM PUBLIKACÍM

2.1 Pasivní a dynamické ovládání optického signálu [1-5]

Optický signál se materiálem šíří prostřednictvím fotonů. Fotony se pohybují optickými vlnovody, přičemž k zesilování, spínání a ukládání informace se používají funkční optické součástky. **Pasivní a dynamické součástky** nemění vlastnosti procházejícího signálu. Pasivní součástky umožňují např. dělení optického výkonu v požadovaném poměru (děliče výkonu neboli splitry), nebo filtrují určitou část optického spektra (spektrální filtry tzv. multiplexory nebo demultiplexory) nebo mění polarizaci procházejícího záření (konvertory polarizace) apod. **Dynamické součástky** využívají vnější elektrický nebo optický signál k ovlivňování nebo řízení procházejícího signálu, jedná se například o optické modulátory, přepínače, laditelné spektrální filtry, optické spínače.

Základní strukturou pro šíření optického signálu je **optický vlnovod**. Jedná se o struktury s vhodnými hodnotami indexu lomu. Obecně platí, že vlnovodná vrstva musí mít nejvyšší hodnotu indexu lomu v daném systému. Pro planární strukturu platí:

$$n_1 > n_0 \geq n_2, \tag{1}$$

kde n_2 je index lomu vzduchu (vnějšího prostředí), n_1 je index lomu vlnovodné vrstvy a n_0 je index lomu substrátu. Je-li index vlnovodu vyšší než index lomu okolního prostředí, zavedené optické záření se pomocí totálních odrazů může šířit vlnovodnou vrstvou, přičemž energie šířícího se záření nemůže z vlnovodu uniknout. Platí-li uvedená podmínka, potom způsob, kterým se optický signál šíří vlnovodem, přesněji jedno z řešení vlnové rovnice pro šíření elektromagnetické vlny daným prostředím, se nazývá optický mod nebo vid. V optickém vlnovodu se může šířit jen omezený počet vidů M, který pro vlnovody se skokovým charakterem hloubkového profilu indexu lomu vypočítáme ze vztahu:

$$M = \frac{2 \cdot d\sqrt{n_1^2 - n_0^2}}{\lambda}, \tag{2}$$

kde d je tloušťka vlnovodné vrstvy, n_1 je index lomu vlnovodné vrstvy, n_0 je index lomu substrátu a λ je vlnová délka optického záření. Vhodná pracovní vlnová délka je další nutnou

podmínkou pro šíření optického vlnovodu strukturou. Praktická ukázka jak rozpoznat vidy v dvourozměrné a jednorozměrné optické struktuře je ukázána na **obr. 1**.

A) Dvourozměrná (planární) vlnovodná struktura

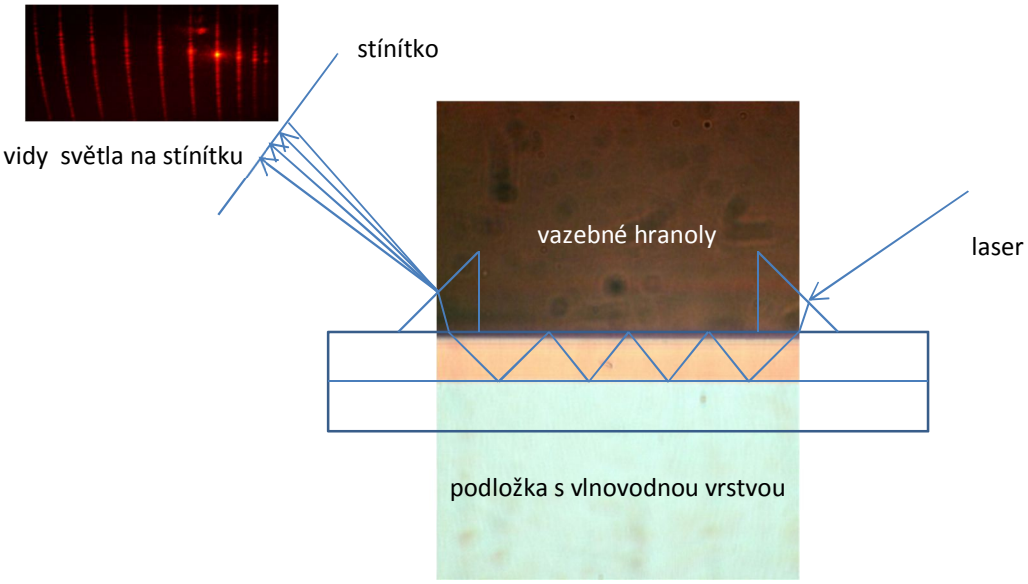

B) Jednorozměrná (kanálková) optická struktura

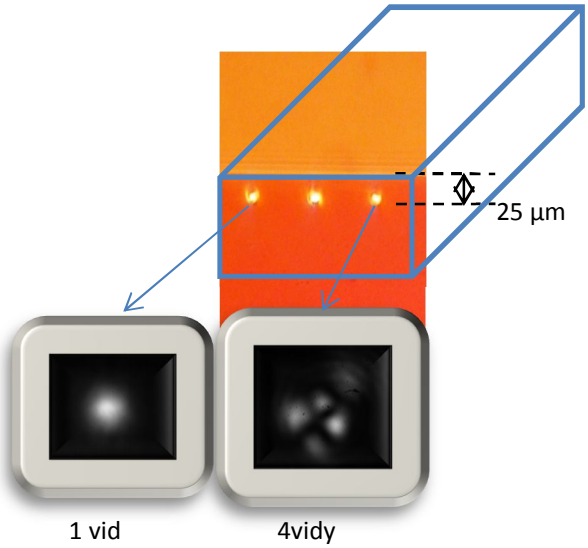

Obrázek 1. Znázornění vidů světla šířícího se jednorozměrnou a dvourozměrnou fotonickou strukturou, jedná se o vlnovody připravené ve skelných podložkách iontovou výměnou $Ag^{+} \leftrightarrow Na^{+}$. Změna indexu lomu je v planární vrstvě až + 0,1 a v kanálkovém optickém vlnovodu okolo + 0,01.

Podle druhu aplikace rozeznáváme druhy optických vlnovodů. Známe například vlnovody planární, kanálkové a vláknové, ve kterých je šíření optického signálu různě prostorově omezeno. V planárním vlnovodu se signál šíří dvěma směry, které jsou dány rovinou vlnovodné vrstvy, v kanálkovém i ve vláknovém vlnovodu je šíření signálu pak omezeno do jednoho směru. Podle hodnoty změny indexu lomu rozlišujeme vlnovody se skokovým nebo gradientním profilem indexu lomu a s vysokou nebo nízkou změnou indexu lomu. Z hlediska množství přenášené informace je dělíme na jedno- a mnoha- vidové, přičemž vláknové vlnovody jsou zpravidla jednovidové se změnou indexu lomu 1×10^{-3} a planární vlnovody, jejichž cílem je vedení a zpravidla zpracování optického signálu na krátkou vzdálenost, mohou být jak jednovidové, tak mnohavidové.

Jednou z velmi důležitých charakteristik optického vlnovodu je jeho optický útlum, který se projevuje jako nežádoucí pokles intenzity (výkonu) optického záření. Vyjadřuje se pomocí koeficientu útlumu α (dB.cm^{-1}) a vypočítá se z následujícího vztahu:

$$\alpha = \frac{1}{L} 10 \log \frac{P_0}{P_L}, \qquad (3)$$

v němž P_0 a P_L je výkon optického záření vstupujícího resp. vystupujícího z materiálu o délce L. Koeficient útlumu α je hlavním faktorem určujícím praktickou použitelnost optických vlnovodů. Kvalitní optické vlnovody mají koeficient útlumu v řádu desetin dB.cm^{-1} a méně. Ukázka změřeného optického útlumu na optické součástce je na **obr.2**.

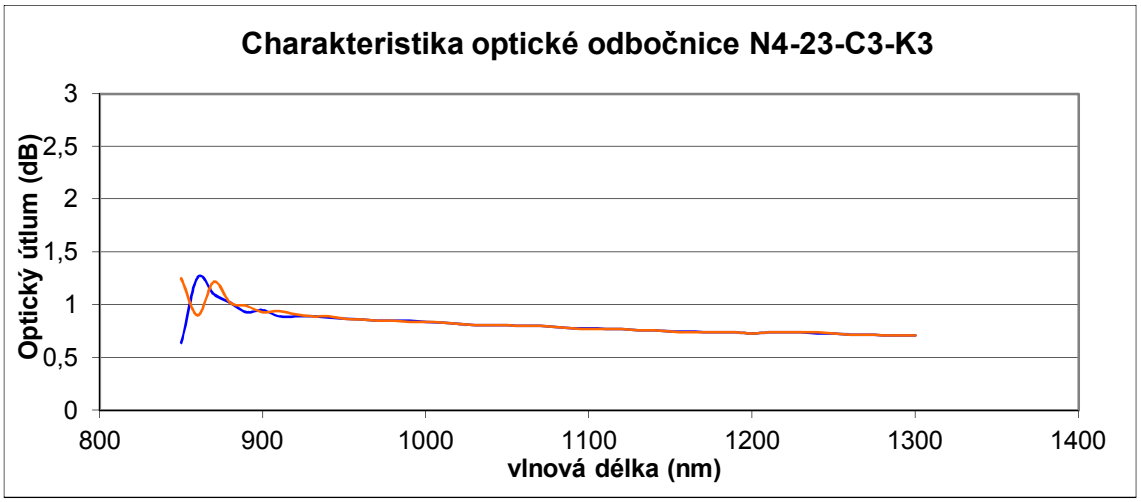

Obrázek 2. Ukázka měření závislosti optického útlumu na vlnové délce u ponořeného kanálkového vlnovodu s vazbami na optické vlákno. Optický signál v celé šířce měřeného spektra nepřesáhne hodnotu 1 dB.cm^{-1}; pro nižší vlnové délky je patrné vedení více vidů. Kanálkový vlnovod je připraveného iontovou výměnou $Ag^+ \leftrightarrow Na^+$ ve skle v rámci spolupráce s firmou Vláknová optika SQS, Nová Paka.

Mezi typické pasivní vlnovodné součástky patří děliče výkonu optického záření tzv. odbočnice nebo splitery. Jedná se o jednorozměrný kanálkový vlnovod, který se v daném místě rozdělí do dvou větví tak, že připomíná tvar písmeneY. Je-li struktura symetrická vůči své podélné ose, pak záření zavedené do jednovidového vstupního vlnovodu se rovnoměrně rozdělí do obou výstupních (jednovidových) větví. Pokud je úhel rozvětvení dostatečně malý, jsou malé i přídavné ztráty vyzařováním a rozptylem optického záření. Při dobré funkci součástky optické záření vycházející z obou větví má poloviční výkon vůči výkonu na vstupu. Dnes jsou vyráběny i nesymetrické děliče výkonu nebo např. děliče, které mají na jeden vstup i 64 výstupů.

Jako typickou dynamickou vlnovodnou součástku lze uvést elektrooptický vlnovodný modulátor, který pracuje na principu Mach-Zehnderova interferometru a funguje jako spínač optického signálu. Je tvořen dvěma jednovidovými vlnovodnými rozvětveními tvaru Y spojenými dvojicí vlnovodů. Vlnovody jsou vytvořeny v materiálu, jehož index lomu lze ovlivňovat přiloženým elektrickým polem. Přiložením napětí na elektrody dochází v horním a dolním vlnovodu ke změně indexu lomu, a tedy k fázovému posuvu. Výstupní rozvětvení pak může být napájeno do obou větví současně s různou fází. Pokud je fáze optického záření v obou větvích stejná, vznikne ve výstupním rozvětvení rozložení pole odpovídající základnímu vidu, který se vlnovodem může šířit, a záření modulátorem prochází s minimálními ztrátami. Přiložíme-li takové napětí, že fáze v jednotlivých větvích se liší o π, vznikne ve výstupním rozvětvení rozložení záření odpovídající vyššímu, antisymetrickému vidu, který se v jedno-vidovém výstupním vlnovodu nemůže šířit. V takovém případě se záření vyzáří mimo výstupní vlnovod; modulátor je tak ve stavu „vypnuto“. Poněvadž odezva elektrooptického materiálu na přiložené napětí je velmi rychlá (řádu desítek femtosekund), umožňuje tento princip velmi rychlou modulaci optického záření relativně malým ovládacím napětím (jednotky voltů). Tyto modulátory se používají v optických komunikačních systémech s přenosovými rychlostmi několika desítek gigabitů za sekundu.

Pokud materiál substrátu vykazuje nelineární optické vlastnosti, je možné na stejném principu vytvořit také optický vlnovodný spínač, u kterého je možné index lomu ovlivňovat vstupujícím optickým signálem. Výzkum v této oblasti se soustředí na vývoj zařízení pracujících na principu “all- optics”, který umožňuje spínání a ovládání optického signálu bez konvertování na signál elektrický. Materiál vykazující nelineární optický jev, totiž pod vlivem silného laserového svazku mění své vlastnosti jako např. index lomu nebo absorpci nelineárně. Příkladem takového optického zařízení může být např. rezonátorový optický spínač, jehož funkce je znázorněna na **obr.3**. Spínač se skládá ze dvou kanálkových vlnovodů

umístěných po stranách mezi, kterými leží kruhový resonátor. Tento kruhový resonátor obsahující např. kovové nanočástice vykazuje nelineární optické jevy - Kerrovy jevy. S využitím křížové fázové modulace, kterou indukuje silný laserový puls, se optický signál v aktivním vlnovodu transportuje do druhého zatím neaktivního vlnovodu – spínač je tím sepnut.

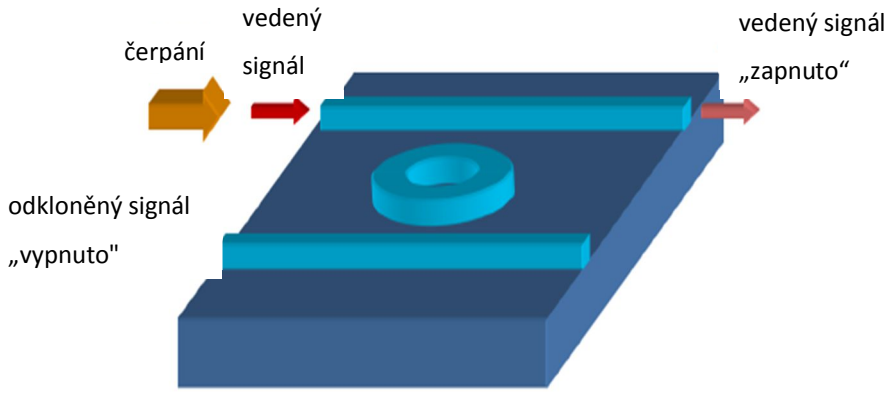

Obrázek 3. Jedno z možných uspořádání optického mikrorezonátoru, který využívá nelineárních optických vlastností pro modulaci optického signálu (převzato z [2])

2.2 Anorganické materiály pro pasivní a dynamické optické členy [5-7]

Index lomu materiálu je pro návrh optické součástky důležitou veličinou. Ze vztahu (4) je zřejmé, že index lomu n je veličina, která je nepřímo úměrná rychlosti šíření optického záření materiálem. Relativní permitivita ε_r je materiálová konstanta a index lomu je pak pomocí permitivity definován jako $n = \sqrt{\varepsilon_r}$. Relativní permitivita (někdy také dielektrická konstanta materiálu) je přímo úměrná polarizaci materiálu a souvisí tedy s elektronovou polarizovatelností jednotlivých atomů nebo molekul.

$$v = \frac{c}{\sqrt{\varepsilon_r}} = \frac{c}{n} \qquad (4)$$

V **Tabulce 1** jsou významné anorganické optické materiály seřazeny podle hodnot indexu lomu. Je zřejmé, že nejvyšší hodnoty indexu lomu nalezneme v krystalických materiálech, nižší pak v materiálech amorfních. Vedle těchto materiálů jsou dnes také zkoumány organické polymerní materiály, které mají obecně nízké hodnoty indexu lomu (např. polymery na bázi teflonu (hodnota indexu lomu 1,297) [8].

Tabulka 1. Optické vlastnosti vybraných optických materiálů index lomu a hranice oblasti s minimální absorpcí – hodnota indexu lomu odpovídá vlnové délce 633 nm [9]

Krystaly	Index lomu	Transparentní oblast [μm]
Al_2O_3	1,7659	0,2 - 5
Diamant	2,4122	0,035 - 10
$LiNbO_3$	2,2864	0,35 - 5,5
$LiTaO_3$	2,1337	0,4 - 5,5
YAG	1,8295	0,4 - 5,0
KTP	1,7619	0,43 - 3,54
KDP	1,5073	0,2 – 1,5
Polovodiče	Index lomu	Transparentní oblast
Si	3,4434 (λ = 2,43 μm)	2,43 - 25
SiC	2,6342	0,488-1,064
ZnO	1,9888	0,45 - 4,0
GaN	2,3848	0,35 - 10
Skla	Index lomu	Transparentní oblast
Fused silica	1,46	0,18 - 3,5
Sodnokřemičitanová skla	1,52	0,31 - 4,6
Borodilicate (BK7)	1.51	0,35 - 2,5
Fosfátová skla	1.52	0,3 - 2,5
Flintová skla	1,58 - 1,62	0,3 - 2,4

Index lomu jako komplexní veličina – nelineární optické jevy

Index lomu materiálu závisí na vlnové délce šířícího se optického signálu. Tomuto jevu říkáme **disperze**. Při tzv. normální disperzi index lomu klesá s rostoucí vlnovou délkou. Příčinou disperze je závislost fázové rychlosti šíření světelné vlny na její vlnové délce při průchodu materiálem.

Vhodný materiál pro pasivní vedení optického signálu nesmí vedený optický signál absorbovat ani rozptylovat. **Absorpce** v materiálu je na jedné straně spektra vlnových délek způsobena fundamentální absorpcí elektronů z valenčního do vodivostního pásu dielektrika a souvisí tedy s šířkou zakázaného pásu dielektrika. Na straně druhé tj. pro vyšší vlnové délky se jedná o infračervenou fononovou absorpci způsobenou vibracemi vazeb struktury dielektrika. Pro daný materiál tedy vždy existuje rozmezí vlnových délek, ve kterém můžeme daný materiál z hlediska nízké-nulové absorpce použít. Meze transparence pro využívané anorganické materiály jsou uvedeny **Tabulce 1**. V anorganických krystalech je například zajímavé si povšimnout vysoké horní hranice transparence diamantu, která je způsobena jeho vysokou kovalencí vazeb spojenou s velkými silovými konstantami a tedy minimální interakcí fononů s procházející vlnou. Polovodiče mají ve srovnání s dielektriky díky menší šířce zakázaného pásu oblast transparence většinou posunutou k vyšším vlnovým délkám – oblast transparence tedy leží ve viditelné oblasti spektra nebo nad ní. U polovodičů je také

naprosto zřejmá souvislost mezi dolní mezí transparence a šířkou zakázaného pásu. Horní mez je u polovodičů dána opět absorpcí krystalové struktury a také s absorpcí spojenou s exitací volných nositelů náboje. Skla jako jeden z nejdůležitějších optických materiálů jsou amorfním prostředím. Mají velkou energii zakázaného pásu (SiO_2 okolo 10 eV), která odpovídá vysoké propustnosti skel v UV oblasti. Jsou také směsí nejrůznějších oxidů, kdy přídavek dalších oxidů např. k SiO_2 snižuje šířku zakázaného pásu, ale hranici propustnosti posouvá k nižším vlnovým délkám. Horní hranice propustnosti křemičitanových skel pak odpovídá vibračním absorpcím teraedrů SiO_4^{3-}.

Rozptyl optického záření v materiálu může být způsoben nečistotami, poruchami-defekty a nehomogenitami v materiálu. Při rozptylu optické záření mění především svůj směr. Může se změnit ale také fáze nebo polarizace záření. Pokud je vlnová délka záření menší, než jsou rozměry nehomogenit, pak se jedná o Rayleighův rozptyl a světlo je na nehomogenitách rozptýleno stejně jako v rozptylce. Rozptyl je pak příčinou zvýšení optického útlumu stejně jako absorpce. Platí, že s rostoucím obsahem nehomogenit stejně jako se zkracující se vlnovou délkou roste optický útlum materiálu.

Pro dynamické ovládání optického signálu se využívají krystalické materiály, které vykazují elektrooptické vlastnosti. Při hledání vhodného materiálu se tedy soustředíme na hodnotu tzv. elektrooptického koeficientu, který je v krystalech tenzorem, tj. pro určité uspořádání měření je většinou měřitelná právě jedna složka daného tenzoru. Hodnoty elektrooptických koeficientů v různých krystalech jsou uvedeny v **Tabulce 2**. Typickými představiteli elektrooptického materiálu jsou monokrystaly niobičnanu lithného a draselného. Přiložené elektrické pole mění posunem atomů vůči sobě rozložení dipólových momentů v materiálu, což ovlivní procházející elektromagnetickou vlnu.

K dynamickému ovládání optického signálu můžeme využívat skutečnost, že např. index lomu materiálu nebo výše popsaná absorpce materiálu mohou za určitých podmínek záviset na intenzitě dopadajícího optického signálu nelineárně. Takovým jevům říkáme **nelineární optické jevy**. Popsaný jev nastává při šíření optického záření s vysokou intenzitou daným materiálem. Silné elektrické nebo magnetické pole optického záření vyvolá prostorové změny v rozložení elektrických nábojů pevné látky. Dochází např. k vychýlení rozložení elektronové hustoty vůči jádru atomu, tj. ke změně polarizovatelnosti atomu. K nelineárním optickým jevům dochází, pokud je elektrické pole optické vlny srovnatelné s elektrickým polem reprezentujícím Coulombovy síly, např. mezi elektrony a jádrem atomu. Rozvoj nelineární optiky tedy nastal až s příchodem laserů s velmi krátkými a vysoce intenzivními laserovými pulsy.

Tabulka 2. Hodnoty elektrooptických koeficientů r a nelineárních optických koeficientů d v nelineárních optických krystalech a hodnoty $\chi 3$ ve vybraných kompozitech na bázi SiO_2

Krystal	Elektrooptický koeficient [pm/V]	Nelineární opt.koeficient [pm/V]	citace
$LiNbO_3$	r_{13}= 9,6 r_{22}= 6,8 r_{33}= 31 r_{51}= 33	d_{31}= 6,25 d_{31} = - 4,5 d_{33}= - 0,27 d_{22} = 2.1	[6]
$LiTaO_3$	r_{33}= 33 r_{13} = 8 r_{22} = 20	d_{31} = - 1 d_{33} = -21 d_{22} = 2.0	[10]
$KNbO_3$	r_{13}= 28 r_{42}= 380 r_{31}= 165		[6]
KDP	r_{41}= 8,8 r_{63}= 10,3	d_{36}=0,44	[10]
Kompozitní materiál	λ [nm]	$\chi 3$ [esu]	
SiO_2	1064	$1{,}8 \times 10^{-14}$	[11]
Cu : SiO_2	1064	$3{,}3 \times 10^{-8}$ $(0{,}8\text{ -}1{,}2) \times 10^{-7}$	[12] [13]
Cu: SLSG	1064	$0{,}9 \times 10^{-8}$	[14]
Ag: SiO_2	1064	$1{,}8 \times 10^{-7}$	[15]
Au: SiO_2	1064	$(0{,}1\text{-}4{,}3) \times 10^{-8}$	[16]

Fyzikálně je nelineární optický jev popsán jako nelineární závislost polarizace prostředí *P* na intenzitě elektrického pole E optického záření:

$$P = \varepsilon_0(\chi^{(1)}E + \chi^{(2)}E^2 + \chi^{(3)}E^3 ...)$$

kde ε_0 je permitivita vakua, $\chi^{(1)}$, $\chi^{(2)}$ $\chi^{(3)}$ je označení pro susceptibilitu prvního, druhého a třetího řádu (v uvedeném vztahu je zanedbána vektorová povaha polarizace *P* a intenzity elektrického pole *E*). První člen ve vztahu popisuje lineární odezvu daného prostředí a popisuje lineární optické jevy. Susceptibilita $\chi^{(1)}$ je vztažena k lineárnímu indexu lomu n_o jako

$$n_{0} = \sqrt{1 + 4\pi\chi^{(1)}}$$

Ostatní optické členy představují nelineární optické jevy. Graficky lze vztah mezi polarizací *P* a intenzitou elektrického *E* a jeho lineární a nelineární povahu znázornit následujícím obrázkem, kde je lineární závislost mezi polarizací a intenzitou elektrického pole znázorněna přerušovanou čárou zatímco nelineární závislost čarou plnou. Slabé elektrické pole dopadajícího signálu způsobí malou lineární odezvu (**Obr. 4a**), kdežto silné pole způsobí vznik asymetrické polarizace s velkým negativním vychýlením (**Obr. 4b**).

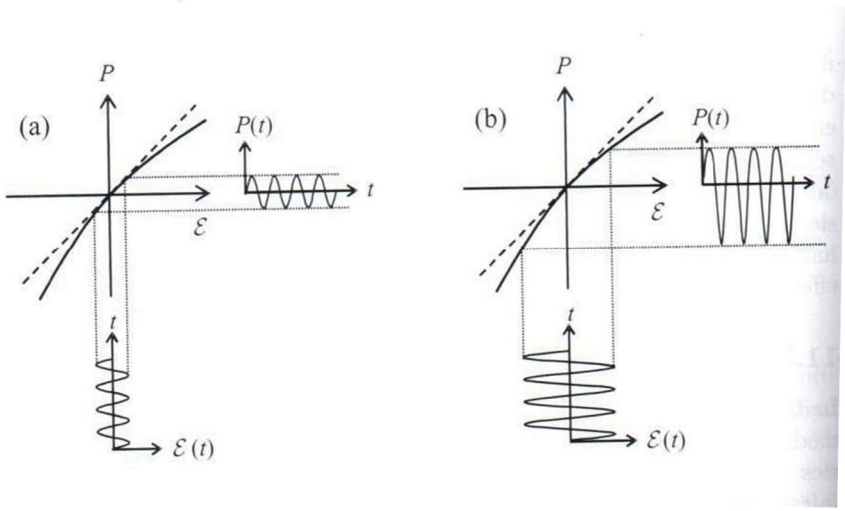

Obrázek 4. Znároznění nelineárních optických jevů (převzato z [6])

Materiál s vysokou optickou nelinearitou je pak charakterizován vysokou hodnotou $\chi 3$ (nebo vysokou hodnotou nelineárního optického koeficientu viz Tabulka 2). Tyto materiály jsou využívány především pro změnu vlnové délky procházejícího optického signálu.

Vedle známých anorganických krystalických materiálů se v současnosti jako jeden z perspektivních materiálů vhodných pro nelineární optické součástky studují skla, která obsahují nanočástice mědi, stříbra nebo zlata [17-19]. Charakteristická je pro ně vysoká hodnota nelineární susceptibility třetího řádu $\chi 3$, porovnání se substrátem bez kovové nanočástice je uvedeno v Tabulce 2. Podstatou tohoto jevu je povrchová plasmonová rezonance přítomných kovových nanočástic. Navíc má optický signál procházející takovým materiálem velmi rychlou odezvu (~50 ps), čímž se blíží vlastnostem elektrického signálu.

Niobičnan lithný [20-22]

Monokrystalický niobičnan lithný je již řadu let známým materiálem, který se vzhledem ke svým mimořádným vlastnostem využívá zejména v nelineární optice, akustice a fotonice. Niobičnan lithný je syntetický krystal a je možné jej dobře pěstovat i ve velkých rozměrech. Mezi jeho největší výhody patří možnost současného pasivního i aktivního ovládání optického signálu v jednom optickém členu.

Niobičnan lithný je kongruentní krystal s přibližně 6% deficitem lithia a dá se tedy snadno dotovat různými prvky. Známé je obohacení vzácnými zeminami (např. Er, Yb, Nd, Tm atd.) pro účely výroby optických zesilovačů a vlnovodných laserů; dále se dotuje také mnohými přechodnými kovy jako např. Fe (pro využití v holografických pamětích), Ti, Cu, Cr, Zn apod.

Niobičnan lithný je jednoosý záporný krystal krystalující v trigonální krystalografické soustavě s prostorovou grupou *R3c* . Díky anisotropii monokrystalu $LiNbO_3$ se v různých krystalografických směrech $LiNbO_3$ šíří optické záření odlišným způsobem. Z toho důvodu se používají krystalografické řezy $LiNbO_3$ s různými orientacemi. Mezi nejpoužívanejší krystalografické řezy $LiNbO_3$ patří řez *Z* a řez *X*; v uváděných pracích byly používány také speciální řezy $LiNbO_3$ označované *Y*, které jsou orientovány buď kolmo na štěpnou rovinu *Y⊥* nebo rovnoběžně se štěpnou rovinou *YII*. Přehled jejich tříindexového a čtyřindexového označení je uveden v **Tabulce 3**.

Tabulka 3. Popis použitých krystalografických řezů $LiNbO_3$ (převzato z [22])

Typ řezu $LiNbO_3$	Popis řezu	Krystalografická rovina {h k l}	Krystalografická rovina {h k i l}
Z	Kolmý na krystalografickou osu *z*	{001}	{0001}
X	Kolmý na krystalografickou osu *x*	{110}	$\{11\bar{2}0\}$
YII (také *Y36*)	Rovnoběžný se štěpnou rovinou	{012}	$\{01\bar{1}2\}$
Y⊥ (také *Y128*)	Kolmý na štěpnou rovinu	{104}	$\{10\bar{1}4\}$

Optická skla [5, 23-26]

Především optická propustnost skel v širokém rozsahu spektra a také snadná opracovatelnost předurčily sklo jako materiál vhodný pro optické a později také fotonické součástky. Skla obecně mohou vykazovat poměrně dobrou homogenitu a navíc se dají jejich vlastnosti snadno měnit pomocí změny jejich chemického složení. Na rozdíl od krystalů se může složení a tedy také vlastnost skla měnit spojitě. Příkladem vhodnosti skla jako důležitého anorganického fotonického materiálu je výroba nízkoztrátových křemenných vláken, kdy je jejich jádro s vyšší hodnotou indexu lomu schopné vést optický signál na velké vzdálenosti.

Sklo má amorfní strukturu a je možné jej nazvat tuhým roztokem zpravidla oxidů ale i jiných chemických sloučenin. Společným znakem všech skel je pravidelné uspořádání jeho strukturních jednotek (dvou až tří atomů) na krátkou vzdálenost. Základní strukturní jednotka je zpravidla tvořena centrálním elektropozitivním prvkem obklopeným různým počtem atomů elektronegativních prvků. Například v křemičitanových sklech je základní strukturní jednotkou tetraedr SiO_4^{3-}, jehož centrálním atomem je křemík obklopený čtyřmi atomy kyslíku. Vedle křemíku známe i další tzv. síťotvorné prvky jako např. B a P. Pokud jsou

do skla přimíseny ještě další prvky jako Na, K, Ca, Mg, dochází k přerušení vazeb Si-O-Si a nastane depolymerace skelné sítě a vlastností skel se mění - modifikují. Kationty modifikátorů leží v dutinách, které vytvoří seskupení strukturní jednotek skla. Modifikátory tedy samy sklo tvořit nemohou díky poměrně vysoké iontovosti vazby. Existují však také prvky intermediální, které mohou být jak modifikátory, tak síťotvornými prvky, jsou to např. Al ale také pravděpodobně Zn. Skla používaná ve fotonice je možné rozdělit na skla

a) s nízkým indexem lomu ($n < 1,7$) – křemičitanová (silikátová) skla, fosforečnanová skla, amorfní Al_2O_3, fluoritová skla,
b) se střední hodnotou indexu lomu ($1,7 < n < 2,0$) – oxynitridová skla,
c) skla s vysokou hodnotou indexu lomu ($n > 2,0$) – amorfní oxidy kovů, chalkogenidová skla a telluridová skla [18].

Pro **návrh optické součástky** je tedy nanejvýš vhodné soustředit se nejprve na její funkci a pro návrh materiálu

a) vybrat pracovní vlnovou délku nebo rozsah vlnových délek, pro které má být materiál transparentní,
b) soustředit se na optický útlum materiálu při dané vlnové délce,
c) navrhnout vhodné uspořádání tj. kombinaci rozměrů a hodnot indexu lomu s ohledem na správné šíření optického záření,
d) zvolit vhodnou technologii přípravy.

Pasivní optické vlnovody: současný stav

V současné době byla vytvořena celá řada nejrůznějších pasivních vlnovodných členů na bázi materiálů krystalických, skelných a v poslední době i polymerních. Vlnovody jsou dnes vytvářeny modifikací nebo návrhy nových materiálů přímo na míru dané funkční součástce. V současné době existují tři hlavní technologické postupy výroby optických vlnovodů. Jednou z možností je nanášení vrstvy daného materiálu s vyšší hodnotou indexu lomu na podložku s nižší hodnotou indexu lomu. K tomuto účelu jsou využívány především různé depoziční techniky jako CVD (Chemical Vapour Deposition) a její modifikace, pulsní laserová deposice, techniky epitaxního růstu nebo techniky sol-gel. Těmito technikami je vytvořena vrstva jiného materiálu na podložce a změnou její tloušťky můžeme ovlivňovat parametry vlnovodu jako např. počet šířených vidů. Na homogenitě, mikrostruktuře a rovnoměrném nanesení stejně tenké vrstvy pak závisí především hodnota optického útlumu

připraveného vlnovodu. Uvedenými technikami je možné vytvářet nejen vlnovody planární ale také vlnovody hřebenové, u nichž je na podložku nebo přímo do štěrbiny mezi materiály nanesen tenký pásek nového materiálu s nižší hodnotou indexu lomu. Takto jsou dnes připravovány především vlnovody z monokrystalického křemíku, nitridů a fosfidů galitých, oxidu zinečnatého, diamantu, yttrium aluminium granátu a dalších materiálů [27-32].

Jinou možností jak připravit optický vlnovod je využít především termální difúzi z nanesené vrstvy nebo iontovou výměnu pro vytvoření tenké vrstvy s odlišným chemickým složením než má původní podložka a tak zvýšit hodnotu indexu lomu. Ve spojení s litografií je tímto způsobem možné připravit i kanálkové struktury vlnovodů. Oproti výše uvedeným nanášecím technikám se tyto vlnovody vyznačují velmi nízkými optickými útlumy a velkou symetrií profilu blízkého pole optického vidu. Omezení těchto technik však plyne z výběru vhodné kombinace podložky a vyměňovaného iontu. Iontová výměna ve skle je nejvíce známá a dosud také velmi často využívaná technika [33, 34]. Vyměňovány jsou především pohyblivé ionty alkalických kovů přítomné ve skelné matrici za jiné vhodné ionty z vnějšího zdroje iontů. Velmi rozšířená je také difúze titanu nebo zinku z napařené kovové vrstvy do $LiNbO_3$ [35] nebo protonová výměna s následným žíháním v uvedeném monokrystalu [36].

Třetím obecným postupem, který je nejmladší, je modifikace povrchu pevné látky intenzivními svazky fotonů, iontů nebo elektronů. Příkladem může být modifikace povrchu skla pulsním laserovým svazkem o dané intenzitě, což má za následek zvětšení objemu v místě dopadu do sklené matrice a následné zvýšení indexu lomu. V krystalech se naopak dopadem uvedeného svazku index lomu snižuje [37].

Současným nejnovějším trendem je lokalizace optického signálu ve vlnovodu, který má menší rozměr než je vlnová délka procházejícího optického signálu. Využívá se při tom obohacení dielektrického materiálu kovovými nanočásticemi. Obor, který se na uvedené možnosti soustředí, se nazývá nanoplasmonika [38].

2.3 Vlastní výsledky výzkumu anorganických optických materiálů pro pasivní a dynamické součástky

V laboratoři materiálů pro fotoniku, jíž jsem součástí, jsme se soustředili na přípravu pasivních a dynamických optických členů difúzními technikami, které nekladou velké nároky na přístrojové vybavení, ale jsou poměrně značně experimentálně náročné a mají omezenou variabilitu v tom smyslu, že je možné kombinovat jen určitý materiál s určitým vhodným

dopantem. V krystalických materiálech byly dosud studovány a prakticky prováděny protonová výměna s následným žíháním v $LiNbO_3$ a $LiTaO_3$ [39-41], a výměna barya v $KTiOPO_4$ (KTP) monokrystalu [42]. Já jsem se konktrétně zaměřila na vlnovody v $LiNbO_3$ a KTP.

Z amorfních materiálů se soustředíme především na křemičitanová skla. Jejich výhodou je velmi dobrá stabilita, odolnost a nejsnazší možnost vazby na optická křemenná vlákna. Navíc ve srovnání s krystaly nebo polymery lze jejich složení a tedy i vlastnosti navrhnout „přesně na míru“ požadavkům konečné fotonické součástky. Výroba je také poměrně levná a snadná. Optické vlnovody v nich byly připraveny následujícími iontovými výměnami: $Ag^+ \leftrightarrow Na^+$ [43-46], $K^+ \leftrightarrow Na^+$ [44,45,47] $Li^+ \leftrightarrow Na^+$ [48-50] $Cs^+ \leftrightarrow Na^+$ [51], $Cu^+ \leftrightarrow Na^+$ [43,52], $Cu^{2+} \leftrightarrow Na^+$ [43,53]. Detailně jsme také studovali iontovou výměnu v elektrickém poli a vytvořili pracovní aparaturu pro uvedený typ iontové výměny [51,53,54]. Jelikož je v našich pracích vždy kladen důraz především na pochopení a popis vztahů mezi optickými, chemickými a strukturními vlastnosti, byla ve spolupráci s Ústavem skla a keramiky VŠCHT (Doc. Martin Míka) substrátová skla také navrhována a modifikována z hlediska jejich složení. To se ukázalo jako zcela klíčové pro vhodnou přípravu optického vlnovodu o předem přesně zadaných parametrech. U připravených optických skel dokážeme také charakterizovat jejich hodnotu indexu lomu, disperzi a homogenitu a u vlnovodných optických vrstev dokážeme stanovit jejich hloubku, počet šířených vidů a optický útlum na vlnové délce 633 nm. K tomuto účelu využíváme techniku vidové spektroskopie, která slouží i jako měřící pracoviště pro naše spolupráce s jinými ústavy popř. pracovišti. Já jsem se ve svých pracích soustředila především na přípravu vlnovodů výměnou $K^+ \leftrightarrow Na^+$ a $Ag^+ \leftrightarrow Na^+$ a také na využití iontové výměny popř. iontové výměny v elektrickém poli v praxi.

V mnohem menší míře byla v naší laboratoři vyzkoušena také technika přípravy vlnovodů pomocí iontové implantace helia a difúze titanu do $Er:LiNbO_3$. Oproti iontové výměně je technika iontové implantace, kterou v laboratoři využíváme ve spolupráci s ÚJF AVČR, technikou neomezených možností, co se týče kombinace dopantu se substrátovým materiálem. Na technické vybavení v podobě urychlovače iontů je však iontová implantace velmi náročná a málo praktická.

2.3.1 Optické krystaly

$LiNbO_3$ – protonová výměna [P1,P3,P4]

Z optických krystalů jsem se ve své práci zaměřila na přípravu planárních optických vlnovodů v niobičnanu lithném. Byla studována příprava optických vlnovodů procesem protonové výměny s následným žíháním – annealed proton exchange (APE). Jedná se o výměnu vodíkového iontu z roztavené vhodné kyseliny adipové a lithné ionty z monokrystalu podle rovnice:

$$LiNbO_3 + xH^+ \rightarrow Li_{1-x}H_xNbO_3 + xLi^+$$

Bezprostředně po iontové výměně mají vlnovody velkou změnu řádného indexu lomu až o 0,12 ale významně se zmenšuje elektrooptický koeficient krystalu (koeficient r_{33} klesne téměř na nulovou hodnotu). Z tohoto důvodu následuje po protonové výměně žíhání, během kterého dochází k difúzi vodíku do větších hloubek, změna indexu lomu přitom klesá a hodnota elektrooptického koeficientu dosahuje původní hodnoty.

V pracích [P1 a P4] byl studován proces APE z kyseliny adipové a zjišťována souvislost mezi změnami chemického složení a optickými vlastnostmi. Po navázání spolupráce s ÚJF AVČR a také s Josef Stefan Institute v Ljublani ve Slovinsku bylo možné pomocí metody NDP (neutron depth profiling) a tedy reakce izotopu ^6Li s termálními neutrony sledovat detailně pohyb lithia během procesu APE. Jako jedno z mála pracovišť jsme dokázali studovat vztah mezi koncentrací lithia a hodnotou indexu lomu. Bylo zjištěno, že lithium je prakticky z 90 % nahrazeno vodíkem během prvního kroku protonové výměny. Následné žíhání způsobuje posun lithia směrem k povrchu až do výše zhruba 60 % celkového obsahu a posun vodíku směrem do hloubky viz obr. 1, 2, 3 v [P1]. I když závislost indexu lomu na hloubce vlnovodné vrstvy zrcadlově odpovídala závislosti koncentrace lithia na hloubce, nebyl potvrzen lineární vztah mezi hodnotou indexu lomu a koncentrací lithia. Byl nalezen semiempirický vztah pro proces APE z kyseliny adipové, který měl pro určité hodnoty obou konstant K1 a K2 lineární tvar, ale pro jiné hodnoty konstant tvar exponenciální [P1].

Během uvedené studie byla také objevena skutečnost, že rychlost, a tedy i míra výměnné reakce lithium – vodík, závisí na použitém krystalografickém řezu niobičnanu lithného. Ukázalo se, že *X* <11-20> krystalografický řez niobičnanu lithného je jak pro pohyb lithia, tak pro pohyb vodíku (zjišťováno metodou ERDA) propustnější nežli krystalografický řez *Z* <0001>. Jako příčina byla nalezena orientace povrchu substrátu vůči štěpné rovině monokrystalu [P3].

Er:$LiNbO_3$ [P22]

Monokrystalický niobičnan lithný je díky velkému množství intristických poruch způsobených deficitem lithia snadné dopovat různými prvky, které svou přítomností mohou kompensovat nerovnováhu náboje. Erbium je, jako jeden z možných dopantů, ve struktuře objemově dotovaného niobičnanu lithného (0,5 mol %) umístěno v polohách lithia a mírně posunuto podél osy *z* o 0,09 nm [P6, 55]. Jeho přítomnost ve struktuře způsobí změnu v absorpčních a luminiscenčních vlastnostech. Hodnotu indexu lomu uvedená koncentrace erbia prakticky nemění [P16].

V niobičnanu lithném včetně jeho formy dotované lanthanoidy je možné připravovat vlnovody několika různými způsoby. V současnosti je nejvíce využívanou technikou difúze titanu z napařené kovové vrstvy. V práci [P22] jsme v niobičnanu lithném dotovaném erbiem porovnali tři různé techniky přípravy vlnovodů a následně i vlastnosti připravených vrstev. Popsány byly především optické vlastnosti v souvislosti se změnami ve struktuře monokrystalu. K přípravě vlnovodů jsme využili difúzi titanu, protonovou výměnu s následným žíháním a iontovou implantaci helia.

Difúze titanu do niobičnanu lithného probíhá nad jeho rekrystalizační teplotou [56] při 1000 °C. Je pravděpodobné, že během procesu přípravy vlnovodů dochází k rekrystalizaci celé struktury Er:$LiNbO_3$. Tomu odpovídá zjištěný téměř nulový stupeň neuspořádanosti struktury [Tabulka 4 v P22]. Struktura monokrystalu je tedy po přípravě vlnovodů poškozena jen minimálně. Titan pravděpodobně obsazuje oktaedrické vakantní polohy v zákrytu za sebou s osou *z*. Vzhledem k vysokému stupni uspořádanosti struktury předpokládáme nízký útlum optického signálu, což se potvrdilo při měření vidovou spektroskopií (velmi zřetelné jednotlivé vidy). Celková změna indexu lomu při použití této metody je v porovnání s uvedenými technikami nejnižší (+0,006) a bude způsobena spíše přítomností *d*-prvku, který celkově zvýší polarizovatelnost materiálu než změnou strukturních parametrů.

Proces protonové výměny probíhá obdobně jako u čistého niobičnanu lithného a přídavek erbia jeho průběh neovlivňuje. Při procesu APE v Er:$LiNbO_3$ byl naměřen vysoký stupeň neuspořádanosti struktury (až 14 %), což odpovídá značné změně strukturního parametru (pravděpodobné je zvětšení strukturního parametru známé jako „swelling“) způsobené úbytkem lithia a umístěním vodíku do planárních rovin v rámci kyslíkových vrstev [P5,55]. Velká změna strukturního parametru způsobuje také značnou celkovou změnu indexu

lomu (+0,06), změna indexu lomu je nejvyšší ze všech porovnávaných technik. I tady velmi zřetelná intenzita optických vidů naznačuje malou hodnotu optického útlumu.

Iontovou implantací He^+ do monokrystalické struktury vzniká zcela jiný typ vlnovodu, jehož vlastnosti souvisí s podmínkami iontové implantace. Změna indexu lomu je přisuzována nejprve vzniku tzv. bariérového vlnovodu [57], později vzniku dvou vrstev, kdy jedna vzniká průletem implantované částice těsně u povrchu a druhá dopadem implantované částice do určité hloubky podle vstupních parametrů implantace. Vlnovod pak vzniká odrazem paprsku od vrstvy, kde částice dopadla a jeho šířením ve vrstvě poškozené průletem implantované částice [58]. Z našich výsledků je patrné, že zatímco dávka při iontové implantaci $1{,}0 \times 10^{14}$ iontů.cm^{-2} nevytváří vlnovodnou vrstvu, dávka $1{,}0 \times 10^{15}$ iontů.cm^{-2} již vede ke tvorbě vlnovodu. Hodnota indexu lomu se zvýší poměrně značně (+0,02). Z výsledků je patrný značný stupeň poškození struktury monokrystalu (2 – 14 %), což potvrzuje, že průletem implantované částice dochází k poškození struktury. Zároveň se zvětší mřížkový parametr, což má za následek zvýšení hodnoty indexu lomu.

V experimentech se objevily poměrně významné rozdíly, které byly pozorovány v chování jednotlivých krystalografických řezů Er:$LiNbO_3$ při iontové implantaci. Skokový charakter indexu lomu byl potvrzen především v řezu *X*, kde byla pozorován malý stupeň poškození struktury (2 %). Gaussovský typ profilu indexu lomu společně s vysokým stupněm poškození (14 %) byl pozorován v řezu *Z* niobičnanu lithného. To znamená, že poškození struktury je závislé na orientaci svazku k povrchu vzorku. Zdá se, že struktura řezu *Z* je průletem iontu mnohem více poškozována než struktura řezu *X*, což způsobí také vyšší hodnotu celkové změny indexu lomu a Gaussovský tvar profilu indexu lomu. Řez *X* je poškozen mnohem více v místě dopadu částic, tj. v hloubce 4 μm, a průlet částic nezpůsobí velké poškození struktury. Následně je celková změna indexu lomu nižší a vlnovod má jasný skokový charakter profilu indexu lomu. Ovlivnění luminiscence erbia v souvislosti s přípravou vlnovodů bude diskutováno v následující kapitole 2.6.

Elektrooptický koeficient v Er:$LiNbO_3$ [P5]

Jednou z důležitých dynamických vlastností niobičnanu lithného je vysoká hodnota elektrooptického koeficientu r_{33} (30.10^{-12} m.V^{-1}), která je využívána např. pro konstrukci Mach-Zhenderova interferometru na bázi Ti: $LiNbO_3$. Tuto důležitou charakteristiku jsme zjišťovali pro proces protonové výměny a následného žíhání v erbiem dotovaném niobičnanu lithném [P5]. Bylo změřeno, že hodnota elektrooptického koeficientu klesá se zvyšujícím se

obsahem vzácné zeminy v monokrystalu: pro obsah lanthanoidů 500 ppm byla naměřena hodnota $29{,}4.10^{-12}$ $m.V^{-1}$ a pro obsah 1000 ppm byla jen $24{,}1.10^{-12}$ $m.V^{-1}$. První krok protonové výměny, tj. samotná výměna lithia za vodík způsobí pokles hodnoty elektrooptického koeficientu pod mez detekce. Ukázalo se, že následné žíhání je pro elektrooptické vlastnosti vlnovodné vrstvy nezbytné. Čím více vodíku obsahovala struktura monokrystalu, tím horší byla hodnota elektrooptického koeficientu, což bylo dobře patrné pro měření r_{33} v různých hloubkách krátce žíhané vlnovodné vrstvy, tj. pro různé optické vidy (viz [P5,obr.5). Hodnota elektrooptického koeficientu úzce souvisela s obsahem lithia a jeho polohou ve struktuře niobičnanu lithného.

Podmínky následného žíhání (kombinaci času a teploty) bylo tedy nutné vhodně nastavit, protože po překročení dané doby žíhání se elektrooptické vlastnosti začaly opět zhoršovat. V této práci se však navzdory předpokladům jiných autorů podařilo prokázat, že spojením procesu APE a Er:$LiNbO_3$ nejsou výrazně zhoršeny elektrooptické vlastnosti substrátu, který je i po APE možné pro modulaci optického signálu elektrickým polem využívat.

Diamant [P14]

Při výrobě optických ovládacích členů je třeba zajistit jejich malý rozměr. Vlnovod nebo-li dráhu paprsku je nutné ohnout nebo zatočit. Přitom útlum vlnovodu vlivem vyzařování z ohybů mimořádně silně závisí na poloměru zakřivení, čím větší je zakřivení vlnovodu tím větší jsou ztráty. Aby byly ztráty v ohybech přijatelně malé, nesmí klesnout poloměr zakřivení pod určitou mez, která u slabě vedoucích vlnovodů (změna indexu lomu jádra vůči obalu např. +0,006) činí až několik milimetrů. Řešením je zvýšení kontrastu indexu lomu, kdy ztráty poklesnou na zanedbatelnou hodnotu. Aktuálně se tedy vytvářejí vlnovody HIC (hight index contrast waveguides), kterými mohou být např. křemíkové nebo diamantové vrstvy na skleněných podložkách.

Nanokrystalický diamant je také jedním z vhodných materiálů pro HIC vlnovody. Mezi jeho význačné vlastnosti patří především tepelná vodivost, nízká absorpce a rozptyl světla v širokém rozsahu spektra, vysoký Youngův modul pružnosti a vysoká stabilita v extrémních podmínkách. Hodnota indexu lomu monokrystalického diamantu je 2,388 pro vlnovou délku 1311 nm. Hodnota nanokrystalické diamantové vrstvy deponované na křemenném, popř. skelném substrátu má obvykle nižší hodnotu, přesto však vlnovody připravené touto kombinací materiálů mají jeden z nejvyšších kontrastů indexu lomu a mohou být využívány

právě jako HIC vlnovody. Uvedený typ vlnovodu se podařilo připravit také nám, kdy ve spolupráci s FÚ AVČR byly získány technikou MW CVD (microwave enhanced plasma chemical vapor deposition) nanokrystalické diamantové vrstvy, které vedly optický signál [P14]. Má práce spočívala především v návrhu a charakterizaci vlnovodných vlastností připravených tenkých vrstev. Tloušťka připravených NCD vlnovodných vrstev byla 380 nm, obsahovala malá zrna a celkově vrstva vykazovala malé množství grafitické fáze, což ukazovalo na její dobrou kvalitu (viz. [P14] obr. 4). Připravené vrstvy vedly jeden optický vid pro vlnové délky 633, 964 1311 a 1552 nm. Hodnota indexu lomu se na rozdíl od dosud publikovaných prací blížila nejvíce hodnotě indexu lomu monokrystalického diamantu (viz [P14] obr. 7).

YAG [21]

Ve spolupráci se skupinou Ing. Kateřiny Rubešové Ph.D. na našem ústavu a s Karlovou univerzitou v Praze byly epitaxním růstem připravovány optické planární vrstvy yttrium aluminium granátu (YAG) se substitucí galium - hliník. Bylo zjištěno, že uvedené vrstvy je možné dotovat přídavkem erbitého iontu a že navržená substituce hliníku galiem velmi příznivě ovlivňuje intenzitu luminiscence erbitého iontu v oblasti 1530 nm. Na připravených vrstvách byly sledovány i vlnovodné vlastnosti. Jelikož se jednalo o depoziční techniku přípravy vlnovodů, počet vedených vidů velmi dobře odpovídal tloušťce připravených vrstev. Přídavek galia zvyšoval hodnotu indexu lomu, která dosahovala hodnoty 1,846 pro vlnovou délku 633 nm.

2.3.2 Optická skla

Iontová výměna $K^+ \leftrightarrow Na^+$ [P2]

Pro optické sensory, které využívají efekt povrchové plazmonové resonance (SPR-surface plasmon resonace) byly v naší laboratoři připravovány nejprve planární a později kanálkové vlnovody pomocí iontové výměny $K^+ \leftrightarrow Na^+$. Tato výměna byla vybrána pro značnou šířku evanescentní vlny, která byla schopna povrchové rezonance s napařenou vrstvou zlata. Pro vlnovody bylo jako substrát vybráno boritokřemičitanové sklo BK7 a dále byly nalezeny vhodné podmínky pro přípravu jednovidového kanálkového vlnovodu. Celá

připravená struktura sensoru se využívala pro detekci hormonů, tj. různých koncentrací chloriového anadotropinu (hCG).

Iontová výměna $Ag^+ \leftrightarrow Na^+$

V letech 1999-2002 jsme pro firmu Color-Chip, Israel zpracovávali studii iontové výměny $Ag^+ \leftrightarrow Na^+$ v různých typech převážně komerčních optických skel. Vybrána byla křemičitanová skla s různým obsahem iontů alkalických kovů a iontů kovů alkalických zemin, ale také skla obsahující nové síťotvorné prvky jako např. skla borito- a fosforečnano-křemičitanová. Připravovány a charakterizovány byly jak planární optické vlnovody, tak později pro vybrané typy skel také struktury kanálkových vlnovodů. Tyto výsledky nebylo možné publikovat.

Iontová výměna $Na^+ \leftrightarrow Ag^+$ v elektrickém poli

Při přípravě planárních optických členů je při konečné realizaci vždy nutná dobrá bezeztrátová vazba optického členu na optické vlákno. Pokud připravujeme planární optický člen iontovou výměnou ve skleněném substrátu, je jednou z podmínek kvalitního napojení optického vlákna tzv. ponoření planární struktury pod povrch substrátu. Ponoření vlnovodné struktury pod povrch zabrání značným ztrátám optického signálu způsobeným právě přítomností povrchu a provádí se reverzibilní iontovou výměnou $Na^+ \leftrightarrow Ag^+$ v elektrickém poli. K tomuto účelu, ale i pro běžnou výměnu iontů urychlenou elektrickým polem, bylo v naší laboratoři realizováno zařízení, které výměnu v elektrickém poli umožňuje. Sledována byla především souvislost mezi obsahem jednomocného modifikátoru, vodivostí skla a hloubkou ponoření vlnovodné vrstvy. Potvrdili jsme, že s rostoucím obsahem sodíku v použitých křemičitanových sklech rostla jejich měrná vodivost a že zvyšování iontové vodivosti skleněných substrátů má pozitivní vliv na hloubku ponoření planárních optických vlnovodů. Obecně bylo zjištěno, že průběh neovlivňuje pouze vodivost substrátu nebo podmínky experimentu, ale že se jedná o komplexní děj, který je ovlivněn více parametry, jako jsou: síla vloženého elektrického pole, koncentrace iontů Ag^+ v připravené planární optické vrstvě, tj. koncentrační gradient působící proti směru elektrického pole při ponořování a také složení, popř. struktura substrátového skla. Za jeden z nejlepších výsledků považujeme dosažení nadprůměrné hodnoty hloubky ponoření optického vlnovodu, tj. až 200 μm pod povrch vzorku v jednom z navržených a připravených typů borito-křemičitanového skla. O tomto skle bylo zjištěno, že má poměrně vysoký stupeň zesítění (3,4), což způsobí, že

v něm termická iontová výměna $Ag^+ \leftrightarrow Na^+$ probíhá pomaleji než u křemičitanových skel s podobným obsahem Na_2O. Naopak zanořování vlnovodů je v něm kvůli vysoké vodivost skla velmi snadné. S přispěním také našich výsledků bylo ve firmě Vláknová optika SQS Nová Paka realizováno a zprovozněno průmyslové pracoviště pro iontovou výměnu v elektrickém poli.

Vývoj optických součástek na bázi iontové výměny

S výše zmíněnou firmou Vláknová optika SQS Nová Paka spolupracujeme od roku 2009. Ve spolupráci s Ústavem skla a keramiky VŠCHT jsem pro tuto firmu pracovala na vývoji nízko-ztrátové širokopásmové odbočnice 1×2 na bázi iontové výměny $Ag^+ \leftrightarrow Na^+$. Vývoj takové odbočnice je experimentálně náročný, především protože je složen z několika kroků a nedá se popsat jednoznačnými matematickými funkcemi. Jednotlivé kroky jsou i s ukázkami stručně popsaných výsledků znázorněny v Tabulce 4. Při volbě vhodného typu skelného substrátu je třeba se soustředit jednak na proveditelnost iontové výměny za daných teplot v poměrně krátkém čase a také na schopnost pohybu iontů stříbra skelnou matricí v elektrickém poli. Ve vhodném typu skla probíhá iontová výměna i následné ponořování vlnovodné vrstvy snadno. Na obrázku v **Tabulce 4 - řádek 1** je znázorněno, jak rozdílně se mohou chovat různá skla vůči elektrickému poli, kdy se za stejných podmínek podaří vlnovod ponořit až 5krát více pod povrch než u jiného typu skelného substrátu. Při výběru skla hraje také důležitou roli jeho odolnost, homogenita a snadnost opracování. Při přípravě odbočnice se iontová výměna provádí přes kovovou masku nanesenou metodou lift-off na skelný substrát. I zde je nutné postupně sledovat výrobek po každém technologickém kroku, protože především kvalita masky ovlivňuje parametry výstupního signálu. Po přípravě skla a nanesení masky následuje iontová výměna, která se provádí ponořením vzorku do taveniny s vyměňovanými ionty při dané teplotě po určitý čas. Podmínkami iontové výměny lze ovlivňovat zejména koncentraci stříbra v kanálkovém vlnovodu. Na obrázcích v Tabulce 4 je patrná ukázka neponořeného kanálkového vlnovodu na skenovacím elektronovém mikroskopu a ukázka koncentračního profilu stříbra po první iontové výměně stanoveného metodou EMA (elektron microprobe analysis).

Tabulka 4. Popis jednotlivých kroků vývoje optické odbočnice 1×2 připravené iontovou výměnou $Ag^+ \leftrightarrow Na^+$ ve vyvíjeném typu optických skel; vývoj probíhal ve spolupráci s firmou Vláknová optika SQS Nová Paka a Ústavem skla a keramiky VŠCHT; výroba odbočnice je realizována (*obrázky a grafy převzaty z výzkumných zpráv připravovaných v rámci spolupráce s uvedenou firmou*)

1. Skelný substrát ⇓ Vztah mezi hodnotou indexu lomu a koncentrací stříbra	**Homogenita** **Kvalita povrchu**  Naleštěný a vybroušený dvoupalcový substrát	**Vhodné složení skla pro oba kroky iontové výměny** 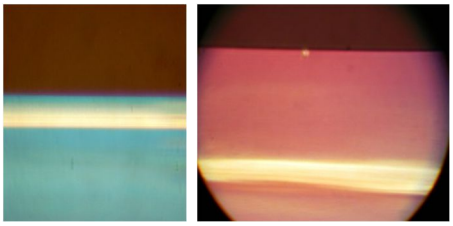 Polarizační mikroskopie (zvětšení 25×): ponoření vlnovodné vrstvy (zářící žlutá vrstva) připravené výměnou **$Ag^+ \leftrightarrow Na^+$**,
2. Litografie ⇓ Vztah mezi šířkou štěrbiny na vzorové masce a skutečnou šířkou štěrbiny	**Vhodný návrh masky** 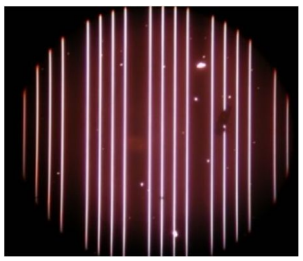 Polarizační mikroskop – kovová maska na skelném substrátu	**Kvalita připravených masek** 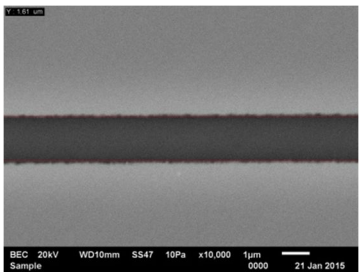 Skenovací elektronový mikroskop – kanálek před iontovou výměnou
3. I. Iontová výměna 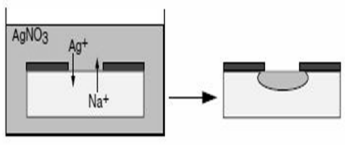 ⇓ Vztah mezi dobou a teplotou iontové výměny a koncentrací stříbra ve vlnovodu	**Podmínky iontové výměny** 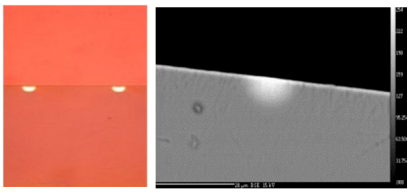 Polarizační a skenovací elektronová mikroskopie – pohled z vybroušené hrany na tvar připraveného vlnovodu	**Charakterizace obsahu stříbra** 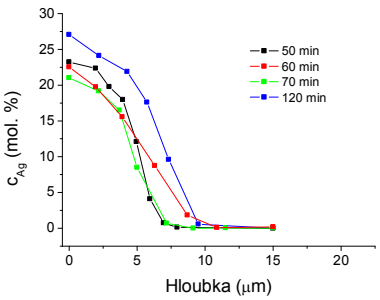 Koncentrační profily Ag^+ iontů stanovené metodou EMA pro různé časy iotové výměny

4. II. Iontová výměna

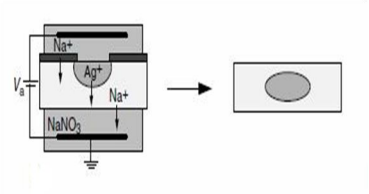

⇓

Vztah mezi dobou a teplotou reverzibilní iontové výměny v elektrickém poli a hloubkou ponoření, tvarem blízkého pole optického signálu a útlumem struktury s vazbou na optické vlákno

Podmínky iontové výměny v elektrickém poli

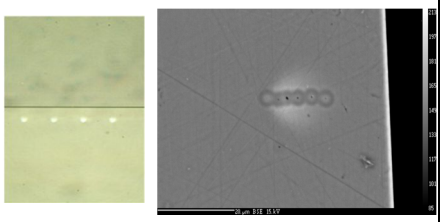

Polarizační a skenovací elektronový mikroskop – pohled z naleštěné hrany na tvar připraveného kanálkového vlnovodu, jednotlivé body na SEM fotografii jsou způsobené proběhlou analýzou

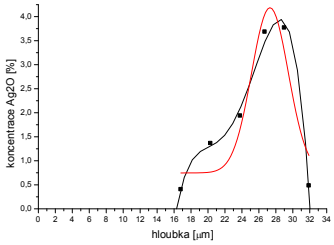

Hloubkový koncentrační profil stříbra (EMA analýza) v kanálkovém vlnovodu

Výstupní parametry kanálkového vlnovodu

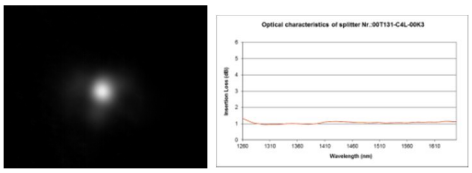

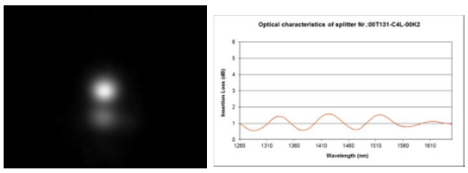

Ukázka blízkého pole optického signálu a měření optického útlumu struktury s vazbou na optické vlákno

5. Odbočnice

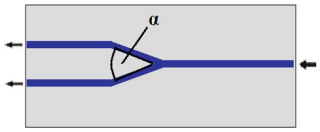

⇓

Konečná realizace struktury a reprodukovatelnost její přípravy

Dělení optického signálu

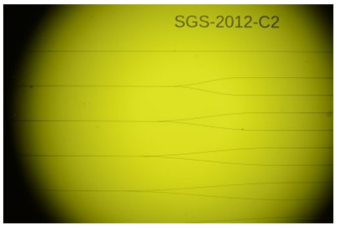

Fotografie struktury odbočnic (polarizační miktroskop) připravených iontovou výměnou ve skleněném substrátu, na vzorku jsou patrné čtyři různé dělící úhly

Charakterizace, opakovatelnost

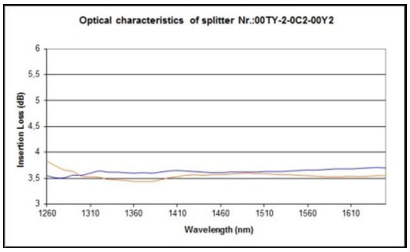

Ukázka spektrální charakteristiky optického útlumu v realizované odbočnice 1×2 s vazbou na vstupní a výstupní vlákno, barva křivek rozlišuje oba výstupy z odbočnice

Druhá iontová výměna probíhá v elektrickém poli a pomocí vstupních parametrů je možné ovlivnit především hloubku ponoření vlnovodu a také tvar blízkého pole optického signálu. Tento tvar by měl pro danou vlnovou délku co nejvíce odpovídat tvaru blízkého pole vstupního optického vlákna (ukázka blízkého pole pro jednovidové a vícevidové blízké pole je v **Tabulce 4**). Pokud tomu tak je, dosahuje součástka nejmenšího možného optického

útlumu. Pokud jsou nalezeny vhodné podmínky pro kanálkový vlnovod a je správně geometricky navrženo dělení svazku v odbočnici, optický dělič je funkční a dosahuje nízkých hodnot optického útlumu (pod 4 $dB.cm^{-1}$).

Při vývoji odbočnic je třeba zvolit pracovní vlnovou délku. I když má připravená odbočnice nízký útlum pro rozsah vlnových délek 1260 až 1610 nm, není zatím funční pro nižší vlnové délky. Na tuto oblast realizace a využití iontové výměny se v budoucnosti hodláme zaměřit.

Kovové nanočástice ve skelné matrici [P7, P10, P13]

V této oblasti výzkumu jsme se společně s Ing. Blankou Švecovou Ph.D. soustředili především na vytváření zlatých kovových nanočástic ve skelné matrici. Kovové nanočástice zlata byly připravovány metodou iontové implantace a následného žíhání. Implantace byla prováděna s různou energií (330 a 1700 keV) a také s různou dávkou implantovaných iontů (1×10^{14}, 1×10^{15}, 1×10^{16} $iontů.cm^{-2}$). Jako substrát byla zvolena křemičitanová skla různého složení. Především byla porovnávána skla s různým obsahem jednomocných modifikátorů a skla s různým stupněm zesítění skelné struktury. Nejprve byly hledány vhodné podmínky iontové implantace a následného žíhání pro vznik nanočástic [P7] ve třech různých typech optických skel. Ukázalo se, že pro vznik nanočástic je potřeba zvolit dávku 1×10^{16} $iontů.cm^{-2}$ nebo vyšší a vzorky následně vyžíhat při teplotě 600 °C. Ukázka připravených kovových nanočástic a jejich distribuce je na obr. 5.

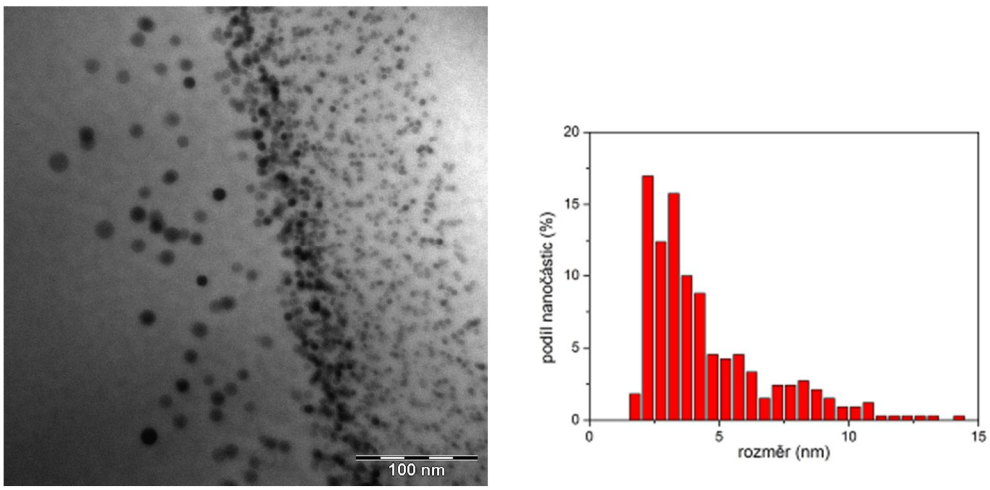

Obrázek 5. Transmisní elektronová mikroskopie kovových nanočástic zlata připravených ve skelném substrátu (sklo GIL49) metodou iontové implantace (*energie 1700 keV, dávka* 1×10^{16} $iontů.cm^{-1}$, *žíhání 5 hod. 600°C*) a diagram distribuce částic (převzato z [5])

Na takto připravených vzorcích byla ve spolupráci s Technickou univerzitou ve Vídni naměřena nelineární optická absorpce metodou Z-scan [P13]. Bylo prokázáno, že koeficient dvoufotonové absorpce je ovlivněn především velikostí nanočástic zlata. S rostoucí velikostí nanočástic rostl měřený koeficient. Nejvyšší hodnota koeficientu dvoufotonové absorpce (TPA koeficient = 16,25 cm/GW) byla pozorována ve skle BK7, kde velikost nanočástic dosahovala 6 až 25 nm.

V průběhu popsaných experimentů se ukázalo, že významným faktorem při tvorbě kovových nanočástic je složení skelného substrátu v souvislosti s teplotou žíhání. Sledování vlivu struktury skla je poměrně ojedinělým přístup, protože většina dosud publikovaných prací používá výhradně komerční skelné substráty. Zaměřili jsme se tedy na vybrané typy skel a zkoumali jeho vliv na tvorbu nanočástic zlata, ale také nanočástic stříbra a mědi [P10]. Zjistili jsme, že tvorbu kovových nanočástic ovlivňuje druh modifikátorů skelné sítě, tj. obsah lithia, sodíku, draslíku, vápníku, hořčíku nebo zinku a to především kvůli různé pohyblivosti iontů během žíhání po iontové implantaci. Bylo zjištěno, že čím více jednomocných modifikátorů skelný substrát obsahuje, tím snadněji se ionty strukturou pohybují a netvoří klastry, popř. nanočástice kovu. Draslík ve skelné struktuře naopak zpomaluje pohyb iontů a skla s vysokým obsahem draslíku se tedy ukázala jako vhodná pro tvorbu nanočástic zlata. Jako síťotvorné prvky byly porovnávány křemík a bor. Z dosud získaných poznatků se zdá, že skla obsahující bor jako síťotvorný prvek usnadňují tvorbu kovových nanočástic. Popsaný výzkum vzhledem ke značné variabilitě složení skla dále pokračuje.

Porovnáme-li schopnost zkoumaných iontů vzácných kovů tvořit nanočástice je patrné, že nejsnadněji se díky nízké afinitě zlata ke kyslíku tvoří nanočástice zlata. Měď a stříbro se dokáží strukturou skla pohybovat rychleji než zlato, což je patrné z naměřených hloubkových koncentračních profilů po iontové implantaci a během následného žíhání. Pro tvorbu nanočástic je tedy důležité navrhnout strukturu skla tak, aby pohybu iontů spíše bránila a podpořila tak vznik kovových nanočástic.

Shrnutí

V oblasti vývoje materilů pro pasivní a dynamické fotonické součástky považuji za nejdůležitější následující zjištěné poznatky a skutečnosti:

a) v laboratoři materiálů pro fotoniku jsme schopni připravovat optické vlnovody s předem zadanými vlastnostmi jak v materiálech krystalických, tak v materiálech amorfních a dokážeme dobře provést základní charakteristiku optického vlnovodu,

b) známe dobře přípravu vlnovodných optických vrstev v niobičnanu lithném, dokážeme v něm vlnovody připravovat různými technikami, známe vztahy mezi vlastnostmi vlnovodu a změnami ve struktuře krystalu,

c) dokázali jsme objasnit různé chování řezů niobičnanu lithného během procesu protonové výměny a následného žíhání,

d) vzhledme k dlouholetému studiu iontové výměny ve sklech a porozumnění vztahům mezi změnami ve skelné struktuře křemičitanových skel dokážeme vhodně navrhnout technologii iontové výměny a složení substrátového skla pro vytvoření optického vlnovodu s požadovanou změnou indexu lomu,

e) dosavadní zkušenosti jsme dokázali aplikovat do výrobního procesu ve firmě Vláknová optika SQS Nová Paka.

2.4 Aktivní ovládání optického signálu [2, 22, 59]

Mezi základní aktivní součástky je možné zařadit vlnové zdroje optického záření jako např. lasery a LED diody (Laser Emited Diods) a optické zesilovače. **Optický zdroj** produkuje optické záření o určité vlnové délce a určité intenzitě.

Optický zesilovač je schopen zesílit intenzitu již vedeného optického záření a slouží k regeneraci signálu, který byl v optickém vláknu v důsledku absorpce a rozptylu světla utlumen. Obecně se zesilovač skládá ze tří základních částí. První z nich je základní materiál, který má vhodné obsazení energetických hladin elektrony. Druhou částí je vnější zdroj, který slouží k iniciaci přeskoků elektronů mezi jednotlivými energetickými hladinami. Poslední částí zesilovače je „optická rezonanční dutina“ obsahující základní materiál a produkující monochromatické koherentní elektromagnetické záření realizovaná např. jako dvě polopropustná zrcadla s danou vzdáleností. Jeho funkce je schematický znázorněna na **obr. 6**.

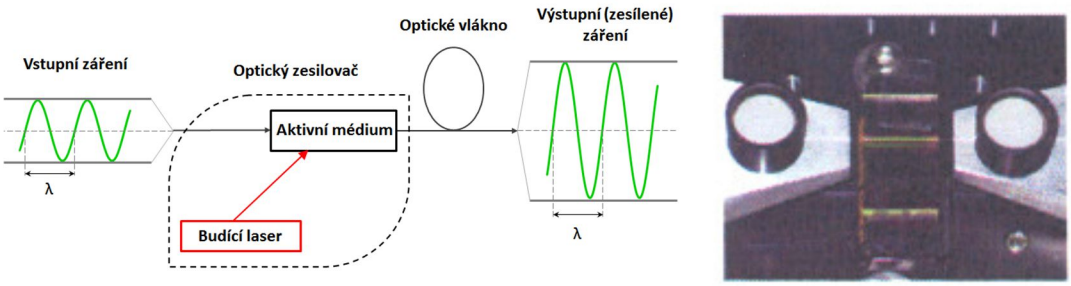

Obrázek 6. Schematické znázornění funkce optického zesilovače a jeho realizace pomocí dvou Braggových mřížek na vstupu a výstupu optického signálu (převzato z [22] a [60])

Reálné koherentní zesilovače vykazují frekvenčně závislý zisk a frekvenčně závislé fázové posunutí s typickými průběhy. Zisk a fázové posunutí určují přenosovou funkci zesilovače. Při dostatečně velkých vstupních amplitudách mohou reálné zesilovače vykazovat saturaci, což je projev nelineárních vlastností, kdy velikost výstupní amplitudy přestává růst lineárně se vstupním signálem. Reálné zesilovače vykazují rovněž šum, takže bez ohledu na vstupní signál se vždy ve výstupním signálu objevuje náhodně fluktuující složka. Zesilovač charakterizují následující vlastnosti: zisk, frekvenční pásmo, fázové posunutí, zdroj čerpání, nelinearita a saturace zisku a šum.

Konstrukce optických zesilovačů nebo optických laserů může být různá. Nejvíce rozšířené jsou vláknové optické zesilovače EDFA (Erbium Doped Fiber Amplifier), u nichž je optický signál zesilován přítomností iontů prvku vzácné zeminy, např. erbia, kterými je dopováno několik metrů dlouhé optické vlákno. Vedený optický signál se šíří jádrem vlnovodu a čerpací záření jedním z jeho plášťů. Čerpací energii erbiovým iontům dodává laserová dioda (polovodičová součástka, v níž dochází k přeměně elektrické energie na laserové záření). Dostatečně dlouhé erbiové vlákno, tj. vlákno s vhodnou koncentrací iontů erbia může, zesílit signál až 10 000×.

Planární optický zesilovač může být realizován např. jako jednorozměrný kanálkový vlnovod obsahující aktivní ionty. Zpravidla je součástí integrované součástky plnící ještě další optické funkce a obě nebo více funkcí je tak lokalizováno v jednom čipu. Příkladem reálně fungující struktury je např. Er:Ti:$LiNbO_3$ vlnovodný laser se synchronizací vidů, který v sobě spojuje kanálkovou strukturu elektrooptického modulátoru s aktivní funkcí erbia dotovaného v povrchové vrstvě. Kontinuálně čerpaný laser generuje krátké pikosekundové impulsy o opakovací frekvenci v oblasti jednotek až desítek GHz, které lze použít jako hodinové impulsy v optickém komunikačním systému. Kvůli poměrně nízké koncentraci iontů erbia na krátké dráze optického signálu nejsou planární zesilovače schopné signál zesilovat tak jako vláknové zesilovače. Aktuálně jsou intenzivně zkoumány možnosti, jak zmiňovanou koncentraci aktivního iontu zvýšit.

Jinou možností konstrukce optického zesilovače nebo laseru je pak tzv. diskový laser. Aktivní prostředí zde tvoří malý disk, který zároveň funguje jako zrcadlo. Výhodou je rovný teplotní profil po celém disku, který umožňuje dosáhnout vysokých výkonů (až 16 kW) s dobrou kvalitou výstupního svazku. Diskové lasery se používají především pro výkonově náročné operace, jako je svařování a řezání kovů.

2.5 Anorganické materiály pro aktivní optické členy [6, 61]

Základním fyzikálním jevem, který se při konstrukci aktivních optických členů využívá, je luminiscence. **Luminiscence** je emise světla založená na energetických přechodech elektronů v atomech. Pokud se v dané látce excitují elektrony z nižší energetické hladiny na vyšší hladinu, tak po určité době dochází k samovolné relaxaci elektronů na nižší energetickou hladinu, což je provázeno uvolněním energie ve formě kvant elektromagnetického záření – fotonů. Emise optického záření se dělí na spontánní a stimulovanou. U spontánní emise světla látkou dochází k náhodné relaxaci elektronů mezi energetickými hladinami. Podstata **stimulované emise** záření spočívá v přechodu elektronů mezi energetickými hladinami, kde je elektronový přechod stimulován vnějším zářením. Jde tedy o kvantový jev, kdy je relaxace elektronů z vyšší excitované hladiny na nižší energetickou hladinu stimulována vnějším podnětem fotonů o vhodné energii rovnající se rozdílu vyšší excitované hladiny a nižší hladiny. Dochází tak k emisi koherentního elektromagnetického záření ve formě fotonů, které vykazují stejné vlastnosti (frekvenci, fázi, polarizaci a směr) jako má dopadající foton.

Základ pevnolátkového aktivního optického členu je tvořen materiálem, který je propustný v dané oblasti spektra, vede optické záření bez výrazných zdrát, a iontem, který má dostatečné množství vhodných energetických přechodů. Ionty s dostatečným počtem energetických hladin jsou prvky s atomovým číslem 21-30, elektronové konfigurace [Ar] $3d^n$ $4s^2$ tzv. *d*-prvky nebo prvky s atomovým číslem 56-70, elektronové konfigurace [Xe] $4f^n$ $6s^2$, tzv. *f*-prvky. Pokud se daný ion dostane do struktury krystalické nebo amorfní látky, dochází k jeho ovlivnění statickými elektrickými poli okolních atomů a iontů. Tato statická elektrická pole se souhrnně označují jako krystalové pole. Ion, který není ovlivněn krystalovým polem, má své diskrétní energetické hladiny odpovídající povoleným kvantovým stavům takového izolovaného iontu – tyto energetické hladiny mají čarový charakter emise. Vlivem krystalového pole jsou ale elektronové obaly iontů deformovány a dochází k jemnému štěpení základních kvantových hladin do multipletů, což je skupina blízkých energetických linií, které mají podobné energie. Rozšíření pásů u lanthanoidů je možné interpretovat jako výsledek rozštěpení na multipletní stavy v důsledku krystalového pole. U *d*-prvků jsou široké emisní pásy výsledkem vibrací 1. hybridizace s kyslíkovými atomovými orbitaly 2p. Charakter emise u *d*-prvků už není přesně čarový, ale zachovává si pásy energií okolo základních kvantových stavů. Naopak u *f*-prvků je vliv krystalového pole stíněn elektrony 5*s* a 5*p,* proto mají *f*-prvky úzké emisní pásy, které není možné krystalovým okolím

snadno ovlivnit. Přehled běžně využívaných aktivních iontů v pevnolátkových laserech je uveden v následující **Tabulce 5**.

Tabulka 5. Přehled běžně využívaných pevnolátkových laserů (převzato z [6])

Laser (označení)	Aktivní iont	Hostitelské prostředí	Vlnová délka [nm]
Ti: safír	Ti^{3+}	Al_2O_3	700 - 1100
Rubidiový laser	Cr^{3+}	Al_2O_3	694
Alexandrit	Cr^{3+}	$BeAl_2O_4$	700 - 820
Cr:LiSAF	Cr^{3+}	$LiSrAlF_6$	780 - 1010
Cr:LiCAF	Cr^{3+}	$LiCaAlF_6$	720 - 840
Cr:forsterit	Cr^{4+}	Mg_2SiO_4	1150 - 1350
Co:MgF_2	Co^{2+}	MgF_2	1500 - 2500 při 77 K
Nd:YAG	Nd^{3+}	$Y_3Al_5O_{12}$	1064
Nd:glass	Nd^{3+}	Fosfátové sklo	1054
Nd:YLF	Nd^{3+}	$LiYF_4$	1047 a 1053
Nd:vanadate	Nd^{3+}	YVO_4	1064
Yb:YAG	Yb^{3+}	$Y_3Al_5O_{12}$	1030 při 100 K
Erbium fibre	Er^{3+}	Optické vlákno-SiO_2	1530 - 1560

V současnosti je výzkum soustředěn především na vláknové, popř. diskové lasery. Z materiálů se jako hostitelská prostředí zkoumají především různé typy skelných substrátů popř. substráty s vysokou hodnotou indexu lomu jako diamant a křemík. Oblast vlnových délek se posunuje k vyšším vlnovým délkám především do oblasti středních vlnových délek (MIR). Jako aktivní ionty jsou v tomto případě využívány ionty Dy^{3+} (silné pásy v oblasti 2,2 μm a 2,9 μm a dva slabší v oblasti 2,4 μm a 4,3 μm, dále pak ionty Tm^{3+} (2 μm), a Ho^{3+} (2,1 μm). Široce-spektrální pevnolátkové lasery pracující v oblasti MIR jsou nezastupitelné, např. při dálkovém snímání parametrů z čidel, spektroskopií s vysokým rozlišením, měření kmitočtů i rozmanitých biologicko-lékařských aplikacích, stejně jako při měření akustooptických jevů pomocí Dopplerových LIDARů [62-65].

Erbium

Iont erbia je v oblasti fotoniky jedním z nejznámějších iontů vzácných zemin využívaných pro svou emisi při vlnové délce okolo 1550 nm tedy v tzv. třetím telekomunikačním okně. Je to oblast velmi nízké absorpce křemičitanových skel jako materiálu pro výrobu křemičitanových optických vláken. **Erbium** patří do skupiny lanthanoidů. U lanthanoidů převládá oxidační stav (III) s částečně zaplněnými orbitaly *4f*. Trivalentní ion erbia obsahuje ve svých valenčních orbitalech 11 elektronů. Právě elektrony v orbitalech *4f* způsobují luminiscenční aktivitu erbitého iontu. Využívají při tom důležité

energetické hladiny $^4I_{11/2}$, $^4I_{13/2}$ a $^4I_{15/2}$, kde probíhá tzv. tříhladinový energetický přechod s emisí na vlnových délkách okolo 1530 až 1535 nm (viz **obr. 7**). Princip tříhladinového energetického přechodu iontu Er^{3+} je zakreslen v energetickém schématu (**obr. 7**) odpovídajícím iontu Er^{3+} ve struktuře $LiNbO_3$. Během tříhladinového energetického procesu dochází k zářivému (vyznačeno červeně) i nezářivému přechodu (vyznačeno modře). K zářivému přechodu ($^4I_{13/2} \rightarrow {}^4I_{15/2}$) dochází buď na principu spontánní emise záření, která nastává samovolně po určité době (tzv. doba života – lifetime) nebo na principu stimulované emise záření. Stimulovaná emise nastává, pokud do opticky aktivní soustavy přijde během doby, kdy jsou elektrony excitovány, jiný stimulující foton o energii rovnající se energetickému rozdílu hladin $^4I_{13/2} \rightarrow {}^4I_{15/2}$, což je v tomto případě ~1530 nm. Pro dobrou účinnost optického zesilovače je kritickou hodnotou populace hladiny $^4I_{13/2}$. Pokud na této hladině dochází k jiným procesům, než je stimulovaná emise, vede to vždy ke ztrátám. Ztrátových procesů může být několik a mohou také úzce souviset s krystalovým polem erbitého iontu. Obecně se může jednat o proces párového zhášení (koncentrační zhášení), nezářivé relaxace (multi-fononová emise), absorpce z excitovaného stavu (up-konverze).

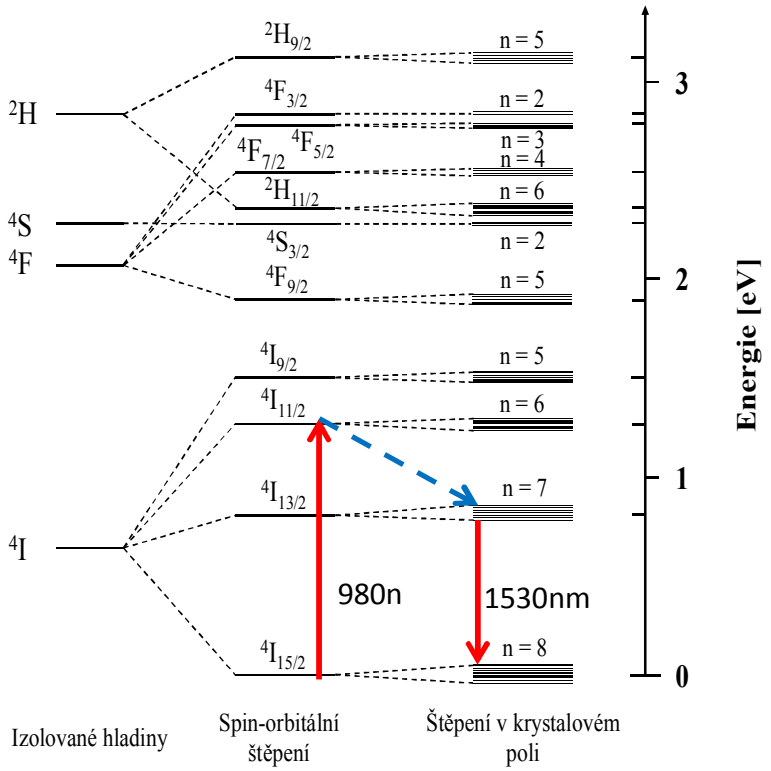

Obrázek 7. Znázornění tříhladinového přeskoku erbitého iontu v jeho energetickém spektru (převzato z [22])

Ačkoliv v případě konstrukce aktivní součástky pracující při vlnové délce 1530 nm jsou vlivy koncentračního zhášení ztrátové, pro jiné využití mohou být naopak požadované. Příkladem může být sensitivní fluorescence využívaná pro efektivní buzení erbium ytterbiových materiálů nebo proces up-konverze, který se využívá pro generaci záření na kratších vlnových délkách.

Příklad typického absorpčního a luminiscenčního spektra erbiového iontu je na **obr. 8**. I z něho je patrné, že efektivita čerpání erbitých iontů (tj. absorpce budícího záření) na vlnové délce 980 nm není příliš vysoká. Z toho důvodu se často používá dopování materiálu směsí iontů a erbium je nejčastěji kombinováno s iontem ytterbitým [66-68]. Ytterbité ionty mají velkou účinnost čerpání při 980 nm, tj. výrazně rozšíří i čerpací pás pro ionty erbia. Po absorpci záření dochází u iontu Yb^{3+} k přeskoku elektronu na hladinu $^2F_{5/2}$. Na této hladině dojde nezářivou cestou k přesunu energie na hladinu $^4I_{11/2}$ atomu Er^{3+} a zde pak dojde k již výše popsané relaxaci na základní hladinu $^4I_{15/2}$.

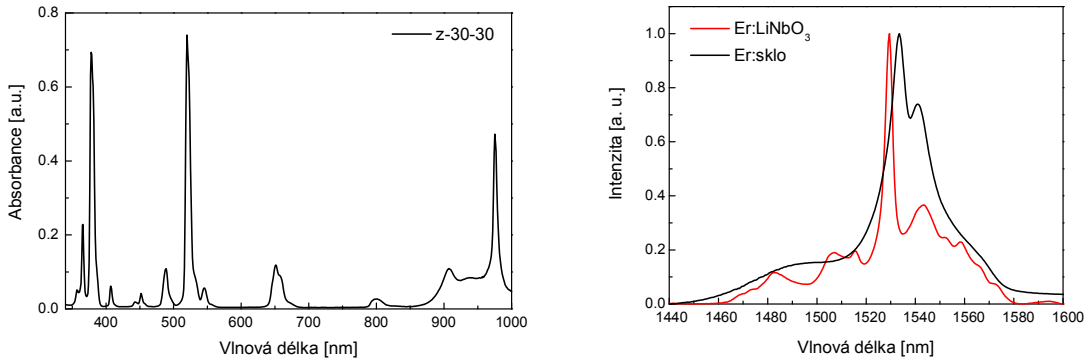

Obrázek 8. Absorpční a luminiscenční spektra pro erbitý iont: (a) absorpční spektrum erbia ve skelné matrici – připravené sklo MM s poměrem erbia:ytterbiu 3:3, (b) porovnání luminiscenčního spektra erbia v připraveném skle MM 0,25 s poměrem erbia:ytterbiu 1:20 a v niobičnanu lithném obsahujícím 0,5 at.% erbia, tj. v amorfní a krystalické struktuře.

Další významnou kombinací iontů, která je nyní intenzivně zkoumána, je kombinace bismutu s různými ionty vzácných zemin [69-71]. Ukazuje se, že využití této kombinace je vhodné pro přípravu optických zesilovačů nebo laserů pracujících v oblasti 1190 až 1550 nm. Je to významná oblast druhého telekomunikačního okna a dosud byla pro tuto oblast využívána pouze fluoritová vlákna dopovaná neodymem a praseodymem (oblast 1300 nm), která však měla velmi silnou absorpci procházejícího záření.

Erbiem byla dopována řada různých optických materiálů. Velmi stručný přehled některých z nich uvádí **Tabulka 6**, ve které jsou uvedeny charakteristické parametry jak pro materiály amorfní tak krystalické. Uvedena je vždy vlnová délka pro emisi z $I_{13/2}$ na $I_{15/2}$. Dále tabulka uvádí některé hodnoty Judd-Ofeltových parametrů Ω_n, na základě kterých je možné určit pravděpodobnosti vnitřních zářivých přechodů pro danou iontovou konfiguraci i jejich doby dosvitu.

Tabulka 6. Materiály vhodné pro dotaci erbitým iontem a jejich Judd-Ofeltovy parametry

Materiál	Vlnová délka [nm]	Ω [10^{-20}cm^2]			Doba dosvitu [ms]	Citace
		Ω_2	Ω_4	Ω_6		
$LiNbO_3$	1535	7,29	2,24	1,27	~200	[72]
$KGd(WO_4)_2$	1548	8,9	0.86	0,92	---	[73]
$LiGdF_4$	1530	0.905	2.47	4.92	4.5	[74]
YAG	--	0.45	0.98	0.62	---	[75]
ZBLAN	--	2,51	1.41	0,97	7200	[76]
Skla fosforečnanová	--	5,42	1,55	0,98	3	[76]
Skla křemičitanová	1535	4,26	0,81	0,46	10	[76]

V posledních deseti letech se výzkum soustředí především na vliv krystalového pole na procesy, které mohou ovlivňovat účinnost laserů a optických zesilovačů. Zkoumána je tedy především přesná poloha erbitého iontu v matrici a souvislost změny jeho polohy nebo změny jeho krystalového pole na jemnou pásovou strukturu energetických hladin. Zajímavé aplikace přináší dopování erbitého iontu do struktury polovodičů, jako je např. křemík [77].

Erbium ve struktuře niobičnanu lithného

Niobičnan lithný má trigononální krystalovou strukturu (*R3c*) s mřížkovými parametry a = 5,15 Å a c = 13,86 Å, jeho hustota je 4,64 g.cm^{-3}. Obecně jsou v niobičnanu lithném možné čtyři polohy pro umístění erbia v jeho struktuře. Jsou to substituční pozice Li^+ a Nb^{5+}, tetraedická vakance a oktaedrická vakance [78]. Protože poloha Li^+ je větší - obklopuje ji 6 atomů kyslíku ve vzdálenosti 2,15 Å (na rozdíl od 2,00 Å u polohy niobu) je substituční poloha lithia pro erbium více stabilní pozicí než substituční poloha niobu. To znamená, že poloha Li by se dala nazvat termodynamickou polohou, kdežto poloha Nb kinetickou polohou z důvodu nízkého difúzního koeficientu erbia [79]. Nejvhodnější analytické metody pro zjišťování přesné polohy erbia v krystalu jsou metoda jemných RBS/kanálovacích skenů a

RTG difrakce s vysokým rozlišením (HR-XRD) v uspořádání pro měření za velmi nízkých úhlů.

Technologií jak dopovat niobičnanu lithný erbiem je několik. Při objemové dopaci je erbium přidáváno přímo do taveniny při růstu krystalu, naopak během lokalizované dotace je obohacena pouze tenká povrchová vrstva. Mezi lokalizované dopace je možné zařadit dopaci z napařené kovové nebo oxidové vrstvy, dopaci z tavenin a iontovou implantaci. Tyto metody jsou podrobněji popsány v následující kapitole 2.7. V objemově dotovaných vzorcích niobičnanu lithného s koncentrací erbia do 1 mol % erbia bylo zjištěno, že erbium (iontový poloměr 88 pm) obsazuje substituční polohy lithného iontu, přičemž je posunuto o (-0,020) až (-0,046) nm podél osy *z* [80,81] Podobně jsou ve struktuře niobičnanu lithného umístěny také jiné lathanoidy a ukázalo se, že posun jednotlivých iontů z pozice Li^+ směrem dolů po ose *z* se zvětšuje se zvyšujícím se poloměrem iontu [82].

Pokud je erbium do struktury niobičnanu lithného dopováno lokalizovaně mohou být použity různé techniky dopace a podle nich dochází k různému strukturnímu uspořádání, ve kterém si erbium hledá svou stabilní pozici. Pokud byla použita metoda dopace z napařené vrstvy erbia nebo oxidu erbitého, pak kombinace metody XSW (X-ray Standing Wave) a optické spektroskopie ukázala, že erbium se nachází v pozici Li^+, ale je posunuto po ose *z* o 0,046 nm [83]. Tento výsledek je shodný s výsledky [82] u objemově dopovaného Er:$LiNbO_3$, což ukazuje na podobnou strukturu okolí erbia u obou technologií dotace. Pokud je použita technika iontové implantace nejsou změny ve struktuře niobičnanu lithného způsobené implantací erbia, popř. následným žíháním zcela objasněny [79, 84]. Z dosud publikovaných výsledků se zdá, že po provedení implantace je dopovaná vrstva amorfizovaná a nelze určit přesnou polohu erbia. Vzhledem k tomu, že při iontové implantaci je struktura krystalu velmi poškozená a implantované vzorky vykazují nízkou luminiscenci okolo 1,5 μm, bylo třeba implantované vzorky vyžíhat. Z předchozích studií [79] plyne, že po vyžíhání při teplotě 500 °C se Er nachází nejpravděpodobněji v poloze Nb, kdežto po vyžíhání při teplotě 1100 °C (kdy by mělo dojít k plné rekrystalizaci a obnově dopovaného krystalu) se Er nachází jak v poloze Li tak poloze Nb. Z výsledků je patrné, že poloha erbia s největší pravděpodobností závisí na zvolené dávce implantovaných iontů a na parametrech následného žíhání. K výše uvedeným zjištění přispěly i naše výsledky (viz kap. 2.6.).

Erbium ve struktuře hexagonálních krystalů

Jako jiné krystaly s hexagonální strukturou významné pro fotonické aplikace byly dopovány erbiem především ZnO a safír (Al_2O_3). Oxid hlinitý má trigonální strukturu (R3c), tj. struktura se velmi podobá struktuře niobičnanu lithného s tím rozdílem, že hliník obsazuje polohy obou kationtů v $LiNbO_3$. Celkově menší iont hliníku však způsobí zkrácení vazeb (a = 4,785 Å, c = 12,991 Å), hustota oxidu hlinitého je 3,97 $g.cm^{-3}$. Ve fotonice se používají safírová vlákna dotovaná erbiem jako vláknové zesilovače nebo lasery. Jako technika pro obohacení oxidu hlinitého erbiem byla využita pouze technika iontové implantace, protože ostatní techniky kvůli vyšší hustotě a kompaktnosti struktury nebylo možné využít. V Al_2O_3 záleží ve srovnání s niobičnanem lithným mnohem více na použité dávce iontové implantace erbia. Erbium implantované do tohoto krystalu při nižších dávkách 1×10^{13} $iontů.cm^{-2}$ obsazuje ze 70 % substituční polohy Al (oktaedrické dutiny) a připravené vrstvy vykazují silný emisní pás při 1550 nm. Při vyšších dávkách dochází k mnohem většímu poškození struktury a dosud bylo publikováno, že atomy erbia leží v intersticiálních polohách. I pro tento krystal je popsán příznivý vliv žíhání po implantaci, vhodná teplota žíhání z hlediska luminiscence je 1200 °C [85-88].

Oxid zinečnatý je dalším optickým materiálem s hexagonální krystalovou strukturou (*Pm6*). Délka vazeb v ZnO je a = 3,252 Å, c = 5,313 Å a hustota je z uvedených krystalů nejvyšší, tj. 5,7 g. cm^{-3}. Díky širokému zakázanému pásu je ZnO přirozeným polovodičem typu n s pevnou excitonovou vazbou (až 60 meV). Nedávno publikovaná možnost připravit z ZnO polovodiče typu p však otevřela nové možnosti pro použití tohoto materiálu ve fotonice jako optického zdroje LED pro UV a VIS oblast spektra [89, 90]. Široký zakázaný pás navíc umožňuje dopování ionty vzácných zemin, díky kterému se rozšíří použitelná oblast spektra až do IR oblasti. Při tom se v tomto materiálu očekává nízké termální zhášení emise [91]. Také ZnO byl dopován erbiem pomocí iontové implantace. Při dopování erbia do tohoto krystalu byly použity většinou nižší implantační dávky okolo 1×10^{14} $iontů.cm^{-2}$. Erbium obsazovalo substituční polohy Zn, což vedlo k měřitelné emisi okolo 1,5 μm [92 - 95].

Erbium ve struktuře skla [5, 96].

Ve srovnání s krystalickými materiály mají skla obsahující ionty erbia široký luminiscenční pás a nižší účinný průřez pásu stimulované emise [97]. Tato vlastnost je výsledkem vlivu amorfní struktury skla v okolí erbitého iontu na jeho energetické hladiny.

Rozšíření emisního pásu a slabší emise se využívají pro realizaci širokopásmových vláknových zesilovačů s nízkým šumem.

V současnosti jsou stále hlavním zdrojem světla polovodičové lasery, které mají oproti sklům dotovaných ionty erbia dvě hlavní výhody: a) polovodičové lasery vykazují zisk v řádech ≈ 100 cm^{-1} [98] a b) polovodičové zdroje světla jsou čerpány elektricky, zatímco skla jsou obvykle čerpána opticky (tj. pomocí optického záření). Výhodou skel dotovaných erbitými ionty je dlouhá doba života na metastabilní energetické hladině (≈ ms), která je několikanásobně větší než u typického polovodičového zesilovače (≈ ns). Takový dlouhý čas znamená, že optický zisk je u skel dotovaných erbitými ionty stabilní a nemění se při kolísání vstupního záření (buzení nebo signálu). Navíc u laserů připravených ve sklech je možné dosáhnout vyšší intenzitu pulzu než u polovodičových laserů [99]. Skla je možné navíc integrovat do optických obvodů.

Pro dotaci erbia se využívají dva základní způsoby: objemová dopace, kdy je erbium přidáváno přímo do vsázky skla jako oxid erbitý, a lokalizovaná dotace do tenké povrchové vrstvy. Pro lokalizovanou dotaci Er do skel je možné použít iontovou výměnu z tavenin obsahujících Er^{3+} ionty, iontovou implantaci nebo depoziční techniky, při kterých se nanese tenká vrstva bohatá na Er^{3+} ionty na povrch skla.

Největším problémem při přípravě optických erbitých skel je v současnosti koncentrační zhášení., které nastává při vyšších koncentracích erbia a dochází při něm k shlukování atomů erbia a párovým interakcím mezi ionty erbia. U integrovaných vlnovodných zesilovačů musí být totiž koncentrace erbitých iontů ve skle o řád vyšší než v optických vláknech, ale například v křemenném skle se klastrování projeví již při malých koncentracích (≈ 0,1 at. %) [96, 100]. Zvýšit koncentraci iontů Er^{3+} a zároveň snížit pravděpodobnost klastrování v křemenném skle pomáhá přídavek Al^{3+} iontů (ve sklech chalkogenidových mají podobný účinek ionty Ga^{3+}). Tyto ionty modifikují skelnou síť a vytváří místo pro začlenění izolovaných Er^{3+} iontů vzácných zemin. Ze stejných důvodů jsou oblíbená mnohasložková hlinito-křemičitanová a foforečnanová skla. Pro zlepšení efektivity čerpání se i ve sklených substrátech často používá výše zmíněná kodopace iontů erbitých ionty ytterbia nebo bismutu. Jiným způsobem, jak zvýšit absorpci Er^{3+} iontů, je změna krystalového pole přítomností nanočástic Si nebo Ag ve skelné struktuře. Tyto nanočástice zabudované do oxidických skel zvyšují účinný průřez stimulované emise o jeden až dva řády. V případě nanočástic Ag byl v poslední době prokázán příznivý vliv na intenzitu luminiscence erbia při vlnové délce 1530 nm, ale není jasný mechanismus, kterým je toto zesílení luminiscence způsobeno. Jedná se buď o transfer mezi energetickými hladinami

stříbra a erbia nebo využití povrchové plasmonové resonance kovových nanočástic (viz [101] a odkazy v něm uvedené).

Pokud se zaměříme na výběr nejvhodnějšího složení skelné matrice pro erbiem dotovaný optický zesilovač, jsou dnes používána různá skla. Výběr typu skla přitom ovlivňuje jak efektivitu buzení, tak šířku emisního pásu, dobu života excitovaného stavu, účinný průřez pásu stimulované emise. Porovnání uvedených charakteristik pro nejběžnější typy používaných skelných substrátů je uvedeno v **Tabulce 7**.

Tabulka 7. Optické a spektroskopické vlastnosti vybraných skel, index lomu n, koncentrace iontů erbia, při které dochází ke koncentračnímu zhášení c_Q, doba života excitovaného stavu τ, účinný průřez pásu stimulované emise σ_p (převzato z [5]).

	n [-]	σ_p [10^{-21} cm^2]	τ [ms]	c_Q [10^{20} cm^{-3}]	Šířka pásu [nm]
křemenné sklo	1,46	7	12	-	11
hlinito-křemičitanové sklo	1,50	5,7	10	3,9-6,0	43
fosforečnanové sklo	1,56	8	10	3,9-8,6	27
fluoridové sklo	1,53	5	9	3,8-5,3	63
amorfní Al_2O_3	1,64	6	7,8	-	55
telluridové sklo	2,10	13	3,3	-	80
VŠCHT sklo	1,51	-	9,8	6,6	20

Kvůli silné fononové absorpci, a tedy malému účinnému průřezu stimulované emise bylo v minulých letech prakticky zavrhnuto využívání křemičitanových skel jako vhodné matrice pro ionty vzácných zemin, a tedy i pro erbium. Ukázalo se, že např. sklo fosforečnanové má větší účinný průřez a je pro erbiový optický zesilovač vhodnější. Přesto se dá říci, že v současnosti je nanejvýš žádoucí kombinace složení právě oxidu křemičitého s ostatními oxidy. Důvodem je především skutečnost, že vazba na běžná křemičitanová skla je oproti vazbě na skla jiných struktur mnohem méně ztrátová a i v kombinaci se substrátovým materiálem, který má horší schopnosti zesílení signálu je pro hromadnou výrobu vhodnější.

O částečnou rehabilitaci křemičitanových skel se ve spolupráci s Ústavem skla a keramiky na VŠCHT zasloužila také naše laboratoř. Na základě originálních úvah o významu chemické bazicity optických skel bylo po řadě experimentů připraveno zinečnato-křemičitanové sklo obsahující erbium, které vykazovalo podobné parametry, jako mají běžná fosforečnanová skla [102, 103]. Přítomnost dané koncentrace zinku zvyšuje bazicitu skla, mění tedy krystalové pole v blízkosti erbitého iontu, způsobuje také pravděpodobně homogenní distribuci erbia ve skle a tím zabraňuje párovým interakcím a koncentračnímu

zhášení luminiscence. V tomto novém typu skla byla hledána optimální koncentrace iontů erbia popř. kombinace erbia a ytterbia v závislosti na konečné aplikaci [104—107]. Mimoto byly určeny Judd-Ofeltovy parametry, které určují pravděpodobnost vnitřních zářivých přeskoků [108]. V uvedeném typu skla byly později připraveny také kanálkové vlnovody, které dokázaly zesílit optický signál o 11 $dB.cm^{-1}$ [109, 110]. Ve výzkumu těchto skel se vzhledem ke komerčnímu zájmu o dané součástky stále pokračuje.

2.6 Vlastní výsledky výzkumu anorganických optických materiálů pro aktivní optické součástky

Výzkum aktivních materiálů v naší laboratoři úzce navazuje na vývoj pasivních optických členů, které byly popsány v předchozí kapitole a materiálů s ním spojených. Jelikož jsme byli schopni připravit optické vlnovody v niobičnanu lithném a ve sklech, snažili jsme se tyto materiály modifikovat tak, aby vykazovaly navíc i zesilovací efekt optického záření. Moje pozornost se soustředila především na obohacení těchto materiálů iontem erbia. Dopovány erbiem byly především niobičnan lithný, ZnO a safír, tj. optické krystaly podobné svou strukturou niobičnanu lithnému. Souvislosti byly hledány především mezi polohou erbitého iontu ve struktuře krystalu a luminiscenčními vlastnostmi v oblasti okolo 1530 nm.

Pozice erbia v krystalové struktuře v objemově dotovaném $LiNbO_3$ [P6]

Pro naše účely podle námi navrhnutého složení byly v dnešní firmě Crytur Turnov připraveny kvalitní monokrystalické podložky niobičnanu lithného dotovaného iontem erbitým popř. směsí iontů erbitých a ytterbitých v koncentracích 0,5 a 1 mol %. Monokrystaly byly rozřezány tak, aby jejich povrchy měly různou krystalografickou orientaci. Získali jsme tak podložky s různě krystalograficky orientovaným povrchem, tj. krystalografické řezy $X\{11\bar{2}0\}$ a $Z\{0001\}$. V těchto krystalech byla s využitím metody RBS/kanálování stanovena pozice erbia, která dobře odpovídala dosud zjištěným výsledkům. Zjistili jsme, že atom erbia ve struktuře niobičnanu lithného obsazuje polohu lithia. Naměřený posun 0,03 nm podle osy *z* (tj. blíže k jedné z rovin kyslíku) souvisí pravděpodobně s větším poloměrem atomu erbia a odpovídal naměřeným hodnotám jiných autorů.

Vliv procesu přípravy optických vlnovodů na pozici erbia v objemově dotovaném $LiNbO_3$ [P22]

Jak bylo popsáno v předcházející kapitole vlnovody v Er: $LiNbO_3$ byly připravovány metodou difuze titanu, metodou protonové výměny a implantací helia. Pro všechny uvedené techniky byl sledován metodou RBS/kanálování stupeň poškození struktury niobičnanu lithného, změna pozice erbitého iontu ve struktuře a její vliv na luminiscenční vlastnosti. Tato studie je ojedinělá, protože není možné srovnávat intenzitu luminiscence mezi jednotlivými pracovišti. U všech použitých technik bylo prokázáno, že ani jedna z nich neovlivňuje pozici energetických pásů v luminiscenčním spektru. Metodou RBS/kanálování s technikou jemných skenů bylo potvrzeno, že erbium není významně vychýleno ze svých poloh. Při přesném měření vlivu procesu APE na pozici erbia metodou XRD byla zjištěna odchylka z původní polohy lithia o 0,09 nm, což oproti původní poloze erbia v substrátu činí odchylku o 0,06 nm [P6]. Porovnáme-li vliv jednotlivých technik přípravy vlnovodů, pak lze říci, že se liší především ve stupni poškození krystalové struktury niobičnanu lithného a také jen velmi málo v intenzitě luminiscenčního pásu při 1535 nm. Nejvíce je intenzita luminiscenčního pásu ovlivněna difúzí titanu i přes to, že strukturní poškození je nejnižší je intenzita luminiscence při 1530 nm nejnižší. Tento jev je možné vysvětlit pomocí transferu fotonů mezi hladinami přítomného *d- a f*-prvku a tedy největší mírou ovlivnění krystalového pole erbitých iontů přítomností titanu. Pro obě další techniky bylo zjištěno větší poškození krystalové struktury ale jen velmi malý pokles intenzity luminiscence.

Poloha erbia v různých monokrystalech po provedení lokalizované dopace [P19]

Kromě niobičnanu lithného jsme erbiem dopovali i jiné optické krystaly, které jsou využívány ve fotonice, jejichž struktura byla co nejvíce podobná struktuře niobičnanu lithného. Provedli jsme iontovou implantaci do monokrystalického Al_2O_3, ZnO a $LiNbO_3$. U všech krystalů byla použita jedna krystalografická orientace tj. řez *Z*. Implantace erbia byla provedena s energií 190 keV a dávkou 1×10^{16} iontů.cm^{-2} a připravené vzorky byly následně žíhány při 1000 °C. Sledován byl stupeň poškození krystalové struktury metodou RBS/kanálování a pomocí jemných skenů také poloha erbia ve struktuře, měřena byla luminiscenční spektra při pokojové teplotě v oblasti 1530 nm. Porovnání výsledků vedlo k zajímavým závěrům. Zatímco ve struktuře niobičnanu lithného a oxidu hlinitého se erbium po implantaci objevilo v intersticiálních polohách, v oxidu zinečnatém nahrazovalo zinek a obsazovalo tedy substituční polohy. Následné žíhání způsobilo v prvních dvou krystalech

hojení struktury s tím, že erbium obsazovalo substituční polohy lithia nebo hliníku. V ZnO tomu bylo naopak a erbium během následného žíhání substituční polohy opouštělo a většina atomů obsadila intersticiální polohy. Naměřená luminiscenční spektra odpovídala pozorovanému chování erbia. Zatímco následné žíhání mělo v niobičnanu lithném a oxidu hlinitém na intenzitu luminiscence příznivý vliv, v ZnO se intenzita luminiscence následným žíháním snižovala.

Z porovnání výsledků plyne, že kongruentní struktura niobičnanu lithného obsahuje nejvíce možných volných pozic pro umístění erbia. Navíc v této struktuře existují jak pevné kovalentní, tak i iontové vazby. Struktura je po implantaci erbia s dávkou 1×10^{16} iontů. cm^{-2} tedy poškozena nejvíce. Při použití vysokých dávek dochází dokonce i k pohybu – vyražení atomů niobu ze svých poloh a erbium se spolu s dalšími ionty krystalu nachází v intersticiálních polohách. Následné žíhání, které je nad teplotou rekrystalizace, dovoluje erbiu usadit se ve struktuře kongruentního krystalu na pozice lithia.

Struktura Al_2O_3 je velmi podobná $LiNbO_3$. Vazby v Al_2O_3 mají však pevný jednotný kovalentní charakter. Proto je možné předpokládat, že pokud použijeme nízké dávky implantace, erbium preferuje prázdné oktaedrické pozice a je umístěno v zákrytu s ionty hliníku [111]. Při vyšších dávkách, jaké byly použity v našem experimentu, však dochází k výrazné destrukci struktury v místě doletu. Prakticky všechno erbium společně s atomy hliníku je v intersticiálních polohách. Žíhání na 1000 °C pravděpodobně nezpůsobuje ve struktuře dostatečné změny na to, aby erbium nahradilo hliník, popř. se umístilo do oktaedrických vakancí.

Struktura ZnO není trigonální, ale již hexagonální (*P6m*), a obahuje jak oktaedrické tak tetraedrické dutiny. Neobsazené tetraedrické dutiny jsou malé a velmi blízko obsazených tetraedrických dutin. Je otázkou, proč nejsou obsazeny oktaedrické dutiny. Implantované erbium tedy nemá po implantaci jinou možnost, něž se umístit do pozic zinku a kvůli nižší pevnosti vazby ZnO je to pravděpodobně snadnější než u oxidu hlinitého. Při implantaci vstupuje erbium do substitučních poloh, protože struktura ZnO je poměrně málo poškozená a zinek obsazuje intersticiální polohy. Následným žíháním je však erbium opět nahrazeno zinkem.

Zajímavá je také otázka iontových poloměrů a rozměrů vakancí, které ve struktuře existují, popř. otázka nábojové rovnováhy, která je implantací porušena, ale po žíhání by se měla alespoň částečně obnovovat. O erbitých iontech je známé, že i přes vysoké atomové číslo mají díky lathanoidové kontrakci poměrně malý poloměr a vejdou se ve struktuře niobičnanu lithného i do jeho volných oktaedrických pozic. Bylo potvrzeno, že malá velikost

nebrání erbiu obsadit ani volné oktaedrické dutiny ve struktuře Al_2O_3. I když jsou zinečnaté ionty oproti iontům hlinitým a lithným srovnatelné nebo menší (iontový poloměr Zn^{2+} je 74 nm [112]) zdá se, že právě těsná hexagonální struktura ZnO nedovoluje erbiu po následném žíhání obsadit polohy zinku. Roli pravděpodobně u implantovaného ZnO hraje také nábojová nestabilita, kterou u safíru díky třímocnému hliníku nepředpokládáme. V niobičnanu lithném dokáže nestabilitu náboje po implantaci pravděpodobně vyrovnat kongruentní struktura krystalu.

Krystalové okolí jednotlivých krystalů ovlivňuje polohy hlavního energetického pásu v luminiscenčním spektru. Ve struktuře oxidu zinečnatého je nejvyšší intenzita luminiscence naměřena při 1537 nm, což je asi o 7 nm více než u niobičnanu lithného. U oxidu hlinitého k posunu nedochází, hlavní intenzita pásu je opět okolo 1530 nm. U oxidu hlinitého se objevuje pás okolo 1543 nm, který je pravděpodobně spojen s existencí erbia v intersticiálních polohách. Posun atomů erbia mimo strukturní polohy hexagonální struktury ZnO je provázen významným snížením intenzity luminiscenčního pásu.

Z výsledků je tedy zřejmé, že v porovnávaných krystalech je pro vysokou hodnotu intenzity luminiscence nezbytné, aby erbium obsazovalo substituční polohy a mělo co nejuspořádanější strukturní okolí.

Shrnutí

V oblasti vývoje materiálů pro aktivní fotonické součástky považuji za nejdůležitější následující zjištěné skutečnosti:

a) ve spolupráci s ÚJF AVČR jsme schopni sledovat pozici erbia ve struktuře krystalů s hexagonální krystalickou mřížkou,

b) jsme schopni popsat pozici erbia a také změny ve struktuře po iontové implantaci erbia v $LiNbO_3$, v Al_2O_3 a také v ZnO a velmi pravděpodobně bychom tuto schopnost dokázali rozšířit jak na jiné lanthanoidy, tak i jiné krystalové struktury

c) dokážeme dobře popsat luminiscenční spektra erbitého iontu a sledovat vliv krystalového pole na posun pásů v luminiscenčním spektru

d) prokázali jsme, že příprava vlnovodů v Er: $LiNbO_3$ pomocí difúze titanu, metodou APE a nebo implantací helia nemění charakter luminiscenčního spektra erbitého iontu a jen velmi málo ovlivní intezitu pásu při 1530 nm, uvedený materiál ve spojení se zkoušenými metodami přípravy vlnovodů může být základem aktivní optické součástky.

2.7 Technologie přípravy tenkých vrstev pro fotoniku

V současnosti existuje celá řada technologií, které je možné použít pro přípravu tenkých vrstev vhodných pro fotoniku. Obecně je možné je rozdělit na **technologie depoziční** nebo technologie využívající selektivní leptání a technologie difúzní. Depoziční technologií je možné připravit vrstvy se skokovou změnou vlatností, např. indexu lomu, ale i ostatních. Naproti tomu ve vrstvách vytvořených technikou difúzní je změna vlastností gradientní. Záleží na konkrétní součástce, pro kterou má vrstva sloužit. Mezi technologie depoziční je možné zařadit napařování, naprašování, epitaxní růst, sol-gel techniky ale také technologie Chemical Vapour Deposition (CVD), Physical Vapour Deposition (PVD), Flame Hydrolysis Deposition (FHD), Pulsed Laser Deposition (PLD) a dále epitaxní metody - Molecular Beam Epitaxy (MBE) a Liquid Phase Epitaxy (LPE). Uvedené techniky se využívají především pro přípravu polovodičových vrstev a pro většinu z nich jsou charakteristické vysoké náklady na vybavení i na jeho provoz. Naopak velkou výhodou těchto metod je možnost velmi přesně řídit složení, tj. vlastnosti a v některých případech kontrolovat růst připravovaných vrstev.

Mezi **technologie difúzní** můžeme zařadit iontovou výměnu, iontovou implantaci a také difúzi z kovových nebo oxidických tenkých vrstev deponovaných na povrch. Dochází k vytvoření vrstvy přímo v podložce a vznikne tak vlnovod s gradientní změnou vlastností. Tento způsob přípravy tenkých vrstev se obvykle vyznačuje poměrně malou náročností z hlediska vybavení (které umožňuje připravit velké množství vzorků najednou), nicméně i přes to jsou vrstvy charakteristické velmi dobrou reprodukovatelností přípravy a nízkými optickými ztrátami. Mezi nejčastěji používané metody patří vysokoteplotní difúze iontů z kovové vrstvy nanesené na povrch podložky (např. difúze Ti [35,113,114] nebo Ag [115] a iontovou výměnu (čistě termická difúze, difúze s využitím vnějšího elektrického pole [96,116,]), která se využívá jak ve sklech, tak v optických krystalech.

Další a nejmladší technologií přípravy tenkých vlnovodných vrstev je tzv. **technologie přímého zápisu** optických vlnovodů do podložky za pomoci vysokovýkonových laserů. Ozáření laserovými pulsy má za následek pokles či nárůst hustoty ozářené části ve srovnání se zbytkem objemu daného materiálu a následně také zvýšení indexu lomu. Tato technika se v současné době používá pro tvorbu kanálkových vlnovodů především v krystalických materiálech, ale také ve sklech obsahujících oxidy těžkých kovů. Jako příklady materiálů terče je možné uvést α-křemen, $LiNbO_3$, safír dopovaný ionty Ti^{3+} a $KY(WO_4)_2$ [117,118].

Iontová výměna

Původně byla iontová výměna využívána převážně k barvení a chemickému tvrzení povrchu skla nebo ke zvýšení chemické odolnosti skel [119]. Později se této metody začalo využívat pro přípravu optických vlnovodů. Optické vlnovody připravené iontovou výměnou mají následující výhody:

a) celý proces je relativně jednoduchý a levný i přes to, že zahrnuje také přípravu masek pomocí litografie;
b) proces je velmi flexibilní vzhledem k volbě výrobních parametrů a vlastnosti vlnovodů mohou tak být snadno optimalizovány;
c) difúzní podstata iontové výměny je příčinou malého ovlivnění kvality vlnovodu tj. jeho optických ztrát vlivem nedokonalostí litografické masky (nedokonale rovných okrajů namaskovaného motivu);
d) kruhový průřez výstupního signálu umožňuje snadné a bezeztrátové navázání na kruhový průřez signálu v optickém vlákně;
e) pokud se jedná o struktury připravené iontovou výměnou na povrchu podložního skla, je relativně snadné propojit vlnovod s jinými materiály, jako jsou polymery a polovodiče.

Iontová výměna iontů z taveniny za ionty z podložky probíhá zpravidla tak, že je substrát při určité teplotě a po určitou dobu ponořen do taveniny, která obsahuje požadované ionty. Hnací silou iontové výměny je difúze. Ionty z taveniny se začnou pohybovat směrem do substrátu a vyměňovat se za slabě vázané ionty v substrátu (např. Li^+, Na^+, K^+), které pak difundují ze skla do taveniny. Změna indexu lomu v připravené vrstvě je pak způsobena jednak vlivem změny chemického složení materiálu (čili prostřednictvím různé polarizovatelnosti vyměněných iontů), ale zároveň také vlivem různé velikosti těchto iontů a následně vznikajícího vnitřního pnutí ve vrstvě (v některých případech i pozorovaným zvětšením objemu vrstvy ve směru kolmém na povrch vzorku).

Asi nejvíce používaným substrátovým sklem je komerčně dostupné borito-křemičitanové sklo IOT BGG31 s přibližně 7% obsahem sodíku. Ve spojení s křemičitanovými skly bylo dosud zkoumáno použití různých vyměňovaných iontů z tavenin anorganických solí, především to byly jednomocné ionty Li^+, K^+, Rb^+, Cs^+, Tl^+ a Ag^+. Za účelem přípravy aktivních vlnovodů ve sklech byly studovány také iontové výměny Cu^+ a Er^{3+} iontů. Nejběžněji je však využívána iontová výměna $Ag^+ \leftrightarrow Na^+$.

Tato technika se dnes využívá ještě pro jiné účely než je tvorba optických vlnovodů. Především jejím spojením s následným žíháním je ji možné použít pro tvorbu kovových nanočástic stříbra ve skelné matrici a využívat tak např. povrchové plazmonové resonance těchto nanočástic.

Iontová implantace [120,121]

Při iontové implantaci dochází k interakci urychlených iontů s pevnou látkou. Důsledkem interakcí energetických iontů s pevnou látkou je řada jevů. Při iontovém implantaci povrchu pevné látky implantované ionty vnikají hlouběji pod povrch, kde postupně interakcemi s atomy bombardované pevné látky ztrácejí svoji energii a zabudovávají se do její struktury. Koncentrační rozdělení dopadlých iontů tvoří tzv. hloubkový koncentrační profil implantované příměsi v pevné látce, který má vždy tvar Gausovy křivky. Výhodou iontové implantace je její značná variabilita v kombinaci implantovaného iontu a bombardované pevné látky a snadná kontrola a řízení vznikajícího hloubkového koncentračního profilu. Koncentrační profil je totiž funkcí pouze dvou dobře měřitelných implantačních parametrů: energie iontů (dané nastaveným urychlovacím napětím) a dávky iontů (dané implantovaným nábojem měřeným integrací iontového proudu dopadajícího na terčík). Iontovou implantací lze dosáhnout vysoké homogenity a také velmi dobré reprodukovatelnosti. Nevýhodou iontové implantace je poměrně značné porušení struktury pevné látky v místě dopadu implantovantované částice, kdy tyto poruchy mohou významně ovlivnit např. optické vlastnosti pevné látky. Toto poškození lze částečně eliminovat následný žíháním. Iontová implantace se původně začala využívat pro modifikaci polovodičů, později se ukázalo, že je možné ji využívat ke změně mechanických, korozních a supravodivých vlastností kovových materiálů, čehož se dnes využívá i komerčně [122].

Pro přípravu optických vlnovodů je iontová výměna využívána spíše zřídka. Pomocí ní je možné připravit tzv. bariérové vlnovody [123]. Pokud se použije dostatečně vysoká energie implantovaného iontu, která svým průletem prakticky nepoškodí strukturu pevné látky a v místě dopadu vytvoří barieru (oblast jiného složení) procházející optický signál se dopadem na tuto vrstvu lomí a začne se vrstvou vytvořenou povrchem látky a vrstvou v místě dopadu implantované částice šířit. Kvůli poruchám, které průlet a dopad implantované částice způsobí, jsou uvedené vlnovody studovány zřídka, vykazují totiž vysoký optický útlum.

Pro fotonické materiály je iontová implantace využívána spíše jako metoda vhodná k obohacení amorfních i krystalických materiálů jinými ionty způsobujícími optickou

aktivitu, tj. např. ionty lanthanoidů nebo vzácných kovů. Přitom je možné říci, že výpočet doletu a konečného rozložení implantované částice se mezi amorfní a krystalickou látkou liší. Zatímco v amorfní látce je dolet ovlivněn energii, dávkou, hmotností a protonovým číslem implantovaných iontů, hmotností a protonovým číslem atomů terče, hustotou a teplotou amorfní pevné látky v krystalickém materiálu terče k těmto vlivům přistupuje ještě vliv krystalografické orientace povrchu vůči svazku. Je-li totiž pevná látky orientována tak, že iontový svazek je rovnoběžný s některým krystalografickým směrem dochází k tzv. kanálování, kdy ionty pronikají podstatně hlouběji. Tohoto jevu je možné využít při zjišťování stupně poškození krystalové struktury dopací aktivních iontů.

V naší laboratoři jsme se soustředili především na technologie, jejichž podstatou je výměna iontů, tj. příprava tenkých vrstev výměnou iontů z tavenin nebo z napařených vrstev. Připravovány tak byly tenké vrstvy s gradientní změnou sledované optické vlastnosti tj. především indexu lomu nebo koncentrace aktivního iontu. Ve spolupráci s Ústavem jaderné fyziky AVČR v Řeži nebo s Helmholtz-centrum Rossendorf dokážeme připravovat a charakterizovat optické vrstvy připravené iontovou implantací. Jak bylo uvedeno výše, tyto technologie se doplňují v tom smyslu, že iontová výměna je omezena vhodnou kombinací substrátu a dopovaného iontu, ale velmi náročná co se týče použitého vybavení. Metoda iontové implantace využívá iontový urychlovač, ale na druhou stranu je schopná kombinovat jakýkoliv materiál substrátu s jakýmkoliv implanatovaným iontem. I proto si myslím, že jsme v současné době pracovištěm, které dokáže připravit tenkou optickou vrstvu požadovaných vlastností a modifikovat její optické vlastnosti v souvislosti s chemickým složením.

2.8 Vlastní výsledky v oblasti technologických procesů přípravy tenkých vrstev pro dynamické i aktivní optické členy

Z technologií, na které jsem se soustředila ve své práci, jsou to především iontová výměna v elektrickém poli, kdy je možné používat poměrně širokou škálu vloženého napětí od 0 V do 2000 V. Pro tuto technologii se podařilo vybudovat základní experimentální pracoviště, na kterém bylo studováno především ponořování tenkých optických vrstev pod povrch skelných substrátů a výzkum souvislosti mezi složením optických skel, jejich vodivostí a snadností ponoření povrchového vlnovodu. Své experimentální zkušenosti jsem pak uplatnila především v aplikačních výstupech pro firmu Color-Chip, Israel a Vláknová optika SQS Nová Paka. Současně jsem se soustředila na iontovou výměnu a iontovou implantaci v optických krystalech a v menší míře také v optických sklech.

Nízkoteplotní dopování erbia: vliv krystalografické orientace řezů niobičnanu lithného na luminiscenci [P3 a P11, P15]

Jako nový způsob lokalizované dotace $LiNbO_3$ erbiem byla v naší laboratoři studována termická difuze erbia z taveniny dusičnanů, při které jsme využívali různé krystalografické řezy niobičnanu lithného [P3,124]. Ukázalo se, že takto připravené vzorky vykazují luminiscenci při 1530 nm a byly prokázány rozdíly v obsahu erbia mezi jednotlivými řezy niobičnanu lithného. Rozhodli jsme se zhotovit speciální řezy niobičnanu lithného s orientací kolmo a rovnoběžně se štěpnou rovinou krystalu (řez rovnoběžný *YII* <10-12> a kolmý řez *Y*⊥ <10-14>). Pomocí nich bylo prokázáno, že štěpná rovina v monokrystalickém niobičnanu lithném usnadňuje pohyb erbia danou strukturou. Tato skutečnost byla později potvrzena pro vyšší teplotu lokalizované dotace [124] a také v safíru [P3]. Ukázalo se, že teplota termické dotace je důležitým faktorem nejen z hlediska rychlosti dotace, ale také z hlediska mechanismu procesu.

V následujících experimentech jsme se proto soustředili na porovnání mechanismu termické difúze při různých teplotách [P11]. Sledovány byly nejen změny v luminiscenčních spektrech v souvislosti s podmínkami přípravy, ale také pohyb lithia a erbia strukturou niobičnanu lithného pomocí metod NDP, RBS a RBS/kanálování. Uvedené výsledky potvrzují skutečnost, že je možné připravit termickou difúzí erbia z taveniny jeho solí velmi tenkou optickou vrstvu erbia v niobičnanu lithném vykazující luminiscenci na 1530 nm. Tloušťka takto připravených vrstev dosahovala maximálně 0,1 μm a obsahovala 7 až 24 at % erbia. Různý obsah erbia odpovídal použitým podmínkám a krystalografickým řezům. Z uvedených výsledků bylo zjištěno, že teplota ovlivňuje mechanismus, kterým ionty erbia do krystalu pronikají. Obecně se podle výsledků SIMS uvádí, že při termické difuzi z taveniny solí erbitých probíhá v materiálu iontová výměna trojmocných iontů erbia z taveniny za ionty lithné [125]. Uvedenému mechanismu, tj. iontové výměně by v našem případě odpovídala mnohem lépe data zjištěná při termické difúzi při nižší teplotě 350 °C (z taveniny dusičnanů), kdy tloušťka vrstvy obsahující erbium poměrně dobře odpovídá tloušťce vrstvy, ve které je patrný úbytek lithia zjištěný metodou NDP. V případě taveniny dusičnanů je třeba si uvědomit, že čas výměny je dlouhý ve srovnání s výměnou erbia v tavenině síranů a že tavenina dusičnanů neobsahuje lithné ionty, což znamená, že iontová výměna není zpomalována. Navíc se v našich pracích ukázalo, že pohyb lithia strukturou je při této teplotě více než pravděpodobný. Zůstává však otázkou, zda při tomto procesu ionty erbité obsazují

polohy lithných iontů. Jelikož nebylo možné naměřit kanálovací spektra je možné v tomto případě předpokládat, že tomu tak není a erbium obsazuje z velké části polohy intersticiální, popř. vychyluje atomy kyslíku a niobu z jejich pravidelných poloh.

Z našich výsledků plyne, že při teplotě 600 °C k iontové výměně erbitých za lithné ionty nedochází. Musíme si však uvědomit, že čas výměny je kratší a tavenina obsahuje lithium. Přesto je patrné, že i když je hloubka, ve které je erbium v povrchu krystalu přítomné mnohem větší, je úbytek lithia ve všech připravených vzorcích prakticky nulový. Předpokládáme tedy jiný mechanismus výměny. Podle [56] může niobičnan lithný při používané teplotě částečně rekrystalovat. Z tohoto důvodu předpokládáme, že po inkorporaci erbia do struktury niobičnanu lithného dochází k vyrovnání náboje částečnou rekrystalizací struktury krystalu, kdy erbium obsazuje ve větší míře polohy niobu a lithium ze struktury krystalu neubývá. Tomuto mechanismu by nasvědčovaly mnohem větší hodnoty intenzit luminiscenčních pásů, kdy je možné předpokládat uspořádanou strukturu kolem atomů erbia. Také výsledky metody RBS a RBS/kanálován ukazují, že po termické difuzi erbia ze síranů jsou vakance ve struktuře krystalu „naplněny “ ionty erbia a po následném žíhání jsou obsazovány polohy niobu (mnohem více erbia se nachází v substitučních polohách).

Budeme-li diskutovat mechanismus termické difuze erbia z hlediska využití různých krystalografických řezů monokrystalu niobičnanu lithného, je zřetelně patrný vliv štěpné roviny na průběh termické difúze. Při obou teplotách bylo ve všech připravených sadách vzorků naměřeno vysoké množství erbia stejně jako byla nalezena vysoká hodnota intenzity luminiscence při 1530 nm právě v řezu kolmém na štěpnou rovinu.

Jako první jsme také publikovali iontovou výměnu erbia a lithia z taveniny dusičnanů v elektrickém poli [P15]. Při tomto experimentu krystalem protékal proud 0,5 mA při napětí 1800 V. K experimentům byl dosud využit pouze řez *Z* niobičnanu lithného. S prodlužujícím se časem iontové výměny se zvyšovala intenzita luminiscenčního pásu při 1535 nm.

Vysokoteplotní dopace erbia: vliv krystalografických řezů niobičnanu lithného a složení napařené vrstvy na luminiscenci [P18]

Jako jiný způsob dotace niobičnanu lithného erbiem byla studována vysokoteplotní dotace z napařené vrstvy obsahující erbium. Pro dotaci erbia byly zvoleny dva různé typy napařených vrstev – kovová vrstva Er a oxidová vrstva Er_2O_3. V obou případech byla difúze provedena při teplotě 1060 °C po dobu 100 h [P18]. Výsledky je možné shrnout do následujících bodů:

a) Charakter luminiscenčního spektra byl pro oba použité způsoby dopace, tj. pro vrstvu kovovou i oxidovou stejný. Pokud byla napařena vrstva s tloušťkou kovu i oxidu 20 nm, nelišily se ani intenzity luminiscenčního pásu při 1535 nm. Naproti tomu při snížení tloušťky napařených vrstev na 10 nm se vyšší intenzita luminiscence objevila u vrstvy Er_2O_3.
b) Intenzita luminiscence dobře odpovídala tloušťkám napařených vrstev, kdy u vzorků připravených z vrstev s tloušťkou vrstev 20 nm se objevila dvojnásobná intenzita luminiscence v porovnání se vzorky připravenými z vrstev o tloušťce 10 nm.
c) Luminiscenční spektra vzorků z vysokoteplotní difúze z napařených vrstev ukazovala na velmi dobré luminiscenční vlastnosti – intenzita luminiscence dosahovala až 20 000 a. u.
d) V luminiscenčním spektru bylo patrných více než 6 luminiscenčních pásů s malou položířkou pásu. Předpokládali jsme tedy vysoké strukturní uspořádání, což se potvrdilo i z kanálovacích RBS spekter, která vykazovala míru uspořádanosti struktury srovnatelnou s čistou nedotovanou strukturou $LiNbO_3$.
e) Pokud porovnáme intenzitu luminiscence mezi použitými řezy *X* a *Z*, je patrné, že pro oba typy vrstev vykazova nejvyšší hodnotu luminiscence řez *Z*.

Tloušťka vrstev připravených uvedenou technologií nepřesáhla podle měření metodou RBS 100 nm, ale podle výpočtu dosahovala až do hloubky 5 až 8 μm, což je za detekčním limitem metody RBS. Koncentrace erbia byla 0,1 až 2,3 at %. V těchto vzorcích nebyl potvrzen výměnný mechanismus erbia za lithium. Analýzy prokazují obsazení poloh niobu i lithia v připravených strukturách. Vzhledem k vysoké teplotě procesu zde zcela jistě dochází k rekrystalizaci struktury niobičnanu lithného. Navíc z výsledků vyplynulo, že ve srovnání s jinými používanými difúzními metodami mají vrstvy připravené uvedeným způsobem zatím nejvyšší hodnoty luminiscence při 1530 nm a jsou tedy vhodné pro přípravu optického zesilovače.

Iontová implantace: vliv experimentálních podmínek na luminiscenci eritých iontů [P8,P9, P12 a P20].

Pro dotování niobičnanu lithného erbiem byla využívána i technika iontové implantace. Ionty Er^+ byly implantovány do monokrystalu za různých podmínek. Vzhledem k možnostem využívaných urychlovačů iontů jsme se soustředili na středně energetickou implantaci při 300

a 500 keV a dávky implantovaného erbia se pohybovaly od 1×10^{15} až do 5×10^{16} iontů.cm^{-2}. Podle použité dávky se koncentrace erbia v připravených vrstvách pohybovala od 0,25 do 8 at. % erbia. Přitom platilo, že čím je použitá dávka ale také energie větší, tím je maximální hodnota v koncentračním profilu, který má tvar Gaussovy křivky, větší. Připravené vrstvy měly maximální koncentraci erbia v hloubkách mezi 60 až 80 nm pod povrchem a nevykazovaly těsně po iontové implantaci prakticky žádnou luminiscenci v oblasti 1530 nm, teprve následné žíhání způsobilo výrazné zlepšení luminiscenčních vlastností.

Diskutován byl také mechanismus přípravy vrstev v souvislosti se změnou luminiscenčních spekter. Obecně je možné předpokládat, že s rostoucí koncentrací erbia ve vrstvě poroste také intenzita luminiscenčního pásu. Ze získaných výsledků je patrné, že použijeme-li pro implantaci vysokou dávku – v našem případě 5×10^{16} iontů.cm^{-2} - intenzita sledovaného luminiscenčního pásu je nižší v porovnání s implantací nižší dávkou. Ve spektru je navíc zřetelná velká intenzita luminiscenčního pásu při 1485 nm. Otázkou byla tedy příčina zhoršení luminiscenčních vlastností, která mohla mít dva důvody:

a) destrukci krystalové struktury během implantace a neschopnost rekrystalizovat během následného žíhání nebo
b) nevhodnou polohu erbia ve struktuře niobičnanu lithného a tvorbu shluků, které luminiscenci zháší.

Ze sledování pohybu erbia a lithia spolu se stupněm uspořádání struktury bylo zjištěno, že bezprostředně po implantaci jsou ionty erbia soustředěny v místě dopadu a jejich okolí je značně zničené. V RBS spektru se objevuje při vysoké dávce 5×10^{16} iontů.cm^{-2} relativní úbytek niobu, který není způsoben výraznou destrukcí povrchu. Intenzita luminiscence pásu 1535 nm je tedy prakticky nulová.

Během následného žíhání dochází k pohybu erbia směrem k povrchu, ale také do hloubky. Tento jev je mnohem patrnější při dávce 1×10^{16} iontů.cm^{-2}. Poškozená struktura během následného žíhání rekrystalizuje a nezávisle na použité dávce, je po 5 hod. žíhání při 1000 °C již z 90 % původní. Z měření RBS metodou jemných skenů, je však patrný výrazný rozdíl v pozici erbia. Zatímco při nižší dávce implantace a po následném žíhání erbium obsazuje převážně substituční polohy pravděpodobně niobu nebo lithia, při dávce vysoké je značná část erbia v poloze intersticiální. Blízkost dvou atomů erbia po implantaci vysokou dávkou vede ke koncentračnímu zhášení luminiscence, tj. k poklesu intenzity luminiscenčního pásu. Přítomnost výrazného luminiscenčního pásu při 1485 nm je s největší pravděpodobností způsobena právě vznikem klastrů erbia.

Iontová implantace: vliv žíhání a vliv krystalografické orientace povrchu vůči dopadajícímu iontovému svazku [P9 a P12]

Vliv následného žíhání a různé krystalografické orientace povrchu krystalu niobičnanu lithného vůči iontovému svazku při iontové implantaci erbia byl studován v [P9 a P12]. V uvedených pracích bylo zjištěno, že následné žíhání ovlivňuje především hojení struktury poškozené dopadem implantované částice. Zhojení strukturního okolí implantovaného erbia a jeho vhodná pozice způsobí charakteristickou luminiscenci erbitého iontu. Zkoumány byly různé teploty žíhání, tj. 350 °C, 600 °C a 1000 °C. Intenzita luminiscence se zvyšovala se zvyšující se teplotou žíhání. Navíc se během experimentů projevily významné rozdíly v chování jednotlivých řezů niobičnanu lithného během žíhání. Ukazuje se, že nejvyšší intenzitu luminiscence a také nejsnadnější pohyb erbia strukturou umožňuje právě řez kolmý na štěpnou rovinu krystalu.

Nejjednodušší příčinou odlišného chování právě řezu $Y\perp$ by bylo vysvětlení, že v řezu $Y\perp$ je koncentrace erbia vyšší a tudíž také intenzita luminiscenčního pásu bude vyšší. Jak tomu bylo např. v našich předchozích pracích [P3,P10a P14]. V případě iontové implantace, kdy je implantována vždy stejná dávka daného iontu, však můžeme tuto příčinu vyloučit, jak ukazují také hloubkové koncentrační profily naměřené metodou RBS. Příčinu je tedy nutné hledat jinde. Z kombinace výsledků pro různé běžné i speciální řezy $LiNbO_3$, kdy erbium bylo implantováno různou dávkou (tj. struktura byla zcela odlišně poškozena) a žíháno při různých teplotách bylo nalezeno následující vysvětlení: Pohyb erbia během následného žíhání je ovlivněn především stupněm poškození struktury, tj. implantační dávkou a následně zvolenou žíhací teplotou.

Při implantaci s dávkou 1×10^{15} iontů.cm^{-2} je možné předpokládat pouze bodové defekty popř. quasiamorfní vrstvu a při následném hojení se pak mnohem více projeví vliv difúze defektů a následně dopantu podle jednotlivých krystalografických směrů tj. vliv řezu. Tento efekt je zřetelný při teplotě žíhání 350 °C, kdy se výrazně sníží koncentrační maximum v RBS koncentračním hloubkovém profilu erbia a profil se stává širším. K největší změně koncentračního profilu RBS dochází v tomto případě v řezu $Y\perp$, což by bylo možné na základě našich předchozích experimentů [P11] vysvětlit rychlou difúzí erbia štěpnou rovinou krystalu. Při vyšší teplotě (600 °C) dochází k celkové rekrystalizaci, která je nejsnadnější podél osy z – struktura v tomto řezu je podle kanálovacích spekter nejvíce podobná původní a proto také luminiscence v tomto řezu je po žíhání na 600 °C již jen o málo nižší než je tomu

v řezu $Y\perp$. V řezu $Y\perp$ je hojení při 600 °C pomalejší, přesto je luminiscence vysoká díky rovnoměrnému rozložení erbia pravděpodobně již v polohách se symetrií C_{3v}.

Při dávkách 1×10^{16} iontů.cm^{-2} je struktura velmi poškozená, o čemž svědčí i významné zvětšení objemu, které je možné doložit zdánlivým úbytkem lithia [P11] – nejvíce mění svůj objem právě řez $Y\perp$. Struktura jednotlivých řezů pak hraje při následném hojení mnohem menší roli, o čemž svědčí menší rozdíly mezi intenzitou luminiscence jednotlivých řezů implantovaných uvedenou dávkou.

Z výsledků je patrné, že stupeň poškození a následný různý mechanismus hojení během žíhání zřetelně ovlivňuje možnost klastrování erbia a také strukturu krystalového okolí erbia. Následně se popsané rozdíly projeví jako rozdílná intenzita luminiscence erbia v jednotlivých krystalografických řezech připravených za stejných podmínek.

Nanášení vrstev Er: $LiNbO_3$ depozičními technikami [P16, P17]

Ve spolupráci s FÚ AVČR a se skupinou Ing. Kateřiny Rubešové Ph.D. na UACH VŠCHT jsme připravovali vrstvy niobičnanu lithného obsahujícího erbium popř. směs erbia a ytterbia pomocí depozičních technik. Vrstvy byly připravovány na safírových podložkách metodou PLD [P16] a také metodou sol-gel [P17]. Technikou PLD se podařilo připravit při vhodné žíhací teplotě vlnovodné vrstvy, které vedly při vyšších vlnových délkách (tj. 964, 1311 a 1552 nm) dva až tři vidy. Index lomu připravených vrstev byl měřen jak metodou vidové spektroskopie tak elipsometrií. Hodnoty indexu lomu si dobře odpovídaly pro obě použité metody a také se shodovaly s teoretickou hodnotou indexu lomu niobičnanu lithného, protože malá koncentrace erbia nebo ytterbia zvýšila index lomu jen o několik tisícin. Vhodné žíhání vrstev vedlo prakticky k vymizení fáze odpovídající $LiNb_3O_8$ a vysoké hodnotě intenzity luminiscence při vlnové délce 1530 nm, která byla srovnatelná s objemově dotovanými substráty. Horší mikrostruktura vrstev se projevila rozšířením absorpčních pásů. Metodou sol-gel se zatím podařilo připravit vrstvy, které mají luminiscenci v dané oblasti spektra, ale díky mikrostrukturním poruchám vykazují velkou absorpci optického záření.

Shrnutí

V uvedených experimentech bylo použito několik způsobů jak dopovat niobičnan lithný ionty erbia. Byly to: a) dopace erbia z taveniny b) dopace erbia z tavenin provedená v elektrickém poli c) iontové implantace erbia d) vysokoteplotní difúze erbia z napařené vrstvy obsahující erbium e) depozice tenkých vrstev Er:$LiNbO_3$ metodou PLD f) depozice

tenkých vrstev Er: $LiNbO_3$ metodou sol-gel. Vlastnosti připravených tenkých vrstev jsme porovnávali s objemově dotovaným niobičnanem lithným obsahujícím 0,5 nebo 1 at. % erbia. Na připravených optických vrstvách byly sledovány především jejich vlnovodné a luminiscenční vlastnosti. Výsledky přehledně shrnuje **Tabulka 8**.

Z uvedených výsledků výplývá, že metody depoziční a také nízkoteplotní dopace erbia při 350 °C je možné použít pro přípravu vlnovodné vrstvy obsahující erbium. Problémem u deponovaných vrstev je jejich rovinnost a homogenita. Právě to způsobuje, že pro krátké vlnové délky se obecně vlnovodné vlastnosti těchto vrstev ztrácejí.

Tabulka 8 Porovnání vlastností tenkých vrstev niobičnanu lithného obsahujících erbium připravených různými technologiemi

Metoda	Luminiscence	Koncentrace Er	Vlnovodné vlastnosti
objemová dopace	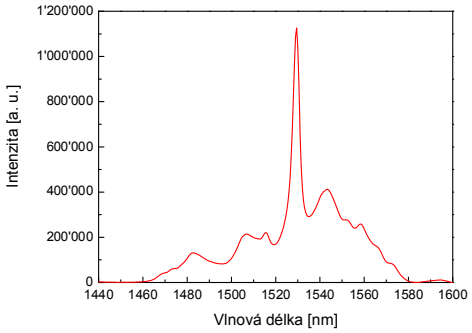	5000 ppm (0,5at.%)	NE
metoda dopace erbia z tavenin provedená v elektrickém poli	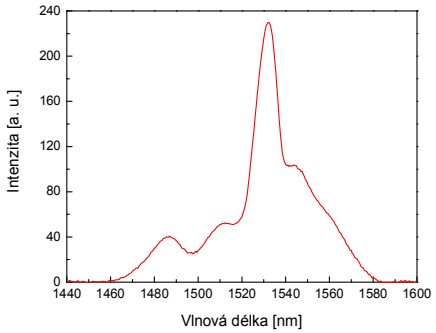	1,3 at % hloubka 60-80 nm	NE
metoda dopace erbia z taveniny	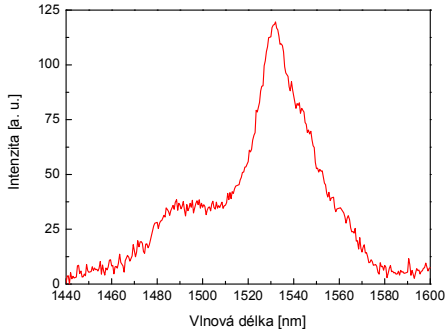	2 až 7 at % hloubka 50 nm	ANO 4-8 vidů, změna indexu lomu

metoda dopace erbia z taveniny	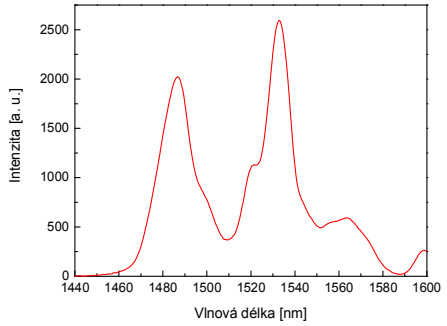	12 až 24 at % hloubka 80 nm	NE
metoda iontové implantace erbia s následným žíháním	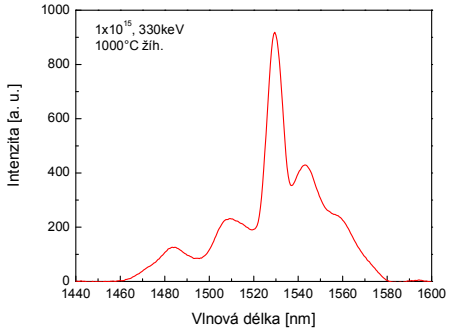	0,25 až 8 at% hloubka 60-80 nm	ANO 1 nepříliš průkazný vid
vysokoteplotní difúze erbia z napařené vrstvy obsahující erbium	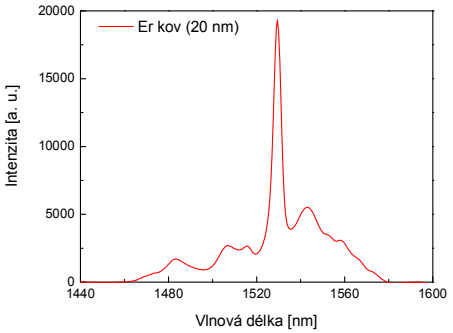	0,1 až 2,3 at % hloubka 5-8 μm	NE
metoda přípravy tenkých vrstev Er:$LiNbO_3$ metodou PLD	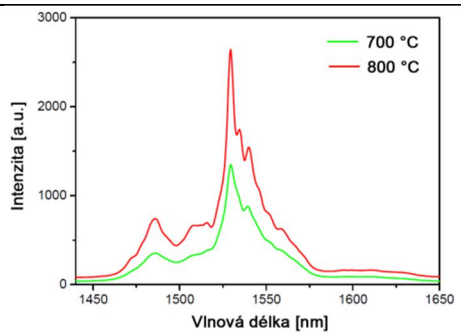	0,5 at % tloušťka vrstvy okolo 1μm	ANO 1-3 vidy pro vlnové délky > 964 nm
metoda přípravy tenkých vrstev Er: $LiNbO_3$ metodou sol-gel	luminiscence zatím nezjištěna	0,5 at % tloušťka vrstvy okolo 1μm	zatím nevedou optický signál

Difúzními technikami byly v niobičnanu lithném připraveny vrstvy s různým obsahem erbia v různých hloubkách a také s různým tvarem hloubkového koncentračního profilu.

Nejvyšší množství erbia obsahovaly vrstvy dopované z taveniny síranů. Tato vrstva měla i přes značně vysoký obsah erbia jasně měřitelnou luminiscenci při 1530 nm. Zřetelně se při použití této techniky projevil pás na vlnové délce 1485 nm, který je charakteristický pro vysoké obsahy erbia ve vrstvách a indikuje klastrování erbitých iontů. Iontovou implantací se připraví mělké vrstvy s poměrně malým obsahem erbia a vysokým stupněm poškození struktury krystalu, což způsobí, že po iontové implantaci je intenzita luminiscence erbia nulová a musí nutně následovat žíhání. Čím je vyšší teplota žíhání, tím jsou pásy ve spektru ostřejší a jejich počet se zvyšuje, což ukazuje na postupné hojení okolní struktury erbia a vhodné krystalové pole pro vznik luminiscence. U vysokoteplotní dotace z napařených vrstev je koncentrace erbia nízká, ale vrstvy jsou hluboké a struktura navykazuje známky poškození, proto se výsledná luminiscence blíží objemově dotovaným vzorkům jak v charakteru, tak v intenzitě luminiscenčního spektra.

V oblasti technologií přípravy tenkých optických vrstev pro fotonické součástky považuji za nejdůležitější následující zjištěné skutečnosti:

a) navrhli jsme a experimentálně jsme potvrdili možnost dopování niobičnanu lithného erbiem z taveniny,

b) ověřili jsme, že dopování niobičnanu lithného erbiem lze provést i v elektrickém poli,

c) prokázali jsme význam krystalografických řezů monokrystalu při difúzních technologiích dopování niobičnanu lithného erbiem a na základě porozumnění probíhajícím dějům jsme objasnili rozdílnou intenzitu pásů luminiscenčního spektra mezi jednotlivými řezy niobičnanu lithného

d) vliv podmínek přípravy na vysokou intezitu luminiscence při 1530 nm se dá zobecnit tak, že vysoké intenzitě luminiscenčního pásu při 1530 nm prospívá vysoká teplota při technologiích popř. při následném žíhání, při které má struktura možnost rekrystalizovat a uspořádat okolí erbitých iontů.

3. ZÁVĚR

Předložená habilitační práce je souborem původních prací, které jsou seřazeny chronologicky za sebou, jak byly publikovány. K pracím je přiložen jen stručný přehled základních pojmů a pak krátké komentáře k jednotlivým publikovaným pracem shrnující nejdůležitější získané poznatky v oblasti anorganických materiálů pro fotoniku. Práce sama je pak rozdělena na tři základní části, kdy první se zabývá materiály vhodnými pro pasivní a dynamické fotonické součástky, druhá pak materiály pro aktivní fotonické součástky a třetí shrnuje a porovnává využívané technologické postupy.

V první části je popsána především příprava planárních optických vlnovodů jako základního fotonického prvku a to jak v materiálech krystalických, především v niobičnanu lithném, tak v materiálech amorfních především v různých typech optických skel. Popsáno, je zde studium souvislostí mezi optickými vlastnostmi, které dokážeme v naší laboratoři dobře charakterizovat, a chemickým složením v připravených optických vrstvách. Uveden je také aplikační výstup v podobě popisu přípravy jednorozměrných optických struktur jako je kanálkový optický vlnovod nebo dělič optického signálu, který byl realizován ve spolupráci s firmou Vláknová Optika SQS Nová Paka. Za nejdůležitější zjištěné poznatky, které plynou z předkládané práce, je možné označit:

a) původní přístup ke studiu souvislostí mezi složením křemičitanových skel, procesem iontové výměny a optickými vlastnostmi především změnou indexu lomu, založený na studiu bazicity skel, který vedl k návrhu složení erbito-ytterbitých křemičitanových optických skel vhodných pro optický zesilovač;
b) vypracování nového postupu přípravy optických vlnovodů v niobičnanu lithném metodou protonové výměny s následným žíháním z netoxické kyseliny adipové, jeho studium a nalezení souvislosti mezi pohybem a koncentrací lithného iontu a změnou indexu lomu;
c) na základě návrhu nových speciálních krystalografických řezů strukturou niobičnanu lithného nalezení souvislostí mezi snadným pohybem iontů štěpnou rovinou krystalu a tedy také rozdílným chováním jednotlivých řezů $LiNbO_3$ při protonové výměně
d) charakterizace vztahů mezi koeficientem β dvoufotonové absorpce a velikostí nanočástic zlata připravených iontovou implanací v různých typech skelných substrátů

V druhé části je popsána především příprava aktivních vrstev pro fotoniku, konktrétně především tenkých vrstev obsahujících erbium jako prvek vykazující luminiscenci při vlnové délce 1530 nm a umožňující tak zesílení optického signálu právě při uvedené vlnové délce. Sledována a popsána je především poloha erbia v různých fotonických krystalech a ovlivňění jeho luminiscence blízkým krystalovým polem, které může být změněno nejen jinou strukturou krystalu, ale např. i různou technikou přípravy vlnovodné vrstvy. Za nejdůležitější nalezené poznatky bych označila:

a) možnost detailního sledování polohy erbia v různých krystalických strukturách pomocí metody RBS/kanálování v různých řezech optických krystalů a nalezení souvislosti mezi jeho polohou, mírou poškození jeho okolí a luminiscenčními vlastnostmi;
b) objasnění vlivu orientace povrchu krystalu vůči iontovému svazku při iontové implantaci na rozdílné luminiscenční vlastnosti vrstev připravených v různých krystalografických řezech fotonických krystalů;
c) prokázání skutečnosti vlivu následného žíhání na rekrystalizaci struktury optických krystalů a pohyb erbia danou strukturou;
d) nalezení možnosti spojit proces protonové výměny s objemově dotovaným Er:$LiNbO_3$ krystalem pro přípravu aktivní vrstvy.

Ve třetí části zaměřené na technologické postupy jsou popsány jednolivé možnosti dopace niobičnanu lithného iontem erbia. Porovnány jsou konktrétně techniky dotace z taveniny, dotace z napařené kovové nebo oxidické vrstvy, iontová implantace erbia, depoziční technika PLD a sol-gel technika. Všemi těmito technikami se podařilo připravit optickou vrstvu obsahující erbium a vykazující luminiscenční vlastnosti. Za nejdůležitější nalezené poznatky v této kapitole bych označila:

a) ojedinělou možnost srovnání intenzity luminiscence pásu při 1530 nm mezi jednotlivými technologiemi;
b) nalezení souvislotsi mezi experimentálními podmínkami jednotlivých technologií a luminiscenčními vlastnostmi erbia;
c) nalezení a ověření skutečnosti, že depoziční techniky jsou pro přípravu vrstev se skokovou změnou vlastností vhodné vzhledem k jejich výrazně vyšší variabilitě složení, ale je třeba dbát na homogenitu připravených optických vrstev, které mohou často vést pouze optický signál s větší vlnovou délkou.

Závěrem bych chtěla říci, že se v naší laboratoři podařilo vytvořit experiemtální pracoviště, které je schopné anorganické materiály modifikovat „na míru“ dané fotonické součástky, a které má značné zkušenosti s charakterizací základních optických a chemických vlastnosti připravených tenkých vrstev.

Seznam zkratek

n ..... index lomu

λ ..... vlnová délka

M ..... počet vedených vidů

d ..... tloušťka vlnovodné vrstvy

α ..... koeficient optického útlumu

P ..... výkon optického záření

εr ..... relativní permitivita nebo dielektrická konstanta materiálu

v..... rychlost šíření optického signálu materiálem

c ..... rychlost světla

YAG ..... ytterium – aluminium granát ($Y_3Al_5O_{12}$)

KTP ..... $KTiOPO_4$

KDP ..... KH_2PO_4

r_{nn} ..... elektrooptický koeficient

d_{nn} ..... nelineární optický koeficient

$\chi 3$ ..... susceptibilita třetího řádu

P..... polarizace

E ..... intenzita elektrického pole

CVD ..... metoda CVD - Chemical Vapour Deposition

PLD ..... Pulsní Laserová Depozice

APE ..... Annealed Proton Exchange - metoda protonové výměny s následným žíháním

NDP ..... metoda Neutron Depth Profiling

K1 a K2 ... konstanty

ÚJF AVČR Ústav jaderné fyziky Akademie Věd České Republiky

Er:$LiNbO_3$ Erbiem dopovaný niobičnan lithný

HIC ..... vlnovody s vysokým kontrastem indexu lomu (hight index contrast)

FÚ AVČR Fyzikální ústav Akademie Věd České Republiky

MW CVD metoda MW CVD - Microwave Enhanced Plasma Chemical Vapour Deposition

NCD ..... nanokrystalický diamant

BK7 ..... označení komerčního boriti-křemičitanového skla

EMA ..... elektronová mikroskopie – Electron Microprobe Analysis

Z-scan ..... metoda měření nelineární optické absorpce

β ..... koeficient dvoufotonové absorpce

TPA ..... koeficient dvoufotonové absorpce

LED..... dioda emitující světlo – Laser Emited Diods

EDFA ..... erbiem dopovaný optický zesilovač – Erbium Doped Fiber Amplifier

MIR ..... oblast středních vlnových délek spektra

$^4I_{15/2}$ ..... spektroskopický term

ZBLAN .... fluoridové sklo obsahující ve své struktuře zirkonium, baryum, lanthanoidy, hliník a sodík

Ω_n ..... Judd- Ofeltovy parametry

RTG ..... rentgenová difrakce

XSW ..... metoda X-ray Standing Wave

c_0 ..... koncentrace, při které dochází ke zhášení iontů erbia

τ ..... doba života excitovaného stavu

σ_p ..... účinný průřez pásu stimulované emise

PVD ..... metoda Physical Vapourr Deposition

FHD ..... metoda Flame Hydrolysis Deposition

MBE ..... metoda Molecular Beam Epitaxy

LPE ..... metoda Liquid Phase Epitaxy

IOT BGG 31 komeční označení borito-křemičitanového skla

SIMS ..... metoda Secondary Ion Mass Spectroscopy

RBS ..... Spektroskopie Rutherfordova zpětného rozptylu (Rutherford Backscattering Spectroscopy)

Literatura

[1] J. Čtyroký, I. Huttel, J. Schrofel, L. Šimková: Integrovaná optika, SNTL Praha 1986

[2] J. Čtyroký, Integrovaná fotonika, dostupné online na http://archiv.otevrena-veda.cz

[3] B.E.A.Saleh, M.C.Teich, Základy fotoniky, 2.sv.1vyd., Univ. Karlova v Praha 1996

[4] J. Schröfel, K., Novotnný: Optické vlnovody, 1986, SNTL, Praha.

[5] B. Švecova - *Disertační práce*: Studium vztahů mezi složením a vlastnostmi optických vrstev připravených různými metodami, VŠCHT, Praha 2010

[6] M. Fox, Optical properties of solids, Oxford University Press, New York, Second Edition, 2010

[7] R.L. Sutherland, Handbook of Nonlinear Optics, Marcel Dekker, New York, 2003.

[8] W.H. Wong, K.K. Liu, K.S. Chan, E.Y.B. Pun: *Polymer devices for photonicsapplications*, Journal of Crystal Growth, 288 (2006).

[9] RefractiveIndex.INFO website: © 2008-2015 Mikhail Polyanskiy

[10] Databáze: http://www.mt-berlin.com/frames_cryst/crystals_frameset1.htm

[11] Stepanov, A. L.: *Nonlinear optical properties of implanted metal nanoparticles in various transparent matrixes: a review.* Rev. Adv. Mater. Sci, 27(2) (2011)115-145.

[12] Stepanov, A. L., Ganeev, R. A., Ryasnyansky, A. I.,Usmanov, T.: *Non-linear optical properties of metal nanoparticles implanted in silicate glass*. Nuclear Instruments and Methods in Physics Research Section B: Beam Interactions with Materials and Atoms, 206, (2003) 624-628.

[13] Wang, Y. H., Wang, Y. M., Lu, J. D., Ji, L. L., Zang, R. G., Wang, R. W.: *Nonlinear optical properties of Cu nanoclusters by ion implantation in silicate glass.* Optics Communications, 283(3), (2010) 486-489.

[14] Ganeev, R. A., Ryasnyansky, A. I., Stepanov, A. L., & Usmanov, T.: *Characterization of nonlinear optical parameters of copper-and silver- doped silica glasses at* λ*= 1064 nm.* physica status solidi (b), 241(4), (2004) 935-944.

[15] Y.H. Wang, S.J. Peng, J.D. Lu, R.W. Wang, Y.G. Cheng and Y.I.Mao, Vacuum 83 (2009) 412.

[16] Wang, Y. H., Lu, J. D., Wang, R. W., Peng, S. J., Mao, Y. L., & Cheng, Y. G. *Optical nonlinearities of Au nanocluster composite fabricated by 300 keV ion implantation*. Physica B: Condensed Matter, 403(19), (2008) 3399-3402.

[17] R.L. Sutherland, Handbook of Nonlinear Optics, Marcel Dekker, New York, 2003.

[18] Chakraborty, P.: *Metal nanoclusters in glasses as non-linear photonic materials*, Journal of materials science, 33(9), (1998) 2235-2249.

[19] F. Gonella, P. Mazzoldi, Handbook of Nanostructured Materials and Nanotechnology,4, Academic, San Diego, 2000.

[20] Arizmendi, L.: *Photonic applications of lithium niobate crystals.,* Phys. Status Solidi A, 201 (2), (2004) 253–283.

[21] Wong, K. K. *Properties of Lithium Niobate*, 1st ed.; INSPEC, IEE: London, 2002.

[22] J. Cajzl - *Diplomová práce:* Erbium ve struktuře niobičnanu lithného a jeho luminiscenční vlastnosti, VŠCHT Praha, 2010.

[23] K.J. Rao, *Sructural chemistry of Glasses*, 1. vyd., Elsevier, 2002

[24] A.K. Varshneya, *Fundamentals of inorganic glasses*, Gulf professional Poblishing, 1994

[25] F. Gan, I. Xu , *Photonics glasses*, World Scientific, 2006

[26] S.O. Kasap, P. Capper, *Glasses for Photonics Integration*, v Springer handbook of electronincs and photonics materials, Springer, 2006

[27] R. A. Soref and J. P. Lorenzo: *Single-crystal silicon: a new material for 1.3 and 1.6 μm integrated-optical components*, Electron. Lett. 21 (21), (1985) 953.

[28] B. Schüppert *et al.*: *Optical channel waveguides in silicon diffused from GeSi allow*, Electron. Lett. 25 (22), (1989), 1500.

[29] N. Takato *et al.*; *Silica-based single-mode waveguides on silicon and their application to guided-wave optical interferometers*, J. Lightwave Technol. 6, (1988),1003.

[30] M.-K. Chin *et al.*: *High-index-contrast waveguides and device*, Appl. Opt. 44 (15), (2005), 3077

[31] J. I. Mackenzie: *Dielectric solid-state planar waveguide lasers: a review*, IEEE J. Sel. Top. Quantum Electron. 13 (3), (2007) 26.

[32] H. Kimura,A.Miyazaki, J.Cryst.Growth 250 (2003) 251.

[33] Izawa, Tatsuo, and Hiroshi Nakagome: *Optical waveguide formed by electrically induced migration of ions in glass plates,* Applied Physics Letters 21.12 (1972) 584-586.

[34] R. V. Ramaswamy and R. Srivastava: *Ion-exchanged glass waveguides: a review,* J. Lightwave Technol. 6 (6), (1988) 984

[35] Schmidt, R. V., and I. P. Kaminow. *Metal-diffused optical waveguides in $LiNbO_3$.,* Applied Physics Letters 25.8 (1974) 458-460.

[36] Jackel, Janet L., C. E. Rice, and J. J. Veselka.: *Proton exchange for high-index waveguides in $LiNbO_3$.*, Applied Physics Letters 41.7 (1982) 607-608.

[37] K. M. Davis *et al.*: *Writing waveguides in glass with a femtosecond laser*, Opt. Lett. 21 (21), (1996) 1729

[38] D. K. Gramotnev and S. I. Bozhevolnyi: *Plasmonics beyond the diffraction limit,* Nature Photon. 4, (2010) 83

[39] Sirotek V. - *Kandidátská práce:* Studium přípravy a vlastností APE vlnovodů v niobičnanu lithném, 1995

[40] Nekvindová P. - *Disertační práce*: Studium optických vrstev v niobičnanu lithném 1999

[41] Salavcová L. - *Disertační práce*: Málovidové optické vlnovody pro použití v pasivních a aktivních fotonických strukturách, 2009

[42] Ondráček F. - D*iplomová práce*: Generace druhé hramonické v optických vlnovodech v KTP, 2002

[43] Třešňáková P. - *Disertační práce*: Optické vlnovody ve skleněných podložkách obsahujících ionty mědi, stříbra a erbia, 2003

[44] Salavcova, L., Svecova, B., Janakova S., Kolek, O., Mika, M., Spirkova, J., Langrova, A.: *Planar optical waveguides in newly developed Er: silicate glasses: A comparative study of K+ and Ag+ ion exchange*. Ceramics− Silikáty, 49(1), (2005) 53-57.

[45] Málek J. - *Diplomová práce*: Příprava a stusium vlastností optických planárních vlnovodů připravených iontovou výměnou ve speciálních silikátových sklech s různým obsahem erbia a ytterbia, 2009

[46] S. Staněk - *Diplomová práce*: Charakterizace optických vlastností vlnovodů v nových Zn-Er, Yb křemičitanových skel, 2011

[47] Svecova, B., et al.: *Ion-exchanged optical waveguides fabricated in novel Er 3+ and Er 3+/Yb 3+-doped silicate glasses: Relations between glass composition, basicity and waveguide properties.,* Materials Science and Engineering: B 149.2 (2008) 177-180.

[48] Kosíková J.- *Disertační práce*: Výukum vlnovodů na bázi výměny iontů K+- Na+ ve skleněných substrátech, 1996

[49] Salavcová L. - *Diplomová práce:* Příprava málovidových optických vlnovodů ve skle s využitím migrace Li+, 2003

[50] Salavcová, L., Nekvindová, P., Červena, J., Langrová, A., Drahoš, V., Špirková, J.. *Lithium migration based fabrication of few-modes planar glass waveguides*, Solid State Phenomena 90, (2003) 577-582.

[51] Drozd A - *Diplomová práce*: Vlnovody ve skleněných podložkách vytvořené iontovou výměnou v elektrickém poli, 1997

[52] Spirkova, J., Tresnakova, P., Malichova, H., Mika, M.: *Cu+ containing waveguiding layers in novel silicate glass substrates.* Journal of Materials Science: Materials in Electronics, 18(1), (2007) 375-378.

[53] Tresnakova, P., Malichova, H., Spirkova, J., Mika, M.: *Fabrication of optical layers containing Er (III) and Cu (I) in silicate glasses*. Journal of Physics and Chemistry of Solids, 68(5), (2007) 1276-1279.

[54] Altšmíd J. - *Diplomová práce*: Vliv vodivosti silikátových skel na proces ponořování optických vlnovodů v elektrickém poli, 2011

[55] Rebouta, L., Smulders, P. J. M., Boerma, D. O., Agulló-López, F., Da Silva, M. F., Soares, J. C. *Ion-beam channeling yields of host and impurity atoms in $LiNbO_3$: Computer simulations,* Physical Review B, 48(6), (1993) 3600.

[56] A. Meldrum, L. A. Boatner, W. J. Weber, R. C. Ewing: *Amorphization and recrystallization of the ABO_3 oxides*, J. Nucl. Mater. 300, 2–3 (2002) 242–254.

[57] P. D. Townsend, P. J. Chandler, L. Zhang, *Opt. Effects of Ion Implantation*, Cambridge University Press, 1994.

[58] V. V. Atuchin: *Causes of refractive indices changes in He-implanted $LiNbO_3$ and $LiTaO_3$ waveguides,* Nucl. Instr. and Methods in Phys. Res. Sect. B: Beam Inter. with Mat. and Atoms 168 (4), (2000) 498–502.

[59] P. Peterka, Vláknové lasery, Academia, 1. Vyd. 2014

[60] Della Valle, G., Festa, A., Sorbello, G., Ennser, K., Cassagnetes, C., Barbier, D., Taccheo, S. *Single-mode and high power waveguide lasers fabricated by ion-exchange*. Optics express, 16(16), (2008)12334-12341.

[61] I.Pelant, J.Valenta: *Luminiscenční spektroskopie*, Academia 2006

[62] Hauglie-Hanssen, C., & Djeu, N.: *Further investigations of a 2-μm Tm: YVO 4 laser. Quantum Electronics,* IEEE Journal of, 30(2), (1994) 275-279.

[63] Lee, C. J., Han, G.,Barnes, N. P.: *Ho: Tm lasers. II. Experiments*. Quantum Electronics, IEEE Journal of, 32(1), (1996) 104-111.

[64] Bourdet, G. L., and G. Lescroart : *Theoretical modelling and design of a Tm: YVO 4 microchip laser,* Optics communications 149.4 (1998): 404-414.

[65] Walsh, B. M., Barnes, N. P., Reichle, D. J., Jiang, S.: *Optical properties of Tm^{3+} ions in alkali germanate glass.* Journal of non-crystalline solids, 352(50), (2006) 5344-5352.

[66] A.J. Kenyon, Prog. *Quant. Electron.* 26 (2002)

[67] X. Feng, S. Tanabe, T. Hanada, *J. Non-Cryst. Solids* 281 (2001)

[68] A. Kozanecki, B.J. Sealy, K. Homewood, *J. Alloy. Compd*. 300-301 (2000)

[69] J. Ruan, E. Wu, H.P. Zeng, et al.: *Enhanced broadband near-infrared luminescenceand optical amplification in Yb-Bi codoped phosphate glasses*, Applied Physics Letters vol. 92,(2008) 101121,

[70] Y. Guang, C. Danping, R. Jing, et al.: *Effects of melting temperature on the broadband infrared luminescence of bi-doped and Bi/Dy co-doped chalcohalide glasses*, Journal of the American Ceramic Society, 90 (11) (2007) 3670-3672.

[71] J. Ruan, G.P. Dong, X.F. Liu, et al.: *Enhanced broadband near-infrared emission and energy transfer in Bi-Tm-codoped germanate glasses for broadband optical amplification*, Optics Letters 34 (16) (2009) 2486-2488.

[72] Amin, J., et al.: *Spectroscopic analysis of Er^{3+} transitions in lithium niobate* Journal of Luminescence 69.1 (1996) 17-26.

[73] Pujol, Maria Cinta, et al.: *Crystalline structure and optical spectroscopy of Er^{3+}-doped $KGd(WO_4)_2$ single crystals.,* Applied Physics B 68.2 (1999) 187-197.

[74] Li, Chun, et al.: *Spectral Properties and Parameters Calculation of Er: $LiGdF_4$ Crystal* Materials Sciences and Applications 2.08 (2011) 1161.

[75] A. A. Kaminskii, A. G. Petrosyan, Denisenko, Butaeva, Fedorov Sarkisovdoi: *Spectrosco pic Properties and 3 μm Stimulated Emission of Er^{3+} ions in the (Y1-xErx)$_3Al_5O_{12}$ and (Lu1-xEr_3)$_3Al_5O_{12}$ Garnet Crystal Systems:* Physica Status Solidi (A), Vol. 71, No. 2, 1982, pp. 291-312.

[76] Tanabe,S.: *Rare-earth-doped glasses for fiber amplifiers in broadband telecommunication*. Comptes Rendus Chimie, 5(12), (2002) 815-824.

[77] Kenyon, A. J.: *Erbium in silicon*, Semiconductor Science and Technology 20.12 (2005)

[78] Lorenzo, A.; Jaffrezic, H.; Roux, B.; Boulon, G.; García-Solé, J. *Lattice location of rare-earth ions in $LiNbO_3$.* Appl. Phys. Lett. 67 (25), (1995) 3735–3737.

[79] Mignotte, C.: *Determination of lattice site locations of erbium ions implanted into $LiNbO_3$ single crystals after annealing at moderate and high temperature.* Applied Surface Science 185 (1-2), **(2001)** 11–26.

[80] Rebouta, L.; da Silva, M. F.; Soares, J. C.; et al.: *Nonaxial sites for Er in $LiNbO_3$,* Applied Physics Letters 70 (9), (1997) 1070–1072.

[81] Macková, A. Groetzschel, R. Eichhorn, F. Nekvindová, P. Špirková, J.: *Characterization of Er:$LiNbO_3$ and APE:Er:$LiNbO_3$ by RBS–channeling and XRD techniques*. Surface and Interface Analysis 36, (2004) 949–951.

[82] Gog, T., Griebenow, M. Materlik, G.: *X-ray standing wave determination of the lattice location of Er diffused into $LiNbO_3$.* Physics Letters A 181 (5), (1993) 417–420.

[83] Baumann, I., Brinkmann, R., Dinand, M., Sohler, W., Beckers, L.; Buchal, Ch.; et al. *Erbium incorporation in $LiNbO_3$ by diffusion-doping,* Applied Physics A, 64, (1997) 33–44.

[84] Fleuster, M., Buchal, Ch., Snoeks, E., Polman, A. *Optical and structural properties of MeV erbium-implanted $LiNbO_3$,* Journal of Applied Physics 75 (1), (1994) 173–180.

[85] Polman A.: *Erbium implanted thin film photonic materials*, J. Appl. Phys. 82 (1997)

[86] E. Alves, M. F. da Silva, J. C. Soares, T. Manteiro, J. Soares, L.: *Santos Effect of crystal orientation on defect production and optical activation of Er-implanted sapphire*, Nucl Instrum Meth B 166-167 (2000), 183-187

[87] G.N. van den Hoven, A. Polman, E. Alves, M.F. da Silva. A.A. Melo, J.C. Soares, J.: *Lattice site and photoluminescence of erbium implanted in α–Al_2O_3,* Mater. Res. 12 (1997), 1401

[88] Alves, E., Da Silva, M. F., Van Den Hoven, G. N., Polman, A., Melo, A. A., Soares, J. C.: *Incorporation and stability of erbium in sapphire by ion implantation*, Nuclear Instruments and Methods in Physics Research Section B: Beam Interactions with Materials and Atoms, 106(1), (1995) 429-432.

[89] Jadwisienczak, W. M., Lozykowski, H. J., Xu, A.,Patel, B.: *Visible emission from ZnO doped with rare-earth ions,* Journal of electronic materials, 31(7), (2002) 776-784.

[90] Özgür, Ü., Alivov, Y. I., Liu, C., Teke, A., Reshchikov, M., Doğan, S., Morkoc, H.: *A comprehensive review of ZnO materials and devices.* Journal of applied physics, 98(4), (2005) 041301.

[91] Cho, H. Morkoc, J. Appl. Phys. 98 (2005) 041301.

[92] Castañeda, L., Morales-Saavedra, O. G., Acosta, D. R., Maldonado, A., Olvera, M. D. L. L.: *Structural, morphological, optical, and nonlinear optical properties of fluorine-doped zinc oxide thin films deposited on glass substrates by the chemical spray technique.* PHYSICA STATUS SOLIDI A APPLICATIONS AND MATERIALS SCIENCE, 203(8), (2006) 1971.

[93] Karthikeyan, B., Sandeep, C. S., Pandiyarajan, T., Venkatesan, P., Philip, R.: *Optical and nonlinear absorption properties of Na doped ZnO nanoparticle dispersions Applied* Physics Letters, 95(2), (2009) 023118.

[94] Kumari, Vinay, et al.: *Nonlinear optical properties of erbium doped zinc oxide (EZO) thin films,* Optics Communications 285.8 (2012) 2182-2188.

[95] Zhou, S., Potzger, K., Von Borany, J., Grötzschel, R., Skorupa, W., Helm, M., , Fassbender, J., *Crystallographically oriented Co and Ni nanocrystals inside ZnO formed by ion implantation and postannealing,* Physical Review B, 77(3), (2008). 035209.

[96] S.I. Najafi, Introduction to Glass Integrated Optics, Artech House, Boston-London, 1992.

[97] Enrichi, F., Mattei, G., Sada, C., Trave, E., Pacifici, D., Franzò, G., Borsella, E.: *Evidence of energy transfer in an aluminosilicate glass codoped with Si nanoaggregates and* Er^{3+} *ions*. Journal of applied physics, 96(7), (2004) 3925-3932.

[98] Palpant, Bruno : *Third-order nonlinear optical response of metal nanoparticles Non-Linear Optical Properties of Matter*, Springer Netherlands, 2006. 461-508.

[99] Shin, Jung H., et al.: *Si nanocluster sensitization of Er-doped silica for optical amplet using top-pumping visible LEDs.,* Selected Topics in Quantum Electronics, IEEE Journal of 12.4 (2006): 783-796.

[100] Kozanecki, A., Sealy, B. J., Homewood, K.: *Excitation of* Er^{3+} *emission in Er, Yb codoped thin silica films,* Journal of alloys and compounds, 300, (2000) 61-64.

[101] Zhang, W., Lin, J., Cheng, M., Zhang, S., Jia, Y.,Zhao, J.: *Radiative transition, local field enhancement and energy transfer microcosmic mechanism of tellurite glasses containing* Er^{3+}, Yb^{3+} *ions and Ag nanoparticles.* Journal of Quantitative Spectroscopy and Radiative Transfer, 159, (2015) 39-52.

[102] MIKA M; SPIRKOVA J; LAHODNY F; et al., Optical sodium-aluminum-silicate glass for photonic components, comprises silica, sodium oxide, alumina and metal oxide, where metal oxide is selected from zinc oxide, magnesium oxide, calcium oxide and bismuth oxide ,Patent Number: CZ201200063-A3; CZ303762-B6, Patent Assignee: VYSOKA SKOLA CHEM TECH

[103] MIKA M; STANEK S; NEKVINDOVA P; et al., Optical luminescent sodium-aluminum-silicate glass for photonic components, comprises silica, sodium oxide, alumina and metal oxide, where metal oxide is selected from magnesium oxide, calcium oxide and zinc oxide , Patent Number: CZ201200064-A3; CZ303767-B6 , Patent Assignee: VYSOKA SKOLA CHEM TECH

[104] O. Kolek.- *Diplomová práce*: Skla pro aktivní optické vlnovody obsahující erbium, VŠCHT, 2003

[105] Svecova, B., et al.: *Ion-exchanged optical waveguides fabricated in novel Er 3+ and Er 3+/Yb 3+-doped silicate glasses: Relations between glass composition, basicity and waveguide propertie,* Materials Science and Engineering: B 149.2 (2008): 177-180.

[106] Salavcova L., et al.: *Formation of optical waveguides in specially designed Er-and Yb-containing silicate glasses by Ag^+/Na^+ ion exchange,* CERAMICS SILIKATY 50.3 (2006) 130.

[107] Salavcova L., et al.: *Channel optical waveguides in various silicate glasses—optimalization of their parameters,* Journal of Materials Science: Materials in Electronics 18.1 (2007): 371-373.

[108] Capek, P., et al.: *Effect of divalent cations on properties of Er 3+-doped silicate glasses,* Optical Materials 27.2 (2004): 331-336.

[109] Ondráček F. et al.: *Er–Yb waveguide amplifiers in novel silicate glasses,* Quantum Electronics, IEEE Journal of 44.6 (2008): 536-541.

[110] Jágerská, J., et al..: *Er–Yb waveguide amplifiers in novel silicate glasses,* 13th Eur. Conf. Integrated Optics ECIO. 2007.

[111] A. Polman, Appl. : *Erbium implanted thin film photonic materials*, Journal of Applied Physics 82.1 (1997): 1-39.

[112] Hausecroft C.E., Sharpen A.G., Anorganická Chemie,VŠCHT Praha, 2014

[113] M. Mattarelli, S. Sebastiani, J. Spirkova, S. Berneschi, M. Brenci, R. Calzolai, A. Chiasera, M.Ferrari, M. Montagna, G. Nunzi Conti, S. Pelli, G.C. Righini, *Characterization of erbium doped lithium niobate crystals and waveguides*, Optical Materials, 28(11), (2006). 1292-1295.

[114] Choi, C. G., Han, S. P., & Jeong, M. Y. *Two-dimensional polymeric optical waveguides for high-density parallel optical interconnection.* Optics communications, 235(1), (2004) 69-73.

[115] Gonella F.: Silver doping of glasses, Ceramics International 41 (5) (2015) 6693–6701

[116] Findakly, T.: *Glass waveguides by ion exchange: a review*, Optical engineering 24.2 (1985): 242244-242244.

[117] Borca, C. N., Apostolopoulos, V., Gardillou, F., Limberger, H. G., Pollnau, M., Salathé, *R. P. Buried channel waveguides in Yb-doped KY (WO 4) 2 crystals fabricated by femtosecond laser irradiation. ,* Applied surface science, 253(19), (2007) 8300-8303.

[118] Özcan, L. Ç., Guay, F., Kashyap, R., Martinu, L. *Fabrication of buried waveguides in planar silica films using a direct CW laser writing technique*, Journal of non-crystalline solids, 354(42), (2008) 4833-4839.

[119] Matusita, K., Mackenzie, J. D., *Improvement of chemical durability of high expansion glasses by ion exchange,* Journal of Materials Science, 13(5), (1978) 1026-1030.

[120] Townsend, P.D. - Kelly, J.C. - Hartley, N.E.W.: Ion Implantation , Sputtering and Their Applications, Academic Press, London, 1976

[121] E. Ryssel, H.Glawisching, Ion Implantation Techniques. Spinger-Verlag, Berlin 1988

[122] Mayer, J.W., Eriksson, L., Davies, J.A.: Ion Implantation in Semiconductors. Academic Press, New York 1970

[123] P. D. Townsend, P. J. Chandler, L. Zhang, *Opt. Effects of Ion Implantation*, Cambridge University Press, 1994.

[124] Perina, V; Vacik, J; Hnatovicz, V., Cervena, J., Kolarova, P., Spirkova-Hradilova, J., Schrofel, J.: *RBS measurement of depth profiles of erbium incorporated into lithium niobate for optical amplifier applications,* NUCLEAR INSTRUMENTS & METHODS IN PHYSICS RESEARCH SECTION B-BEAM INTERACTIONS WITH MATERIALS AND ATOMS 139 (1-4), (1998) 208.

[125] Sada, C., et al.: *Erbium doping of $LiNbO_3$ by the ion exchange process*., Applied physics letters 72.26 (1998) 3431-3433.

Seznam původních publikací zařazených do habilitační práce

[P1] Spirkova-Hradilova J; **Nekvindova, P**; Vacik, J;Cervena, J., Schrofel, J.: The possibility of tailoring the n(e) vs c(Li) relationship in lithium niobate optical waveguides, OPTICAL MATERIALS 15 (4) (2001) 269-278

[P2] Dostalek, J; Ctyroky, J; Homola, J., Brynda, E., Skalsky, M., **Nekvindova, P.,** Spirkova, J., Skvor, J., Schrofel, J. : Surface plasmon resonance biosensor based on integrated optical waveguide,SENSORS AND ACTUATORS B-CHEMICAL 76 (1-3) (2001) 8-12

[P3] **Nekvindova, P;** Spirkova, J; Vacik, J; Cervena, J., Perina, V., Schrofel, J.: Importance of crystal structure of the substrate for diffusion technologies of waveguides fabrication, INTERNATIONAL JOURNAL OF INORGANIC MATERIALS 3 (8) (2001) 1245-1247

[P4] **Nekvindova, P**; Spirkova, J; Cervena, J; Budnar, M., Razpet, A., Zorko, B., Pelicon, P. Annealed proton exchanged optical waveguides in lithium niobate: differences between the X- and Z-cuts, OPTICAL MATERIALS 19 (2) (2002) 245-253

[P5] **Nekvindova, P**; Cervena, J; Capek, P, Mackova, A., Perina, V., Schrofel, J., Spirkova, J: Features of APE waveguides in different Er : $LiNbO_3$ and (Er+Yb): $LiNbO_3$ cuts: electrooptical coefficient $r_{(33)}$), OPTICAL MATERIALS 24 (3) (2003) 527-535

[P6] Mackova, A; Groetzschel, R; Eichhorn, F; et al., Characterization of Er:$LiNbO_3$ and APE : Er:$LiNbO_3$ by RBS-channeling and XRD techniques, SURFACE AND INTERFACE ANALYSIS 36 (8) (2004) 949-951

[P7] Malinsky, P.; Mackova, A.; Bocan, J., Svecova, B., **Nekvindova, P.:** Au implantation into various types of silicate glasses, Au implantation into various types of silicate glasses, NUCLEAR INSTRUMENTS & METHODS IN PHYSICS RESEARCH SECTION B-BEAM INTERACTIONS WITH MATERIALS AND ATOMS 267 (8-9) (2009) 1575-1578.

[P8] Svecova, B.; **Nekvindova, P.;** Mackova, Oswald, J., Vacik, J., Groetzschel, R. ;Spirkova, J.: Conference: NUCLEAR INSTRUMENTS & METHODS IN PHYSICS RESEARCH SECTION B-BEAM INTERACTIONS WITH MATERIALS AND ATOMS 267 (8-9) (2009) 1332- 1335.

[P9] Mackova, A.; Malinsky, P.; Svecova, B., **Nekvindova, P.**, Groetzschel, R.: Study of Er^+ ion-implanted lithium niobate structure after an annealing procedure by RBS and RBS/channelling, NUCLEAR INSTRUMENTS & METHODS IN PHYSICS RESEARCH SECTION B-BEAM INTERACTIONS WITH MATERIALS AND ATOMS 268 (11-12) (2010) 2042-2045.

[P10] Svecova, B.; **Nekvindova, P.;** Mackova, Malinsky, P., Kolitsch, A., Machovic, V., Stara, S., Mika, M., Spirkova: Study of Cu^+, Ag^+ and Au^+ ion implantation into silicate glasses, JOURNAL OF NON-CRYSTALLINE SOLIDS 356 (44-49 (2010) 2468-2472

[P11] Cajzl, J., **Nekvindova, P**., Svecova, B., Spirkova, J., Mackova, A., Malinsky, P., Vacik, J., Oswald, J. and Kolitsch, A. (2012), in Advances and Applications in Electroceramics II: Ceramic Transactions, Volume 235 (eds K. M. Nair and S. Priya), John Wiley & Sons, Inc., Hoboken, NJ, USA.

[P12] **Nekvindova, P.**; Svecova, B.; Cajzl, J., Mackova,Malinsky, P.,Oswald, J.,Kolistsch, A., Spirkova, J.; Erbium ion implantation into different crystallographic cuts of lithium niobate, OPTICAL MATERIALS 34 (4) (2012) 652-659

[P13] Husinsky, W.; Ajami, A.; **Nekvindova, P.**, Svecova, B., Pesicka, J., Janecek, M.: Z-scan study of nonlinear absorption of gold nano-particles prepared by ion implantation in various types of silicate glasses, OPTICS COMMUNICATIONS 285 (10-11) (2012) 2729-2733

[P14] Prajzler, V.; Varga, M.; **Nekvindova P.,**Remes Z., Kromka A.: Design and investigation of properties of nanocrystalline diamond optical planar waveguides OPTICS EXPRESS 21 (7) (2013) 8417-8425

[P15] Cajzl, J.; **Nekvindova, P**.; Svecova, B.; Mackova, A.,Malinsky, P., Oswald, J.,Vacik, J., Spirkova, J.): Electric field-assisted erbium doping of LiNbO3 from melt , SCRIPTA MATERIALIA 68 (9) (2013) 739-742

[P16] Jelinek, M.; Oswald, J.; Kocourek, T, Rubesova, K., **Nekvindova, P**.,Chvostova, D., Dejneka, A.); Zelezny, V., Studnicka, V.,Jurek, K.: Optical properties of laser-prepared Er-and Er,Yb-doped $LiNbO_3$ waveguiding layers , LASER PHYSICS 23 (10) (2013)

[P17] Jakes, V.; Rubesova, K.; Erben, J., **Nekvindova, P.**, Jelinek, M.: Modified sol-gel preparation of $LiNbO_3$ target for PLD, OPTICAL MATERIALS 35 (12) (2013) 2540-2543

[P18] **Nekvindova, P.**; Cajzl, J.; Svecova, B., Mackova, A., Malinsky, P.,Oswald, J.,**,** Vacik J., Spirkova, J.: Erbium diffusion from erbium metal or erbium oxide layers deposited on the surface of various $LiNbO_3$ cuts , OPTICAL MATERIALS 36 (2) (2013) 402-407 .

[P19] Mackova, A.; Malinsky, P.; Pupikova, H., **Nekvindova, P**.; Cajzl, J.; Sofer, Z.; Wilhelm, R. A.); Kolitsch, A.; Oswald, J.: The structural changes and optical properties of $LiNbO_3$ after Er implantation using high ion fluencies , NUCLEAR INSTRUMENTS & METHODS IN PHYSICS RESEARCH SECTION B-BEAM INTERACTIONS WITH MATERIALS AND ATOMS 332 (2014) 74-79

[P20] Mackova, P. Malinsky, H. Pupíková, P.Nekvindová, J. Cajzl, B. Svecová, J. Oswald, R.A. Wilhelm, A. Kolisch; A comparison of the structural changes and optical properties of $LiNbO_3$, Al_2O_3 and ZnO after Er^+ ion implantation; NUCLEAR INSTRUMENTS & METHODS IN PHYSICS RESEARCH SECTION B-BEAM INTERACTIONS WITH MATERIALS AND ATOMS 331 (2014) 182-186

[P21] Hlasek, T., Rubesova K., Jakes J., **Nekvindova, P**. Oswald J., Kucera M., Hanus, M: Influence of gallium on infrared luminescence in Er^{3+}doped Yb_3A_{l5}-$yGayO_{12}$ films grown by the liquid phase epitaxy, JOURNAL OF LUMINESCENCE 164 (2015) 90-93

[P22] Cajzl J., Nekvindová P., Macková A., Malinský P., Oswald J., Staněk S., Vytykáčová S. and Špirková : Optical waveguides in Er:$LiNbO_3$ fabricated by different techniques – a comparison, *submited to the Optical Materials*

ELSEVIER

Optical Materials 15 (2001) 269–278

OPTICAL Materials

www.elsevier.nl/locate/optmat

The possibility of tailoring the n_e vs c_{Li} relationship in lithium niobate optical waveguides

Jarmila Špirková-Hradilová [a,*], Pavla Nekvindová [a], Jiří Vacík [b], Jarmila Červená [b], Josef Schröfel [c]

[a] *Department of Inorganic Chemistry, Institute of Chemical Technology, Technicka 5, 166 28 Prague, Czech Republic*
[b] *Department of Neutron Physics, Nuclear Physics Institute, Academy of Sciences of the Czech Republic, 250 68 Řež, Czech Republic*
[c] *Department of Microelectronics, Faculty of Electrical Engineering, Czech Technical University, 166 27 Prague, Czech Republic*

Received 19 June 2000; accepted 10 July 2000

Abstract

We present results of our study of concentration profiles of lithium (c_{Li}) in annealed proton exchanged (APE) waveguiding layers as measured by the neutron depth profiling (NDP) method. This non-destructive method, based on the $^6Li(n,\alpha)^3H$ reaction induced by thermal neutrons, allowed easy monitoring of c_{Li} profiles in a large number of samples fabricated under various fabrication conditions. Our systematic study revealed that, though every particular waveguide could be characterised by very similar mirror-shaped extraordinary refractive index (n_e) as well as c_{Li} depth profiles, in contrast with up to now generally accepted opinion, there was no linear relationship which unambiguously attributed Δn_e to Δc_{Li}. The most important fabrication step appeared to be the post-exchange annealing, during which the lithium atoms were transported towards the sample surfaces. The annealing regime pre-destined not only the depth distribution of the lithium atoms but, as a consequence of it, also other properties of the waveguiding region. That knowledge allows us to fabricate the APE waveguides with a priori given properties for a wide range of special applications. We have also formulated the n_e vs c_{Li} semi-empirical relationship, which was proved to fit all our fabricated APE waveguides.

PACS: 42.79.Gn; 82.65.Fr; 52.40.Hf; 41.75.Ai; 81.70.Jb

Keywords: Lithium niobate; Optical waveguides; Annealed proton exchange (APE); Lithium concentration profiles; Neutron depth profiling

1. Introduction

The proton exchange technique of fabrication of optical waveguides in lithium niobate single crystalline wafers is based on a reaction between the surface of the wafers with an appropriate proton source:

$$LiNbO_3 + xH^+ \rightarrow Li_{1-x}H_xNbO_3 + xLi^+.$$

The as-exchanged waveguides have a large increase of the extraordinary refractive index value ($\Delta n_e \leqslant +0.12$); however, they are not stable and their electro-optic properties, represented by the coefficient r_{33}, are degraded almost to zero. To restore the value and to stabilise the waveguide

* Corresponding author. Fax: +42-0-2-311-2206.
E-mail address: jarmila.spirkova@vscht.cz (J. Špirková-Hradilová).

0925-3467/01/$ - see front matter
PII: S0925-3467(00)00042-2

properties, a second fabrication step, annealing (A), is necessary.

Proton exchanged optical waveguides in lithium niobate have been intensively studied since their discovery in 1982 [1]. The possibility of easy fabrication of the low-loss waveguides with a high threshold of optical damage allows for their applications in a large range of integrated optics devices such as polarisers, switches, splitters, electro-optic frequency shifters, etc. Another very promising application is in sensitive sensor structures based on few-mode waveguides with strong evanescent fields. For better tailoring of the waveguide parameters for any kind of applications, a good knowledge of the relationship between optical properties and composition of the waveguiding region is highly helpful.

Secondary ion mass spectrometry (SIMS) has already been used [2–9] to profile concentrations of incorporated hydrogen as well as concentrations of lithium remaining in the treated layers. The results of the published measurements indicate a strong correlation between the extraordinary refractive index (n_e) depth profiles and lithium concentration (c_{Li}) profiles. However, the small number of the measured samples does not allow for any precise considerations on interrelations between both (n_e and c_{Li}) parameters. Much more attention has been paid to the correlation of concentration profiles of incorporated hydrogen with the refractive index profiles, but these results lead to diverging conclusions.

Recently, several papers appeared dealing with the crystal structure of proton exchanged (PE) and annealed proton exchanged (APE) layers [9–11]. The authors identified as many as seven different crystalline phases that may exist, according to the fabrication conditions, in the waveguiding region. No doubt that many discrepancies between the published results may be explained on the basis of different crystalline structures of the fabricated waveguides.

We present the results of our systematic study of distributions of lithium atoms in PE as well as APE optical waveguides fabricated under a large variety of experimental conditions. For this, neutron depth profiling (NDP) measurement is a perfect tool that enables us to characterise a large number of samples. For understanding the studied relationship better, we show, in this paper, some typical examples of the results obtained for Z-cut wafers, which may help us to explain the most important features of the problem. General conclusions are then made on the basis of all the obtained results gained by the measurement of more than 300 samples of the Z- as well as the X-cuts. All of the measured samples have been characterised with their fabrication conditions, the extraordinary refractive index (n_e) depth profiles and the lithium concentration (c_{Li}) depth profiles in the waveguiding regions. In this paper, we do not present any considerations on the concentrations of the in-diffused hydrogen. However, we have made some necessary ERDA and IR reflection spectra measurements in order to get some basic information on the behaviour of hydrogen (or OH groups) in the treated layers. The results are not in contradiction with the presented considerations on the behaviour of lithium and they will be published later in another paper.

2. Experimental approach

2.1. Fabrication of the samples (proton exchange PE and post-exchange annealing A)

The samples used in the experiments were congruent, Z-cut, lithium niobate ($LiNbO_3$) wafers polished on one side, with typical dimensions of $25 \times 5 \times 0.7\ mm^3$. The thoroughly pre-cleaned samples were mounted in platinum holders and placed in individual silica or platinum beakers that contained the reaction melt consisting of pure or lithium-salt-containing adipic acid [1]. The heating source was an ordinary laboratory oven. The PE waveguides were fabricated at a temperature of 213°C for times ranging from 30 min to 6 h. (The setting of the temperature of the reaction melt at 213°C comes from our experiments on the com-

[1] Adipic acid ($HOOC–(CH_2)_4–COOH$) is similar to benzoic acid (which is usually used for proton exchange) in acidity, but it is a non-toxic, safe to use and an environmentally much more friendly proton source than benzoic acid [12,13].

position of the reaction melt. According to our thermodynamic considerations, at a temperature of about 210°C the concentration of H_3O^+ ions in the reaction melt is highest, which makes the proton exchange process at this temperature progress most efficiently. Using either lower or higher temperatures of the reaction melt than approximately 210°C resulted in fabrication of PE waveguides which had smaller Δn_e and supported less numbers of modes. These results will be published in detail elsewhere.) The as-exchanged samples were immediately washed with distilled water and acetone in order to remove the remnants of the reaction melt, and then they were annealed at temperatures ranging from 250°C to 500°C for various time periods (30 min to 100 h) in another laboratory oven under ambient atmosphere. The annealing was usually done immediately after the proton exchange.

2.2. Measurement

The waveguides were optically characterised at $\lambda = 633$ nm using the prism coupling technique. The extraordinary refractive index (n_e) depth profiles of the fabricated waveguides were reconstructed from the effective index spectra by means of the inverse WKB procedure [14], using piecewise linear approximation to the actual index profiles.

Lithium concentration depth profiles (c_{Li}) in the as-exchanged as well as post-exchanged annealed waveguides were measured by NDP [15,16]. The method is based on the reaction of thermal neutrons with ^{6}Li: ^{6}Li(n,α)^{3}H. The fabricated samples were irradiated with a thermal neutron beam from a 6 m long neutron guide (the neutron intensity was 10^7 neutrons cm^{-2} s^{-2}) and the charged reaction products were recorded by means of an Si(Au) surface barrier detector. The accuracy of the NDP method was 5% of the c_{Li} value and the depth resolution was 10 nm. Thus, the absolute values of concentrations of lithium, as presented in c_{Li} depth profiles in the diagrams, represent, in fact, the concentrations of ^{6}Li. The natural abundance of the "NDP active" ^{6}Li isotope is 7.5%; however, in the actual samples, the ^{6}Li/^{7}Li ratio may significantly vary (e.g., due to artificial depletion of the ^{6}Li isotope from the original natural materials). Thus, to avoid uncertainty induced by this variation, for some considerations, we rely on relative changes of c_{Li} instead of absolute values.

3. Results and discussion

3.1. n_e and c_{Li} depth profiles

The NDP lithium concentration (c_{Li}) profiles of the as-exchanged waveguides are presented in Figs. 1 and 2. Fig. 1 clearly shows a difference between the guides fabricated using pure and lithium-containing (buffered) reaction melts for the same time of the proton exchange (4 h). When the pure adipic acid was used, practically all the lithium was "washed out" from the sample surfaces. After using lithium-containing adipic acid as the reaction melt, much more lithium (30–40%) was always found in the surfaces of much shallower (1 μm in Fig. 1) exchanged layers. Longer times of the proton exchange reaction resulted in fabrication of deeper PE waveguides (Fig. 2), but the depths of the as-exchanged layers in our experiments never exceeded 3 μm. The shapes of both the functional depth profiles, c_{Li} and n_e, always had a step-like character and the as-exchanged waveguides supported, according to their fabrication conditions, one, two or three modes. The depths of the waveguides estimated from the mode

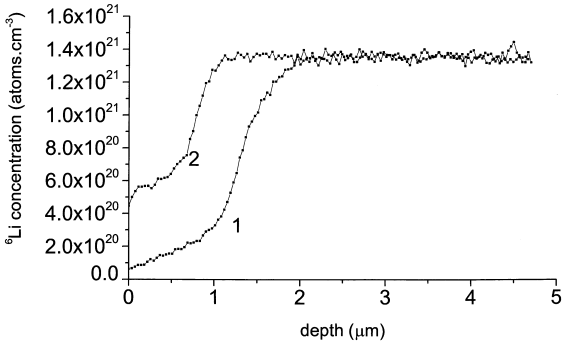

Fig. 1. Lithium concentration depth profiles of the Z-cuts as-exchanged (4 h) in pure (1) and lithium (0.5 mol%)-containing (2) adipic acid.

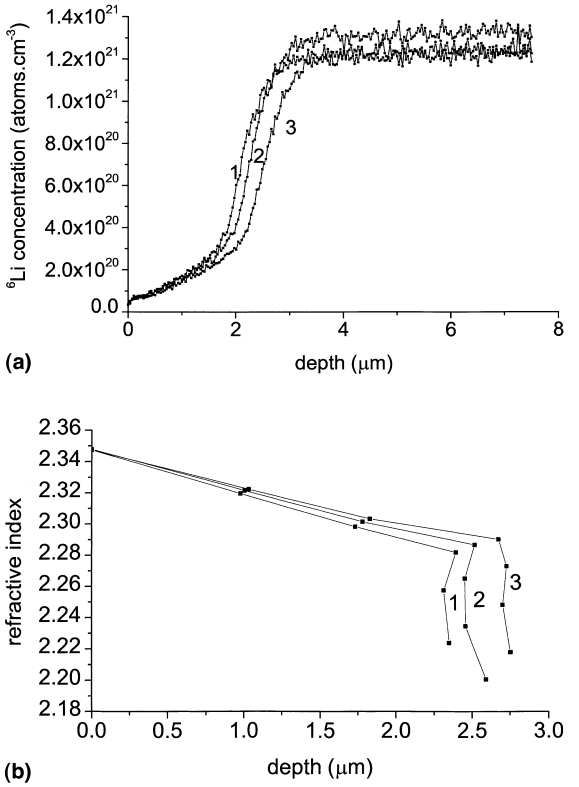

Fig. 2. c_{Li} (a) and n_e (b) depth profiles of the Z-cuts as-exchanged 4 h (1), 5 h (2) and 6 h (3) in pure adipic acid.

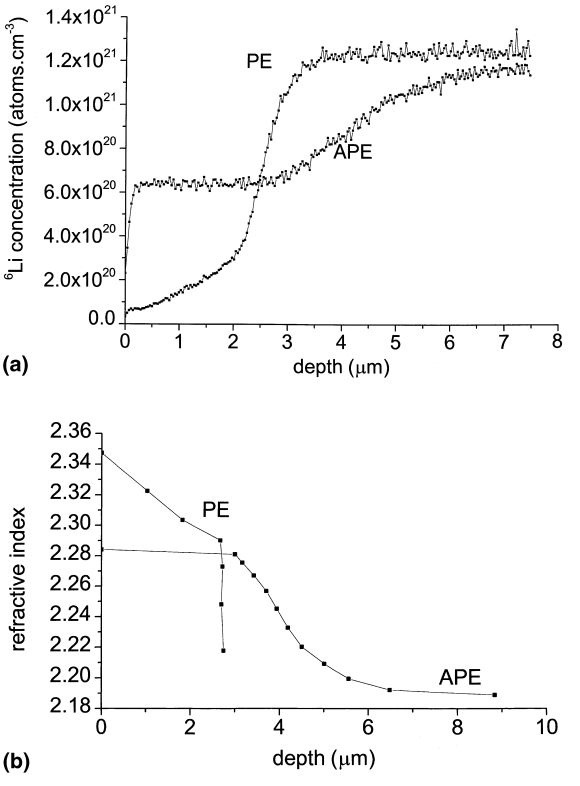

Fig. 3. c_{Li} (a) and n_e (b) depth profiles of the as-exchanged (PE) and annealed (APE) Z-cut (PE: 4 h, lithium-containing adipic acid; A: 1.5 h, 350°C).

spectroscopy measurement corresponded well to those obtained by the NDP measurement.

Generally, the as-exchanged waveguides suffer from high optical loss and degradation of their electro-optical properties as well as poor stability of their optical properties. It is well known that these drawbacks can be easily overcome by post-exchange annealing, during which the incorporated hydrogen diffuses deeper into the substrate (see [2–9]). However, much less is known about the behaviour of lithium during annealing.

The shapes of both the profiles, n_e as well as c_{Li}, dramatically change when the as-exchanged samples are annealed in ambient atmosphere (see Fig. 3). We have observed the well-known transition of the shapes of the n_e as well as c_{Li} profiles from step-like for the PE waveguides to graded after annealing the sample, indicating, thus, a massive transport of lithium ions towards the samples surfaces. The total amount of out-diffused lithium is determined by the first fabrication step, the proton exchange reaction, but its concentration in the exchanged layer is gradually supplemented by the consequent diffusion of lithium from the bulk substrate. Thus, the resulting concentrations of lithium on the surfaces of the annealed waveguides depend strongly on the regime of annealing.

Fig. 4(a) shows the c_{Li} profiles of the annealed (APE) waveguides that were fabricated from the pure adipic acid for various times of the proton exchange reaction and then annealed for 1.5 h at 350°C. Refractive index depth profiles of the waveguides in Fig. 4(b) very clearly show two different types of waveguides (graded index for the waveguides with shorter proton exchange (1–3) and step-like ones for the waveguides fabricated by the longer proton exchange (4–6)). This trend is less evident for the lithium concentration profiles,

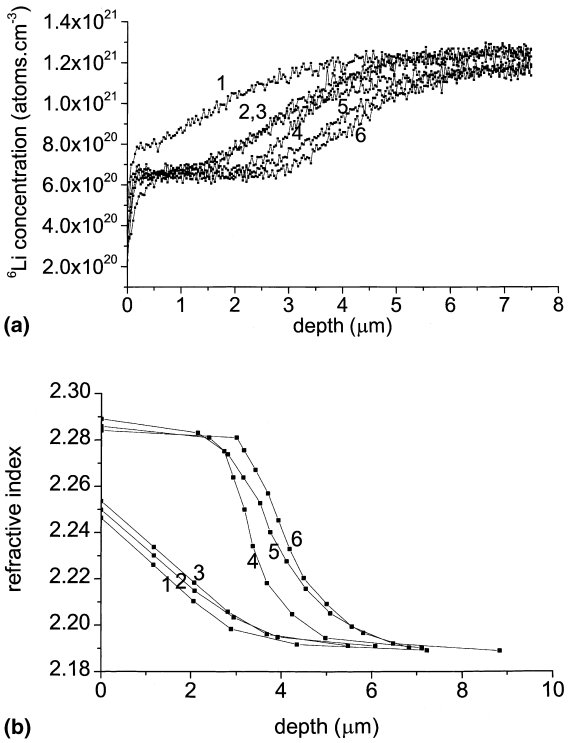

Fig. 4. c_{Li} (a) and n_e (b) depth profiles of the APE waveguides proton exchanged for various times in pure adipic acid [PE: 1 h (1), 2 h (2), 3 h (3), 4 h (4), 5 h (5) and 6 h (6); A: 1.5 h at 350°C].

the shapes of which reflect a smooth, slow movement of the lithium ions towards the surface of the samples. Longer times of the proton exchange reaction mean also longer times for re-establishing the stable structure of the exchanged layer so that, in fact, there are two diffusion processes which occur at practically same time: (a) exchange of lithium for hydrogen from the reaction melt and (b) further progression of lithium via the sample surfaces, which may be also considered as the next step in the exchange of lithium for the already indiffused hydrogen in the outermost surface layers of the samples.

From the NDP measurement, it follows that, in the annealed waveguides, there exist several compositional phases which are relatively stable. One of them is formed during the annealing in the surfaces of the samples and is characterised by a concentration of ^{6}Li of approximately 6×10^{20} atoms cm^{-3}, i.e., about 55% of the original amount

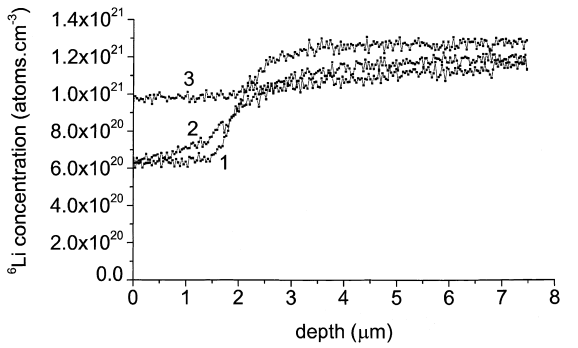

Fig. 5. Effect of post-exchange annealing (A) on c_{Li} depth profiles: various times of annealing [PE: 2 h in pure adipic acid; A: 300°C for 0.5 h (1), 24 h (2) and 100 h (3)].

of lithium remains in the surface. This phase was always found when the as-exchanged guides were annealed for 1.5 h at temperatures in the range of 300–350°C. Several examples of the formation of this compositional phase are given in Fig. 4(a) (c_{Li} profiles 2–6) and Fig. 5 (c_{Li} profiles 1 and 2). On the contrary, this generally obtained value of c_{Li} was not found for the samples annealed in air at relatively low temperatures (e.g., see c_{Li} profile 1 in Fig. 6 for the sample annealed 90 min at 250°C) or for the samples annealed at temperatures up to 350°C for very long times (e.g., the sample annealed for 100 h, see c_{Li} profile 3 in Fig. 5). A similar effect was also observed when the samples were annealed at temperatures higher than 350°C for relatively short times (curve 4 in Fig. 6).

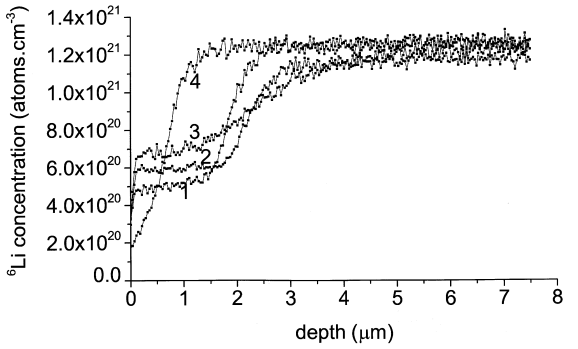

Fig. 6. Effect of post-exchange annealing (A) on c_{Li} depth profiles for various temperatures of annealing [PE: 2 h in pure adipic acid; A: 1.5 h at 250°C (1), 300°C (2), 350°C (3) and 450°C (4)].

The high mobility of lithium ions, owing to their very small size and partly ionic character, makes their movement through the lithium niobate structure easy when some energy is provided. In the first fabrication step, the proton exchange, transport of lithium ions occurs via the substitution of H^+ for Li^+, and the c_{Li} profiles of the as-exchanged samples are very similar to each other (see, e.g., Fig. 2(a)). The longer times of the proton exchange reaction result in the same concentration steps of the c_{Li} depth profiles, which differ only by the depths of the respective PE waveguides. The energy added later in the form of post-exchange annealing makes the lithium ions move again. Now, their movement is ruled predominantly by their high mobility via "empty" sites in the structure. It means that the annealing regime should be considered to be the most important parameter in the fabrication of waveguides with desired properties.

In Fig. 7, the extraordinary refractive index (n_e) depth profiles of the waveguides (the c_{Li} profiles of which are shown in Fig. 6) are compared. The similar surface concentrations of lithium correspond with the very similar surface n_e values of the respective guides. The significantly changed n_e profile of the guide annealed at 350°C (n_e profile 5) gives evidence of the importance of the annealing temperature and corresponds well with the findings of Korkishko and Fedorov [11]. The authors affirm that annealing at temperatures above 320°C results in dramatic changes of crystal structure of

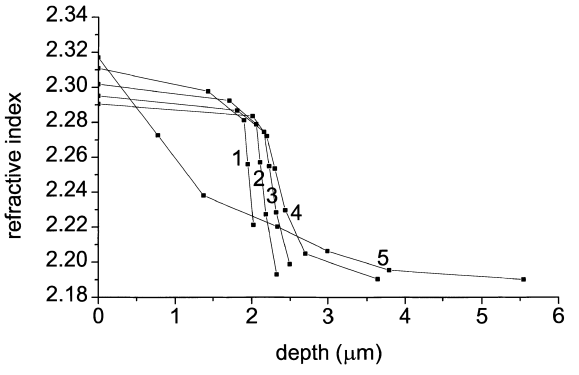

Fig. 7. Effect of post-exchange annealing (A) on evaluation of the n_e depth profiles for various temperatures of annealing [PE: 2 h in pure adipic acid; A: 1.5 h at 250°C (1), 275°C (2), 300°C (3), 325°C (4) and 350°C (5)].

the as-exchanged region which, in this particular case, leads to a transition from the step-like n_e depth profile to the graded one. The same trend is clearly demonstrated also by the c_{Li} profiles of the APE guides in Fig. 6, where the guide annealed at 350°C has graded character of lithium distribution (c_{Li} profile 3), in contrary to those annealed at lower temperatures. Annealing at 450°C (curve 4 in Fig. 6) completely destroyed the waveguiding properties of the sample. It means that, for better tailoring of waveguiding properties, it is highly recommendable to avoid using higher annealing temperatures and to rely, rather, on a slow redistribution of the lithium ions during the longer annealing procedures at lower temperatures.

3.2. Relationship between n_e and c_{Li}

In Fig. 8, we plot the n_e vs c_{Li} relationship for the as-exchanged (PE) and the post-exchange annealed (APE) samples fabricated from pure (a) and buffered (b) adipic acid. Obviously, the annealing removes, to a quite high extent, the differences in the refractive index values as well as the distribution of lithium ions in the as-exchanged layers, which were consequences of the different acidities of the reaction melts used for the proton exchange reaction. "Empty space" near the surfaces of PE layers, from which the lithium ions were washed out during the proton exchange, is now filled with lithium ions from deeper layers of the unchanged substrates. This effect is particularly evident for the waveguides that were proton exchanged in pure adipic acid. As will be demonstrated in the following, the shapes of the resulting n_e vs c_{Li} relationship of the APE waveguides can be easily influenced by the regime of annealing so that, for the same PE waveguides, it is, in principle, possible to obtain a variety of guides with different n_e vs c_{Li} relationships.

Figs. 9 and 10 show the effect of proton exchange times on the n_e vs c_{Li} relations in the annealed guides. The appearance of two types of n_e vs c_{Li} relations (step-like for the longer times of the "hard" exchange reaction in pure adipic acid and graded for "softer" fabrication conditions when short times and less acidity melts were used for the proton exchange) may be explained by the already

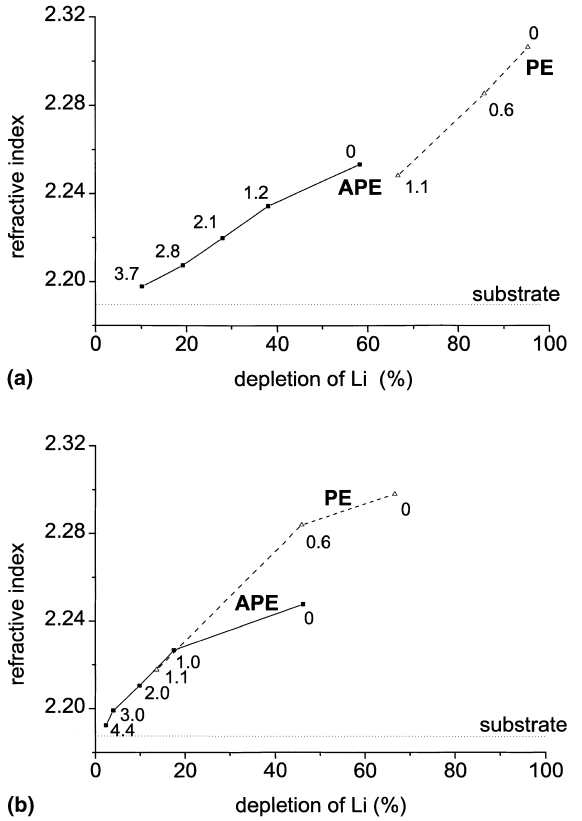

Fig. 8. Plot of n_e vs depletion of lithium (as measured in the depth of particular modes) for PE and APE waveguides fabricated from pure (a) or lithium (0.5 mol%)-containing (b) adipic acid (PE: 4 h, A: 1.5 h at 350°C). The numbers in the figures stand for the depths (in μm) of the particular modes.

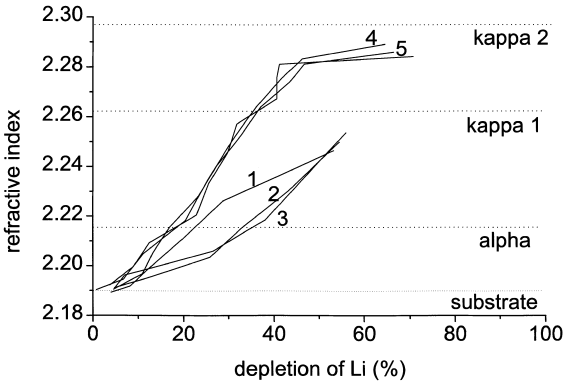

Fig. 9. Evaluation of the relationship between n_e and c_{Li} for the APE waveguides for various times of proton exchange reaction [PE: 1 h (1), 2 h (2), 3 h (3), 4 h (4) and 5 h (5) in pure adipic acid; A: 1.5 h at 350°C]. The regions of particular structural phases are denoted according to [11].

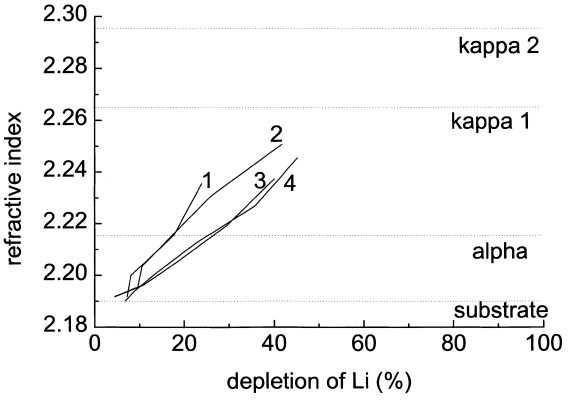

Fig. 10. Evaluation of the relationship between n_e and c_{Li} for the APE waveguides for various times of proton exchange reaction [PE: 1 h (1), 4 h (2), 5 h (3) and 6 h (4) in buffered (0.5 mol% of Li) adipic acid; A: 1.5 h at 350°C]. The regions of particular structural phases are denoted according to [11].

reported (e.g., [9–11]) existence of several structural phases within the waveguiding layers. It also corresponds well with the discontinuity in the transition of the waveguide characteristics from the step-like to the graded ones. As has been demonstrated above, the continuous redistribution of lithium may be accompanied by a sudden change of the n_e profiles. These discontinuities are evidently connected with the changes of structural properties of the waveguiding layers. A possibility of transition from one structural phase to another affecting the crystal structure of the fabricated waveguides has been already reported in the literature (e.g., [10]).

As has been stated above, the regime of the annealing is the most important step of the APE fabrication procedure. The curves in Fig. 11 illustrate the changes of the n_e vs c_{Li} relationships for the waveguides proton-exchanged for 2 h in the pure adipic acid and then annealed for various times at 300°C. The step-like characteristics of the waveguides, which were formed by short heating at that rather low annealing temperature, change to graded ones after 9 h of the heating. Waveguides 3 and 4 in Fig. 11 are the most interesting ones as both of them represent waveguides with

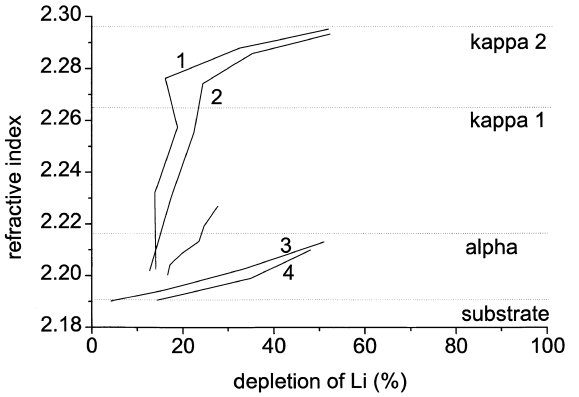

Fig. 11. Evaluation of the n_e vs c_{Li} relationship of the APE waveguides which were proton exchanged for 2 h in pure adipic acid and then annealed for various times at 300°C [A: 0.5 h (1), 1.5 h (2), 9.25 h (3) and 24 h (4)]. The regions of particular structural phases are denoted according to [11].

the so-called *alpha* phase structure [11]. Waveguides consisting mostly of the *alpha* phase are known to have low optical loss and higher values of electro-optic coefficient r_{33} as their structures are very similar to that of the untreated virgin substrate, and therefore, they are expected to be the most suitable ones for practical applications.

The importance of annealing temperature is demonstrated in Fig. 12 for the samples, which were proton-exchanged for 2 h from pure adipic acid (similar to the guides in Fig. 11), but were now annealed for 90 min at various temperatures. The results of the n_e vs c_{Li} relationships are in a good agreement with the already mentioned findings of Korkishko and Fedorov [10] concerning the critical temperature of annealing. Our results give evidence that careful annealing may help tailor the properties of the samples so that the resulting characteristics of the fabricated guides fit a desired purpose. For instance, the short annealing of the as-exchanged sample (illustrated in Fig. 12) at temperatures higher than 350°C, as well as the longer annealing of the PE samples at 300°C (curves 3 and 4 in Fig. 11), may "move" the n_e vs c_{Li} curves to the lowest part of the diagram, i.e., predominantly to the region of the *alpha* phase.

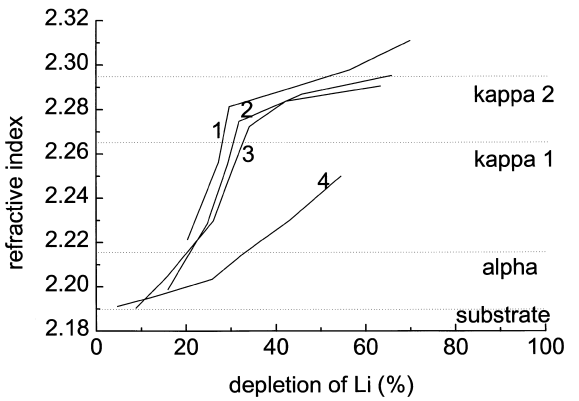

Fig. 12. Evaluation of the n_e vs c_{Li} relationship of the APE waveguides proton exchanged for 2 h in pure adipic acid and annealed for 1.5 h at various temperatures [A: 250°C (1), 300°C (2), 325°C (3) and 350°C (4)]. The regions of particular structural phases are denoted according to [11].

The experimental data of all the fabricated waveguides were found to fit the following functional dependence of n_e vs c_{Li}:

$$n_e = \frac{A_1 - B_1}{1 + e^{K_1((A_2 - c_{Li})/(c_{Li} - B_2))^{K_2}}} + B_1, \qquad (1)$$

where A_1 and B_1 are the surface and substrate values, respectively, of n_e (as determined by mode spectroscopy), A_2 and B_2 stand for the surface and substrate values, respectively, of c_{Li} (in atoms cm^{-3}, as determined by NDP) and K_1 and K_2 are empirical, case-dependent constants, which are closely connected with the orientation of the cuts and structural phase of the fabricated waveguide. (In our experiments, the values of A_1 for the APE samples were always lower than 2.32 and A_2 varied in a range between 6.00×10^{20} and 1.35×10^{21} atoms cm^{-3}.)

The fit of the calculated and the measured data is demonstrated in Fig. 13 for a series of APE waveguides fabricated from buffered (containing 0.5 mol% of lithium) adipic acid for various times of the proton exchange. A similar functional dependence was found for the depth profiles of the refractive index values as well as for the values of the local concentrations of lithium in the waveguiding layers. It should be mentioned that the actual shape of function (1) is determined by the values of the case-dependent constants K_1 and K_2. If $K_1 \geqslant 0$ and $K_2 = 1$, then the solution of Eq. (1) is a straight line. This may explain some of the

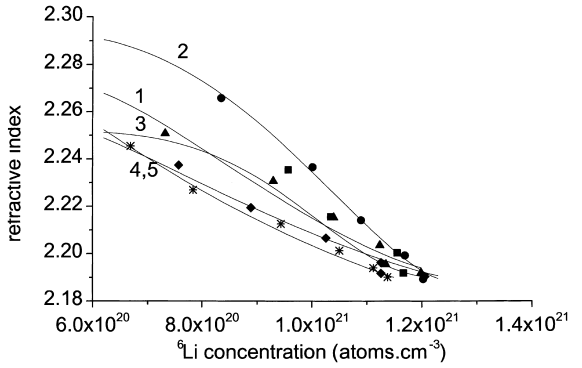

Fig. 13. The fit of experimental and calculated data of the n_e vs c_{Li} relationship for the APE waveguides fabricated from buffered (containing 0.5 mol% of Li) adipic acid for various times of proton exchange [PE: 1 h (1 – triangles), 2 h (2 – squares), 4 h (3 – circles), 5 h (4 – diamonds) and 6 h (5 – stars); A: 1.5 h, 350°C].

discrepancies between the already published conclusions, where some authors [6,8] stated the linear dependence between n_e (or Δn_e) and the concentrations of the constituents of the waveguiding layers, while other authors [3,17] found non-linear shapes of this functional dependence. We have proved that it is possible to control the APE process in such a way that the resulting waveguides may really reveal linear shapes of the n_e vs c_{Li} dependence. The details of the fitting will be published elsewhere.

4. Conclusions

The NDP measurement revealed a high mobility of the small Li^+ ions through the lithium niobate structure. The subsequent annealing results in moving the lithium ions towards the surface of the exchanged layers. The total amount of the outdiffused lithium is given by the first fabrication step, the proton exchange in the reaction melt, but the resulting properties of the waveguides depend strongly on the second fabrication step, the regime of the annealing.

We have demonstrated how the properties of the APE waveguides, namely, their n_e vs c_{Li} relationship, may be easily tailored by a large variety of fabrication conditions. The waveguides suitable for the most practical applications are expected to be few-mode ones. Moreover, in order to get low optical loss and high value of the coefficient r_{33}, they should consist only of the *alpha* phase, which is characterised by a small increment of the extraordinary refractive index ($\Delta n_e \leqslant +0.03$). According to our results, there is another parameter which should be taken into account in the fabrication of APE waveguides – the n_e vs c_{Li} relationship itself. Even for, e.g., weakly guided waveguides with graded refractive index profiles, there are quite a few possible variations of this relationship, which can be intentionally tailored for a desired purpose. Different contents of lithium ions in the waveguides and different shapes of their distribution might also influence their electro-optic properties and attenuation (at least, the intrinsic scattering of the guided radiation is expected to be lower in the waveguides with lower contents of lithium ions which are homogeneously distributed). These interconnections are now a subject of our investigation.

Acknowledgements

This research has been supported by the Grant Agency of the Czech Republic (Projects 102/99/1391 and 102/99/D017), by the research programme "Chemistry and technology of materials for technical applications, health and environment protection" (CEZ: MSM 223100002) and last, but not least, by the International Atomic Energy Agency (CPR CZR 10031).

References

[1] J.L. Jackel, C.E. Rice, J. Veselka, Appl. Phys. Lett. 41 (1982) 607.
[2] C. Canali, A. Carnera, G. Della Mea, P. Mazzoldi, S.M. Al Shukri, A.C.G. Nutt, R.M. De La Rue, J. Appl. Phys. 59 (8) (1986) 2643.
[3] M. McWright Howerton, W.K. Burns, P.R. Sheat, A.S. Greenblatt, J. Quant. Electron. 77 (3) (1991) 593.
[4] R. Richter, T. Bremer, P. Hertel, E. Krätzig, Phys. Stat. Sol. A 114 (1989) 765.
[5] R.G. Wilson, S.W. Novak, J.M. Zavada, A. Loni, R.M. De La Rue, J. Appl. Phys. 66 (12) (1989) 6055.

[6] S.T. Vohra, A.R. Mickelson, S.A. Asher, J. Appl. Phys. 66 (11) (1989) 5161.
[7] G.R. Paz-Pujalt, D.D. Tuschel, G. Braunstein, T. Blanton, S. Tong Lee, L.M. Salter, J. Appl. Phys. 76 (7) (1994) 3981.
[8] J.M. Zavada, H.C. Casey Jr., R.J. States, S.W. Novak, A. Loni, J. Appl. Phys. 77 (6) (1995) 2697.
[9] Yu.N. Korkishko, V.A. Fedorov, M.P. De Micheli, P. Baldi, K. El Hadi, A. Leycuras, Appl. Opt. 35 (36) (1996) 7056.
[10] Yu.N. Korkishko, V.A. Fedorov, Tech. Phys. Lett. 21 (9) (1995) 752.
[11] Yu.N. Korkishko, V.A. Fedorov, J. Appl. Phys. 82 (3) (1997) 1010.
[12] V. Sirotek, J. Hradilová, J. Schröfel, J. Čtyroký, in: PHOTONICS'95, Prague, 23–25 August 1995, in: European Optical Society Annual Meetings Digest Series, vol. 2A, p. 151.
[13] P. Kolářová, J. Hradilová, P. Novák, J. Schröfel, J. Vacík, J. Čtyroký, in: PHOTONICS'95, Prague, 23–25 August 1995, in: European Optical Society Annual Meetings Digest Series, vol. 2A, p. 190.
[14] J.M. White, P.F. Heinrich, Appl. Opt. 15 (1976) 151.
[15] J. Vacík, J. Červená, V. Hnatowicz, V. Havránek, D. Fink, Acta Phys. Hungarica 75 (1–4) (1994) 369.
[16] P. Kolářová, J. Vacík, J. Špirková-Hradilová, J. Červená, Nucl. Instrum. Meth. Phys. Res. B 141 (1998) 498.
[17] S. Kapphan, A. Breitkopf, Phys. Stat. Sol. A 133 (1992) 15.

ELSEVIER

Sensors and Actuators B 76 (2001) 8–12

SENSORS AND ACTUATORS B CHEMICAL

www.elsevier.nl/locate/sensorb

Surface plasmon resonance biosensor based on integrated optical waveguide

J. Dostálek[a], J. Čtyroký[a], J. Homola[a,*], E. Brynda[b], M. Skalský[a], P. Nekvindová[c], J. Špirková[c], J. Škvor[d], J. Schröfel[e]

[a]*Institute of Radio Engineering and Electronics, Academy of Sciences of the Czech Republic, Chaberská 57, 18251 Prague, Czech Republic*
[b]*Institute of Macromolecular Chemistry, Academy of Sciences, Heyrovského nám. 2, 16206 Prague, Czech Republic*
[c]*Institute of Chemical Technology, Technická 5, 16628 Prague, Czech Republic*
[d]*SEVA IMUNO Prague, Prague, Czech Republic*
[e]*Faculty of Electrical Engineering, Czech Technical University, Technická 2, 16627 Prague, Czech Republic*

Abstract

We report a sensor based on spectral interrogation of surface plasmon resonance (SPR) in an integrated optical waveguide-coupled SPR sensing device. We present theoretical analysis of the integrated optical SPR sensor structure leading to a device design optimized for operation in aqueous environments. We demonstrate that the fabricated laboratory prototype of the sensor is capable of measuring bulk refractive index changes smaller than 1.2×10^{-6}. In conjunction with specific biomolecular recognition elements (monoclonal antibodies against human chorigonadotropin (hCG)) the sensor is used for the detection of hCG. The sensor is demonstrated to be capable of detecting 2 ng of hCG present in 1 ml of 1% bovine serum albumin solution.

Keywords: Optical waveguides; Surface plasmon resonance; Optical sensors; Biosensors

1. Introduction

The use of optical waveguides in biosensors offers numerous benefits such as potential for the development of miniaturized, compact and rugged sensing elements, and prospect of fabrication of multiple sensors on one chip. In addition, in conjunction with fiber optics, planar optical waveguides may allow for the development of sensing devices which may be used remotely from both the source and detector, with the potential for sensor multiplexing. The first surface plasmon resonance (SPR) integrated optical sensors have been described in late 1980s [1]. Since then, various integrated optical SPR sensors using slab waveguides, channel waveguides and even more complex waveguide structures have been demonstrated [2–6]. These integrated optical SPR sensors are based on the measurement of variations in the optical power transmitted by an integrated optical SPR sensing element and thus are sensitive to instabilities in light source and waveguide in/out-coupling efficiency.

In this paper, we present an integrated optical SPR sensor based on the use of a broadband optical source and spectral interrogation of SPR. This approach offers more accurate and robust SPR measurement than conventional approaches relying on the intensity modulation [2–6].

2. Theory

The integrated optical waveguide SPR sensor structure is shown in Fig. 1. It consists of a channel waveguide locally covered with a planar (multi)layer structure supporting surface plasmons. The multilayer contains an SPR-active metal (usually gold) and other layers that promote adhesion (e.g. chromium) or adjust the operating range of the sensor (e.g. tantalum pentoxide). Light propagates through the waveguide and excites surface plasmons in the multilayer structure if the phase velocities of the waveguide mode and that of the surface plasmon match. In comparison with traditional guided modes of dielectric waveguides, surface plasmons' propagation constant depends strongly on the wavelength. Therefore, the matching condition between a guided mode of an integrated optical waveguide and a surface plasmon supported by a planar multilayer may be fulfilled only within a narrow spectral band. Thus, when a broadband light is launched into the waveguide, the transmitted spectrum exhibits a narrow dip associated with the

* Corresponding author. Tel.: +42-2-688-1804; fax: +42-2-688-0222.
E-mail address: homola@ure.cas.cz (J. Homola).

0925-4005/01/$ – see front matter
PII: S0925-4005(01)00559-7

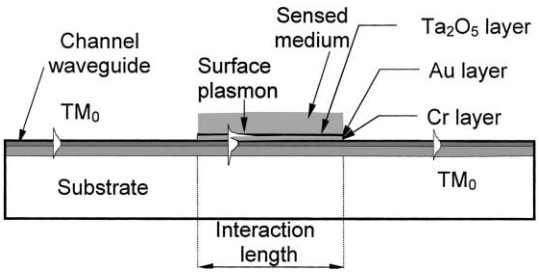

Fig. 1. Integrated optical waveguide-coupled SPR sensor.

transfer of optical energy into surface plasmons. As the propagation constant of a surface plasmon is highly sensitive to changes in refractive index distribution within its evanescent field, the spectral position of the SPR dip in the transmitted spectrum depends on the refractive index of dielectrics adjacent to the SP supporting structure (sensed medium) ''seen'' by the surface plasmon.

To simulate light propagation through the waveguide-coupled SPR sensor, we use the equivalent planar waveguide approach and the mode expansion and propagation method (MEP) [7]. In this method, the waveguide structure is subdivided into longitudinally uniform sections, and in each section, the set of eigenmodes is calculated. The relations among modal amplitudes at the interface between the longitudinal sections are obtained from the continuity of the transversal field components. Perfectly conducting electric (for TE modes) or magnetic (for TM modes) walls are introduced to discretize the spectrum of radiation modes of the waveguide. In order to account for waveguide refractive index profile, the graded-index integrated optical waveguide is simulated as a stack of twelve, 500 nm thick layers with a constant refractive index [8].

2.1. Integrated optical SPR sensor

Fig. 2 presents normalized spectral transmission for the waveguide-coupled SPR sensor consisting of a single-mode integrated optical $K^+ \leftrightarrow Na^+$ ion exchanged waveguide in BK7 and a gold layer calculated for two different refractive indices of the sensed medium.

As follows from the simulations presented in Fig. 2, the theoretical refractive index sensitivity of the spectral integrated optical SPR sensor is about 6000 nm/RIU (RIU: refractive index unit).

2.2. Integrated optical SPR sensor for aqueous environment

The operating wavelength of the sensor is determined by the refractive index profile of the waveguide, properties of the SPR-active metal layer, and the refractive index of the sensed medium. In biosensing applications the sensor is desired to be sensitive in a particular region of refractive indices, usually around 1.33 (aqueous environment) in a particular wavelength region (usually between 0.6 and

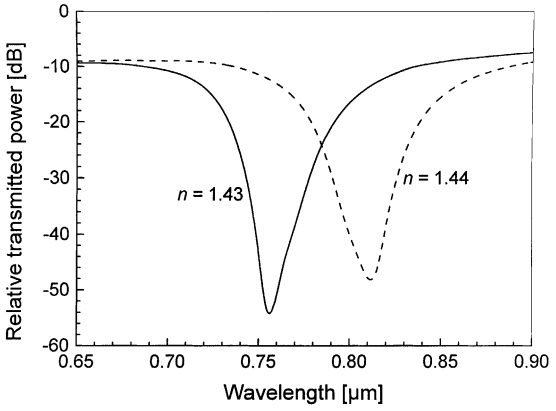

Fig. 2. Spectral dependence of the TM_0 mode transmission through the $K^+ \leftrightarrow Na^+$ ion exchanged waveguide with 2 nm thick adhesion chromium layer and 60 nm thick gold film (interaction length: 1.8 nm) calculated for two different refractive indices of the sensed medium.

0.9 μm). In this wavelength range, SPR sensors based on $K^+ \leftrightarrow Na^+$ ion exchanged waveguides in BK7 exhibit SPR at the refractive index around 1.44 (Fig. 2). In order to shift the operating point of the sensor towards aqueous environment, a thin high refractive index dielectric overlayer can be employed [9]. In this work we use tantalum pentoxide which was chosen for its high refractive index and good environmental stability. Fig. 3 illustrates the tuning of the operating point of the integrated optical SPR sensor by means of a tantalum pentoxide overlayer.

A tantalum pentoxide overlayer of the thickness of 30 nm shifts the refractive index operating point by about 0.11 RIU. In principle, various dielectrics may be used for the tuning overlayer. A shift in the resonant wavelength due to the presence of the overlayer is proportional to $(1 - n^2_{\text{sensed}}/n^2_{\text{overlayer}})t_{\text{overlayer}}$, where n_{sensed}, $n_{\text{overlayer}}$, $t_{\text{overlayer}}$ denote refractive index of the sensed medium, refractive index of the tuning overlayer and overlayer thickness, respectively [10]. Therefore, the use of overlayers with higher refractive

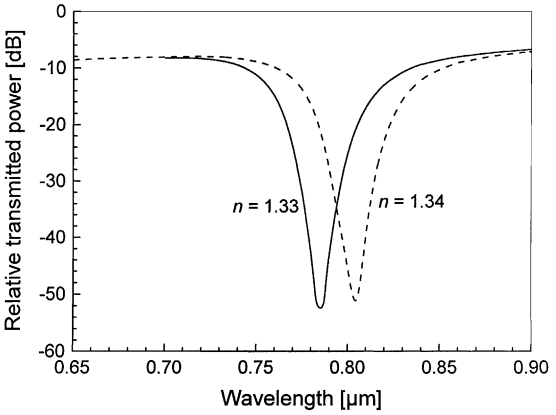

Fig. 3. Spectral dependence of the TM_0 mode transmission through the $K^+ \leftrightarrow Na^+$ ion exchanged waveguide with 2 nm thick adhesion chromium layer, 60 nm thick gold film, and 30 nm thick tantalum pentoxide overlayer (interaction length: 1.8 mm) calculated for two different refractive indices of the sensed medium.

indices allows for thinner overlayers and potentially better sensor sensitivity. As follows from Figs. 2 and 3, the presence of the tantalum pentoxide overlayer decreases the bulk refractive index sensitivity by a factor of three to about 2000 nm/RIU.

3. Experimental

3.1. Reagents

Human choriogonadotropin (hCG; urine, 5000 mIU/mg) and monoclonal antibody against β subunits of human choriogonadotropin (a-hCG), were obtained from Seva Immuno, Prague. Dextran sulfate sodium salt (DS; from dextran with an average molecular weight of 10,000), bovine serum albumin (BSA, 99% by electrophoresis), and glutaraldehyde (GA) were from Sigma. Solutions were prepared in citrate buffer (0.1 M) pH 4 (CB) and phosphate-buffered physiological saline, pH 7.4 (PBS).

3.2. Sensor fabrication and experimental setup

Waveguides used throughout this work were fabricated by ion exchange in BK7 glass substrates. The substrates were coated with resist in which channel waveguide pattern was formed using lithography. The substrates were coated with Ti–Al and channels were exposed using the lift-off process. The $K^+ \leftrightarrow Na^+$ ion exchange was accomplished by immersing the substrates into KNO_3 salt melt kept at the temperature of 375°C; in order to ensure single-mode performance of the waveguides, rather short diffusion time (typically 30 min) was used. The waveguide exhibits TM ↔ TE polarization cross-coupling of about 25 dB and its loss is estimated to about 1 dB per cm. In the second stage of fabrication, the waveguides were coated by an adhesion-promoting chromium film (thickness: 2 nm), a gold film (thickness: 60 nm), and a tantalum pentoxide overlayer (thickness: 30 nm) by vacuum evaporation.

The configuration of the developed integrated optical SPR sensor system is shown in Fig. 4. A pigtailed superluminescent diode (SLD) (SLD-371, Superlum Ltd., Russia) with the power of 0.9 mW in a single-mode fiber, FWHM of 72 nm, and the central wavelength of 816 nm was used as a source of polychromatic light. Light from the pigtail fiber (SF) (SM800, Fibercore Ltd., UK) was directly coupled into the integrated optical sensor element (SE). After propagating through the sensor chip, the light was collimated using a microscope objective (MO), TM polarization was selected by a dichroic polarizer (P) (POLACOR 800-HC, Corning Inc., USA; extinction ratio >50 dB) and coupled into a multimode optical fiber (MF) (FT 400-EMT, Thorlabs Inc., USA) by a collimator (C) (Zeiss-Jena GmbH, Germany). The optical fiber was connected to the input of a spectrograph (S) (SD2000, Ocean Optics Inc., USA). Transmitted spectra were acquired by the spectrograph and normalized with respect to the spectrum corresponding to sensor response when no sample was present (Fig. 5). A total of 64 spectra were averaged to reduce spectrum noise. The centroid method was used to quantify the shift of the position of the SPR transmission minimum; typically 200 points closest to the minimum of the SPR dip were used in centroid calculation. A Teflon flow cell (FC) was attached to the sensing element to contain a measured liquid sample during experiments. The FC (volume ∼2 μl) was interfaced with Teflon tubing (inner diameter: 0.5 mm); the sample flow was controlled by a syringe pump (Uniflows Ltd., Japan) at a flow rate of 20 μl/min.

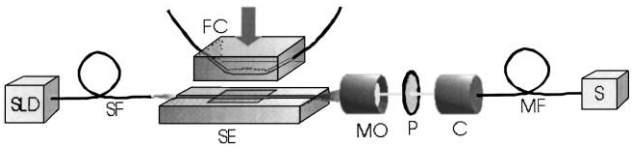

Fig. 4. Integrated optical SPR sensor: experimental setup.

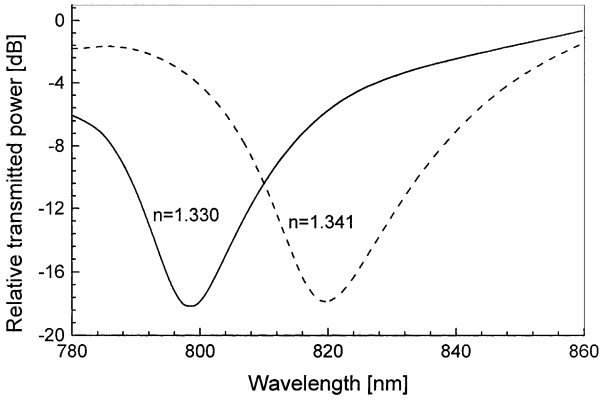

Fig. 5. Normalized spectral dependence of TM transmission through the $K^+ \leftrightarrow Na^+$ ion exchanged waveguide with 1.7 mm stripe comprising 1.5 nm thick chromium layer, a 60 nm thick gold film, and a 30 nm thick tantalum pentoxide overlayer, measured for two different refractive indices of the sensed medium.

3.3. Sensor functionalization

The sensor surface cleaned in solution of 10% hydrogen peroxide (H_2O_2) and sulfuric acid (H_2SO_4) mixed in 1:5 ratio was functionalized with a double-layer of a-hCG molecules using the immobilization technique described in [11]. Assemblies consisting of alternating molecular layers of an a-hCG and DS were formed by alternating adsorption from the a-hCG and DS solutions. The solutions were used in the following order: CB, a-hCG in CB (0.1 mg/ml), CB, DS in CB (1 mg/ml), CB, a-hCG in CB, CB. Then, the assembly was incubated with 0.5 wt.% glutaraldehyde in CB for 30 min to cross-link a-hCG. DS was washed out of the cross-linked antibody network with PBS (Fig. 6).

The first a-hCG monolayer was adsorbed on Ta_2O_5 mainly due to the hydrophobic interaction. By changing

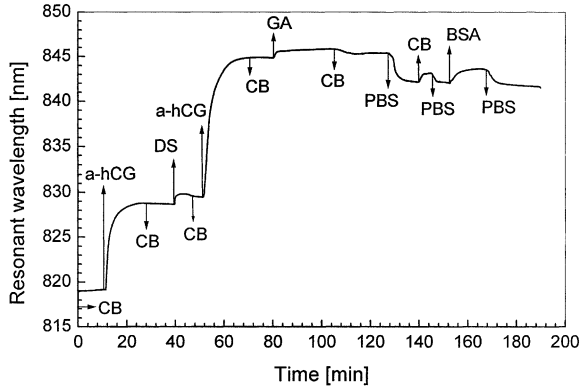

Fig. 6. Preparation of a-hCG double-layer on tantalum pentoxide surface of an integrated optical SPR sensor. Arrows indicate exchange of solutions; a-hCG: 0.1 mg/ml CB, DS: 1 mg/ml CB, GA: 0.5% in CB.

the solution DS layer and the second a-hCG layer were successively adsorbed due to electrostatic attraction between DS polyanions and a-hCG molecules positively charged below their isoelectric point in CB at pH 4. Glutaraldehyde cross-linked covalently a-hCG molecules via reactive aminogroups. In PBS at pH 7.4, the net electrical charge of a-hCG reverted to a negative one and DS polyanions were expelled from the a-hCG network [11,12]. A decrease in sensor response measured in CB before and after soaking the a-hCG/DS/a-hCG assembly with PBS (Fig. 7) was probably due to the desorption of DS and some a-hCG molecules, which were not strongly bound in the network. The full reversibility of sensor response to 1% BSA solution indicated a solid coating of the sensor surface with a-hCG double layer which prevented the non-specific adsorption of BSA on Ta_2O_5 support.

As Fig. 6 indicates, the adsorption of a monolayer of a-hCG produces a shift in the resonant wavelength of about 9.7 (the first monolayer) and 15.5 nm (the second layer). This discrepancy is probably caused by different arrangements of proteins in these monolayers. Based on a more detailed theoretical analysis and assuming the refractive index of the protein monolayer is equal to 1.45, these shifts were found to correspond to antibody monolayer thickness of about 4.3 nm

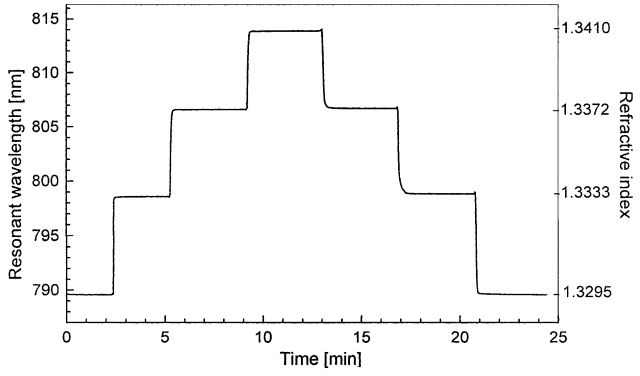

Fig. 7. Temporal sensor response to variations in the refractive index of sample.

(the first monolayer) and 7.4 nm (the second layer). These values are within expected dimensions of a-hCG molecule as given in [13].

3.4. Integrated optical SPR refractometry

In order to demonstrate sensor's potential as a refractometer, we flowed liquid samples (mixtures of ethyleneglycol and water) of known refractive indices across the surface of the sensing element and recorded the sensor response, Fig. 7 (refractive indices of samples are given at the wavelength of 800 nm). In the performed refractometric experiment, the sensor was found to exhibit baseline drift of less than 1 nm/h at the flow rate of 20 μl/min and 0.4 nm/h for static sample. The bulk refractive index sensitivity attained by the sensor was as high as 2100 nm/RIU. The baseline noise was determined to be about 0.0025 nm (standard deviation) which corresponds to the sensor resolution better than 1.2×10^{-6} RIU. It should be noted that the sensor response was quite fast. It suggests that the multilayer is not porous and thus not permeable for liquid samples. Relatively good reproducibility attained in the refractometric experiment (better than 2% of the response) indicates that the tantalum pentoxide layers were stable in aqueous environment.

3.5. Integrated optical SPR biosensing

The integrated optical SPR sensor has been used for biosensor-based detection of human choriogonadotropin (hCG). The sensor functionalized with a double-layer of a-hCG (Fig. 7) was incubated with BSA (1% in PBS), then sample solutions containing 2, 5, and 10 ng/ml of hCG in the BSA solution were flowed across the sensor surface. Finally the sensor surface was incubated in BSA (1% in PBS) again. The sensor response (Fig. 8) shows the resonant wavelength shift of 0.3 nm for hCG concentration $c_{\mathrm{hCG}} = 2$ ng/ml, 0.95 nm for $c_{\mathrm{hCG}} = 5$ ng/ml, and 1.02 nm for $c_{hCG} = 10$ ng/ml.

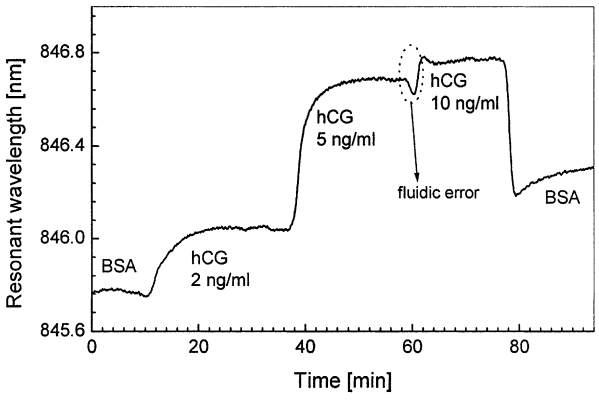

Fig. 8. Response of an integrated optical SPR sensor functionalized with a double-layer of a-hCG to hCG present in BSA solution. Arrows indicate exchange of solutions; 1% BSA in PBS, hCG 2, 5 and 10 ng/ml in 1% BSA solution.

It also suggests, that approximately 50% of antigen was bound irreversibly.

4. Discussion

There seems to be a very good agreement between the theoretical predictions and experimental results in terms of the SPR dip position and bulk refractive index sensitivity. The observed difference (less than 5%) is probably due to discrepancies of the used thin film parameters from the models employed in simulations. The depth of the experimentally observed SPR dips is considerably lower than the figures predicted by the theoretical analysis. This is likely due to uncertainties in the thin film parameters, scattering at imperfect interfaces of the layered structure, TM $\leftrightarrow$ TE light polarization conversion in the waveguide structure and spectrograph resolution.

A limit for hCG detection with a biosensor prepared by immobilization of a double a-hCG layer on the integrated optical SPR sensor is estimated to be of about 1 ng/ml. The obtained detection limit is comparable with that attained in ELISA experiments — using the same a-hCG/hCG pair, the standard semiquantative ELISA was able to detect hCG in the concentration of 1.2 ng/ml.

5. Conclusions

We have reported a new integrated optical SPR sensor based on the use of broadband radiation and spectral interrogation of SPR condition. We have demonstrated that the sensor may be applied to refractometry where it allows resolving refractive index variations smaller than 1.2×10^{-6}. In conjunction with specific biomolecular recognition elements (monoclonal antibodies against hCG) the sensor has been used for the detection of hCG. The sensor was capable of detecting 2 ng/ml hCG present in 1% bovine serum albumin solution.

Future work will aim at introducing referencing for compensating for long-term drifts and non-specific effects producing background refractive index variations. This will result in robust biosensor technology desired in many areas such as medicine, environmental monitoring, and biotechnology.

Acknowledgements

The authors would like to thank Dr. Václav Malina for thin film deposition. The authors acknowledge the support of the Grant Agency of the Czech Republic, contracts No. 102/99/0549 and 102/00/1536.

References

[1] H.J.M. Kreuwel, P.V. Lambeck, J. van Gent, T.J.A. Popma, Surface plasmon dispersion and luminescence quenching applied to a planar waveguide sensors for measurement of chemical concentrations, Proc. SPIE 789 (1987) 218–224.
[2] C.R. Lavers, J.S. Wilkinson, A waveguide-coupled surface plasmon resonance sensor for an aqueous environment, Sens. Actuators B 22 (1994) 475–481.
[3] R.D. Harris, J.S. Wilkinson, Waveguide surface plasmon resonance sensors, Sens. Actuators B 29 (1995) 261–267.
[4] M.N. Weiss, R. Srivastava, H. Grogner, Experimental investigation of a surface plasmon-based integrated-optic humidity sensor, Electron. Lett. 32 (1996) 842–843.
[5] J. Homola, J. Čtyroký, M. Skalský, J. Hradilová, P. Kolárová, A surface plasmon resonance based integrated optical sensor, Sens. Actuators B 38/39 (1997) 286–290.
[6] C. Mouvet, R.D. Harris, C. Maciag, B.J. Luff, J.S. Wilkinson, J. Piehler, A. Brecht, G. Gauglitz, R. Abuknesha, G. Ismail, Determination of simazine in water samples by waveguide surface plasmon resonance, Anal. Chim. Acta 338 (1997) 109–117.
[7] G. Sztefka, H.P. Nolting, Bidirectional eigenmode propagation for large refractive index steps, IEEE Photon. Technol. Lett. 5 (1993) 554–557.
[8] J. Čtyroký, J. Homola, Modeling of surface plasmon resonance waveguide sensor by complex mode expansion and propagation method, Opt. Quantum Electron. 29 (1997) 301–311.
[9] J. Čtyroký, J. Homola, M. Skalský, Tuning of spectral operation range of a waveguide surface plasmon resonance sensor, Electron. Lett. 33 (1997) 1246–1248.
[10] J. Homola, On the sensitivity of surface plasmon resonance sensors with spectral interrogation, Sens. Actuators B 41 (1997) 207–211.
[11] E. Brynda, M. Houska, J. Škvor, J.J. Ramsden, Immobilization of multilayer bioreceptor assemblies on solid substrates, Biosens. Bioelectron. 13 (1998) 165–172.
[12] E. Brynda, M. Houska, A. Brandenburg, A. Wikerstal, J. Škvor, The detection of human β_2-microglobulin by grating coupler immunosensor with three-dimensional antibody networks, Biosens. Bioelectron. 14 (1999) 363–368.
[13] M. Marquart, J. Deisenhofer, R. Huber, Crystallographic refinement and atomic models of the intact immunoglobulin molecule Kol and its antigen binding fragment at 3.0 and 1.9 Å resolution, J. Mol. Biol. 141 (1980) 369–391.

ELSEVIER

International Journal of Inorganic Materials 3 (2001) 1245–1247

International Journal of Inorganic Materials

Importance of crystal structure of the substrate for diffusion technologies of waveguides fabrication

P. Nekvindová[a], J. Špirková[a,*], J. Vacík[b], I. Červená[b], V. Peřina[c], J. Schröfel[c]

[a]*Department of Inorganic Chemistry, Institute of Chemical Technology Prague, 166 28 Prague, Czech Republic*
[b]*Nuclear Physics Institute, Czech Academy of Sciences, 250 68 Řež, Czech Republic*
[c]*Department of Microelectronics, Czech Technical University, 16627 Prague, Czech Republic*

Abstract

Effect of different crystallographic structure of various substrate cuts on diffusion processes into optical crystals is demonstrated for lithium niobate and sapphire. After the low or moderate temperature diffusion processes the X-cuts, which are parallel to the C_3 axis, always contained much more dopants comparing with the Z-cuts, which are oriented perpendicularly to the C_3. This has been proved for annealed proton exchange (APE) technology for fabrication of optical waveguides in lithium niobate and for the moderate temperature incorporation of erbium ions into both materials. Thus the possibility of localized doping by Er^{3+} diffusion at moderate (lower then 500°C) temperature is for the first time demonstrated for sapphire single crystal wafers. The strong anisotropy of the doping is explained on the bases of suitable orientation of the cleavage planes to the substrates surfaces in the X-cuts that allows for better penetration of the diffusing particles into the material.

Keywords: Lithium niobate; Sapphire; Optical waveguides; Erbium doping; Annealed proton exchange; Crystal structure

1. Introduction

Single crystal lithium niobate (C^6_{3v}) is one of the most popular optoelectronic material for fabrication of dynamical optical waveguides which are widely used in various types of highly sophisticated optoelectronic devices and structures. Moderate temperature approach for the waveguide fabrication in lithium niobate — annealed proton exchange (APE) [1] — is based on an exchange reaction between the substrate wafers and a suitable proton source, typically an acid. The PE ($H^+ \leftrightarrow Li^+$) reaction usually occurs at temperatures between 150 and 250°C. For fabrication of high quality stable optical waveguides the second fabrication step — the annealing of the as-exchanged waveguides at temperatures around 350°C — is necessary.

Another very interesting optical crystal is sapphire (D^6_{3d}), which is used e.g. as the basic component of the tunable Ti-sapphire laser. It is a very promising material for optoelectronic structure of a new generation.

Doping of both materials with laser active ions opens a possibility to use them as optical amplifiers and waveguide lasers, which may integrate the passive/dynamical and active function of the guide on the same substrate. For that the localized doping with the laser active elements, which are presented only in the surface (waveguiding) layers of the substrates, is highly desirable.

The aim of the presented paper is to summarize our experience on behavior of differently oriented crystal cuts in the processes of moderate temperature diffusion technologies for fabrication of optical waveguides in lithium niobate and to present new results on the doping into sapphire, which were obtained by utilizing our previous knowledge of the subject.

2. Moderate temperature doping with H^+ and/or Er^{3+}

2.1. Lithium niobate

Two principal types of the lithium niobate substrate wafers are used for the optical waveguides fabrication — the Z-cuts (0001), perpendicular to the C_3 axis, and the X-cuts (11-20), which are perpendicular to the Z-cuts. The structure of the Z-cuts reveals open channels in the structure, so that one would expect that in this cut the

*Corresponding author. Fax: +420-23-112-206.
E-mail address: jarmila.spirkova@vscht.cz (J. Špirková).

1466-6049/01/$ – see front matter
PII: S1466-6049(01)00150-7

doping should be easier, i.e. the doped layers would be deeper and the amount of the incorporated foreign particles would be higher as comparing with the X-cuts. However, as follows from the experiments, the opposite is true.

We have done a systematic study [2–5] of a large number of PE and APE lithium niobate samples, which were fabricated in the Z- and X-cuts under very different fabrication conditions of the proton exchange reaction as well as the post-exchange annealing of the as-exchanged (PE) samples. The results of the study allowed us to disclose quite general findings as follows: the prevailing mechanism of H^+ incorporation into the Z-cut structure is substitution of H^+ for Li^+, which is accompanied by some interstitial H^+ diffusion. X-cuts revealed the same extent of the $H^+ \leftrightarrow Li^+$ substitution as was observed in the Z-cuts waveguides fabricated under the same fabrication condition. However, intensities of ν(O–H) vibration bands in the IR reflection spectra of the fabricated waveguides, as well as ERDA measurements of the H^+ concentration depth profiles, always gave evidence for much more hydrogen incorporated in the X-cuts. It means, that the $H^+ \leftrightarrow Li^+$ substitution is in the X-cut strongly accompanied by the interstitial in-diffusion of hydrogen. H^+ species then form a barrier that prevents lithium to move during the post-exchange annealing of the PE samples towards the surfaces of the wafers, causing thus typical step-like shapes of the X-cuts depth characteristics.

Moderate temperature Er^{3+} doping [6–9] into lithium niobate wafers made from a mixture of erbium containing nitrates was far more successful in the X-cuts, where the amount of the incorporated erbium (up to 10 mole %) was approximately 10 times higher compared with that incorporated into the Z-cuts. Sada et al. [9] explained these phenomena on the bases of a small depletion of lithium atoms nearby the surface of the samples as the multivalent $Er^{3+} \leftrightarrow 3Li^+$ ion-exchange process. The process which is more favourable in the X-cuts as there is the higher surface density of the lithium atoms compared with the Z-cuts.

However, we have observed in our erbium containing X-cuts the increased concentration of hydrogen which, evidently, was incorporated into the samples during their treatment in the erbium-containing melts of the nitrates. This finding, as to our opinion, explains the reported [9] small depletion of lithium in the shallow surface layers of the erbium-containing X-cuts. The erbium nitrate always contains some hydrate water and it causes, due to the covalent nature of erbium, a hydrolytic reaction in the reaction melt which results in the presence of some H^+ (in fact H_3O^+) particles in the reaction bath. Thus, simultaneously with the in-diffusion of erbium, occurs also a weak proton exchange ($H^+ \leftrightarrow Li^+$) reaction. This may be also an explanation for the waveguiding properties, which we have noticed with our erbium containing X-cuts.

We suggest that this strong anisotropy of the doping with Er^{3+} as well as with H^+ is in a close connection with the orientation of the substrate cuts towards the more open planes of lithium niobate. The surface of the X-cuts opens access to the cleavage planes {01–12} which vacancies help moving particles to penetrate into the crystal (interstitial in-diffusion) moreover to those incorporated into the structure via substitution (e.g. H^+ for Li^+). To prove this hypotheses we studied the moderate-temperature diffusion of erbium ions into the sapphire, which structure is very similar to that of lithium niobate, but it is well known to be extremely resistant against in-diffusion of foreign particles. The constituents of the structure ($A1_2O_3$) do make the ion-exchange mechanism of the in-diffusion unlikely, so that only interstitial in-diffusion is to be expected.

2.2. Sapphire

Diffusion of erbium into the sapphire occurred by immersing the thoroughly pre-cleaned one side polished (11–20) and (1–102) wafers (supplied by AVTEX, Czech Republic) into a bath of molten nitrates ((KNO_3 + $Er(NO_3)_3$ in the weight ratio 10:1) and kept at 350°C for times ranging from 5 to 120 h. The fabricated samples were then studied by SEM, RBS and photoluminiscence spectra measurement. In the 'X-cuts' (11–20) there were found up to 1 mole % of erbium on the surfaces of approx. 400 nm thick erbium containing layers. In spite of it in the (1–102) cuts the contents of erbium were by one order of magnitude lower. Fig. 1 shows an example of RBS depth profile and absorption (380 nm) and emission (435 nm) of the $^4I_{15/2} \rightarrow {}^4G_{11/2}$ transition of Er^{3+} incorporated into the sapphire (11–20) cut by diffusion doping for 120 h at 350°C.

These first results correspond well with those already obtained for lithium niobate and fulfilled our expectation. In practice that means, that a suitable orientation of the substrate cut may really help to introduce the mobile particles from melt into the substrate.

3. Conclusion

We have proved that it is in principle possible to control the diffusion mechanism of H^+ and Er^{3+} into the lithium niobate and sapphire single crystals by using the suitable orientation of the substrate wafer towards the cleavage planes of the crystal. The X-cuts (11–20) of the both single crystalline materials allow for much better incorporation of foreign particles into the structure. This effect is explained on the bases of better access of the X-cut surfaces to the more open planes of the crystals.

Acknowledgements

This research has been supported by the projects 102/99/1391 and 102/99/D017 (Grant Agency of the Czech Republic), CPR CZR 10031 (International Atomic Energy

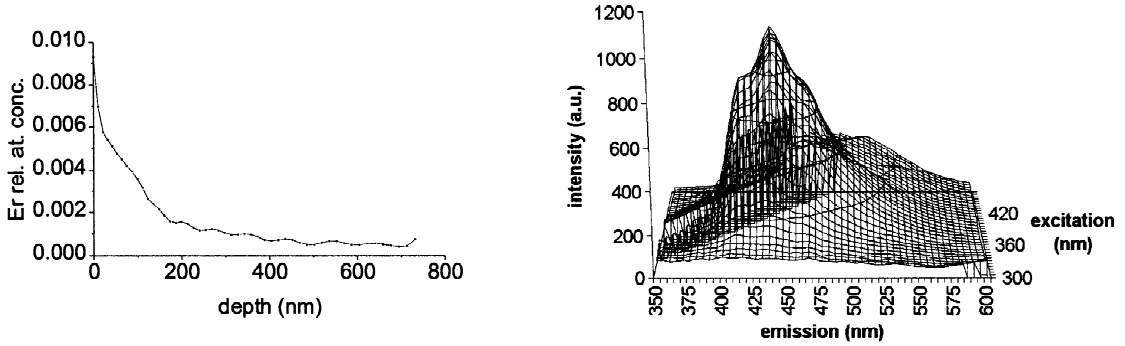

Fig. 1. RBS depth profile and emission photoluminescence spectrum showing the $^4I_{15/2} \rightarrow {}^4G_{11/2}$ transition of Er^{3+} incorporated into the sapphire (11–20) cut (diffusion of Er: 120 h, 350°C).

Agency) and by the Research Programme CEZ: MSM 2231 00002. The authors thank Dr. Gabriela Kuncova for providing the photoluminescence spectra measurement.

References

[1] Jackel JL, Rice CE, Veselka JL. Appl Phys Lett 1982;41:607.
[2] Kolářová P, Vacík J, Špirková-Hradilová J, Červená J. NIM (Nucl Instrum Meth Chem Res) B 1998;141:498.
[3] Špirková-Hradilová J, Nekvindová P, Vacík J, Červená J, Scbröfel J. In: Adv. Mat. and Opt. Syst for Chem, and Biol. Detection, Proceedings of SPIE, Vol. 3858, 1999, p. 190.
[4] Nekvindová P, Špirková-Hradilová J, Vacík J, Červená J, Schröfel J. In: PHOTONICS PRAGUE'99 (Prague, 21–23 June, 1999), p. 117.
[5] Špirková-Hradilová J, Nekvindová P, Vacík J, Červená J, Schröfel J. Opt Mater 2001;15:269.
[6] Hradilová J, Kolářová P, Schröfel J, Čtyroký J, Peřina V. In: Opt. Systems Design and Production II, Proceedings of SPIE, Vol. 2775, 1996, p. 647.
[7] Peřina V, Vacík J, Hnatowicz V, Červená J, Kolářová P, Špirková-Hradilová J, Schröfel J. NIM (Nucl Instrum Meth Chem Res) B 1998;139:208.
[8] Nekvindová P, Špirková-Hradilová J, Schröfel J, Slunečko M, Peřina V, Vacík J. In: Adv. Mat. and Opt. Syst for Chem, and Biol. Detection, Proceedings of SPIE, Vol. 3858, 1999, p. 180.
[9] Sada C, Borsella E, Caccavale F, Gonella F, Segato F, Korkishko YuN, Fedorov VA, Morozova TM, Battaglin G, Polloni R. Appl Phys Lett 1998;72:3431.

ELSEVIER

Optical Materials 19 (2002) 245–253

OPTICAL Materials

www.elsevier.com/locate/optmat

Annealed proton exchanged optical waveguides in lithium niobate: differences between the X- and Z-cuts

Pavla Nekvindová [a], Jarmila Špirková [a,*], Jarmila Červená [b], Milos Budnar [c], Alenka Razpet [c], Benjamin Zorko [c], Primož Pelicon [c]

[a] *Department of Inorganic Chemistry, Institute of Chemical Technology, Technická 5, 166 28 Prague, Czech Republic*
[b] *Department of Neutron Physics, Nuclear Physics Institute, Academy of Sciences of the Czech Republic, 250 68 Řež, Czech Republic*
[c] *Department of Medium and Low Energy Physics, Josef Stepan Institute, Jamova 39, SI-1001 Ljubljana, Slovenia*

Received 9 July 2001; accepted 14 July 2001

Abstract

This article summarizes results and assessments of our systematic fabrication and characterization of proton exchanged (PE) and annealed proton exchanged (APE) waveguides study in lithium niobate. This study focused on different behavior of crystallographically diverse X(1 1 $\bar{2}$ 0) and Z(0 0 0 1) substrate cuts during waveguides fabrication, and differences in characteristics of the resulting waveguides. Non-toxic adipic acid was used as a proton source, and the waveguides properties were defined by a mode spectroscopy (waveguides characteristics) and neutron depth profiling (NDP, lithium concentration and distribution), infrared vibration spectra and elastic recoil detection analysis (ERDA, concentration and depth distribution of hydrogen). It was discovered that the X-cuts structure is more permeable for moving particles (lithium and hydrogen ions), which leads to a higher effectiveness of the PE process within the X-cut. The explanation of this phenomenon is based on the fitting X-cuts orientation towards cleavage planes of lithium niobate crystal. Higher content of interstitial hydrogen in the X-cuts then prevents lithium from free movement during the post-exchange annealing in direction to the surface of samples, and so causes a typical step-like shape of the depth concentration profiles of lithium within the X-cuts. A free transport of lithium within the Z-cuts is being reflected in a gradient shape of the lithium depth concentration profiles and extraordinary refractive index, as well the last but not least, in a trouble-free good reproducibility of the waveguides fabrication within the Z-cuts.

PACS: 42.79.Gn; 82.65.Fr; 52.40.Hf; 41.75.Ai; 81.70.Jb
Keywords: Lithium niobate; Optical waveguides; Annealed proton exchange (APE); Lithium concentration depth profiles; Hydrogen concentration depth profiles; X-cut; Z-cut

1. Introduction

Single-crystal lithium niobate ($LiNbO_3$) is an important ferroelectric material for various applications in linear and non-linear optical devices.

* Corresponding author. Fax: +42-0-2-2431-1010.
E-mail address: jarmila.spirkova@vscht.cz (J. Špirková).

0925-3467/02/$ - see front matter
PII: S0925-3467(01)00186-0

One of its typical utilization are annealed proton exchange (APE) planar (channel) optical waveguides [1]. Proton exchange (PE) is based on a reaction of the lithium niobate wafer with a suitable acidic source

$$LiNbO_3 + xH^+ \rightarrow Li_{1-x}H_xNbO_3 + xLi^+,$$

which results in a large increase of the extraordinary refractive index n_e. The as-exchanged waveguides suffer from high optical loss and degradation of electro-optic figure of merit. However, they can be substantially improved by the annealing of the as-exchanged samples. Properties of the resulting APE waveguides strongly depend on the exchange conditions as well as on any subsequent annealing conditions.

We have carried out a systematic research into relationship between the change of refractive index and the redistribution of lithium after the PE and after the post-exchange annealing [2]. Now we extend our prior investigation to include both Z- and X-cut wafers and present the differences in the properties of the waveguides fabricated under the same fabrication conditions in both types of cuts.

Let us first recall what has already been published on the different behavior of the X- $(1\,1\,\bar{2}\,0)$ and the Z-cuts $(0\,0\,0\,1)$ APE waveguides fabricated using the same technological procedures:

- X-cut waveguides are always deeper [3,4];
- n_e values on the surfaces of the X-cut samples are higher [5,6];
- Li-depletion depth profiles, as measured by SIMS, were not the exact complements of the SIMS or ERDA hydrogen depth profiles in both types of the cuts, indicating thus that the standard ion exchange model, i.e., substitution of Li^+ for H^+, was not sufficient [7–9];
- Two types of mechanism of H^+ in-diffusion into lithium niobate were assumed: Li^+ for H^+ substitution (s, ≈75%) and interstitial H^+ in-diffusion (i, ≈25%). The calculated hydrogen diffusion coefficients were $D_s^X = 3.4 \times 10^{-12}$ cm^2 s^{-1} and $D_i^X = 1.3 \times 10^{-11}$ cm^2 s^{-1} for the X-cuts, and $D_s^Z = 5.0 \times 10^{-12}$ cm^2 s^{-1} and $D_i^Z = 1.4 \times 10^{-11}$ cm^2 s^{-1} for the Z-cuts [10];
- Existence of seven crystallographic phases in the structure of the waveguiding layers was explicitly connected with the Li/H ratio [11].

Although there were quite a lot of evidences on the different characters of the X- and Z-cuts, an explanation why it is so has not been yet explicitly studied in the literature. The intention of the present study was to summarize the different behavior of both types of the cuts as it was observed in our experiments, and to discuss it on the basis of a different structure of the pertinent cuts.

2. Experiments

2.1. Fabrication of the samples (PE and post-exchange annealing A)

The samples used in the experiments were congruent Z- and X-cuts of lithium niobate one side polished wafers with typical dimensions $25 \times 5 \times 0.7$ mm^3 (mostly provided by AVTEX, Czech Republic). The thoroughly pre-cleaned samples were mounted on a platinum holder and placed into individual silica or platinum beakers that contained reaction melt consisting of pure or lithium salt containing adipic acid. The heating source was an ordinary laboratory oven. The PE waveguides were fabricated at a temperature of 213°C for times ranging from 30 min to 6 h. Setting of the temperature of the reaction melt at 213°C comes from our experiments concerning the composition of the reaction melt. According to our thermodynamic considerations, at the temperature about 210°C there is the highest concentration of H_3O^+ ions in the reaction melt, which makes the PE process at this temperature to progress most efficiently. Applying either lower or higher temperatures of the reaction melt than ≈210°C resulted in fabrication of the PE waveguides which had smaller Δn_e and supported less number of modes. The as-exchanged samples were immediately washed with distilled water and acetone in order to remove the remnants of the reaction melt and then they were annealed at temperatures ranging from 250 to 500°C for various times (30 min–100 h) in another laboratory oven under

ambient atmosphere. The annealing was usually done immediately after the PE.

2.2. Measurement

The waveguides were optically characterized at $\lambda = 633$ nm using the prism coupling technique. The extraordinary refractive index (n_e) depth profiles of the fabricated waveguides were reconstructed from the effective index spectra by means of inverse WKB procedure [12] using piecewise linear approximation to the actual index profiles.

Lithium concentration depth profiles (c_{Li}) in the as-exchanged as well as post-exchanged annealed waveguides were measured by the neutron depth profiling (NDP) [13,14]. The method is based on a reaction of thermal neutrons with ^{6}Li:^{6}Li (n,α) ^{3}H. The fabricated samples were irradiated with a thermal neutron beam from a 6 m long neutron guide (neutron intensity was 10^7 n cm^{-2} s^{-2}) and the charged reaction products were recorded by means of Si(Au) surface barrier detector. The accuracy of the NDP method is 5% of the c_{Li} value, the depth resolution is 10 nm. Natural abundance of the "NDP active" ^{6}Li isotope is 7.5%, however, in the actual samples the ^{6}Li/^{7}Li ratio may significantly vary (e.g., due to artificial depletion of the ^{6}Li isotope from the original natural materials). Thus, to avoid uncertainty induced by this variation, for some considerations we rely on relative changes of c_{Li} instead of their absolute values.

Depth profiles of incorporated hydrogen were measured by elastic recoil detection analysis (ERDA) [15,16]. The $^4He^+$ beam from the Tandem accelerator with 1.8 MeV with the beam currents below 10 nA was used for this measurements. Reflection geometry was taken with the incident angle of 75° relative to the surface normal and the take-off angle of 24° with respect to the surface normal. The beam doses of up to 100 μC were obtained by the simultaneous Rutherford backscattering spectroscopy (RBS) measurement, the method being also used for the determination of the sample matrix composition. The 6 μm thick Al foil placed in front of the ERDA detector was used to stop scattered He^+ ions and prevent them from scattering into detector. With this ERDA setup were achieved the detection limit of 0.1 at.%, detectable depth of up to 0.5 μm with the depth resolution 30 nm.

3. Results

In the course of our systematic investigation of the relations between concentration profiles of lithium (c_{Li}) and the waveguiding properties, especially refractive index (n_e) profiles, we have noticed some peculiarities in the X-cut samples. One of them is illustrated in Fig. 1 showing typical examples of lithium concentration (c_{Li}) profiles of the APE X- and Z-cut samples. The Z-cuts revealed the already described [2] transition of the c_{Li} depth profiles from the step-like for the PE guides to graded after annealing (1.5 h), the c_{Li} depth profiles of the X-cuts maintain more or less step-like character even after annealing of the PE guides. The same trends were observed also for the refractive index (n_e) depth profiles (Fig. 2).

Similar observations are also illustrated in Fig. 3, now for the guides annealed for very long times (100 h). The c_{Li} profiles of the X-cut maintain the step-like shape even after such a long annealing but both the n_e profiles (Fig. 4) are graded with different Δn_e which is lower for the Z-cut sample. Unlike the cases where the annealing times are short, the depths of the X-cut waveguides after a long annealing time are shallower compared with those in the Z-cut samples.

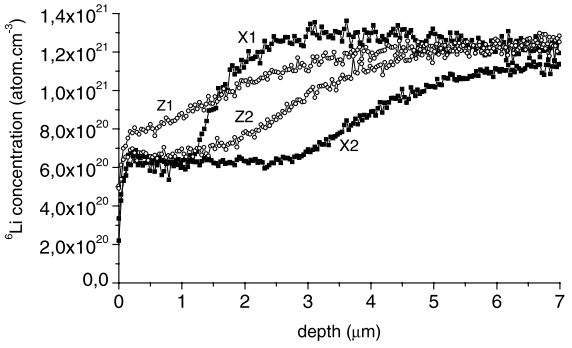

Fig. 1. Comparison of the c_{Li} depth profiles of the APE waveguides fabricated using different time of PE in the X- and Z-cuts. (X1 and Z1 PE: 1 h, X2 and Z2 PE: 3 h, 213°C in pure adipic acid; A: 1.5 h, 350°C).

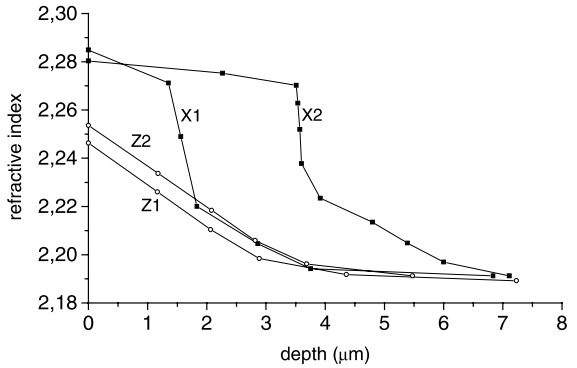

Fig. 2. Comparison of the n_e depth profiles of the APE waveguides from Fig. 1. (X1 and Z1 PE: 1 h, X2 and Z2 PE: 3 h, 213°C in pure adipic acid; A: 1.5 h, 350°C).

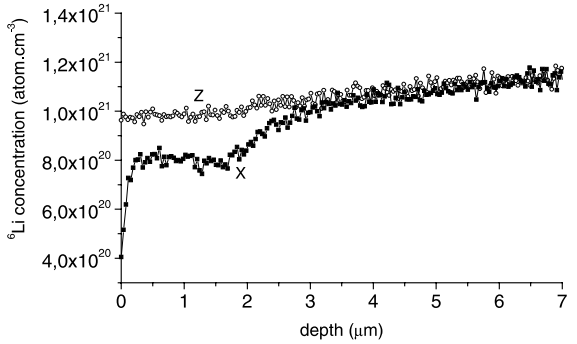

Fig. 3. Comparison of the long time annealing effect on the c_{Li} depth profiles of the waveguides fabricated in the X- and Z-cuts under the same fabrication conditions. (PE: 2 h, 213°C in pure adipic acid; A: 100 h, 300°C).

Large number (about 300) of the measured samples fabricated in both types of the cuts, and using a variety of the fabrication conditions, lead to fairly general findings. The results clearly demonstrated the well-known fact that the as-exchanged PE guides in the X-cuts were always deeper and supported higher number of modes comparing with the guides fabricated using the same experimental conditions of PE in the Z-cuts.

The differences between both types of the cuts became even more significant after the post-exchange annealing of the PE samples. Though the c_{Li} profiles of the Z-cut APE waveguides tended to be graded with longer times of the annealing, in the X-cuts was always observed a tendency to

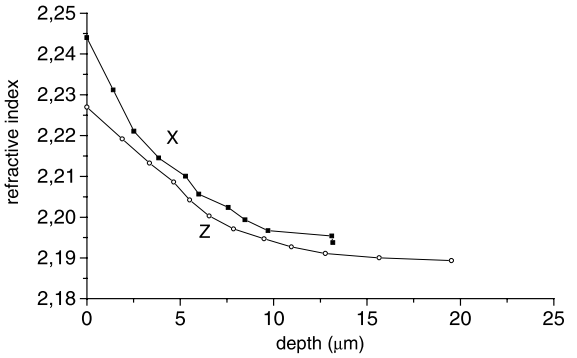

Fig. 4. Comparison of the long time annealing effect on the n_e depth profiles of the waveguides fabricated in the X- and Z-cuts under the same fabrication conditions. (The points in the figure represent particular modes, so that the position of the last mode gives also the depth of the particular guide.) (PE: 2 h, 213°C in pure adipic acid; A: 100 h, 300°C).

persist the step-like shapes of the APE c_{Li} depth profiles.

Fig. 1 illustrates another interesting feature. The lithium concentrations on the surfaces of the samples tended to keep a relatively stable value of 6×10^{20} at. cm^{-3} corresponding approximately to a 55% depletion of lithium. This stable phase is in the X-cuts established sooner and can be observed in deeper layers of the samples (curves X1 and X2 in Fig. 1). However, the pertinent n_e values differ in both types of the cuts. The stable compositional phase corresponds to the $\Delta n_e + 0.09$ for the X-cut samples and about +0.06 for the Z-cuts.

Quite generally, the relationship between lithium concentration values (c_{Li}) and the pertinent n_e values of the guides fabricated under the same conditions are in both types of the cuts different. It

Table 1
Comparison of the areas under the ν(OH) absorption bands at 3500 cm^{-1} in the reflection infrared spectra of the X- and Z-cut PE and APE samples fabricated in pure adipic acid at 213°C and post-exchange annealed at 300°C in air

Fabrication	X-cut	Z-cut
Standard (virgin substrate)	0.251	0.199
PE: 2 h, A: 0.5 h	2.324	0.132
PE: 2 h, A: 1.5 h	2.442	–
PE: 2 h, A: 14 h	2.472	0.005
PE: 2 h, A: 24 h	2.628	0.006
PE: 2 h, A: 100 h	2.760	0.001

means that the contributions into the increments of the extraordinary refractive indices are not the same in the X- and the Z-cuts.

In Table 1 there are summarized the intensities of the ν(OH) absorption bands at 3500 cm^{-1} in the infrared vibration spectra of the APE waveguides. From the X- and Z-cut pairs, the X-cut samples always contained much more hydrogen incorporated in the waveguiding layer.

These observations made us to study the origin of that phenomena beginning with the direct measurement of the hydrogen concentration in the PE and APE layers. We fabricated very shallow optical layers (Figs. 5 and 6), resulting from very short times of the PE reaction, which enabled the

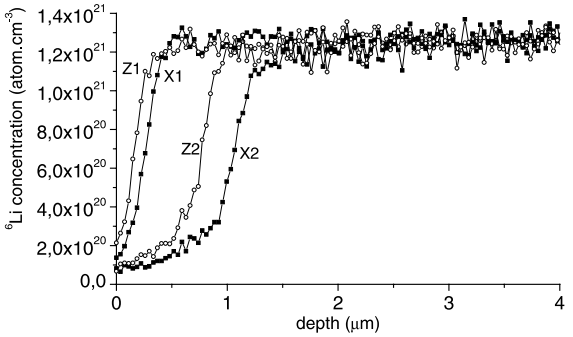

Fig. 5. Comparison of the lithium concentration (c_{Li}) depth profiles of the PE X- and Z-cuts samples for the short (curves X1 and Z1) and long (curves X2 and Z2) times of PE (PE: 5 min and 1 h, 213°C in pure adipic acid).

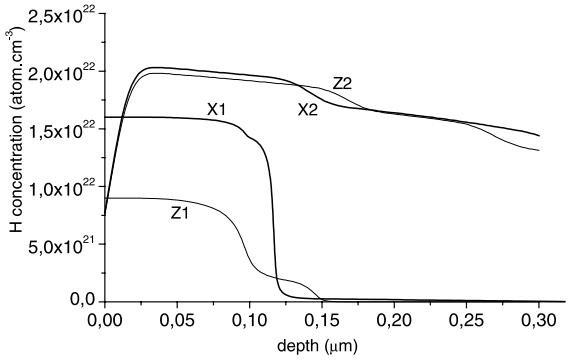

Fig. 6. Comparison of the hydrogen concentration (c_H) depth profiles of the PE X- and Z-cuts samples for the short (curves X1 and Z1) and long (curves X2 and Z2) times of PE (PE: 5 min and 1 h, 213°C in pure adipic acid).

ERDA measurement to characterize the whole PE area in the surfaces of the samples. The figures show the comparison of the c_{Li} and c_H depth profiles of the PE guides fabricated in pure adipic acid for 5 min and 1 h. It is obvious that the rate of lithium out-diffusion is always slower in the Z-cuts. The rate of in-diffusion of hydrogen can be compared only in very shallow layers (see the curves X1 and Z1 in Fig. 6) and evidently it is substantially higher in the X-cuts. The c_{Li} profiles of the 1 h PE samples show that the concentrations of lithium in 3 μm depths already reached its substrate values (curves X2 and Z2 in Fig. 5). However, the treated layers still contained the in-diffused hydrogen (the depth to which the ERDA measurement can refer is less than 0.5 μm so that the exact depth of the H-containing layers could not be determined).

Diffusion of hydrogen then does not entirely correspond with lithium out-diffusion. It may be explained by the fact that the mechanism of its entry into lithium niobate structure cannot be expressed as a simple substitution of lithium, and be assumed that it is accompanied by an interstitial diffusion, and/or the migration of hydrogen inside the bulk of the samples, which are the processes fundamentally independent of lithium movement from the surface out.

Figs. 7 and 8 indicate c_{Li} and c_H samples depth profiles from Figs. 5 and 6, at this time, after being annealed at 300°C for a 90 min period. The lithium movement from PE shallow layers (fabricated by means of short PE) in direction towards surfaces

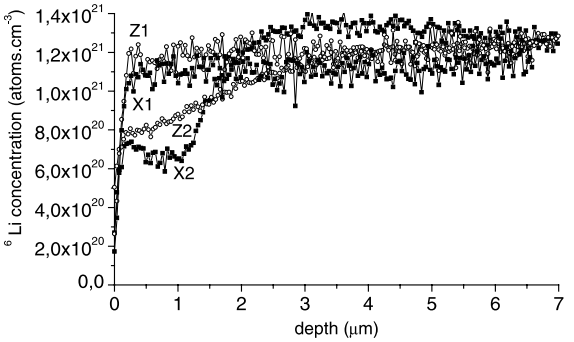

Fig. 7. Comparison of the lithium concentration (c_{Li}) depth profiles for the samples of Figs. 5 and 6 after the annealing (A: 1.5 h, 300°C).

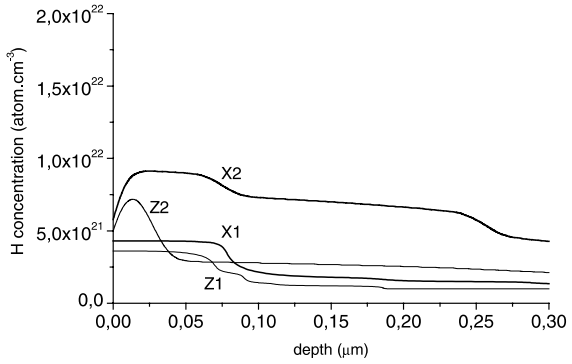

Fig. 8. Comparison of the hydrogen concentration (c_H) depth profiles for the samples of Figs. 5 and 6 after the annealing (A: 1.5 h, 300°C).

of the samples causes its concentration to be practically nearly balanced out up to a bulk value within the entire volume of the optical layer. As well hydrogen concentration profiles (X1 and Z1 curves in Fig. 8) indicated a drop of the hydrogen content already in a depth, where it was measurable by the ERDA method. In layers deeper than 0.1 μm the hydrogen concentrations are already constant in both the cuts. A small difference in their values, i.e., higher concentration of hydrogen within the X-cut, is quite consistent with other measured values, (although here it could also be interpreted as an experimental error).

Even more interesting are c_{Li} profiles of the PE layers fabricated by longer PEs. Both the X2 and Z2 curves in Fig. 7 indicate the so characteristic difference already mentioned earlier. The gradient shape of depth c_{Li} documents the movement of lithium in direction towards the surface having to be continuous during the Z-cut annealing. Quite different is the situation in case of the X-cut, where the c_{Li} profile is of a much more complicated shape. Lithium is quite distinctively slowed down by a certain barrier when moving towards the surface, which causes its accumulation, in this case, in a depth of about 2–4 μm, where the lithium concentration is higher than its corresponding substrate value. Due to this fact, we can observe the so typical step-like shape of the c_{Li} depth profile. Slight accumulation of lithium in a very thin subsurface layer (<0.5 μm) is also the commonly observed phenomenon in the X-cuts of APE waveguides.

The hydrogen concentration profiles in these samples (X2 and Z2 samples in Fig. 8) gives a quite clear idea about the hydrogen volume contained in the APE samples surfaces. A clear loss of its concentration in the Z-cut that already appears in a very shallow layer (>0.05 μm) documents not only its lower initial concentration after PE but also the fact that hydrogen moves within the Z-cuts substantially slower than within the X ones, where it penetrates deeper in the substrate during the annealing process. It is certainly necessary to keep in mind that the ERDA measurement only affects a very shallow layer, up to 0.5 μm, so it does not give any information about hydrogen distribution within the entire waveguide layer volume, but, nevertheless, from the measurement of the very short-time PE layers it is obvious that the samples always contained more hydrogen within the X-cuts than the Z ones. This assessment is in a good agreement with the information obtained upon an indirect determination of the hydrogen content of the PE as well as APE waveguides fabricated in both the types of cuts, i.e., from comparison of the OH stretching vibrations bands intensity in the infrared reflection spectra.

Table 2
Comparison of Li (depleted): H ratios in the X- and Z-cuts PE waveguides fabricated in pure adipic acid at 213°C

Cut	Fabrication (min)	NDP-areas	ERDA-areas	Li:H
X-cut	5	4.057×10^{21}	1.86×10^{21}	1:0.45
	10	3.29×10^{21}	3.52×10^{21}	1:1.07
	60[a]	5.01×10^{21}	5.85×10^{21}	1:1.16
Z-cut	5	3.18×10^{21}	9.54×10^{20}	1:0.30
	10	4.66×10^{21}	2.90×10^{21}	1:0.62
	60[a]	4.88×10^{21}	5.77×10^{21}	1:1.18

[a] The compared areas refer only to the depths of 0.3 μm; the layers in both the cuts are in this depth already H-saturated.

Table 2 indicates the comparison of areas underneath the c_H and c_{Li} depth concentration profiles of PE samples in the X- and Z-cuts. Again, from the comparison of the short PE time samples it follows that significantly more hydrogen "flows" into the X-cuts than into the Z ones. After the longer PE times the shallow layers are already H-saturated, so that there was found similar concentration of hydrogen. An interesting finding is the fact that after short time periods of the PE a ratio of hydrogen and lithium is not 1:1 as one would expect in the event of a substitution reaction. According to these assessments it seems that both processes, i.e., movement of hydrogen into the lithium niobate surface layer and movement of lithium out of this layer, act independent of each other, and that lithium moves faster than hydrogen. If we then compare the speed of movement of these particles within both the types of cuts, then it is clear that lithium moves within the X-cuts faster than it does within the Z ones.

4. Discussion

To discuss the obtained results one should bear in mind two things:

The base of processes taking place during the PE and the post-exchange annealing, and the structure of lithium niobate.

The PE includes Li^+ for H^+ substitution and, very probably, also an interstitial in-diffusion of the hydrogen into the lithium niobate structure. What does the already reported [3–6] higher rate of the PE in the X-cut structure really mean? Does it mean a faster substitution of Li^+ for H^+ because of better accessibility of lithium atoms in the X-cut structure or does it mean a larger amount of the incorporated hydrogen in the X-cuts after the same PE procedure as in the Z-cuts?

Our results show that the rate of the Li^+ for H^+ substitution in the beginning of the PE, i.e., for very short times of the PE, is really higher in the X-cuts (see Figs. 5,6 and Table 2). The amount of the in-diffused hydrogen is also always larger in the X-cuts and even after some time of PE it is larger than that which would correspond completely to a simple Li^+ for H^+ substitution. Hence one may assume that the extent of the interstitial H^+ in-diffusion strongly depends on the orientation of the cuts being more efficient in the X-cuts than in the Z-cuts.

The post-exchange annealing causes a massive transport of lithium towards the samples surfaces [2]. This transport can be partly considered as a "secondary" PE inside the subsurface layers of the PE samples, where the already in-diffused hydrogen forms the diffusion source, and partly as an independent pervading of the moving Li^+ and H^+ particles through the lithium niobate structure. The progression of lithium towards the samples surfaces, and that of hydrogen inside the bulk crystal, depend not only on the annealing temperature but also on the availability of suitable vacant positions. Longer periods of PE reaction enable to start the secondary progression of the diffusing particles, so that both processes, the PE and the post-exchange annealing, may occur at the same time. The smooth characters of the c_{Li} depth profiles of the APE Z-cuts (Fig. 7) show a non-interrupted motion of the lithium particles when some energy is added by annealing. On the other side, the outlasting step-like character of the c_{Li} depth profiles in the X-cuts gives evidence for a barrier, which prevents the lithium ions move smoothly towards the surface of the wafer. It is expected that this barrier is, in fact, positively charged area with higher concentration of the in-diffused hydrogen which makes the moving lithium to heap up before it reaches the very surface of the wafer. However, much measurement of the hydrogen depth profiles, especially in deeper layers of the waveguides, is needed to complete the understanding of that phenomenon.

Similar anisotropy of the diffusion processes in the X- and the Z-cuts has been already described for erbium ions which were in-diffused into the lithium niobate X-, Y- and Z-cuts at a moderate temperature in melts containing erbium nitrate [17–19], as well as by a high-temperature diffusion of erbium from the metal erbium thin film evaporated onto the substrate surfaces. In the latter case, the surface concentration of erbium in the X-cuts higher than that in the Z-cuts was reported ([20] and references therein).

Now why is the rate of incorporation of hydrogen (and Er^{3+}) higher in the X-cuts than in the Z-cuts? Structure of the Z-cuts, which are oriented perpendicularly to the C_3 axis, reveals the well-known channel structure [21]. On the other hand, the structure of the X-cut is less dense that the Z-cut one (the density of the X-cuts is one quarter lower than that of the Z-cuts [22]). Moreover, it shows a layered-type situation with the following sequences: –oxygen–lithium–oxygen–niobium–oxygen–vacancy–. The layers of the vacancies form the cleavage planes ($\{0\,1\,\bar{1}\,2\}$) [23], which are in this type of the cuts oriented perpendicularly to the surfaces of the wafers. The easy access of the vacant sites helps introducing the diffusing particles into the structure of the X-cuts in a higher rate than into the Z-cuts. This easy access to vacant sites of the cleavage planes also explains why both the migrating Li^+ and H^+ ions keep moving within the X-cuts faster, and why hydrogen penetrates into the substrate greater depths within these cuts.

Resulting waveguides characteristics, i.e., a change of extraordinary refractive index, then represent a result of co-action of a number of elements. Fig. 9 indicates an example of difference between n_e and c_{Li} APE waveguides within both types of the cuts. It is obvious that this regards quite different waveguides, and it is a question as how much this is only caused by the fact that a radiation of TM polarization is distributed within the Z-cuts and the TE polarization within the X-cuts. Various options of this relationship (between n_e and c_{Li}), i.e., the fact that more c_{Li} values can correspond with one n_e value and vice versa, and how this relationship may be changed by modification of experimental conditions, we had even observed within the scope of the same cut (refer to [2]). At first sight, it seems obvious that a higher concentration of hydrogen within the waveguide layer contributes to an increase of the extraordinary refractive index, but a key factor for resulting waveguide characteristics shall also be the hydrogen distribution inside the waveguiding layer. According to our preliminary results, it appears that a shift of the curve of dependency between n_e and c_{Li} into the α phase area, and due to this, even substantial improvement of the waveguide quality is connected with a lower concentration, and, at the same time, a homogenous hydrogen distribution within the waveguide layer, i.e., by its progress into the substrate deep layers. However, these assessments are necessary to be examined to be made more accurate by further studying.

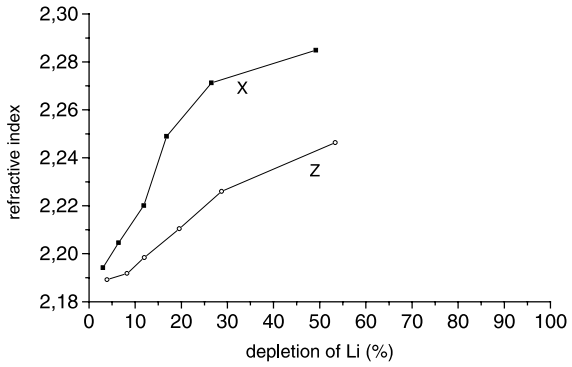

Fig. 9. Plot of n_e vs. depletion of lithium (as measured in the depth of particular modes) for the X- and Z-cuts fabricated under the same conditions (PE: 1 h, 213°C in pure adipic acid, A: 1.5 h, 350°C).

5. Conclusions

A systematic study of PE and APE waveguides within the lithium niobate X- and Z-cuts had been conducted focusing on differences between both the crystallographically different cuts. The process of the waveguide layer formation during the PE, and subsequent annealing, is a very complicated one, where the waveguide gets stabilized already during PE longer periods. According to our results this process does not mean a pure exchange of $H^+ \leftrightarrow Li^+$, but, in harmony with already earlier presented opinions, this substitution is accompanied with a hydrogen interstitial diffusion. Nevertheless, a range of these two processes substantially varies in both the types of cuts. It was discovered that the X-cuts $(1\,1\,\bar{2}\,0)$ are significantly better passable for moving particles than those of Z $(0\,0\,0\,1)$. This "better permeability" of the X-cuts is, most likely, caused by a suitable, particularly perpendicular orientation of the X-cuts towards crystal cleavage planes allowing easier movement of particles due to the fact that these can take advantage of their own easily available vacant

sites. Hydrogen then proceeds faster within the X-cuts into greater substrate depths. Its higher concentration closer to the samples surfaces creates a barrier preventing the lithium ions to freely move towards the surface, and so causes a typical step-like shape of the lithium depth concentration profiles within the X-cuts.

Acknowledgements

This research has been supported by the Grant Agency of the Czech Republic (Projects 102/99/1391 and 102/99/D017), by the Research Programme "Chemistry and technology of materials for technical applications, health and environment protection" (CEZ: MSM 223100002), and last but not least, by the International Atomic Energy Agency (CPR CZR 10031).

References

[1] J.L. Jackel, C.E. Rice, J.J. Veselka, Appl. Phys. Lett. 41 (1982) 607.
[2] J. Špirková-Hradilová, P. Nekvindová, J. Vacík, J. Červena, J. Schröfel, Opt. Mater. 15 (4) (2000) 269.
[3] G.R. Paz-Pujalt, D.D. Tuschel, G. Braunstein, T. Blanton, S.T. Lee, L.M. Salter, J. Appl. Phys. 76 (7) (1994) 3981.
[4] J.L. Jackel, Integrated optical circuits, SPIE 1538 (1991) 54.
[5] A. Loni, R.M. De La Rue, J.M. Winfield, J. Appl. Phys. 61 (1) (1987) 64.
[6] J.M. Carbrera, J. Olivares, M. Carrascosa, J. Rams, R. Müller, E. Diéguez, Adv. Phys. 45 (5) (1996) 349.
[7] R.G. Wilson, S.W. Novak, J.M. Zavada, A. Loni, R.M. De La Rue, J. Appl. Phys. 66 (12) (1989) 6055.
[8] A. Loni, R.M. De La Rue, J.M. Zavada, R.G. Wilson, S.W. Novak, Electron. Lett. 27 (14) (1991) 1245.
[9] C. Canali, A. Carnera, G. Della Mea, P. Mazzoldi, S.M. Shukri, A.C.G. Nutt, R.M. De La Rue, J. Appl. Phys. 59 (8) (1985) 2643.
[10] T. Sendeep, S.T. Vohra, A.R. Mickelson, S.E. Asher, J. Appl. Phys. 66 (11) (1989) 5161.
[11] Yu.N. Korkishko, V.A. Fedorov, S.M. Kostritskij, J. Appl. Phys. 84 (5) (1998) 2411.
[12] J.M. White, P.F. Heinrich, Appl. Opt. 15 (1976) 151.
[13] J. Vacík, J. Červená, V. Hnatowicz, V. Havránek, D. Fink, Acta Phys. Hunga. 75 (1–4) (1994) 369.
[14] P. Kolářová, J. Vacík, J. Špirková-Hradilová, J. Červená, Nucl. Instrum. Meth. Phys. Res. B 141 (1998) 498.
[15] J. Tirira, Y. Serruys, P. Trocellier, Forward Recoil Spectrometry, Plenum Press, New York, 1996.
[16] B. Zorko, M. Budnar, Vacuummist 15/4 (1995) 10.
[17] J. Hradilová, P. Kolářová, J. Schröfel, J. Čtyroký, J. Vacik, V. Peřina, Proc. SPIE 2775 (1996) 647.
[18] C. Sada, E. Borsela, F. Caccavale, F. Gonella, F. Segato, Yu.N. Korkishko, V.A. Fedorov, T.M. Morozova, A.G. Battaglin, R. Polloni, Appl. Phys. Lett. 72 (1998) 3431.
[19] P. Nekvindová, J. Špirková-Hradilová, J. Schröfel, V. Peřina, J. Mater. Res. (in press).
[20] F. Caccavale, F. Segato, I. Mansour, J.M. Almeisa, A.P. Leite, J. Mater. Res. 13 (6) (1998) 1672.
[21] S. Abrahams, J. Reddy, J. Bernstein, J. Phys. Chem. Solids 27 (1996) 997.
[22] A. Rauber, Chemistry and physics of lithium niobate, in: Current Topics in Materials Science, 1, North-Holland, Amsterdam, 1978.
[23] R.S. Weis, T.K. Gaylord, Appl. Phys. A 37 (1985) 191.

Available online at www.sciencedirect.com
SCIENCE DIRECT®
Optical Materials 24 (2003) 527–535
OPTICAL Materials
www.elsevier.com/locate/optmat

Features of APE waveguides in different Er:$LiNbO_3$ and (Er + Yb):$LiNbO_3$ cuts: electrooptical coefficient r_{33}

Pavla Nekvindová [a,*], Jarmila Červená [b], Pavel Čapek [c], Anna Macková [b], Vratislav Peřina [b], Josef Schröfel [c], Jarmila Špirková [a]

[a] Department of Inorganic Chemistry, Institute of Chemical Technology, 166 28 Prague, Czech Republic
[b] Department of Neutron Physics, Nuclear Physics Institute, Academy of Sciences of the Czech Republic, 250 68 Řež, Czech Republic
[c] Department of Microelectronics, Czech Technical University, 166 27 Prague, Czech Republic

Received 18 February 2003; accepted 3 March 2003

Abstract

Our contribution represents a systematic study of optical layers fabricated by the annealed proton exchange (APE) method in various cuts (X, Y, Z) of lithium niobate that was doped in bulk with erbium (500 ppm) and mixture of erbium and ytterbium in weight portion 1:9 (1000 ppm). Rutherford backscattering spectrometry (RBS), elastic recoil detection analysis (ERDA) and neutron depth profiling (NDP) methods have been used for monitoring a composition of fabricated optical layers, i.e. changes of the concentration of the rare earths (RE), hydrogen and lithium. We have used mode spectroscopy and a Mach–Zehnder interferometer to monitor the relevant properties, i.e. changes in the effective refractive index and the electrooptical coefficient r_{33}. The obtained results show that during the APE process, there is no loss of the rare earths from the substrate and that during the treatment of the as-exchanged samples the hydrogen concentration increases while the lithium concentration decreases. Waveguiding properties and composition of the RE doped waveguides were not substantially changed compared with those fabricated in pristine lithium niobate. The presence of the doping ions decreases the r_{33}, however, a carefully designed APE technology can increase the r_{33} almost to the value of the pristine $LiNbO_3$. A correlation between the uniform distribution of lithium and high values of the electrooptic coefficient r_{33} was found. According to our results the proton exchange not necessarily lowers the efficiency of the 1.5 μm emission and certainly does not lower the concentration of the RE.

PACS: 42.70; 42.82.E; 78.66; 78.20.J; 81.40
Keywords: Lithium niobate; Optical waveguides; Annealed proton exchange; Erbium; Ytterbium; Electrooptical properties

1. Introduction

Single crystals of lithium niobate are frequently used in photonics and integrated optics due to its excellent properties. For emission at 1550 nm ($^4I_{13/2} \rightarrow {}^4I_{15/2}$), lithium niobate is doped with erbium ions [1–5], or with a mixture of erbium and

* Corresponding author. Fax: +420-2-311-2206.
E-mail address: pavla.nekvindova@vscht.cz (P. Nekvindová).

0925-3467/$ - see front matter © 2003 Published by Elsevier B.V.
doi:10.1016/S0925-3467(03)00088-0

ytterbium ions [6]. Basically, such doping can be a bulk doping or a localised doping from an external source. A suitable combination of the bulk or localised erbium doping and a simultaneous preparation of optical waveguides by using titanium diffusion have been proved to be successful [7–9] and several optical amplifiers and lasers based on such technology have been already demonstrated [10].

One of the reasons for the high popularity of lithium niobate for optoelectronics applications is the high value of the electrooptical coefficient r_{33} (30×10^{-12} m V^{-1}). However, only a limited number of lithium niobate devices such as Ti:$LiNbO_3$ Mach–Zehnder [11] modulators have been used so far because of their poor electrooptic performance.

The annealed proton exchange (APE) [12] technology for fabrication of the waveguides in connection with the rare earth doped lithium niobate was mentioned only scarcely. It has usually been stated that this combination is not suitable for a good function of the active waveguides as the presence of hydrogen has a killing effect on the excited Er^{3+} electrons shortening their lifetimes, which then results in a drastically reduced optical gain [9,10].

The aim of this paper is to present properties of the APE waveguides in the bulk doped Er:$LiNbO_3$ and (Er + Yb):$LiNbO_3$ *X*- and *Z*-cuts. We mainly focused on the relations between the composition of the waveguiding layers and important properties of the waveguides, especially the value of the electrooptical coefficient r_{33}, and how it can be increased by a carefully designed APE process.

2. Experimental

Single crystals doped either with erbium or mixture of erbium and ytterbium (1:9) were grown by the Czochralski technique from congruent melts of the relevant elements oxides with 500 ppm of erbium oxide and 1000 ppm of mixture of erbium and ytterbium oxides (AVTEX, Czech Republic). The three crystallographically different types of substrate wafers (one or both sides polished) of lithium niobate (*Z* (0 0 0 1), *X* (11–20) and *Y* (1–100)), were used with dimensions of $25\times5\times0.7$ mm and $30\times5\times0.7$ mm.

Thoroughly pre-cleaned samples were immersed into a proton source, which was a pure or buffered (i.e. containing 0.5 mol% of Li^+) adipic acid in a quartz crucible. This system was closed with ground glass joint and heated in a common laboratory oven at a temperature of 213 °C for the desired times. The as-exchanged samples were immediately washed with distilled water and acetone to remove the proton source residues and annealed subsequently in the air in the laboratory oven. Two sets of the samples were fabricated. For a study of the waveguiding layers composition the proton exchange (PE) times were 1 and 3 h and, subsequently, the post-exchange annealing (A) was done for 1.5 h at 350 °C. To ensure the fabrication reproducibility as well as the accuracy of the measurement, the same samples were doubled or even tripled. The second set of the samples was fabricated for the measurement of the electrooptic coefficient r_{33}. The annealing times of the samples (that were proton exchanged for 2 h) were from 30 min to 100 h at temperatures of 300 and 350 °C.

2.1. Measurement

Distribution of hydrogen and erbium in the fabricated optical layers were determined by Rutherford backscattering spectrometry (RBS) and elastic recoil detection analysis (ERDA), respectively. The RBS and ERDA measurement were performed in a vacuum chamber simultaneously by 2.745 MeV ion beam from an electrostatic accelerator. The RBS measurement was performed under 170° laboratory scattering angle. In the ERDA measurement the protons recoiled under an angle of 30° were registered with a surface barrier detector covered with a 12 μm thick mylar stopping foil. The RBS and ERDA spectra were evaluated using the GISA [13] and the SIMNRA [14] PC codes, respectively.

Lithium concentration depth profiles (c_{Li}) in the as-exchanged (PE) as well as the post-exchanged annealed (APE) waveguides were measured by the neutron depth profiling (NDP) [15,16]. The method is based on a nuclear reaction of thermal neutrons with ^{6}Li: ^{6}Li(n,α)^{3}H. The fabricated

samples were irradiated with a thermal neutron beam from a 6 m long neutron guide (neutron intensity was 10^7 neutrons $cm^{-2} s^{-2}$) and the charged reaction products were recorded by means of Si(Au) surface barrier detector. The accuracy of the NDP method is 5% of the c_{Li}-value, the depth resolution is 10 nm. The natural abundance of the "NDP active" ^{6}Li isotope is 7.5%, however, in the actual samples the ^{6}Li/^{7}Li ratio may significantly vary (e.g. due to an artificial depletion of the ^{6}Li isotope from the original natural materials). Thus, to avoid uncertainty induced by this variation, for some considerations we rely on relative changes of c_{Li} instead of their absolute values.

The waveguides properties were characterized at $\lambda = 633$ nm using the two-prism mode spectroscopy. The refractive index depth profiles of the waveguides were reconstructed from the measured effective index spectra by means of the inverse WKB procedure [17] using piecewise (step-by-step) linear approximation to the actual index profiles.

The electrooptical coefficient r_{33} was measured using a Mach–Zehnder interferometer (see Fig. 1) with a He–Ne laser (633 nm, 10 mW) as a light source. The laser light was split to two beams through a divider; one of the beams was the reference one and the other beam coupled into and out of the measured sample using the BGO prisms. An adjustable high voltage power supply 0–1200 V was applied to the sample using a couple of electrodes. The divider was used to create interference between both beams. The interference pattern was magnified by a microscopic objective and monitored using a lock-in synchronous amplifier. The electrooptic coefficient value was than derived from the measured half-wave voltage.

The bulk values of the electrooptical coefficient were also measured using the above-mentioned experimental set-up. For the measurement of the substrate mode guiding, one half of the surface was covered with an aluminium thin layer so that the proton exchange occurred only in the uncovered area (see Fig. 2A). The light beam was then coupled in through the PE layers and the substrate mode was coupled out in the second (originally Al covered) half using also the BGO prisms (Fig. 2B).

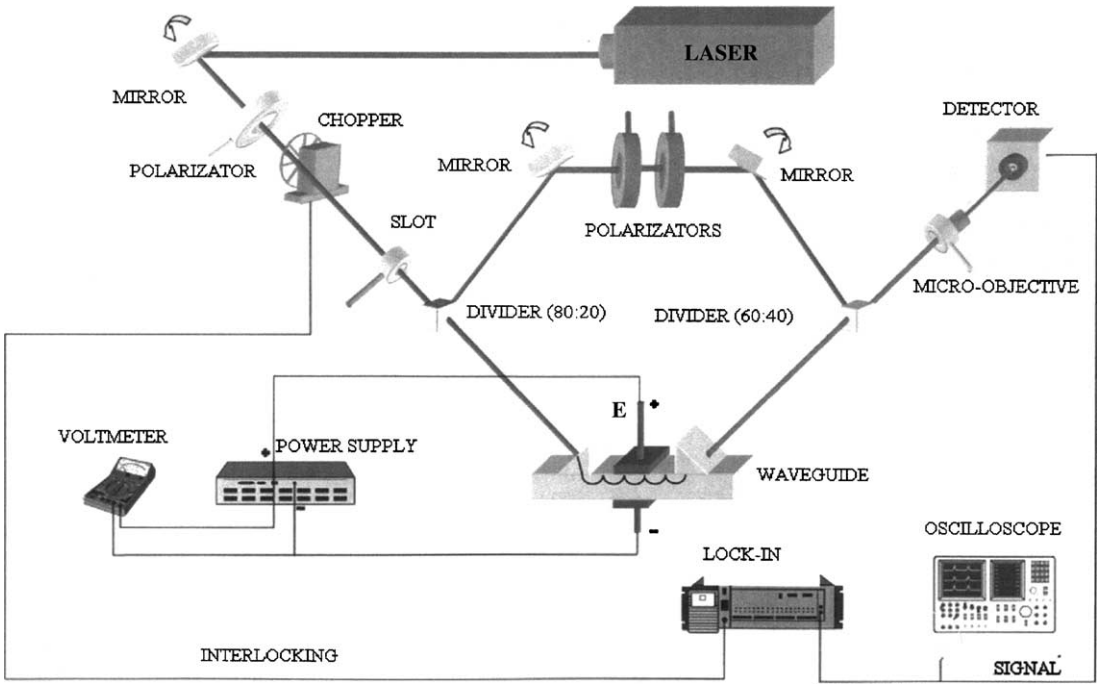

Fig. 1. The r_{33} measurement set-up.

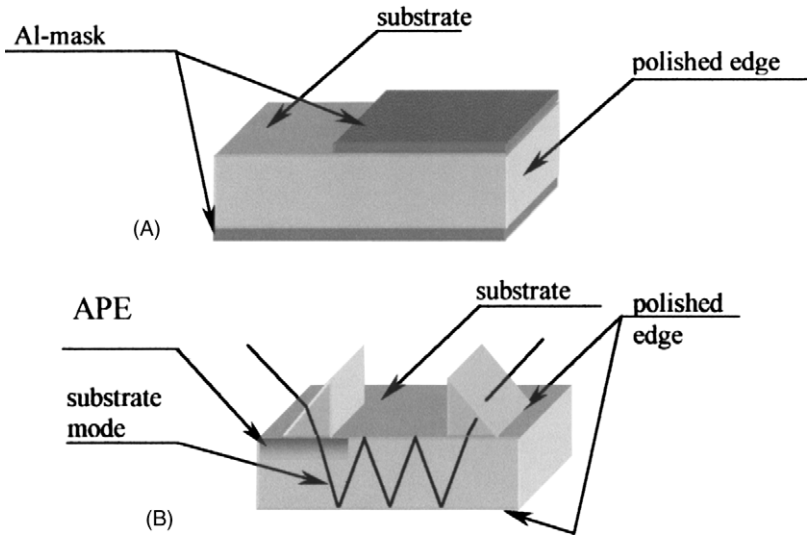

Fig. 2. Details of the measurement of the r_{33} substrate value: (A) masking, (B) propagation of the optical signal during the measurement in the APE waveguide.

The absorption spectra of the samples were taken in a range of 200–1000 nm using the UV-1601 (Shimadzu) absorption spectrophotometer.

3. Results

3.1. The properties of the pristine (untreated) samples

The prime factor which significantly affects the properties of the fabricated waveguides is the composition of the bulk single crystals. Our attention was paid to this fact and the single crystals doped with rare earth ions were analysed by RBS, ERDA, NDP and absorption spectroscopy methods. The surface concentrations of erbium, hydrogen and that of ^{6}Li were found to be 0.13 ± 0.01, 0.001 mol% and 1.35×10^{20} atom cm^{-3}, respectively, in the crystals doped with 500 ppm of erbium. In the crystals doped with a mixture of 1000 ppm of Er and Yb (weight ratio 1:9) during the crystal growth the same contents of Li and H were found as in the former case. The total content of RE was twice as high (i.e. 0.24 mol%) comparing with the former (RBS is not able to distinguish between Er and Yb).

As expected, the presence of ytterbium in the erbium doped lithium niobate caused a significant broadening of the absorption band at about 980 nm with three distinct bands showing an increasing maximum intensity at 918, 956 and 980 nm (Fig. 3) in the absorption spectrum. It was interesting to find that the intensities of these bands differed when comparing *X*-, *Y*- and *Z*-cuts of the (Er + Yb):$LiNbO_3$ samples. The 980 nm band had almost the same intensity in all three types of the cuts but the intensity of the 956 nm band was significantly lower in *Y*-cut.

The results of the r_{33} coefficient measurement of the RE doped wafers are shown in Table 1. It is clear that the RE doping makes the r_{33} value decreased while increasing the total concentration of the RE.

3.2. Annealed proton exchanged waveguides in Z-, X- and Y-cuts of $LiNbO_3$

The behaviour of the individual cuts during the reaction in the acid melts differ each other. This fact must be kept in mind when the waveguides are being fabricated. There is a high risk of a surface damage in *X*- and *Y*-cuts during the treatment in the reaction melts, therefore the so called buffered

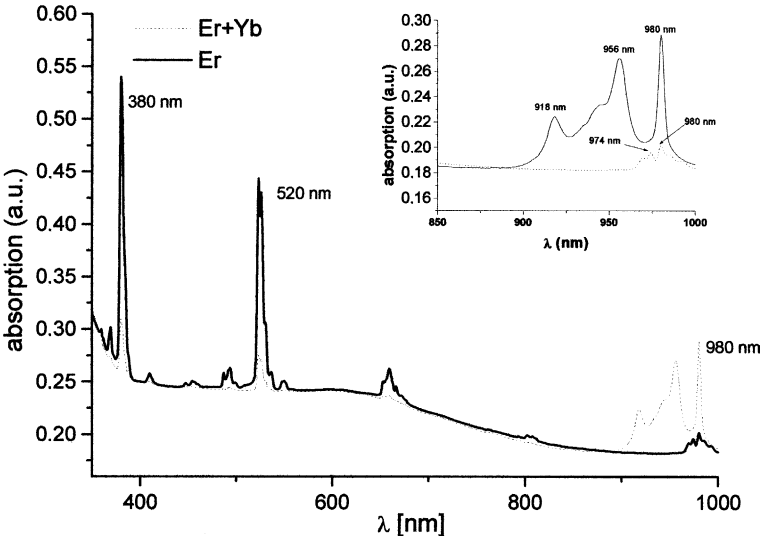

Fig. 3. Absorption spectra of $LiNbO_3$ doped with Er (500 ppm) and Er + Yb (1000 ppm).

Table 1
Dependence of the value of the r_{33} on the RE content in the Z-cut of lithium niobate

Mode	Average voltage U_π (V)	Average value of $r_{33} \times 10^{-12}$ (mV^{-1})		Standard deviation $\Delta r_{33} \times 10^{-12}$ (mV^{-1})	95% confidence interval for average $r_{33} \times 10^{-12}$ (mV^{-1})	95% confidence interval for standard deviation $\Delta r_{33} \times 10^{-12}$ (mV^{-1})
Subs.	123.9	30.60	±	1.42 (4.64%)	30.60 ± 2.09	⟨0.5; 4.07⟩
Er 500 ppm	128.1	29.40	±	0.82 (2.79%)	28.74 ± 1.02	⟨0.49; 2.37⟩
1Er:9Yb 1000 ppm	153.8	24.10	±	0.69 (2.86%)	24.10 ± 0.97	⟨0.42; 1.99⟩

adipic acid (i.e. in our case containing 0.5 mol% of lithium) was used for the fabrication of the APE waveguides in all three types of the cuts. Only shorter (i.e. 1 h) times of the proton exchange were applied for Y-cuts as the risk of the surface damage in them is even higher than in X-cuts. The results of the experiments (see Table 2) were as follows:

(i) The APE process did not change the concentrations of erbium and ytterbium which means that "washing out" of the RE from the exchanged layers did not occur.
(ii) The PE process, as expected, made the lithium concentration in the fabricated waveguides decreased while that of hydrogen increased.
(iii) After the proton exchange the contents of the in-diffused hydrogen differed in various types of the cuts, being lower on the surface of Z-cut comparing with X-cuts. This is a consequence of a better permeability of X-cuts for the diffusing particles as we already proved in [18]. During the annealing the hydrogen migrated faster into deeper layers in the X-cut substrates so that after the APE process the hydrogen concentration was lower in the measured shallow (up to 500 nm) subsurface layers. These results were almost the same for the waveguides fabricated in both pristine and RE doped substrates (taking into account the accuracy of the ERDA measurement, i.e. 2 mol% of the actual H concentration).

Table 2
The APE layers composition as measured by the NDP, RBS and ERDA methods

Sample	Nb (at.%)	Er (at.%)	Li (surface) $\times 10^{21}$(atom cm^{-3})	Li (depletion) (at.%)	H (at.%)
Z-cut					
(Er); PE, 1 h	20	0.13	0.5154	12.4	11.0
(Er + Yb); PE, 1 h	20	0.24	0.5160	12.35	14.0
(Er); PE, 3 h	20	0.12	0.6682	10.1	12.0
(Er + Yb); PE, 3 h	20	0.22	0.6217	10.8	16.0
Y-cut					
(Er); PE, 1 h	20	0.14	0.6322	10.6	14.0
(Er + Yb); PE, 1 h	20	0.25	0.6003	11.1	17.0
X-cut					
(Er); PE, 1 h	20	0.10	0.7537	8.8	9.0
(Er + Yb); PE, 1 h	20	0.26	0.7697	8.6	8.0
(Er); PE, 3 h	20	0.14	0.6623	10.2	7.0
(Er + Yb); PE, 3 h	20	0.25	0.6402	10.5	6.0

Fig. 4 shows the comparison of the refractive index depth profiles of the APE waveguides fabricated using the same experimental conditions in both RE doped and pristine substrates. The well-known step-like n_e profiles of the APE waveguides in the *X*-cut were observed again in the RE doped samples, though slightly different from those in the pristine (i.e. undoped) wafers (see Fig. 4A). More significant differences were observed in the properties of the APE waveguides in the *Z*-cuts (Fig. 4B) where a distinct shift of the refractive index values in the surfaces of samples was found due to a higher content of the RE. The typical few-modes gradient character of the n_e depth profiles in the *Z*-cuts was observed in the RE doped samples as well.

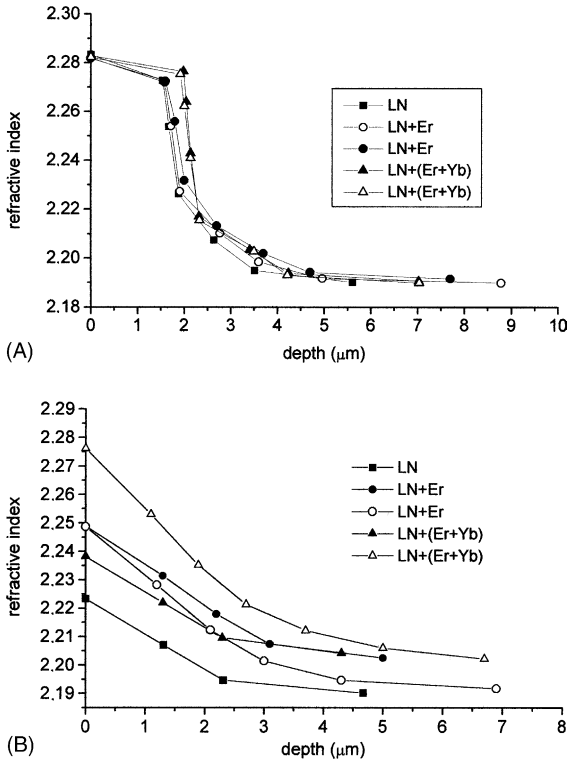

Fig. 4. Comparison of the APE waveguides properties in pristine and doped Er:$LiNbO_3$ and (Er + Yb):$LiNbO_3$: (A) *X*-cut, (B) *Z*-cut (PE: adipic acid + 0.5 mol% Li, 3 h, 213 °C, A: 1.5 h, 350 °C).

The electrooptic coefficients r_{33} for each particular mode of the waveguides were measured in the *Z*-cut samples (see Section 2) immediately after the proton exchange and then several times again during the post-exchange annealing. Electrooptic properties, which were deteriorated after the PE to an undetectable value of the r_{33} recovered almost completely after the post-exchange annealing. It is demonstrated in Fig. 5 that if we observe the r_{33} value for different modes (various depths) in one waveguide the r_{33} value increases with increasing depth of the particular modes. The α-structural phase is likely to appear in the maximum depth of the waveguiding layer, which is in a close vicinity to the original crystal structure, so it is not surprising that also the r_{33} value is the highest in that part of the waveguide.

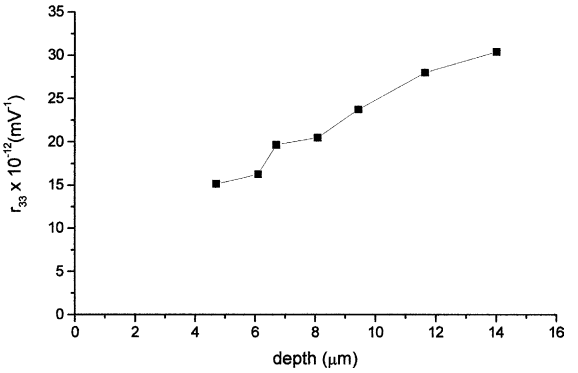

Fig. 5. Electrooptic coefficient r_{33} dependence on the depths of particular modes in the APE Er:$LiNbO_3$ (PE: pure adipic acid, 2 h, 213 °C, A: 10 h, 350 °C).

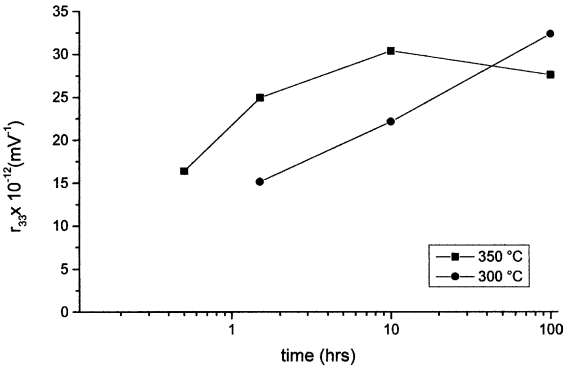

Fig. 7. Effect of annealing temperature on the r_{33} value in Er:$LiNbO_3$ (PE: pure adipic acid, 2 h, 213 °C, A: 30 min to 100 h, 300 and 350 °C).

We compared the r_{33} values that were measured always at the last mode, (i.e. in the maximum depth of the PE waveguides) for various post-exchange annealing times (Fig. 6). The same trend as for the r_{33} values obtained for the non-exchanged substrates could be observed also here, it means that the highest r_{33} values were found in the APE waveguides fabricated in the pristine lithium niobate and they decreased in the RE doped substrates.

Another important finding is that the r_{33} did not increase monotonously with the time when the annealing temperature was higher than 350 °C but it reached its maximum (Fig. 7) and then its value decreased. We noted that lower annealing temperature (300 °C) makes the r_{33} value increased steadily without reaching any maximum even after 100 h of the annealing, and that the r_{33} values of the waveguides annealed at 300 °C are higher compared with the former. As we expected that the changes of the r_{33} originated in the migration of lithium during the annealing, the lithium depth distribution curves in several samples were determined by the NDP method and the r_{33} values were then attributed to the pertinent lithium concentrations (Fig. 8). The measurement showed that the higher depletion of lithium in the waveguiding layer is always accompanied with the decreasing r_{33} value, as we expected. Moreover, the lithium distribution plays an important role also in the samples annealed at 300 °C where quite a large

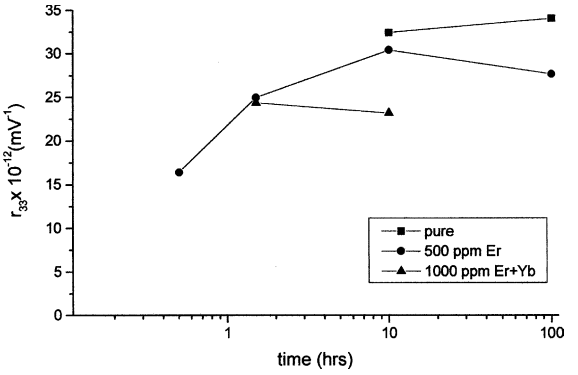

Fig. 6. Effect of annealing times on the r_{33} values in RE doped $LiNbO_3$ (PE: pure adipic acid, 2 h, 213 °C, A: 30 min to 100 h, 350 °C).

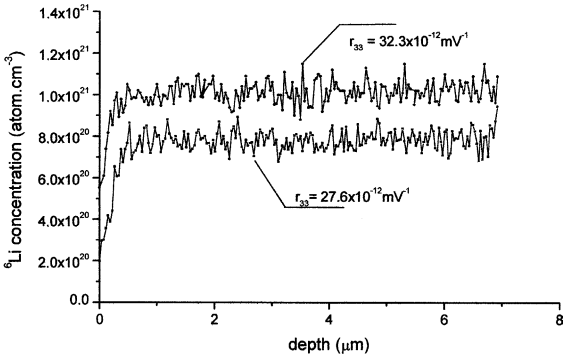

Fig. 8. Depletion of lithium in the APE waveguide from Fig. 4 (see text) (PE: pure adipic acid, 2 h, 213 °C, A: 100 h, 300 and 350 °C).

depletion of lithium was observed but the distribution of the non-depleted lithium within the waveguiding layer is almost homogeneous. In these waveguides we found the highest values of the r_{33}.

4. Discussion

At present it is generally accepted that the combination of the erbium doping into lithium niobate and the APE fabrication of the waveguides is not suitable for utilisation in optical amplifiers or waveguide lasers. As reported, it is so mainly because of the hydroxyl (hydrogen) presence in the waveguide zone, which results in decreasing the lifetime $^4I_{13/2}$ energy level [10].

On the other side, our results show that a sophisticatedly designed APE process, namely the regime of the post-exchange annealing, may have a positive effect on the properties of the waveguides as this way the value of the r_{33} can be increased so that the observed decrease of the r_{33} value in the RE doped substrate might be at least compensated.

According to our NDP measurement the long times of the post-exchange annealing cause a uniform distribution of lithium in the waveguiding layers. It seems that the mobility of lithium is so high that the main process that occurs during the annealing is not the ion exchange itself (i.e. migration of protons deeper into the substrate and migration of lithium towards the surface) but more likely an independent migration of lithium to the surfaces of the wafers. The values of the r_{33} increased with the gradual changes of lithium displacement resulting in the almost homogenous distribution of lithium in the waveguiding layers.

The presence of the hydrogen incorporated during the APE process was found to have a negative effect on the r_{33} value, which tended to increase with the decreasing concentration of OH in the waveguides during the annealing process. This finding is important when dealing with the main problem (i.e. the already mentioned shortening of excited electrons lifetimes due to hydrogen present in the waveguides) that is associated with the APE technology for fabrication of the erbium-doped waveguides in lithium niobate. We have found that a well designed regime of the annealing may lead to the fabrication of the α-phase APE waveguides with a homogeneous distribution of lithium and a negligible content of hydrogen, in which the r_{33} was 32.3×10^{-12} mV^{-1} (Fig. 8).

Another option for fabrication of high gain active waveguides is to use a suitable cut of lithium niobate, especially *X*-cut. The structure of *X*-cut enables the moving particles to use available vacancies of the cleavage planes to move faster inside the structure and that results in a quicker decrease of the hydrogen (OH) content in the waveguide region (as confirmed by IR spectra and ERDA) [18].

5. Conclusion

The study of the APE layers in lithium niobate doped with erbium and with the mixture of erbium and ytterbium points to the conclusion as follows:

- The rare earth (RE) content in lithium niobate does not decrease during the process of the proton exchange (PE).
- The PE process in the RE doped lithium niobate is controlled by the same mechanism as that in lithium niobate, i.e. the hydrogen content increased while the lithium content decreased. Also the rate of the PE for various cuts maintains the same trend as that one in the undoped lithium niobate, i.e. the PE process is faster in *Y*-cuts and slower in *Z*-cuts.
- The process of the waveguide formation by APE method is the same in the pristine lithium niobate as well as in the RE doped one. Therefore the waveguide layers, which were fabricated using the same experimental conditions in both types of the cuts (doped and undoped), had almost the same refractive index profiles.
- The addition of the RE into the lithium niobate substrates causes partial decrease of the coefficient r_{33} value, but it can be increased again almost to its original magnitude using a sophistically designed regime of the annealing. The reason for that are the homogeneous distribu-

tion of lithium and a very low content of hydrogen in the long time-annealed waveguiding layers.

- As to our opinion the APE process itself might not be in principle a cause for the observed degradation of active properties of the erbium doped lithium niobate. Similarly as above, the carefully designed APE technology may help to lower the hydrogen content in the waveguides, which is considered as the main obstacle in using the APE waveguides in active integrated optics structures.

Acknowledgements

This research has been supported by the Grant Agency of the Czech Republic (project 102/99/D017) and by the Research Programme "Preparation and properties of advanced materials—modelling, characterization, technology" (CEZ:MSM 223100002).

References

[1] I. Baumann, R. Brinkmann, M. Dinand, W. Sohler, L. Beckers, Ch. Buchal, M. Fleuster, H. Holzbrecher, H. Paulus, K.-H. Muller, Th. Gog, G. Materlik, O. Witte, H. Stolz, W. von der Osten, Appl. Phys. A 64 (1997) 33.

[2] D.L. Veasey, J.M. Gary, J. Amin, J.A. Aust, IEEE J. Quant. Electron. Lett. 33 (1997) 1647.

[3] R. Brinkman, Ch. Buchal, St. Mohr, W. Sohler, H. Suche, Integr. Photon. Res. 5 (1990) PD1.

[4] V. Bermúdez, M.D. Serrano, J. Tornero, E. Diéguez, Solid State Commun. 112 (1999) 699.

[5] L. Rebouta, M.F. da Silva, J.C. Soares, D. Serrano, E. Diéguez, F. Agulló-López, J. Tornero, Appl. Phys. Lett. 70 (9) (1999) 1070.

[6] E. Cantelar, F. Cussó, Appl. Phys. B 69 (1999) 29.

[7] I. Baumann, R. Brinkmann, M. Dinand, W. Sohler, S. Westernhofer, IEEE J. Quant. Electron. 32 (1996) 1695.

[8] P. Becker, R. Brinkmann, M. Dinand, W. Sohler, H. Suche, Appl. Phys. Lett. 61 (1992) 1257.

[9] Edmond J. Murphy (Ed.), Integrated Optical Circuits and Components, Design and Applications, Marcel Dekker, 1999, p. 127 (Chapter 6).

[10] A.C. Cino, S. Riva Sanseverino, M.P. De Micheli, K.El. Hadi, F. Cusso, G. Lifante, SPIE Proc. 3280 (1998) 152.

[11] M. Seino, M. Mekada, T. Namiki, T. Yamane, H. Nakajima, Tech. Dig. European Conference on Optical Communication, ECOC'89, 1998.

[12] T. Suzuki, O. Eknoyan, H.F. Taylor, J. Lightwave Technol. 11 (2) (1993) 285.

[13] J. Saarilahti, E. Rauhala, Nucl. Instr. and Meth. B 64 (1992) 734.

[14] M. Mayer, Technical Report IPP 9/113, Max-Planck-Institut für Plasmaphysik, Garching, Germany 1997.

[15] J. Vacík, J. Červená, V. Hnatowicz, V. Havránek, D. Fink, Acta Phys. Hungarica 75 (1–4) (1994) 369.

[16] P. Kolářová, J. Vacík, J. Špirková-Hradilová, J. Červená, Nucl. Instr. and Meth. B 141 (1998) 498.

[17] J.M. White, P.F. Heinrich, Appl. Opt. 15 (1976) 151.

[18] P. Nekvindová, J. Špirková, J. Červená, M. Budnar, A. Razpet, B. Zorko, P. Pelicon, Opt. Mater. 19 (2002) 245.

SURFACE AND INTERFACE ANALYSIS
Surf. Interface Anal. 2004; **36**: 949–951
Published online in Wiley InterScience (www.interscience.wiley.com). DOI: 10.1002/sia.1808

SIA

Characterization of Er:$LiNbO_3$ and APE:Er:$LiNbO_3$ by RBS–channeling and XRD techniques

A. Mackova,[1]* R. Groetzschel,[2] F. Eichhorn,[2] P. Nekvindova[3] and J. Špirkova[3]

[1] Institute of Nuclear Physics, Czech Academy of Sciences, Řež 250 68, Czech Republic
[2] Institute of Ion Beam Physics and Material Analysis, Forschungzentrum Rossendorf, Dresden, Germany
[3] Institute of Chemical Technology, Prague, Czech Republic

Received 3 July 2003; Revised 27 November 2003; Accepted 27 November 2003

The samples of erbium-doped lithium niobate (Er:$LiNbO_3$) were prepared by the standard Czochralski method and treated by the annealed proton exchange (APE) procedure to create a planar waveguide for further optical application. The positions of Er atoms in the crystal lattice of pristine and APE treated Er:$LiNbO_3$ samples were studied by the Rutherford backscattering spectrometry (RBS)–channeling method. The Er^{3+} ion positions in the pristine and the APE treated Er:$LiNbO_3$ samples are compared. X-ray diffraction (XRD) was used to determine the damage to the crystal structure caused by the APE treatment. It was found that the APE treatment leads to significant crystal structure damage and to shifts of the Er^{3+} ions from their positions in the pristine crystal. Copyright © 2004 John Wiley & Sons, Ltd.

KEYWORDS: Er:$LiNbO_3$; RBS–channeling study; APE treatment; optical waveguides

INTRODUCTION

Optical amplifiers and lasers based on materials doped with rare earth atoms have large application potential. Lithium niobate ($LiNbO_3$), due to its very favourable electro-optical, acousto-optical and non-linear properties, is one of the most popular materials for these applications.[1] Several techniques have been established to fabricate low-loss optical waveguides based on lithium niobate.[1] One of the most used ones is the annealed proton exchange (APE) and this technique has been used in this study to fabricate planar waveguides. Proton exchange (H^+ for Li^+) takes place in a liquid proton source, typically an acid. This procedure increases the extraordinary refractive index, but it also causes changes of the crystal structure of the treated layers. To optimize the active function of the fabricated APE optical waveguides in Er:$LiNbO_3$ it is very important to know the exact positions of the Er^{3+} ions in the structures of both APE treated and non-treated Er:$LiNbO_3$.

Although several RBS–channeling studies of the lattice site location of rare earth ion positions in Er:$LiNbO_3$ have been performed,[2–4] until now the exact positions of the Er^{3+} ions have not been fully clear. RBS–channeling analysis is very suitable for the determination of the position of Er atoms in the crystal lattice due to its sensitivity to atoms in interstitial positions. In this study the Er atom positions in the pristine and the APE treated Er:$LiNbO_3$ samples were determined by the RBS–channeling method for the first time. Complementary information on the crystal structure damage caused by the APE treatment was determined using the XRD technique.

*Correspondence to: A. Mackova, Institute of Nuclear Physics, Czech Academy of Sciences, Rez 25068, Czech Republic.
E-mail: mackova@ujf.cas.cz
Contract/grant sponsor: Grant Agency of the Czech Republic;
Contract/grant number: 102/01/D069.

EXPERIMENTAL

The congruent Er:$LiNbO_3$ single crystal containing 5000 ppm of Er was grown by the standard Czochralski method (Avtex Turnov). The crystal was cut into 0.7 mm thick wafers corresponding to x ($\langle 11\text{–}20\rangle$), y ($\langle 01\text{–}10\rangle$) and z ($\langle 0001\rangle$) cuts, in which the planar waveguides were fabricated by the APE process at 213 °C for 3 h using adipic acid as the proton source. The waveguides were single mode at $\lambda = 1.5\,\mu m$ and the proton profile reaches about 10 μm deep into the wafer, as does also the depletion of lithium. The RBS–channeling experiments were performed at the Forschungzentrum Rossendorf, Dresden, Germany using the beam of 1.8 MeV alpha particles from a van de Graaff accelerator and standard measuring procedure.[5] The signals of the Er atoms and the host lattice Er:$LiNbO_3$ in RBS spectra are well separated due to scattering kinematics. From the angular scan through different axial channels the Er atom positions in the crystalline lattice were obtained for the pristine and the APE treated Er:$LiNbO_3$. The angular scans along the $x\langle 11\text{–}20\rangle$, $y\langle 01\text{–}10\rangle$ and $z\langle 0001\rangle$ axes were measured for pristine Er:$LiNbO_3$ samples and for the samples treated by the APE technique (the samples were denoted: 470x-cut, 491y-cut and 487z-cut.)

XRD measurements were performed on D5005 (Siemens/Bruker AXS) with 1/4 circle Eulerian cradle and CuK_α radiation ($\lambda = 0.154$ nm). The samples were adjusted at high-angle Er:$LiNbO_3$ reflections with θ and χ axes; diffractograms were measured by 1 : 2 coupled scans (size step = 0.05°). The

net planes of used reflections were approximately parallel to the surface (surface normal || momentum transfer vector), i.e. the beam path was symmetric at the sample.

RESULTS

RBS–channeling

In the structure of the $LiNbO_3$ crystal four different lattice sites are available which may be occupied by foreign ions: two substitutive octahedral sites (Li^+ and Nb^{5+}), an additional free octahedron and a tetrahedral vacancy site. The scan along the ⟨0001⟩ axis of pristine Er:$LiNbO_3$ can be used to identify any position out of the *z*-axis, i.e. the tetrahedral site. The angular scan of the Nb host atoms through the ⟨0001⟩ axis is practically identical to that of Er atoms (see Fig. 1), so that it can be concluded that the Er atoms are located in three possible positions along the *z*-axis, i.e. the Nb^{5+}, Li^+ sites or the structural octahedral site. To determine precisely the Er position inside the Li^+ octahedron the scans through the ⟨01–10⟩ and ⟨11–20⟩ axes were measured (see Fig. 1). If the Er atoms sit in the octahedral position a maximum in the scan through the ⟨11–20⟩ axis should be seen,[3] but this is not the case. From the measured angular scan shapes of pristine Er:$LiNbO_3$ samples (Fig. 1, first row) and from the simulations published in Ref. 4 we can conclude that the Er^{3+} ions sit on the Li^+ sites but they are shifted slightly in the direction along the *z*-axis. The shift along the *z*-axis direction of about 0.03 nm was found for the pristine Er:$LiNbO_3$ samples in accord with the data reported earlier for Yb^{3+} ions in Yb:$LiNbO_3$.[3] We have performed the same analysis of angular scans for APE treated samples—3 cuts (Fig. 1, second row) and it indicates about 0.09 nm shift of the Er^{3+} ions in the *z*-axis direction. The shift of Er atoms after the APE treatment corresponds to the expansion of the Er:$LiNbO_3$ cell volume observed by XRD analysis. In the case of APE treated samples we observed the crystal lattice damages in RBS–channeling spectra which are indicated by an increase of RBS yield from the APE treated sample in comparison with that from pristine samples observed in aligned spectra.

XRD

The XRD diagrams for the reflections (0 0 6) and (0 0 12) from the *z*-cut of the pristine and the APE treated samples are shown in Fig. 2. The APE treated samples exhibit higher intensity compared to the pristine ones. The proton exchange disturbs the formerly nearly perfect crystal lattice of Er:$LiNbO_3$, so that the primary extinction is reduced and the reflected intensity grows. The APE treated samples show a clear shoulder at the low-angle side of the reflection curve indicating a deformed crystal lattice. A layer with a deformed lattice obviously exists in the APE treated samples, the presence of which is manifested in a different manner for differently orientated substrate cuts. Whereas the *z*-cut sample exhibits a layer with a more imperfect lattice (possibly due to point defects) without any change of the net plane distance, on the *x*-cut and *y*-cut samples layers with an increased net plane distance are observed. This result corresponds well with the published data concerning increasing crystal cell volume[6] and Er atom shift observed in the present RBS–channeling measurement.

CONCLUSIONS

The RBS–channeling measurements show that the Er^{3+} ions in pristine Er:$LiNbO_3$ are located in the Li^+ site but they are shifted by 0.03 nm in the *z*-direction. The

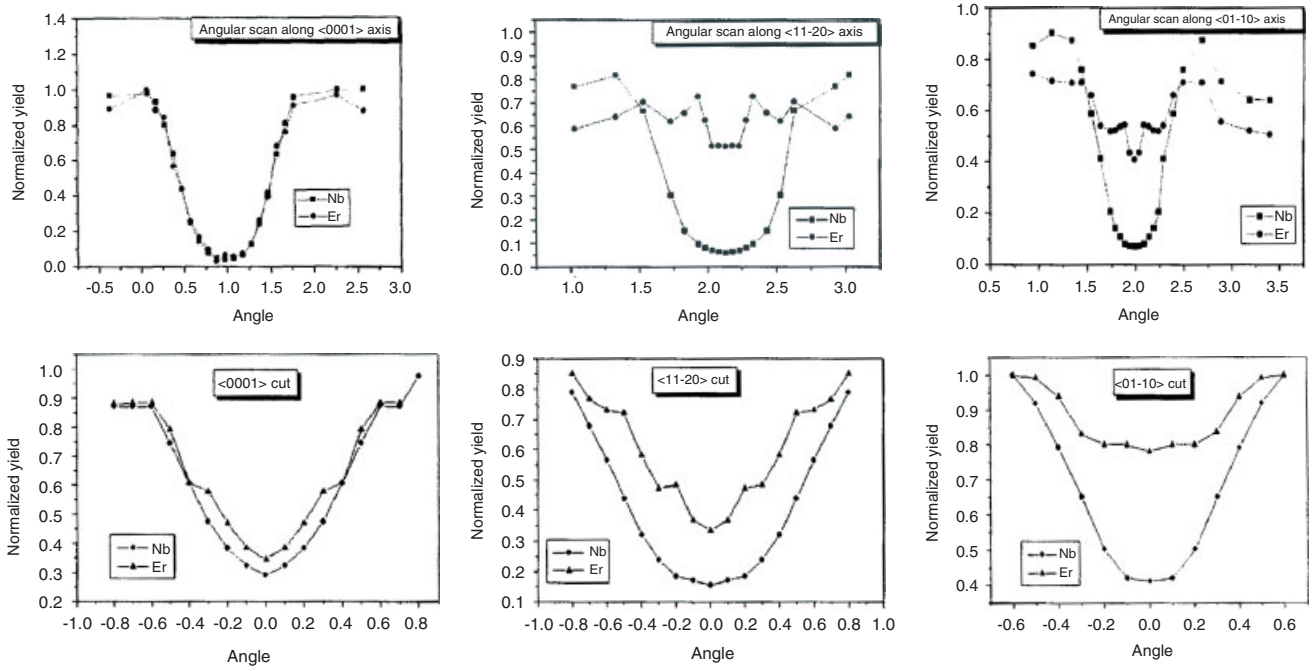

Figure 1. Comparison of angular scans along axes ⟨0001⟩, ⟨11–20⟩, ⟨01–10⟩ of the pristine samples (first row) of Er:$LiNbO_3$ and APE treated samples (second row).

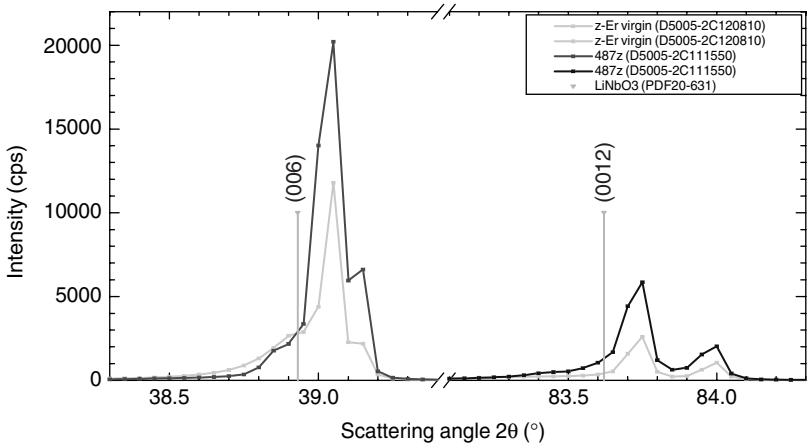

Figure 2. XRD measurement of the *z*-cut ⟨0001⟩ of pristine and APE treated Er:$LiNbO_3$ sample.

shift from the Li^+ site is connected with the larger size of the Er^{3+} ion, which is forced to move towards the larger oxygen triangle. The shift of 0.09 nm observed in the APE treated samples can be explained by the enlarged volume of the Er:$LiNbO_3$ elementary cell and also by the crystal damage created by the APE treatment. Both effects were confirmed by RBS–channeling analysis and by XRD measurement.

Acknowledgement

This work was supported by the Grant Agency of the Czech Republic under the Project number 102/01/D069.

REFERENCES

1. Sohler W, Suche H. *Integrated Optical Circuits and Components.* Marcel Dekker: New York, 1999; p. 127.
2. Lorenzo A, Loro H, Munoz Santiuste JE, Terrile MC, Boulon G, Bausa LE, Garcia Sole J. *Opt. Mater.* 1997; **8**: 55.
3. Lorenzo A, Jaffrezic H, Roux B, Boulon G, García Solé J. *Appl. Phys. Lett.* 1995; **67**: 3735.
4. Rebouta L, Smulders PJM, Boerma DO, Agullo-Lopez F, da Silva MF, Soares JC. *Phys. Rev. B.* 1993; **48**: 3600.
5. Feldman LC, Mayer JW, Picraux ST. *Materials Analysis by Ion Channeling*. Academic Press: London, 1982.
6. Zhou F, Matteo AM, De La Rue RM, Ironside CN. *Electron. Lett.* 1992; **28**: 87.

Nuclear Instruments and Methods in Physics Research B 267 (2009) 1575–1578

Contents lists available at ScienceDirect

Nuclear Instruments and Methods in Physics Research B

journal homepage: www.elsevier.com/locate/nimb

Au implantation into various types of silicate glasses

P. Malinský [a,b], A. Macková [a,b,*], J. Bočan [a], B. Švecová [c], P. Nekvindová [c]

[a] Nuclear Physics Institute, Academy of Sciences of the Czech Republic, 250 68 Rez, Czech Republic
[b] Department of Physics, Faculty of Science, J. E. Purkinje University, Ceske mladeze 8, 400 96 Usti nad Labem, Czech Republic
[c] Department of Inorganic Chemistry, Institute of Chemical Technology, Technicka 5, 166 28 Prague, Czech Republic

ARTICLE INFO

Article history:
Available online 20 February 2009

PACS:
42.70.Ce
78.67.Bf
62.23.Pq

Keywords:
Au^+ ion implantation
Glasses
Depth profiling
RBS
UV–vis optical absorption

ABSTRACT

The implantation of gold ions into three types of silicate glass was studied. The energies of the implanted Au^+ ions were 1701 keV, and the fluences of the ions were 1×10^{14}, 1×10^{15}, 3×10^{15} and 1×10^{16} cm^{-2}. The as-implanted samples were annealed in air at two temperatures (400 and 600 °C). The Au concentration depth profiles were investigated using Rutherford Backscattering Spectrometry (RBS) and compared to simulated profiles from the SRIM. The structural changes were studied by UV–vis absorption spectroscopy. The obtained mono-mode waveguides were characterised using Dark Mode Spectroscopy at 671 nm to yield information on the refractive index changes. The results showed interesting differences depending on the type of glass and the post-implantation treatment. The obtained data were evaluated on the basis of the structure of the glass matrix, and the relations between the structural changes, waveguide properties and absorption, which are important for photonics applications, were formulated.

1. Introduction

Metal nanocluster composite glasses (MNCGs) are interesting for their potential application in non-linear optics due to the third-order optical non-linear responses of their metal nanoclusters [1]. Glasses containing metal colloids can be prepared using several techniques, such as melt doping, ion exchange or ion implantation [2]. As compared to the other techniques, ion implantation allows the synthesis of high-density metal nanoclusters in the glasses with well-defined dopant depth profiles [3]. Post-implantation annealing can control the size as well as non-linear properties of the nanoclusters [4,5]. In this paper, we have focused on the high-energy ion implantation of Au^+ ions into three types of silicate glasses conducted under various conditions. Silicate glasses were selected as they are important materials for various nanotechnology applications because of their low cost, easy manufacture, high chemical stability, transparency and flexibility in chemical composition [6]. The glasses used differed in their chemical compositions especially in terms of the concentration of the monovalent modifier (Na) and the network elements (Si and B). The glass containing gold nanoclusters exhibited enhanced third-order susceptibility $\chi^{(3)}$ at 532 nm [4], which, as a measure of optical non-linearity, can be considered as a figure of merit for its potential utilisation in photonics devices. Moreover, ions of gold have a low enough diffusivity (when compared to e.g. silver ions [7], which are too fast) to allow the study of the processes that occur during annealing. The main aim of this project was to study and subsequently formulate the relations between the chemical composition of the glass substrate and the formation of the Au nanoparticles.

2. Experiment

We have used three types of optical glasses with varying chemical compositions, namely specially designed Glasses A and B (made at the Glass Institute Hradec Kralove Ltd., Czech Republic) and a commercially available Glass C (BK7). The glasses varied especially in their concentrations of monovalent and divalent modifies (Na_2O, K_2O, CaO, MgO) as well as their network formers (SiO_2, B_2O_3). The compositions of the glasses determined by X-ray Fluorescence (XRF) are provided in Table 1.

Au^+ ions were implanted into the silicate glasses on a new Tandetron 4130 MC accelerator at the Nuclear Physics Institute in Prague, Czech Republic. The energy of the implanted Au^+ ions was 1701 keV. The fluences of the Au^+ ions into Glass A were 1×10^{14}, 1×10^{15}, 3×10^{15} and 1×10^{16} cm^{-2}, whereas the fluences used in the cases of Glasses B and C were 1×10^{14}, 1×10^{15} and 1×10^{16} cm^{-2}. The as-implanted glasses A were annealed at temperatures of 400 °C for 5 and 25 h or 600 °C for 5 h. The depth distribution and diffusion profiles of the implanted Au were

* Corresponding author. Address: Nuclear Physics Institute, Academy of Sciences of the Czech Republic, 250 68 Rez, Czech Republic. Tel.: +420 266172102.
E-mail address: mackova@ujf.cas.cz (A. Macková).

0168-583X/$ - see front matter © 2009 Elsevier B.V. All rights reserved.
doi:10.1016/j.nimb.2009.01.161

Table 1
The compositions of the silicate substrates (in wt.%).

Substrate	SiO_2	Na_2O	Al_2O_3	CaO	MgO	K_2O	B_2O_3	BaO
Glass A	63.2	24.4	1.1	5.6	5.3	0.5	–	–
Glass B	88.0	8.7	3.3	–	–	–	–	–
Glass C	68.3	8.8	–	0.1	–	8.1	12.1	2.5

investigated using Rutherford Backscattering Spectrometry (RBS) with 2.0 MeV He^+ ions. The incoming angle was 0° while the scattering angle was 170°. The measurements were evaluated with the Gisa 3.99 [8] and compared with a simulation in the SRIM 2003 [9]. The UV–vis absorption spectra were collected using a CARY 50 dual-beam spectrometer in transmission modes ranging from 300 to 1000 nm. The implanted samples were also studied by Dark Mode Spectroscopy (DMS) at 671 nm for possible waveguiding properties. The method is based on coupling the light into the surface of the substrate through a prism. This results in the phenomenon of the so-called 'dark modes', which are in fact a consequence of the interference effect produced by the reflectivity of light at a single point on the coupling-prism interface. The waveguiding properties of the sample are then evaluated employing the well-known IWKB procedure. The accuracy of the method (refractive index value) is currently mentioned as 2×10^{-4} [10].

3. Results and discussion

3.1. Implantation versus simulation

The typical depth profiles of the implanted Au ions in Glasses A and B as determined from the RBS spectra are shown in Fig. 1(a) and 1(b), respectively. Glass C contains a larger amount of Ba and hence RBS is not capable of determining the depth profile or the integral amount of Au with reasonable precision for this glass. The depth profiles of the glasses implanted at a fluence of 1×10^{14} cm^{-2} are not presented because of the extremely low concentration, making a comparison of the values over two orders of magnitude in one figure unconstructive. The profiles calculated with the SRIM 2003 code for the implanted glasses (1×10^{16} cm^{-2}, 1701 keV) are shown in Fig. 1(a) and 1(b) for comparison.

Fig. 1(a) and 1(b) indicate that the SRIM simulation results are in good agreement with the varying density of the glass. The projected range R_P and range straggling ΔR_P calculated using the SRIM 2003 are $R_P = 378.9$ nm and $\Delta R_P = 68$ nm for Glass A and

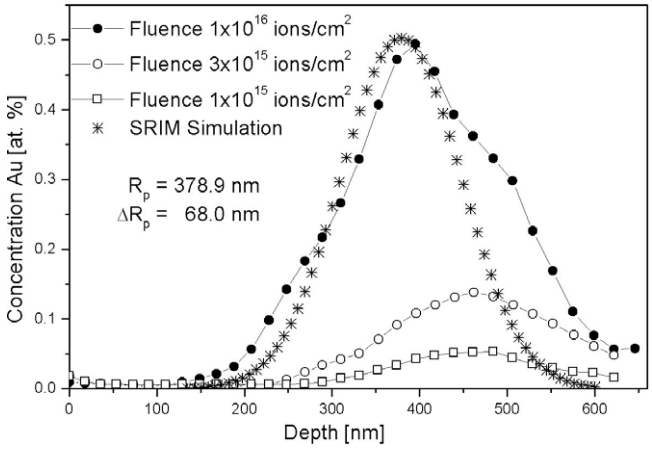

Fig. 1a. The depth profiles of the implanted Au in Glass A for the different fluences compared to the SRIM simulation.

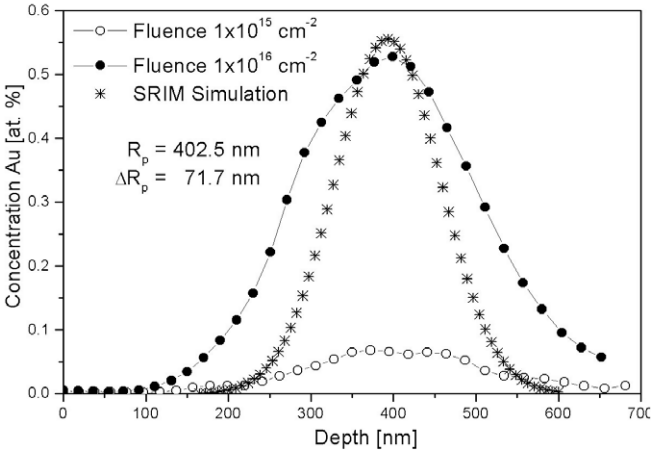

Fig. 1b. The depth profiles of the implanted Au in Glass B for the different fluences compared to the SRIM simulation.

$R_P = 402.5$ nm and $\Delta R_P = 71.7$ nm for Glass B, with Glasses A and B differing in their composition and density. In Fig. 1(a) and 1(b), we observed two evident disagreements between the simulation and measured data. First, the measured depth profiles are broader than the simulated ones, which may be caused by higher straggling of the implanted ions. Second, the maximal concentration is shifted towards the surface as compared to the simulated values mainly for Glass A and at higher fluences. This disagreement is not surprising since the SRIM code does not take into account the structural changes of a glass matrix caused by ion irradiation. Consequently, Glass B, which is similar to silica glass (in terms of the network's cross-linking), yielded better agreement of the simulation with the experimental data, unlike Glass A, which, being more basic (as compared to the rather covalent Glass B), provided much worse agreement. This may indicate that the structure of the treated thin layers had become more covalent (i.e. cross-linked to a higher extent) as a consequence of the depletion of oxygen from the glass surface. A different degree of cross-linking of the glass network was reported e.g. in [11].

3.2. Post-implantation annealing

The annealing conditions, especially temperature, play the main role in creating gold nanoparticles in glass. Therefore, Glass A was annealed at temperatures below or near the glass transition temperature $T_g = 615$ °C (as determined by Differential Thermal Analysis). The gold concentration profile changes caused by the different methods of annealing of Glass A are shown in Fig. 2(a) and 2(b). The Au depth profiles presented in Fig. 2(a) describe the Au distribution for the various annealing conditions for the samples implanted at 1×10^{15} cm^{-2}. A change of Au depth profile was observed after the long-time annealing at 400 °C, namely for 25 h, when the Au was redistributed and formed an Au layer without a significant concentration maximum.

The Au depth profiles in Glass A implanted at 1×10^{16} cm^{-2} are presented in Fig. 2(b). The concentration profiles of the non-annealed samples and samples annealed at 400 °C and 600 °C for 5 h were similar. The depth profile of the sample annealed at 400 °C for 25 h was narrower with a higher concentration maximum than the other samples. A substantial change of the Au depth profile occurred after the long-time annealing and could have been caused by the Ostwald ripening mechanism [12].

The RBS measurement of the Au integral amount is summarised in Table 2. The Au integral amount stayed the same for the as-implanted Glass A after a short-time annealing of 4 h at 400 °C.

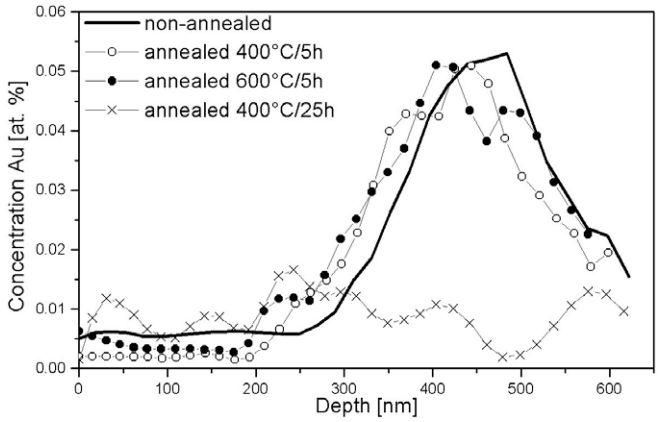

Fig. 2a. The Au depth distribution in as-implanted and as-annealed samples. A comparison is made for a fluence of 1×10^{15} cm^{-2} in Glass A.

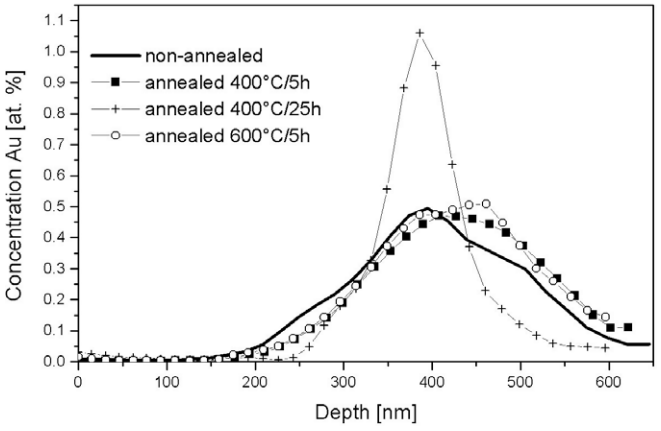

Fig. 2b. The Au depth distribution in as-implanted and as-annealed samples. A comparison is made for the fluence of 1×10^{16} cm^{-2} in Glass A.

Increasing temperature and time caused a broadening of the depth profiles and a decrease of the Au maximum concentration in the samples implanted at the lowest fluence (1×10^{14} cm^{-2}). The decrease was so significant that the depth profiles could not be measured by RBS. Glass A implanted at a medium fluence (1×10^{15} cm^{-2}) exhibited a similar behaviour after annealing for 25 h, where the integral amount was decreased to 64% of the original value, see Table 2. The integral amount for the samples with the Au implanted at a fluence of 1×10^{16} cm^{-2} is the same for all the samples with or without annealing.

We can hence conclude that the glass samples implanted at low and medium ion fluences show similar behaviour after the long-time annealing. The Au is redistributed in the glass substrate and creates a constant concentration profile with no significant maximum. Completely different Au depth profile changes were observed in Glass A when implanted at a high ion fluence (see Fig. 2(b) for where the sharp peak concentration occurred).

Table 2
The Au integral amount comparison before and after the annealing procedure for Glass A.

The As-implanted Au Glass A			
Au integral amount [cm^{-2}]	1.5×10^{14}	0.94×10^{15}	0.83×10^{16}
Au Glass A annealed at 400° for 5 h			
Integral amount [cm^{-2}]	1.5×10^{14}	0.91×10^{15}	0.85×10^{16}
Au Glass A annealed at 600° for 5 h			
Integral amount [cm^{-2}]	–	0.99×10^{15}	0.90×10^{16}
Au Glass A annealed 400° for 25 h			
Integral amount [cm^{-2}]	–	0.64×10^{15}	0.87×10^{16}

– RBS was not able to measure the depth profile.

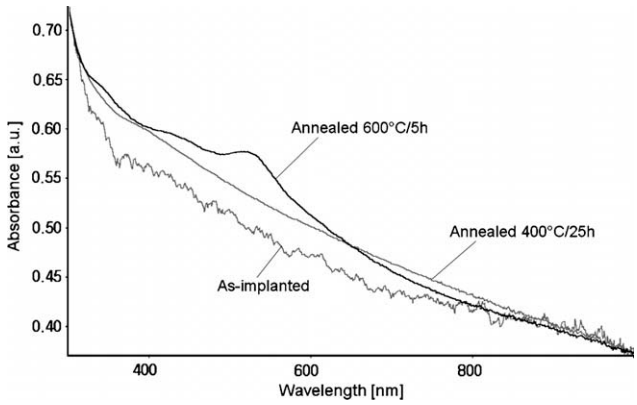

Fig. 3. The UV–vis absorption spectra of the three samples: (a) as-implanted, (b) as-annealed at 600 °C for 5 h and (c) as-annealed at 400 °C for 25 h in Glass A.

Table 3
The waveguiding properties measured with DMS at 671 nm. The refractive index values are given for TE polarisation.

Glass	Au$^+$ fluence (cm^{-2})	$n_{substrate}$	Number of guided modes	n	Δn
A	1×10^{14}	1.504	–	–	–
	1×10^{15}		–	–	–
	3×10^{15}		1	1.505	0.001
	1×10^{16}		1	1.505	0.001
C	1×10^{14}–1×10^{16}	1.512	–	–	–
B	1×10^{14}, 1×10^{15}	1.475	–	–	–
	1×10^{16}		1	1.477	0.002

3.3. Optical properties

The glasses that were implanted at the highest fluence (i.e. 1×10^{16} cm^{-2}) and subsequently annealed at the highest temperature (600 °C) changed from colourless to red. The colour red, which appeared in all three glass types and which was confirmed also by the appearance of the pertinent peak (at 532 nm) in the UV–vis absorption spectra (see e.g. the absorption spectrum for Glass A in Fig. 3) indicated the presence of colloid particles of gold. Glasses A and B had that peak with similar intensities and located at exactly 532 nm while Glass C differed in both, with a lower intensity of the 'red' peak shifted to a shorter wavelength (550 nm). Obviously, these findings are related to the structure of the glasses used and deserve further analysis.

The waveguiding properties as measured by DMS are shown in Table 3. The waveguiding effect was found only in Glasses A and B after applying higher fluences (3×10^{15} and 1×10^{16} cm^{-2}). The refractive index increments Δn in the waveguides ranged from 0.001 to 0.002, which is sufficient for the creation of single-mode waveguides.

4. Conclusion

Three silicate glasses were implanted with 1701 keV Au$^+$ ions using fluences ranging from 1×10^{14} to 1×10^{16} cm^{-2}. A small disagreement between the predicted Au depth profiles calculated by the SRIM and the measured Au depth profiles was observed in correlation with the varying structures of the glasses. A dramatic change of the Au concentration depth profiles was observed after

long-time annealing (25 h) at 400 °C. The presence of gold colloid particles was identified in the glass implanted at 1×10^{16} cm^{-2} and annealed at the highest temperature (600 °C), as proved by UV–vis spectroscopy. The results showed a certain similarity between Glasses A and B, both being silicate glasses. Glass C (BK7), on the other hand, revealed stronger resistance to the ion implantation as well as its consequences. A likely reason is that Glass C is a boron-silicate glass. Boron, with a much smaller size when compared to silicon, makes the structure of the glass network less open and denser than the mostly silicate network, which results in lower penetrability of the glass for the incoming particles (ions). Our experiments lead us to believe that rather than the concentration of monovalent (more mobile) modifiers in the glass (in our case sodium ions), it is the network-forming elements that are decisive for the behaviour of the glass in the ion implantation process applied here.

Acknowledgements

MEYS Grant Nos. 6046137302, LC06041, Grant Agency of the Czech Academy of Sciences KJB 100480601, and Czech Science Foundation Grant No. 106/05/0706 have supported the research.

References

[1] C. Sinha, S. Bhattacharyya, Current Topics Atomic, Molecular and Optical Physics, World Scientific Publishing Co., Singapore, 2006, p. 237.
[2] F. Gonella, Metal nanoclusters composite silicate glasses, Rev. Adv. Mater. Sci. 14 (2007) 134.
[3] P. Mazzoldi, G. Mattei, Phys. Stat. Sol. (a) 3 (2007) 621.
[4] K. Fukumi, A. Chayahara, K. Kadono, T. Sakaguchi, Y. Horino, J. Appl. Phys. 75–76 (1994) 3075.
[5] G. De Marchi, G. Mattei, P. Mazzoldi, C. Sada, A. Miotello, J. Appl. Phys. 92–98 (2002) 4249.
[6] H. Bach, N. Neuroth, Properties of Optical Glasses, Springer, Berlin, 1995.
[7] F. Gonella, E. Cattaruzza, A. Quaranta, S. Ali, N. Argiolas, C. Sada, Solid State Ionics 177 (2006) 3151.
[8] J. Saarilahti, E. Rauhala, Nucl. Instr. and Meth. B 64 (1992) 734.
[9] J.F. Ziegler, Stopping and Range of Ions in Matter: SRIM – 2003, <http://www.srim.org>.
[10] P.D. Townsend, P.J. Chandler, L. Zhang, Optical Effects of Ion Implantation, Cambridge University Press, 1994.
[11] P. Colomban, J. Non-Crystalline Solids 323 (2003) 180.
[12] T. Stelzner, G. Angra, F. Falk, E. Wendler, W. Wesch, R. Schulz, S. Christiansen, Nucl. Instr. and Meth. B 257 (2007) 172.

Nuclear Instruments and Methods in Physics Research B 267 (2009) 1332–1335

Contents lists available at ScienceDirect

Nuclear Instruments and Methods in Physics Research B

journal homepage: www.elsevier.com/locate/nimb

Er^+ medium energy ion implantation into lithium niobate

B. Svecova [a,*], P. Nekvindova [a], A. Mackova [b,c], J. Oswald [d], J. Vacik [b,e], R. Grötzschel [f], J. Spirkova [a]

[a] Department of Inorganic Chemistry, Institute of Chemical Technology, Technicka 5, 166 28 Prague, Czech Republic
[b] Nuclear Physics Institute, Academy of Sciences of the Czech Republic, v.v.i., 250 68 Rez, Czech Republic
[c] Department of Physics, Faculty of Science, J.E. Purkinje University, Ceske Mladeze 8, 400 96 Usti nad Labem, Czech Republic
[d] Institute of Physics, Academy of Sciences of the Czech Republic, v.v.i., Cukrovarnicka 10, 162 53 Prague, Czech Republic
[e] Research Centrum Rez, 250 68 Rez, Czech Republic
[f] Institute of Ion Beam Physics and Materials Research, Forschungszentrum Rossendorf, 01314 Dresden, Germany

ARTICLE INFO

Article history:
Available online 29 January 2009

PACS:
85.40.Ry
42.70.Hj
61.85.+p
25.40.Cm

Keywords:
Lithium niobate
Erbium
Ion implantation
Photoluminescence

ABSTRACT

Erbium-doped lithium niobate (Er:$LiNbO_3$) is a prospective photonics component, operating at 1.5 μm, which could find its use chiefly as an optical amplifier or waveguide laser. In this study, we have focused on the properties of the optically active Er:$LiNbO_3$ layers, which are fabricated by medium energy ion implantation under various experimental conditions. Erbium ions were implanted at energies of 330 and 500 keV with fluences of 1.0×10^{15}, 2.5×10^{15} and 1.0×10^{16} cm^{-2} into $LiNbO_3$ single-crystalline cuts of various orientations. The as-implanted samples were annealed in air at 350 °C for 5 h. The depth distribution and diffusion profiles of the implanted Er were measured by Rutherford Backscattering Spectroscopy (RBS) using 2 MeV He^+ ions. The projected range R_P and projected range straggling ΔR_P were calculated employing the SRIM code. The damage distribution and structural changes were described using the RBS/channelling method. Changes of the lithium concentration depth distribution were studied by Neutron Depth Profiling (NDP). The photoluminescence spectra of the samples were measured to determine whether the emission was in the desired region of 1.5 μm. The obtained data made it possible to reveal the relations between the structural changes of erbium-implanted lithium niobate and its luminescence properties important for photonics applications.

1. Introduction

Single-crystalline lithium niobate ($LiNbO_3$, LN) is one of the most widely used photonic materials thanks to its unique combination of properties see [1,2]. After doping with rare earth ions, LN crystals become suitable for use as optical amplifiers, lasers or up-convertors. A laser emission of around 1.5 μm (the wavelength commonly used in telecommunication [3]) can be achieved by doping erbium into lithium niobate. A thin surface layer of lithium niobate, containing erbium ions (Er:$LiNbO_3$), can be, in principle, fabricated in several ways (see [4] and the references therein): doping during a growth process, diffusion from an erbium metal layer evaporated on the surface of an LN wafer, ion exchange from a molten erbium salt and, last but not least, ion implantation.

Many papers (see e.g. [5] and the references therein) have already been published on the erbium implantation into lithium niobate, which have described on the implantation process and the luminescence of the implanted samples. However, only a few of them have thoroughly dealt with the structural properties of the implanted lithium niobate thin wafers. While Mignotte et al. [6,7] have recently reported on the relationships between the composition and properties of Er:$LiNbO_3$, a complete, systematic study of the impact of the erbium-implantation process on the properties and structure of the implanted lithium niobate is yet to be conducted.

In this study, we have focused on erbium doping by the implantation of Er^+ ions into various cuts of single-crystalline lithium niobate. The ion implantation method has great potential for application in terms of most of the substrate materials as well as-implanted ions. By setting the implantation parameters (such as ion fluence, beam energy and ion current), we can control the final structure of the treated materials and their implantation-relevant characteristics, e.g. the concentration and depth of the dopant ions, the number of the introduced defects and extent of damage induced in the thin layer implanted [8]. In the case of lithium niobate, its disrupted crystalline structure (caused by the ion implantation) can be reconstructed through subsequent annealing at elevated temperatures (above 500 °C, see [9,10]). However, annealing at higher temperatures may, in the case of higher concentrations of erbium ions, lead to the formation of clusters that, because of the pair interactions of the erbium ions, cause an unde-

* Corresponding author. Tel.: +420 220 444 003; fax: +420 224 311 010.
E-mail address: blanka.svecova@vscht.cz (B. Svecova).

0168-583X/$ - see front matter © 2009 Elsevier B.V. All rights reserved.
doi:10.1016/j.nimb.2009.01.041

sired effect known as concentration quenching of the 1.5 μm luminescence (see e.g. [5]). Moreover, annealing at higher temperatures caused damage to the lithium niobate structure, which in many cases proved to be irreversible. Hence, based on our previous experience with ion diffusion into lithium niobate [11], annealing at lower temperatures (⩽350 °C) was applied for the recovery of the lithium niobate structure. The lower annealing temperatures have, in the authors' opinion, an additional benefit: the processes occurring during the annealing should proceed in the various crystallographic cuts at different rates, which could help comprehend the importance of particular crystallographic orientations in the diffusive processes inside lithium niobate.

The subject of this study consists of (i) implantation of Er^+ ions into various crystallographic cuts of single-crystalline lithium niobate using different conditions of the implantation, and (ii) characterisation of the as-implanted and the annealed erbium-containing thin layers using a combination of chemical analysis and structure defining as well as photoluminescence methods.

The aim of this study was to discover how the different crystal structures of the particular lithium niobate cuts affect the erbium-implantation process and migration (diffusion) of the erbium ions during the thermal treatment of the as-implanted lithium niobate wafers.

2. Experiments

In this study, we have used various $LiNbO_3$ cuts (made by the Czochralski method in Crytur Turnov, Czech Republic), namely commonly used *X* cuts ⟨11–20⟩, *Z* cuts ⟨0001⟩ and specially designed *Y* cuts, i.e. parallel *Y*II ⟨10–14⟩ and perpendicular *Y*⊥ ⟨01–12⟩ to the cleavage plane.

Thoroughly pre-cleaned $LiNbO_3$ wafers were implanted with Er^+ ions using medium energies (330 or 500 keV). The ion fluence ranged from 1.0×10^{15} to 1.0×10^{16} cm^{-2}. The implantations were performed by a 500 kV implanter in Forschungszentrum Rossendorf, Germany. The beam was scanned through an aperture of typically 1×1 cm^2, resulting in a beam current density on the target of typically 0.25 μA/cm^2. During implantation, the crystals were tilted by 7° to avoid the channelling of the erbium ions into the $LiNbO_3$ crystalline structure. For the recovery of the structure, the as-implanted samples were annealed for 5 h in air at 350 °C.

The concentration profiles of the incorporated erbium ions were studied by Rutherford Backscattering Spectroscopy (RBS). The analysis was performed at the Tandetron 4130 MC accelerator using a 2.0 MeV He^+ ion beam. The He^+ ions, backscattered under a 170° laboratory scattering angle, were detected by the ULTRA-ORTEC silicon detector. The collected data were evaluated using the GISA 3 computer code [12] and transformed into concentration depth profiles.

The structural changes (structural damage, amount of the introduced defects), which occurred during the ion implantation and subsequent annealing, were examined by the RBS/channelling measurements using a beam of 1.8 MeV He^+ ions from the van de Graaff accelerator in Forschungszentrum Rossendorf, Germany.

A few samples that were implanted with Er^+ ions at high fluences (1.0×10^{16} cm^{-2}) were characterised for the depth concentration profiles of lithium by Neutron Depth Profiling (NDP), i.e. a method based on the $^6Li(n,^4He)^3H$ nuclear reaction of thermal neutrons with the ^6Li isotope [13,14].

The photoluminescence (PL) spectra of the samples were collected in the region of around 1535 nm at room temperature using front-side excitation (from the implanted side) at 980 nm. PL was detected by a Ge detector with a two-step thermoelectric cooler. All the PL spectra were corrected on the spectral sensitivity of the Ge detector.

3. Results and discussion

3.1. Erbium concentration depth profiles (RBS)

The RBS analysis confirmed that the implanted erbium ions were present in all of the inspected $LiNbO_3$ cuts. Fig. 1 demonstrates that the amount of the incorporated erbium corresponds well to the increasing implantation fluence, and the depths of the as-implanted layers range from 70 to 90 nm depending on the energy of the implantation (330 or 500 keV, respectively). For the *X* cut samples, these trends are illustrated in Fig. 1. The results for the *Z* and *Y* cuts were similar to those of the *X* cut.

The obvious differences between the cuts were shown in Fig. 2, when the high ion fluences (1.0×10^{16} cm^{-2}) were applied. At *Y*⊥ cut, the erbium concentration maximum was shifted slightly closer to the surface and its value was slightly higher than those for the *X*, *Z* and *Y*II cuts. In any case, however, these differences were very far from those (much more dramatic) found in the case of erbium-ion exchange doping [15].

As for the post-implantation annealing, it did not cause any dramatic changes in the erbium concentration depth profiles. The substantial change in concentration profiles occurred at *Y*⊥ cut (1.0×10^{16} cm^{-2} and 330 keV), when it got 6% broader.

3.2. SRIM simulation

The statistical distribution of the implanted ions can be described by a Gaussian function centred at the projected range R_P with a half-width ΔR_P straggling. The R_P and ΔR_P values depend on the energy and mass of the implanted ion as well as on the density of the substrate used.

The measured concentration depth profiles of the as-implanted erbium ions corresponded to the SRIM 2006 [16] projected range calculation and had a typical bell-shape distribution, especially when the highest fluence was used (1.0×10^{16} cm^{-2}, see Fig. 1). In Fig. 2, we can see that the measured profile is broader than the calculated one. The SRIM code does not take into account the surface sputtering effects and the dynamic changes of the substrate composition during the implantation process, which can apparently lead to an error in the estimated concentration profile when the implantation fluence is high. The projected range R_p and range straggling ΔR_P of the erbium ions calculated by SRIM are R_p = 69.9 nm, ΔR_p = 21.9 nm and R_p = 99 nm, ΔR_p = 30.5 nm

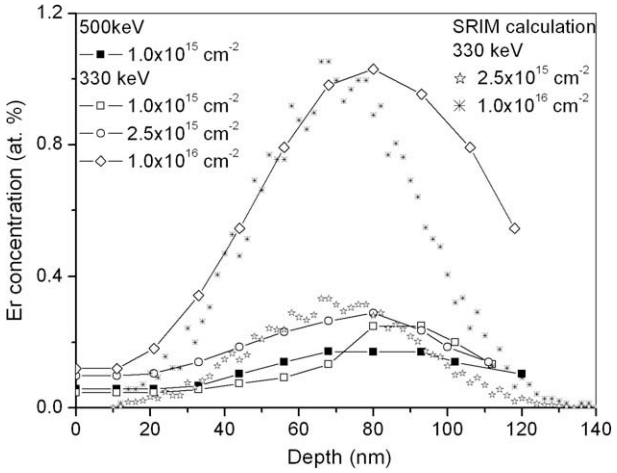

Fig. 1. The dependence of the erbium concentration depth profiles on the implantation Er^+ ion fluence (lithium niobate *X* cuts). The full Er depth profile cannot be extracted from the RBS spectra due to overlap with the Nb edge.

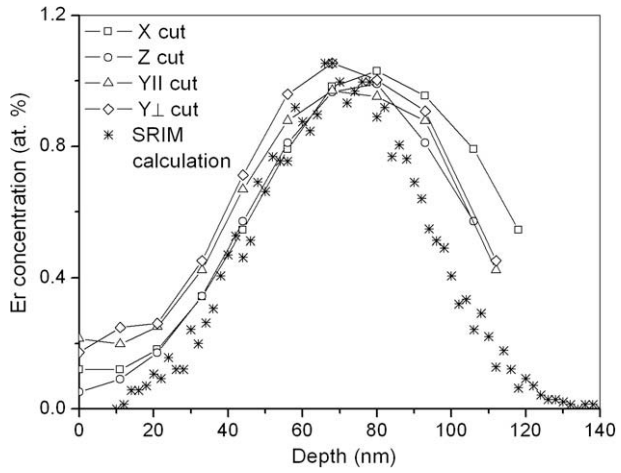

Fig. 2. The erbium-profile comparison of the various as-implanted (1.0×10^{16} cm^{-2} and 330 keV) lithium niobate cuts.

depending on energies of the implanted ions (330 or 500 keV, respectively).

By comparing the erbium concentration depth profiles of the substrates with different crystallographic orientations (see Fig. 2), it is possible to conclude that the *Z* cut manifests a narrower erbium depth profile and better agreement with the predicted data. The *Y*II cut also exhibits a broader bell-shape depth distribution of the erbium ions as compared to the SRIM simulation, which makes it similar to the *X* cut behaviour. More significant disagreement with the SRIM code is observed in the as-implanted *Y*⊥ cuts, where the depth profile broadens and obvious maximum shift towards the surface in the as-implanted samples appears.

3.3. Structural damage and defects revealed by RBS/channelling

The data obtained by RBS/channelling illustrate how the ion implantation induced considerable damage (amorphisation) of the surface layers of the LN crystal (shown for the *X* cut in Fig. 3). With increasing fluence, we observed a deepening of the modified layer, namely the amount of disorder saturated first at the most probable depth (corresponding to the projected range of ions) and then over a widening depth interval. An increase of the energy of the doping caused a higher number of defects which reached deeper into the substrate. These effects occurred regardless of the crystallographic orientation of the cuts.

After the post-implantation annealing, a partial reconstruction of the surface layer occurred (see Fig. 4). The thickness of the damaged layer substantially decreased and so did the yield from the depth behind the modified layers.

3.4. Changes in lithium distribution (NDP)

The NDP measurement showed that the lithium concentration in the LN surface layer had decreased after Er^+ ion implantation (see Fig. 5). The decline of the lithium concentration is seen on both lines of the energy spectra (see the inset), but more distinctively on the α-line (due to the higher stopping power of the alpha particles). In all measured samples, the measured depth profiles of lithium showed a drop-off close to the surface to about 92% of the nominal (i.e. bulk) value, measured by NDP, which slowly changed to 94% at the depth of about 100 nm and finally recovered to 100% at greater depth. The decrease of the lithium concentration spanned the layer of about 130 nm, which roughly corresponded to the implanted erbium depth distribution (see Fig. 2). The decrement in the lithium concentration was probably caused by the swelling of the surface layer implanted by the Er^+ ions with a high fluence (>10^{15} cm^{-2}). This effect (swelling of the crystalline substrate arising from ion implantation with a high fluence) had already been observed in LN systems [17,18] as well as in other oxide crystals (e.g. Al_2O_3 [19], a-SiO_2 [20], etc.). In the present case, the 'swelling-effect' observed on the LN crystal by NDP (for the first time) is very pronounced and deserves further analysis.

3.5. Optical properties

The PL spectra of the erbium-implanted samples were collected in the 1.5 μm region before and after annealing. The as-implanted samples (unannealed) did not show any desired photoluminescence at 1.5 μm, which was attributed to the $^4I_{11/2} \rightarrow {}^4I_{15/2}$ transition. However, it appeared after the post-implantation annealing although no significant change of the erbium concentration profiles had occurred. The intensity of the emission band increased with the increasing fluence of the implantation and also depending on the crystallographic orientation of the substrate cut in the sequence: $X \rightarrow Y\text{II} \rightarrow Z \rightarrow Y\perp$. The highest intensity of the photoluminescence appeared in the annealed *Y*⊥ cut sample that was implanted using 1.0×10^{16} cm^{-2} fluence and 330 keV (see Fig. 6).

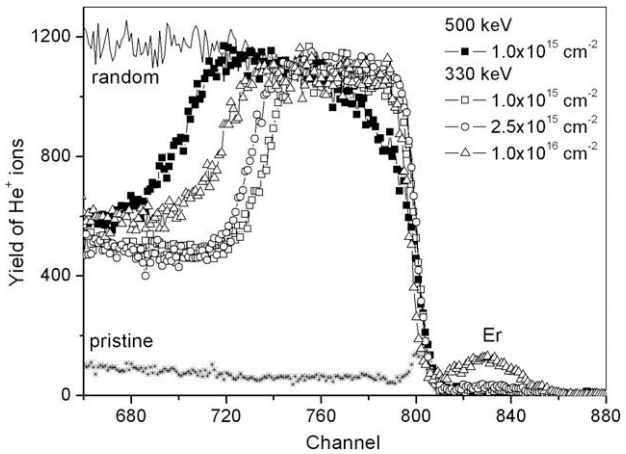

Fig. 3. The RBS/channelling spectra of the lithium niobate *X* cuts implanted under various implantation conditions.

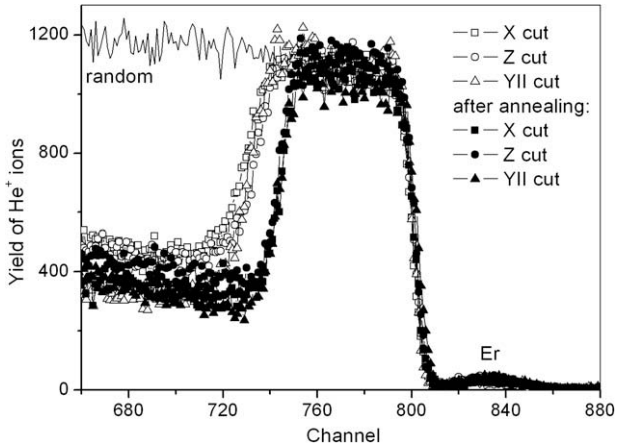

Fig. 4. The RBS/channelling spectra of the various as-implanted and annealed lithium niobate cuts. Reconstruction of the annealed surface layers is evident.

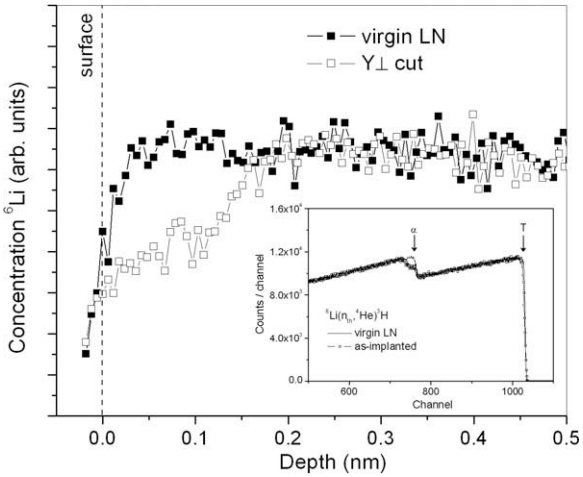

Fig. 5. The lithium distribution changes in the as-implanted $Y\perp$ cut (1.0×10^{16} cm^{-2} and 330 keV) determined by NDP. In the detail, the normalised energy spectra from the reaction ^{6}Li(n,^{4}He)^{3}H measured on pristine-irradiated samples are shown. The spectra consist of the triton (T) and alpha (α) lines. The drop-off of the alpha line represents a decline of the Li content in the subsurface layer.

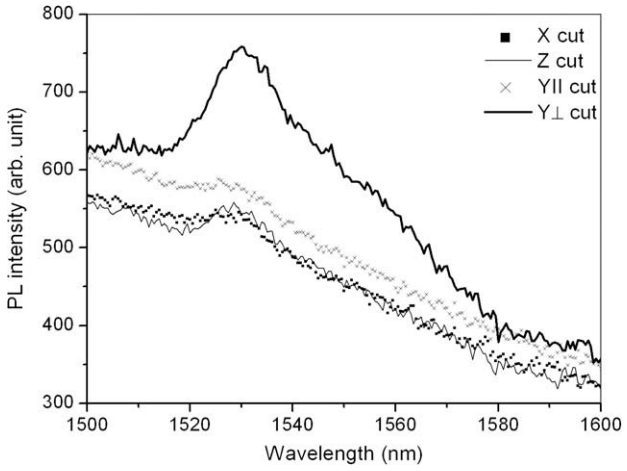

Fig. 6. The 1.5 μm photoluminescence spectra observed in the erbium-implanted (1.0×10^{16} cm^{-2} and 330 keV) samples which were annealed for 5 h at 350 °C.

Fig. 6 clearly also shows that the annealing has a different impact on the PL properties in the various crystallographic cuts. The PL intensity of the annealed samples was substantially improved in the $Y\perp$ cut, while remaining rather weak in the other cuts. In our opinion, this effect cannot be unambiguously attributed merely to the recovery of the lithium niobate crystal structure, i.e. to the presence or absence of the amorphous layer in which the PL measurements occurred. A similar effect has been observed in special silicate glasses [21] into which erbium was in-diffused by the ion-exchange reaction. Moreover, some of the samples revealed significant enhancement of the 1.5 μm luminescence after the annealing of the as-exchanged samples, or, the sought luminescence had not appeared until the samples were annealed, which could not have been caused by the re-crystallisation of the Er-doped matrix as the silicate glass surface undoubtedly remained amorphous. Our explanation of the observed behaviour of the thin erbium-doped layers is that the annealing caused a better distribution of the erbium ions, which in the as-implanted sample (as well as in the as-exchanged samples in our previous experiments) was rather random, leading to the formation of clusters and thus to pair interaction, which is one of the main problems in erbium-doped materials. Annealing in the erbium as-implanted thin layers could thus cause both dissolution of the erbium clusters that were formed during the doping and recovery of the original lithium niobate structure, in which the erbium ions will be allowed to occupy only several well-defined sites, preventing their interactions. Indubitably, this effect is closely related to the crystallographic orientation of the cuts, indicating that the diffusive processes in the $Y\perp$ cuts are much simpler than in the other ones used. This finding may be of some importance in the design of erbium-doped photonics devices and will be further examined.

4. Conclusion

In summary, erbium was implanted into lithium niobate single-crystalline wafers of various crystallographic orientations. The different conditions of the implantation were reflected in the properties of the resultant thin surface layers, especially the extent of the introduced structural defects, the concentration depth profiles of both the incorporated erbium and depleted lithium and, finally, optical properties. Our results confirmed that Er^+ ion implantation has a different effect on the various crystallographic cuts of LN. The post-implantation annealing is beneficial for the character and intensity of the erbium-induced photoluminescence at 1.5 μm, which is important for its potential utilisation for photonics devices.

Acknowledgements

The research has been supported by the LC06041, MSM 6046137302 and KJB 100480601 research programs, and the student grant of the Institute of Chemical Technology in Prague No. 101/08/0016. The implantation experiment was done within the Research Infrastructures Transnational Access (RITA) Contract No. 025646. The NDP measurements were supported by the Project No. IAA200480702.

References

[1] K.K. Wong, Properties of Lithium Niobate, INSPEC, London, 2002.
[2] L. Arizmendi, Phys. Stat. Sol. (a) 201 (2004) 253.
[3] A.J. Kenyon, Prog. Quantum Electron. 26 (2002) 225.
[4] L. Tsonev, Opt. Mater. 30 (2008) 892.
[5] A. Polman, J. Appl. Phys. 82 (1997) 1.
[6] C. Mignotte, Appl. Surf. Sci. 185 (2001) 11.
[7] C. Mignotte, Nucl. Instr. and Meth. B 187 (2002) 95.
[8] P.D. Townsend, P.J. Chandler, L. Zhang, Optical Effects of Ion Implantation, Cambridge University Press, 1994.
[9] M. Fleuster, Ch. Buchal, E. Snoeks, A. Polman, J. Appl. Phys. 75 (1994) 173.
[10] S.M.M. Ramos, B. Canut, P. Thévenard, D.B. Poker, J. Phys. Chem. Solids 57 (1996) 513.
[11] P. Nekvindova, J. Spirkova, J. Cervena, M. Budnar, A. Razpet, B. Zorko, P. Pelicon, Opt. Mater. 19 (2002) 245.
[12] J. Saarilahti, E. Rauhala, Nucl. Instr. and Meth. B 64 (1994) 734.
[13] R.G. Downing, G.P. Lamaze, J.K. Langland, J. Res. Natl. Inst. Stand. Technol. 98 (1993) 109.
[14] J. Vacik, J. Cervena, V. Hnatowicz, V. Havranek, J. Hoffmann, S. Posta, D. Fink, R. Klett, Nucl. Instr. and Meth. B 142 (1998) 397.
[15] P. Nekvindova, J. Spirkova-Hradilova, J. Schröfel, V. Perina, J. Mater. Res. 16 (2001) 333.
[16] <www.srim.org>.
[17] B. Canut, R. Brenier, A. Meftah, P. Moretti, S. Ould Salem, S.M.M. Ramos, P. Thevenard, M. Toulemonde, Nucl. Instr. and Meth. B 91 (1994) 312.
[18] B. Canut, S.M.M. Ramos, R. Brenier, P. Thevenard, J.L. Loubet, M. Toulemonde, Nucl. Instr. and Meth. B 107 (1996) 194.
[19] S.M.M. Ramos, N. Bonardi, B. Canut, S. Della-Negra, Phys. Rev. B 57 (1998) 189.
[20] C. Trautmann, J.M. Costantini, A. Meftah, K. Schwartz, J.P. Stoquert, M. Toulemonde, in: J.C. Barbour, S. Roorda, D. Ila, M. Tsujioka (Eds.), Atomistic Mechanisms in Beam Synthesis and Irradiation of Materials, MRS Symposia Proceedings No. 504, Materials Research Society, Pittsburgh, 1999, p. 123.
[21] L. Salavcova, A. Mackova, J. Oswald, B. Svecova, S. Janakova, J. Spirkova, M. Mika, J. Phys. Chem. Solids 68 (2007) 891.

Nuclear Instruments and Methods in Physics Research B 268 (2010) 2042–2045

Contents lists available at ScienceDirect

Nuclear Instruments and Methods in Physics Research B

journal homepage: www.elsevier.com/locate/nimb

Study of Er^+ ion-implanted lithium niobate structure after an annealing procedure by RBS and RBS/channelling

A. Mackova [a,b,*], P. Malinsky [a,b], B. Svecova [c], P. Nekvindova [c], R. Grötzschel [d]

[a] Nuclear Physics Institute, Academy of Sciences of the Czech Republic, v.v.i., 250 68 Rez, Czech Republic
[b] Department of Physics, Faculty of Science, J.E. Purkinje University, Ceske mladeze 8, 400 96 Usti nad Labem, Czech Republic
[c] Department of Inorganic Chemistry, Faculty of Chemical Technology, Institute of Chemical Technology, Technicka 5, 166 28 Prague, Czech Republic
[d] Institute of Ion Beam Physics and Materials Research, Forschungszentrum Rossendorf, 01314 Dresden, Germany

ARTICLE INFO

Article history:
Available online 25 February 2010

Keywords:
Lithium niobate
Erbium
Ion implantation
RBS/channelling

ABSTRACT

Erbium-doped lithium niobate (Er:$LiNbO_3$) is a prospective photonics component, operating at $\lambda = 1.5$ μm, which could be used as an optical amplifier or waveguide laser. We have focused on the structure of Er:$LiNbO_3$ layers created by 330 keV erbium ion implantation (fluences 1.0×10^{15}, 2.5×10^{15} and 1.0×10^{16} cm^{-2} 1) in the *X*, *Z* and two various *Y* crystallographic cuts of $LiNbO_3$. Five hours annealing at 350 °C was applied to recrystallize the as-implanted layer and to avoid clustering of Er. Depth distribution of implanted Er has been measured by Rutherford Backscattering Spectroscopy (RBS) using 2 MeV He^+ ions. Defects distribution and structural changes have been described using the RBS/channelling method. Data obtained made it possible to reveal the relations between the crystallographic orientation of the implanted crystal and the behaviour during the restoration process. The deepest modified layer has been observed in the perpendicular *Y* cut, which also exhibits the lowest reconstruction after annealing. The shallowest depth of modification and good recovery after annealing were observed in the *Z* cut of $LiNbO_3$. Since Er-depth profiles changed significantly in the perpendicular *Y* cut, we suppose that the crystal structure recovery inhibits Er mobility in the crystalline structure.

1. Introduction

Single crystals like lithium niobate ($LiNbO_3$, named as "LN") are frequently doped with optically active rare earth or transition metal ions for a variety of applications in optical devices such as solid state lasers, amplifiers, sensors [1,2]. The crystalline field in the surroundings of the active ions and their distribution in various centres can strongly affect the optical properties. The ion implantation technique is one of the ways (see [3] and the references therein) to form active optical layers. Ion implantation into LN in order to form colloids or nanoparticles has already been performed by several groups [4–7]. It is well known when using low-fluence implantation, point-defect and simple-defect clusters are generated, whereas a fluence greater than 10^{15} cm^{-2} causes layer amorphisation with significant volume expansion [8]. However, subsequent annealing is known to have a beneficial influence on the reconstruction of the damaged structure as well as on optical properties like intensity of luminescence. However, complicating factor is the temperature of annealing. As has been already reported, unlike other ABO_3 materials, the ion- implanted niobates and tantalates after annealing at temperatures of 825–925 K do not recrystallize epitaxially but instead new crystals nucleated and grew in the amourphous region [9]. Differences in the nanoparticle or precipitate formation in the different LN cuts during annealing were attributed to the directional character of the stress fields created during the implantation process and the anisotropic re-distribution of vacancies and interstitials [6,8].

Here we have focused on erbium doping by implantation of Er^+ ions into various cuts of single-crystalline lithium niobate. Precipitates formation was not expected at this stage [6,7], but the anisotropy in Er distribution in LN crystal structure could be attributed to early stage implant accumulation, which is influenced by radiation-stimulated diffusion, implantation fluence and by damages introduced during ion implantation [10].

The Er distribution and aggregation in the LN crystal lattice significantly influences the luminescent properties. We have already found significant differences of the photoluminiscence (PL) bands intensities between various crystallographic cuts of the Er-impanted LN (with the highest one observed at the $Y_\perp$) [11], and in this paper we are going to explain why do they occur. In order to get that information, we have studied how the process of recovery during the post-implantation annealing of Er:LN affects the migration of erbium ions through the different crystal structures of the particular lithium niobate cuts.

* Corresponding author. Address: Nuclear Physics Institute, Academy of Sciences of the Czech Republic, v.v.i., 250 68 Rez, Czech Republic.
E-mail address: mackova@ujf.cas.cz (A. Mackova).

0168-583X/$ - see front matter © 2010 Elsevier B.V. All rights reserved.
doi:10.1016/j.nimb.2010.02.021

2. Experimental

In this study, we have used various $LiNbO_3$ cuts (synthesized by the Czochralski method in Crytur Turnov, Czech Republic), namely the commonly used *X* cuts ⟨11–20⟩, *Z* cuts ⟨0001⟩ and specially designed *Y* cuts, i.e. "parallel" Y_{II} ⟨10–14⟩ and "perpendicular" $Y_{\perp}$ ⟨01–12⟩ to the cleavage plane. Thoroughly pre-cleaned $LiNbO_3$ wafers were implanted with 330 keV Er ions, 7° off-axis to avoid channelling. The ion fluence ranged from 1.0×10^{15} to 1.0×10^{16} cm^{-2}; in this paper, we present only the results of the lower implantation fluences (1.0×10^{15} and 2.5×10^{15} cm^{-2}). Different effects on Er-depth profiles after annealing appeared only in the case of the highest fluence, as described in [11]. The implantations were performed using a 500 kV implanter in the Institute of Ion-Beam Physics and Materials Research, Forschungszentrum Rossendorf, Germany. The beam was scanned through an aperture of typically 1×1 cm^2, resulting in a beam current density of typically 0.25 μA/cm^2 on the target. For the recovery of the structure, the as-implanted samples were annealed for 5 h in air at 350 °C.

The concentration profiles of the incorporated erbium ions were studied by Rutherford Backscattering Spectroscopy (RBS). The analysis was performed on a Tandetron 4130 MC accelerator using a 2.0 MeV He^+ ion beam. He^+ ions were detected at the scattering 170°.

The collected data were evaluated and transformed into concentration depth profiles using the GISA 3 computer code [12]. In order to study damages introduced by the implantation process, the influence of the annealing procedure on the recovery of the host lattice was examined by RBS/channelling measurements using a 1.7 MeV He^+ beam from the Van de Graaff accelerator in the Institute of Ion-Beam Physics and Materials Research, Forschungszentrum Rossendorf, Germany.

3. Results and discussion

3.1. Erbium concentration depth profiles (RBS) in the as-implante and post-implantation-annealed samples

The RBS depth profiles were measured for all of the LN cuts (*X*, *Z*, Y_{II} and $Y_{\perp}$ implanted with Er ions at fluences 1.0×10^{15} cm^{-2} and 2.5×10^{15} cm^{-2}). The statistical distribution of the implanted ions can be described by a Gaussian function centred at the projected range R_p with half-width ΔR_P. The measured concentration depth profiles of as-implanted Er ions are compared with SRIM 2003 [13] projected range calculation. The projected range R_p and range straggling ΔR_P of erbium ions calculated by SRIM are $R_p = 70$ nm, $\Delta R_p = 22$ nm. The comparison with the values R_p and ΔR_p obtained from RBS depth profiles for different fluences is shown in Table 1.

We have confirmed that as per the literature [14] the increasing fluence makes the concentration depth profiles shift to shallower depths. There is an interesting finding concerning the particular types of LN cuts. The behaviour of the particular cuts is different and the concentration maxima are shifted to the surface in the order from the deepest one to the shallowest: $X \rightarrow Z \rightarrow Y_{II}$, $Y_{\perp}$ (see Figs. 1a, b and 2a, b) erbium concentration depth profiles (RBS) in the post-implantation-annealed samples.

Moreover, in the case of lower fluences (for 1.0×10^{15} cm^{-2}, see Figs. 1b, 2b; for 2.5×10^{15} cm^{-2}, see Figs. 1a, 2a), the Er-depth profiles are influenced more significantly by the annealing procedure than for highest fluence used (1.0×10^{16} cm^{-2}, see [11]). We suggest that with increasing implantation fluence larger Er clusters could be created because of the higher level of damage induced and the exceeding solubility limit of Er in LN [2], even if the implantation temperature was not so high as to enable the crystal structure re-growth in the modified layer [15–17]. We observed that the annealing procedure influenced Er profiles for both *Y* cuts more significantly than for other cuts (see Fig. 2a, b and compare them with Fig. 1a, b). In the $Y_{\perp}$ cut, the erbium concentration maximum disappeared and the Er concentration at depth Rp decreased. Hence, the erbium ions migrate most significantly through the structure of both *Y* cuts. On the contrary, the most marginal changes in Er-depth profiles were exhibited by the *Z* cut samples after the annealing procedure. These interesting discrepancies in Er profiles after the annealing procedure in various cuts could be explained in the following way.

(i) When the amount of defects in the various cuts differ, so does the level of recovery during the annealing procedure, (ii) in some cuts a better migration of defects through the structure of cuts is the reason for a more significant recovery [14], (iii) erbium has a different mobility in the recovered or damaged structure of the various cuts. We have used RBS/channelling to shed more light onto these mechanisms.

3.2. Structural information about as-implanted and as-annealed samples (RBS/channeling)

Data obtained by RBS/channelling illustrate how ion implantation induced considerable damage into the surface layers of the LN crystal implanted with 2.5×10^{15} cm^{-2} (see Fig. 3a and b) and with 1.0×10^{15} cm^{-2} (Fig. 4a and b). With increasing fluence, we observed a slight deepening of the modified layer. The discrepancies between fluence 2.5×10^{15} cm^{-2} and 1.0×10^{15} cm^{-2} was not as pronounced as when compared with 1.0×10^{16} cm^{-2} fluence (see [11]).

After the post-implantation annealing, a partial reconstruction of the surface layer occurred (see Figs. 3 and 4). For all of the cuts, the thickness of the damaged layer decreases. However, differences in restoration of the modified structure for the various cuts were observed after the annealing procedure. As mentioned above, the cut mostly affected by ion implantation according to RBS Er profiles is the $Y_{\perp}$ cut, whereas the smallest impact of implantation was found in the *Z* cut. This was confirmed also by the measured RBS/channelling spectra (see Fig. 3b). After annealing, the thinner, modified layer was found in the *Z* cut, but the restoration of the $Y_{\perp}$ is the less significant one.

Even though the differences in the RBS/channelling spectra were not so pronounced, we could observe that for all fluences (see also in [11]), recovery after the annealing procedure was mostly significant in the *Z* cut, unlike in both *Y* cuts, where it was the least profound one. Our results confirmed the previously observed differences in the various types of sample cuts [16,17].

It can be concluded that: (i) the amount of disordered atoms in the implanted region was similar in all cuts (the yield in the RBS-aligned spectra is comparable with the random spectra), but the thicknesses of the modified layer differed for the various cuts, which means that the depth of the introduced defects differed for the various cuts as well; (ii) the migration of the defects also differed, and we have observed better migration of defects in the *Z* cut as compared to the $Y_{\perp}$ cut; (iii) Er migration is strongly

Table 1
Projected ranges *Rp* and range straggling Δ*Rp* of implanted Er determined from RBS depth profiles for the different crystallographic orientation of LN implanted using various fluences.

LN cut	Fluence 1.0×10^{15} cm^{-2}		Fluence 2.5×10^{15} cm^{-2}		Fluence (11) 1.0×10^{16} cm^{-2}	
	R_p (nm)	ΔR_p (nm)	R_p (nm)	ΔR_p (nm)	R_p (nm)	ΔR_p (nm)
X cut	84	42	74	30	76	25.5
Z cut	81	27.5	75	28	74	28.5
Y_{II} cut	80	28	72	25.5	73	27
$Y_{\perp}$ cut	80	29.5	75	24.6	72	27.5

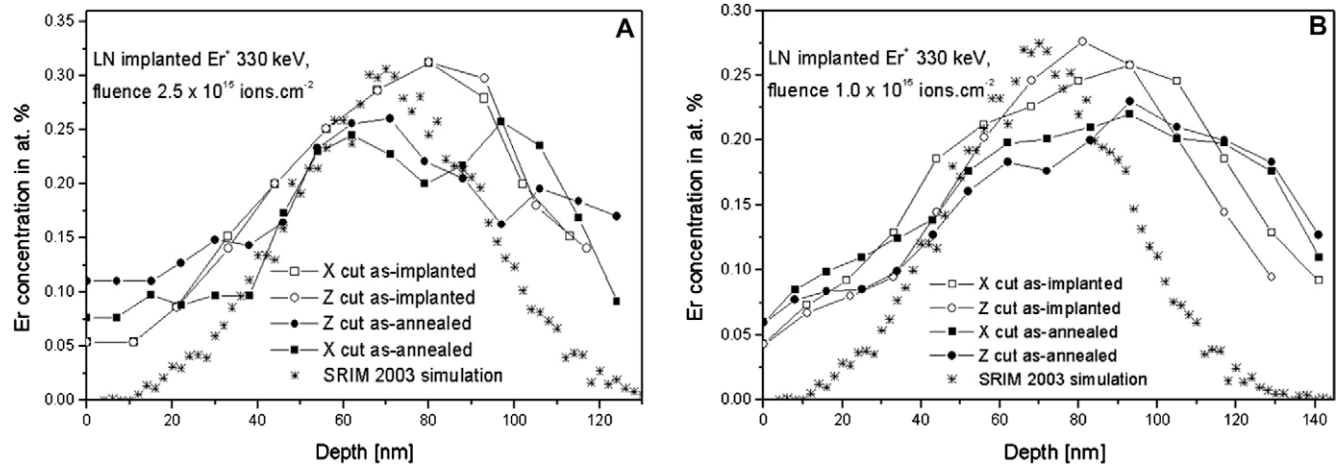

Fig. 1. The Er-depth profiles in different LN *X* and *Z* cuts measured by RBS for implantation fluence (A) 2.5×10^{15} cm^{-2} and (B) 1.0×10^{15} cm^{-2} – comparison of as-implanted samples and as-annealed samples.

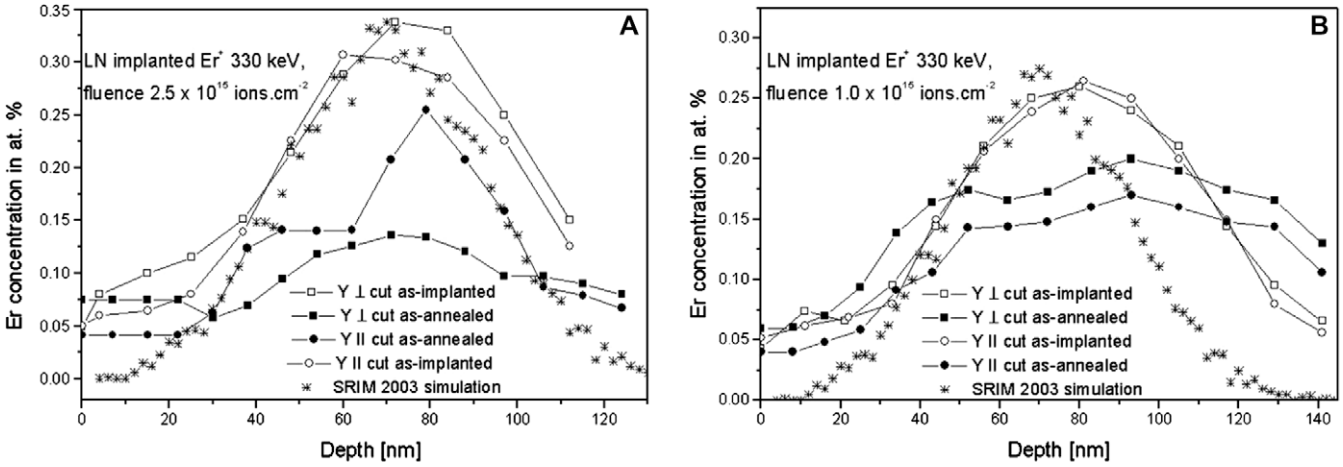

Fig. 2. The Er-depth profiles in different LN Y_{II} and $Y_{\perp}$ cuts measured by RBS for implantation fluence (A) 2.5×10^{15} cm^{-2} and (B) 1.0×10^{15} cm^{-2} – a comparison of the as-implanted and as-annealed samples.

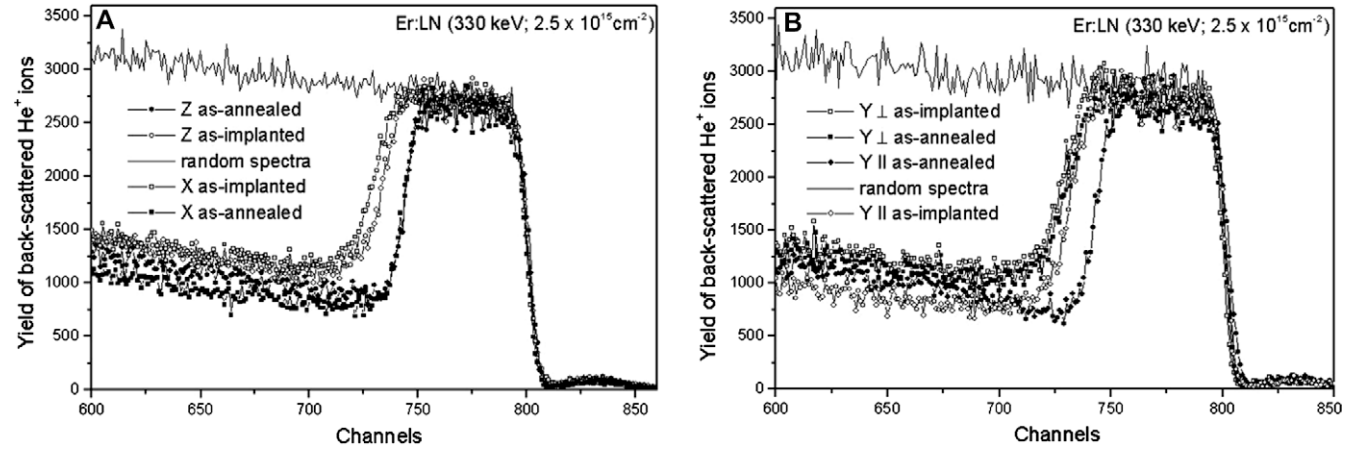

Fig. 3. The RBS/channelling spectra in different LN cuts for the implantation fluence of 2.5×10^{15} cm^{-2} – a comparison of the as-implanted samples and as-annealed samples (A) *X* and *Z* cuts and (B) $Y_{\perp}$ and Y_{II} cuts.

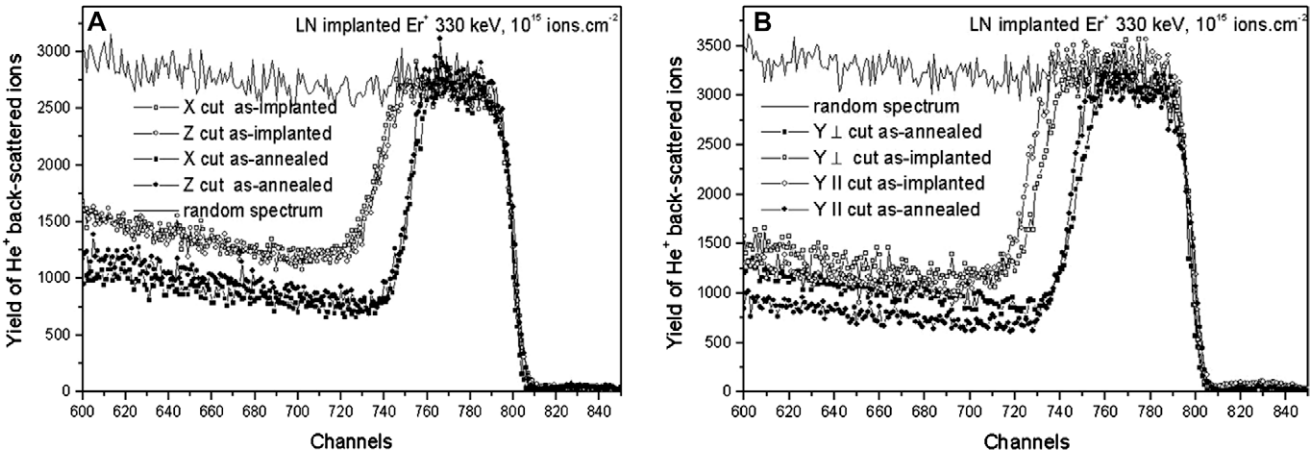

Fig. 4. RBS/channeling spectra in different LN cuts for implantation fluence 1.0×10^{15} cm^{-2} – comparison of as-implanted samples and as-annealed samples *X* and *Z* cuts (A) and $Y_{\perp}$ and Y_{II} cuts (B).

influenced by the ability of recovery for each type of the cut, i.e. the Er ions seem to be more mobile in the damaged structure of $Y_{\perp}$ cut.

4. Conclusion

Erbium doped single-crystalline lithium niobate has been currently one of the most significant materials for construction of optical amplifiers and lasers. It has been found that not only suitable concentration of the erbium ions, but also their site symmetry and surrounding in the structure of the thin optical layer have important impact on the thought photoluminescence properties, i.e. on the intensity and width of the 1535 nm emission bands. However, it has not been yet made clear why also various crystallographic cuts of the lithium niobate make such differences of the photoluminescence behaviour. Results presented in this paper showed that the RBS and RBS/channelling are efficient tools to follow motions of the implanted ions both during the implantation and during the post-implantation annealing. The measurements done in thin erbium implanted surface layers in different crystallographic lithium niobate cuts proved that the migration of the Er ions through the LN structure in the $Y_{\perp}$ cut is the best because of the lower ability of the recovery, i.e. the worsened migration of defects through the structure of this cut. We suppose that the recovery of the interface between the modified and the non-modified LN structure decreased the mobility of the Er implanted particles because of the migration of the introduced defects.

Acknowledgements

The research has been supported by the LC06041, 106/09/0125 and student grant 101/08/9001 research programs. The implantation experiment was conducted within the Research Infrastructures Transnational Access (RITA), Contract No. 025646.

References

[1] A.J. Kenyon, Prog. Quant. Electron. 26 (2002) 225.
[2] A. Polman, J. Appl. Phys. 82 (1997) 1.
[3] L. Tsonev, Opt. Mater. 30 (2008) 892.
[4] K.K. Wong, Properties of Lithium Niobate, INSPEC, London, 2002.
[5] L. Arizmendi, Phys. Status Solidi A 201 (2004) 253.
[6] M. Rahmani, L.H. Abu-Hassan, P.D. Townsend, I.H. Wilson, G.L. Destefanis, Nucl. Instrum. Meth. B 32 (1988) 56.
[7] A. Kling, J.C. Soares, M.F. da Silva, Nucl. Instrum. Meth. B 141 (1998) 268.
[8] S. Jetschke, H. Karge, K. Hehl, Phys. Status Solidi A 77 (1983) 207.
[9] A. Meldrum, L.A. Boatner, W.J. Weber, R.C. Ewing, J. Nucl. Mater. 300 (2002) 242.
[10] O.A. Plaksin, Y. Takeda, H. Amekura, N. Umeda, K. Kono, N. Okubo, N. Kishimoto, Appl. Surf. Sci. 241 (2005) 213–217.
[11] B. Svecova, P. Nekvindova, A. Mackova, J. Oswald, J. Vacik, R. Grotzschel, J. Spirkova, Nucl. Instrum. Meth. B 267 (2009) 1332.
[12] J. Saarilahti, E. Rauhala, Nucl. Instrum. Meth. B 64 (1994) 734.
[13] <http://www.srim.org>.
[14] L.C. Feldmann, J.W. Mayer, S.T. Picraux, Material Analysis by Ion Channelling, Academic Press, New York, 1982.
[15] G. Kuri, G. Materlik, V. Hagen, R. Wiesendanger, Appl. Phys. A 73 (2001) 265.
[16] C. Mignotte, Appl. Surf. Sci. 185 (2001) 11.
[17] C. Mignotte, Nucl. Instrum. Meth. B 187 (2002) 95.

Journal of Non-Crystalline Solids 356 (2010) 2468–2472

Contents lists available at ScienceDirect

Journal of Non-Crystalline Solids

journal homepage: www.elsevier.com/ locate/ jnoncrysol

Study of Cu^+, Ag^+ and Au^+ ion implantation into silicate glasses

B. Svecova [a,*], P. Nekvindova [a], A. Mackova [b,c], P. Malinsky [b,c], A. Kolitsch [d], V. Machovic [e], S. Stara [a], M. Mika [f], J. Spirkova [a]

[a] Department of Inorganic Chemistry, Faculty of Chemical Technology, Institute of Chemical Technology, Technicka 5, 166 28 Prague, Czech Republic
[b] Nuclear Physics Institute, Academy of Sciences of the Czech Republic, v.v.i., 250 68 Rez, Czech Republic
[c] Department of Physics, Faculty of Science, J. E. Purkinje University, Ceske mladeze 8, 400 96 Usti nad Labem, Czech Republic
[d] Institute of Ion Beam Physics and Materials Research, Forschungszentrum Rossendorf, 01314 Dresden, Germany
[e] Laboratory of Molecular Spectroscopy, Institute of Chemical Technology, Technicka 5, 166 28 Prague, Czech Republic
[f] Department of Glass and Ceramics, Faculty of Chemical Technology, Institute of Chemical Technology, Technicka 5, 166 28 Prague, Czech Republic

ARTICLE INFO

Article history:
Received 15 October 2009
Received in revised form 9 February 2010
Available online 28 June 2010

Keywords:
Ion implantation;
Silicate glasses;
Metal nanoparticles;
Rutherford backscattering

ABSTRACT

A study of the ion implantation of Cu^+, Ag^+ or Au^+ ions into different types of silicate glasses is reported. The energy of the implanted ions was 330 keV and the implantation fluence was kept at 1×10^{16} cm^{-2}. The samples were characterised by various analytical methods: Rutherford backscattering spectrometry for the concentration depth profiles of the implanted atoms, Raman spectroscopy for the structure of the samples and also by UV–VIS absorption spectroscopy. The obtained data were evaluated on the bases of the structure of the glass matrix and the relations between the structural changes and optical properties, important for photonics applications, were formulated.

The main focus was the impact of various types and concentrations of glass network modifiers (e.g. Li, Na, K, Mg, Ca or Zn) as well as glass network formers (Si, and B) on the projected range of the implanted ions. Interesting results were also provided by a study of the annealing of the as-implanted samples in various types of glass substrates. The study showed that each of the implanted ions migrated in the substrates with different glass structures via unique mechanisms.

1. Introduction

The metal nanocluster composite glasses (MNCGs), which are synthesised by ion implantation, have been shown to be promising non-linear photonic materials (see [1,2] and the references therein). Metal nanoclusters (nanoparticles) embedded in glasses enhance the third-order optical response at a wavelength around the characteristic surface plasmon resonance (SPR) of the metal cluster. The enhanced magnitude of the optical non-linearities of such MNCGs and the amazingly short temporal responses (in a time domain below picoseconds) of these non-linearities have unambiguously opened a new dimension in the area of photonics, bringing the scientific community closer to success in the realisation of all-optical switching devices [3,4].

Such glasses containing dispersed nanoparticles can be prepared by a variety of physical and chemical methods [5–7], especially ion implantation, ion exchange, sol–gel technique, etc. The advantage of the ion implantation method is the formation of high-density nanoparticles in solids in a well-defined space of an optical device because of the high controllability of the depth distribution of the implanted elements together with the ability to exceed the low solubility limitation [8]. The size, shape, lattice structure, distribution and composition of the embedded metal nanoclusters are influenced by the preparation procedure (i.e. beam energy, choice of the implanted ion and its fluence) and, last but not least, the composition of the used material. Subsequent treatment further promotes the nanoparticle precipitation and in the case of thermal annealing reduces irradiation-induced damage in the material.

In the past few years, several research groups have studied the synthesis of nanometre-sized particles of noble metals embedded especially in silica glass, occasionally in soda–lime silicate glasses [9–11]. Besides noble metal implantation (Cu, Ag, and Au), sequential ion implantation of two metal species (see [5,12,13]) or co-implantation of noble metal, an oxidising or reducing ion (atom) [14–16] has been done to form alloy metal nanoclusters and thus influence the resulting non-linear properties. Several works on metal–ion-implanted colloid generation in bulk glass have shown that optical properties depend also on the annealing atmosphere (e.g. [5,17,18]). Nowadays, it seems obvious that very good non-linear properties (considered as the $\chi 3$ coefficient measured by the Z-scan method) are revealed by the material having homogeneously distributed small-sized nanoparticles (approx. 5 to 20 nm, see [3,4,19,20]).

In this paper, we report on the Cu^+, Ag^+ and Au^+ room-temperature ion implantation into different types of glasses. All the ions belong to the 11th group of elements with the general valence shell electron configuration d^{10} s^1, so that similar properties of the

* Corresponding author.
E-mail address: blanka.svecova@vscht.cz (B. Svecova).

0022-3093/$ – see front matter © 2010 Elsevier B.V. All rights reserved.
doi:10.1016/j.jnoncrysol.2010.03.031

ions with the same valence can be expected (of course with respect to their various atomic weight). All the implanted materials are silicate-based glasses that form a basis with gradually changing properties (as concentration or type of the modifiers, optical basicity or the various extents of network cross-linking, etc.). The penetration of ions during ion implantation through different glass matrices was studied by Rutherford Backscattering Spectroscopy (RBS) and compared to the SRIM simulation. The migration of implanted ions during subsequent annealing was also investigated. The results were evaluated in terms of finding and understanding the relations between the properties of the implanted material and the incoming particle, which may be of the crucial importance in designing e.g. nanoparticle-based components for special applications.

2. Experimental procedures

In this study, we used glass substrates with different chemical compositions, namely several specially-designed glass types GIL and Glass B (made at the Glass Institute Hradec Kralove Ltd., Czech Republic) as well as glass type GZ (specially designed at the Institute of Glass and Ceramics, Institute of Chemical Technology Prague, Czech Republic) and the commercially available BK7 and silica glass. The glasses varied especially in their concentrations of monovalent (Li_2O, Na_2O, and K_2O) or divalent (CaO, MgO, and ZnO) modifiers as well as their network formers (SiO_2, and B_2O_3). The compositions of the glasses determined by X-ray fluorescence (XRF) or electron microprobe analysis (EMA) as well as the density of the glass substrates are provided in Table 1. The volume occupied by one mole of a glass containing N components was characterised by the glass molar volume V_m and calculated from formula [21]

$$V_m = \frac{M_m}{\rho}, \quad (1)$$

where M_m is glass molar mass (g mol^{-1}) and ρ is the glass density (g cm^{-3}). Glass molar mass was calculated from Eq. (2):

$$M_m = \sum_{i=1}^{N} M_{mi} x_i, \quad (2)$$

where M_{mi} are the molar masses of oxides (g mol^{-1}) and the x_i are the molar parts of oxides. The values of V_m for used glasses are given in Table 1.

The thoroughly pre-cleaned glass substrates were implanted with Cu^+, Ag^+ or Au^+ ions at an energy of 330 keV while the ion fluence was kept at 1×10^{16} cm^{-2}. The implantations were performed by the 500 kV implanter in the Ion Beam Centre, Forschungszentrum Dresden-Rossendorf, Germany. The as-implanted glasses were annealed in air at temperatures of 600 °C for 1 or 5 h.

Table 1
The composition of the glass samples used (in mol%).

Glass	Density [g cm^{-3}]	V_m [cm^{3}mol^{-1}]	SiO_2	B_2O_3	Li_2O	Na_2O	K_2O	Other components
BK7	2.50	25.70	73	11	–	9	6	As_2O_3, BaO
GIL11	2.37	24.65	67	–	20	3	–	Al_2O_3
GIL13K	2.48	26.67	62	29	–	–	9	Al_2O_3
GIL49	2.49	23.81	73	–	–	14	–	Al_2O_3, CaO, MgO
GIL56	2.41	25.48	79	–	–	18	1	Al_2O_3
Glass B	2.32	26.27	94	–	–	5	–	Al_2O_3
GZ4	2.63	24.04	73	–	–	14	–	Al_2O_3, ZnO
GZ5	2.44	23.78	73	–	–	14	–	Al_2O_3, MgO
GZ6	2.50	24.05	73	–	–	14	–	Al_2O_3, CaO
Silica glass	2.20	27.26	100	–	–	–	–	–

The depth distribution profiles of the implanted atoms were measured using Rutherford backscattering spectrometry (RBS) with 2.0 MeV He^+ ions. The incoming angle was 0° while the scattering angle was 170°. The measurements were evaluated with the Gisa 3.99 [22] and compared with simulated profiles of the implants in the SRIM 2008 [23]. The accuracy of the method is mentioned to be 5 nm. The Raman spectra were collected at 200 nm under the glass surface using a LabRam system Jobin Yvon model Labram HR equipped with the 532 nm line laser, the power on the head of the laser was 50 mW. The objective ×50 was used to focus the laser beam on the sample. The scattered light was analysed by spectrograph with a holographic grating of 600 g/mm, a slit width of 100 μm and a confocal hole of 400 μm. The adjustment of the system was regularly checked using a silicon sample. The acquisition time was 20 s and twenty accumulations were co-added to obtain a spectrum. The UV–VIS absorption spectra were collected using a CARY 50 dual-beam spectrometer in transmission modes ranging from 300 to 800 nm.

3. Results and discussion

3.1. The ion implantation — results

The glasses shown in Table 1 were implanted with Cu^+, Ag^+ or Au^+ ions with the same experimental conditions: a beam energy of 330 keV, a fluence of 1×10^{16} cm^{-2}. The concentration depth profiles of the implanted ions were measured using RBS and simulated by the SRIM 2008. The statistical distribution of the implanted ions can be described by a Gaussian function centred at the projected range R_P with a half-width ΔR_P straggling. The summarisation of the simulated SRIM 2008 parameters R_P and ΔR_P for all the implanted glasses and ions is presented in Table 2 and compared to the R_P and ΔR_P values calculated from the real implant depth profiles (determined by RBS) extrapolated by the Gaussian function.

It was confirmed that the lighter (and smaller) the implanted ions, the deeper the projected range (see Table 2). This trend is similar for the R_P values obtained by the SRIM simulation as well as by the RBS measurement. It is obvious that the lighter the implanted ion is, the more sensitively the SRIM simulation reacts to the varying density of the materials used, i.e. the differences in the simulated R_P value between the samples implanted with the lighter ion Cu^+ are greater with even a small change of the density of the substrate than the differences between the R_P values of the SRIM simulation for the Ag^+ or Au^+ ions.

We supposed that the same trend would also be found in the actual experiment. However, the R_P values obtained from the RBS measurement did not follow the trend observed with the SRIM simulation

Table 2
Comparisons of the R_P and ΔR_P parameters from the SRIM calculation and RBS depth profiles extrapolated by the Gaussian function [cm^{3}mol^{-1}].

Substrate	Cu^+			Ag^+		Au^+	
	SRIM $R_P/\Delta R_P$ [nm]	RBS $R_P/\Delta R_P$ [nm]	RBS peak[a] [nm]	SRIM $R_P/\Delta R_P$ [nm]	RBS $R_P/\Delta R_P$ [nm]	SRIM $R_P/\Delta R_P$ [nm]	RBS $R_P/\Delta R_P$ [nm]
BK7	245/73	–	–	147/40	161/60	96/19	106/47
GIL11	250/72	252/82	226	143/36	182/63	100/19	111/32
GIL13K	246/67	221/65	198	139/36	122/64	97/19	97/31
GIL49	237/70	242/85	254	139/37	143/55	96/19	101/35
GIL56	246/75	255/83	245	143/37	159/56	99/19	101/32
Glass B	251/70	250/92	234	147/38	117/100	102/21	102/39
GZ4	239/72	[b]	[b]	137/38	125/78	94/20	103/36
GZ5	245/72	244/91	226	140/36	116/55	97/19	102/32
GZ6	243/73	221/91	223	140/37	146/61	96/20	91/32
Silica glass	270/78	244/90	207	147/38	135/59	107/21	116/39

– RBS was not able to measure the depth profile because of the barium shielding.
[a] The position of the maximum concentration.
[b] The Cu concentration depth profile could not be evaluated because of the very low Cu concentration.

(mentioned above). The measured RBS profiles correspond well to the Gaussian function only for heavy ion, i.e. Au^+, while the Gaussian function practically does not describe the RBS profiles of Cu (compare the R_P values obtained by extrapolation of measured concentration profiles and the position of concentration maximum). In Table 2 we can also see that the R_P values for Cu differed from SRIM simulation mostly. Generally, it is possible to say that for lighter elements the SRIM simulation does not correspond well. Evidently, there is another factor that has a substantial impact on the migration of the incoming ion through the matrix of the glass and, regarding the results obtained, it will be the structure of the glass rather than its density. To explain those differences occurring with glasses of similar density, we need to make considerations based on the glass structure and binding interactions. Therefore, the influence of the glass structure on the behaviour of the implanted ion will be discussed below.

It is very interesting to note (see Table 2) that differences between measured concentration profiles of Ag^+ ions are the most pronounced, i.e. type of glass and its structure affect the Ag range of all the implanted ions mostly.

Contrary, the R_P values obtained from the RBS measurement of glasses implanted with Au^+ ions are in a good agreement with the simulated values. The ion range of Au^+ ions is affected rather by the density on the glass than by glass structure.

3.2. The ion implantation — discussion

The ion penetration through the glass during ion implantation is dependent on properties of the ion (beam energy and ion mass) and properties of the substrate used (composition and density). The well-known influence of density of the glass on the ion penetration was in our experiment provable only at glasses implanted with heavier Au^+ ions. This trend is not perspicuous in the glasses implanted with lighter ions (Cu, and Ag), in some glasses is even reverse (i.e. Cu^+ and Ag^+ ions do not have the deepest penetration in silica glass). For this reason, we studied the relationships between the ion penetration and the molar volume V_m or we focused directly on the structure of the glass network.

From Tables 1 and 2 it is apparent that ranges of Cu^+ and Ag^+ ions in glasses with high V_m values are obviously the smallest ones which can be explained by the high number of collisions (and i.e. a high stopping power) of the implanted ions with particles of the substrate in glasses with high molar volume V_m.

If we focused directly on the structure of glass network it is possible to divide the used glasses from the point of view of:

a) a different amount of monovalent modifiers (Na^+),
b) a different type of monovalent modifiers (Li^+, Na^+, and K^+),
c) a different type of divalent modifiers (Ca^{2+}, Mg^{2+}, and Zn^{2+}) or
d) a different type of network formers (SiO_2, and B_2O_3).

Regarding a) The simplest type of glass from the point of view of its structure is the silica glass built-up only from deformed tetrahedron units [$SiO_{4/2}$] [24]. The addition of the modifier into the glass network results in a 'breaking' of the Si–O–Si linkage, with a new terminal (non-bridging) oxygen appearing in the glass structure. In the Raman spectra, the addition of modifiers caused a growth of the peak around 1090 cm^{-1}, which corresponds to the stretching mode [25]. Fig. 1 provides a comparison of the Raman spectra of our three types of glass, where the concentration of the monovalent modifier varies. For silica glass, the stretching mode had a very small Raman intensity, but the peak intensity significantly increased in the glass containing 14% Na_2O (GIL49). We suppose that the migration of the implanted ion through the glass matrix will be more difficult in glass having a higher degree of cross-linking (i.e. in glass having lower stretching mode's intensity).

When comparing as-implanted glasses with different concentrations of a monovalent one-type modifier (see Fig. 2), it can be seen that the implanted Ag^+ ions penetrated to the greatest depth in glass containing the highest amount of Na (GIL56, glass with 18% Na_2O), while the smallest ion range was recorded in Glass B with the smallest content of Na (glass with 5% Na_2O) as well as in silica glass (despite their low density). It could be explained by fact that both types of glass (Glass B and silica glass) possess the highest amount of network cross-linking. The behaviour of Cu^+ ions in the glasses with various content of monovalent modifier was similar to the behaviour of Ag^+ ions. The penetration of Au^+ ions reacted to the addition of the monovalent modifier less pronounced. A possible explanation is that gold being the heaviest ion causes greater damage in the glass matrix than lighter ions regardless to the structure of particular type of the glass.

Concerning b) On the other hand, when we compare glasses with different types (though of similar concentrations) of monovalent modifier (Li^+, Na^+, and K^+), it is apparent that ion penetration through the material depends on the mass or size (understood here as the ionic radius) of each modifier. We assume that the degree of cross-linking of the glass structure is in this case similar (because of the similar amount of the modifier) and the stopping power of each glass

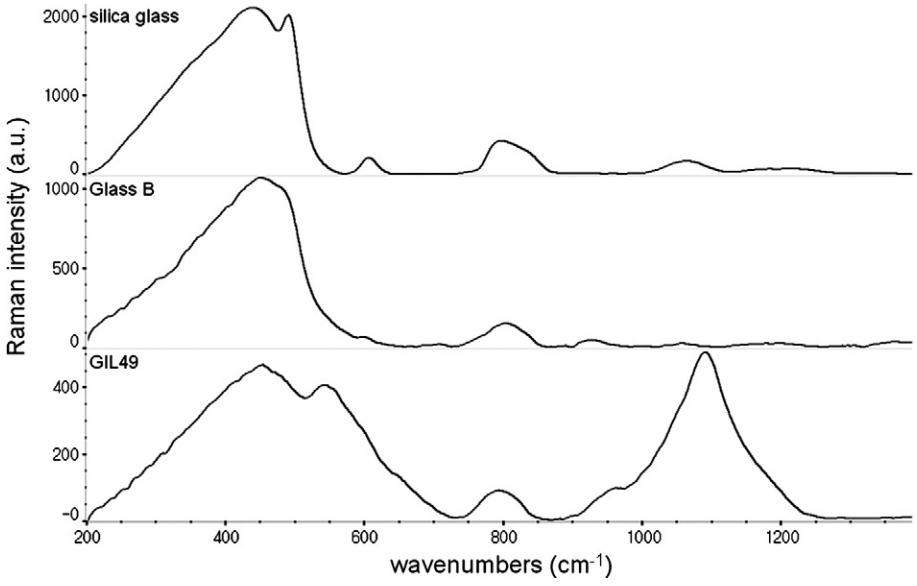

Fig. 1. The Raman spectra of the glasses (not implanted) with a different degree of modification of the glass structure.

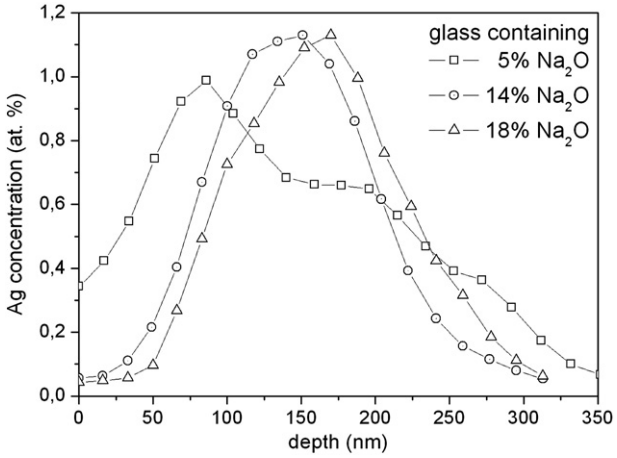

Fig. 2. Ag depth concentration profiles in the glasses with a different concentration of the monovalent modifier (Na), experimental conditions: a beam energy of 330 keV, a fluence of 1×10^{16} cm^{-2}.

containing a different type of the modifier increases in the sequence: Li–glass → Na–glass → K–glass, depending on the increasing mass or size of the modifiers, what correspond to the increasing V_m values of glasses used. The glasses containing Li_2O (GIL11) are more permeable than the glasses containing Na_2O (GIL56) and K_2O (GIL13K) (demonstrated for Au^+ ions in Fig. 3).

Regarding c) In this case, we compare the glasses with different types of divalent modifier (Ca^{2+}, Mg^{2+}, and Zn^{2+}). The divalent modifier plays a similar role in the glass as a monovalent modifier (i.e. its higher concentration generates a higher amount of non-bridging oxygens in the glass structure). Our glasses with different types of divalent modifier varied in their density, and we supposed that the ion range would be the smallest in the Zn–glass (GZ4) (according to the SRIM simulation). Nevertheless, from the results of the Cu^+ and Au^+ as-implanted samples, it is evident that the smallest ion range has been surprisingly found in the Ca–glass (GZ6). The possible explanations could be the size of divalent modifiers or the ionic character of the Ca–O bond, which makes the glass network less permeable for incoming ions (see e.g. [26]).

Another interesting feature is the possibility of various oxidation states of the ions embedded in the matrix that could vary from I to III. In our opinion, the resulting valence will follow the so-called stable oxidation states, i.e. Cu (II), Ag(I) and Au(III). If so, it would also change the ionic/covalent character of the bonding interactions between the terminal oxygen atoms and the implanted ions. This may explain the rather unexpected behaviour of the silver ions during ion implantation, which does not correlate well with the periodic table sequence Cu → Ag → Au. However, discussion on this subject is in this moment beyond the scope of this paper, but it will be closely observed and presented elsewhere.

Concerning d) The used glasses can be compared also in terms of the network formers, i.e. we can compare the glasses whose structural element is SiO_2 and/or B_2O_3. For the given set of glasses, the resulting trend is not clear, however, glasses containing B_2O_3 seem to be more permeable (the projected range of the implanted ions is deeper). We suppose that the explanation of the longer-range ion in glasses containing boron is the small mass or size of boron in comparison with silicon.

3.3. The post-implantation annealing — results

The glasses implanted with Ag^+ ions were annealed at 600 °C for 5 h in the air. The annealing of the as-implanted glass containing Li_2O (GIL11) led to the formation of a crystalline phase and degradation of the glass. The concentration profile of Ag in the as-annealed glass GIL13K (the glass containing K_2O) was substantially different than the profiles of all other types of used glasses (demonstrated in Fig. 4 for glass GIL49 and GIL13K). The maximum concentration of the Ag^+ in glass GIL13K (containing K_2O) was slightly shifted towards the glass substrate, but not reduced. The

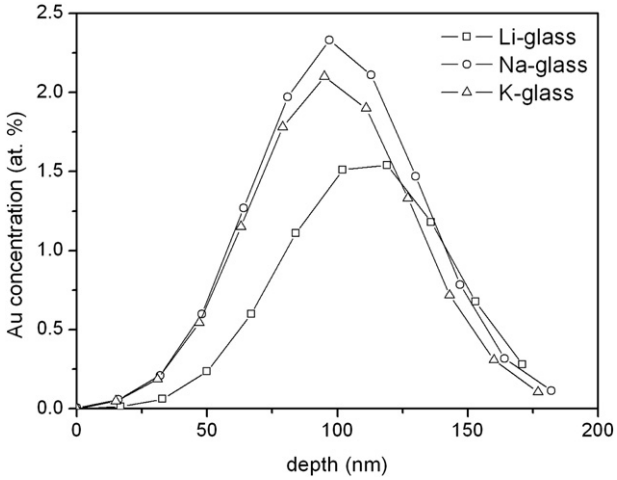

Fig. 3. Au depth concentration profiles in the glasses with a different type of monovalent modifier (Li^+, Na^+, and K^+), experimental conditions: a beam energy of 330 keV, a fluence of 1×10^{16} cm^{-2}.

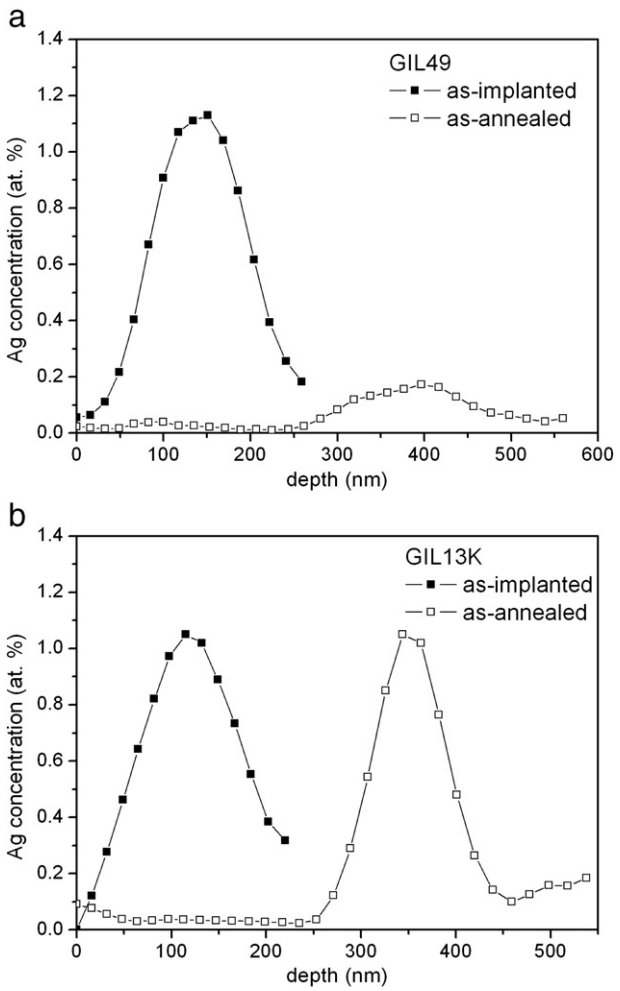

Fig. 4. Ag depth concentration profiles in the two types of glasses before and after annealing, experimental conditions: a beam energy of 330 keV, a fluence of 1×10^{16} cm^{-2}, annealing at 600 °C for 5 h in the air.

maximum concentration of the implanted ions significantly decreased after annealing in the samples made in all other types of the glasses, with the most significant reduction (up to 85 %) being observed in the glasses GIL49 implanted with Ag^+ ions and annealed for 5 h.

The migration of Ag^+ ions through the glass was very fast at the annealing conditions applied. Due to the low weight of the Cu^+ ion, we expected also fast penetration of the Cu^+ ions during the subsequent annealing through the glass structure, therefore we annealed the samples implanted with Cu^+ and Au^+ ions at the same temperature (600 °C) but for a shorter time (1 h). We annealed only samples made in two types of glass (i.e. GIL49 and GIL13K), where, according to the results of the Ag implantation, we expected the most significant difference of the ion migration through the glass structure. From the RBS measurements of the samples annealed for 1 h, it was evident that Au^+ ions moved through the glass structure slowly, i.e. the R_P values of glass GIL49 implanted with Au^+ ions changed from 101 to 94 nm, while glass GIL49 implanted with Cu^+ ions the R_P values changed from 242 to 224 nm. The concentration maximum at both annealed samples was shifted towards the surface which has been observed also in [20]. The R_P values of Cu^+ and Au^+ ions in glass GIL13K after short time annealing changed as follows: from 198 to 158 nm for Cu and from 97 to 75 nm for Au respectively.

3.4. The post-implantation annealing — discussion

A different mass or size of individual ions of Cu^+, Ag^+, and Au^+ was revealed at differing speeds of ion movement in the structure during the subsequent annealing. The deepest ion ranges observed at the glasses implanted with Ag^+ ions are caused by the annealing length being five times greater. For glasses containing monovalent modifiers, it seems probable that the Ag^+ ions moved through glass during annealing by the ion exchange mechanism. The different behaviour of all the implanted ions in the glass GIL13K caused by annealing could be explained on the basis of the low permeability of the glasses containing K_2O. Bigger and heavier potassium ions hamper the free movement of the incoming ion through the glass matrix, thus causing clustering (nanoclustering) of the implanted ions during the post-implantation annealing. The presence of Au nanoclusters in the glass was confirmed during the measurements of the absorption spectra, where the band at 412 nm was observed in the as-annealed sample in the glass GIL13K (see Fig. 5).

4. Conclusion

Different types of silicate glasses were implanted with Cu^+, Ag^+ or Au^+ ions using similar experimental conditions. It was found that the measured concentration profiles did not follow the expected trend (i.e. the higher the density of the glass, the lower the ion penetration as was predicted with the SRIM simulation) and a significant influence of the glass structure was proved. The ion range was affected mostly by molar volume of the glass and the presence of a monovalent modifier (Na^+) in the glass structure. The increasing concentration of glass modifier (Na^+) makes the glass structure less cross-linked and hence more permeable to an incoming ion. When we compare glasses with different types (but similar concentrations) of monovalent modifier, it is apparent that the ion penetration through a material depends on the mass of each modifier.

One well-known fact was confirmed, i.e. that light ions (Cu^+, and Ag^+) migrate during the post-implantation annealing through the glass structure faster than the heavier Au^+ ions. The ion migration during annealing was mostly hampered in glass containing K_2O, which in the case of Au^+ ions and the annealing conditions applied led to the formation of nanoparticles.

Our findings, which were confirmed also by Raman spectroscopy and absorption spectroscopy, can be useful in tailoring the desired properties of optical devices on the MNCGs, i.e. the choice of the bulk glass and the ion implantation conditions used.

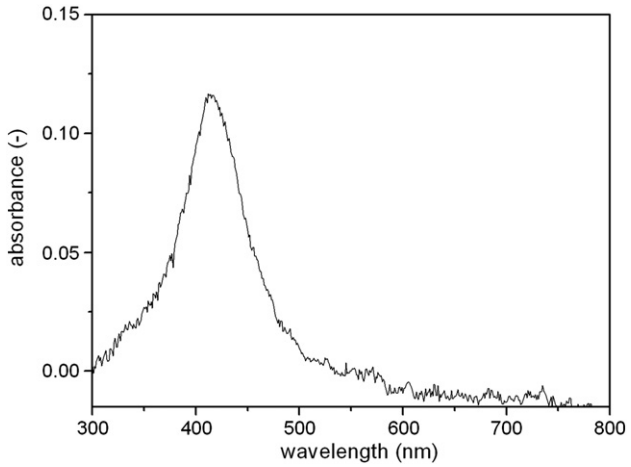

Fig. 5. The absorption spectra of the glass GIL13K implanted with Au^+ ions, experimental conditions: a beam energy of 330 keV, a fluence of 1×10^{16} cm^{-2}, annealing at 600 °C for 1 h in the air.

Acknowledgements

The research has been supported by the LC06041 research program, Grant No. 6046137302 from the Ministry of Education, Youth and Sports, Grant No. 106/09/0125 from the Czech Science Foundation, and the student grant of the Institute of Chemical Technology in Prague No. 101/08/9001. The implantation experiment was done within the Research Infrastructures Transnational Access (RITA) Contract Number 025646.

References

[1] C. Sinha, S. Bhattacharyya, Current Topics Atomic, Molecular and Optical Physics, World Scientific Publishing Co., Singapore, 2006, pp. 237–264.
[2] F. Gonella, P. Mazzoldi, in: H.S. Nalwa (Ed.), Handbook of Nanostructured Materials and Nanotechnology, Vol. 4, Academic, San Diego, 2000, p. 81.
[3] Optical Nonlinearity in Photonic Glasses, in: S. Kasap, P. Capper (Eds.), Springer Handbook of Electronic and Photonic Materials, 1st ed, Springer, New York, 2006, pp. 1063–1074.
[4] P. Chakraborty, J. Mater. Sci. 33 (1998) 2235.
[5] F. Gonella, Rev. Adv. Mater. Sci 14 (2007) 134.
[6] R.A. Ganeev, A.I. Ryasnyansky, Appl. Phys. B 84 (2006) 295.
[7] L. Armelao, R. Bertoncello, E. Cattaruzza, S. Gialanella, S. Gross, G. Mattei, P. Mazzoldi, E. Tondello, J. Mater. Chem. 12 (2002) 2401.
[8] P.D. Townsend, P.J. Chandler, L. Zhang, Optical Effects of Ion Implantation, Cambridge University Press, 1994.
[9] M. Dubiel, H. Hofmeister, E. Wendler, J. Non-Cryst. Solids 354 (2008) 607.
[10] M. Dubiel, H. Hofmeister, G.L. Tan, K.-D. Schicke, E. Wendler, Eur. Phys. J. D 24 (2003) 361.
[11] A.L. Stepanov, D.E. Hole, A.A. Bukharaev, Vacuum 64 (2002) 169.
[12] B. Joseph, H.P. Lenka, P.K. Kuiri, D.P. Mahapatra, R. Kesavamoorthy, Int. J. Nanosci. 6 (2007) 423.
[13] F. Gonella, E. Cattaruzza, G. Battaglin, F. D'Acapito, C. Sada, P. Mazzoldi, C. Maurizio, G. Mattei, A. Martorana, A. Longo, F. Zontone, J. Non-Cryst. Solids 280 (2001) 241.
[14] B. Joseph, S. Mohapatra, H.P. Lenka, P.K. Kuiri, D.P. Mahapatra, Thin Solid Films 492 (2005) 35.
[15] D. Ila, R.L. Zimmerman, C.I. Muntele, P. Thevenard, F. Orucevic, C.L. Santamaria, P.S. Guichard, S. Schiestel, C.A. Carosella, G.K. Hubler, D.B. Poker, D.K. Hensley, Nucl. Instrum. Methods B 191 (2002) 416.
[16] S. Nakao, S.X. Wang, L.M. Wang, M. Ikeyama, Y. Miyagawa, S. Miyagawa, Nucl. Instrum. Methods B 175–177 (2001) 202.
[17] J.-X. Xu, F. Ren, D.-J. Fu, Ch.-Z. Jiang, Physica A 373 (2006) 341.
[18] R.H. Magruder III, L. Yang, R.F. Haglund Jr., C.W. White, L. Yang, R. Dorsinville, R.R. Alfano, Appl. Phys. Lett. 62 (1993) 1730.
[19] D. Ila, E.K. Williams, S. Sarkisov, C.C. Smith, D.B. Poker, D.K. Hensley, Nucl. Instrum. Methods B 141 (1998) 289.
[20] F. Fukumi, A. Chayahara, K. Kadono, T. Sakaguchi, Y. Horino, J. Appl. Phys. 75 (1994) 3075.
[21] C.A. Harper (Ed.), Handbook of Ceramics, Glasses, and Diamonds, McGraw-Hill Professional, 2001, 5.24.
[22] J. Saarilahti, E. Rauhala, Nucl. Instrum. Methods B 64 (1992) 734.
[23] J.F. Ziegler, Stopping and Range of Ions in Matter: SRIM — 2008, www.srim.org.
[24] K.J. Rao, Structural Chemistry of Glasses, 1st ed Elsevier, 2002.
[25] P. Colomban, J. Non-Cryst. Solids 323 (2003) 180.
[26] B. Švecová, J. Špirková, S. Janáková, M. Míka, Mater. Sci. Eng. B 149 (2008) 177.

Advances and Applications in Electroceramics II

Ceramic Transactions, Volume 235

Edited by
K. M. Nair
Shashank Priya

A John Wiley & Sons, Inc., Publication

STUDY OF THE DIFFUSION FROM MELTED ERBIUM SALT AS THE SURFACE-MODIFYING TECHNIQUE FOR LOCALIZED ERBIUM DOPING INTO VARIOUS CUTS OF LITHIUM NIOBATE

Jakub Cajzl, Pavla Nekvindova, Blanka Svecova, and Jarmila Spirkova
Department of Inorganic Chemistry, Faculty of Chemical Technology, Institute of Chemical Technology, Technicka 5, 166 28 Prague, Czech Republic

Anna Mackova, Petr Malinsky, and Jiri Vacik
Nuclear Physics Institute, Academy of Sciences of the Czech Republic, v.v.i., 250 68 Rez, Czech Republic
Department of Physics, Faculty of Science, J. E. Purkinje University, Ceske mladeze 8, 400 96 Usti nad Labem, Czech Republic

Jiri Oswald
Institute of Physics, Academy of Sciences of the Czech Republic, Cukrovarnicka 10, 162 53 Prague, Czech Republic

Andreas Kolitsch
Helmholtz-Zentrum Dresden Rossendorf, 01314 Dresden, Germany

ABSTRACT
The results of the localized doping of erbium into lithium niobate (LN), mainly via diffusion from melted erbium salt (TD – thermal diffusion), are presented. Two different temperatures, 350 and 600 °C, as well as commonly used and specially cut LN wafers were applied. The samples were characterized by Rutherford Backscattering Spectroscopy (RBS) for the erbium concentration depth profiles and by Photoluminescence Spectroscopy for the emission around 1530 nm. The samples revealed thin erbium-doped layers that contained from 7 to 24 at. % of erbium. The luminescence without the post-diffusion annealing appeared in all of the LN cuts. As expected, when a higher temperature of TD was used, the luminescence intensity increased. However, the big differences in the luminescence intensity were found between the various LN cuts. A higher value of luminescence intensity was always detected in the $Y_{\perp}$ cut <10–14>, which is perpendicular to the crystal cleavage plain. To clarify the different penetration of the crystallographic orientation of LN for incoming erbium ions as well as the mechanism of the thermal diffusion process, the erbium site in the LN structure was studied using a combination of RBS/channeling and Neutron Depth Profiling (NDP) methods.

1. INTRODUCTION

Erbium-doped lithium niobate ($Er:LiNbO_3$, Er:LN) is, thanks to its suitable properties and mainly because of the possibility of transmission of the signal in the third telecommunication window, a very attractive material for photonics devices[1-3]. However, the doping of LN with Rare-Earth elements is very demanding, so that most of the devices are formed from bulk-doped LN in which the waveguiding layer is consequently created by high-temperature diffusion of titanium or zinc[4,5]. Therefore, the creation of an optically active waveguiding thin layer by an erbium localized doping into the LN surface is a tempting question to research. Actually, such an approach has already been studied and the localized doping of erbium from metal erbium or an erbium oxide film is currently being used[6]. This approach has also become our long-term task and within it we are going to compare

techniques and eventually suggest a feasible approach for the localized doping of erbium into LN leading to the construction of a real thin-film optical amplifier. In one of our previous papers[7,8], we reported on novel technology of the localized LN doping using a moderate-temperature diffusion of Er^{3+} from the melt of nitrates. We have tested this approach on several different crystallographic cuts of LN and found that all of the doped cuts revealed the emission at 1.5 μm. The amount of the in-diffused erbium depended strongly on the crystallographic orientation of the pertinent cuts. Similar results were also obtained for diffusion from the melts of sulfates performed at the higher temperature; this experiment was originally done by Sada et al.[9]. As expected, the crucial factor for a successful doping is the temperature of the diffusion, and it is true not only for the rate of the diffusion but also for the mechanism involved. Several interesting questions still remain unanswered, such as why the intensity of the luminescence is different in different crystallographic cuts after the thermal diffusion and what the basic processes occurring during the diffusion that affect the sites of the incorporated erbium are. The basic problem is whether the process is based on the exchange of erbium ions for lithium ions.

In this study, we are going to report on our experiments on the doping of erbium from the melts containing erbium salts conducted at two different temperatures into commonly used and specially cut LN wafers. The samples were characterized by luminescence measurement and by ion-beam techniques such as RBS (Rutherford Backscattering Spectroscopy) for the amount of the incorporated erbium. Using the RBS/channeling method and NDP (Neutron Depth Profiling), we were able to study the mechanism of the thermal diffusion process.

2. EXPERIMENT

For the experiments, we used wafers of LN with various crystallographic orientations (pulled by the Czochralski method) supplied by Crytur Turnov (Czech Republic). The wafers were oriented and labeled as follows: standard X cuts <11–20> and Z cuts <0001> and specially executed Y cuts with respect to the cleavage plane of the LN crystal, namely a parallel Y_{II} cut <10-12> and perpendicular $Y_{\perp}$ cut <10-14>. All of the wafers were ground on both sides and polished on one side to optical quality. The dimensions of the wafers were 12 × 7 mm with a thickness of 0.7 mm. Before the experiments, the wafers were treated by ultrasound-assisted cleaning in isopropanol.

For the doping of erbium, two erbium salt-containing multi-component melts were used: a two-component nitrate melt and a four-component sulfate melt (see Table I). The compositions of the melts differed according to thought temperature of the diffusion. The actual composition was based on our previous experiments[7,8] on finding suitable melts that would allow for doing the diffusion experiments mechanisms of that could have differed each from other. The criteria for the suitable melts were, besides a feasible and user friendly experimental procedure, mainly that the melts would not make any harm to the single-crystalline surfaces of the samples. Unfortunately it was found that it was not possible to find any melts that would fulfill the expected criteria for both temperatures of the diffusion; it means that the actual compositions of the melts differed not only in the particular components but also in the actual content of erbium. The amount of erbium nitrate was as high as possible but simultaneously below the level that would allow for the separation of Er_2O_3 that may occur at higher temperatures. Any diffusion of the large potassium cation did not expect. The doping from the nitrate melts carried out at 350 °C for 168 hours. The sulfate melt consisted, according to[9], of Li_2SO_4, Na_2SO_4 and K_2SO_4 (100 wt. %), into which 1 wt. % of $Er_2(SO_4)_3$ was added. The doping from this melt was carried out at 600 °C for 40 hours. Therefore, two basic sets of the samples were prepared and in order to ensure a good reproducibility of the results the experiments using both of the melts were repeated.

The doping was done in an oven using platinum crucibles. To ensure the homogeneity of the doping media, the melts were heated for at least 3 hours prior to the doping process.

For the recovery of the LN structure, the as-doped samples were annealed for 5 hours at 600 °C in oxygen.

Table I. The erbium-melts composition

Melt	Component *	Content [wt. %]
Nitrates	KNO_3	90
	$Er(NO_3)_3$	10
Sulfates	Li_2SO_4	70.7
	Na_2SO_4	9.9
	K_2SO_4	19.4
	$Er_2(SO_4)_3$	1.0

*As some of the components, e.g. erbium nitrate, lithium or erbium sulfates, occur as hydrated salts, the compositions of the melts were evaluated for the anhydrous ones.

The concentration profiles of the incorporated erbium ions were studied by RBS. The analysis was performed at a Tandetron 4130 MC accelerator using a 2.0 MeV He^+ ion beam. The backscattered He^+ ions were detected at a laboratory angle of 170°. The collected data were evaluated and transformed into concentration-depth profiles using the GISA 3 computer code[10]. The RBS/channeling analysis was performed to study the structural changes in the surface layer containing Er and to obtain information on the Er position in crystal after thermal diffusion. The RBS/channeling measurements were performed using a 1.7 MeV He^+ beam from the Van de Graaff accelerator in the Helmholtz Zentrum.

The photoluminescence spectra of the Er doped samples were collected within the range of 1440–1600 nm at room temperature. A pulse semiconductor laser POL 4300 emitting at 980 nm was used for the excitation of the luminescence. The luminescence radiation was detected by a two-step-cooled Ge detector J16 (Teledyne Judson Technologies). To scoop the specific wavelengths, a double monochromator SDL-1 (LOMO) was used. For the evaluation, all of the luminescence spectra were transformed to the base level and after the abstraction of the baseline the normalizing was done with help of reference samples.

The lithium concentration depth profiles in the prepared samples were measured by Neutron Depth Profiling (NDP). The method is based on a reaction of a thermal neutron with ^6Li: ^6Li (n,α) ^3H. The fabricated samples were irradiated with a thermal neutron beam from a 6 m long neutron guide (the neutron intensity was 10^7 neutrons.cm^{-2}.s^{-2}) and the charged reaction products were recorded by means of a Si(Au) surface barrier detector. The accuracy of the NDP method is 5% of the concentration value of Li, c_{Li}, the depth resolution is 10 nm. The natural abundance of the "NDP active" ^6Li isotope is 7.5%, but in the actual samples the $^6Li/^7Li$ ratio may significantly vary (e.g., due to the artificial depletion of the ^6Li isotope from the original natural materials). Thus, to avoid the uncertainty induced by this variation, for some considerations we rely on the relative changes of c_{Li} rather than their absolute values.

3. RESULTS

According to our previously conducted research[7,8], we assumed that the amount of the incorporated erbium in the doped thin-surface layers will be strongly affected mainly by the temperature of the doping but also by the type of the different crystallographic cuts. Four

types of various LN cuts were doped at two different temperatures, i.e., 350 °C and 600 °C. The actual temperatures were selected on the basis of previous experiments showing that at 350 °C the migration of lithium ions can be expected and at 600 °C the damaged LN crystal structure might be recrystalized[11] (the experimental conditions and composition of the melts used for the doping have been mentioned above in Chap. 2). The crucial property that was followed was the intensity of the luminescence at 1.5 μm, which was measured by luminescence spectroscopy in the reflection arrangement. The RBS method was used to determine the integral amount and depth distribution of the incorporated erbium, while the NDP method was a useful tool to follow the migration of lithium during the doping process. With the help of RBS/channeling, we were able to evaluate the structural changes after the TD and the amount of Er in the interstitial position of the LN structure.

3.1 LUMINESCENCE

In this chapter, we are going to compare the intensities of the luminescence bands occurring between 1400 nm and 1600 nm, with special attention to the band at 1530 nm, as it is particularly important for the potential utilization of the pertinent material in photonic devices. The samples doped at 350 °C from the nitrate melt revealed the maximal 1530 nm band intensity around 200 a.u. being the highest in the $Y_{\perp}$ cut perpendicular to the cleavage plane and decreasing in the order: $Y_{\perp} \rightarrow Z \rightarrow Y_{\parallel} \approx X$[7,8].

The samples doped from the sulfate melt revealed a much higher intensity of the luminescence at 1530 nm; the intensity of the best ones reached up to 4000 a.u. (i.e., 20 times higher than the highest intensity of luminescence observed in samples fabricated using nitrate melt). Compared with TD from the nitrate melt, the $Y_{\perp}$ cut also revealed a high intensity of 1530 nm luminescence. Surprisingly, intensive luminescence was detected at the Z cuts, which was even higher than that at the $Y_{\perp}$ cut (see Fig 1b).

In the spectra of the samples doped from the sulfate melt, a distinctive band at 1490 nm was also found, which can be attributed to the irradiative transition $^4I_{15/2} \rightarrow {}^4I_{13/2}$ (like the emission at 1530 nm) and is a consequence of a fine splitting of the Er^{3+} levels $^4I_{15/2}$ and $^4I_{13/2}$ in the crystal field of the LN. This band is much deeper in the samples prepared by doping from the sulfate melt.

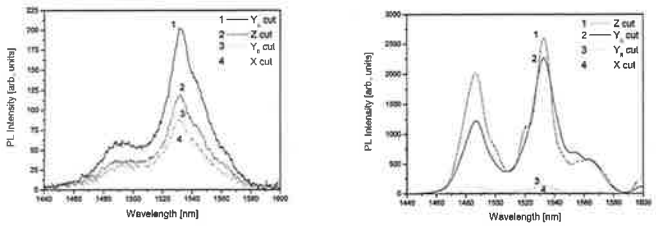

a) b)

Fig. 1 The luminescence spectra of the erbium-doped LN samples prepared from the melt of a) nitrate melt (168 hrs at 350 °C), b) sulfate melt (40 hrs at 600 °C)

3.2 ERBIUM-CONCENTRATION PROFILES AND STRUCTURAL CHANGES IN LN

The concentration-depth profiles of the erbium incorporated in all of the LN samples prepared by doping from the nitrate melt are shown in Fig. 2a. Obviously, the surface

concentration of erbium differs in the particular samples, but it does not exceed the range from 2 at. % to 7 at. %. The shape of the concentration-depth profiles showed an exponential decrease of the erbium content towards depths of approximately 40 nm under the surface of the samples. The highest concentration of erbium was found in the Z and $Y_{\perp}$ cuts, which also had very similar shapes of the depth-concentration profiles. The lowest concentration of erbium was found in the $Y_{\parallel}$ cut.

The erbium doping from the sulfate melt was performed in all four types of cuts. The obtained concentration-depth profiles of erbium differed when compared with samples conducted in nitrates and are displayed in Fig. 2b. In Fig. 2b it is evident that the concentration profile of erbium is maximal at the surface and is decreasing towards the LN depth like the profiles observed with samples fabricated in nitrate melt. However, it is possible to see clearly the very high concentration of erbium reaching 24 at. %, which means that almost one quarter of the surface (in terms of atomic concentration) is occupied with erbium. Such a high concentration of erbium even changed the appearance of the samples that showed a coloring similar to that of the interference images. The experiments were rather demanding, and therefore, to be sure that the results would be fully reproducible, we repeated the experiments with sulfate melt. In all of the prepared samples, the surface concentration of erbium was rather different in particular LN cuts (ranging from 12 at.% to 24 at.%). The highest concentrations of erbium were in all of the sets of the samples always found in the $Y_{\perp}$ and the Z cuts. The depths of the doped layers reached 70 up to 100 nm.

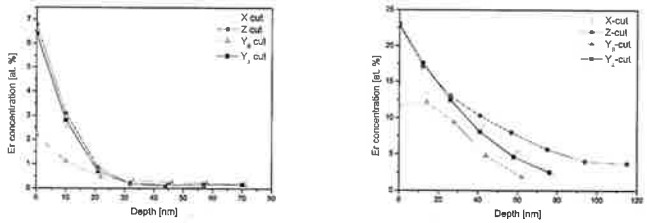

a) b)

Fig. 2 The depth-concentration profiles of the erbium incorporated into various LN cuts by diffusion from the a) nitrate melt (168 hrs at 350 °C), b) sulfate melt (40 hrs at 600 °C)

An RBS/channeling analysis would enable us to determine the amount of Er atoms incorporated in the interstitial sites looking along the main axis of each crystallographic cut. However, the prepared erbium-doped samples, both from the nitrate and sulfate melts, were so disordered as to make directing the channeling and evaluating the positions of the erbium atoms in this way impossible. The number of disordered atoms is comparable to an amorphous structure; it means that the thermal diffusion causes a high modification of the crystalline structure. In the RBS random spectra, we can observe Nb depletion, see Figure 3a. The depletion of Nb in the surface layer was observed in all of the cuts of LN with Er incorporated by diffusion from the sulfate melt. The depleted amount of Nb was about 5–7 at. %.

Results that are even more interesting were obtained after annealing the sample sets doped at 600 °C from the sulfate melt (the experimental conditions of annealing were mentioned above in Chapter 2). In these samples, the erbium-surface concentrations decreased and erbium atoms were redistributed to a depth. Moreover, differences between the particular

LN cuts appeared. The best movement of erbium atoms was observed in the $Y_{\perp}$ cut, where the erbium-containing layer reached up to 0.5 μm and the erbium surface concentration decreased to 18 at.% (Fig. 3). The other LN cuts currently revealed the 10 at.% concentration of erbium even in 0.1 μm depths.

Such samples also allowed the directing of the channeling spectra so that the position of the erbium could be evaluated. The samples after the annealing procedure exhibited a higher level of ordered structure as compared to the non-annealed samples, which enabled us to find the channeling direction and compare the amount of Er incorporated in the substitutional and interstitial positions. It is obvious that 52 at. % of Er atoms were located in the interstitial positions in the $Y_{\perp}$ cut and the remaining amount of Er atoms was placed in the substitutional position of this cut. This phenomenon was observed only in the mentioned cut, not in the other cuts investigated.

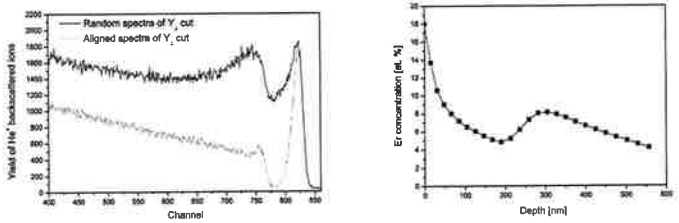

a) b)

Fig. 3 The RBS channeling spectra of $Y_{\perp}$ cut of LN fabricated by TD in sulfate melt (a), calculated erbium concentration-depth profile (b)

3.3 LITHIUM CONCENTRATION PROFILES

All of the annealed samples were measured using the NDP method to determine the changes of the concentrations of lithium in the surfaces of the samples. This method is a suitable tool as we know from our previous experience, because the measurement does not make any changes in the distribution of the lithium atoms. The results of the measurement are shown for the samples doped at lower temperature (from the nitrates melt) in Fig. 4a and those doped at higher temperature (from the sulfates melt) in Fig. 4b.

The depth-concentration profiles displayed in Fig. 4a for the samples doped at 350 °C clearly show the depletion of lithium from the surface, thus increasing its concentration towards the subsurface areas of the samples. The percentual depletion of lithium was evaluated from the integral-area ratio above the depth profiles of lithium reaching down to 0.5 μm (see Table II). From the comparison of those areas, it can be seen that on the surfaces of the samples doped at 350 °C about 20 at. % of lithium is missing. Table II also shows that the depletion of lithium is bigger in the X and $Y_{\perp}$ cuts while the lowest depletion is in the Z cut.

The samples doped at higher (600 °C) temperatures are dramatically different. The concentration-depth profiles show that the depletion of lithium is located in a very narrow area below the surface of the samples. At a depth of 10 nm under the surface, the concentration of lithium in all of the samples is practically the same as in the virgin LN samples. Substantial differences were noted between particular cuts: according to the integral amount the biggest depletion occurred in the X cut while in the other cuts the depletion was

much smaller. The depth to which the depletion of lithium (10 nm) reached does not in any case correspond with the depth where erbium was still detected (up to 100 nm).

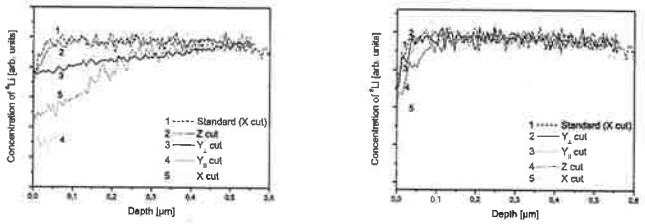

a) b)

Fig. 4 The depth-concentration profiles of lithium in various LN cuts doped with erbium from the melts of a) nitrates (168 hrs at 350 °C), b) sulfates (40 hrs at 600 °C).

Table II. The percentual depletion of lithium calculated from the integral amount of the lithium concentration profiles

	Integral amount [atoms/cm^2]	Percentual depletion of lithium [%]
Nitrates : LN $Y_{\parallel}$ cut	2.28×10^{16}	26.4
Nitrates : LN $Y_{\perp}$ cut	1.41×10^{16}	16.3
Nitrates : LN X cut	2.33×10^{16}	27.0
Nitrates : LN Z cut	2.93×10^{15}	3.4
Sulfates: LN $Y_{\parallel}$ cut	3.03×10^{15}	3.5
Sulfates : LN $Y_{\perp}$ cut	2.44×10^{15}	2.8
Sulfates : LN X cut	9.27×10^{15}	10.7
Sulfates: LN Z cut	5.52×10^{15}	6.4

4. DISCUSSION

The presented results provide evidence that it is in principle possible – using purely thermal diffusion of erbium from erbium-containing salts – to prepare a very thin optical layer on the surface of the LN crystal that reveals luminescence at 1530 nm. The thickness of layers prepared in this way was maximally 0.1 μm, which is, in terms of the experimental conditions used, in good agreement with the results of Sada[12] and Caccavale[13]. As expected, the crucial factor that influenced the process of thermal diffusion was temperature, which affected not only the rate of the penetration of the diffusing erbium ion but also the mechanism of how it occurred. Generally, on the bases of the results obtained by SIMS, it can be argued that the thermal diffusion of erbium is in fact an ion exchange of the erbium ions from the melt for the lithium ions from the surface of the LN crystals[1]. This mechanism is in the case of diffusion from the melt of nitrates likely to occur at lower temperatures, where the thickness of the in-diffused layer corresponds approximately with the thickness of the lithium-depleted layer.

It is also important to bear in mind that the process of diffusion from the nitrates-melt is much slower and takes a very long time, so that, in principle, ion exchange may also take place. This has also been confirmed in our earlier papers[7,8], where we gave evidence that erbium in-diffusion was always accompanied by the migration of lithium through the

structure of the LN. The question is whether the erbium ions would occupy the sites freed by lithium ions. In the case of samples with the highly disordered surface layer there is no sense to talk about the Er position, because this position is random in the randomly ordered structure.

A slightly different situation arises at the diffusion performed at higher (600 °C) temperatures. According to our results, it is unlikely that an exchange of erbium for lithium ions occurs there. One should remember that the time of the diffusion is much shorter and lithium is already present in the melt used for the diffusion of erbium. Even though the amount of erbium incorporated into the LN surface is much higher (as compared with the lower temperature approach), depletion of lithium is practically zero; this indicates that the mechanism of the higher-temperature diffusion will be different. According to[11], the structure of the LN crystal at such a temperature may partly recrystallize. This idea leads us to believe that after the incorporation of erbium ions into the LN structure a balancing of the charges may occur in such a way that erbium ions (during the recrystallization) may occupy the positions of niobium while the amount of lithium remains unchanged. This hypothesis is verified by the highest intensities of the 1530 nm luminescence bands, which are evidence of a better ordering of the erbium surrounding and moreover the depletion of lithium atoms is very low. During the post-diffusion annealing the recrystallization process follows on – erbium ions from the interstitial sites move to the substitutional sites. The differences between the various cuts were found: in the $Y_{\perp}$ cut more than 52% of incorporated Er after the annealing procedure were in the interstitial sites while in the Z cut the amount of Er in interstitial sites remained 93 - 99% as to the random RBS/channeling spectrum.

Concerning the mechanism of the thermal diffusion from the point of view of different single-crystalline lithium niobate cuts, the importance of the crystallographic orientation of the cuts with respect to the cleavage plane is patently evident. The greatest amount of incorporated erbium as well as the highest intensity of the 1530 nm were always connected with the specially designed $Y_{\perp}$ cut <10–14>. If one accepts the concept of an ion exchange process of the erbium incorporation, then for comparison one can use the well-known method of proton exchange (PE or APE) for the fabrication of optical waveguides in lithium niobate in the standard X, Y and Z cuts of LN. The rate of proton exchange is always higher in the X cuts than in the Z cuts; this has also been proven in our research concerning the migration of lithium through the LN structure and the greatest depletion of lithium in the X cuts [see Fig.4]. Then, why was the highest erbium concentration not found also in the X cut? Actually, the opposite is true. In light of this, the ion-exchange mechanism of erbium incorporation does not seem likely.

5. CONCLUSION

The thermal diffusion of erbium at two temperatures into commonly, as well as specially cut LN wafers, was performed. The thin layers which were prepared contained different amounts of erbium, i.e., 7–24 at. % depending on the crystallographic orientations of the wafer surfaces at a depth of less than 100 nm. As expected, the intensity of the luminescence corresponds well with the amount of incorporated erbium. The highest luminescence intensity therefore was even more obvious when the higher temperature was applied. Moreover, the positive effect of annealing on the layer containing erbium was also verified. Using the RBS/channeling and NDP methods, the mechanism of TD was studied and the following facts became evident:

i) For the mechanism of the process of incorporating erbium into the LN structure it was found that rather than the amount of erbium in the melt used for the diffusion it is the temperature of the process that is strongly determinative. While the mechanism of the ion exchange is more likely at 350 °C (lithium-atom depletion was detected in the surface layer),

at a 600 °C temperature the mentioned mechanism was not proved. It is interesting that despite the fact no depletion of lithium occurred (probably because the high content of it in the used sulfates melt, it evidently occurred the in-diffusion of erbium. It indicates that the mechanism of incorporation of erbium via ion exchange is under those actual conditions unlikely.

ii) The ability of erbium to penetrate into the LN structure is clearly influenced by the sample surface crystallographic orientation. The highest erbium content and the highest luminescence intensity at 1530 nm were always observed in the $Y_{\perp}$ cut <10–14> perpendicular to the cleavage plane.

iii) After TD, the position of the erbium atoms was not possible to determine using RBS/channeling spectroscopy since the majority of the atoms have been deflected from their positions and therefore most of the erbium atoms are located in the interstitial positions. The subsequent annealing caused a recrystallization of the structure, erbium penetration deeper into the LN substrate and its occupation of the substitution positions.

REFERENCES

1K.K. Wong, Properties of Lithium Niobate, INSPEC (2002) London.
2L. Arizmendi, Phys. Stat. Sol. (a) 201 (2004) 253.3W.
3Sohler et al., IEICE TRANS. ELECTRON E88–C (5) (2005) 990.
4 G. Singh, S. Gupta, S. Bothra, V. Janyani and R. P. Yadav, Proc. SPIE 8069, (2011) 80690W.
5E. Cantelar, R. Nevado, G. Martín, J.A. Sanz-García, G. Lifante, F. Cusso, M.J. Hernandéz, P.L. Pernas, J. Lumin. 87-89 (2000) 1096.
6I. Bauman, R. Brinkmann, M. Dinand, W. Sohler, L. Beckers,Ch. Buchal, M.Fleuster, H. Holzbrecher, H. Paulus, K.-H. Muller, Th.Gog, G. Materlik, O.Eitte, H.Stolz, W.von der Osten, Appl. Phys. A 64, (1997) 33.
7J. Hradilová, P. Kolářová, J. Schrofel, J. Čtyroký, J. Vacík, J. Peřina, Proc. SPIE 2775 (1996) 187.
8V.Peřina, J.Vacík, V.Hnatovitz, J. Červená, P. Kolářová, J. Špirková-Hradilová, J. Schröfel, Nucl. Instrum. Methods Phys. Res., Sect. B 139 (1-4), (1998), 208–212.
9C. Sada, F. Caccavale, F. Segato, B. Allieri, L.E. Depero, Optical Materials 19 (1) (2002) 23–31.
10J. Saarilahti, Nucl. Instr. Methods Phys. Res. B 64 (1994) 734.
11A. Meldrum, J. Nucl. Mater. 300 (2002) 242.
12C.Sada et al., Appl. Phys. Lett. 72 (1998) 3431.
13F.Caccavale, C. Sada, F. Segato, N.Yu. Korkishko, V.A. Fedorov, T.V. Morozova, J. Non. Cryst. Solids 245 (1999) 135.

ACKNOWLEDGEMENT

The authors acknowledge support from the following grants: Czech Science Foundation 106/10/1477 and 106/09/0125, TA01010237. This work has also been supported by the European Community as an Integrating Activity 'Support of Public and Industrial Research Using Ion Beam Technology (SPIRIT)' under EC contract no. 020 and 227012.

Optical Materials 34 (2012) 652–659

Contents lists available at SciVerse ScienceDirect

Optical Materials

journal homepage: www.elsevier.com/locate/optmat

Erbium ion implantation into different crystallographic cuts of lithium niobate

P. Nekvindova [a,*], B. Svecova [a], J. Cajzl [a], A. Mackova [b,c], P. Malinsky [b,c], J. Oswald [d], A. Kolistsch [e], J. Spirkova [a]

[a] Department of Inorganic Chemistry, Faculty of Chemical Technology, Institute of Chemical Technology, Technicka 5, 166 28 Prague, Czech Republic
[b] Nuclear Physics Institute, Academy of Sciences of the Czech Republic, v.v.i., 250 68 Rez, Czech Republic
[c] Department of Physics, Faculty of Science, J. E. Purkinje University, Ceske mladeze 8, 400 96 Usti nad Labem, Czech Republic
[d] Institute of Physics, Academy of Sciences of the Czech Republic, v.v.i., Cukrovarnicka 10, 162 53 Prague, Czech Republic
[e] Helmholtz-Zentrum Dresden Rossendor, 01314 Dresden, Germany

ARTICLE INFO

Article history:
Received 29 June 2011
Received in revised form 20 September 2011
Accepted 21 September 2011
Available online 15 November 2011

Keywords:
Lithium niobate
Erbium
Ion implantation
Luminescence

ABSTRACT

Single crystals like lithium niobate are frequently doped with optically active rare-earth or transition-metal ions for a variety of applications in optical devices such as solid-state lasers, amplifiers or sensors. To exploit the potential of the Er:$LiNbO_3$, one must ensure high intensity of the 1.5 μm luminescence as an inevitable prerequisite. One of the important factors influencing the luminescence properties of a lasing ion is the crystal field of the surrounding, which is inevitably determined by the crystal structure of the pertinent material. From that point it is clear that it cannot be easy to affect the resulting luminescence properties – intensity or position of the luminescence band – without changing the structure of the substrate. However, there is a possibility to utilise a potential of the ion implantation of the lasing ions, optionally accompanied with a sensitising one, that can, besides the doping, also modify the structure of the treated area od the crystal. This effect can be eventually enhanced by a post-implantation annealing that may help to recover the damaged structure and hence to improve the desired luminescence.

In this paper we are going to report on our experiments with ion-implantation technique followed with subsequent annealing could be a useful way to influence the crystal field of LN. Optically active Er:$LiNbO_3$ layers were fabricated by medium energy implantation under various experimental conditions. The Er^+ ions were implanted at energies of 330 and 500 keV with fluences ranging from 1.0×10^{15} to 1.0×10^{16} ion cm^{-2} into $LiNbO_3$ single-crystal cuts of both common and special orientations. The as-implanted samples were annealed in air and oxygen at two different temperatures (350 and 600 °C) for 5 h. The depth concentration profiles of the implanted erbium were measured by Rutherford Backscattering Spectroscopy (RBS) using 2 MeV He^+ ions. The photoluminescence spectra of the samples were measured to determine the emission of 1.5 μm.

It has been shown that the projected range *Rp* of the implanted erbium depends on the beam energies of implantation. The concentration of the implanted erbium corresponds well with the fluence and is similar in all of the cuts of lithium niobate used. What was different were the intensities of the 1.5 μm luminescence bands not only before and after the annealing but also in various types of the crystal cuts. The cut perpendicular to the cleavage plane ⟨10–14⟩ exhibited the best luminescence properties for all of the experimental conditions used. In order to study the damage introduced by the implantation process, the influence of the annealing procedure on the recovery of the host lattice was examined by RBS/channelling. The RBS/channelling method serves to determine the disorder density in the as-implanted surface layer.

1. Introduction

Because of its unique properties, lithium niobate continues to be used as an advanced material in the photonics field [1–3]. Its outstanding properties of the single-crystalline lithium niobate allow modulating and simultaneously also amplifying optical radiation. But actually single crystalline lithium niobate is in fact a congruent crystal and the real ratio of lithium to niobium is not 1:1 as one would expect, but about 6% of lithium is missing. This fact allows for its easy doping with for instance magnesium but also in our case with laser-active ions such as erbium [4,5]. Erbium ions are currently used in telecommunication systems, because electrons overleaping between energy levels $^4I_{13/2} \rightarrow {}^4I_{15/2}$ (1450–1650 nm) are

* Corresponding author.
E-mail address: pavla.nekvindova@vscht.cz (P. Nekvindova).

0925-3467/$ - see front matter © 2011 Elsevier B.V. All rights reserved.
doi:10.1016/j.optmat.2011.09.011

able to produce an emission just in the third telecommunication window. The significant loss of optical gain at the wavelength causes the green upconversion at energy levels $^2H_{11/2} \rightarrow {}^4I_{15/2}$ (cca 520 nm), $^4S_{3/2} \rightarrow {}^4I_{15/2}$ (cca 550 nm) and $^4F_{9/2} \rightarrow {}^4I_{15/2}$ (660 nm) [6]. Generally in the crystalline materials, the above-mentioned resulting luminescence properties could be strongly affected by the crystal-field surroundings of the lasing atoms. Used technologies as well as eventual sensitizers can change the crystal field surroundings of the lasing atoms [7–9] and thus increase the luminescence by 1.5 μm luminescence as well as decrease the undesirable upconversion in the UV–VIS.

Currently, it is possible to say that the research of erbium-doped lithium niobate (Er:LN) progresses in several directions. The development of functional optical thin-layer amplifiers is now one of the main streams. Many technologies have been developed to dope lithium niobate with erbium. These methods can be divided into bulk and thin-film doping. Erbium bulk doping occurs directly during the crystal pulling. A rather small amount of erbium ions (about 0.5 mol. %) was usually doped into crystal, which places relatively heavy demands on the well-quality-crystal fabrication. The combination of bulk doping with the waveguide preparation by titanium in-diffusion led to the fabrication of a functional laser amplifier, and up until today several integrated optical devices have been constructed [10,11].

It has been known that thin film layers or waveguides have many advantages over their bulk-doped alternatives; the main advantages are lower pump powers in the case of the waveguide form. There are a number of technologies to prepare erbium-containing thin layers, which could be divided into incorporation (ion-implantation, thermal-diffusion) and deposition methods (sol/gel method, PLD technique) [12–16].

Despite the fact that ion-implantation technique offers great versatility in how to affect the luminescence spectra by many sensitizers, its potentialities have not been extensively studied yet. This is mainly because of significant damage introduced into the crystal structure during implantation and the necessity of subsequent (post-implantation) annealing. It has been found that a suitable annealing temperature for the structure recovery lies between 500 and 1000 °C [17,18]. It could be assumed that the knowledge of consequences of annealing of different LN cuts will lead to better understanding of the processes that results in changing of the intensity of the luminescence and how they could be utilised to increase the thought luminescence properties of erbium doped into LN.

Our group has recently addressed detailed studies of the possibility of the diffusion of erbium ions from a melt of erbium-salt into the LN substrate surface [19,20]. During the research, it became clear that different crystallographic cuts of LN absorb different amounts of erbium ions from the doping melt. We have paid some attention to that problem and found that the largest amount of erbium as well as the strongest 1.5 μm luminescence intensity was found in the special LN cut ⟨10–14⟩ which we call the *Y* perpendicular and have marked as $Y\perp$. It is the one that is perpendicular to the cleavage plane of the LN crystal.

Here, we will focus on a systematic study of the ion implantation of erbium into various crystallographic cuts of LN. The main problem is whether the importance of crystallographic orientation of the crystal cuts is valid only when the diffusion technique is applied or if it has general validity.

2. Experiments

In this study, various $LiNbO_3$ cuts have been used (synthesised by the Czochralski method in Crytur Turnov, Czech Republic), namely the commonly used *X* cuts ⟨11–20⟩, *Z* cuts ⟨0001⟩ and specially designed *Y* cuts, i.e. 'parallel' Y_{II} ⟨01–12⟩ and 'perpendicular' $Y\perp$ ⟨10–14⟩ to the cleavage plane. Thoroughly pre-cleaned $LiNbO_3$ wafers were implanted with an energy of 330 keV and 500 keV Er ions, 7° off-axis to avoid channelling. The ion fluence of 1.0×10^{15}, 2.5×10^{15} and 1.0×10^{16} ion cm^{-2} was used. The implantations were performed using a 500 kV implanter in the Helmholtz-Zentrum Dresden Rossendorf, Germany. The beam was scanned through an aperture of usually 1×1 cm^2, resulting in a beam current density of typically 0.25 μA/cm^2 on the target. For the recovery of the structure, the as-implanted samples were annealed for 5 h at 350 °C in air or for the same time in oxygen at 600 °C.

The concentration profiles of the incorporated erbium ions were studied by Rutherford Backscattering Spectroscopy (RBS) in the Nuclear Physics Institute in Rez, Czech Republic. The analysis was performed on a Tandetron 4130 MC accelerator using a 2.0 MeV He^+ ion beam. He^+ ions backscattered at a laboratory angle of 170° were detected.

The collected data were evaluated and transformed into concentration depth profiles using the GISA 3 computer code [21]. In order to study the damages introduced by the implantation process, the influence of the annealing procedure on the recovery of the host lattice was examined by RBS/channelling measurements using a 1.7 MeV He^+ beam from the Van de Graaff accelerator in the Helmholtz-Zentrum Dresden Rossendorf, Germany.

The photoluminescence spectra of the implanted samples were collected within the range of 1440–1600 nm at room temperature. A pulse semiconductor laser POL 4300 emitting at 980 nm was used for the excitation of the electrons. The luminescence radiation was detected by a two-step-cooled Ge detector J16 (Teledyne Judson Technologies). To scoop specific wavelengths, a double monochromator SDL-1 (LOMO) was used. For the evaluation, all of the luminescence spectra were transformed to the base level and after abstraction of the baseline the normalisation was performed with the help of reference samples.

3. Results

The ion implantation was performed under different conditions mentioned above into all the LN cuts. The as-implanted samples were annealed at two different temperatures, namely 350 °C and 600 °C. The possible migration of lithium through the structure was assumed to occur already at the lower temperature, and recrystallisation of the damaged LN structure was expected to take place at the higher temperature [22]. The subsurface layers in LN enriched by Er were prepared in this way, with the Er concentration maximum being about 1 at.%, achieved in the case of the implantation fluence of 1.0×10^{16} ion cm^{-2}. The maximum of the Er concentration was detected at the depth of 70–90 nm depending on the LN cut. The main attention was paid to the luminescence spectra measured around 1530 nm. Between the particular fabrication steps, the concentration-depth profiles of erbium were checked by the RBS method. All of the annealed samples were also analysed by the RBS/channelling method to determine the changes in the crystal structure.

3.1. Luminescence

The luminescence spectra were measured in the range of 1440 and 1600 nm in all of the prepared samples; the measurement was performed between every fabrication step. In Fig. 1, the annealing effect on the luminescence intensity of the peak at 1530 nm is demonstrated for the *Z*-cut sample, where the erbium ions were implanted under the following conditions: 330 keV and 1.0×10^{16} ion cm^{-2}. In Fig. 1a, no luminescence at 1530 nm was found in any of the as-implanted samples, and similar behaviour was found with all of the LN cuts implanted at lower ion fluences, i.e. for 1.0×10^{15} ion cm^{-2} and 2.5×10^{15} ion cm^{-2}. The positive effect of post-implantation annealing at a luminescence intensity of the 1530 nm peak is shown

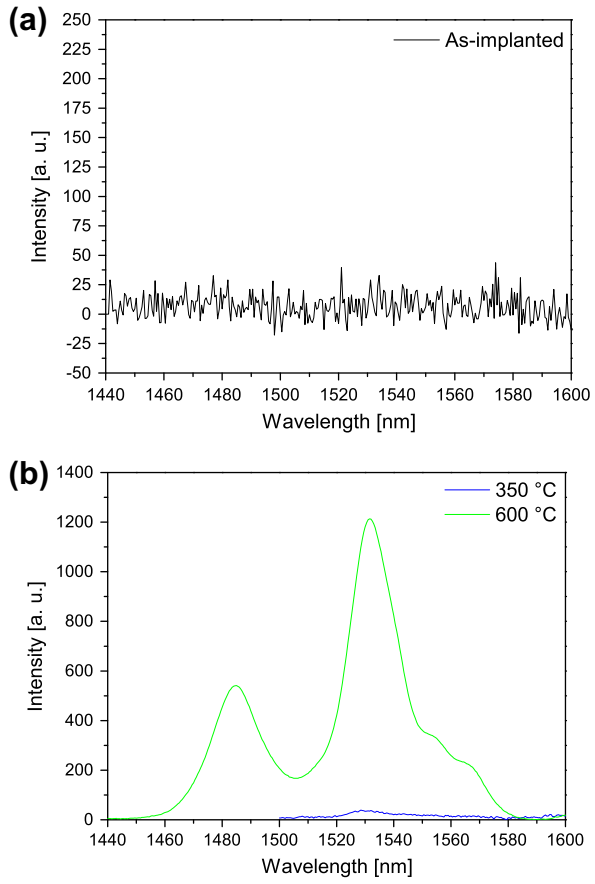

Fig. 1. The influence of the annealing temperature on the 1.5 μm luminescence spectra in the *Z*-cut of LN implanted with erbium (1.0×10^{16} cm^{-2} and 330 keV) and annealed at 350 and 600 °C.

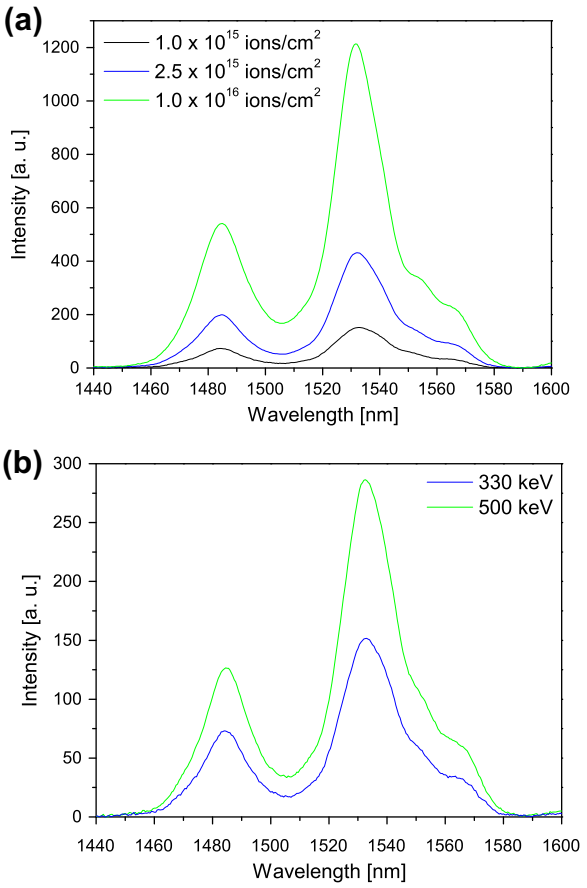

Fig. 2. The influence of the implantation conditions – energy and fluence – on the 1.5 μm luminescence spectra in the *Z*-cut of LN implanted with erbium and annealed at 600 °C.

in Fig. 1b. It is obvious that a noticeable luminescence peak at 1530 nm was observed at an annealing temperature of 350 °C and the differences between the various LN cuts became clearly visible [23]. A significant increase of the luminescence intensity at 1530 nm occurred after annealing at 600 °C. Moreover, in Fig. 1b another strong luminescence peak at 1485 nm appeared after annealing at 600 °C, and such peaks are visible in all of the collected spectra. The intensities of those peaks follow a trend similar to the peak at 1530 nm according to the experimental conditions. Our results have confirmed the well-known fact about the positive effect of annealing at the luminescence intensity of 1530 nm of the ion-implanted layers [17].

Thanks to this significant increase of the luminescence intensity, the results of the particular ion-implantation conditions could be compared. In Fig. 2, the luminescence intensities of the annealed *Z*-cuts samples are compared for different ion fluences (see Fig. 2a) as well as for different ion-beam energies (see Fig. 2b). If we compared the intensity of the luminescence around 1530 nm of the samples implanted with different fluences (the beam energy is still the same, i.e. 330 keV) and annealed at 600 °C, the result is not surprising. As expected, with the higher ion fluence used, the higher luminescence intensity appeared at 1530 nm (Fig. 2a).

If one compares the luminescence spectra of the annealed samples implanted at different energies, the results are far less predictable. Although the same fluences have been used (1.0×10^{15} ion cm^{-2}), the luminescence intensity is higher when higher energy was used for the implantation (Fig. 2b), despite the fact that the integrated amount of erbium should be the same according to the ion fluence.

In Fig. 3 the effect of the LN crystallographic orientation facing the ion beam on the consequent luminescence spectra is shown for the optical layers fabricated under the same conditions. Principally, the results for two different ion fluences are presented: 330 keV and 1.0×10^{15} ion cm^{-2} (Fig. 3a) and 330 keV and 1.0×10^{16} ion cm^{-2} (Fig. 3b). After comparing the intensities in particular cuts, it became apparent that luminescence intensity is always the highest in the $Y\perp$ cut, which is perpendicular to the LN cleavage plane. Major differences between the cuts were observed in the samples implanted using lower fluences (i.e. 1.0×10^{15} ion cm^{-2} and 2.5×10^{15} ion cm^{-2}).

Generally, it is possible to say that the luminescence intensity around 1530 nm in the Er:LN layers fabricated by ion implantation was significantly affected:

(i) by post-implantation annealing – clearly visible luminescence peaks appeared after annealing at 600 °C,
(ii) by conditions of the ion implantation process, both fluence and ion-beam energy, and
(iii) by the crystallographic orientation of the single-crystal facing to the ion beam. The best intensity of the luminescence was found in the $Y\perp$ cut ⟨10–14⟩ of LN implanted with higher energy (330 keV) as well as with higher fluence (1.0×10^{16} ion cm^{-2}), which was annealed at 600 °C.

3.2. Erbium depth concentration profiles

The erbium concentration depth profiles and its changes after post-implantation annealing were measured by the RBS method

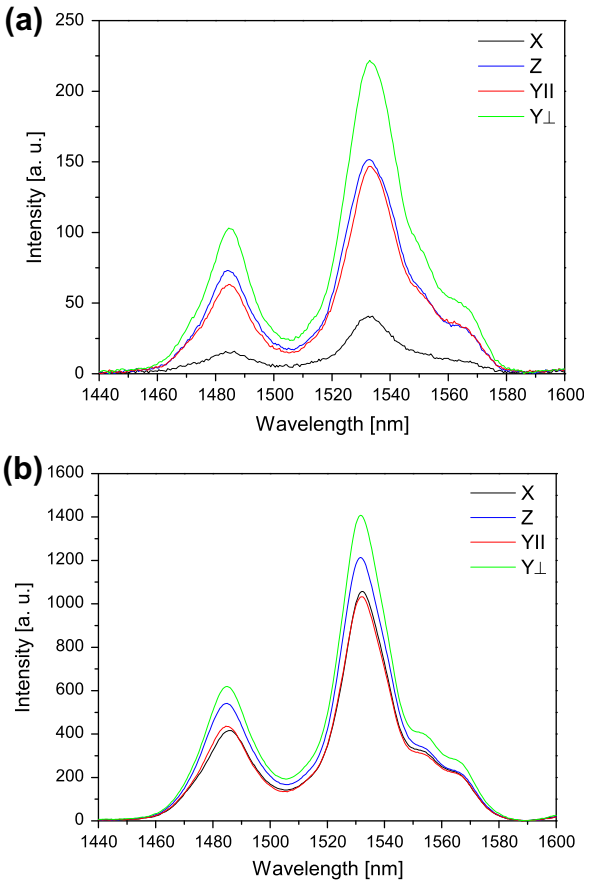

Fig. 3. The comparison of the 1.5 μm luminescence spectra in various cuts of LN implanted with erbium at a fluence: (a) 1×10^{16}cm^{-2} and (b) 1×10^{15}cm^{-2}, energy: 330 keV and annealed at 600 °C.

for all of the prepared samples, namely between every single fabrication step. The statistical distribution of the implanted ions in the as-implanted samples could be described by a Gaussian function, and all of the depth profiles of the as-implanted samples were smoothed in this way. Although the shapes of the erbium depth concentration profiles changed after annealing, the Gaussian function could be applied at most of erbium depth concentration profiles despite the fact that the depth profiles of the annealed samples changed. For some samples (bearing an [a] in Table 1), two concentration maximums appeared after the annealing, as a consequence of which the Gaussian function cannot be applied. The effect was mainly found in the layers implanted with a fluence of 2.5×10^{15} ion cm^{-2}.

For all of the Gaussian functions, the maximum concentration depths, i.e. projected range (Rp) with range straggling (ΔRp), as well as the value of the maximum concentration (H) and maximal integrated amount (I), were evaluated. Table 1 shows the parameter values mentioned above for the measured Er:LN layers depending on the experimental conditions.

3.2.1. As-implanted samples

For Er^+ implantation into LN at 330 keV, the concentration profiles calculated by SRIM 2008 simulation have the following parameters: the Rp value is 70 nm and the ΔRp value is 22 nm (see [23,24]). Table 1 shows that the results detected in our experiments correspond well with the simulation: the average value of Rp = 77 nm. If we compare the observed Rp values in Table 1 for the as-implanted (not-annealed) samples, it becomes clear that, generally, the projected range Rp is larger for particles implanted with lower fluences. Comparing the value of the projected range for various cuts, very small differences have been found. The ΔRp values in RBS measured profiles are slightly higher than the values obtained by a SRIM 2008 simulation, and neither the fluence nor the LN crystallographic cut used have affected the value. With the increasing ion-implantation fluence, the damage of the subsurface layer increases and causes lower ion-penetration depth in the crystalline material. This phenomenon has been observed in our case, where the depth of the incorporated ions Rp is the decreasing function of the implantation fluence. The SRIM 2008 simulation [25] does not take into account the crystalline structure in the different implanted cuts and the growing number of disordered atoms during the high fluence implantation, so a small deviation of the concentration maximum depth in comparison to the simulated projected range could be expected. The real energetic straggling of ions penetrating matter is higher owing to the energy deviations caused by the damage of crystalline structure, which is developed simultaneously with the implantation as was observed elsewhere [26].

From Table 1, it clearly arises that the maximal concentration values (H) increase in proportion to the implanted erbium fluence in the range from 0.25 at.% (for 1.0×10^{15} ion cm^{-2}) to 1.05 at.% (for 1.0×10^{16} ion cm^{-2}). A similar trend was found for the value of the integrated erbium amount (I). The amount of the implanted erbium increases according to the increased ion-implantation fluence used so that the integral amount in proportion to the fluence increased from 1.22×10^{15} cm^{-2} (for 1.0×10^{15} ion cm^{-2}) to 5.92×10^{15} cm^{-2} (for 1.0×10^{16} ion cm^{-2}). Determining the integral amount for the lowest fluence 1.0×10^{15} ion cm^{-2} should take into account the higher uncertainty because of the implantation fluences close to the detection limit of the RBS.

Neither the maximal concentration value H nor the integral amount value I depends on the crystallographic orientation of LN.

3.2.2. As-annealed samples (350 °C)

The noticeable changes of erbium depth concentration profiles occurring after post-implantation annealing at 350 °C are shown in Table 1, which also demonstrates a significant shift of the Gaussian maximum Rp deeper into the substrate. This shift is more evident when the lower fluence 1.0×10^{15} ion cm^{-2} is used.

In this case, it is interesting to compare the values of the erbium concentration maximum H before and after annealing at 350 °C (see Table 1). As expected, the erbium concentration maximum H decreased while the concentration profile became broader only for lower fluences (i.e. 1.0×10^{15} ion cm^{-2} and 2.5×10^{15} ion cm^{-2}). On the contrary, for higher fluences 1.0×10^{16} ion cm^{-2}, the erbium concentration maximum increased and all of the curves characterising the concentration profiles shifted deeply into the substrate. The behaviour of the erbium depth concentration profiles during annealing is also shown for the Z cuts of LN in Fig. 4. From the comparison of three erbium concentration profiles diverging at the annealing temperature used for fluences of 1.0×10^{16} ion cm^{-2} (Fig. 4a) and 1.0×10^{15} ion cm^{-2} (Fig. 4b), it is obvious that the shapes of the profiles differed substantially with the fluence of ion implantation. To this point, the changes of erbium concentration profiles are similar for all of the LN cuts.

However, the influence of the crystallographic orientation to the structure recovery as well as to the erbium ions moving through the crystal structure became more profound after annealing at 350 °C. As Table 1 shows, there are different changes of erbium depth concentration profiles shapes depending on the pertinent crystallographic orientation of the LN cut. For the samples implanted with lower fluence (i.e. 1.0×10^{15} ion cm^{-2}), it seems that smaller changes of concentration profiles were found with the Z cut while more significant ones were always associated

Table 1
The characteristic value (projected range *Rp*, range straggling Δ*Rp*, maximum concentration *H*, integrated amount *I*) of the erbium depth concentration profile determined by the RBS in various crystallographic orientations of LN as well as for different annealing temperatures.

LN cut	Fluence 1.0×10^{15} ion cm^{-2}				Fluence 2.5×10^{15} ion cm^{-2}				Fluence 1.0×10^{16} ion cm^{-2}			
	Rp [nm]	Δ*Rp* [nm]	*H* [at.%]	*I* [10^{15} cm^{-2}]	*Rp* [nm]	Δ*Rp* [nm]	*H* [at.%]	*I* [10^{15} cm^{-2}]	*Rp* [nm]	Δ*Rp* [nm]	*H* [at.%]	*I* [10^{15} cm^{-2}]
X cut	84	42.0	0.25	1.53	74	30.0	0.31	2.63	76	25.5	0.98	5.3[b]
X cut 350 °C	88	46.3	0.20	1.66	80[a]	31.7	0.26	2.50	81	31.5	1.05	6.10
X cut 600 °C	63	27.5	0.11	1.46	69	21.1	0.08[c]	2.37	–	–	–	5.92
Z cut	81	27.5	0.27	1.40	75	28.0	0.31	2.36	74	28.5	0.99	5.0[b]
Z cut 350 °C	95	41.1	0.18	1.59	76	30.2	0.23	2.29	79	24.7	1.12	5.68
Z cut 600 °C	61	36.9	0.14	1.37	74	28.1	0.28	2.74	69	25.6	0.92	6.23
Y_{II} cut	80	28.0	0.26	1.22	72	25.5	0.22	1.58	73	27.0	0.96	5.40[b]
Y_{II} cut 350 °C	88	46.3	0.15	1.52	76	22.8	0.25	1.27	79	24.5	1.16	5.69
Y_{II} cut 600 °C	66	35.2	0.17	1.55	72	24.0	0.26	2.00	69	25.2	0.69	6.69
$Y\perp$ cut	80	29.5	0.26	1.46	75	24.6	0.34	2.20	72	27.5	1.05	5.22[b]
$Y\perp$ cut 350 °C	90	58.0	0.17	1.63	74	18.7	0.33	1.13	79	29.2	1.04	5.49
$Y\perp$ cut 600 °C	71	31.2	0.19	1.68	69	21.1	0.13[c]	2.38	–	–	–	7.04

[a] The profile has two peaks here, it is thus difficult to set the maximum concentration depth.
[b] Undervalued integrals.
[c] Depth concentration profiles are likely to be diffused.

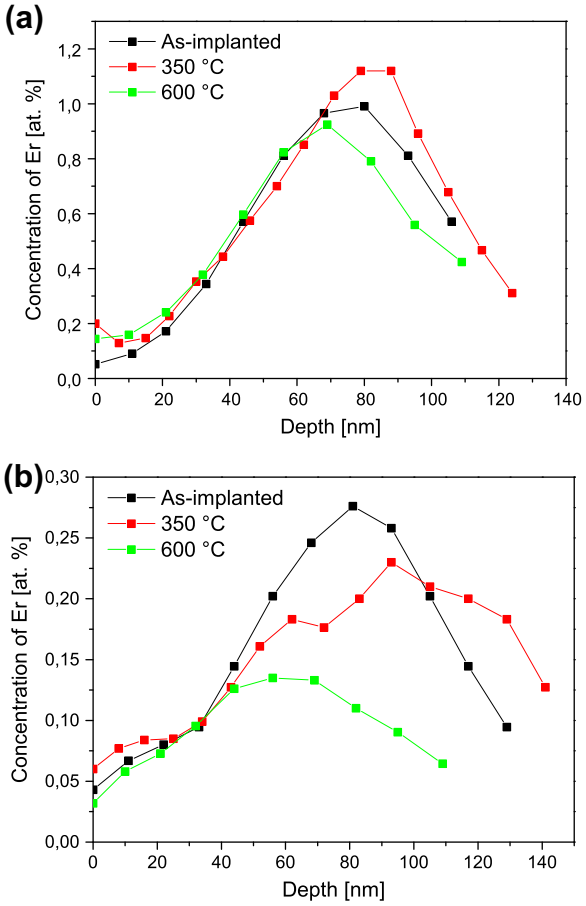

Fig. 4. The erbium depth concentration profile changes caused by annealing at different temperatures in the *Z*-cut of LN for various fluences of ion implantation (a) 1×10^{16} cm^{-2} (b) 1×10^{15} cm^{-2}.

with the $Y\perp$ cut. These findings have already been reported in more detail in our paper [24].

3.2.3. As-annealed samples (600 °C)

After a very positive effect of annealing on the luminescence at 1530 nm had been proved, all of the implanted samples were annealed at 600 °C. According [22], the re-crystallisation of the damaged structure could be assumed at this temperature. The changes of the erbium depth concentration profiles are shown at the Table 1, and for *Z* cut also in Fig. 4. Significant changes were above all registered at the *Rp* and *H* values. A decrease of concentration maximum *H* and a shift of *Rp* value to the depth and extension of concentration profiles are evident for all of the cuts as well as for all ion implantation conditions (see Table 1). As mentioned above, the shift of Er maximum concentration *H* towards the surface of the substrates after annealing was observed. The shift of concentration is more pronounced for the lower implantation fluences (i.e. 1.0×10^{15} ion cm^{-2}) and less pronounced for the fluence 1.0×10^{16} ion cm^{-2} (see also Fig. 4). The *Rp* value obtained from the concentration depth profiles of as-annealed samples at 600 °C implanted at the lower fluence was extracted with higher uncertainty owing to the depth profiles, where the maximum concentration decreases with the increasing annealing temperature close to the detection limit of the RBS analysis and becomes insignificant in some cases.

If we focused on the substrate crystallographic orientation effect, small, though clearly visible, effects could be noticed. During annealing, the more significant erbium depth concentration profiles shift to the surface was found in the *X* cut (about 21 nm), while in the $Y\perp$ cut the difference in *Rp* values is only 9 nm.

The results mentioned above have described the changes of the erbium concentration profile caused by post-implantation annealing in detail. It was proved that:

(i) erbium does not escape from structure of the LN single-crystal during annealing, it moves in every direction inside the substrate;
(ii) annealing at 350 °C does not cause any dramatic changes of the erbium depth concentration profiles; more profound changes did not occur until the annealing temperature was increased to 600 °C;
(iii) migration of erbium through the structure during the annealing is strongly influenced with both applied ion fluence and annealing temperature; setting of those two parameters determines the resultant state of the implanted thin layer;
(iv) from Table 1, it is obvious that using low ion fluences strongly shifts the projected range (*Rp* value) towards the surface and the maximal concentrations of erbium (*H* value) after the annealing are lower while higher fluences do not

practically change the *Rp* values, but the *H* value decreased and the concentration profile became broader only after annealing at higher temperatures.

3.3. Structure recovery

The luminescence of erbium in the LN structure is affected not only by its concentration, but, even more importantly, by its locations and surroundings. To estimate the extent of that effect, the RBS/channelling spectra were measured with a special aim of recording the changes occurring during the annealing in the structure of the crystal. The main attention was paid to the crystal structure reconstruction ability in various LN cuts.

The study of structure damage and its recovery during annealing at 350 °C has been described in our previous papers [23,24]. The RBS/channelling analysis shows that after the implantation for all of the fluences a modified layer appeared. The thickness of the modified layer corresponded to the Er implanted region and slightly differed for the various cuts. The amount of the disordered atoms in the modified layer is 100% and the implanted layer became amorphous. With increasing fluence, we observed a slight deepening of the modified layer, the difference between the samples implanted using 2.5×10^{15} ion cm^{-2} and 1.0×10^{15} ion cm^{-2} was not so pronounced as compared with the samples implanted using 1.0×10^{16} ion cm^{-2} fluence. Furthermore, in [23,24] it was shown that annealing at 350 °C caused slight restoration of the samples exhibited as a decrease of the modified layer thickness. Even though the differences in the RBS/channelling spectra were not so pronounced, we could observe that for all of the fluences the recovery after the annealing procedure was mostly significant in the *Z* cut, unlike in both *Y* cuts. We can see the shallower modified layer appearing after annealing at 350 °C, which can be connected with the recovery at the interface of the implanted and un-implanted layer. The amount of disordered atoms, which are placed off their original position in the crystalline structure in the implanted region, does not change.

However, very significant changes in the crystal structure were found after annealing at 600 °C. The comparison of the RBS/channelling spectra for various annealing temperatures is shown for the *Z* cut in Fig. 5. Similar trends were found in all of the studied crystallographic cuts. Contrary to the annealing at 350 °C, the amount of disordered atoms decreased after annealing at 600 °C from 100% to 17% in *Z* cut, 76% in $Y\perp$ cut, 93% in Y_{II} cut and in 71% in *X* cut (see Fig. 6) for the samples implanted using 2.5×10^{15} ion cm^{-2}. Comparing the Er integral amount in the aligned and random direction did not show any differences between the samples annealed at 350 °C and the as-implanted samples. The number of Er atoms aligned along the *z* axis in the annealed samples at 600 °C is lowered to 20%, while that along the *x*, *y* parallel and *y* perpendicular is lowered to 54%, 88% and 58%, respectively, as compared to the Er amount viewed in the random direction. This effect could be explained in terms of the movement of Er atoms into substitution positions along the *z* axis.

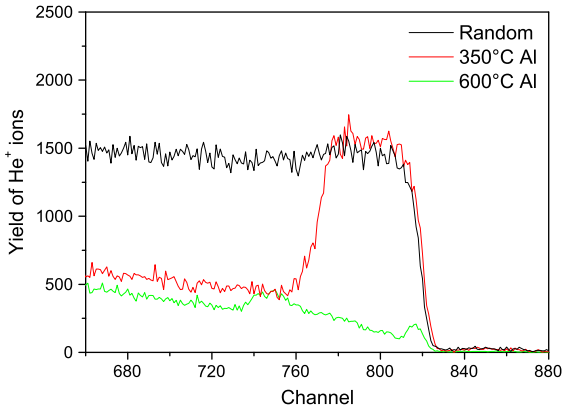

Fig. 5. The RBS channelling spectra in *Z*-cut of LN implanted with erbium (1.0×10^{15} cm^{-2}, 330 keV) and annealed at different temperatures.

The mentioned results allowed the team to assume that the mechanism of the various LN cuts recovery is different; the same is true for erbium migration through the crystal structure. The results could be summarised as follows:

(i) the crucial factor for recovering damaged crystal structure is a choice of the temperature of the post-implantation annealing;
(ii) the recovery of crystal structure preferably occurs along the *z* axis, i.e. in the *Z* cut of LN. For all of the other investigated cuts, a slower reconstruction of the crystal structure was found.

4. Discussion

From our results, the question arises of what the key factor for the erbium luminescence at 1530 nm is. Evidently, it is not the amount of the implanted ions only. The ion implantation performed with higher energy through the same fluence results in the formation of a layer containing an equal number of erbium ions but found in greater depths with a smaller variation of their distribution (thinner layer); despite this, however, the luminescence is stronger. In our case, those differences are not so distinguished, because of the vicinity of both implantation energies (330 and 500 keV). It seems that the surroundings of the erbium ions are whatever matters, and then it stands that with the increasing energy of the doping the damage of the implanted layers is smaller than that of the layer above it (i.e. of the one which the implanted ions flies through). In the area of incidence of the slowed-down ions, the extent of the damage is similar. This perception would provide a good explanation of the luminescence intensity increasing when using equal fluences but higher energies of ion implantation.

Bearing in mind the above-mentioned facts and our previously acquired findings, we may start to discuss the causation of the significantly stronger luminescence always found in the substrate cut perpendicular to the cleavage plane of the crystal. The most simple explanation would be based on the fact that in the $Y\perp$ cut the concentration of erbium ions is at the higher end and therefore also the intensity of the luminescence band would higher, according to our findings reported in [19,22]. However, this is not the case of the ion implantation where the amounts of the doping ions are always the same, as can be confirmed by the RBS erbium depth concentration profiles. The reason for the fact mentioned must be then sought in something else, and the surrounding of the erbium ions is probably whatever matters the most. The results of the experiments when the erbium ions were implanted into crystallographically different cuts (commonly used as well as specially prepared ones) using various fluences (i.e. the structure of the formed layers exhibited various extents of damage) and the as-implanted samples were then annealed at various temperatures, which would offer the explanation as follows.

The origin of the different luminescence is the different mechanism of the recovery of the damaged implanted structure in the LN wafers. The migration of erbium in the course of annealing is affected first of all by the degree of the damage of the structure and then by the annealing temperature applied. Using the implantation fluence 1.0×10^{15} ion cm^{-2}, one can expect only point defects, possibly the formation of a quasi-amorphous layer, which makes the subsequent recovery more vulnerable to the influence

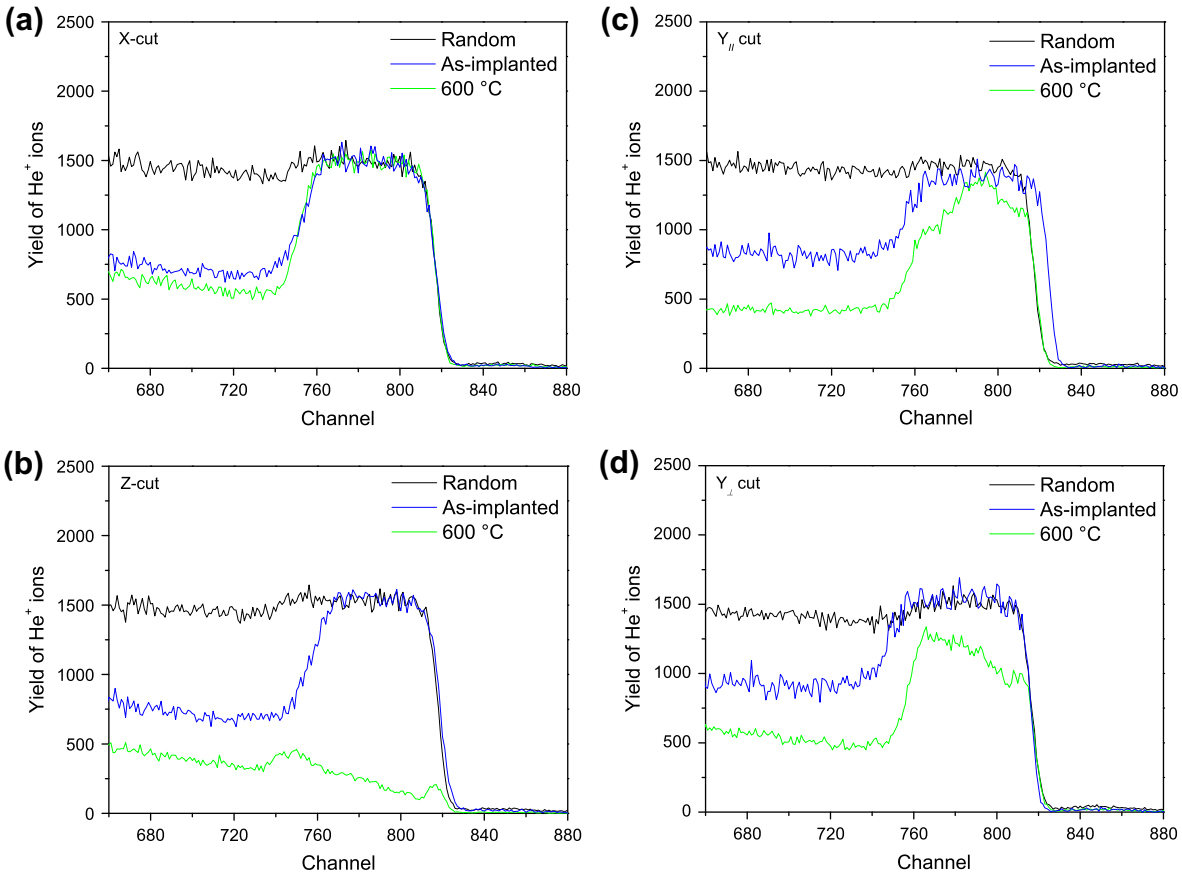

Fig. 6. The RBS channelling spectra in various cuts of LN implanted with erbium (2.5×10^{15} cm^{-2}, 330 keV) and annealed at 600 °C (a) *X*-cut (b) *Z*-cut (c)Y_{II} cut (d) $Y\perp$ cut.

of the diffusion of the defects [27]. This effect becomes more profound at 350 °C, when the *H* value (i.e. the maximum concentration of erbium) in the erbium depth concentration profiles lowers and the shape of the profiles broadens. The most evident change of the RBS concentration profile was found with the $Y\perp$ cut, which can be explained (regarding our previous experience) on the basis of the rapid diffusion of erbium through cleavage plane of the crystal. Using a higher annealing temperature (600 °C) makes the overall re-crystallisation easier, and it applies especially for the *z* axis, where the structure of the crystal – according to the channelling RBS spectra – resembles the most the virgin one, which is why the luminescence in this cut is after the annealing at 600 °C only slightly weaker than in the $Y\perp$ cut. In the latter, the recovery at 600 °C is slower despite the luminescence being rather strong, probably because the erbium ions have been already settled in the C_{3v} sites.

After applying the fluence of 1.0×10^{16} ion cm^{-2}, the structure becomes totally damaged, evidence of which is the ostensible depletion of lithium [23]; particularly in the $Y\perp$ cut, that effect was the most pronounced. However, during the recovery, the structure of the cuts evidently plays a much smaller role, as the intensities of the luminescence of the particular cuts are similar. The extent of the damage and the effect of the post-implantation annealing very likely also influenced the possibility of the clustering of erbium ions as well as the structure of their neighbourhood. The hypothesis is confirmed by the fact that the obtained RBS erbium depth concentration profiles are very similar for all of the cuts. Moreover, after annealing at 350 °C, a slight increase of the erbium concentration was noted. Subsequently, those differences are reflected in the differing intensity of the luminescence of the samples prepared in particular crystallographic cuts using the same conditions.

5. Conclusions

In the paper, a rather complex study of the possibilities of affecting the 1530 nm luminescence of the implanted erbium ions into different crystallographic cuts of lithium niobate is summarised. Erbium was implanted using various implantation conditions and the samples varied by the regimen of the post-implantation annealing. The implanted layers contained at most 1 at.% of erbium, the concentration depth profiles had a Gaussian shape with the maximal depth reaching around 140 nm. The as-implanted layers did not reveal any luminescence properties at 1530 nm, but it dramatically changed after annealing.

It was proved that erbium implantation into LN depends on the specific crystallographic orientation of the sample surface. The best luminescence was always observed in $Y\perp$ ⟨10–14⟩ cuts even when various experimental conditions of preparation were applied. Moreover, corresponding with our previously acquired findings, the results generally demonstrate the important role of the LN cleavage plane. This plane allows the easy movement of erbium ions under all thermal treatments that is thermal diffusion or post-implantation annealing. In such a case, also an easier dissolution of erbium clusters is predictable.

Acknowledgements

We appreciate the grants of the Czech Science Foundation No. P106/10/1477, LC 06041, MSMT 6046137302 and SPIRIT 020.

References

[1] K.K. Wong, Properties of Lithium Niobate, INSPEC, London, 2002.
[2] L. Arizmendi, Phys. Stat. Sol. (A) 201 (2004) 253.

[3] A. Polman, J. Appl. Phys. 82 (1997) 1.
[4] D.L. Zhang, D.C. Wang, E.Y.B. Pun, J. Appl. Phys. Lett. 18 (2001) 1205.
[5] L. Tsonev, Opt. Mater. 30 (2008) 892.
[6] V.G. Babajanyan, Laser Phys. 15 (11) (2005).
[7] M.N. Palatnikov, J. Crystal, Growth 291 (2006) 390–397.
[8] Ai-hua Li, J Lum. 128 (2008) 239–244.
[9] De-Long Zhang, J. Appl. Phys. 99 (2006) 023101.
[10] C. Becker, IEEE J. Sel. Top. Quant. Electron 6 (1) (2000) 101.
[11] W. Sohler et al., IEICE Trans. Electron E88–C (5) (2005) 990.
[12] C. Buchal et al., Annu. Rev. Mater. Sci. 24 (1994) 125.
[13] C. Mignotte, Appl. Surf. Sci. 185 (2001) 11.
[14] C. Sada et al., Opt. Mater. 30 (6) (2008) 892.
[15] M.P.F. Graca et al., J. Phys: Condens. Matter 19 (2007) 016213.
[16] M. Jelínek, Laser Phys. 19 (2) (2009) 265.
[17] M. Fleuster et al., J. Appl. Phys. 75 (1) (1994) 173.
[18] C. Mignotte, Nucl. Instr. Methods Phys. Res. B 187 (2002) 95.
[19] P. Nekvindova et al., Int. J. Inorg. Mater. 3 (8) (2001) 1245.
[20] P. Nekvindova et al., J. Mater. Res. 16 (2) (2001) 333.
[21] J. Saarilahti, Nucl. Instr. Methods Phys. Res. B 64 (1994) 734.
[22] A. Meldrum et al., J. Nucl. Mater. 300 (2002) 242.
[23] B. Svecova et al., Nucl. Instr. Methods Phys. Res. B 267 (2009) 1332.
[24] A. Mackova et al., Nucl. Instr. Methods Phys. Res. B 268 (2010) 2042.
[25] www.srim.org.
[26] L.C. Feldmann, J.W. Mayer, S.T. Picraux, Material Analysis by Ion Channelling, Academic Press, New York, 1982.
[27] S. Jetschke, H. Karge, K. Hehl, Phys. Stat. Sol. (A) 77 (1983) 207.

Optics Communications 285 (2012) 2729–2733

Contents lists available at SciVerse ScienceDirect

Optics Communications

journal homepage: www.elsevier.com/locate/optcom

Z-scan study of nonlinear absorption of gold nano-particles prepared by ion implantation in various types of silicate glasses

W. Husinsky [a], A. Ajami [a,*], P. Nekvindova [b], B. Svecova [b], J. Pesicka [c], M. Janecek [c]

[a] Institute of Applied Physics, Vienna University of Technology, Wiedner Huaptstrasse 8-10 Wien-1040, Austria
[b] Department of Inorganic Chemistry, Faculty of Chemical Technology, Institute of Chemical Technology, Technicka 5, 166 28 Prague, Czech Republic
[c] Charles University, Faculty of Mathematics and Physics, Department of Physics of Materials, Ke Karlovu 5, 121 16 Prague, Czech Republic

ARTICLE INFO

Article history:
Received 21 March 2011
Received in revised form 19 December 2011
Accepted 25 January 2012
Available online 9 February 2012

Keywords:
Silicate glass
Metal nano-particles
Nonlinear absorption
Au+ ion implantation
Z-scan
Ultra short lasers

ABSTRACT

Metal nano-clusters composite glasses synthesized by ion implantation have been shown as promising nonlinear photonic material. In this paper, we report on the nonlinear absorption measurements of gold nano-particles implanted in four structurally different types of silicate glasses. All targets containing gold nano-particles in a layer 500 nm under the surface of the glass have been prepared by ion implantation with subsequent annealing. The targets were characterized by UV–VIS absorption spectroscopy, transmission electron microscopy (TEM) and by the Z-scan technique. The resulting nano-particles differed in size, range of particle size and shape as well as depth distribution characteristic for glasses with different chemical compositions. With the Z-scan technique, it can be shown that the nano-particles produced in silicate glasses exhibit substantial two-photon absorption (TPA). The TPA coefficient differed depending on size, shape, and depth distribution of the metal nano-clusters and the structure and composition of the glass substrates. The highest TPA coefficient (16.25 cm/GW) was found for the glass BK7 in which the largest non-spherical nano-particles have been observed in the thinnest layer.

1. Introduction

Glass substrates have recently attracted growing interest due to the fact that they can serve as substrates for nano-structured systems with remarkable optical nonlinear properties [1]. Glass substrates possess overall advantages as compared to many crystals or polymers. In particular, the composition of the glass can be well designed and tuned according to the needs of the encompassed photonic components and also their fabrication is usually feasible and inexpensive [2]. Silicate glasses (i.e., glasses based on silica SiO_2) are both chemically and thermally stable, and it is rather simple to fabricate waveguides compatible with currently used optical fibers.

The metal nano-cluster composite glasses synthesized by ion implantation have been shown as particularly promising nonlinear photonic materials [1,3–6]. Nanometric metal particles can exhibit a nonlinear optical response several orders of magnitude larger than bulk metals due to a phenomenon referred to as surface plasmon resonance. When the particle size ranges from nanometer to a few tens of nanometers, confinement results in the possibility of resonantly exciting the electron gas collectively by coupling with an appropriate oscillating electromagnetic field. As the local electric field in the particles is enhanced due to the oscillation of the electron gas, the metal nonlinear optical response can be amplified as compared to the bulk solid one [7].

Recent experiments have shown that standard glass substrates containing nano-particles of Au can be regarded as one of the most promising nonlinear optical materials [8–16]. The experiments have shown that such materials exhibit very strong nonlinear third-order susceptibility. $\chi^{(3)}$ contains a real and an imaginary part. The real part of the susceptibility is related to the refractive index while the imaginary part determines the absorption coefficient. Therefore, a strong third-order nonlinear optical response might manifest itself as a noticeable change in the refractive index or in the absorption coefficient or in both.

The third-order nonlinear optical process is responsible for nonlinear behaviors such as the optical Kerr effect, two-photon absorption, third harmonic generation and many more. These phenomena can be observed in almost all materials when they are irradiated with high intense laser radiation such as ultrashort laser pulses. For the Kerr effect and two-photon absorption, the nonlinear optical response is observed as a linear intensity dependence in the refractive index and in the absorption coefficient respectively.

$$n(I) = n_0 + \gamma I \tag{1.a}$$

$$\alpha(I) = \alpha_0 + \beta I \tag{1.b}$$

where n_0 is the linear refractive index, γ is the nonlinear index of refraction, α_0 is the linear absorption coefficient, β is the two-photon

* Corresponding author.
E-mail address: ali_ajami80@yahoo.com (A. Ajami).

0030-4018/$ – see front matter © 2012 Elsevier B.V. All rights reserved.
doi:10.1016/j.optcom.2012.01.044

absorption coefficient and I denotes the irradiance of the laser beam within the nonlinear medium.

The ratio of the imaginary to the real parts of the third-order nonlinear susceptibility is given by $\beta/k\gamma$ (where k is the wave number) which determines the absorptive and refractive contributions to the third-order nonlinear susceptibility. Depending on this ratio, metal nano-cluster composite materials can be employed for different applications. For instance, in the case $\beta > k\gamma$, the absorptive property can be exploited for a variety of optical limiting applications (protective devices etc.) [17,18] whereas for $\beta < k\gamma$, the refractive properties can be exploited for all-optical switching devices [14,19].

Third-order nonlinear optical properties of metal/dielectric nanocomposite materials depend significantly on many factors regarding both the materials themselves (metal and host medium kinds, metal particles concentration, size and shape) and the excitation laser (wavelength, intensity, pulse width) [13,20–23].

Several different experimental methods can be employed to measure TPA coefficients such up-converted fluorescence emission [24], transient absorption [25], four-wave mixing [26] and the Z-scan technique [27,28]. Among these methods the Z-scan technique, which was first introduced by Sheik-Bahae et al. in 1989 [29], is a particularly sensitive technique. It is especially suitable for non-fluorescence materials such as metal nano-cluster composite materials for which the up-converted fluorescence emission experiment is not an appropriate method for measuring TPA coefficient. In this technique the nonlinear medium is translated along the laser beam propagation direction through the focal point of a tightly focused laser beam. The transmitted energy through the sample is entirely collected using a convergent lens and detected by a diode. The measured signal is a V-shape curve from which the nonlinear absorption coefficient can be extracted.

We had previously found significant differences of the ion penetration depth for various glass substrates when implanted with Au^+ ions [30]. In this paper we focused on the measurement of nonlinear absorption and the study of the relationship between the nonlinear absorption and the size, depth distribution and shape of gold nanoparticles and also the structure of silicate glasses. Four types of silicate glasses with different compositions (the variation was mainly due to different concentrations of monovalent modifiers and, therefore, in the extent of cross-linking of glass matrix) were chosen according to our previous study [31]. The glasses were implanted with Au^+ ions under identical conditions; the nucleation of metal nanoparticles was initiated during the subsequent annealing of the as-implanted glasses. In the case of post-implantation annealing, the conditions were also kept identical for all prepared samples. Formation and evolution of the metal nano-particles in the glass substrates were studied by absorption spectroscopy and TEM. Nonlinear absorption was measured by the open aperture Z-scan technique.

We have also addressed the question, if and in how far it is possible to influence and control the nonlinear properties of the resulting composite glass–metal material. The results were evaluated in terms of finding and understanding the relations between the properties of the composite glass–metal material and the properties of the implantation particles, which may be of crucial importance in designing e.g. nano-particles based components for special applications.

2. Experimental

2.1. Preparation of samples

We have used four types of optical silicate glasses, namely specially designed GIL49 and Glass B (made at the Glass Institute Hradec Kralove Ltd., Czech Republic) and commercially available silica glass and BK7. The used glasses varied especially in the concentration of monovalent modifiers (Na_2O, K_2O) as well as their network formers (SiO_2, B_2O_3). The compositions of the glasses can be found in Table 1.

The thoroughly pre-cleaned glass substrates were implanted with Au^+ ions at an energy of 1701 keV while the ion fluence was kept at 1×10^{16} ions cm^{-2}. The implantation was performed at the Tandetron 4130 MC accelerator at the Nuclear Physics Institute in Prague, Czech Republic. The as-implanted glasses were annealed in air at temperature of 600 °C for 5 h.

2.2. Characterization of sample properties

The depth distribution and diffusion profiles of the implanted Au were investigated using Rutherford Backscattering Spectrometry (RBS) with 2.0 MeV He^+ ions at the Nuclear Physics Institute in Prague, Czech Republic and have already been reported in Ref. [30]. UV–VIS absorption spectra were collected using a dual-beam spectrometer (CARY 50) in transmission modes ranging from 300 to 1000 nm at the Institute of Chemical Technology Prague, Czech Republic.

Nano-particle microscopy characterization was done by a TEM (JEOL 2000 FX) equipped with an energy dispersive X-ray analyzer (Link AN 10000) at the Faculty of Mathematics and Physics, Charles University Prague, Czech Republic. The samples were prepared with a dimple grinder (Gatan Inc.) and by ion polishing procedure with a precise ion polishing system (Gatan PIPS) for thin foil preparation for TEM.

Nonlinear absorption was measured applying the open aperture Z-scan technique for ultrashort laser radiation. A Ti:sapphire laser (FEMTOPOWER Compact PRO) was used that delivers ultra short laser pulses at a repetition rate of 1 kHz each pulse having a maximum energy of 1 mJ with a spectrum centered at 790 nm. The duration of the shortest pulses for this system, estimated as the full width at half maximum (FWHM) of a Gaussian temporal profile, is 25 fs. There is a possibility for pulses to be stretched up to a few hundreds of femto-second using a Dazzler system (an acousto-optic programmable dispersive filter). An autocorrelator (model: ENV40CSG, Femtolasers) was employed to measure the pulse duration. The laser beam power was measured using a digital power meter in front of the sample prior to each measurement. A 175 mm focal length plano-convex lens was used to focus the 15 mm diameter laser beam within the sample. The Rayleigh range and beam waist radius were measured to be 0.28 mm and 11 μm respectively considering this fact that the beam quality factor is 2 for our laser system. The sample mounted on a translating stage was moved 6 mm from 3 mm before the focus to 3 mm after the focus in about 40 steps. The schematic of the experimental setup is shown in Fig. 1 and has been described in detail elsewhere [32].

3. Results

3.1. Linear absorption spectra and characteristics of nano-clusters

The measurements of the optical absorption spectra indicated different spectra for as-implanted and as-annealed samples as shown in Fig. 2. It can be seen from Fig. 2 that no significant increase of the linear absorption in UV–VIS region occurred for any prepared sample after the ion implantation. After annealing, except for the silica glass, the targets attained a pink–red color, which was proven by the presence of an absorption peak in UV–VIS region. Although the

Table 1
The compositions of the silicate substrates (in wt.%).

Glass substrate	SiO_2	Na_2O	Al_2O_3	CaO	MgO	K_2O	B_2O_3	BaO
GIL49	63.2	24.4	1.1	5.6	5.3	0.5	–	–
Glass B	88.0	8.7	3.3	–	–	–	–	–
BK7	68.3	8.8	–	0.1	–	8.1	12.1	2.5
Silica glass	100	–	–	–	–	–	–	–

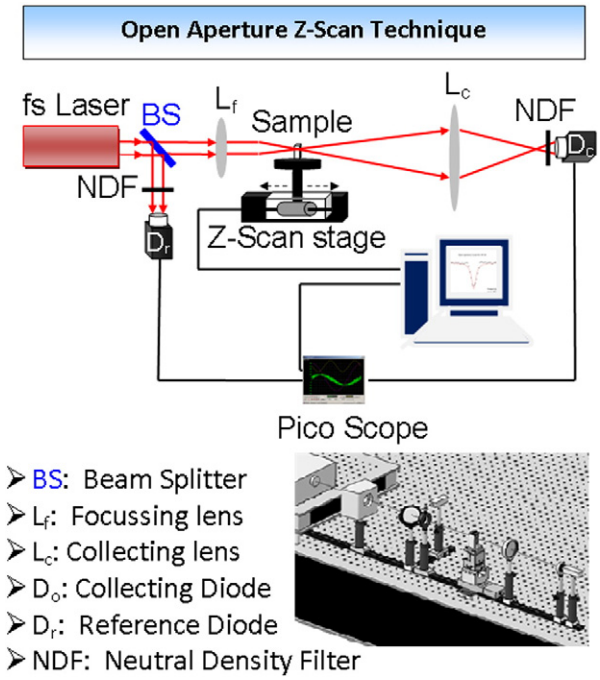

Fig. 1. Schematic of the Z-scan experimental setup.

experimental conditions were kept identical for the treatment of all samples but their absorption spectra showed different peaks after annealing. Two as-annealed samples GIL49 and BK7 each one showed one absorption peak at 525 nm and 560 nm respectively but as-annealed glass B showed two absorption peaks at 415 and 520 nm.

Glasses with absorption in the visible region after annealing were characterized by TEM and details of the results will be published separately. TEM analysis confirmed the presence of metal nano-particles in as-annealed glasses at a depth corresponding well to the depth of the maximum Au concentration measured by RBS. The most relevant results of the characterization of the nano-structures obtained by TEM analysis for all samples are summarized in Table 2.

From Table 2, it is evident that the size and shape of the gold nano-particles differ for the various types of glass although all the glasses were treated under identical conditions. Nano-particles observed in glass B were small (1–7 nm) and were present in a relatively broad layer of 350 nm. In glass GIL49, nano-particles with different sizes from 1 to 15 nm were found in a layer of 250 nm. Nano-particles in BK7 glass were typically 6–25 nm and were concentrated in a narrow layer of 100 nm.

3.2. Determinations of TPA coefficients

In the first step we have determined the laser parameter regime in which TPA can be clearly attributed (from the measured Z-scans) to the existence of gold nano-clusters. By varying the pulse duration from 25 fs to 200 fs (possible range of our laser system) we observed no dependence on the pulse duration. We decided to perform all the measurements with the shortest pulses possible (25 fs). Furthermore, it had to be verified that no nonlinear absorption is due to the glass substrates themselves. For this purpose, we first determined the intensity at which the standard glass (i.e. non implanted glass) starts exhibiting nonlinear absorption. The pulse energy threshold for nonlinear absorption of the standard glasses was determined to be 50 nJ. Therefore, all the Z-scan measurements for the as-implanted and as-annealed samples were performed with pulse energies lower than 50 nJ. In this intensity regime the Z-scan results depend on the laser pulse energy, i.e. the nonlinear absorption of the sample increases with increasing pulse energy (see Fig. 4).

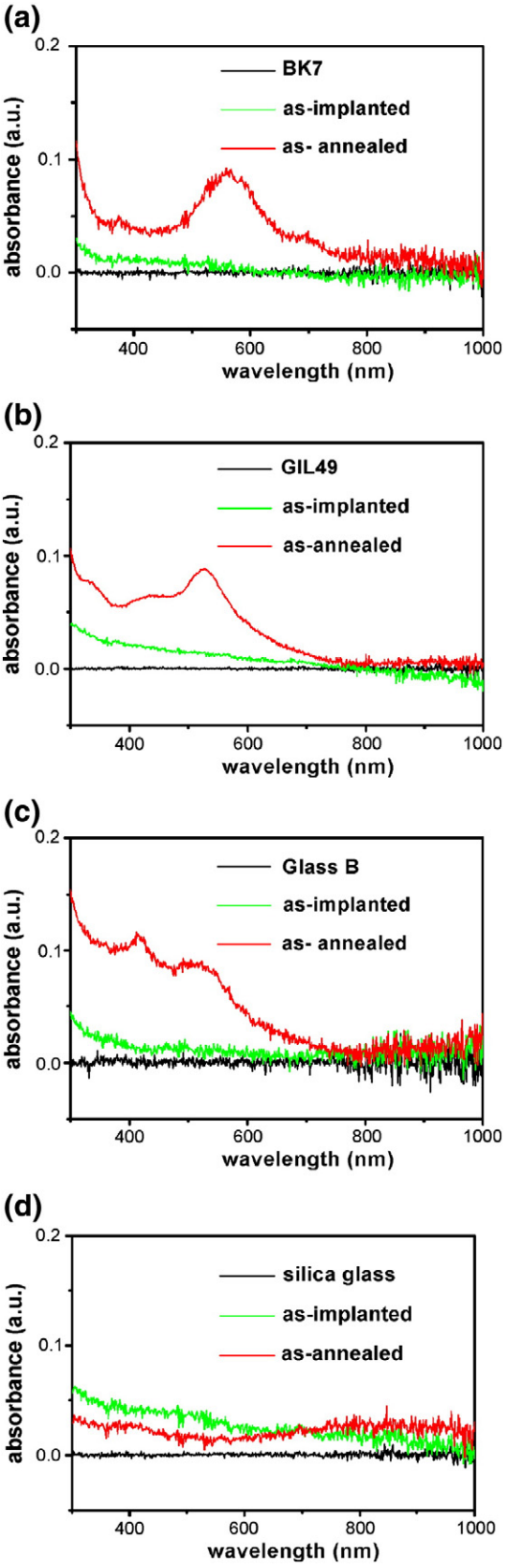

Fig. 2. UV–VIS absorption spectra of four different types of silicate glass substrates implanted and annealed under identical conditions. (a) BK7; (b) GIL49; (c) glass B; (d) silica glass.

Table 2
The TEM analysis of four different silicate glass substrates implanted and annealed under identical conditions.

Glass substrate	Thickness of layer with nano-particles	Size of nano-particles	Shape of nano-particles
Silica glass	Not measured	Not measured	Not measured
GIL49	250 nm	1–15 nm	Spherical
Glass B	350 nm	1–7 nm	Spherical
BK7	100 nm	6–25 nm	Non-spherical

In the next step, the as-implanted glasses were measured. It was found that only as-implanted glass BK7 showed nonlinear absorption. The TPA coefficient was determined by fitting Eq. (2) to the Z-scan experimental data.

$$T(z) = \sum_{n=0}^{\infty} \frac{(-q_0)^n}{(n+1)^{3/2}(1+x^2)^n} \tag{2}$$

where q_0 is $\beta L I_0$, β is the TPA coefficient, L is the thickness of the sample (gold nano-particles layer), $x = z/z_0$, z is the sample position, z_0 is the Rayleigh range and I_0 is the maximum on-axis intensity at the focal point of the laser beam within the sample. It should be noted that Eq. (2) is used to extract the pure TPA coefficient under assumption of negligible excited state absorption and three-photon or higher order nonlinear absorption as described in Ref. [32]. The obtained TPA coefficient for as-implanted BK7 is 11.08 cm/GW.

In the next step, the influence of annealing on the TPA of the resulting nano-composite material has been studied. Fig. 3 shows Z-scans of as-implanted and as-annealed BK7 performed with the same pulse energy of 30 nJ. It is evident from Fig. 3 that the TPA for BK7 showed a 40% increase after annealing. Fig. 4 shows Z-scans of as-annealed glass BK7 measured with different pulse energies. As can be seen from Fig. 4, the normalized absorbance increases linearly with laser pulse energy (laser intensity), which is an indication of TPA due to the presence of gold nano-particles in BK7. The same measurements were performed for all other as-annealed samples. The obtained TPA coefficients for all samples are summarized in Table 3 and also are compared in Fig. 5.

The highest TPA coefficient of 16.25 cm/GW was obtained for as-annealed BK7 that had developed the largest non-spherical nano-particles in the thinnest layer of 100 nm whereas the smallest TPA coefficient of 2.46 cm/GW was obtained for as-annealed silica glass that showed no absorption in the UV–VIS region. It should also be mentioned that the linear absorption at a wavelength of 790 nm was negligible for all samples. Hence no saturation of absorption at this wavelength for these samples can be expected.

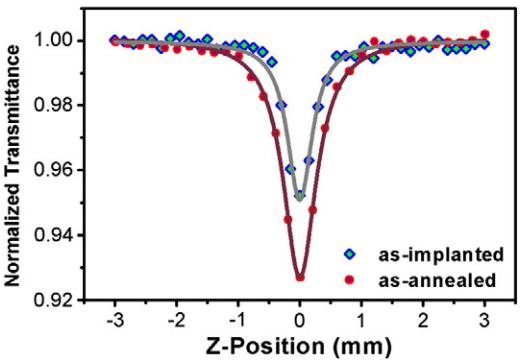

Fig. 3. Z-scans of the as-implanted and as-annealed glass BK7 measured with the same pulse energy of 30 nJ. Blue solid line represents the best fit to the experimental data for the as-implanted sample and red solid line is for the as-annealed sample.

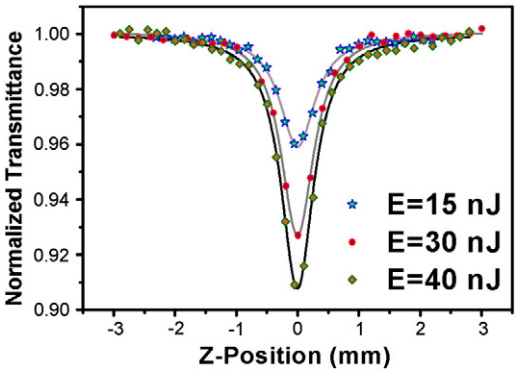

Fig. 4. Z-scans of as-annealed glass BK7 possessing a 100 nm thick layer of gold nano-particles after annealing performed with different pulse energies.

4. Discussion

A different nucleation of gold nano-particles observed in our glasses after the annealing process is probably related to the glass composition, especially to a different extent of cross-linking of glass structure. The ion implantation process caused the different range of structure damage in glass (so called de-polymerization of the glass [31]) according to the glass composition and structure. Therefore, the subsequent annealing process results in different speed in the recovery of the glass matrix. Consequently gold nano-particles observed in glasses after the post-implantation annealing by TEM exhibit different size, shape and distribution.

The metal nano-particles absorb part of the UV–VIS spectra, which results in the coloration of the glass. The absorption of these glasses in the UV–VIS region is given by a characteristic surface plasmon resonance frequency of the metal nano-particles. The characteristic wavelength of the surface plasmon resonance of gold is centered around 535 nm [6], i.e. at wavelength observed also in our glasses. The results showed that the shape of the absorption band, its intensity and position in the spectrum are affected by the size, shape and distribution of nano-particles in the glass. The thinner layers (in which metal nano-particles are distributed in the glass) and the larger particle size both result in a better-defined absorption band. Decreasing the size of the gold nano-particles in the glass and extending the layer in which nano-particles are present result in shifting the absorption band toward shorter wavelengths.

The enhancement of the nonlinear response of the glass observed after implantation (in the case of BK7) and after annealing is caused due to the presence of gold nano-particles in glass. This is because of the phenomenon referred to as surface plasmon resonance: The electron gas in the nanoscale particles is forced to resonate by the oscillating electromagnetic field of the laser radiation. This results in an enhancement of the local electric field, and thus an increase in the optical nonlinear response of the metal nano-particles implanted in the glasses. This causes an increase of several orders of magnitude in optical nonlinear response of metal nano-particles compared to that of the bulk solid one.

From our data in Tables 2 and 3, it becomes evident that the size of the nano-particles is the most relevant factor for the TPA coefficient. Measurements of the linear absorption spectra also show that the characteristic surface plasmon resonance feature is maximal for the largest clusters [33–37].

Table 3
TPA coefficients of nano-composite glasses prepared by ion implantation in different silicate glasses under identical conditions.

Glass substrate	Silica glass	Glass B	GIL 49	BK 7
TPA coefficient (cm/GW)	2.46	5.21	7.75	16.25

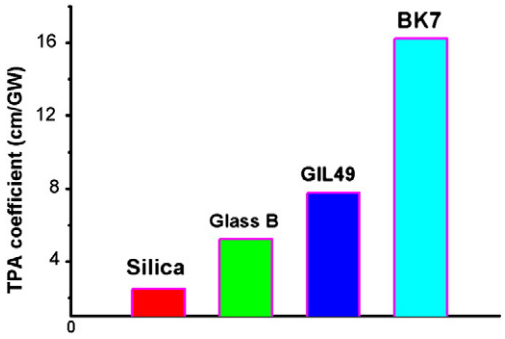

Fig. 5. TPA coefficients of nano-composite glasses prepared by ion implantation in different silicate glasses under identical conditions.

But also the shape and the layer thickness can have a substantial influence. Our results indicate that non-spherical nano-particles in glass BK7 show higher TPA coefficient than spherical ones in glass GIL49 and glass B. If the surface of a metal nano-particle is rough, the surface plasmons (SP) are strongly scattered leading to the accumulation of the electromagnetic field density [27]. This causes an enhancement of the local electric field and thus an increase in polarization. This is an indication of a susceptibility enhancement and a strong nonlinear response of the nano-composite material.

Moreover, our results showed that the composition and structure of the used glass have significant impact on the resulting nonlinear optical properties.

One should notice that the metal nonlinear response is indeed further amplified by the SPR phenomenon, which depends significantly on the difference of the dielectric constant of the nano-particles and the host medium. Therefore, the metal alone cannot explain by itself the highly nonlinear response of the nano-composite media. This indicates that the substrate plays an important role in two aspects: First, it affects the size, shape and distribution of the metal nano-particles formed in the composite material (which are responsible for the strength of nonlinear response of metal nano-particles) and secondly, as mentioned above, the dielectric contrast between the particles and the substrate is responsible for amplification of the local electric field which thus determines the strength of the nonlinear optical response of the metal nano-particles. Why BK7 develops the largest gold nano-particles and shows the highest TPA coefficient is still unclear and will be the subject of further investigation.

5. Conclusion

It was shown that the nucleation of gold nano-particles and their parameters (such as size, shape and distribution in glass matrix) depend on the glass composition and structure. It is due to the different extent of de-polymerization of the glass during the implantation and therefore the different conditions for the nucleation of the gold nano-particles.

We could establish that the increase of the TPA coefficient is mainly caused by increasing the size of gold nano-particles presented in the glass. The TPA coefficient ranges from 2.5 to 16.3 cm/GW depending on the glass composition and its structure, although we kept the conditions of the preparation of the nano-composite glass identical. The highest value of TPA coefficient was found for glass BK7 under these conditions: Au^+ implantation, beam energy of 1701 keV, ion fluence of 1×10^{16} ion cm^{-2}, post-implantation annealing in air at 600 °C for 5 h.

Acknowledgments

Some of us acknowledge the financial support by the Agency of the Czech Republic, grants LC06041, MSMT 6046137302 and MSM No. 21/2010 SPIRIT020.

References

[1] P.C.S. Kasap, Springer Handbook of Electronic and Photonic Materials, Springer, New York, 2006.
[2] N.N.H. Bach, The Properties of Optical Glass, Springer-Verlag, Berlin, 1998.
[3] R.L. Sutherland, Handbook of Nonlinear Optics, Marcel Dekker, New York, 2003.
[4] P. Chakraborty, Journal of Materials Science 33 (1998) 2235.
[5] R.W. Boyd, Nonlinear optics, Academic, San Diego, 2003.
[6] F. Gonella, P. Mazzoldi, Handbook of Nanostructured Materials and Nanotechnology, 4, Academic, San Diego, 2000.
[7] B. Palpant, Non-linear optical properties of matter, 1, Springer, 2006.
[8] W. Rechberger, A. Hohenau, A. Leitner, J.R. Krenn, B. Lamprecht, F.R. Aussenegg, Optics Communications 220 (2003) 137.
[9] A.I. Ryasnyanskiy, B. Palpant, S. Debrus, U. Pal, A.L. Stepanov, Optics Communications 273 (2007) 538.
[10] A. Lesuffleur, P. Gogol, P. Beauvillain, B. Guizal, D. Van Labeke, P. Georges, Journal of Applied Physics 104 (12) (2008) Art. No.: 124310.
[11] F.Z. Henari, A.A. Dakhel, Journal of Applied Physics 104 (3) (2008) Art. No.: 033110.
[12] W. Wang, Y. Wang, Z. Dai, Y. Sun, Applied Surface Science 253 (2007) 4673.
[13] A.I. Ryasnyanskiy, B. Palpant, S. Debrus, U. Pal, A. Stepanov, Journal of Luminescence 127 (2007) 181.
[14] N. Venkatram, R. Sai Santosh Kumar, D. Narayana Rao, S.K. Medda, S. De, G. De, Journal of Nanoscience and Nanotechnology 6 (2006) 1990.
[15] J.T. Seo, S.M. Ma, Q. Yang, R. Battle, L. Creekmore, B. Tabibi, W.J. Kim, J.H. Heo, W.S. Yun, D.H. Ha, S.S. Jung, E. Bryant, C. Payne, W. Yu, V. Colvin, Proceedings of the IEEE 1 (2006) 258.
[16] A.I. Ryasnyanskiy, B. Palpant, S. Debrus, U. Pal, A.L. Stepanov, Physics of the Solid State 51 (2009) 55.
[17] S. Sreeja, S. Mayadevi, S.R. Suresh, P.G.L. Frobel, N. Smijesh, R. Philip, C.I. Muneera, PRO 1391 (2011) 618.
[18] G. Vinitha, A. Ramalingam, Proceedings of World Academy of Science, Engineering and Technology, 64, 2010.
[19] H. Inouye, K. Tanaka, I. Tanahashi, T. Hattori, H. Nakatsuka, Japanese Journal of Applied Physics, Part 1: Regular Papers and Short Notes and Review Papers 39 (2000).
[20] E. Shahriari, W. Mahmood Mat Yunus, Digest Journal of Nanomaterials and Biostructures 5 (2010) 939.
[21] Y.H. Wang, F. Ren, Q.Q. Wang, D.J. Chen, D.J. Fu, C.Z. Jiang, Physics Letters, Section A: General, Atomic and Solid State Physics 357 (2006) 364.
[22] E. Cattaruzza, G. Battaglin, P. Calvelli, F. Gonella, G. Mattei, C. Maurizio, P. Mazzoldi, S. Padovani, R. Polloni, C. Sada, B.F. Scremin, F. D'Acapito, Composites Science and Technology 63 (2003) 1203.
[23] J. Olivares, J. Requejo-Isidro, R. Del Coso, R. De Nalda, J. Solis, C.N. Afonso, A.L. Stepanov, D. Hole, P.D. Townsend, A. Naudon, Journal of Applied Physics 90 (2001) 1064.
[24] C. Xu, W.W. Webb, Journal of the Optical Society of America B: Optical Physics 13 (1996) 481.
[25] J.D. Bhawalkar, G.S. He, P.N. Prasad, Reports on Progress in Physics 59 (1996) 1041.
[26] Q. Yang, J. Seo, S. Creekmore, G. Tan, H. Brown, S.M. Ma, L. Creekmore, A. Jackson, T. Skyles, B. Tabibi, H. Wang, S. Jung, M. Namkung, Journal of Physics Conference Series 38 (2006) 144.
[27] P. Wang, Y. Lu, L. Tang, J. Zhang, H. Ming, J. Xie, F.H. Ho, H.H. Chang, H.Y. Lin, D.P. Tsai, Optics Communications 229 (2004) 425.
[28] R.A. Ganeev, A.I. Ryasnyansky, A.L. Stepanov, C. Marques, R.C. Da Silva, E. Alves, Optics Communications 253 (2005) 205.
[29] M. Sheik-Bahae, A.A. Said, T.-H. Wei, D.J. Hagan, E.W. Van Stryland, IEEE Journal of Quantum Electronics 26 (1990) 760.
[30] P. Malinský, A. Macková, J. Bočan, B. Švecová, P. Nekvindová, Nuclear Instruments and Methods in Physics Research Section B: Beam Interactions with Materials and Atoms 267 (2009) 1575.
[31] B. Svecova, P. Nekvindova, A. MacKova, P. Malinsky, A. Kolitsch, V. Machovic, S. Stara, M. Mika, J. Spirkova, Journal of Non-Crystalline Solids 356 (2010) 2468.
[32] A. Ajami, W. Husinsky, R. Liska, N. Pucher, Journal of the Optical Society of America B: Optical Physics 27 (2010) 2290.
[33] Y.H. Wang, Y.M. Wang, J.D. Lu, L.L. Ji, R.G. Zang, R.W. Wang, Optics Communications 283 (2010) 486.
[34] S. Nah, L. Li, J.T. Fourkas, Journal of Physical Chemistry A 113 (2009) 4416.
[35] R. Sreeja, R. Reshmi, M. George, M.K. Jayaraj, Proceedings of SPIE 7155 (2008) Art. No.: 715521.
[36] X. Liu, Y. Tomita, K. Yasui, K. Kojima, K. Chikama, Proceedings of SPIE 7722 (2010) Art. No.: 77222A.
[37] J. Shin, K. Jang, K.S. Lim, I.B. Sohn, Y.C. Noh, J. Lee, Applied Physics A: Materials Science and Processing 93 (2008) 923.

Design and investigation of properties of nanocrystalline diamond optical planar waveguides

Vaclav Prajzler,[1] Marian Varga,[2,3] Pavla Nekvindova,[4] Zdenek Remes,[2] and Alexander Kromka[2,*]

[1]*Department of Microelectronics, Faculty of Electrical Engineering, Czech Technical University in Prague, Technicka 2, 166 27 Prague 6, Czech Republic*
[2]*Institute of Physics, Academy of Sciences of the Czech Republic, v.v.i., Cukrovarnicka 10/112, 162 53 Prague 6, Czech Republic*
[3]*Institute of Electronics and Photonics, FEI STU, Ilkovičova 3, SK-812 19 Bratislava, Slovak Republic*
[4]*Institute of Chemical Technology, Technicka 5, 166 28 Prague 6, Czech Republic*
[*]*kromka@fzu.cz*

Abstract: Diamond thin films have remarkable properties comparable with natural diamond. Because of these properties it is a very promising material for many various applications (sensors, heat sink, optical mirrors, chemical and radiation wear, cold cathodes, tissue engineering, etc.) In this paper we report about design, deposition and measurement of properties of optical planar waveguides fabricated from nanocrystalline diamond thin films. The nanocrystalline diamond planar waveguide was deposited by microwave plasma enhanced chemical vapor deposition and the structure of the deposited film was studied by scanning electron microscopy and Raman spectroscopy. The design of the presented planar waveguides was realized on the bases of modified dispersion equation and was schemed for 632.8 nm, 964 nm, 1 310 nm and 1 550 nm wavelengths. Waveguiding properties were examined by prism coupling technique and it was found that the diamond based planar optical element guided one fundamental mode for all measured wavelengths. Values of the refractive indices of our NCD thin film measured at various wavelengths were almost the same as those of natural diamond.

OCIS codes: (230.7390) Waveguides, planar; (220.1920) Diamond machining; (120.5710) Refraction; (220.0220) Optical design and fabrication.

References and links

1. O. A. Williams, A. Kriele, J. Hees, M. Wolfer, W. Mueller-Sebert, and C. E. Nebel, "High Young's modulus in ultra thin nanocrystalline diamond," Chem. Phys. Lett. **495**(1-3), 84–89 (2010).
2. P. Achatz, J. A. Garrido, M. Stutzmann, O. A. Williams, D. M. Gruen, A. Kromka, and D. Steinmuller, "Optical properties of nanocrystalline diamond thin films," Appl. Phys. Lett. **88**(10), 101908 (2006).
3. D. M. Gruen, "Nanocrystalline diamond films," Annu. Rev. Mater. Sci. **29**(1), 211–259 (1999).
4. A. Melloni, R. Costa, G. Cusmai, and F. Morichetti, "The role of index contrast in dielectric optical waveguides," Int. J. Mat. Prod. Tech. **34**(4), 421–437 (2009).
5. I. Bello, Y. M. Chong, Q. Ye, Y. Yang, B. He, O. Kutsay, H. E. Wang, C. Yan, S. K. Jha, J. A. Zapien, and W. J. Zhang, "Materials with extreme properties: Their structuring and applications," Vacuum **86**(6), 575–585 (2012).
6. P. W. May, "Diamond thin films: a 21st-century material," Philos. Trans. R. Soc. Lond. A **358**(1766), 473–495 (2000).
7. P. Djemia, C. Dugautier, T. Chauveau, E. Dogheche, M. I. Barros, and L. Vandenbulcke, "Mechanical properties of diamond films: A comparative study of polycrystalline and smooth fine-grained diamonds by Brillouin light scattering," J. Appl. Phys. **90**(8), 3771 (2001).
8. T. Sharda, T. Soga, and T. Jimbo, "Optical properties of nanocrystalline diamond films by prism coupling technique," J. Appl. Phys. **93**(1), 101–105 (2003).
9. M. Varga, T. Izak, A. Kromka, M. Vesely, K. Hruska, and M. Michalka, "Study of diamond film nucleation by ultrasonic seeding in different solutions," Central European J. Phys. **10**(1), 218–224 (2012).

#183297 - $15.00 USD Received 10 Jan 2013; revised 20 Feb 2013; accepted 28 Feb 2013; published 29 Mar 2013

10. M. Funer, C. Wild, and P. Koidl, "Novel microwave plasma reactor for diamond synthesis," Appl. Phys. Lett. **72**(10), 1149–1151 (1998).
11. R. Ulrich and R. Torge, "Measurement of thin film parameters with a prism coupler," Appl. Opt. **12**(12), 2901–2908 (1973).
12. M. J. Adams, *An Introduction to Optical Waveguides* (John Wiley & Sons Ltd., 1981).
13. V. Prajzler, J. Klapuch, O. Lyutakov, I. Huttel, J. Spirkova, P. Nekvindova, and V. Jerabek, "Design, Fabrication and Properties of Rib Poly(methylmethacrylimide) Optical Waveguides," Radioengineering **20**, 479–485 (2011).
14. M. Bass, C. DeCusatis, J. M. Enoch, V. Lakshminarayanan, G. Li, C. MacDonald, V. N. Mahajan, and E. VanStryland, *Handbook of Optics, Optical Properties of Materials, Nonlinear Optics, Quantum Optics,* (McGraw-Hill 2009).
15. E. D. Palik, *Handbook of Optical Constants of Solids* (Academic Press, 1985).
16. A. Kromka, O. Babchenko, T. Izak, K. Hruska, and B. Rezek, "Linear antenna microwave plasma CVD deposition of diamond films over large areas," Vacuum **86**(6), 776–779 (2012).
17. Z. Remes, H. Kozak, O. Babchenko, S. Potocky, E. Ukraintsev, B. Rezek, and A. Kromka, "Grazing angle reflectance spectroscopy of organic monolayers on nanocrystalline diamond films," Diamond Related Materials **20**(7), 882–885 (2011).
18. D. Franta and I. Ohlidal, "Influence of lateral dimensions of the irregularities on the optical quantities of rough surfaces," J. Opt. A, Pure Appl. Opt. **8**(9), 763–774 (2006).

1. Introduction

Nanocrystalline diamond (NCD) thin films are of special interest in photonics and micro/nanophotonics structures because of their unique properties as low absorption and scattering in wide spectral range, high thermal conductivity, high density, large Young's modulus and high stability under extreme operating conditions [1–3]. The table value of the diamond refractive index is approximately 2.3876 at λ = 1 311 nm. Refractive index of synthetically prepared NCD film usually has lower value but NCD deposited on silica on silicon substrate has still high index contrast. The waveguides created this way are known as high index contrast (HIC) waveguides and have much higher index contrast than common photonic materials (polymers, optical glasses and crystals) [4]. Useful HIC waveguides can be used for small bending radius structures or compact and ultra dense photonics integrated circuits. Because of the combination of high chemical stability and thermal conductivity with attractive optical properties diamond is beginning to find applications in optical components (especially those for IR region) suitable for using in harsh environments [5]. Conventional IR materials such as ZnS, ZnSe and Ge, suffer from the disadvantage of being brittle, easily damaged and having low chemical resistance.

Deposition of thin single-crystalline diamond film has not been up to now fully successful. Recently, fabrication processes of diamond films having NCD and/or ultrananocrystalline (UNCD) structures were presented [6]. Such structures made by an approach based on microwave plasma enhanced chemical vapor deposition (MW PECVD), however only a few of the deposited diamond films had acceptable waveguiding properties.

Here we are going to present NCD planar waveguides, which we proved to support fundamental TE/TM modes in the wavelength range from 473 nm to 1 552 nm. The design of the presented planar waveguides was done on the base of modified dispersion equation and then, an actual NCD film was deposited by microwave plasma enhanced chemical vapor deposition (MW PECVD). This is going to be an approach, different of those already published [7, 8], which will lead to deposition of such diamond layers that would be very close to genuine diamond.

2. Experimental

Before the diamond deposition the surface of silicon substrate (10 × 10 mm^2) was processed by thermal oxidation and 1 420 nm thick silica film was formed. Prepared silica-silicon arrangement was mechanically seeded in an ultrasonic bath in deionized water/UDD (Ultra Dispersed Diamond) powder solution [9]. The NCD deposition was done from a gas mixture of methane and hydrogen (hydrogen gas flow of 400 sccm, methane gas flow of 2 sccm) in a MW PECVD reactor using an ellipsoidal cavity resonator [10]. The deposition was performed

#183297 - $15.00 USD Received 10 Jan 2013; revised 20 Feb 2013; accepted 28 Feb 2013; published 29 Mar 2013

at the total gas pressure of 5 kPa, microwave power of 2 500 W, and the substrate temperature was 990 °C.

The surface morphology and grain size of deposited diamond film were measured by scanning electron microscopy (SEM, e LiNE writer, Raith GmbH) and the diamond character of the films was studied by Raman spectrometer (Renishaw InVia Reflex) with the excitation wavelength of 325 nm.

The TE polarized reflectance spectra were measured under variable angle of incidence in the spectral range of 600-1 200 nm using a prototype spectrometer. The measurement setup uses a halogen lamp as a light source, monochromator with grating blazed at 750 nm, NIR polarizer in rotary mount, simple rotary sample stage with 1° precision and Si photodiode as a detector.

Waveguiding properties of NCD film were examined by using Metricon 2010 prism-coupler system. The apparatus works on a principle of dark mode spectroscopy [11] (see Fig. 1). The measured NCD sample is brought into contact with the base of a couple prisms by means of a pneumatically-operated coupling head. A small air gap between the waveguide film and the prism is formed. A laser beam strikes the base of the prism and is totally reflected at the prism base onto a photodetector. At certain discrete values of the incident angle Θ, called mode angles, photons can tunnel across the air gap into the waveguide film and enter into a guided optical propagation mode, causing a sharp drop of the intensity of light reaching the detector.

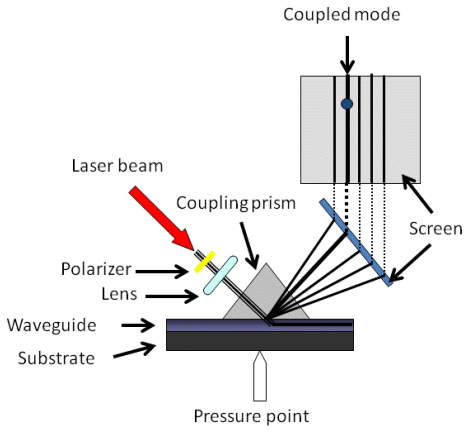

Fig. 1. Schematic view of the dark mode spectroscopy measurement.

3. Results and discussions

3.1 Modeling of the nanocrystalline diamond optical planar waveguides

The dimensions of the waveguides were calculated by using modification dispersion equation [12, 13]. The cross-section view of the design waveguide structure is shown in Fig. 2. Before the deposition, dimensions of the NCD waveguides were designed with help of the refractive index values listed in the tables presented in Table 1.

#183297 - $15.00 USD Received 10 Jan 2013; revised 20 Feb 2013; accepted 28 Feb 2013; published 29 Mar 2013

Fig. 2. Schematic view of the optical planar NCD waveguide structure.

Table 1. Tabular Refractive Indices of the Silicon (Si), Silica (SiO_2) and Natural Diamond (D) Used for Modeling [14, 15]

Wavelength (nm)	Refractive index		
	Si [14]	SiO_2 [15]	*D* [15]
	n_{Si}	n_{SiO2}	n_D
473	4.4676	1.4639	2.4383
632.8	3.8816	1.4570	2.4122
850	3.6621	1.4525	2.3978
964	3.6089	1.4509	2.3939
1260	3.5128	1.4474	2.3882
1311	3.5073	1.4468	2.3876
1552	3.4762	1.4440	2.3855
1625	3.4693	1.4431	2.3851

For the waveguide structure described above, the mode calculations performed for operating wavelengths of 632.8 nm, 964 nm, 1 310 nm and 1 550 nm for TE as well TM polarization are shown in Fig. 3.

From the calculations it follows, e.g., that if we want the deposited film to guide one single mode, the thickness of the diamond film (h_{NCD}) should not exceed 200 nm at 632.8 nm (see Fig. 3(a)) and for the 1 550 nm the diamond film (h_{NCD}) should not be thicker than approx. 450 nm (see Fig. 3(d)). The thickness of the buffer SiO_2 film (h_{SiO2}) was set according to the calculated one, which ensures that the out-coupled energy of the evanescent wave would be less than 1% (This calculation procedure has been already described in [12, 13]). Calculations made clear that to ensure the above-mentioned conditions the thickness of the silica film should not be less than 900 nm for all considered wavelength. Therefore we used silica-on-silicon substrate with thickness of the silica film to be around 1 420 nm, which is fully sufficient.

#183297 - $15.00 USD Received 10 Jan 2013; revised 20 Feb 2013; accepted 28 Feb 2013; published 29 Mar 2013

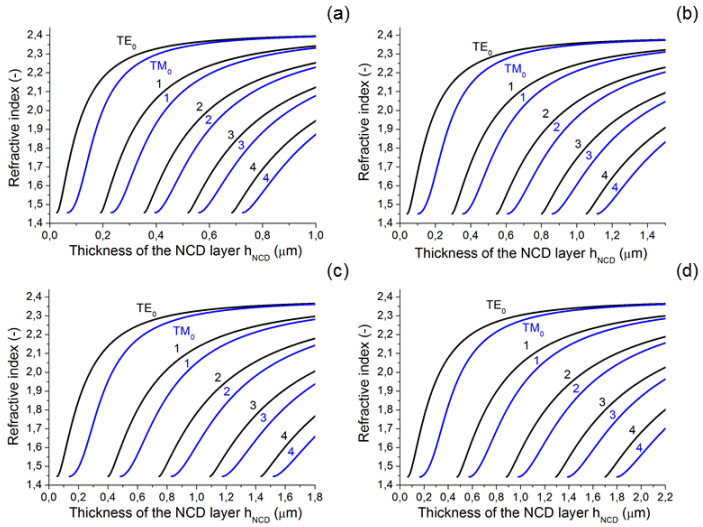

Fig. 3. Mode calculations of the diamond optical planar waveguides, (a) λ = 632.8 nm, (b) λ = 964 nm, (c) λ = 1 310 nm and (d) λ = 1 550 nm.

3.2 Morphology, thickness and optical properties of NCD

Top view SEM image is shown in Fig. 4(a) and the appropriate Raman spectrum in Fig. 4(b). Raman spectrum exhibits two sharp peaks, first one is centered at 521 cm^{-1} and it is assigned to the silicon substrate; the second one centered at 1 332 cm^{-1} is well known as the so called diamond peak and it is related to sp^3 bonds. The wide band located at 1 580 cm^{-1} is known as the G-band ("graphite-band") and is related to the sp^2 phases (i.e. amorphous phases) preferentially localized at grain boundaries [16].

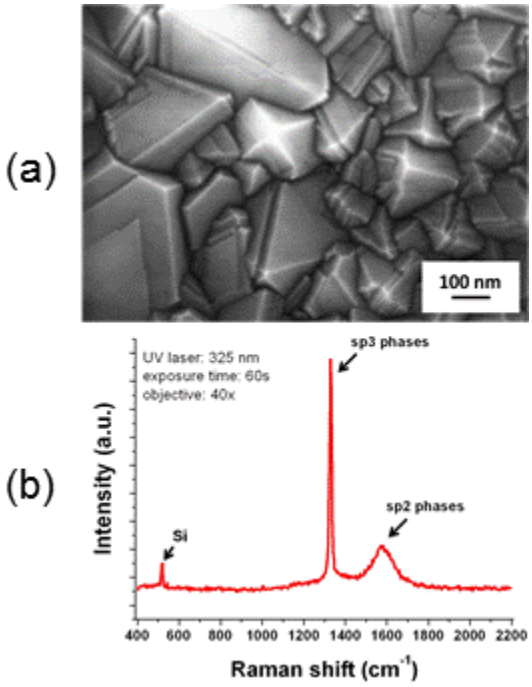

Fig. 4. (a) Top view SEM image and (b) Raman spectrum of the deposited NCD film.

#183297 - $15.00 USD Received 10 Jan 2013; revised 20 Feb 2013; accepted 28 Feb 2013; published 29 Mar 2013

In Fig. 5 we compare the measured and calculated TE reflectance spectra of thin NCD film deposited on silica/silicon substrate. The spectra were measured using TE polarized light under different angles of the incidence. The interferences shift to lower wavelengths with the increasing angle of incidence because of the increased optical path in thin films. Theoretical spectra were calculated with the optical parameters interpolated from Table 1 using commercial software (*Film Wizard*) for advanced modeling of the optical spectra of thin film multilayers. For calculations the effective medium approximation (EMA) was applied [17], to describe the index of refraction of the NCD film supposing that NCD film consists of crystalline diamond with the index of refraction n_D given by Table 1 and the sp^2 phases with the complex index of refraction n_{nonD} of the highly absorbing non-diamond phase at grain boundaries. The unknown Cauchy parameters of the n_{nonD} were found by the fitting procedure:

$$n_{NCD} = \left\{(1-\xi)\sqrt[3]{n_D} + \xi\sqrt[3]{n_{nonD}}\right\}^3 \qquad (1)$$

Here $\xi \in (0,1)$ is a fraction of the sp^2 phase in the NCD film. The index of refraction n_{surf} related to the surface film was modeled within the EMA with the index of refraction given by the formula:

$$n_{surf} = (1+\sqrt[3]{n_{NCD}})^3 / 8 \qquad (2)$$

The thickness of the SiO_2 (1 420 nm), NCD (380 nm) and the surface film (42 nm) as well as the complex index refraction of non-diamond phase and its volume fraction ξ (2%) were optimized during the fitting process. The reflectance spectra measured at angles 20° and 25° were fitted simultaneously. The good agreement between the calculated and measured spectra is shown in Fig. 5 for both angles and it proofs the validity of the estimated thickness and the refraction index shown in Fig. 7. The calculated thickness of the surface film (42 nm) suggests the surface rms roughness to be about 21 nm [18].

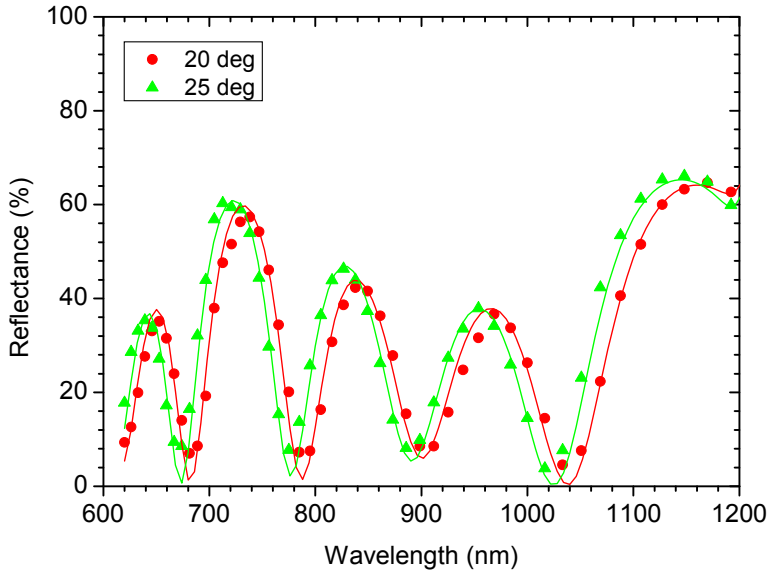

Fig. 5. Measured (scattered points) and calculated (solid curves) TE reflectance spectra of NCD film (calculated thickness 380 nm, surface rms roughness 21 nm) on Si substrate coated by the SiO_2 film (calculated thickness of 1 420 nm) under the angle of incidence of 20 and 25 degrees.

#183297 - $15.00 USD Received 10 Jan 2013; revised 20 Feb 2013; accepted 28 Feb 2013; published 29 Mar 2013

3.3 Waveguiding properties of the NCD film

Waveguiding properties of the NCD films were measured by prism-coupling system at five wavelengths: 473 nm, 632.8 nm, 964 nm, 1 311 nm and 1 552 nm. The obtained data are summarized in Table 2.

Waveguiding measurements of the mode spectra for both polarizations (TE and TM) proved that values of the refractive indices for TE and TM modes are almost identical. Based on this observation, further we present only TE modes. Figure 6 shows TE guided mode spectra for four longer wavelengths.

Table 2. Waveguiding Properties of the Deposited NCD Film: Angle of Incidence of the TE Modes

Wavelength	(nm)	473	632.8	964	1 311	1 552
Angle of incidence	(degree)	–26°42′	–14°28′	–14°31′	–20°58′	–25°16′

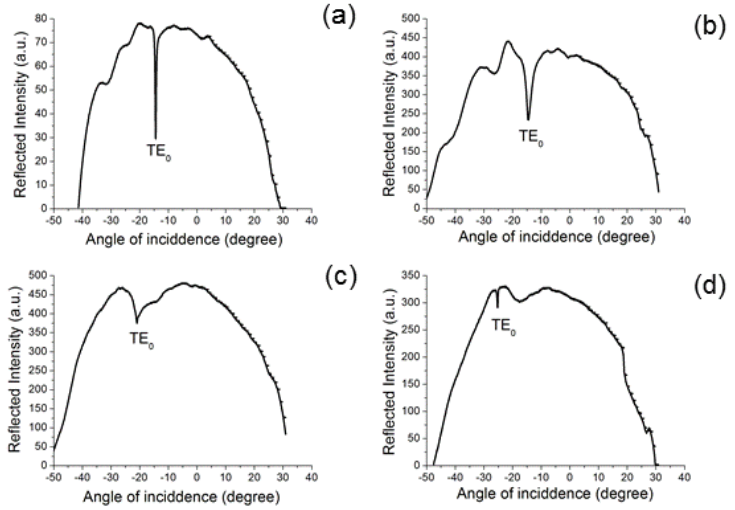

Fig. 6. TE guided mode spectrum for the NCD film at (a) 632.8 nm, (b) 964 nm, (c) 1 311 nm and (d) 1 552 nm.

From results shown in Fig. 6 and summarized in Table 2 it is clearly evident that the NCD films exhibit waveguiding properties. Refractive indices of the deposited films were calculated using the angles given in the Fig. 6(a)-6(d), the wavelengths of the measurement and, if needed, the thickness of the waveguiding films (380 nm). Figure 7 plots refractive indices of the measured NCD film used in this study and data presented in the previously mentioned works [7, 8] are added to compare them with those of the natural diamond [15].

#183297 - $15.00 USD Received 10 Jan 2013; revised 20 Feb 2013; accepted 28 Feb 2013; published 29 Mar 2013

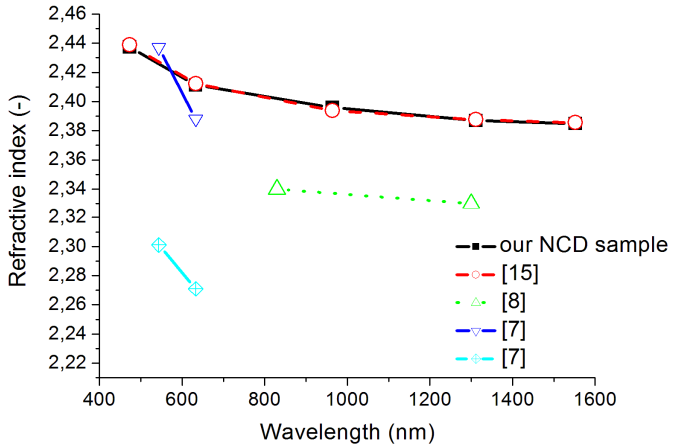

Fig. 7. Comparison of refractive indices of genuine diamond waveguide, our thin film and the films reported in [7, 8, 15]. The indices of our thin film (full line) coincide with those of genuine diamond (dash curve)

According the calculation mentioned above it was expected that the deposited NCD film having a thickness of 380 nm will support 2 TE modes at the wavelengths of 964 nm and shorter. At the longer wavelengths there would be noticeable one TE mode only. However, the measurement showed that the deposited films actually supported always just one mode at all applied wavelengths.

Optical properties of the NCD films examined by prism coupling technique have been reported only by limited number of works [7, 8]. Sharda et al. [8] reported about refractive index measurements at two wavelengths, 830 nm and 1 300 nm for the microcrystalline and nanocrystalline diamond films, with thickness ranging from 883 to 4 100 nm that were deposited on silicon substrate. They found the refractive indices of 2.34 and 2.33 at the wavelenghts of 830 and 1 300 nm, respectively [8]. Djemia et al. [7] reported about refractive index measurements at two wavelengths, 543.5 nm and 632.8 nm, for the polycrystalline and smooth fine-grained diamond films deposited on a titanium alloy by a two step microwave CVD with 2 μm and 5 μm thicknesses of the diamonds films. Their polycrystalline films had the refractive indices of 2.437 and 2.388 at 543.5 and 632.8 nm, respectively. For the smooth fine-grained diamond films they found the values of the refractive indices 2.301and 2.271 at 543.5 and 632.8 nm, respectively.

In comparison with presented works [7, 8] our thin film was grown on the Si-SiO_2 substrate. This approach allows for using wider range of wavelengths for waveguiding, as well as IR spectra measurement. This is of particular interest for sensoric applications. Moreover, in both papers [7, 8] the NCD films were deposited on optically non-transparent substrates, which are rather mirrors and from the text in [7] it is not clear if the conditions for waveguiding properties are fulfilled. What concerns the NCD films deposited on Si [8] there could be found a planar waveguide by the dark mode spectroscopy, however that waveguide cannot be in principle of any practical use. Moreover, our NCD film much more resembles the natural diamond refractive indices than the films reported in [7] and [8], what gives an evidence of its high optical quality.

4. Conclusion

In this paper we presented a modified approach to deposit diamond thin layers. The waveguiding structure of our deposited layers was calculated for various operating wavelengths for TE as well as TM polarization by using modified dispersion equation and

#183297 - $15.00 USD Received 10 Jan 2013; revised 20 Feb 2013; accepted 28 Feb 2013; published 29 Mar 2013

actual waveguiding properties of the deposited Si/SiO_2/NCD planar optical element were confirmed by prism-coupling technique. Even thought that our diamond film was thin (380 nm) and consisted of small grains, a high optical quality of diamond film was confirmed. This was in a good agreement with Raman measurements which detected a sharp diamond characteristic line centered at rounding values 1 332 cm^{-1}. Our Si/SiO_2/NCD planar optical element revealed only one fundamental mode for all the measured wavelengths (473 nm, 632.8 nm, 964 nm, 1 311 nm and 1 552 nm). The comparison with cited references [7, 8] shows the merit of our work, as refractive index of our diamond is very close to the genuine one in spite of the reference above (see Fig. 7). Moreover, we also found that our NCD had a surface conductivity, which makes it potentially interesting for application as new sensors family based of functionalized diamond.

Acknowledgments

This research is supported by the Ministry of Industry and Trade of the Czech Republic under project FR-TI3/797, by the grant CTU no. SGS11/156/OHK3/3T/13 and by the grants P108/11/0794, P108/12/G108, LH12186 (MSMT KONTAKT II). This work was carried out in frame of the LNSM infrastructure.

#183297 - $15.00 USD Received 10 Jan 2013; revised 20 Feb 2013; accepted 28 Feb 2013; published 29 Mar 2013

Available online at www.sciencedirect.com

SciVerse ScienceDirect

Scripta Materialia 68 (2013) 739–742

Scripta MATERIALIA

www.elsevier.com/locate/scriptamat

Electric field-assisted erbium doping of $LiNbO_3$ from melt

J. Cajzl,[a] P. Nekvindová,[a,*] B. Švecová,[a] A. Macková,[b,c] P. Malinský,[b,c] J. Oswald,[d] J. Vacík[b] and J. Špirková[a]

[a]*Department of Inorganic Chemistry, Faculty of Chemical Technology, Institute of Chemical Technology, Technická 5, 166 28 Prague, Czech Republic*

[b]*Nuclear Physics Institute, Academy of Sciences of the Czech Republic, v.v.i., 250 68 Řež, Czech Republic*

[c]*Department of Physics, Faculty of Science, J.E. Purkinje University, České mládeže 8, 400 96 Ústí nad Labem, Czech Republic*

[d]*Institute of Physics, Academy of Sciences of the Czech Republic, v.v.i., Cukrovarnická 10, 162 53 Prague, Czech Republic*

Received 16 October 2012; accepted 4 January 2013
Available online 11 January 2013

This paper presents a new approach for $LiNbO_3$ doping with erbium from melt by means of an electric field-assisted process. The doping was done at medium temperature (350 °C), using a two-component reaction melt containing 10 wt.% $Er(NO_3)_3$. The electric field-assisted procedure substantially reduced the time needed for erbium incorporation into the $LiNbO_3$ surface. After the 25 min procedure, the amount of the in-diffused erbium was as high as 1.4 at.%.

Keywords: Luminescent materials; Rare earth; Crystalline oxides; Ionic diffusion; Electrochemistry

Lithium niobate ($LiNbO_3$) is one of the most widely used materials in optoelectronics and photonics because of its unique combination of special properties—in particular its electro-optic, acousto-optic and ferroelectric effects—as well as its high Curie temperature ($T_c = 1150$ °C). Lithium niobate is often doped with rare-earth elements for use mainly as an optical amplifier or waveguide laser in various telecommunication bands. Er^{3+} ions are frequently utilized as dopants due to their $I_{13/2} \rightarrow I_{15/2}$ transitions, which exhibit emission at 1.5 μm – this wavelength falls into the most widely used C telecom band (window). Erbium-doped lithium niobate (Er:$LiNbO_3$) has, therefore, received much attention. In addition, this material makes it possible to simultaneously amplify and modulate an incoming optical beam.

Erbium doping of lithium niobate straight from a melt of erbium salt is an attractive way of preparing laser-active thin layers. The advantage of this method lies in its significant acceleration of the doping process, and also in the easy and undemanding execution of the experiments. For the preparation of thin layers doped with erbium from melt, several kinds of erbium melts with different melting temperatures of mainly around 350 and 600 °C have so far been used [1–4]. The mechanism of erbium doping into $LiNbO_3$ from melt is assumed to involve either ion exchange of three lithium ions by one erbium ion [4,5] or diffusion of erbium ions into the $LiNbO_3$ substrate [1–3]. Our group has recently reported detailed studies on the possibility of the doping of erbium ions from a melt of erbium salt into the surface of the $LiNbO_3$ substrate [3]. It was demonstrated that the amount of the incorporated erbium and the mechanism – as well as the speed – of the doping process are mostly dependent on the temperature of doping. The in-doped erbium amount is not only influenced by temperature, but is also strongly affected by the concentration gradient of erbium in the reaction melt during the doping process. To a large degree, the concentration gradient can hence be controlled an electric field.

The aim of this paper is to describe experiments involving the erbium doping of $LiNbO_3$ from melt with the assistance of an electric field. The main focus-apart from the performance of the experiments – is on luminescence measurements in the region near a wavelength of 1.5 μm. We measured the concentration-depth profiles of erbium and lithium using Rutherford backscattering spectrometry (RBS) and neutron depth profiling (NDP).

* Corresponding author. Tel.: +420 220444003; e-mail: pavla.nekvindova@vscht.cz

1359-6462/$ - see front matter © 2013 Acta Materialia Inc. Published by Elsevier Ltd. All rights reserved.
http://dx.doi.org/10.1016/j.scriptamat.2013.01.006

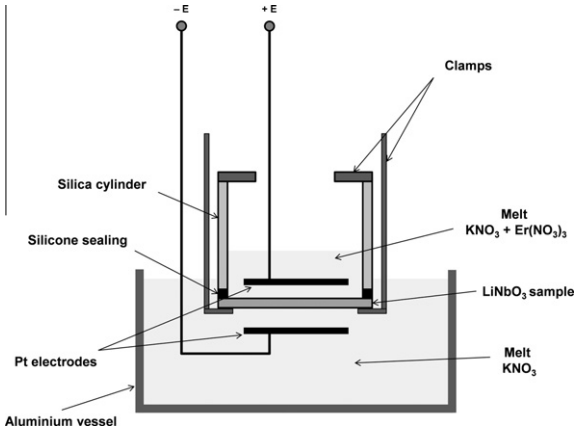

Figure 1. A scheme of the electric field-assisted erbium doping of $LiNbO_3$ from melt.

Electric field-assisted erbium doping of $LiNbO_3$ from melt was carried out at a temperature of 350 °C for about 20–25 min, with a maximum electric voltage of 2000 V and an electric current of about 0.5 mA. Since $LiNbO_3$ is an electrical insulator, it was necessary to use high voltages in these erbium doping experiments. In the first experiments, the high voltages often caused cracking and even breakage of the samples. However, by optimizing the voltage ramp in the first minutes of the experiments, it turned out that damage to the samples could mostly be avoided. In addition, single-crystal $LiNbO_3$ is quite sensitive to temperature changes, so that the samples had to be carefully preheated to the doping temperature before they were submerged into the melt.

In this study, Z cuts $\langle 0001 \rangle$ of $LiNbO_3$ were used. These $LiNbO_3$ single crystals were synthesized by the Czochralski method in Crytur Turnov, Czech Republic. Samples with dimensions of 25 mm × 25 mm × 0.7 mm were cleaned with isopropyl alcohol in an ultrasonic bath. The experiments were carried out in a vertical muffle furnace (see Fig. 1), and the overall process was as follows: (i) salt mixture I was put into an aluminium vessel and salt mixture II was put into a silica beaker. Then the aluminium vessel and the silica beaker were inserted into a muffle furnace and the salt mixtures were melted at a temperature of 350 °C. Salt mixture I (consisting of KNO_3) was used as the anode (−) melt and the salt mixture II (consisting of KNO_3 and $Er(NO_3)_3$, 90:10 wt.%) was used as the cathode (+) melt. (ii) The sample of $LiNbO_3$ was held in an aluminium tool and the silica cylinder was stuck onto the sample with a silicone paste. The inner diameter of the silica cylinder was 18 mm. (iii) Both electrodes were placed onto the aluminium tool. (iv) The aluminium tool with the sample was put into the muffle furnace and the sample was tempered for about 20 min. (v) The tool with the sample was lowered into the aluminium vessel and immersed in melt I. From the silica beaker, melt II was drawn into a pipette and then poured into the silica cylinder (which was positioned on the upper side of the sample). This made it possible to immerse both the lower and the upper sides of the sample in melts I and II, respectively. (vi) By controlling the main electric field, a slow voltage ramp increase was started. The electric current was automatically controlled by the system according to the electric voltage and the electrical conductivity of the system between the electrodes. (vii) When the electric voltage reached the maximum possible value of the electric source, ~2000 V, the corresponding value of the electric current was then maintained at a constant level by manual adjustment of electric voltage for the given time period, ~20-25 min. Throughout the experiment, values of the electric field and current were recorded at 1 min intervals. (viii) After a given time, the electric field was switched off. Melt II in the silica cylinder was removed as quickly as possible by a pipette, and the aluminium tool, with the sample, was taken out of the aluminium vessel (which contained melt I) and out of the furnace. Subsequently, the sample was removed from the aluminium tool and remained tempering while positioned on the silica cylinder. (ix) Finally, the sample was separated from the silica cylinder and the remaining silicone paste was cleaned off with isopropyl alcohol.

Silica-glass samples were utilized to setup the parameters for the electric-field system. The experiments then made use of single-crystal $LiNbO_3$ wafers. This study presents data from three selected experiments that we carried out with $LiNbO_3$ samples. The maximum maintained electric current values, as well as the maximum electric voltage values achieved and the total durations of the experiments with the electrical conductivity values, are summarized in Table 1. The voltage and current behaviors were similar throughout all three experiments. The example of the electric voltage and current behaviors of the third experiment (with the electrical conductivity behavior) are shown in Figure 2. In the first 6 min, the electric voltage and current increased to the maximum value, then the electric current remained constant while the electric voltage slowly decreased – thus the electrical conductivity of the sample increased too. The values of the electrical conductivity were calculated from the electric voltage and current values, and from the diameter of the silica cylinder and the thickness of samples.

According to the literature and our research [5,8,9], post-diffusion annealing of the samples has a positive influence on the luminescence intensity, as well as on

Table 1. The durations, the maximum electric current and voltage values, and the minimum and maximum electrical conductivity values for all three experiments.

Experiment No.	Duration of the experiment [min]	Maximum maintained electric current [mA]	Maximum electric voltage [V]	Minimum electric conductivity [mS m^{-1}]	Maximum electric conductivity [mS m^{-1}]
1	19	0.52	1850	3.06×10^{-4}	2.30×10^{-3}
2	20	0.18	2000	1.96×10^{-4}	9.17×10^{-4}
3	25	0.61	1600	3.13×10^{-4}	1.16×10^{-2}

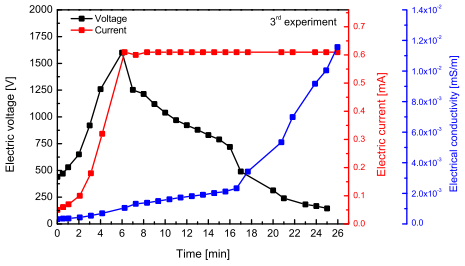

Figure 2. Electric voltage and current behaviors (with the electrical conductivity behavior) of the third experiment.

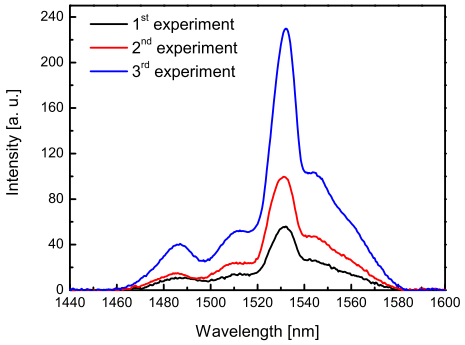

Figure 3. Luminescence spectra of samples from all three experiments annealed at 1000 °C for 5 h in dry oxygen.

other luminescence characteristics. Therefore, all three samples were annealed. The temperature of annealing was set to 1000 °C. The annealing process lasted for 5 h and was carried out in an atmosphere of dry oxygen.

The photoluminescence spectra of the prepared samples were collected within the range of 1440–1600 nm at room temperature. A pulse semiconductor laser, POL 4300, emitting at 980 nm, was used for electron excitation. Luminescence radiation was detected by a two-step-cooled Ge detector J16 (Teledyne Judson Technologies). A double monochromator (SDL-1, LOMO) was used to select specific wavelengths. For the evaluation, all luminescence spectra were transformed to the base level, and after baseline abstraction normalization was performed by means of reference samples.

The concentration-depth profiles of the incorporated erbium were studied by RBS in the Tandetron laboratory, Nuclear Physics Institute of ASCR, Czech Republic. The analysis was performed on a Tandetron 4130 MC accelerator, using a 2.0 MeV He^+ ion beam. He^+ ions, backscattered at a laboratory angle of 170°, were detected. The collected data were evaluated and transformed into concentration-depth profiles using the GISA 3 computer code [6] using cross-section data from IBANDL [7]. The erbium detection limit of this method is between 0.1 and 0.2 at.% – below this limit, erbium cannot be detected with the requisite accuracy due to the statistical noise in the recorded RBS spectrum.

Lithium concentration-depth profiles in the prepared samples were measured by NDP. This technique is based on the reaction of thermal neutrons with ^{6}Li:^{6}Li (n,α) ^{3}H. The fabricated samples were irradiated with a thermal neutron beam from a 6 m long neutron guide (with a neutron intensity of 10^7 neutrons cm^{-2} s^{-2}) and the charged reaction products were recorded by means of a Si (Au) surface barrier detector. The nominal accuracy of the NDP method is 5% of the concentration value of Li, c(Li), the depth resolution is 10 nm. The natural abundance of the "NDP active" ^{6}Li isotope is about 7.5%, but in the actual samples the ^{6}Li/^{7}Li ratio may significantly vary (e.g. due to an artificial depletion of the ^{6}Li isotope from the original natural materials). Therefore, in order to avoid the uncertainty induced by this variation, for some considerations we rely on the relative changes of c(Li) rather than on their absolute values.

The luminescence spectra of the prepared samples were measured in the region around a wavelength of 1.5 μm. After doping, all the samples had zero luminescence intensity with no clear luminescence bands (peaks), and there were also no differences between the three samples. For the recovery of the $LiNbO_3$ structure, all the in-diffused samples were annealed for 5 h at 1000 °C in dry oxygen. The luminescence spectra of the annealed samples are depicted in Figure 3. As can be seen from the spectra, the luminescence intensity is relatively high, and substantially increased as compared to the non-annealed samples; moreover, there are several distinctive luminescence bands (peaks) present. The most intense luminescence band is around 1532 nm, while the other luminescence bands are around 1486 and 1510 nm. The sample with the highest luminescence intensity is from the third experiment.

Erbium concentration-depth profiles of the doped samples showed a curve progression similar to samples prepared by common diffusion techniques, i.e. the highest erbium concentration was located at the surface of the samples and slowly decreased with depth according to a Gaussian-type behaviour. The highest erbium concentration of 1.3 at.% was found in the sample provided by the third experiment, which had the highest maintained electric current (0.61 mA) and lasted the longest (25 min) of all three experiments. The depth at which the highest portion of erbium was found was in the first 40 nm of the surface layer. All three samples exhibited an inhomogeneous distribution of erbium, which was apparent from the "coloured maps" on the surface of the doped samples. Due to this inhomogeneity, the RBS method was inconvenient to measure the erbium concentration in the samples. From successful RBS measurements, it is clear that after doping the maximum depth was about 80 nm and the maximum erbium concentration was as high as 1.4 at.%. All the samples were then annealed at 1000 °C in dry oxygen; the erbium concentration-depth profiles of the annealed samples are shown in the Figure 4. Annealing of the samples caused a lowering of the erbium concentration-depth profiles in the surface layer and the in-diffusion of erbium deep into the sample. In addition, the "coloured maps" on the surface of the samples almost vanished with the annealing.

Lithium concentration-depth profiles were measured by the NDP method in all three samples, both non-annealed and annealed, at 1000 °C. The NDP measurements showed that neither the non-annealed nor the annealed samples exhibited significant lithium depletion in the surface area.

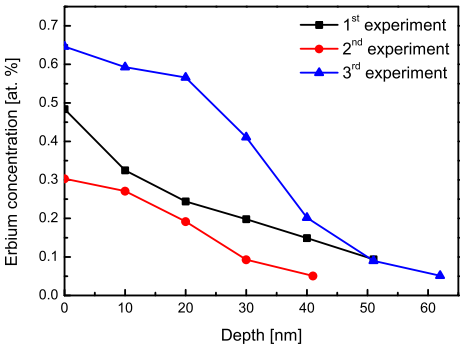

Figure 4. Erbium concentration-depth profiles of samples from all three experiments annealed at 1000 °C in dry oxygen.

Since single-crystal $LiNbO_3$ is a dielectric material with high electrical resistivity, it was interesting to study whether it is possible to use electric-field assistance for erbium doping of $LiNbO_3$ samples from melts and how large the amounts of in-doped erbium would be. By applying the electric field, it is possible to considerably shorten the time needed for erbium doping from melt: in less than 25 min, as much as 1.4 at.% erbium was found in the surface layer, whereas by using the classic non-electric field-assisted doping from melt which we previously reported [3] (which lasts for 168 h = 7 days) a maximum of 7 at.% erbium was obtained in the surface layer.

The values of electrical conductivity for the as-grown $LiNbO_3$ range between 10^{-6} and 10^{-5} mS m^{-1} [5]. Measured values of electrical conductivity in the beginning of our experiments were higher, i.e. of order the order of 10^{-4} mS m^{-1}. Moreover, it can be seen from the electric current and voltage spectra that as the time progresses, the electric voltage lowers, i.e. the electric conductivity of the material rises. The increase in the electric conductivity could be attributed to the influence of the incorporation of erbium ions in the structure of $LiNbO_3$. The incorporation of erbium therefore makes it more likely for charge transfers to occur between ions in the crystal structure.

The lack of luminescence intensity within the as-doped samples was probably caused by a large modification of the surface structure or by the creation of erbium clusters, which induced luminescence quenching [10]. The lack of significant lithium depletion in the doped (and annealed) samples excludes the process of the erbium ion exchange for lithium, thus indicating erbium diffusion into the $LiNbO_3$ structure.

In future experiments, it should be possible to achieve higher amounts of erbium through the use of higher temperatures (>350 °C). Longer durations of the doping experiments with substantially higher electric voltages (the critical effective field or dielectric strength of congruent $LiNbO_3$ is ~5.8 MV m^{-1} [11]) could also be applied to increase the erbium content in the doped samples; the maximum theoretical value of the critical field for 0.7 mm thick, congruently grown $LiNbO_3$ samples would be ~4000 V. Finally, the electrical conductivity is non-negligibly affected by the thickness of the samples: the thicker the samples, the higher the electric currents through the samples, and thus the higher the amount of erbium detected.

The prospect of electric field-assisted erbium doping of $LiNbO_3$ from melt led us to design a new doping method based on our previous laboratory experience with electric field-assisted ion doping of glasses. We were able to successfully establish the optimum conditions for electric field-assisted erbium doping of $LiNbO_3$ from melt based on our experimental findings. The best results were obtained using an electric current of ~0.5 mA and an electric voltage of ~1800 V. The results obtained showed that it is possible to enrich the surface of the $LiNbO_3$ material with erbium by using this electric field-assisted doping from melt method. It was proved that the higher the electric current used during the experiments, the higher the amounts of erbium that were detected on the surface, and thus the higher the luminescence intensity that was measured. The intensity of luminescence around a wavelength of 1.5 μm of the erbium-doped samples was substantially increased by the post-doping annealing, which was done at 1000 °C for 5 h in an atmosphere of dry oxygen. After the annealing, three distinct luminescence peaks, with a narrow peak width of ~9 nm developed, which points to a favourable arrangement of the crystal structure surrounding the erbium ions.

The research has been supported by the Czech Science Foundation under the Projects No. P106/10/1477, Nos. TA01010237, P106/09/0125 and the Project of the Internal Grant Agency of J.E. Purkinje University (IGA UJEP) No. 5322215000301. Some parts of this research were realised at the CANAM LM2011019 (Center of Accelerators and Nuclear Analytical Methods) infrastructure.

[1] V. Peřina, J. Vacík, V. Hnatowitz, J. Červená, P. Kolářová, J. Špirková-Hradilová, J. Schröfel, Nucl. Instrum. Methods Phys. Res. Sect. B 139 (1998) 208.
[2] P. Nekvindová, J. Špirková-Hradilová, J. Schröfel, M. Slunečko, V. Peřina, J. Vacík, Proc. SPIE-Int. Soc. Opt. Eng. (1999) 180.
[3] J. Cajzl, P. Nekvindová, B. Švecová, J. Špirková, A. Macková, P. Malinský, J. Vacík, J. Oswald, A. Kolitsch, Adv. Appl. Electroceram. II: Ceram. Trans. 235 (2012) 95.
[4] C. Sada, F. Caccavale, F. Segato, B. Allieri, L.E. Depero, Opt. Mater. 19 (2002) 23.
[5] K.K. Wong, Properties of Lithium Niobate, first ed., INSPEC, IEE, London, 2002.
[6] J. Saarilahti, E. Rauhala, Nucl. Instrum. Methods Phys. Res. Sect. B 64 (1992) 734.
[7] IBANDL. <http://www-nds.iaea.org/ibandl/>.
[8] A. Meldrum, L.A. Boatner, W.J. Weber, R.C. Ewing, J. Nucl. Mater. 300 (2002) 242.
[9] P. Nekvindová, J. Špirková, J. Červená, M. Budnar, A. Razpet, B. Zorko, P. Pelicon, Opt. Mater. 19 (2002) 245.
[10] D. Boivin, T. Föhn, E. Burov, et al., Proc. SPIE 7580 (2010), http://dx.doi.org/10.1117/12.841369.
[11] A.K. Bandyopadhyay, P.C. Ray, V. Gopalan, Eur. Phys. J. B 65 (2008) 525, http://dx.doi.org/10.1140/epjb/e2008-00356-9.

Optical properties of laser-prepared Er- and Er,Yb-doped $LiNbO_3$ waveguiding layers

2013 Laser Phys. 23 105819

(http://iopscience.iop.org/1555-6611/23/10/105819)

Laser Phys. **23** (2013) 105819 (5pp) doi:10.1088/1054-660X/23/10/105819

Optical properties of laser-prepared Er- and Er,Yb-doped $LiNbO_3$ waveguiding layers

M Jelínek[1,2], J Oswald[1], T Kocourek[1,2], K Rubešová[3], P Nekvindová[3], D Chvostová[1], A Dejneka[1], V Železný[1], V Studnička[1] and K Jurek[1]

[1] Institute of Physics ASCR v.v.i., Na Slovance 2, 18221 Prague 8, Czech Republic
[2] Czech Technical University in Prague, Faculty of Biomedical Engineering, nam. Sitna 3105, Kladno, Czech Republic
[3] Institute of Chemical Technology, Technická 5, 166 28 Prague 6, Czech Republic

E-mail: jelinek@fzu.cz

Received 21 August 2013
Accepted for publication 26 August 2013
Published 17 September 2013
Online at stacks.iop.org/LP/23/105819

Abstract
Doped $LiNbO_3$ films were prepared from Er- and Er,Yb-doped monocrystalline targets using laser ablation. SiO_2/Si was used as a substrate. Polycrystalline films were synthesized at substrate temperatures of 650–800 °C. The influence of the deposition conditions on the film crystallinity, surface morphology, dopant concentration, optical properties (using the *m*-line technique and spectroscopic ellipsometry), and luminescence was studied. The films were luminescent at 1530 nm and were waveguiding.

(Some figures may appear in colour only in the online journal)

1. Introduction

$LiNbO_3$ (LNO) is a material that has unique piezoelectric, optical, and photoelastic properties, and exhibits mechanical and chemical stability. LNO can be used in many applications as a laser frequency doubler, as an optical parametric oscillator (OPO) and a quasi-phase-matched doubler, in information and image storage, for coherent optical amplification, as a waveguide substrate, for SAWs, and so on. By doping $LiNbO_3$ the field of applications becomes much larger. Doped LNO can be used for photorefractive recording (Fe and Mn dopants), for high harmonic generation (Er), for holographic storage (Fe:Cu, Fe, Ce:Cu, Fe:Mn, Ru, Tm, Tb, Ce:Mn, Er), for resistance to powerful light radiation (MgO), in ferroelectric materials (Co), for upconversion (triply doped Tm, Yb, and Nd), for increased photoconductivity (Sc), for increased upconversion (Ho), as a 1.5 μm laser (MgO + Er), for increased photoconductivity (Zn + Nd), for its photorefractive properties (Mn), for second harmonic generation (Zn, Er, and Eu), for two color holograms (Tb), in an OPO (Mg), for holography (Zn:Fe, Cr:Cu, Tb, Fe, Mn, and Ce), for non-volatile holograms (Ru), for holographic gratings (Fe:Mn, Ce:Mn, Ce:Cu, and Fe:Cu), for emission at 1.5 mm (Er), for cw generation at 929 nm (Zn), for cw generation at 1.3 mm (Nd), in lasers in the blue–green spectral domain (Nd + Zn), for surface acoustic waves—SAWs (MgO), in a cw laser (Zn + Nd), and so on.

For this contribution, we studied laser-prepared thin films of Er- and Er,Yb-doped LNO. LNO:Er^{3+} is a key material for devices operating in the third telecommunication window. Yb^{3+} co-doping improves the pumping efficiency [1]. There are not enough experimental data in the field, and systematic characterization is needed [2].

2. Experimental details

Deposition. Our doped LNO films were prepared by KrF excimer pulsed laser deposition (PLD). Two monocrystalline, bulk-doped $LiNbO_3$ targets were used—one was cut from LNO:Er crystal (light violet color, 10 000 ppm of Er), and the second was cut from LNO:Er:Yb (light violet color, 9000 ppm of Yb, 1000 ppm of Er). The layers were fabricated

Table 1. Deposition conditions and optical constants of doped $LiNbO_3$—measured by *m*-line and by spectroscopic ellipsometry (T_S—substrate temperature, thickness*—measured by profilometer, Ra—film roughness, *n*-refractive index, thickness**—calculated). Target $LiNbO_3$: Er–Er = 10 000 ppm, layers LNE—1, 2, 3, 4; target $LiNbO_3$:Er:Yb–Er = 1000 ppm and Yb = 9000 ppm, layers LNE—5, 6, 7, 8.

Deposition of doped $LiNbO_3$					*m*-line			Ellipsometry measurement		
Sample	T_S (°C)	Thickness* (nm)	Ra (nm)	Wavelength (nm)	Mode no.	*n*	Thickness** (nm)	*n*	*k*	Thickness** (nm)
LNE-1	650	1170	2.1	473	—	—	—	—	—	—
LNE-2	700	1060	1.8	633	—	—	—	—	—	—
LNE-3	750	980	2.9	964	2	2.234	1025	2.158	0.008	960
				1552	1	2.212	983	1.891	0.004	
LNE-4	800	1000	3.5	964	3	2.234	1226	2.155	0.008	1065
				1311	2	2.215	1222	1.982	0.003	
				1552	2	2.205	1239	—	—	
LNE-5	650	1040	3.9	—	—	—	—	—	—	—
LNE-6	700	1050	1.4	—	—	—	—	—	—	—
LNE-7	750	1030	3.1	1311	2	2.200	1137	—	—	1100
				1552	2	2.188	1161	1.968	0.006	
LNE-8	800	860	2.9	964	3	2.231	1248	2.211	0.010	910
				1311	2	2.213	1240	2.015	—	
				1552	2	2.203	1251	—	—	

at substrate temperatures, T_S, between 650 and 800 °C on SiO_2/Si(100) substrates—see table 1. The substrate was heated to T_S and cooled down at a rate of 100 °C per 15 min. A laser fluence of 2 J cm^{-2}, an oxygen pressure of 30 Pa and a target–substrate distance of 40 mm were used. Because the refractive index of Si ($n = 3.42$) is higher than that of LNO ($n_0 = 2.29$, $n_e = 2.2$), an appropriate buffer layer is needed for the LNO waveguide structure. An amorphous SiO_2 layer ($n = 1.46$) was found to offer several advantages for this purpose [3]. The thickness of our SiO_2 buffer layer was 3 μm.

Analysis. The film thickness and roughness were determined with an Alpha-step profilometer (Talystep Tencor 500) by scanning a diamond tip (radius 5 mm, 60°) over the 0.5 mm surface layer. For crystallinity measurement, a parallel beam geometry and detector scan with a stationary sample and grazing angle of incidence (GAOI) were used. The topology and dopand concentration were studied using a SEM (scanning electron microscope) (EDAX Jeol Superprobe 733) and a microprobe with a wavelength dispersive spectrometer (WDS). The optical properties, i.e. the refractive index and the thickness of the waveguide films, were measured with the prism coupling method (Metricon model 2010, USA) at five wavelengths (473, 632, 964, 1311, 1552 nm) for both TE and TM polarizations. For waveguides, the Metricon Model 2010 provides a WKB calculation based on Chiang's method [4] of the effective index versus the depth. The accuracy of n_e measurement is ±0.0001 at a wavelength of 632 nm. Variable angle spectroscopic ellipsometry (VASE) measurements were carried out to investigate the optical properties (*n* and *k*) of the LNO thin films. The VASE (J.A. Woollam, Inc.) spectrometer was operated in rotating analyzer (RAE) mode in the spectral range 1–6 eV, at incidence angles 65°, 70°, and 75° at room temperature. The luminescence of erbium in the targets and in the layers was determined by an SDL1 spectrometer between 1450 and 1650 nm. The spectra were excited by a semiconductor laser with an emission wavelength of 980 nm.

3. Results and discussion

Surface morphology. Our films were very smooth (at 400× magnification) with very few small droplets on the surface—see figure 1. At higher magnifications (4000×), the surface resembled strewn sand. At T_S of 800 °C, we observed shallow cracks in the film. The surfaces of films created from an Er-doped target and from an Er,Yb-doped target were very similar. The film roughness Ra was between 2 and 4 nm—see table 1.

XRD. All the prepared samples were polycrystalline. We found a layered two-phase system consisting of LNO and $LiNb_3O_8$ (L8) peaks. As T_S increased, the LNO peaks increased (for both types of targets), relative to the $LiNb_3O_8$ peaks. The best crystallization was found for Er:Yb:LNO layers at the highest T_S (800 °C)—see figure 2. The SiO_2 buffer layer was found to be amorphous. In our previous LNO study, for the same deposition conditions, we found only LNO peaks in the XRD spectra [5]. We can deduce that the development of only the LNO phase of the doped layers is influenced by the dopands.

Composition. Transport in the undoped LNO target material and contamination of the LNO layers have been studied recently [5, 6]. Here, we focused on the transport of dopants. The erbium concentration in one monocrystalline bulk target was 10 000 ppm, i.e. 1 at.%. The concentration of Er and Yb in the other monocrystalline target was 1000 ppm Er and 9000 ppm Yb. Compared with the dopant concentrations in the targets, in the Er:LNO films, we found approximately six-fold lower concentration of Er (0.13–0.16 at.%), and in the Er:Yb:LNO layers, approximately five-fold lower concentration of Yb (0.17–0.19 at.%), The detection limit of the WDS method was 0.02 at.% (0.15 wt%) for Er and 0.005 at.% (0.03 wt%) for Yb. We did not observe any systematic changes in the dopant concentrations with substrate temperature. The concentration

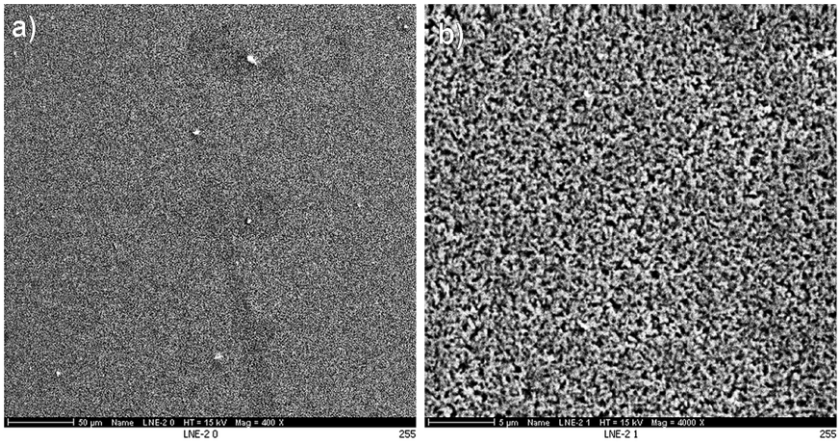

Figure 1. Topology of Er:$LiNbO_3$ film on SiO_2/Si for $T_S = 700\,°C$ (a)—400×, (b)—4000× magnification).

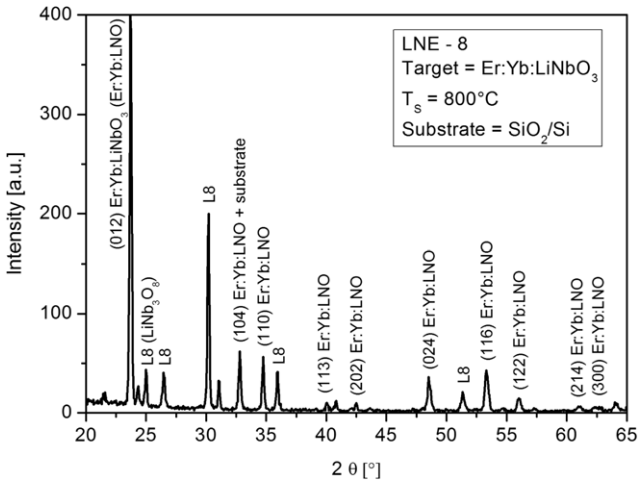

Figure 2. XRD spectrum of Er:Yb:LNO film ($T_S = 800\,°C$, L8 = $LiNb_3O_8$).

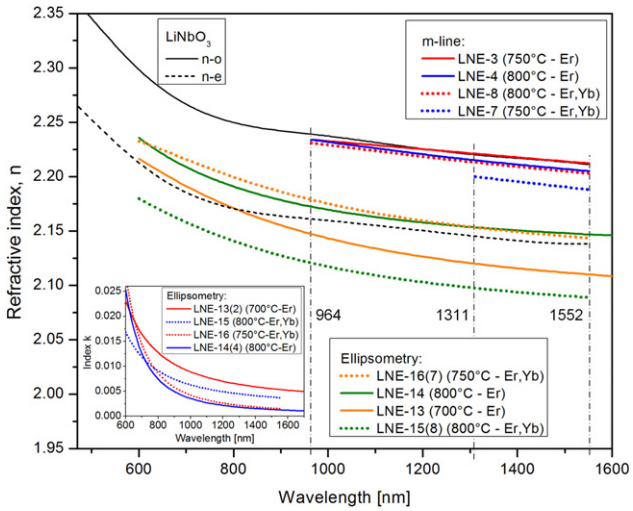

Figure 3. Optical constants (n, k) of Er:$LiNbO_3$ and Er:Yb:$LiNbO_3$ layers measured by spectroscopic ellipsometry and by the *m*-line technique (compared to virgin $LiNbO_3$ [5]).

of Li was stoichiometric and remained unchanged for both targets and both temperatures. We did not observe a decrease in Li in the presence of heavier elements, as was claimed in [7]. The reason could be a higher deposition pressure and a relatively short target–substrate distance.

M-line. Samples created at higher T_S (750 and 800 °C) were waveguiding, for both types of targets (Er- and Er,Yb). It was possible to find one, two, or three waveguide modes, but only at longer wavelengths (964, 1311, and 1552 nm)—see table 1 and figure 3. No waveguiding was found in the visible region. The exciting laser beam was TE polarized. No modes were found for the TM polarization. From this measurement, it follows that the change of refractive index n_o, with T_S, or with target (Er- and Er,Yb) is small. For the doped LNO, the wavelength dependence of n and the measured values are similar to the dependence for the undoped LNO. (This similarity is also confirmed by Metricon measurements of Er:LNO (0.5 at.% of Er) and undoped LNO bulk materials)—see table 2. We can see that the concentration of dopants is too small to have a substantial impact on the refractive index, but it can be deduced that the value of n could strongly depend on the arrangement of grains in the polycrystalline layer. When we can identify three guiding modes in the layer, the accuracy of measurement is ±0.0001 at a wavelength of 632 nm, and we can then calculate the depth profile of the refractive index—see figure 4 and table 1. We see that n is decreases from $n = 2.231$ at the top layer to the value of ∼2 (last mode, close to the substrate). The largest change in n is mainly in the first stage of film growth.

Ellipsometry. Our evaluation of the ellipsometric spectra of the waveguiding layers was performed using a five-phase structural optical model consisting of ambient (air), a surface roughness layer, the LNO layer, the SiO_2 buffer layer and the Si substrate. The roughness layer was taken into account, and on the basis of the effective medium approximation, the roughness layer consisted of 50% of LNO and 50% of void.

The ellipsometric data were analyzed with the software package WVASE32. The obtained effective surface roughness value, ∼50 nm, was mainly caused by near surface inhomogeneity of the film. The calculated LNO thickness ∼750 nm correlates well with the expected value. The

Table 2. Wavelength dependence of the refractive index of both virgin LNO and Er:LNO (Er concentration of 0.5 at.%) bulk crystals for various crystal cuts and beam polarizations measured by the *m*-line technique (Metricon Prism Coupler).

Wavelength (nm)	*n* of Xcut LNO TE	*n* of Xcut LNO TM	*n* of Zcut LNO TE	*n* of Zcut LNO TM	*n* of Xcut + Er:LNO TE	*n* of Xcut + Er:LNO TM
473	2.2645	×	×	×	×	
632	2.2024	×	×	2.2032	2.2024	1.9348
964	2.1614	1.9377	×	2.0163	2.1604	1.9327
1311	2.1455	1.9277	×	2.0025	2.1449	1.9263
1552	2.1370	1.9221	2.2108	1.9958	2.1370	1.9211

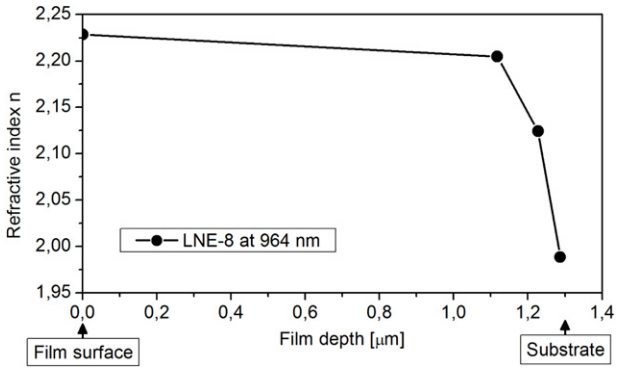

Figure 4. Depth profile of the refractive index (layer LNE-8, $T_S = 800\,°C$).

dielectric functions of the LNO film were fitted by the Cauchy dispersion relation with Urbach tail absorption. The optical model applied to the evaluation of the SE data was additionally improved considering the ∼20 nm intermix region between the SiO_2 and LNO layers. The calculated refractive index and extinction coefficient values are summarized in figure 3 and table 1.

It is observed that ellipsometry gives lower values of the refractive index compared to the *m*-line technique, but the ellipsometry spectral dependence obviously shows similar behavior. (Figure 3 presents the spectral dependence of the refractive index for the bulk [8] from *m*-line and from ellipsometry.) A possible reason for the origin of this discrepancy can be found in the lower sensitivity of the prism coupling technique than in the spectroscopic ellipsometry [9] to sample inhomogeneities and imperfections such as haze, surface roughness, flatness, and thickness variations. In the ellipsometry model, this non-uniformity in depth was partially taken into account with two additional interlayers, while the *m*-line experiments are modeled for a single waveguide core and for the substrate materials. Moreover, the waist of the beam used in our ellipsometric measurements was approximately 2 mm, while in the *m*-line setup, it was approximately 0.1–0.2 mm.

Luminescence. The luminescence related to the $^4I_{13/2}$–$^4I_{15/2}$ transition of Er^{+3} ions was observed on all prepared samples. The luminescence spectra of the prepared layers were compared to target ones—see figure 5(a). The luminescence peaks of the layers are broader than the target ones in contrast to spectra published in [10]. This is probably caused by inhomogeneous broadening in polycrystalline

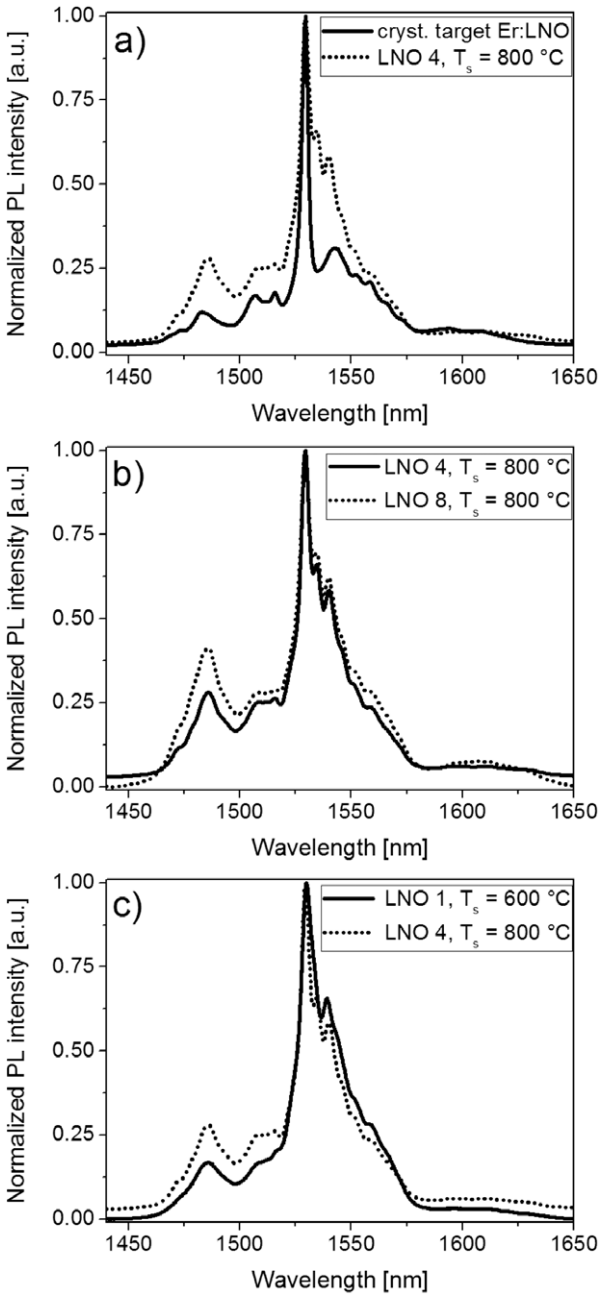

Figure 5. (a) Comparison of the normalized spectra for the crystalline target and LNO four layer; (b) comparison of normalized spectra samples LNO 4 and LNO 8 prepared from different targets at $T_S = 800\,°C$; (c) comparison of normalized spectra samples LNO 1 and LNO 4 prepared from the same target Er:LNO at different temperatures, 600 °C and 800 °C, respectively.

layers due to different crystal field in the vicinity of Er^{+3} ions. The shape of the luminescence spectra of layers prepared at the same temperature was practically independent of the used target—see figure 5(b). The shape of the luminescence spectra only slightly depends on preparation temperature T_S—see figure 5(c). There is a small broadening of the peaks due to the poorer crystalline quality of low temperature layers.

4. Conclusions

Polycrystalline and waveguiding layers of Er:LNO and Er:Yb:LNO were prepared using the pulsed laser deposition method. The $LiNbO_3$ phase, admixed with $LiNb_3O_8$ (L8), was observed by x-ray diffraction measurement. The intensity of doped LNO peaks increased with T_S, while the intensity of the L8 peaks decreased. The films were waveguiding. We observed loss of Er (∼6×) and Yb (∼5×) during transport of material from the targets to the substrate. Two or three waveguide modes at 964, 1311, and 1552 nm were observed by the *m*-line technique at layers created at higher substrate temperatures (750, 800 °C). The spectroscopic ellipsometry measurements essentially confirmed the results obtained by the *m*-line tests. The concentrations of dopants are very low, i.e. the extinction coefficient *k*, measured by ellipsometry, is also very low, and it is close to the value for undoped LNO. We observed luminescence from Er near 1530 nm from all the films. The shape of the signal was similar to that of the targets. The signal can be improved by better optimization of the thickness of the SiO_2 layer [3].

Acknowledgments

We thank the Grant Agency of the Czech Republic for grants P106/10/1477 and P204/11/1011 and the Czech Technical University in Prague for grant SGS 12/167/OHK4/2T/17.

References

[1] Cantelar E and Cusso F 2003 *J. Lumin.* **102/103** 525
[2] Fedorov V A, Korkishko Yu N, Sanz-Garcia J A, Cantelar E, Nevado R, Lifante G and Cusso F 2001 *Appl. Phys.* B **73** 449
[3] Wang X, Ye Z, He J, Cao L and Zhao B 2004 *Mater. Lett.* **58** 3597
[4] Chiang J 1985 *J. Lightwave Technol.* **LT/3** 385
[5] Jelinek M, Havránek V, Remsa J, Kocourek T, Vincze A, Bruncko J, Studnička V and Rubešová K 2013 *Appl. Phys.* A **110** 883
[6] Jelinek M, Kocourek T, Zemek J, Studnička V, Nekvindová P, Remsa J, Vincze A and Havránek V 2011 *E-MRS ICAM IUMRS 2011 Spring Meeting (Nice)* (*Book of Abstracts*) P2-2
[7] Canulescu S, Papadopouiou E L, Anglos D, Lippert Th, Schneider C W and Wokaun A 2009 *J. Appl. Phys.* **105** 063107
[8] Zelmon D E, Small D L and Jundt D 1997 *J. Opt. Soc. Am.* B **14** 3319
[9] www.metricon.com/ellipsometry.html
[10] Grishin A M and Khartsev S I 2012 *Opt. Lett.* **37** 419

Optical Materials 35 (2013) 2540–2543

Contents lists available at ScienceDirect

Optical Materials

journal homepage: www.elsevier.com/locate/optmat

Modified sol–gel preparation of $LiNbO_3$ target for PLD

V. Jakeš [a,*], K. Rubešová [a], J. Erben [a], P. Nekvindová [a], M. Jelínek [b]

[a] Institute of Chemical Technology Prague, Technická 5, 166 28 Prague 6, Czech Republic
[b] Department of Applied Optics, Institute of Physics AS CR, v.v.i., Na Slovance 2, 182 21 Prague 8, Czech Republic

ARTICLE INFO

Article history:
Received 17 January 2013
Received in revised form 13 June 2013
Accepted 24 July 2013
Available online 22 August 2013

Keywords:
Lithium niobate
PLD
Sol–gel
Pechini polyesterification
Transmittance

ABSTRACT

When preparing $LiNbO_3$ thin layer by PLD, the maximal density of polycrystalline target is important. In this work, we prepared the precursor powders by sol–gel method and used them at PLD target synthesis. The gels were synthesized by Pechini polyesterification, using citric acid and ethylene glycol as an organic matrix constituents, and then decomposed using various temperatures (800, 600 and 400 °C) and atmospheres (air, nitrogen and oxygen in sequence). Out of several combinations tested, the decomposition at 800 °C in nitrogen followed by the oxidation at 400 °C in oxygen was found to be the best way to achieve the minimal particle size of powder precursor resulting in denser targets. The prepared targets were characterized by XRD and SEM.

The optimized process was subsequently used for preparation of $LiNbO_3$ target. Thin layers prepared by PLD from this target resulted smoother than the layers prepared from commercial monocrystalline target.

1. Introduction

Lithium niobate, due to its optical properties and the possibility of their tuning by doping, is one of the well-known and widely studied materials for possible photonic applications nowadays [1]. It can be used either as a bulk material or in the form of thin layer in electrical, optical and acoustic applications. Thin films of $LiNbO_3$ have been successfully prepared by various deposition techniques such as chemical vapor deposition [2], liquid phase epitaxy [3], epitaxial growth from melt [4] and sol–gel [5]. Pulsed Laser Deposition (PLD) is considered to be a suitable method, too, since it is able to deposit layers of complex oxide systems and the deposition conditions can be tuned to meet the requests on the resulting layer. So far, the $LiNbO_3$ targets used for PLD were either polycrystalline, prepared by solid state reaction, or monocrystalline, prepared by Czochralski method. As the substrate, either sapphire or Si with the buffer layer of SiO_2 are used [6–9]. Up to our knowledge, targets prepared by sol–gel process have not been used in the PLD.

For preparation of mixed oxides there are several wet synthesis routes, in general called sol–gel methods [10]. Among them, one of the most used in bulk material preparation is so called "modified Pechini method" [11]. The key step in this route is the polyesterification reaction between an α-hydroxycarboxylic acid (e.g. citric acid) and a polyalcohol (e.g. ethylene glycol) in a water solution containing metal ions. Citric acid is used mainly due to its ability to form stable complexes with the majority of metal cations [12]. If the cation is available only in the form of insoluble or hard-to-handle compounds (as is the case of Nb_2O_5 and $NbCl_5$, respectively, the most common compounds of Nb^V), the citrate complex must be prepared separately before the polyesterification reaction itself takes place. In our work, niobium citrate is prepared via the fluorocomplexes of niobium (V) and so called niobic acid ($Nb_2O_5{\cdot}xH_2O$) [13].

With a view to the pulsed laser deposition (PLD) of niobate thin layers, the bulk density/porosity of the target could be one of the crucial parameters that influence the quality of prepared film. To achieve the minimal porosity of a target, precursor grain size should be minimal to enhance solid state reaction and densification at the sintering of the final target.

From this point of view, sol–gel methods are well applicable in powder precursor preparation. The precursors not only have the advantage of high chemical homogeneity, but they are also of smaller grain size and highly reactive, in comparison to the precursors prepared by solid state reaction. In addition to it, the particle size of the precursor can be further decreased by the decomposition of a gel in appropriate atmosphere [14]. And last but not least, sol–gel method is a low-temperature and cost-effective process.

In this work, the improvement of the Pechini method is suggested as a new approach to $LiNbO_3$ targets fabrication by sol–gel technique. The main attention is paid to the influence of decomposition/oxidation atmosphere and temperature on the grain size of precursor powder. Our optimized procedure was then

* Corresponding author. Tel.: +420 220 443 765.
E-mail address: vit.jakes@vscht.cz (V. Jakeš).

0925-3467/$ - see front matter © 2013 Elsevier B.V. All rights reserved.
http://dx.doi.org/10.1016/j.optmat.2013.07.019

used at $LiNbO_3$ target preparation, which, as far as we know, is the first time PLD target was prepared by sol–gel method. This target was used to deposit thin layers of $LiNbO_3$ by PLD. The quality of prepared thin films was compared with those prepared using monocrystalline target.

2. Experimental

2.1. Target preparation

$LiNbO_3$ precursor powders were prepared by the Pechini polyesterification. The solution of niobium (V) was prepared in the following way: Nb_2O_5 was first dissolved in concentrated hydrofluoric acid at 80 °C and then precipitated in the form of $Nb_2O_5{\cdot}xH_2O$ by the addition of concentrated ammonia. Afterwards, the precipitate was filtered and washed, first by diluted ammonia (5% w/w solution) to remove fluoride anions (in the form of ammonium fluoride), and then thoroughly washed by water (to remove the residual ammonia). After filtration and washing, $Nb_2O_5{\cdot}xH_2O$ was immediately dissolved in the water solution of citric acid (molar ratio Nb:citric acid = 1:4) at 90 °C. After complete dissolution, Li_2CO_3 and ethylene glycol were added (molar ratio citric acid:ethylene glycol = 1:4) and the solution was heated first at 80 °C to remove solvent water. Then the temperature was raised up to 130 °C to promote a polyesterification reaction. Conditions of a subsequent thermal/atmosphere processing are summarized in Table 1 together with samples marking. Next to these samples, a reference sample LN–Air was prepared with decomposition of the precursor powder in air for 2 h at 500 and 800 °C. Due to lithium loss during the PLD process, all samples contained additional 10% (w/w) of lithium. The last step in the samples preparation was the sintering of pressed pellets at 1100 °C in air for 12 h.

2.2. Deposition

The final target for PLD was prepared using selected gel decomposition process as described in the Results part (3 h at 800 °C in nitrogen, followed by 1 h at 400 °C in oxygen). The target was doped with 10% (w/w) excess of Li^+. From the prepared target, thin layers were prepared using KrF excimer PLD and their roughness and thickness were compared with layers prepared from commercial monocrystalline target. The layers were deposited on SiO_2/Si or sapphire (0001) substrates at the temperatures of 650, 700 and 750 °C. Laser frequency used was 10 Hz and its fluency was 2 J cm^{-2}. The distance target-substrate was 40 mm and the deposition took place in oxygen atmosphere with the gas pressure of 30 Pa.

2.3. Samples characterization

The phase composition of sol–gel prepared samples was determined by XRD. The device used was X'pert Pro θ–θ powder diffractometer with parafocusing Bragg–Brentano geometry using Cu Kα radiation (λ = 1.5418 Å, U = 40 kV, I = 20 mA). Data evaluation was performed in the software package HighScore Plus. Scanning electron microscopy was carried out using TESCAN Vega3 equipped with an EDS analyzer (Oxford Instruments INCA 350). All presented pictures were taken in secondary electrons regime.

Deposited film thickness and roughness were measured by Alpha-step profilometer (Talystep Tencor 500) with diamond tip (radius 2 μm, 60°). Optical transmission was measured by Shimadzu spectrometer UV 1601 in the wavelength range 200–1100 nm.

Table 1
Heat treatment of the samples.

Air	N2	O2	Sample
240 °C	800 °C	400 °C	LN 8/4
2 h	3 h	1 h	
		600 °C	LN 8/6
		1 h	
	600 °C	400 °C	LN 6/4
	3 h	1 h	
		600 °C	LN 6/6
		1 h	

3. Results

Precursor gels were prepared by sol–gel process and after drying in the air at 240 °C, they were decomposed in various atmospheres and temperature regimes according to Table 1. From these precursor powders, final samples were sintered and their phase composition was determined by XRD. Since all the obtained patterns were very similar, only the pattern of sample LN 6/6 is shown in Fig. 1. All prepared samples were almost monophase, they contained pure $LiNbO_3$ phase with the traces of Li_3NbO_4. This is caused by the necessary excess of lithium needed at PLD deposition and corresponds with the phase diagram Li_2O–Nb_2O_5 [15].

The sintered samples were cross cut and after polishing observed by SEM (selected photos shown in Figs. 2 and 3). Using the ImageJ software, porosity of the samples was calculated, the results are shown in Table 2. As can be seen, the sample prepared in 800 °C (N_2)/400 °C (O_2) regime is the least porous, with less than 30% pore area, compared to the other samples that had a larger pore area. This can be attributed to the fact that, in nitrogen atmosphere, the organic matrix decomposes but the amorphous carbon remains within the sample, creating barrier that impedes the sintering of precursor grains at high temperature. Later, when treating the sample in oxygen atmosphere, considerably lower temperature is sufficient to oxidize the carbon, but it is not high enough to sinter the grains.

Supposedly, the smaller the grains the better is their packing and as a consequence, the smaller pores are formed and consequently the higher density is achieved. When treating the precursor at 600 °C in nitrogen, the organic matrix is not decomposed sufficiently and the following treatment in oxygen results in

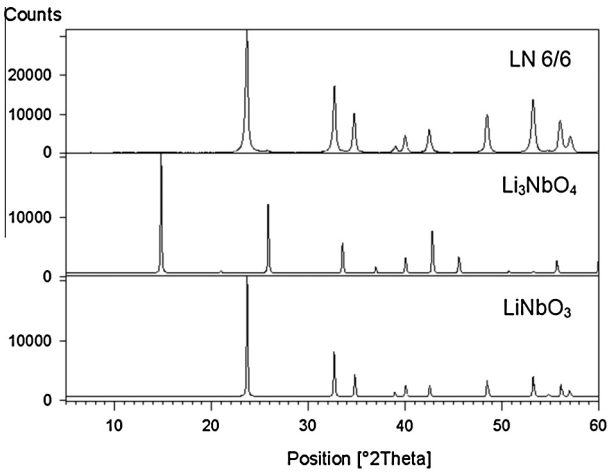

Fig. 1. XRD pattern of selected sample (LN 6/6) and reference patterns of $LiNbO_3$ and Li_3NbO_4.

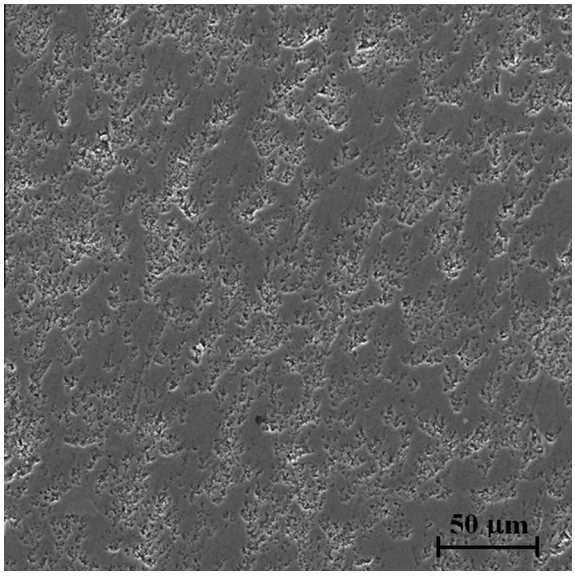

Fig. 2. SEM photograph of the polished sample LN 8/4 (500× magnification).

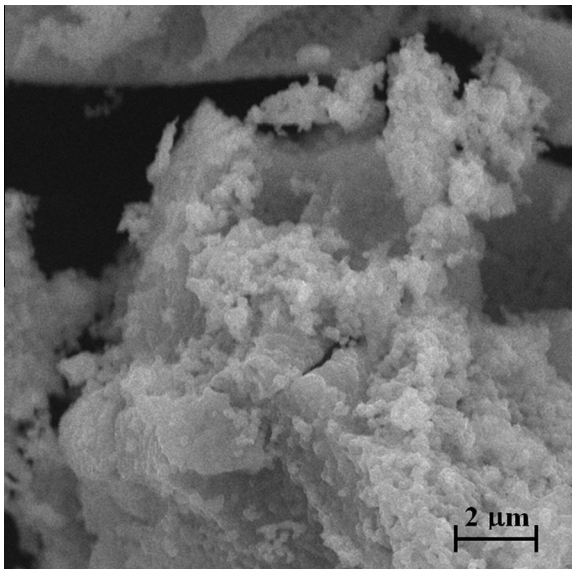

Fig. 4. SEM photograph of the precursor powder LN–Air (10k× magnification).

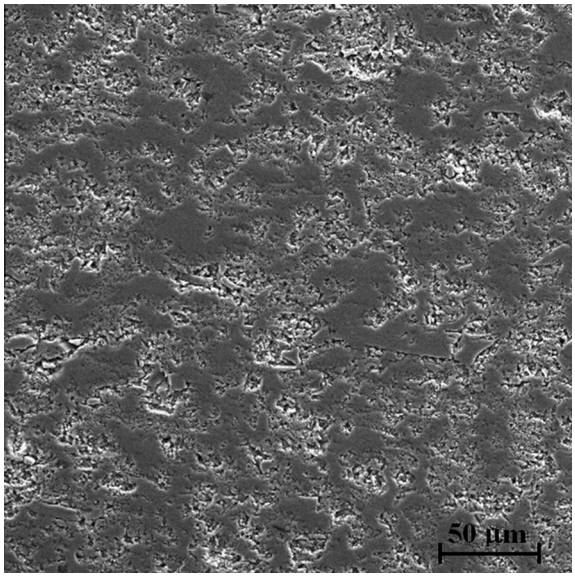

Fig. 3. SEM photograph of the polished sample LN 6/4 (500× magnification).

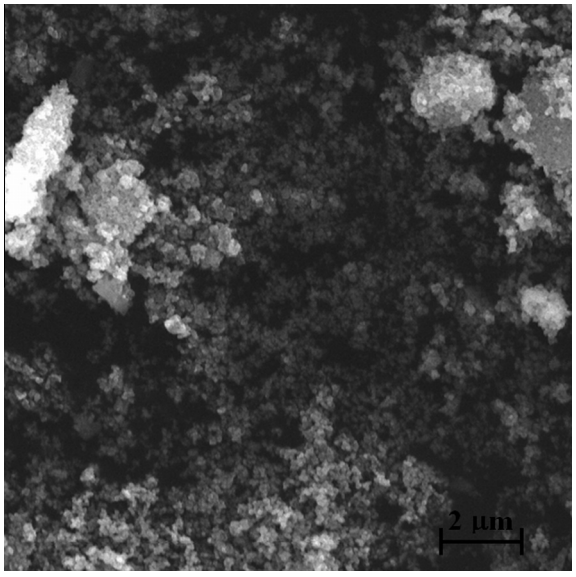

Fig. 5. SEM photograph of the precursor powder LN 8/6 (10k× magnification).

Table 2
Porosity of the prepared samples.

Sample	Porosity (%)
LN–Air	33
LN 6/4	53
LN 6/6	43
LN 8/4	29
LN 8/6	40

exothermic process within the sample. The elevated temperature then leads to further sintering of the grains. This fact is illustrated in Figs. 4 and 5, where the difference in grain size of the precursor powders is evident.

Using the most efficient regime of gel decomposition (800 °C in N_2/400 °C in O_2), target for PLD was prepared and used for deposition of thin films on SiO_2/Si and sapphire (0001) substrate at various substrate temperatures (650, 700 and 750 °C). Table 3 shows the marking of the samples. The same table summarizes the roughness and thickness of the prepared thin layers. All layers deposited from our polycrystalline target were thicker than the layers from monocrystalline target. The roughness of the layers deposited on SiO_2/Si substrate was lesser compared to corresponding layers deposited from the monocrystal.

Visually, all layers were shiny, but layers prepared from polycrystalline target appeared darker compared to layers from the monocrystal. The transmission spectra of the films deposited on sapphire substrate were collected. These measured spectra are shown in Fig. 6. All samples started to be transparent in the wavelength range from 280 to 300 nm.

Table 3
Summary of deposition conditions, roughness and thickness of the samples.

Target	$LiNbO_3$ monocrystal						$LiNbO_3$ (polycrystalline, sol–gel)					
Substrate	SiO_2/Si			Sapphire (0001)			SiO_2/Si			Sapphire (0001)		
Sample No.	1	2	3	4	5	6	7	8	9	10	11	12
Substrate temperature (°C)	650	700	750	650	700	750	650	700	750	650	700	750
Film thickness (nm)	500	700	600	500	600	600	1050	1000	1000	750	1000	1000
Film roughness (nm)	4	2	3	2	2	2	2	1	1	2	4	3

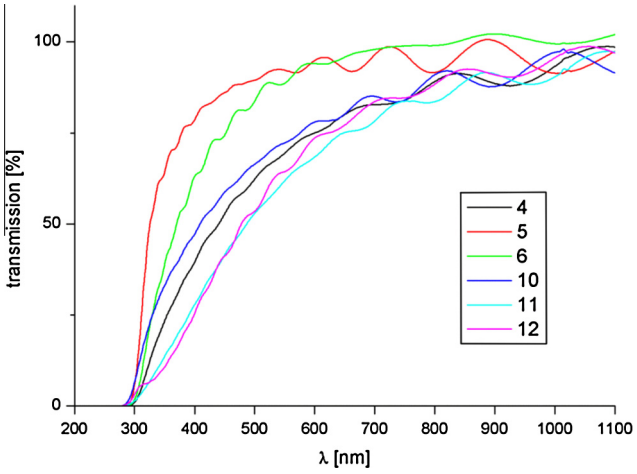

Fig. 6. Transmission spectra of $LiNbO_3$ layers prepared on sapphire substrate.

4. Conclusions

With respect to the minimal porosity of the sintered samples, the thermal processing of sol–gel prepared samples was investigated. After the preparation of the samples by Pechini polyesterification, the precursor gels were heat treated for 3 h in nitrogen at 600 or 800 °C followed by 1 h treatment in oxygen at 400 or 600 °C. From the SEM micrographs of the precursor powders and the polished sintered samples, the combination 800 °C (N_2) and 400 °C (O_2) was chosen as the most effective.

This heat treatment sequence was then used to prepare $LiNbO_3$ target doped with 10% Li^+ (w/w) that was subsequently used for deposition of thin layers to SiO_2/Si and sapphire (0001) substrate. The transmission, roughness and thickness of thin layers deposited from this target were compared with layers deposited under the same conditions from commercially available monocrystalline $LiNbO_3$ target. The layers prepared using our polycrystalline target were smoother and thicker than those deposited from $LiNbO_3$ monocrystal under similar conditions.

Acknowledgement

This work was supported by the Grant Agency of the Czech Republic as Grant No. P106/10/1477.

References

[1] L. Arizmendi, Phys. Stat. Sol. A 201 (2004) 253.
[2] M. Kadota, Y. Suzuki, Y. Ito, Jpn. J. Appl. Phys. 50 (2011) 07HD10.
[3] Y. Lu, P. Dekker, J.M. Dawes, J. Cryst. Growth 311 (2009) 1441.
[4] T. Kawaguchi, D.H. Yoon, M. Minakata, Y. Okada, M. Imaeda, T. Fukuda, J. Cryst. Growth 152 (1995) 87.
[5] S. Satapathy, P. Verma, P.K. Gupta, C. Mukherjee, V.G. Sathe, K.B.R. Varma, Thin Solid Films 519 (2011) 1803.
[6] X. Wang, Z. Ye, G. Li, B. Zhao, J. Cryst. Growth 306 (2007) 62.
[7] S. Shandilya, K. Sreenivas, R.S. Katiyar, V. Gupta, Indian J. Eng. Mater. Sci. 15 (2008) 355.
[8] G.C. Budakoti, R.S. Rawat, J. Cryst. Growth 310 (2008) 4205.
[9] J.-W. Son, S.S. Orlov, B. Phillips, L. Hesselink, J. Electroceram. 17 (2006) 591.
[10] M. Kakihana, J. Sol–Gel Sci. Technol. 6 (1996) 7.
[11] M.P. Pechini, Inventor; sprague electric company assignee. US patent No. 3330697, July 11 (1967).
[12] L.G. Sillén, A.E. Martell, J. Bjerrum, Stability Constants of Metal–Ion Complexes, Chemical Society, London, 1964.
[13] D. Dhak, S.K. Biswas, P. Pramanik, J. Eur. Ceram. Soc. 26 (2006) 3717.
[14] K. Rubešová, T. Hlásek, V. Jakeš, D. Sedmidubský, J. Hejtmánek, J. Sol–Gel Sci. Technol. 64 (2012) 93.
[15] L.O. Svaasand, M. Eriksrud, G. Nakken, A.P. Grande, J. Cryst. Growth 22 (1974) 230.

Optical Materials 36 (2013) 402–407

Contents lists available at ScienceDirect

Optical Materials

journal homepage: www.elsevier.com/locate/optmat

Erbium diffusion from erbium metal or erbium oxide layers deposited on the surface of various $LiNbO_3$ cuts

P. Nekvindova [a,*], J. Cajzl [a], B. Svecova [a], A. Mackova [b,c], P. Malinsky [b,c], J. Oswald [d], J. Vacik [b], J. Spirkova [a]

[a] Department of Inorganic Chemistry, Faculty of Chemical Technology, Institute of Chemical Technology, Technicka 5, 166 28 Prague, Czech Republic
[b] Nuclear Physics Institute, Academy of Sciences of the Czech Republic, v.v.i., 250 68 Rez, Czech Republic
[c] Department of Physics, Faculty of Science, J.E. Purkinje University, Ceske mladeze 8, 400 96 Usti nad Labem, Czech Republic
[d] Institute of Physics, Academy of Sciences of the Czech Republic, v.v.i., Cukrovarnicka 10, 162 53 Prague, Czech Republic

ARTICLE INFO

Article history:
Received 15 January 2013
Received in revised form 13 September 2013
Accepted 30 September 2013
Available online 30 October 2013

Keywords:
Lithium niobate
Erbium
Erbium oxide
Diffusion doping
Luminescent materials

ABSTRACT

In this paper the doping of erbium from thin layers deposited on the $LiNbO_3$ surface with an emphasis on the relations between changes in the $LiNbO_3$ structure and the luminescence properties of Er:$LiNbO_3$ have been studied. The erbium-containing layers were primarily characterised in terms of the luminescence at 1.5 μm. The obtained results showed a high level of structural ordering in the samples after indiffusion of Er at high-temperature. This was apparent from the luminescence results, where more than 6 quite narrow luminescence bands were found, and also from the RBS/channeling analysis which showed, that the doped structure has similar degree of ordering as the bulk crystal $LiNbO_3$. In terms of luminescence intensity at 1.5 μm a better source for the erbium doping seems to be the erbium oxide layer. The highest luminescence intensity values were among the cuts achieved in the *Z* cut.

1. Introduction

Lithium niobate ($LiNbO_3$, LN) is a well-known material in the field of photonics because of its ability to combine active and passive optical beam control [1]. In order to create an optically active material that could be used as an optical amplifier or waveguide laser, the LN is doped with laser-active ions such as erbium to form erbium-doped lithium niobate (Er:$LiNbO_3$ or Er:LN) [2–5].

Currently, there are several methods used for erbium doping [6–8]. The doping from a thin erbium metal film, deposited on the substrate surface, is the first and thus far the most common approach for introducing erbium into the lithium niobate. Another suitable source of doping has been found in erbium oxide [7]. Thin layers prepared in this way were investigated in detail; it was found that the concentration of erbium reached approximately 0.1–0.2 at.% at a depth of several microns (i.e., up to 6 μm) and such erbium-rich layers displayed high-intensity luminescence at 1.5 μm [8]. A study of the structure of the doped layers revealed that erbium atoms preferentially occupied the lithium sites [9]. The implantation of erbium ions into the lithium niobate [10,11] and the diffusion of erbium ions from a melt of erbium containing salts [12,13] are also known.

For several years, we have utilised an alternative method of Er:LN-layer fabrication with emphasis on the relations between the changes in the LN structure and the luminescence properties of Er:LN. We have also considered possible ways to influence the luminescence properties by modifying the crystal field surrounding the erbium ions. We have already reported the doping from the melt [14,15] and the techniques of ion implantation [16–18] into various LN cuts. In order to make the subject of our interest more complete, we have performed some experiments using the techniques of doping from a thin Er metal film deposited on various LN cuts.

In this paper, we present the results of our experiments carried out on the doping of erbium from the thin layers deposited on the LN surface, the layers being either Er metal or Er_2O_3. The layers used as the doping source had a thickness of 10 and 20 nm. The erbium-containing layers were primarily characterised in terms of their luminescence at 1.5 μm. The concentration depth profiles of erbium and lithium in the doped samples and the changes of their structure were also investigated. An entirely new idea was to compare the results of such doping into commonly used and specially designed lithium niobate substrate cuts to see the possible differences arising from the migration of the incorporated erbium ions through a differently oriented crystalline matrix.

2. Experiments

For the experiments, we used wafers of LN with various crystallographic orientations (pulled by the Czochralski method) supplied by Crytur Turnov (Czech Republic). The wafers were oriented and

* Corresponding author. Tel.: +420 220 444 003; fax: +420 224 311 010.
E-mail address: pavla.nekvindova@vscht.cz (P. Nekvindova).

0925-3467/$ - see front matter © 2013 Elsevier B.V. All rights reserved.
http://dx.doi.org/10.1016/j.optmat.2013.09.027

labelled as follows: standard X cut $\langle 11-20\rangle$ and Z cut $\langle 0001\rangle$, and specially executed Y cuts with respect to the cleavage plane of the LN crystal, namely a parallel Y_{II} cut $\langle 10-12\rangle$ and perpendicular $Y_{\perp}$ cut $\langle 10-14\rangle$. All wafers were polished on both sides, with one side polished to optical quality. The dimensions of the wafers were 12×7 mm with a thickness of 0.7 mm.

The experimental conditions of the erbium doping from thin erbium metal and oxide films deposited on the crystal surface were chosen according to an already published experiment [7]. The thicknesses of the deposition source layers were 10 nm and 20 nm for both Er metal layers and Er_2O_3 layers (custom-made by Crytur Turnov – Czech Republic by magnetron sputtering on the crystal surface). For these experiments, only Z cuts were used. The diffusion of erbium from both kinds of layers was carried out at 1060 °C for 100 h in a tube furnace in a dry O_2 atmosphere. These experiments were repeated in order to verify the results. Based on previous results, further studies were conducted only with samples doped from 20-nm thick layers. Using these samples, we focused on the behaviour of the different cuts. The experiments were performed with the X, Z, Y_{II}, $Y_{\perp}$ cuts of $LiNbO_3$.

The concentration depth profiles of the incorporated erbium atoms were studied by Rutherford Backscattering Spectroscopy (RBS) at the Nuclear Physics Institute in Řež, Czech Republic. The analysis was performed by the Tandetron 4130 MC accelerator using a 2.0 MeV He^+ ion beam. He^+ ions incoming at normal incidence were backscattered and detected at a laboratory angle of 170°. The RBS spectra were evaluated using the GISA 3.99 [19] code utilising cross-section data from IBANDL [20]. The RBS depth resolution is better than 10 nm and the detection limit of Er concentration in this case is about 0.1 at.%. The detection limit mentioned above can be achieved for the region of backscattered He^+ ions, where the Er signal is not overlapped by the Nb signal from the LN substrate. Consequently, this detection limit for Er is implementable up to an analytical depth of about 150 nm. In order to study the changes in the lithium niobate structure caused by the erbium in-diffusion, the RBS/channelling measurements, using a 1.7 MeV He^+ beam from the Van de Graaff accelerator in the Helmholtz-Zentrum Dresden Rossendorf, Germany, were performed. The value of the minimal yield χ_{min} was determined by the integration of the regions of interest in random and aligned spectra using the usual procedure reported, e.g., in [21].

The lithium concentration depth profiles in the prepared samples were measured by Neutron Depth Profiling (NDP). The method is based on a reaction of a thermal neutron with ^6Li:$^6Li(n,\alpha)\,^3H$. The fabricated samples were irradiated with a thermal neutron beam from a 6-m long neutron guide (the neutron intensity was 10^7 nth $cm^{-2}\,s^{-1}$) and the charged reaction products were recorded by a Hamamatsu PIN diode detector. The nominal accuracy of the NDP method is ~5% of the concentration value of Li, c_{Li}; the nominal depth resolution is ~10 nm.

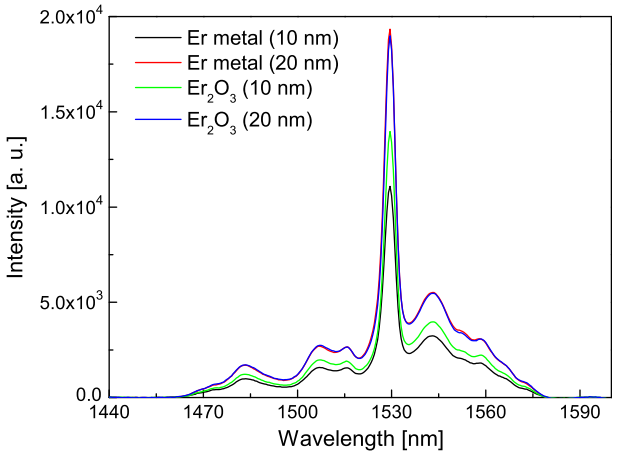

Fig. 1. The luminescence spectra of the erbium-doped LN samples prepared by doping from the erbium metal and erbium oxide layers deposited on the Z cut of LN. (*Experimental conditions*: 1060 °C; 100 h; atm. O_2.)

Table 1
The comparison of luminescence intensity at 1529 nm of the erbium-doped samples prepared from the 20-nm thick layers of Er metal or Er_2O_3 deposited on the surface of various LN cuts. (*Experimental conditions:* 1060 °C; 100 h; atm. O_2.)

Er sources	Z cut	X cut	$Y_{\perp}$ cut	Y_{II} cut
Luminescence intensity (rel.%)				
Metallic Er	100	16	81	43
Er_2O_3	100	10	60	40

The photoluminescence spectra of the prepared samples were collected within the range of 1440–1600 nm at room temperature. A pulse semiconductor laser POL 4300 emitting at 980 nm was used for the excitation of the electrons. The luminescence radiation was detected by a two-step-cooled Ge detector J16 (Teledyne Judson Technologies). To scoop specific wavelengths, a double monochromator SDL-1 (LOMO) was used. For the evaluation, all of the luminescence spectra were transformed to the base level and the baseline was abstracted.

3. Results

3.1. Luminescence properties

Fig. 1 shows a comparison of the luminescence spectra in the region around 1.5 μm for samples prepared by erbium diffusion from an Er metal layer and an Er_2O_3 layer of various thicknesses. It is obvious that all samples revealed the highest intensity at a wavelength of 1529 nm. Moreover, there are evident 6 emission bands with a narrow spectral width at wavelengths of 1483 nm, 1507 nm, 1516 nm, 1529 nm, 1543 nm and 1559 nm. The measured spectra are similar to the spectra obtained from a bulk-doped Er:LN crystal [14,22]. As expected, the luminescence intensity corresponded well with the thicknesses of the deposited source layers, i.e., the intensity was always higher for the 20-nm thick source layers. The comparison of both erbium sources is not so ambiguous. The luminescence intensity at 1529 nm was higher for the 10-nm thick Er_2O_3 deposited layers than for the 10-nm thick metal deposited ones. No differences between the luminescence intensity of the two erbium sources were observed for the 20-nm thick source layers. To verify the results, we repeated the experiments with the second set of the LN wafers, which proved the results described above.

The behaviour of variously oriented LN cuts was studied using the samples that were doped from 20-nm thick films of both erbium metal and erbium oxide; the doping conditions were otherwise identical. The resulting luminescence spectra showed similar shapes of the luminescence spectra with the 6 above-described narrow luminescence bands for all the samples. The spectra of the various cuts differed especially in the intensity of the 1529 nm band, which was the highest in the Z cuts for both types of the doping sources. Values of the intensity of luminescence at 1529 nm are stated in Table 1. Data are compared to the Z cut which luminescence intensity was considered to be 100%.

3.2. Erbium concentration in the prepared layers

In Fig. 2, the RBS spectrum of the Er metal layer deposited before the actual diffusion was compared with that of the erbium-containing layer after the diffusion. The random RBS spectrum of the sample with the deposited erbium layer clearly

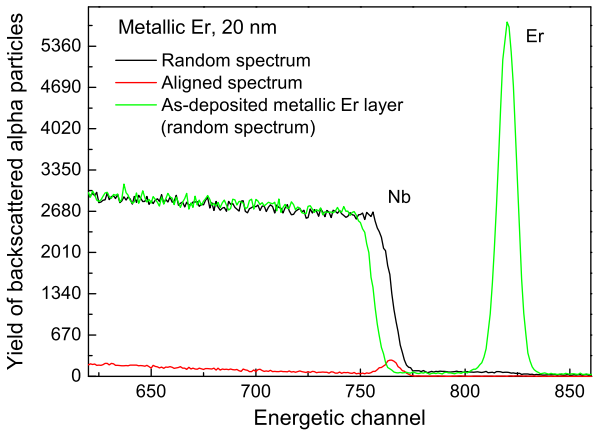

Fig. 2. The RBS spectrum – a comparison of the results coming from the erbium metal deposited on the crystal surface with that obtained after the diffusion in the *Z* cut. (*Experimental conditions*: 1060 °C; 100 h; atm. O_2.)

showed the presence of erbium on the surface of the lithium niobate substrate, and its integral amount was evaluated as 5.8×10^{16} at. cm^{-2} (see Fig. 2 – the green[1] curve). After the in-diffusion at elevated temperature, the signal of erbium was significantly lower, and the integral amount of erbium detected in the sub-surface layer of LN decreased to 0.2×10^{16} at. cm^{-2} simultaneously with the shift of niobium reaching the edge towards higher energies (see Fig. 2 – the black curve). This effect is connected to the fact that the in-diffusion of the whole amount of the deposited erbium into the lithium niobate sample has proceeded deeper into the substrate, and thus Er is detected only on the surface of the sample. The red curve in Fig. 2 represents the measured aligned spectrum which was used for the calculation of disordered atoms. The RBS spectrum detected for Er_2O_3 deposited layers is conformable to the described spectrum of the Er metal layer and is shown in Fig. 4b.

The erbium depth concentration profiles obtained for various LN cuts are shown in Fig. 3, which provides a comparison of the erbium depth concentration profiles for thin erbium films prepared by diffusion from the metal deposited on the surface (Fig. 3a) and those arising from diffusion from an erbium oxide layer (Fig. 3b). From these figures, it is obvious that the erbium concentration in surface and sub-surface layers was about 1.0–2.3 at.% for the in-diffusion from the oxide layers, and 0.2–1.0 at.% from the erbium metal layers. Nevertheless, it is necessary to keep in mind that the depth resolution of RBS is about 10 nm, so the accurate position of the erbium profile in the frame of a 10-nm thick sub-surface layer is burdened by high uncertainty. In the *Z* cuts of LN the results were verified by repeating the experiments with samples having a 10-nm thick diffusion source (not shown). The shapes of the depth concentration profiles were very similar for both thin-film sources. The surface concentration of erbium is rather low, approximately 0.2 at.%, and the layer possibly reaches deeper than 80 nm. Unfortunately, the erbium concentration at a greater depth is below the detection limit of the RBS measurement in the used combination of host element and matrix. Except for the mentioned uncertainty, a higher erbium surface concentration was again obvious in the layers performed from the Er_2O_3 as well as in the sample prepared from the layer having a thickness of 20 nm.

Concerning erbium concentration profiles in various cuts, we were not able to determine for certain in which cut the diffusion process took place preferably. For the diffusion from the deposited

[1] For interpretation of colour in Fig. 2, the reader is referred to the web version of this article.

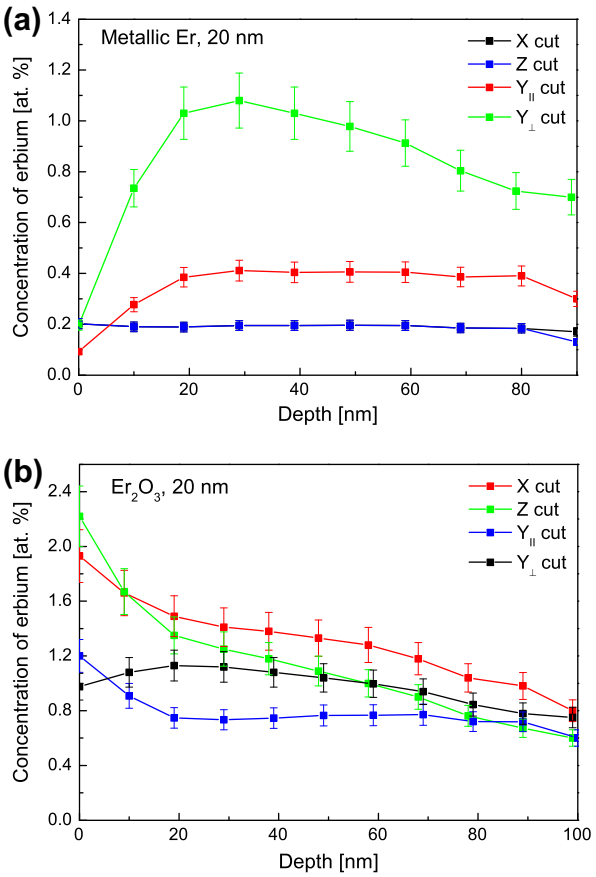

Fig. 3. The depth concentration profiles of the erbium-doped LN samples prepared from the 20-nm thick layers of erbium metal (A) or erbium oxide (B) deposited layers on the surface of various LN cuts. (*Experimental conditions*: 1060 °C; 100 h; atm. O_2.)

metal layers, the $Y_\perp$ cut behaved quite differently, because it had a higher erbium concentration in the surface layer after the diffusion. The diffusion from the Er_2O_3 layers into the *X* and *Z* cuts, as well as into both *Y* cuts, exhibited a striking similarity. The depth concentration profiles, with a higher concentration in the surface layer, was found with the first LN cuts, achieving values up to 2.3 at.%.

3.3. Lithium concentration in the prepared layers

From the RBS extracted erbium concentration values in the fabricated layers only a small depletion of lithium ions could be assumed. Therefore, in all the samples, prepared by diffusion from the deposited Er metal layers, lithium concentration depth profiles were measured by the high-statistics NDP method. The NDP measurements however showed that within the 5% accuracy of the method no significant lithium depletion in the surface area of any cut was observed.

3.4. Structural changes – RBS/channeling

Since the luminescence properties of the prepared thin films were good and the RBS measurement showed about 2 at.% of the erbium concentration in the surface, the changes in the LN structure caused by the diffusion process were interesting to investigate. The RBS/channeling technique was used for the investigation. The yield of backscattered ions, in the aligned spectrum

along the chosen crystallographic axes, is very sensitive to the number of disordered atoms of the host matrix.

The RBS/channeling spectra of the samples, where the in-diffusion of erbium from the oxide layers was applied, are presented in Fig. 4 (the spectra for erbium metal layer were shown only for the *Z* cut, see Fig. 2). The minimal yields for both erbium sources used are summarised in Table 2. From Fig. 4, it is obvious that in the aligned spectra the erbium signal was significantly lowered, which can be explained by a higher erbium amount in the substitution position viewing along the *x* and *z* axes (about 80% and 92%, respectively). It means that erbium is localised in some preferential C_{3v} sites in the crystalline matrix. Table 2 clearly shows that the minimal yield in the aligned spectrum is comparable for all cuts and has a value of about 4–7% for erbium in-diffused from the metal layers. Moreover, the values of the minimal yields are comparable to the minimal yields of the virgin (untreated) LN crystal, thus indicating negligible damage of the original structure.

In the case of erbium in-diffusion from the oxide layers, the values of the minimal yields are slightly higher in all the investigated cuts, i.e., about 6–10%, which may be connected to the increased disorder introduced into the sub-surface layer after erbium in-diffusion. Erbium atoms in the surface layer (more than 70%) sites are mostly located in interstitial positions. RBS/channeling analysis proved that the induced disorder of the density of the atoms, deduced from the spectra after the erbium in-diffusion from the erbium metal layer, is comparable to the crystalline structure of the virgin (untreated) sample. The erbium concentration in the LN surface layer is very low and in the accessible analytical depth seems to be homogeneous in the case of the erbium in-diffusion from the metal layer. Nevertheless, the thin film structure was ordered in the extent of more than 90% in all the samples. This fact could be a likely reason for the high intensity of 1529 nm luminescence observed in the presented samples.

Table 2
The minimum yield χ_{min} of backscattered ions in the aligned spectrum relative to the random spectrum in the various LN crystallographic cuts also shown for various erbium sources of the deposited layers.

Er sources	*X* cut	*Z* cut	$Y_{\perp}$ cut	Y_{II} cut
χ_{min} of LN in various crystallographic LN cuts (%)				
Metallic Er – 10 nm	–	4	–	–
Metallic Er – 20 nm	4	5	8	4
Er_2O_3 – 10 nm	–	4	–	–
Er_2O_3 – 20 nm	8	10	8	6

4. Discussion

This section discusses the usage of various sources of erbium ions in the form of thin layers evaporated on the surfaces of the samples. The study focused on the suitability of particular diffusion sources for use in photonics, i.e., mainly in terms of the best performance in the luminescence properties. In principle, it is possible to calculate how many atoms each type of layer (with a certain thickness) contains: the erbium metal layer with a thickness of 20 nm contains about 6.5×10^{16} Er atoms per cm^2, the 20-nm layer of Er_2O_3 would contain only about 5.4×10^{16} Er atoms per cm^2. These values corresponded well with the integral amounts of erbium

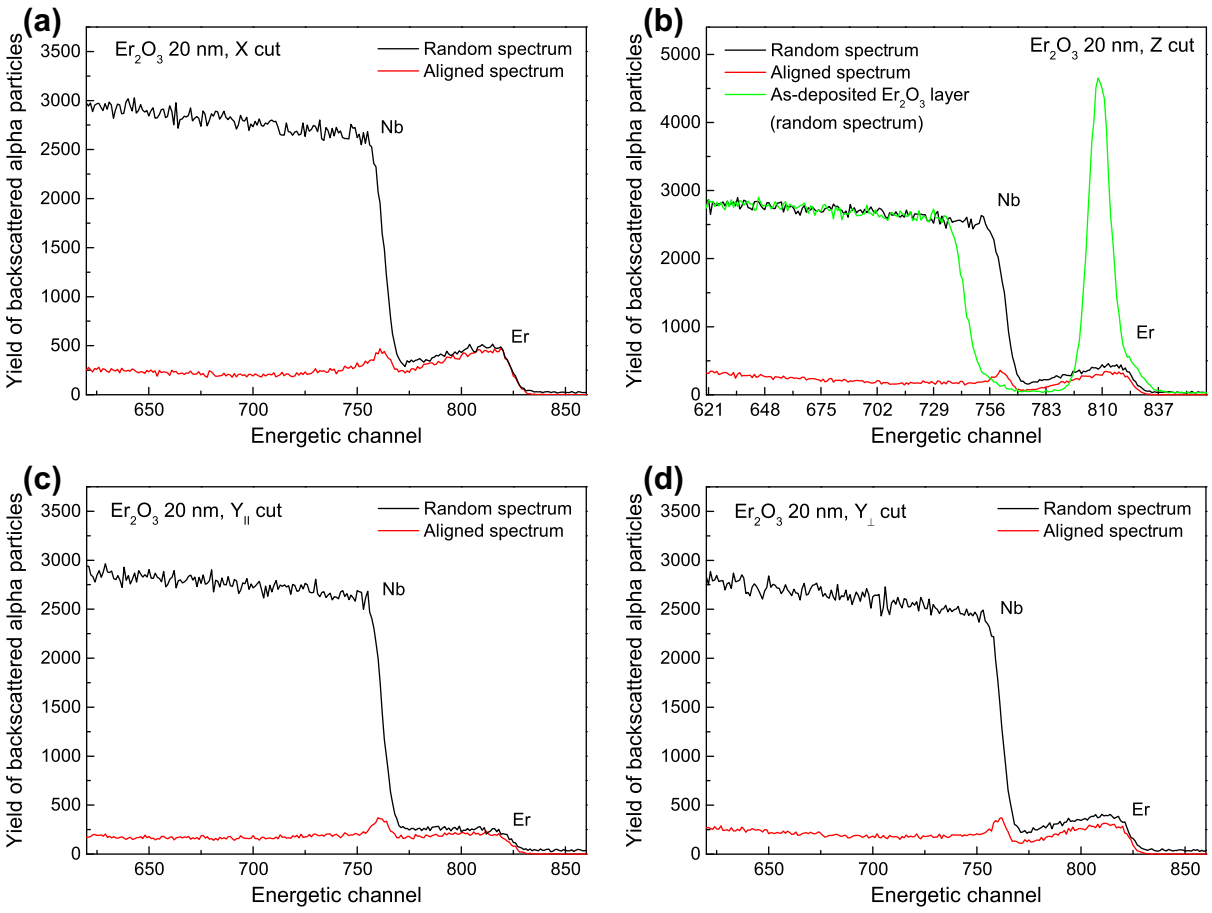

Fig. 4. The RBS channelling spectra of various LN cuts fabricated by diffusion from 20-nm thick erbium oxide layers deposited on the surface. (*Experimental conditions*: 1060 °C; 100 h; atm. O_2.)

Table 3
The calculated values of estimated depth l containing diffused erbium ions in *Z* cut of LN.

	Er				Er_2O_3			
	C (at.%[a])	$C_{measured}$ (at. cm^{-2})	$C_{calculated}$ (at. cm^{-2})	*l* (μm)	*C* (at.%[a])	$C_{measured}$ (at cm^{-2})	$C_{calculated}$ (at. cm^{-2})	*l* (μm)
10 nm	0.2	–	3.2×10^{16}	8.6	0.2	–	2.7×10^{16}	7.2
20 nm	1.0	5.8×10^{16}	6.5×10^{16}	3.4	0.5	3.7×10^{16}	5.4×10^{16}	5.7

[a] 1 at.% ≅ 1.893×10^{20} at. cm^{-3}.

found by the RBS analysis of the actual deposited metal or oxide erbium layers (see Fig. 3 – 5.8×10^{16} at. cm^{-2}). If we presume that the erbium concentration value of the "constant (steady) part" of the erbium concentration depth profiles (found by the RBS) is the same both in the surface region and in the whole doped depth region (also constant) – i.e., for deposited 10-nm erbium metal or Er_2O_3 *Z*-cut samples, the constant erbium concentration is about 0.2 at.% – we can then calculate the estimated depth of the in-diffused erbium. That means to calculate how deep the erbium ions diffuse into the sample after the high temperature diffusion process from the defined depth of evaporated erbium or oxide layer. The estimated thicknesses of the diffused erbium layers, prepared from metallic erbium, as well as from the Er_2O_3 evaporated layers mentioned above, were calculated from the following equations (relationships):

$$l(\text{Er layer}) = 100 \cdot \frac{1}{C(\text{at.}\%)} \cdot \frac{V(\text{evap.1.})}{V(1\ \text{cm}^3)} \cdot \frac{\rho(\text{Er, metal})}{\rho(\text{LiNbO}_3)} \cdot \frac{M(\text{LiNbO}_3)}{M(\text{Er})} \quad (1)$$

$$l(\text{Er}_2\text{O}_3\ \text{layer}) = 100 \cdot \frac{1}{C(\text{at.}\%)} \cdot \frac{V(\text{evap.1.})}{V(1\ \text{cm}^3)} \cdot \frac{\rho(\text{Er}_2\text{O}_3)}{\rho(\text{LiNbO}_3)} \cdot \frac{M(\text{LiNbO}_3)}{\frac{1}{2} \cdot M(\text{Er}_2\text{O}_3)} \quad (2)$$

In the above equations are the following variables: *l* [m] is the estimated thickness of diffused Er layer, *C* [at.%; at./cm^3] is the erbium concentration (value estimated from the constant "steady" part of the erbium concentration profile), N_A [mol^{-1}] is the Avogadro constant, *M* [kg/mol] is a molar mass, ρ [kg/m^3] is a density, *V* (evap.) [m^3] is the volume of the evaporated layer, *V* (1 cm^3) [m^3] is the volume of 1 cm^3 – i.e. 10^{-6} m^3.

The calculated values of estimated diffusion depth containing erbium ions are summarised in Table 3.

It is evident that the calculated values correspond well with the depth obtained by SIMS for the doping from the metal erbium layer [7]. Nevertheless in our case, measuring the real doped samples, the concentrations on the surface and the total concentrations measured towards the depth of 80 nm were much lower, thus indicating that the erbium reached beyond depth detection limits of the RBS method.

With a simple presumption that the intensity of luminescence is proportional to the amount of erbium (without considering the depletion of erbium), we may expect that a higher content of erbium in the samples doped from the erbium metal layer will also result in higher luminescence. However, our findings are not fully unambiguous with that presumption. The samples doped from 10-nm thick Er_2O_3 layers had higher luminescence intensities than those doped from the Er metal layers having the same thickness. The differences diminished with the samples that were prepared from 20-nm thick layers, although we have never found that samples doped from the Er_2O_3 layers would have lower luminescence intensities than those doped from the Er metal layers. Nonetheless, the luminescence intensity is substantially affected by other factors, such as concentration quenching and the ordering of the structure around the erbium ion in the doped layer. Concentration quenching is not very likely to occur in the case of the doping from the Er metal layer, since the maximum concentration of erbium was found to be very low even in the shallow sub-surface layer. For the concentrations found in the samples doped from the Er_2O_3 layers (2.3 at.%), we would have expected luminescence quenching, but then the luminescence intensities would have been higher in those samples.

The luminescence intensities, and above all the shapes of the luminescence bands, are highly affected by the surroundings of the erbium ions. The rather high ordering of the structure – as follows from the RBS/channeling spectra (see Fig. 4) – indicated a re-crystallisation of the structure, which occurs at 600 °C and above. Consequently, Er-ion surroundings are well ordered and the majority of erbium ions occupy the substitution positions of the most likely lithium or niobium ions. Thanks to this fact, the luminescence intensity is rather high for both types of layers – Er metal and Er_2O_3. If erbium occurs in higher concentrations, as in the samples made by the diffusion from erbium oxide, then it is localised at interstitial sites, which makes the structure much less ordered and lowers the intensity of the luminescence. The only explanation of the higher intensity of the luminescence in the samples doped from erbium oxide (as compared to the samples doped from erbium metal) is the more feasible way of how erbium ions incorporate into the lithium niobate structure, or the presence of oxygen atoms from erbium oxide in the doped layers. However, such a hypothesis is still a matter of further investigation.

As to the comparison of the suitability of particular crystallographic cuts of lithium niobate for the mentioned applications, it is clear that the crystallographic cut orientation is a very important factor influencing the luminescence properties of the doped samples. Within all the used samples, it was always the *Z* cut that exhibited the highest intensity of luminescence. Since we compared the samples that were annealed significantly above the temperature of re-crystallisation (i.e., about 600 °C), we can assume that the rate of the re-crystallisation process is the highest along the *z*-axis of LN and the crystal structure along this direction would have the highest degree of ordering. However, this hypothesis cannot be fully confirmed, as the differences that were found between various cuts are rather small and almost 100% ordering was measured in all our samples.

5. Conclusions

The luminescence spectra of the samples that were doped with erbium from two different thin film sources evaporated onto single-crystal $LiNbO_3$ samples – erbium metal and Er_2O_3 – were studied in detail. In the luminescence spectra of the doped samples, there appeared 6 narrow bands around a wavelength of 1529 nm, which indicated a good structural ordering of the erbium-ion crystal field. Such a low disordering is similar to that of virgin (undoped) LN. In terms of the luminescence properties around a wavelength of 1.5 μm, the erbium oxide layer seems to be a better source for the doping than the erbium metal layer. The highest intensity of the luminescence was always found in the *Z* cut. The results confirmed that this type of erbium doping of lithium niobate is the best alternative for utilisation in photonic structures, e.g., optical amplifiers.

Acknowledgements

The research has been supported by the Czech Science Foundation (project No. P106/10/1477 and No. 106/09/0125). Some parts of this research were realised at the CANAM infrastructure (LM2011019), under the project SPIRIT (No. 227012) and Technological Agency of the Czech Republic (project No. TA01010237).

References

[1] B.E.A. Saleh, M.C. Teich, Fundamentals of Photonics, first ed., John Wiley & Sons, New York, 1991.
[2] A. Polman, F.C.J.M. van Veggel, Broadband sensitizers for erbium-doped planar optical amplifiers: review, Journal of the Optical Society of America B 87121 (5) (2004) 871–892.
[3] L. Arizmendi, Photonic applications of lithium niobate crystals, Physica Status Solidi A 201 (2) (2004) 253–283.
[4] K.K. Wong, Properties of Lithium Niobate, first ed., INSPEC, IEE, London, 2002.
[5] L. Tsonev, Luminescent activation of planar optical waveguides in $LiNbO_3$ with rare earth ions Ln^{3+} – a review, Optical Materials 30 (6) (2008) 892–899.
[6] M.N. Palatnikov, I.V. Biryukova, N.V. Sidorov, et al., Growth and concentration dependencies of rare-earth doped lithium niobate single crystals, Journal of Crystal Growth 291 (2006) 330–397.
[7] I. Baumann, R. Brinkmann, M. Dinand, W. Sohler, L. Beckers, C. Buchal, et al., Erbium incorporation in $LiNbO_3$ by diffusion-doping, Applied Physics A 64 (1997) 33–44.
[8] D.L. Zhang, J.P. Wang, P.R. Hua, et al., Locally Er-doped near-stoichiometric $LiNbO_3$ crystals prepared by standard Er diffusion and post-VTE treatment, The American Ceramic Society 92 (8) (2009) 1739–1747.
[9] M. Dinand, W. Sohler, Theoretical modeling of optical amplification in Er-doped Ti:$LiNbO_3$ waveguides, IEEE Journal of Quantum Electronics 30 (5) (1994) 1267.
[10] M. Fleuster, C. Buchal, E. Snoeks, A. Polman, Optical and structural properties of MeV erbium-implanted $LiNbO_3$, Journal of Applied Physics 75 (1) (1994) 173–180.
[11] C. Mignotte, Determination of lattice site locations of erbium ions implanted into $LiNbO_3$ single crystals after annealing at moderate and high temperature, Applied Surface Science 185 (1–2) (2001) 11–26.
[12] P. Nekvindová, J. Špirková-Hradilová, J. Schröfel, M. Slunečko, V. Peřina, J. Vacík, Localized moderate-temperature Er^{3+} doping into optical crystals (Proceedings Paper), Proceedings of SPIE—International Society for Optical Engineering (1999) 180–189.
[13] C. Sada, F. Caccavale, F. Segato, B. Allieri, L.E. Depero, Erbium incorporation in $LiNbO_3$ crystals obtained by ion-exchange process, Optical Materials 19 (1) (2002) 23–31.
[14] V. Peřina, J. Vacík, V. Hnatovitz, J. Červená, P. Kolářová, J. Špirková-Hradilová, J. Schröfel, RBS measurement of depth profiles of erbium incorporated into lithium niobate for optical amplifier applications, Nuclear Instruments and Methods in Physics Research, Section B: Beam Interactions with Materials and Atoms 139 (1–4) (1998) 208–212.
[15] J. Cajzl, P. Nekvindová, B. Švecová, J. Špirková, A. Macková, P. Malinský, J. Vacík, J. Oswald, A. Kolitsch, Study of the diffusion from melted erbium salt as the surface – modifying technique for localized erbium doping into various cuts of lithium niobate, Advances and Applications in Electroceramics II: Ceramic Transactions 235 (2012) 95–105.
[16] B. Svecova, P. Nekvindova, A. Mackova, J. Oswald, J. Vacik, R. Grötzschel, J. Spirkova, Er^{+} medium energy ion implantation into lithium niobate, Nuclear Instruments and Methods in Physics Research B 267 (2009) 1332.
[17] A. Mackova et al., Study of Er^{3+} ion-implanted lithium niobate structure after an annealing procedure by RBS and RBS/channelling, Nuclear Instruments and Methods in Physics Research B 268 (2010) 2042.
[18] P. Nekvindova, B. Svecova, J. Cajzl, A. Mackova, P. Malinsky, J. Oswald, A. Kolistsch, J. Spirkova, Erbium ion implantation into different crystallographic cuts of lithium niobate, Optical Materials 34 (4) (2012) 652–659.
[19] J. Saarilahti, E. Rauhala, Nuclear Instruments and Methods B 64 (1992) 734.
[20] IBANDL. <http://www-nds.iaea.org/ibandl/>.
[21] J.R. Tesmer, M.A. Nastali, Handbook of Ion Beam Spectroscopy, Materials Research Society, 1995.
[22] M. Mattarelli, S. Sebastiani, J. Spirkova, S. Berneschi, M. Brenci, R. Calzolai, A. Chiasera, M. Ferrari, M. Montagna, G. Nunzi Conti, S. Pelli, G.C. Righini, Characterization of erbium doped lithium niobate crystals and waveguides, Optical Materials 28 (2006) 1292–1295.

Nuclear Instruments and Methods in Physics Research B 331 (2014) 182–186

Contents lists available at ScienceDirect

Nuclear Instruments and Methods in Physics Research B

journal homepage: www.elsevier.com/locate/nimb

A comparison of the structural changes and optical properties of $LiNbO_3$, Al_2O_3 and ZnO after Er^+ ion implantation

A. Mackova [a,b], P. Malinsky [a,b,*], H. Pupikova [a,b], P. Nekvindova [c], J. Cajzl [c], B. Svecova [c], J. Oswald [d], R.A. Wilhelm [e,f], A. Kolitsch [e]

[a] Nuclear Physics Institute of the Academy of Sciences of the Czech Republic, v.v.i., 250 68 Rez, Czech Republic
[b] Department of Physics, Faculty of Science, J.E. Purkinje University, Ceske mladeze 8, 400 96 Usti nad Labem, Czech Republic
[c] Department of Inorganic Chemistry, Institute of Chemical Technology, Technicka 5, 166 28 Prague 6, Czech Republic
[d] Institute of Physics, Academy of Sciences of the Czech Republic, v.v.i., Cukrovarnicka 10, 162 53 Prague, Czech Republic
[e] Institute of Ion Beam Physics and Materials Research, Helmholtz-Zentrum Dresden-Rossendorf, 01314 Dresden, Germany
[f] Technische Universität Dresden, 01062 Dresden, Germany

ARTICLE INFO

Article history:
Received 25 September 2013
Received in revised form 22 November 2013
Accepted 22 November 2013
Available online 13 February 2014

Keywords:
Er ion implantation
Crystals
Depth profiles
RBS
RBS/channelling
Photoluminescence

ABSTRACT

This paper reports on the structural as well as compositional changes of $LiNbO_3$, Al_2O_3 and ZnO crystals, implanted with Er^+ ions at 190 keV a with fluence of 1.0×10^{16} cm^{-2} into the <0001> crystallographic cuts. Post-implantation annealing at 1000 °C in oxygen atmosphere was also done. The chemical compositions and erbium concentration-depth profiles of implanted layers were studied by Rutherford Backscattering Spectrometry (RBS) and compared to SRIM simulations. The same value of the maximum erbium concentration (up to 2 at.%) was observed at a depth of about 40 nm for all crystals. The structural properties of the prepared layers were characterised by RBS/channelling. The relative numbers of disordered atoms in the prepared implanted layers were compared with each other and discussed for various crystals. It has been found that erbium is located in $LiNbO_3$ and in Al_2O_3 preferably in interstitial positions, unlike ZnO, where the largest amount of erbium (about 83%) is placed in substitutional positions after the implantation. The erbium position in the host matrix was substantially influenced by the annealing procedure. In ZnO, after the annealing, the erbium amount in substitutional positions significantly decreased; in $LiNbO_3$ and Al_2O_3 the increase of erbium in substitutional positions was observed simultaneously with the improvement of the quality of the reconstructed host matrix. Since we are interested in the relationship between structural changes and optical properties, the erbium luminescence properties were measured in the region of wavelength 1440–1650 nm for all crystals. After ion implantation $LiNbO_3$ samples had zero luminescence intensity, while ZnO and Al_2O_3 samples had one significant luminescence band at 1537 and 1530 nm, respectively. The annealing improved the luminescent properties significantly in all investigated crystalline materials.

1. Introduction

Due to their unique properties, lithium niobate ($LiNbO_3$,) and sapphire (Al_2O_3) continue to be used as advanced materials in the field of photonics [1,2]. Since single crystalline lithium niobate is grown as congruent crystal, it allows an easy doping with laser active ions, such as erbium [3,4]. Particularly, the incorporation of erbium in structure of sapphire is interesting for optical waveguide applications [5]. The zinc oxide (ZnO) is a wide band-gap natural n-type semiconductor with a large exciton-binding energy of 60 meV that has attracted much attention nowadays. The recently reported ability to obtain p-type ZnO has opened new possibilities for photoelectronic light-emitting devices including lasers operating in the near ultraviolet (UV) and blue spectral range [6–8]. The wide and direct band-gap in ZnO makes it suitable as a host for optically active Er ions, since it allows for emission at wavelength 1.5 μm as well as in the entire visible region. In addition the advantage is that the effect of the thermal quenching of the photoemission is expected to be low [9]. The efficient incorporation of the erbium into the host matrix, the particular erbium position in the structure and therefore the effect of the erbium crystal-field surroundings on the luminescence properties of the erbium ions are very important to study.

* Corresponding author at: Nuclear Physics Institute of the Academy of Sciences of the Czech Republic, v.v.i., 250 68 Rez, Czech Republic. Tel.: +420 777126346.
E-mail address: malinsky@ujf.cas.cz (P. Malinsky).

http://dx.doi.org/10.1016/j.nimb.2013.11.047
0168-583X/

The structure of the three mentioned crystals ($LiNbO_3$ – ***R3c***, Al_2O_3 – ***R3c***, ZnO – ***P6$_3$mc***) have similar basic oxygen hexagonal lattice differing mainly in the occupation of the octahedral and tetrahedral vacant sites of the appropriate ions. The ion-implantation technique is a way to form active optical layers in these crystals (see [4] and the references therein). In this paper the thin layers containing erbium have been prepared by ion implantation in three optical crystals, i.e. $LiNbO_3$, Al_2O_3 and ZnO. Experimental conditions of the ion implantation and post-implantation annealing were deliberately chosen identical. The main attention is focused on the structural and compositional changes comparison and also on the influence of various crystals fields on the 1.5 μm luminescence of erbium ions.

2. Experimental

In this study, the *Z* cuts <0001> of congruent lithium niobate (supplied by Crytur Turnov, Czech Republic), sapphire (supplied by AVTEX Turnov, Czech Republic) and ZnO (supplied by Gemma Korea Corporation, South Korea) were used. Thoroughly precleaned wafers were implanted with 190 keV Er^+ ions, 7° off-axis to avoid channelling. An ion fluence of 1.0×10^{16} cm^{-2} was applied. The implantations were performed using a 200 kV implanter at the Helmholtz-Zentrum, Dresden-Rossendorf, Germany. The beam was scanned through an aperture of typically 1×1 cm^2, resulting in a beam current density of typically 0.25 μA/cm^2 on the target. For the recovery of the structure, the as-implanted samples were annealed at a temperature of 1000 °C for 5 h in dry oxygen atmosphere [9].

The concentration profiles of the implated erbium ions were studied by Rutherford Backscattering Spectrometry (RBS). The analysis was performed at a Tandetron 4130 MC accelerator of the Academy of Sciences of the Czech Republic using a 2.0 MeV He^+ ion beam. He^+ ions backscattered at a laboratory angle of 170° were detected. In order to study the damages introduced by the implantation process, the influence of the annealing procedure on the recovery of the host lattice was examined by RBS/channelling measurements using a 1.7 MeV He^+ beam from a van-de-Graaff accelerator at the Ion Beam Center of the Helmholtz-Zentrum, Dresden-Rossendorf.

The photoluminescence spectra of the implanted samples were collected within the range of 1440–1650 nm at room temperature. A semiconductor laser POL 4300 emitting at 980 nm was used for the electron excitation. The luminescence radiation was detected by a two-step-cooled Ge detector J16 (Teledyne Judson Technologies). To scoop specific wavelengths, a double monochromator SDL-1 (LOMO) was used. Synchronous detection technique was implemented by chopping the laser beam at a modulation frequency of about 35 Hz, and by employing a lock-in amplifier (EG&G 5205). For the evaluation, all of the luminescence spectra were transformed to the base level.

3. Results

3.1. Er depth profiles

RBS was used for erbium depth profile determination in all prepared structures. The range R_P, defined as the depth of the maximum erbium concentration, and ΔR_P characterising the profile standard deviation are summarised in Table 1. The results show that the measured R_P agree with those from the SRIM simulation within the uncertainties of the RBS measurement for as-implanted samples.

The measured values of ΔR_P exceed those from the SRIM [10] simulation by a factor of 1.6–2. The difference is obviously caused by the energy straggling of the ions implanted, which is supposed to be higher in a crystalline material due to the possible channelling of implanted ions and the modified structure of the implanted layer.

Post-implantation annealing alters the depth profiles of implanted erbium. For each crystal, different changes of the erbium concentration-depth profiles were obvious. The erbium

Table 1
A summary of the erbium profile parameters (R_P and ΔR_P) in as-implanted and as-annealed samples of LiNbO3, Al_2O_3 and ZnO implanted with Er^+ ions (190 keV) into the <0001> crystallographic cuts.

	Er-implanted **$LiNbO_3$** $1.0 \times 10^{16}$$cm^{-2}$		Er-implanted **Al_2O_3** $1.0 \times 10^{16}$$cm^{-2}$		Er-implanted **ZnO** $1.0 \times 10^{16}$$cm^{-2}$	
	Rp (nm)	ΔRp (nm)	Rp (nm)	ΔRp (nm)	Rp (nm)	ΔRp (nm)
SRIM simulation	43	15	42	10	38	10
<0001> cut as-implanted	54	22	40	19	39	19
<0001> cut as-annealed	*	*	54	14	49	22

* R_P and ΔR_P parameters were not determined for the annealed erbium depth profiles as they have a non-Gaussian character.

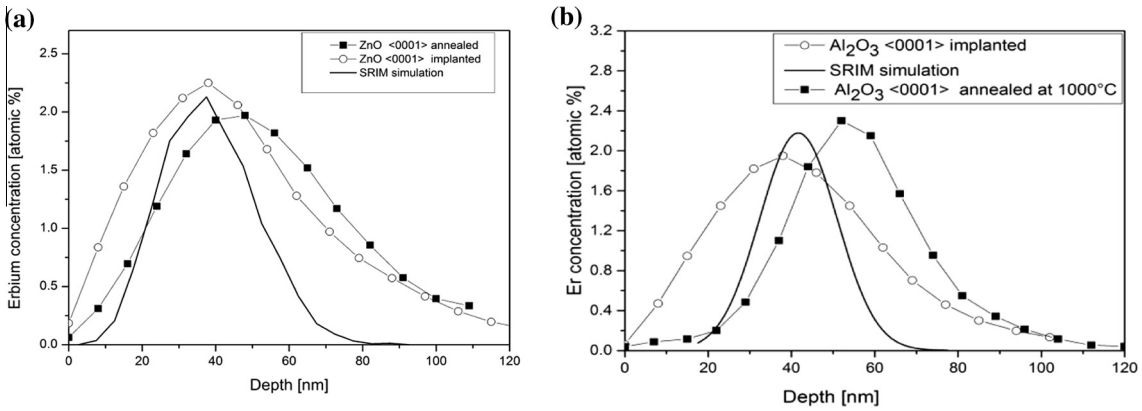

Fig. 1. Er concentration-depth profiles in as-implanted and as-annealed <0001> cuts of ZnO (1a) and Al_2O_3 (1b) compared to the SRIM simulation. The samples were implanted by 190 keV Er^+ ions with an ion fluence of 1.0×10^{16} cm^{-2}. The annealing procedure was done for 5 h at 1000 °C in O_2 atmosphere.

depth-concentration profiles for $LiNbO_3$ exhibited a shift of the concentration maximum to the surface, a decrease of the maximum concentration and a broadening of the erbium profile [not shown – the results have been published in 11]. Erbium concentration-depth profiles compared for as-implanted and as-annealed ZnO are presented in Fig. 1a. It is clear that the depth-concentration profile in this crystal showed a decrease of the erbium concentration maximum as well as the profile broadening but the concentration maximum was shifted deeper. For the Al_2O_3 crystal, the erbium concentration-depth profile was narrower after the annealing and the maximum concentration was slightly shifted to the depth. For Al_2O_3, these changes are presented in Fig. 1b. Moreover, all erbium depth-concentration profiles are also compared to the corresponding SRIM-simulated ones.

3.2. Structural changes

The structure of as-implanted and as-annealed samples was examined using the RBS/channelling method. Fig. 2 presents the random and aligned spectra of both as-implanted (2a) and as-annealed (2b) samples of Al_2O_3. The same spectra determined in the $LiNbO_3$ have been published in [11]. For the ZnO, these types of spectra are shown in Fig. 3. The relative concentration of the displaced atoms N_D/N was calculated from the area of the deeper-lying disordered peak using a common procedure [12]; the minimum yield χ_{min} was determined as well (see [12] for details). For various crystals, these values are summarised in Table 2. It is evident from the results that a considerable amount of damage is created in the near-surface region corresponding to the depth of the implanted layer in the all investigated crystalline samples. Using the identical implantation conditions, the highest relative disorder N_D/N (71%) was introduced by implantation in Al_2O_3 while the lowest (44%) in ZnO.

The annealing procedure had a significant influence on crystal recovery in $LiNbO_3$ and ZnO where the relative disorder introduced in the buried layer decreased from 64% to 12% and 44% to 5%, respectively (see Table 2). The implanted structure was completely reconstructed by annealing in the ZnO case, because the minimum yield after annealing (5%) was close to the minimum yield of the virgin ZnO crystals. In Al_2O_3, the disordered host matrix was recovered only partially; mere 30% (see Fig. 2b) of the defects introduced by implantation was reconstructed by the annealing procedure.

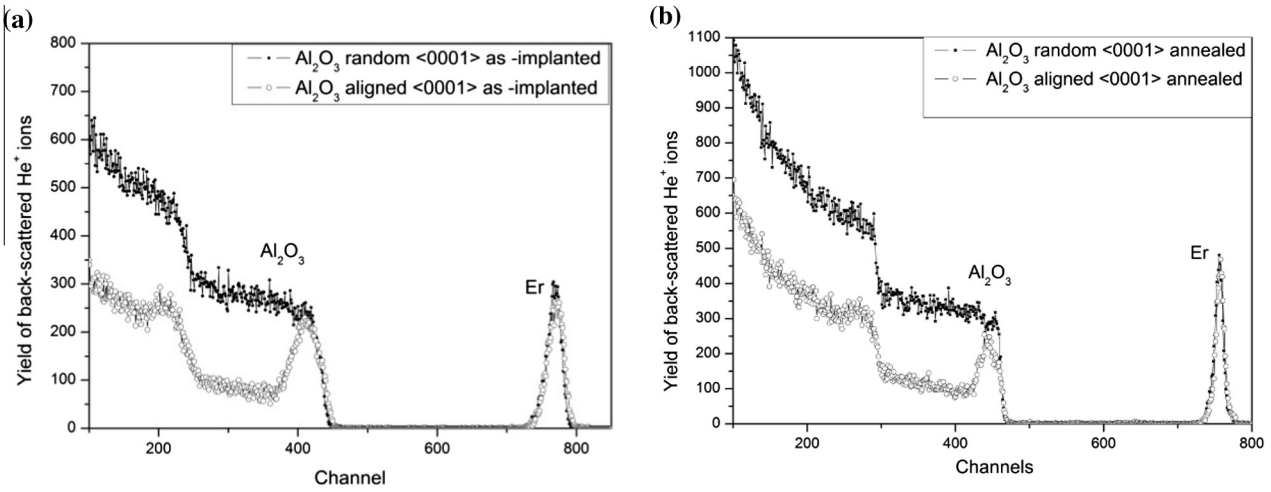

Fig. 2. The RBS/channelling spectra for <0001> Al_2O_3 determined in as-implanted (a) and as-annealed (b) samples. The samples were implanted by 190 keV Er^+ ions with an ion fluence of 1.0×10^{16} cm^{-2}. The annealing procedure was done for 5 h at 1000 °C in O_2 atmosphere.

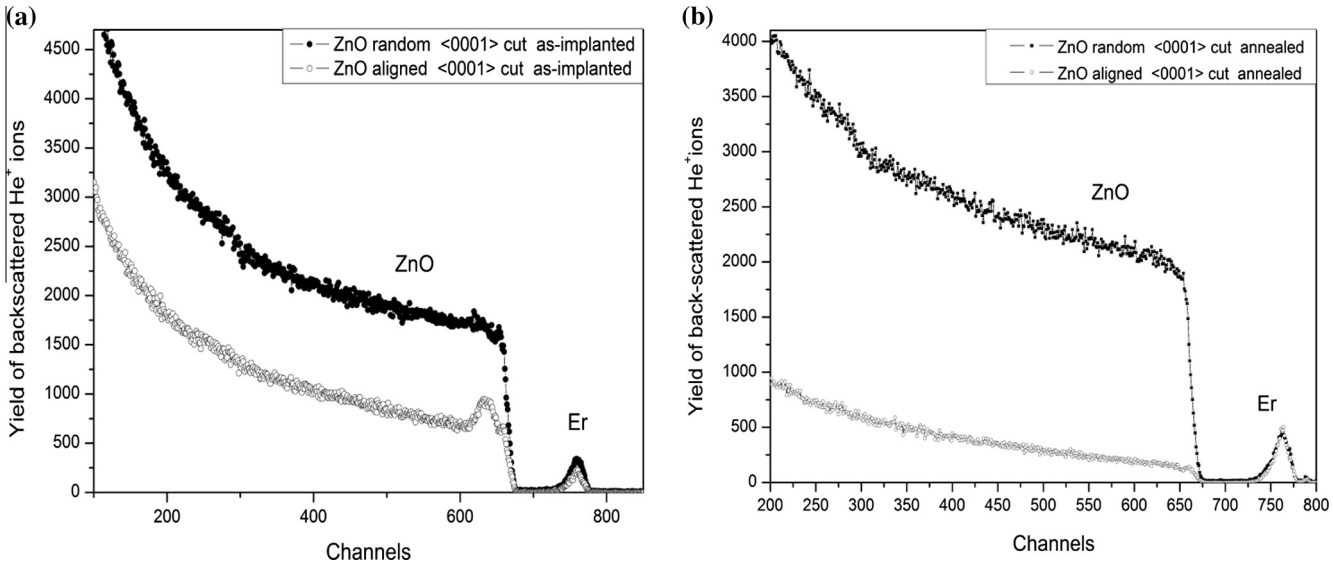

Fig. 3. The RBS/channelling spectra for <0001> ZnO determined in as-implanted (a) and as-annealed (b) samples. The samples were implanted by 190 keV Er^+ ions with an ion fluence of 1.0×10^{16} m^{-2}. The annealing procedure was done for 5 h at 1000 °C in O_2 atmosphere.

Table 2
A summary of the minimum yields and the relative number of the disordered atoms for $LiNbO_3$, Al_2O_3 and ZnO implanted by 190 kV Er^+ ions with a fluence of 1×10^{16} cm^{-2} and subsequently annealed for 5 h at 1000 °C in O_2 atmosphere.

	Er-implanted **$LiNbO_3$** $1.0 \times 10^{16}cm^{-2}$		Er-implanted **Al_2O_3** $1.0 \times 10^{16}cm^{-2}$		Er-implanted **ZnO** $1.0 \times 10^{16}cm^{-2}$	
	N_D/N (%)	χ_{min} (%)	N_D/N (%)	χ_{min} (%)	N_D/N (%)	χ_{min} (%)
<0001> cut as-implanted	64	65	71	72	44	46
<0001> cut as-annealed	12	14	49	51	5	8

We have compared the relative number of erbium atoms in substitutional positions in as-implanted samples and annealed samples along the main crystallographic axis <0001>, where the erbium displacement from the substitutional position in the host matrix has the greatest influence on the back-scattered ion yield in channelling direction. The fraction of the implanted erbium atoms entering substitutional positions after implantation and post-annealing was determined from the change in the area of the erbium signal (for details, see [12]). Using the above-mentioned implantation conditions, no significant erbium preferential substitutional position was observed after the implantation in $LiNbO_3$ and Al_2O_3. This means that more than 90% of erbium atoms were found at interstitial positions. Fig. 4a shows a fine angle scan determined in an as-implanted ZnO. When we are following the shape of back-scattering yield appropriate to the Zn and Er signal in RBS spectrum depending on the ion incident angle, we can see in Fig. 4a, that the Er yield is very close to the one of Zn. It can be concluded, that 83% of the erbium is located at substitutional positions, which are ordered along the axis of <0001> crystallographic axis in agreement with the results presented in [13,14].

The substitutional fraction of erbium atoms was analysed also after the annealing, when the crystalline matrix was partly or fully reconstructed in ZnO, $LiNbO_3$ and Al_2O_3. It was published in [11] that in $LiNbO_3$ the erbium fraction in substitutional positions is about 56% after the annealing. In the case of Al_2O_3, the erbium relative amount at substitutional positions after annealing was increased only slightly, to 20%. The behaviour during the annealing of the ZnO crystal was different. In ZnO, a decrease of erbium amount in substitutional positions to 15% was observed see Fig. 4b.

3.3. Luminescence properties

The luminescence properties were measured from 1440 to 1650 nm with erbium as-implanted samples of all the mentioned crystals. After implantation, $LiNbO_3$ samples had zero luminescence intensity with no clear luminescence bands [11]. Fig. 5 shows the luminescence spectra of erbium implanted and annealed (a) Al_2O_3 and (b) ZnO samples. The main luminescence band with the highest intensity was measured in Al_2O_3 around 1530 nm and in ZnO around 1537 nm. The luminescence spectra of erbium implanted Al_2O_3 had another diffused peak around 1543 nm. The luminescence spectra of both crystal samples are similar but have some important differences: (i) the spectrum of erbium implanted ZnO is shifted by 7 nm towards higher wavelengths as compared with the erbium implanted Al_2O_3 spectrum; (ii) the luminescence band around 1543 nm is half the height of the main luminescence band in Er^+ implanted Al_2O_3, whereas in erbium implanted ZnO this luminescence band is less than quarter the height. After post-implantation annealing of both samples (Al_2O_3 and ZnO) revealed the highest intensity of luminescence at a wavelength of 1526 nm. The value of highest measured intensity was slightly lower in ZnO. In addition there are evident 6 significant emission bands in the both luminescence spectra (see Fig. 5). More detailed information on the fine erbium structure and hence the representation of the individual structural of binding states of erbium in the crystal matrix could be provided by luminescence at low temperatures. This measurement as well a detailed study of luminescence will follow in our future work.

4. Discussion

When the structural changes of $LiNbO_3$, Al_2O_3 and ZnO as well as the positioning of Er in these crystals are compared with the previous studies [14–16], it may be assumed that $LiNbO_3$ has more free substitutional sites where Er could be placed than Al_2O_3 and ZnO. It was suggested in [15] that low Er ion implantation fluence leads to a preferential occupation of free octahedral sites in Al_2O_3 and that the occupational preferences of dopants are connected to the ionic radii [15,16]. If the Er amount exceeds the limit of the Er amount incorporated in Al_2O_3 at implantation fluence of the order of 1×10^{16} cm^{-2}, then some Er is segregated and annealing supports Er precipitation in a heavily damaged crystal structure. After the annealing, a high amount of Er still remains in interstitial positions [15], which is in agreement with our observations.

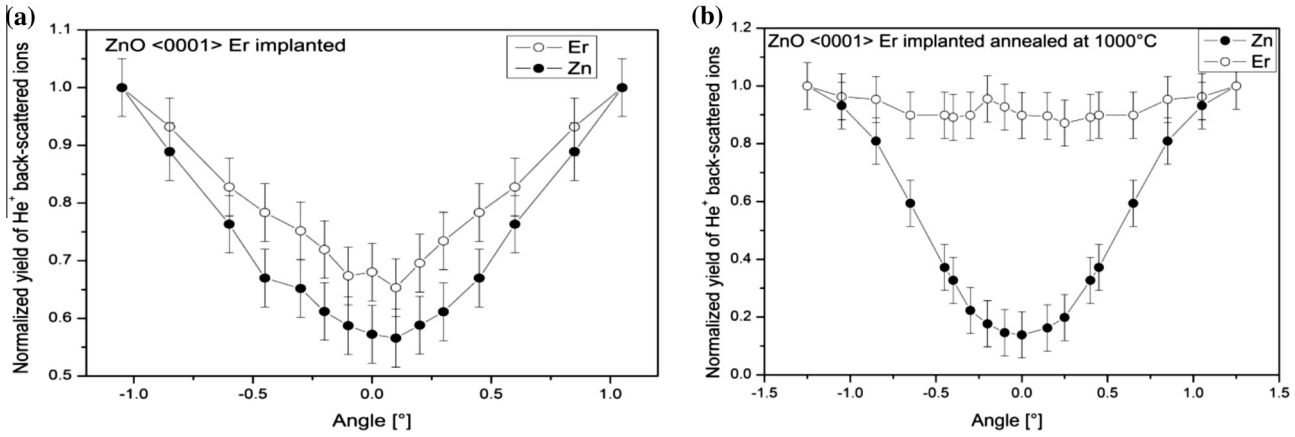

Fig. 4. A fine angle scan determined from a RBS/channelling analysis for the <0001> cut (a) as-implanted and (b) as-annealed ZnO samples. The samples were implanted by 190 keV Er^+ ions with an ion fluence of 1.0×10^{16} cm^{-2}. The annealing procedure was done for 5 h at 1000 °C in O_2 atmosphere.

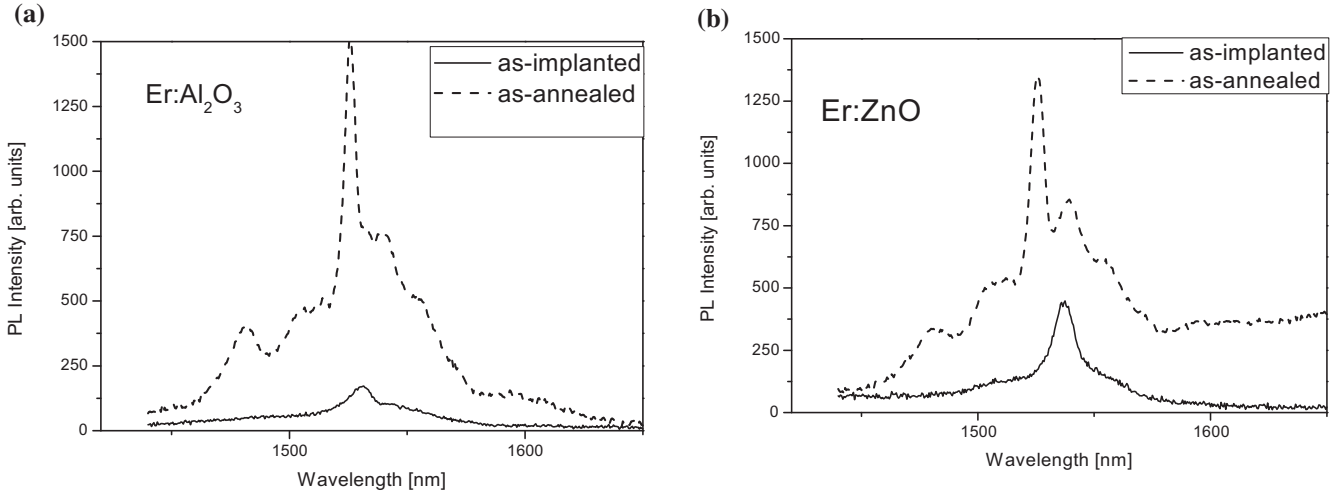

Fig. 5. The luminescence spectrum of the crystals: (a) Al_2O_3 and (b) ZnO. The samples were implanted by 190 keV Er^+ ions with an ion fluence of 1.0×10^{16} cm^{-2}. The annealing procedure was done for 5 h at 1000 °C in O_2 atmosphere.

In case of $LiNbO_3$ we suppose Er occupies vacant Li sites as was observed earlier in Er enriched $LiNbO_3$ thin layers prepared by Er diffusion [17]. Despite their high atomic number, erbium ions are known to have, due to the lanthanide contraction, relatively small radii. It may thus be assumed, and it has been proven, that it can occupy free octahedral sites in the Al_2O_3 structure see [15]. In ZnO erbium ions occupied the Zn sites after ion implantation and post-implantation annealing caused the Zn comeback to the original sites, while the erbium ions migrate to interstitial positions. In the case a certain role could be played by charge instability, which is not supposed to be in sapphire because of trivalent aluminium. In $LiNbO_3$, it may be balanced by the congruent crystal structure behaviour.

5. Conclusions

From the RBS and RBS/channelling measurements it follows that erbium ions were positioned in $LiNbO_3$ and in Al_2O_3 preferably in the interstitial sites, unlike ZnO, where the largest amount of erbium (83%) was placed in substitutional positions, after the implantation. The erbium position in the host crystal structures was substantially influenced by the annealing procedure: in ZnO after the annealing, the amount of Er in substitutional positions significantly decreased, whereas in the case of $LiNbO_3$ and Al_2O_3, the amount of erbium in substitutional positions increased simultaneously with the improved quality of the reconstructed host matrix. All the as-implanted samples, except for $LiNbO_3$, exhibited after ion implantation noticeable luminescence. The luminescence spectrum of erbium implanted ZnO had lower intensity of the luminescence band around 1543 nm than compared to erbium implanted Al_2O_3. This behaviour corresponds to the different probability of emission transitions between sublevels of $I_{13/2}$ and $I_{15/2}$ electronic levels in erbium ions. The annealing improved the luminescent properties significantly in all investigated crystalline materials.

Acknowledgements

The research has been supported by project P108/12/G108 and realised at the CANAM (Center of Accelerators and Nuclear Analytical Methods) LM 2011019. It has been supported by the European Community as an Integrating Activity SPIRIT under EC contract No. 227012.

References

[1] A.J. Kenyon, Recent developments in rare-earth doped materials for optoelectronics, Prog. Quant. Electron. 26 (2002) 225.
[2] T. Volk, M. Wöhlecke, Lithium Niobate – Defects, Photorefraction and Ferroelectric Switching, Springer, Berlin, 2009. ISBN: 978-3-540-70765-3.
[3] A. Polman, Erbium implanted thin film photonic materials, J. Appl. Phys. 82 (1997) 1.
[4] L. Tsonev, Luminescent activation of planar optical waveguides in $LiNbO_3$ with rare earth ions Ln^{3+} – a review, Opt. Mater. 30 (2008) 892.
[5] E. Alves, M.F. da Silva, G.N. van den Hoven, A. Polman, A.A. Melo, J.C. Soares, Incorporation and stability of erbium in sapphire by ion implantation, Nucl. Instr. Meth. B 106 (1995) 429.
[6] D.C. Reynolds, D.C. Look, B. Jogai, C.W. Litton, T.C. Collins, W. Harsch, G. Cantwell, Neutral-donor-bound-exciton complexes in ZnO crystals, Phys. Rev. B 7 (1998) 12151.
[7] W.M. Jadwisienczak, H.J. Lozykowski, A. Xu, B. Patel, Visible emission from ZnO doped with rare-earth ions, J. Electron. Mater. 31 (2002) 776.
[8] Ü. Özgür, Y.I. Alivov, C. Liu, A. Teke, M.A. Reshchikov, S. Doğan, V. Avrutin, S.J. Cho, H. Morkoç, A comprehensive review of ZnO materials and devices, J. Appl. Phys. 98 (2005) 041301.
[9] C. Buchal, S.P. Withrow, C.W. White, D.B. Poker, Ion implantation of optical materials, Annu. Rev. Mater. Sci. 24 (1994) 125.
[10] www.srim.org, website, access date 2013-11-13.
[11] A. Macková, P. Malinský, H. Pupíková, P. Nekvindová, J. Cajzl, Z. Sofer, R.A. Wilhelm, A. Kolitsch, J. Oswald, The structural changes and optical properties of $LiNbO_3$ after Er implantation using high ion fluencies, 21st international conference on ion beam analysis (IBA), Nucl. Instr. Meth. B 21 (2013) 21–24.
[12] J.R. Tesmer, M.A. Nastasi, Handbook of Modern Ion Beam Analysis, Materials Research Society, Michigan, 1995. ISBN: 155-8-992545.
[13] S.M.C. Miranda, M. Peres, T. Monteiro, E. Alves, H.D. Sun, T. Geruschke, R. Vianden, K. Lorenz, Rapid thermal annealing of rare earth implanted ZnO epitaxial layers, Opt. Mater. 33 (2011) 1139.
[14] A. Mackova, P. Malinský, Z. Sofer, P. Šimek, D. Sedmidubský, M. Mikulics, R.A. Wilhelm, A study of the structural and magnetic properties of ZnO implanted by Gd ions, 21st international conference on ion beam analysis (IBA), Nucl. Instr. Meth. B (2013).
[15] E. Alves, R.C. da Silva, M.F. da Silva, J.C. Soares, Solubility and damage annealing of Er implanted single crystalline α-Al_2O_3, Nucl. Instr. Meth. B 139 (1998) 313.
[16] E. Alves, E. Rita, U. Wahl, J.G. Correia, T. Monteiro, J. Soares, C. Boemare, Lattice site location and optical activity of Er implanted ZnO, Nucl. Instr. Meth. B 206 (2003) 1047.
[17] I. Baumann, S. Bosso, R. Brinkmann, R. Corsini, M. Dinand, A. Greiner, K. Schafer, J. Sochtig, W. Sohler, H. Suche, R. Wessel, Er-doped integrated optical devices in $LiNbO_3$, IEEE J. Sel. Top. Quant. 2 (1996) 355.

Nuclear Instruments and Methods in Physics Research B 332 (2014) 74–79

Contents lists available at ScienceDirect

Nuclear Instruments and Methods in Physics Research B

journal homepage: www.elsevier.com/locate/nimb

The structural changes and optical properties of $LiNbO_3$ after Er implantation using high ion fluencies

A. Macková [a,b,*], P. Malinský [a,b], H. Pupíková [a,b], P. Nekvindová [c], J. Cajzl [c], Z. Sofer [c], R.A. Wilhelm [d,f], A. Kolitsch [d], J. Oswald [e]

[a] Nuclear Physics Institute, Academy of Sciences of the Czech Republic, v.v.i., 250 68 Rez, Czech Republic
[b] Department of Physics, Faculty of Science, J.E. Purkinje University, 400 96 Usti nad Labem, Czech Republic
[c] Department of Inorganic Chemistry, Institute of Chemical Technology, 166 28 Prague, Czech Republic
[d] Institute of Ion Beam Physics and Materials Research, Helmholtz Zentrum, 01314 Dresden, Germany
[e] Institute of Physics, Academy of Sciences of the Czech Republic, v.v.i., 162 53 Prague, Czech Republic
[f] Technische Universität Dresden, 01062 Dresden, Germany

ARTICLE INFO

Article history:
Available online 15 March 2014

Keywords:
Implanted lithium niobate
Erbium implantation
RBS channeling structural study
Luminesent properties

ABSTRACT

The structural and compositional changes of $LiNbO_3$ implanted with 190 keV Er^+ ions into various crystallographic cuts with fluencies of 1×10^{16} and 5×10^{16} cm^{-2} were studied. The effect of post-implantation annealing at 1000 °C in oxygen atmosphere was also examined. Concentration depth profiles of implanted erbium, determined by Rutherford Backscattering Spectrometry (RBS), are broader than those from the SRIM simulation. The maximum erbium concentration (of up to 8 at.%) is observed at the depth of about 50 nm, for all crystal cuts. The structure of the implanted layers were characterised by RBS-channelling method. The lower relative number of disordered atoms in the crystalline matrix was observed in the lithium niobate (LN) implanted at a fluence of 1×10^{16} cm^{-2}, where also the preferential position of the erbium in substitutional sites was observed when compared to the randomly distributed erbium in interstitial positions at a fluence of 5×10^{16} cm^{-2} after the annealing. Surface-morphology changes at the highest implantation fluencies were studied using Atomic Force Microscopy (AFM). Since we were interested in the relation between the structural changes and optical properties, erbium luminescence properties were measured in the region of 1440–1650 nm. The positive effect of post-implantation annealing on the luminescence properties caused by structural recovery was proved.

1. Introduction

Due to its unique properties, lithium niobate ($LiNbO_3$, LN) is widely used in photonics [1–3]. Nowadays the development of optical thin-layer amplifiers is one of the main research directions. Crystalline lithium niobate is a good candidate for modulation and amplification of the optical radiation. In this connection various technologies for doping of lithium niobate with optically active erbium ions are of interest [4,5] and the ion-implantation is one of the promising techniques to form active optical layers in LN [3], which enables to form colloids or nanoparticles in LN and has already been used by several groups [6–9]. The structural changes in LN caused by ion implantation and by post-implantation annealing have not been well clarified yet. The position of implanted erbium atoms in the LN crystal structure and effects of internal electrostatic fields on the optical (e.g. luminescent) properties are important topics to study.

Erbium implantation in LN structure and the effect of post-implantation annealing was studied in [4] and the structural changes in LN matrix caused by ion implantation in [5]. It was shown that ion implantation leads to extensive amorphization of the as-implanted thin surface layer. Post-implantation annealing performed at higher temperatures (around 1000 °C) resulted in full recovery (i.e. recrystallisation) of the LN structure. Implanted erbium atoms were found to locally deform LN crystal structure, which means that the LN structure had to adapt to incorporated erbium atoms. In our former works [10,11] it was shown that incorporation of erbium into the LN depends on the choice of crystallographic orientation of the sample surface.

This work is focused on further study of erbium implantation using high ion fluencies into various crystallographic cuts of LN. The position of implanted erbium atoms in the LN structure after

* Corresponding author at: Nuclear Physics Institute, Academy of Sciences of the Czech Republic, v.v.i., 250 68 Rez, Czech Republic.
E-mail address: mackova@ujf.cas.cz (A. Macková).

http://dx.doi.org/10.1016/j.nimb.2014.02.033
0168-583X/

the ion implantation – and also after subsequent annealing – is studied in detail. Also the effect of ion implantation into different crystallographic cut orientations of LN on the luminescence properties is studied.

2. Experimental

$LiNbO_3$ was synthesised by the Czochralski method (Crytur Turnov, Czech Republic). The experiments were accomplished on X cuts (11–20), *Z* cuts (0001) and specially designed *Y* cuts, i.e. 'parallel' $Y_{\parallel}$ (01–12) and 'perpendicular' $Y_{\perp}$ (10–14) to the cleavage plane. Thoroughly pre-cleaned $LiNbO_3$ wafers were implanted with 190 keV energy Er^+ ions (7° off-axis to avoid channelling) with fluencies of $1.0 \times 10^{16}\,cm^{-2}$ and $5.0 \times 10^{16}\,cm^{-2}$. The implantation was performed thanks to the 200 kV implanter in the Helmholtz-Zentrum, Dresden-Rossendorf, Germany. The beam was scanned through an aperture of typically $1 \times 1\,cm^2$, resulting in a beam current density of typically 0.25 μA/cm^2 on the target. As-implanted samples were annealed at a temperature of 1000 °C for 5 h in dry oxygen atmosphere (for details see [4]).

The concentration profiles of the incorporated erbium ions were studied by Rutherford Backscattering Spectroscopy (RBS). The analysis was performed thanks to a Tandetron 4130 MC accelerator using a 2.0 MeV He^+ ion beam. He^+ ions backscattered at a laboratory angle of 170° were detected. RBS spectra were evaluated using the GISA 3.99 [12] code and SIMNRA 6.06 [13] codes, utilising cross-section data from IBANDL [14]. Structural and compositional changes induced by the ion implantation and post-implantation annealing were examined by RBS/channelling measurements using a 1.7 MeV He^+ beam at VdG accelerator in the Helmholtz-Zentrum, Dresden-Rossendorf.

The surface morphology and roughness were examined by Atomic Force Microscopy (AFM). The AFM Ntegra Spectra from NT-MDT was used in a tapping mode. The arithmetic average height parameter (R_a) was defined as the average absolute deviation of the roughness irregularities from the mean line over one sampling length. Root-mean-square roughness (RMS) is the standard deviation of the distribution of surface heights [15].

The photoluminescence spectra of the implanted samples were collected within the range of 1440–1650 nm at room temperature. A pulsed semiconductor laser POL 4300 emitting at 980 nm was used for the excitation of electrons. Luminescence radiation was detected by a two step-cooled Ge detector J16 (Teledyne Judson Technologies). To scoop specific wavelengths, a double monochromator SDL-1 (LOMO) was used. For the evaluation, all the luminescence spectra were transformed to the base level; after the substraction of the baseline, the normalisation was done using a reference sample.

3. Results

The erbium depth profiles from LN samples with the different crystallographic orientations implanted to the fluencies of 1×10^{16} and $5 \times 10^{16}\,cm^{-2}$ are presented in Fig. 1a and b

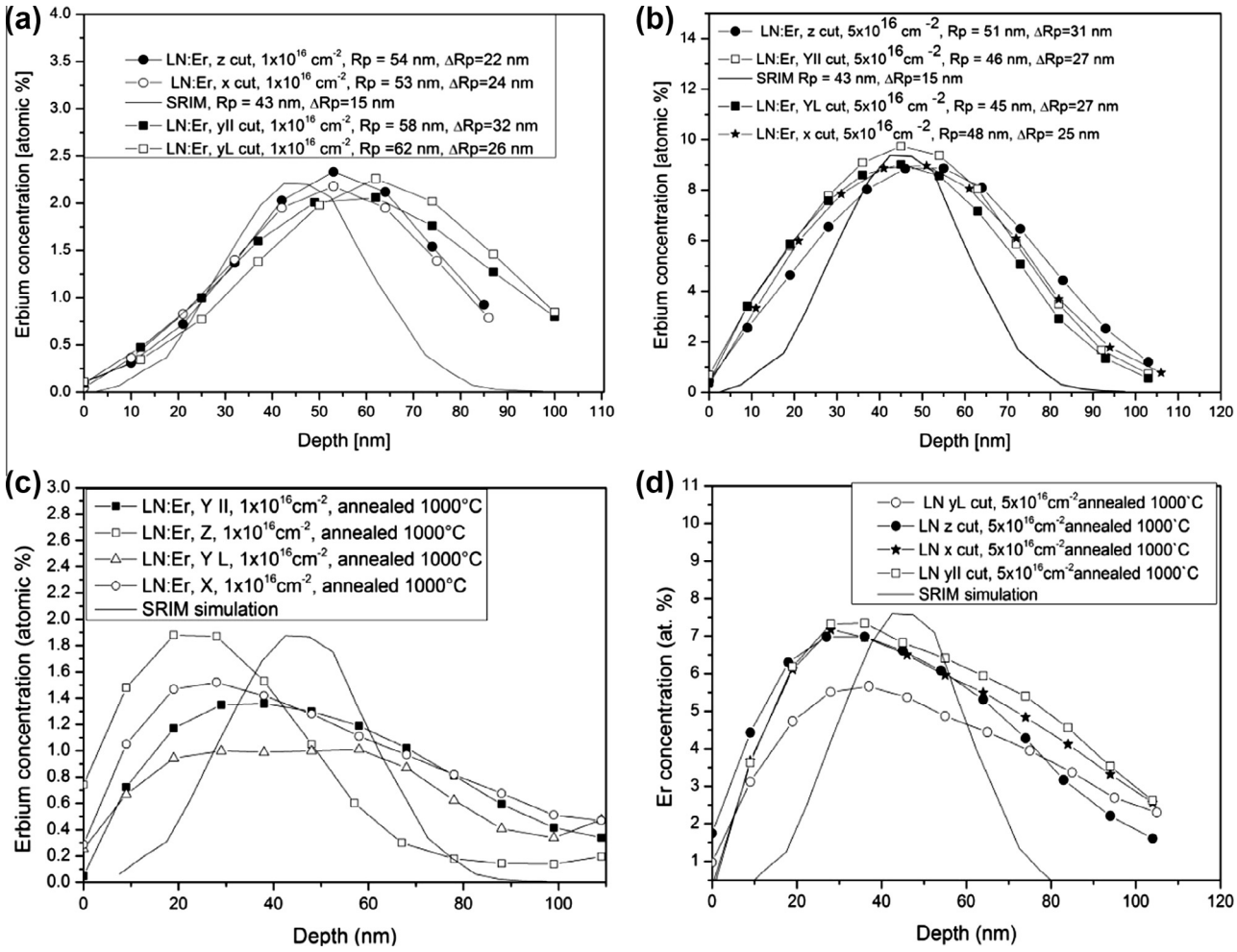

Fig. 1. Erbium depth profiles determined from RBS for various crystallographic orientations of LN: (a) implanted to $1 \times 10^{16}\,cm^{-2}$, (b) implanted to $5 \times 10^{16}\,cm^{-2}$, (c) implanted to $1 \times 10^{16}\,cm^{-2}$, annealed at 1000 °C, (d) implanted to $5 \times 10^{16}\,cm^{-2}$, annealed at 1000 °C.

respectively. The depth profiles are compared with those simulated by SRIM code [16]. The range R_P, defined as the depth of the maximum erbium concentration, and ΔR_P characterising the profile width are shown in Fig. 1. The measured R_P agree with those from the SRIM simulation within the uncertainties of the RBS measurement for as-implanted samples. The measured values of ΔR_P exceed by a factor of 1.6–2 those from SRIM simulation. The difference is obviously caused by the energy straggling of the ions implanted, which is supposed to be higher in a crystalline material due to the possible channelling of implanted ions and structure of the implanted layer. By post-implantation annealing the depth profiles of implanted erbium are significantly altered. The erbium depth profiles for both fluencies used in our experiment are shown in Fig. 1c (1×10^{16} cm^{-2}) and d (5×10^{16} cm^{-2}). Shift of the concentration maximum to the surface, decrease of the maximum concentration and a broadening of the erbium profile are observed on the annealed samples. More significant changes are observed on the LN samples implanted to lower fluence. Most pronounced changes of the depth profile is seen on *Y* cut perpendicular to the cleavage plane ($Y_\perp$), where erbium diffusion into the LN interior appeared. R_P and ΔR_P parameters were not determined for the annealed erbium depth profiles as they have a non-Gaussian character. The erbium concentration depth profiles after annealing have a diffusion non-symmetric shape (see Fig. 1c and d).

The changes in the surface morphology caused by ion implantation were studied using the AFM technique. It was found that all the implanted samples had a very smooth surface with a RMS = 0.50–2.00 nm (for a 10×10 μm scan) without obvious signs of damage. After the implantation, the $Y_\perp$ and *Z* cuts had an almost smooth surface, the X cut had slight changes of surface roughness, and the surface of the Y_{II} cut had significantly changed surface morphology. Fig. 2 depicts the AFM images of the Y_{II} cut sample doped with fluencies of (a) 1×10^{16} cm^{-2} for illustration scan 20 x 20 microns is used in the Figure 2a and (b) 5×10^{16} cm^{-2}. On the sample implanted to higher fluence more surface 'bumps' are seen. The maximal height of the 'bumps' was about 20 nm. The RMS of the surface roughness was 0.66 nm (R_a = 0.44 nm, for scan size of 10×10 μm^2) for the fluence of 1×10^{16} cm^{-2} and 0.98 nm (R_a = 0.65, for scan size of 10×10 μm^2) for the fluence of 5×10^{16} cm^{-2}. The standard bulk doped Y_{II} cut of Er:$LiNbO_3$ exhibited a smooth surface with no such bumps on the surface and the *RMS* of the surface roughness was 0.72 nm (R_a = 0.46 nm, for scan size of 10×10 μm^2). On the basis of this observation, it may be concluded that the occurrence of the surface defects is related to the crystallographic orientation of the substrate and the relaxation of surface energy induced by ion implantation.

The structure of as-implanted and post-annealed samples was examined using the RBS-channelling method; the typical aligned

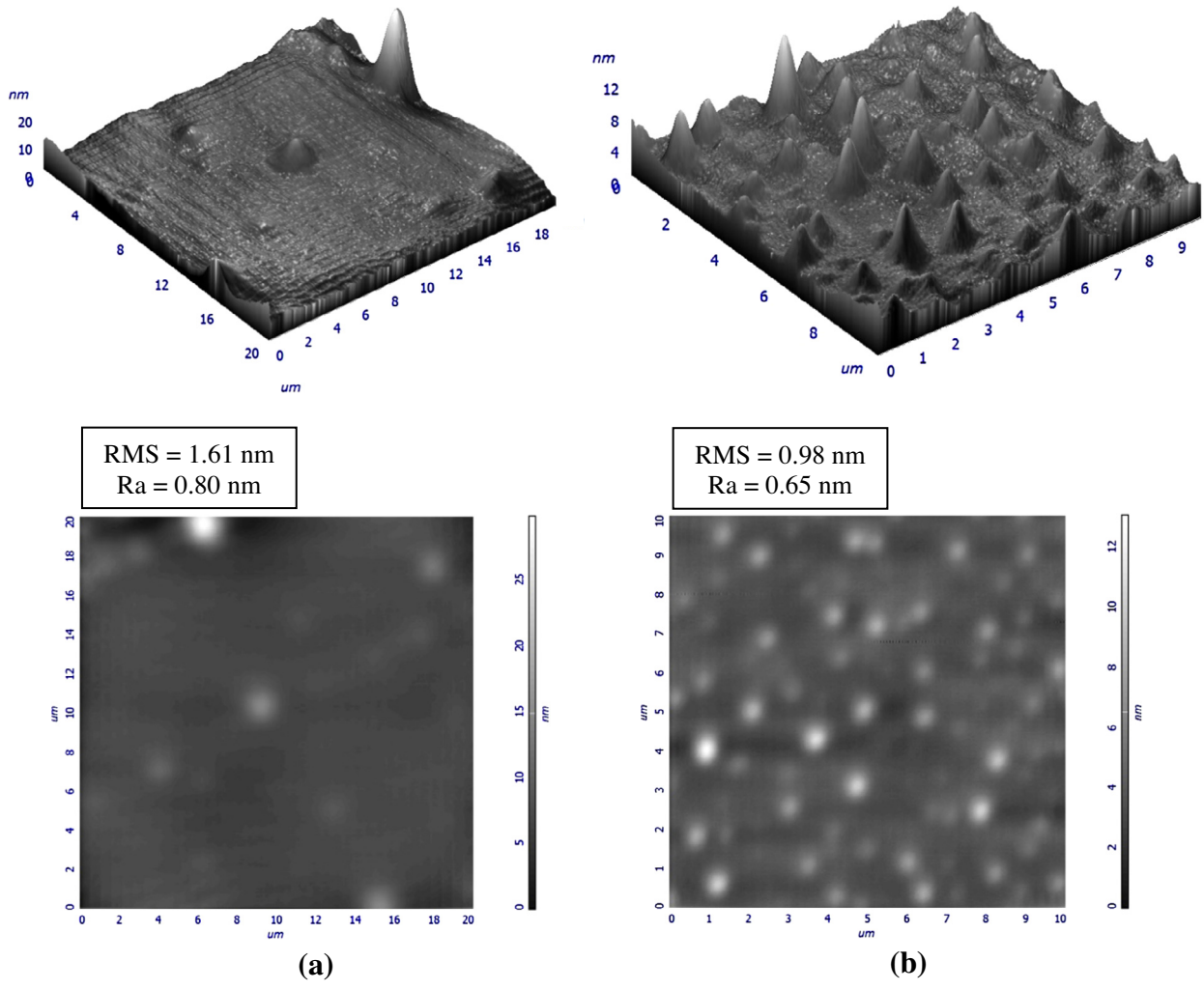

Fig. 2. Surface changes caused in Y_{II} cut of $LiNbO_3$ by ion implantation (a) 1×10^{16} cm^{-2} and (b) 5×10^{16} cm^{-2}.

Table 1
Minimum yields and the relative number of disordered atoms for implantation fluences of 1×10^{16} cm^{-2} and 5×10^{16} cm^{-2} in as-implanted and as-annealed samples.

LN cut	Fluence 1×10^{16} cm^{-2}		Fluence 5×10^{16} cm^{-2}	
	N_D/N [%]	χ_{min} [%]	N_D/N [%]	χ_{min} [%]
X-cut	61	63	79	80
X-cut 1000 °C	12	14	18	22
Z-cut	64	65	75	76
Z-cut 1000 °C	12	14	32	33
Y_{II}-cut	67	68	74	75
Y_{II}-cut 1000 °C	9	11	19	21
$Y_{\perp}$cut	69	70	70	71
$Y_{\perp}$-cut 1000 °C	24	26	22	24

and random spectra are shown in Fig. 3. Fig. 3a and b presents the random and aligned spectra for as-implanted and as-annealed samples and ion fluencies of 1×10^{16} cm^{-2} and 5×10^{16} cm^{-2} respectively. The relative concentration of the displaced atoms N_D/N was calculated from the area of a deeper-lying disordered peak using a common procedure [18] with the minimum yield χ_{min} determined by usual procedure too [18] (see Table 1). The disorder induced by ion implantation increases slightly with increasing ion-fluence, but even for the lower fluence of 1×10^{16} cm^{-2} it is above 60% (see Table 1). For the fluence of 5×10^{16} cm^{-2}, the depletion of Nb in the very surface layer is also observed (see the random spectrum in Fig. 3b).

After annealing at 1000 °C, a significant recovery of crystalline structure in the implanted layer is observed, the relative disorder is reduced from more than 60% to less than 20% of disordered atoms for an implantation fluence 1×10^{16} cm^{-2} (see Table 1). In the case of the fluence 5×10^{16} cm^{-2}, the crystal quality was also improved, the relative disorder density was decreased from more than 70% to about 19% (see Fig. 3b). As expected, the crystal recovery was slightly lower after the annealing procedure for the higher implantation fluence. However, the annealing temperature is suitable to recover a highly disordered structure created at both implantation fluencies.

The fraction of the implanted erbium atoms entering substitutional positions after implantation and post-annealing was determined from the change in the area of the depth profile, see [18]. At the implantation fluencies used, no significant preferential substitutional position was observed after the implantation. Substitutional fraction of erbium atoms was analysed after the annealing, when the crystalline matrix was partly reconstructed. After the annealing at 1000 °C of the samples implanted to the fluence 1×10^{16} cm^{-2}, the erbium fraction in substitutional positions (Li, Nb) of about 56% was observed. In the samples implanted at the fluence of 5×10^{16} cm^{-2} no difference in between integral amount of erbium observed in the random and aligned spectra is observed even after the annealing. The normalised yield of backscattered He^+ ions as a function of the incoming ion-beam angle is presented in Fig. 4a for *Z* cut implanted at the fluence 1×10^{16} cm^{-2}. In the case of the fluence 5×10^{16} cm^{-2} no significant changes of the integral amount of erbium is observed see Fig. 4b, erbium is hence positioned randomly in the host LN matrix.

The luminescence spectra of the prepared samples were measured in the wavelength region of 1440–1650 nm. After implantation, all the samples had zero luminescence intensity. The luminescence spectra of the annealed samples doped with implantation fluences of 1×10^{16} cm^{-2} and 5×10^{16} cm^{-2} are depicted in Fig. 5. It is seen that in this case the luminescence bands are intensive and narrow and the main peak around 1530 nm appears. There are significant differences between the spectra from the samples implanted to different fluencies. The samples implanted at the fluence of 5×10^{16} cm^{-2} have a more distinctive luminescence peak around 1483 nm and hardly visible luminescence peaks in the region around 1510 nm. The samples implanted with a higher fluence have lower luminescence intensity. For both fluencies, the highest luminescence intensity occurs in the *Z* and $Y_{\perp}$ cuts.

4. Discussion

From the results it follows that immediately after the implantation erbium ions are packed in a thin layer and the surrounding of the erbium ions is strongly damaged, which results in a significantly deteriorated (almost zero) luminescence intensity. The RBS spectra also revealed relative depletion of niobium, which – as to the AFM measurement – was not caused by a strongly damaged surface of the sample. Following annealing (1000 °C – which is above the temperature of recrystallization of lithium niobate) [17] caused dispersion of erbium ions both towards the surface and deeper into the substrate. This effect was even more pronounced when the implantation was done with lower fluence (1×10^{16} cm^{-2}). The annealing caused healing (recovery) of the LN structure, while it appeared that this effect is not primarily dependent on the used implantation fluence, because after 5 h of annealing at 1000 °C, as much as 80% of the structure was comparable to the original untreated lithium niobate structure. However, the luminescence properties were not the same for the samples

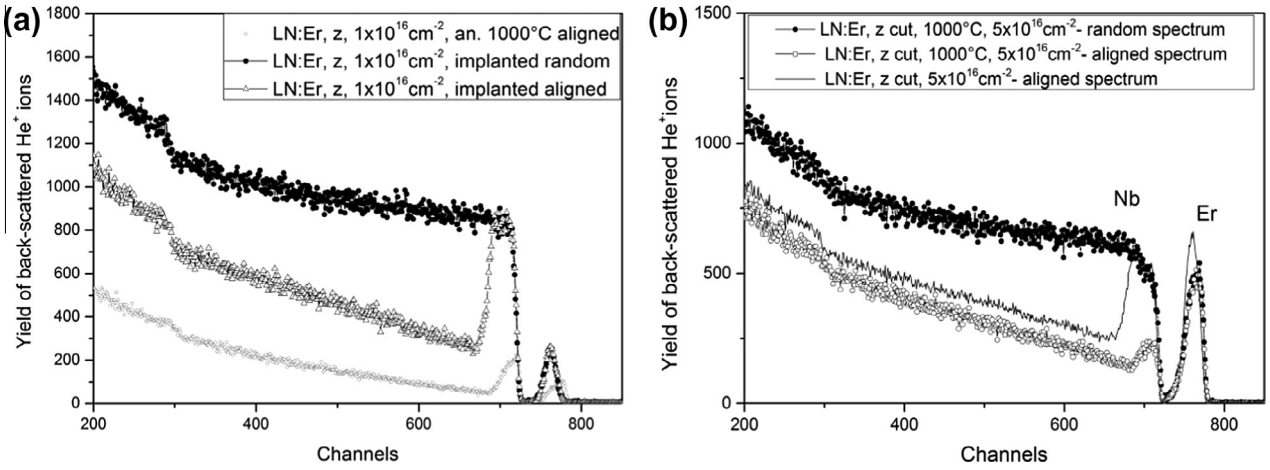

Fig. 3. The RBS-channelling spectra changes caused by annealing at 1000 °C in the *Z* cuts of LN for various fluencies of ion implantation (a) 1×10^{16} cm^{-2}, (b) 5×10^{16} cm^{-2}.

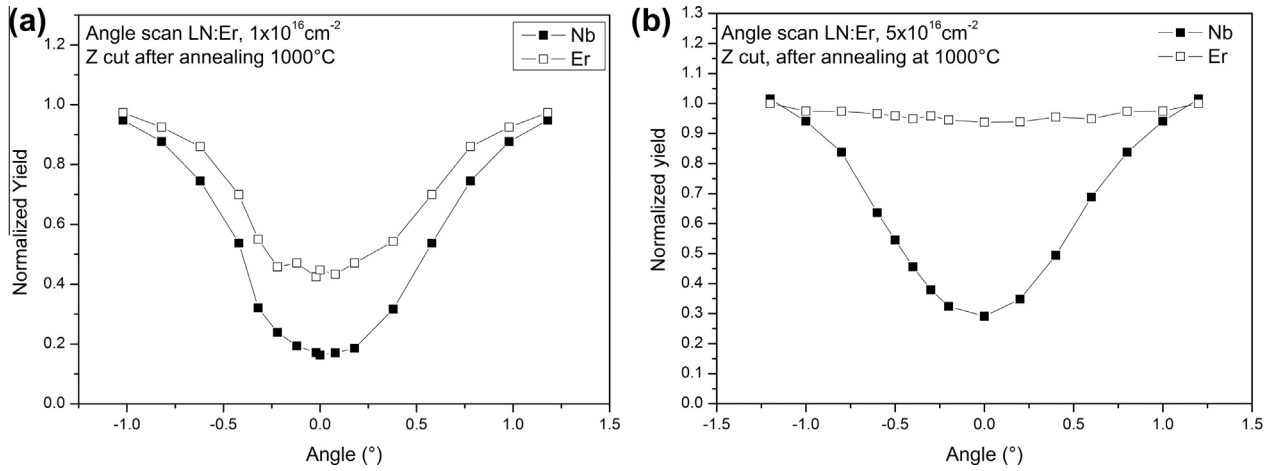

Fig. 4. Erbium fine angle scan determined from the RBS channelling analysis for the *Z* cut, with LN after annealing at 1000 °C: (a) an ion-implantation fluence of 1×10^{16} cm^{-2}, (b) an ion-implantation fluence of 5×10^{16} cm^{-2}.

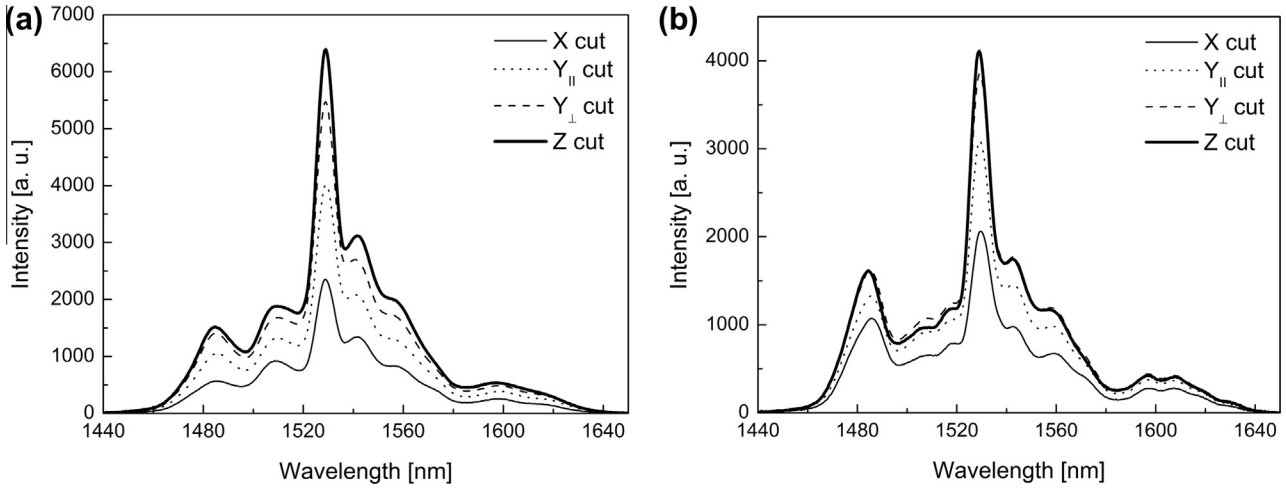

Fig. 5. The luminescence spectra of the annealed samples doped with implantation fluences of (a) 1×10^{16} cm^{-2} and (b) 5×10^{16} cm^{-2}. The energy of implantation was 190 keV. Annealing: 1000 °C, 5 h, atm. O_2.

doped with different implantation fluencies which could be explained with the help of detailed scans of the RBS measurement. Low fluencies of the ion implantation introduced such amount of erbium ions that was just sufficient for their optimal distribution. This appeared to be similar to the erbium bulk-doped lithium niobate crystals where the erbium ions occupy the substitutional sites of lithium atoms [19]. The higher implantation fluencies introduced bigger amounts of erbium ions, which due to their tendency to form clusters, flocked together and were forced to occupy interstitial positions as well. The effect of clustering of erbium ions has been already well described (e.g. [20]), and leads to substantial lowering of the luminescence intensity around 1535 nm due to concentration quenching (pair interactions). This cluster-induced luminescence quenching behaviour we also expect in our samples having relatively high content of incorporated erbium (implantation dose 5×10^{16} cm^{-2}, which is 5-times higher than former experiments). In this case, it would be reasonable to prolong the annealing procedure to obtain information on the suggested erbium-cluster decay, which is planned in our future work.

5. Conclusion

Various cuts of LN crystalline samples were implanted by 190 keV Er^+ ions with the fluencies of 1×10^{16} cm^{-2} and 5×10^{16} cm^{-2}. The RBS analysis shows that erbium concentration depth profiles are significantly influenced by the annealing at 1000 °C where the erbium concentration profile change is more pronounced for the lower implantation fluence. The erbium concentration depth profiles became asymmetric after the annealing, due to the recrystallization of the LN structure. In agreement with our previous studies, the $Y_\perp$ crystallographic orientation is the orientations most affected by the implantation procedure. The increase of surface "bumps" measured by AFM was observed only for the Y_{II} cut, all other cuts have almost smooth surface. This effect is probably associated with the higher surface energy of this crystallographic cut and could also be a consequence of easy spreading of the tension along the crystal-cleavage plane. The RBS-channelling analysis provided information on a significant reconstruction of the LN crystalline structure after the annealing which is caused mainly by a decrease of the relative number of disordered atoms. The lower relative number of disordered atoms in the crystalline structure was observed in the LN samples implanted using 1×10^{16} cm^{-2}, where the preferential position of the erbium in substitutional sites was observed when compared to the randomly distributed erbium in interstitial positions at a fluence of 5×10^{16} cm^{-2} after the annealing. The luminescence properties showed that the implantation introduced a different defect density and location, e.g. created a different ordering around erbium

atoms, which implies differences in luminescence spectra. It was also found that the higher implantation 5×10^{16} cm^{-2} had lower luminescence intensity compared with the sample implanted 1×10^{16} cm^{-2}, which is probably caused by the formation of erbium clusters in the LN structure, which is worsening the desired luminescence properties.

Acknowledgements

The research has been realised at the CANAM (Center of Accelerators and Nuclear Analytical Methods) infrastructure and has been supported by project No. P108/12/G108.

References

[1] A.J. Kenyon, Prog. Quantum Electron. 26 (2002) 225.
[2] A. Polman, J. Appl. Phys. 82 (1997) 1.
[3] L. Tsonev, Opt. Mater. 30 (2008) 892.
[4] C. Buchal, Annu. Rev. Mater. Sci. 24 (1994) 125.
[5] C. Mignotte, Appl. Surf. Sci. 185 (2001) 11.
[6] M.P.F. Graca, J. Phy. Condens. Matter 19 (2007) 016213.
[7] K.K. Wong, Properties of Lithium Niobate, INSPEC, London, 2002.
[8] L. Arizmendi, Phys. Status Solidi A 201 (2004) 253.
[9] M. Rahmani, L.H. Abu-Hassan, P.D. Townsend, I.H. Wilson, G.L. Destefanis, Nucl. Instr. Meth. Phys. Res. B 32 (1988) 56.
[10] P. Nekvindová, J. Spirkova, J. Schröfel, V. Perina, J. Mater. Res. 16 (2) (2001) 333.
[11] B. Svecova, P. Nekvindova, A. Mackova, J. Oswald, J. Vacik, R. Grotzschel, J. Spirkova, Nucl. Instr. Meth. Phys. Res. B 267 (2009) 1332.
[12] J. Saarilahti, E. Rauhala, Nucl. Instr. Meth. Phys. Res. B 64 (1992) 734.
[13] M. Mayer, SIMNRA version 6.06, Max-Planck-Institut fur Plasmaphysik, Garching, Germany, 2011. Available at: http://home.rzg.mpg.de/~mam/Download.html
[14] IBANDL, http://www-nds.iaea.org/ibandl/
[15] E.S. Gadelmawla, M.M. Koura, T.M.A. Maksoud, I.M. Elewa, H.H. Soliman, J. Mater. Process. Technol. 123 (2002) 133–145.
[16] <www.srim.org>
[17] A. Meldrum, L.A. Boatner, W.J. Weber, R.C. Ewing, J. Nucl. Mater. 300 (2–3) (2002) 242–254.
[18] J.R. Tesmer, M.A. Nastasi, Handbook of Ion Beam Spectroscopy, Materials Research Society, 1995.
[19] P.M. Mattarelli, S. Sebastiani, J. Spirkova, S. Berneschi, M. Brenci, R. Calzolai, A. Chiasera, M. Ferrari, M. Montagna, G. Nunzi Conti, S. Pelli, G.C. Righini, Opt. Mater. 28 (2006) 1292–1295.
[20] D. Boivin, T. Föhn, E. Burov, et al., Proc. SPIE (2010) 75802B-1–9.

Journal of Luminescence 164 (2015) 90–93

Contents lists available at ScienceDirect

Journal of Luminescence

journal homepage: www.elsevier.com/locate/jlumin

Influence of gallium on infrared luminescence in Er^{3+} doped $Yb_3Al_{5-y}Ga_yO_{12}$ films grown by the liquid phase epitaxy

T. Hlásek [a,*], K. Rubešová [a], V. Jakeš [a], P. Nekvindová [a], J. Oswald [b], M. Kučera [c], M. Hanuš [c]

[a] Department of Inorganic Chemistry, University of Chemistry and Technology Prague, Technická 5, Prague 6 166 28, Czech Republic
[b] Institute of Physics v.v.i., Academy of Sciences of the Czech Republic, Cukrovarnická 10, Prague 6 162 00, Czech Republic
[c] Charles University, Faculty of Mathematics and Physics, Ke Karlovu 5, Prague 2 121 16, Czech Republic

ARTICLE INFO

Article history:
Received 12 December 2014
Received in revised form
21 March 2015
Accepted 24 March 2015
Available online 1 April 2015

Keywords:
Liquid phase epitaxy
Optical materials
Luminescence
Ytterbium aluminium garnet
Er^{3+}-doping
Ga doping

ABSTRACT

Erbium (Er^{3+}) doped ytterbium garnet $Yb_3Al_{5-y}Ga_yO_{12}$ ($y=0$, 0.55 and 1.1, YbAGG) thick films were grown by the isothermal liquid phase epitaxy method (LPE) on LuAG or YAG substrates. The influence of gallium on the photoluminescent properties of Er^{3+} is presented in this paper. Room temperature transmission and emission spectra were measured for the 0.5 at% Er^{3+}:YbAGG films with a different doping level of Ga. Also Er^{3+}:$Yb_3Al_{3.9}Ga_{1.1}O_{12}$ ($y=1.1$) films with a different doping level of erbium (0.5, 1 and 2 at%) were tested. The presence of gallium significantly affects the fine splitting and total intensity of erbium emission in an infrared region (the transition $^4I_{13/2} \rightarrow {}^4I_{15/2}$). Even at the highest doping level of erbium (2 at%), no up-conversion luminescence was observed, resulting in a maximum efficiency of the infrared emission. The lifetime of luminescence at 1530 nm was studied for all samples.

1. Introduction

Garnets with general formula $A_3B_5O_{12}$, where A is yttrium or rare-earth metal and B is trivalent d- or p-block metal (e.g. Al, Ga, Fe or their combination), are promising host materials for many optical applications. The main benefits of these materials are a wide transparency range, good thermal conductivity, isotropic optical properties, high thermal and chemical stability and the ability to modify both refractive index and lattice parameter with a composition change [1]. Thanks to these characteristics, the garnets have been used as a host material for many optical activators such as Cr^{4+} [2], Nd^{3+} [3], Ce^{3+} [4], Yb^{3+} [5] or Er^{3+} [6].

Among the rare-earth ions, Er^{3+} has been one of the most studied activators in recent years. Due to its energy level structure, Er^{3+} can emit violet, green, red and infrared light. With minor changes of composition (co-doping, the concentration of erbium), the material with a single color emission can be prepared [7–9]. Material which exhibits up-conversion emission in the visible spectral range could be applied in color displays, optoelectronics, sensor technology, solid state lasers or bio-imaging [10,11]. Additionally, the IR emission of erbium is used for the optical amplification of signal in the third telecommunication window [12].

The infrared emission of erbium (the transition $^4I_{13/5} \rightarrow {}^4I_{15/2}$) has a sharp maximum at 1530 nm with spectral width of around 10 nm and, due to its parity-forbidden nature, the emission has a long lifetime (~ms). However, the low absorption cross-section of Er^{3+} decreases the efficiency of luminescence by NIR excitation (approx. 980 nm). To overcome this phenomenon, Yb^{3+} has been successfully used as a sensitizer in many host materials such as $LiNbO_3$ [13,14], $KY(WO_4)_2$ [15], $NaYF_4$ [16] or YAG [17,18]. The energy transfer from ytterbium ($^2F_{5/2}$) to erbium ($^4I_{11/2}$) is highly effective when ytterbium is used as a part of the host material and not just as a co-dopant (e.g. in $Yb_3Al_5O_{12}$) [19].

For the preparation of waveguide structures with good amplifying effect, a precise control of the lattice parameter and refractive index is very important for both an optical active film and substrate. The substitution of gallium for aluminum is one possible way to increase the refractive index and adjust the lattice parameter [20,21]. But, to our best knowledge, there is no work dedicated to the influence of gallium substitution on the IR emission of Er^{3+} in YbAG.

In this work, we studied the effect of gallium substitution on the IR emission of erbium ions in planar waveguide films prepared by liquid phase epitaxy (LPE). Two different sets of samples were

* Corresponding author. Tel.: +420 220 443 765.
E-mail address: hlasekt@vscht.cz (T. Hlásek).

http://dx.doi.org/10.1016/j.jlumin.2015.03.030
0022-2313/

prepared to investigate the effect of gallium and erbium concentration on luminescent properties of $(Yb,Er)_3(Al,Ga)_5O_{12}$. Our aim was to prepare waveguide structures with pure IR emission.

2. Experimental

The single crystalline epitaxial garnet films Er:$Yb_3Al_{5-y}Ga_yO_{12}$ (where $y=0$, 0.55 and 1.1) were prepared from $PbO–B_2O_3$ flux by the standard isothermal dipping technique; the details were published elsewhere [22,23]. The films were grown from a supercooled melt solution at constant supercooling onto the $Y_3Al_5O_{12}$ (YAG) or $Lu_3Al_5O_{12}$ (LuAG) substrates of (1 1 1) crystallographic orientation and 20 mm in diameter. The growth temperature was in the range of 967–996 °C with the supercooling of 14–18 °C.

The phase composition and film orientation were determined by X-ray diffraction (XRD). The device used was the Expert Pro θ–θ powder diffractometer with parafocusing Bragg–Brentano geometry using the CuK_α radiation ($\lambda=1.5418$ Å, $U=40$ kV, $I=20$ mA). Data evaluation was performed in the software package HighScore Plus.

The photoluminescence spectra of the prepared films were collected within the range of 1440–1650 nm at room temperature. Semiconductor laser POL 4300 emitting at 980 nm was used for the excitation. The luminescence radiation was detected by a two-step-cooled Ge detector J16 (Teledyne Judson Technologies). To scoop specific wavelengths, a double monochromator SDL-1 (LOMO) was used. A synchronous detection technique was implemented by chopping the laser beam at a modulation frequency of about 35 Hz, and by employing a lock-in amplifier (EG&G 5205). For evaluation, all luminescence spectra were transposed to the base level. For the decay measurement, the Er^{3+} luminescence was excited by a laser pulse (980 nm). The photoluminescence (PL) intensity was captured by a fast detector with rising and falling edge of 60 μs. The progress of PL was recorded on the memory oscilloscope. A tungsten lamp and a single grating spectrometer MDR 23 were used as a source of monochromatic light for transmission measurement. A pyroelectric detector was used for detection of transmitted light and also for a relative calibration of the incident light intensity. A synchronous detection technique was used to suppress a noise. All measurements were performed at room temperature.

Waveguiding properties were measured with m-line mode spectroscopy on the Metricon Prism Coupler device. For the samples that guided three and more optical modes, it was possible to evaluate the refractive index depth profiles [24]. The refractive index profiles of the waveguides were reconstructed from the measured effective index spectra by means of inverse WKB procedure (Wentzel–Kramers–Brillouin approximation – a method for finding approximate solution to linear partial differential equations with spatially varying coefficients). Our measurement was done using the prism with the effective range of refractive index value from 1.2 to 2.02 (for 633 nm) at the operating wavelength 1552 nm in the TE polarization. The determined properties were: the number of guided optical modes, the overall change of waveguides refractive index, and the layer thickness. The accuracy of n_e measurement is ± 0.0001 for the 1552 nm wavelength.

3. Results and discussion

Precise control of the lattice parameter and refractive index is very important for the preparation of waveguide structures. The substitution of gallium for aluminum is one possible way to increase the refractive index and adjust the lattice parameter [20,21]. In this work, we studied the effect of gallium substitution on the IR luminescence of erbium.

The essential technology demands on high quality planar waveguide are good lattice match of the film and substrate, suitable ratio of waveguide/substrate refractive indices, and good surface morphology. All these requirements can be achieved by choice of a suitable substrate and/or by Ga substitution for Al ions in the YbAG garnet lattice. Measured lattice parameters of LuAG and YAG single crystal substrates were 12.918 and 12.008 Å, respectively, and that of YbAG film was 11.942 Å. In order to obtain high quality films with good surface morphology, the film-substrate lattice mismatch must be minimized. The composition and lattice constants of studied samples are summarized in Table 1. The lattice mismatch of optimized samples Yb-3–Yb-5 with Ga content $y=1.1$ (grown on YAG substrate) does not exceed 0.01 Å. The films have high quality optical surface with optical transmission close to the theoretical limit and also good waveguide properties. The film Yb-2 grown at higher lattice mismatch (Ga content $y=0.55$) had rough surface which partly scattered light, rendering is not suitable for waveguide applications. The film Yb-1 (YbAG:Er without Ga doping), which was grown onto LuAG substrate for better lattice mismatch, had good optical properties, but no waveguide effect was observed since its refractive index was close to that of the substrate. In spite of higher lattice mismatch of samples Yb-1 and Yb-2, both films are single crystalline with good emission properties and serve here as reference systems.

The epitaxial growth of the films was checked by X-ray diffraction – a typical diffractogram is shown in Fig. 1. In the range of 20–70° 2θ, the only visible diffraction peak is (4 4 4). This fact confirms the epitaxial growth of all prepared films. The detailed structure of the (4 4 4) reflection is displayed in the inset of Fig. 1.

The influence of gallium substitution on the room temperature emission spectra (the erbium transition $^4I_{13/2}\rightarrow{}^4I_{15/2}$ excited at 980 nm) in the samples of composition $Er_{0.015}Yb_{2.985}Al_{5-y}Ga_yO_{12}$ (where $y=0$, 0.55 and 1.1) is shown in Fig. 2. As can be seen in our set of samples, the total intensity of the emission could be enhanced even by a small amount of gallium. Besides the overall intensity,

Table 1
Summary of the composition and lattice constants of $Yb_{3-x}Er_xAl_{5-y}Ga_yO_{12}$ epitaxial films.

Sample	Ga content	Er [at%]	Substrate	a [Å]
Yb-1	$y=0$	0.5% ($x=0.015$)	LuAG	11.942
Yb-2	$y=0.55$	0.5% ($x=0.015$)	YAG	11.958
Yb-3	$y=1.1$	0.5% ($x=0.015$)	YAG	11.997
Yb-4	$y=1.1$	1% ($x=0.03$)	YAG	11.997
Yb-5	$y=1.1$	2% ($x=0.06$)	YAG	11.997

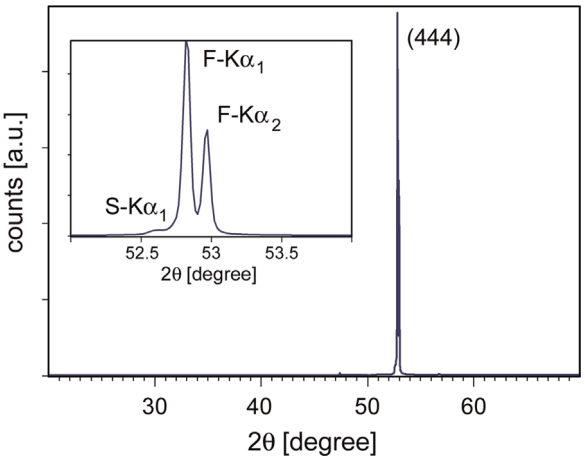

Fig. 1. X-ray diffraction pattern of the Yb-4 film (F—film, S—substrate).

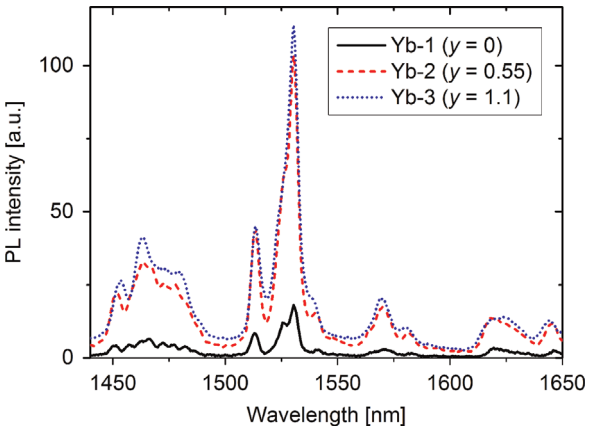

Fig. 2. Room temperature emission spectra of Er-doped films with different content of gallium, λ_{ex}=980 nm, Er^{3+} concentration is 0.5 at%.

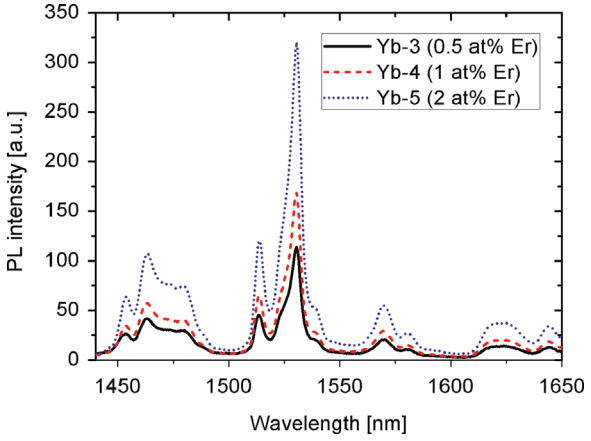

Fig. 3. Room temperature Er^{3+} emission spectra of Er_x:$Yb_{3-x}Al_{3.9}Ga_{1.1}O_{12}$ films with different content of erbium, λ_{ex}=980 nm.

gallium affects also the relative intensity of almost all emission bands. On the other hand, the position of emission bands is affected only slightly by the presence of gallium. This phenomenon is probably caused by the change of the crystal field symmetry around Er^{3+} ions and it is well noticeable in the range of 1440–1500 nm. Regardless of the gallium concentration, the essential emission remains at 1530 nm. The emission spectrum of the sample without gallium is in good agreement with emission spectrum measured from bulk ceramics of the same composition [19]. Fig. 3 shows the room temperature emission spectra of the films with composition Er_x:$Yb_{3-x}Al_{3.9}Ga_{1.1}O_{12}$ (where x=0.015, 0.03 or 0.06; the content of gallium is constant). The intensity of the IR emission increases with increasing content of erbium up to 2 at%. If the excitation wavelength of 980 nm is used, the visible up-converted emission from level $^4I_{11/2}$ will be expected for Er:YbGaAG system. The up-converted emissions would be visible at the wavelengths of about 550 nm ($^4S_{3/2}\rightarrow{}^4I_{15/2}$) and 650 nm ($^4F_{9/2}\rightarrow{}^4I_{15/2}$). The room temperature emission in this region was measured in all samples. Even at such a high doping level of erbium, no up-conversion emission was observed, which documents the maximal efficiency of the IR emission.

The decay curves of the IR luminescence at 1530 nm are shown in Fig. 4 and the lifetimes of the same emission for all samples are listed in the Table 2. The measured data were fitted by one-exponential function for all samples. The fit was more accurate for the samples containing gallium. This could be caused by some non-radiative transitions in pure YbAG. On the other hand, the lifetime of the IR emission at 1530 nm is only slightly affected by the concentration of both erbium and gallium (in the studied

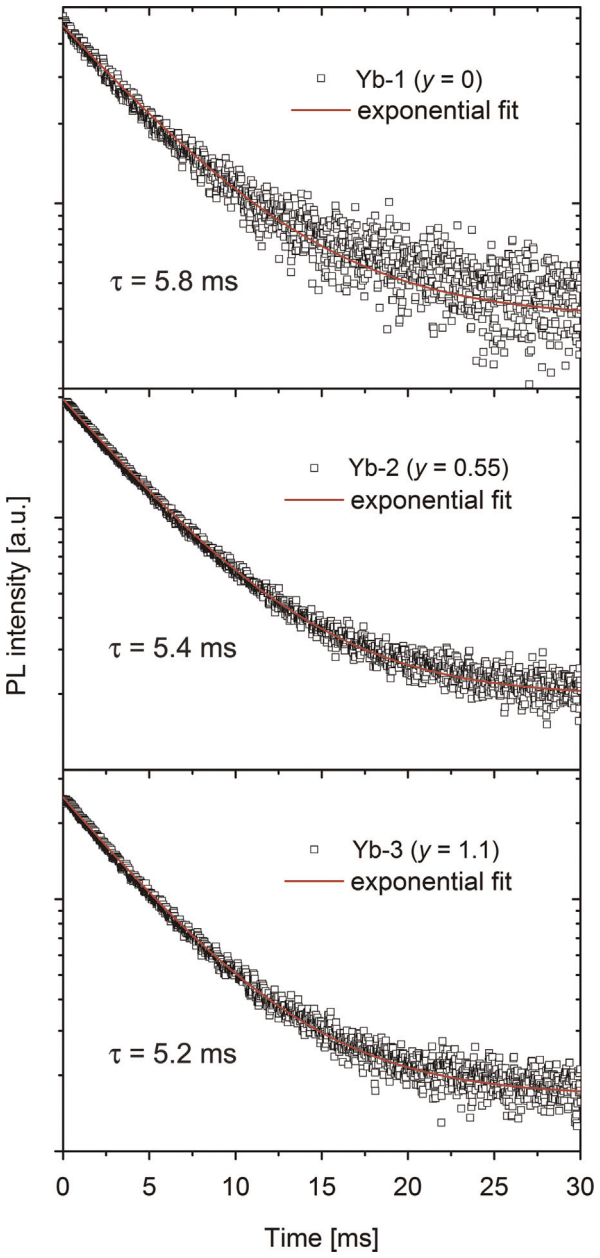

Fig. 4. Measured Er^{3+} decay curves and one-exponential fit (solid lines) of the IR emission (λ_{em}=1530 nm) in films doped with with 0.5% of Er and different gallium content (y), λ_{ex}=980 nm, PL intensity is in logarithmic scale.

Table 2
Lifetime of the Er^{3+} luminescence at 1530 nm.

	Yb-1	Yb-2	Yb-3	Yb-4	Yb-5
Lifetime, τ [ms]	5.8	5.4	5.2	5.3	5.1

The accuracy of lifetime determination is smaller than $\pm$0.05 ms.

range of concentration). These lifetimes are comparable with the ones in the YAG and YbAG single crystals [25,26].

Fig. 5 shows the room temperature spectra of absorption coefficients for the films with different content of gallium. The spectra were calculated from transmission measurement, the sample Yb-2 was corrected for scattered light as mentioned above. The position of absorption bands is not influenced by changes in crystal field of Yb^{3+} ions. However, the relative intensity of absorption bands is slightly affected by the presence of gallium. The 4f–4f absorption

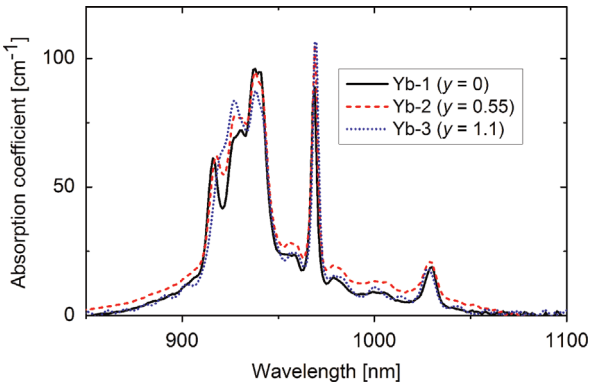

Fig. 5. Room temperature absorption spectra of the Er-doped YbAG films with Er content of 0.5% and different content of gallium.

Table 3
Thickness, refractive index and number of propagation modes in samples.

Sample	Thickness Δm (μm) m-line	Refractive index at λ=1552 nm	Number of guided modes (λ=1552 nm)
Yb-1	21.3	–	–	0
Yb-2	17.4	–	–	0
Yb-3	19.0	17.6	1.8445	7
Yb-4	13.7	13.1	1.8460	5
Yb-5	13.5	13.5	1.8457	5
YbAG	–	–	1.8217 [27]	–

The accuracy of refractive index value measurement is ±0.0001 for the 1552 nm wavelength, the accuracy of film thickness value is ±0.5 μm.

lines in Er^{3+} were not observed in the transmission spectra due to low Er^{3+} concentration, low thickness of films, and optical interference in films Yb-3 though Yb-5. With respect to pumping mechanism, the most important region of the absorption spectrum is the sharp band of Yb^{3+} transition $^2F_{7/2}\rightarrow{}^2F_{5/2}$ at approx. 970 nm. In this region the absorption is enhanced by 20% by the presence of gallium. This phenomenon could contribute to the enhanced IR emission of Er^{3+} in samples containing gallium. Changes in the concentration of Er^{3+} ions (in the range of 0.5–2 mol%) have no significant effect on both position and relative intensity of all Yb^{3+} absorption bands.

Waveguiding properties at 1552 nm were also studied and the results are summarized in the Table 3. It is obvious from the table that all films with the highest content of gallium were multi-mode waveguides at the wavelength of 1552 nm. The prepared films guided 5–7 optical modes. The number of optical modes increased with the thickness of the film. The total refractive index change was 0.02 compared to the pure YbAG for all the samples with the highest content of gallium. The film thickness 13–17 μm was calculated by the WKB calculation. For these samples, the thickness determined by the m-line spectroscopy was in good agreement with the one calculated from the mass change after deposition of the films (see Table 3).

The samples Yb-1 and Yb-2 do not exhibit waveguiding effect. In the case of the sample Yb-1, the reason is an inappropriate ratio of refractive indices of the film and the LuAG substrate. In the second case (the sample Yb-2), the high value of optical loss comes from high lattice mismatch (as discussed above).

4. Conclusions

The single-crystalline thick films with the composition $(Er,Yb)_3(Al,Ga)_5O_{12}$ were successfully prepared by the liquid phase epitaxy on LuAG or YAG substrates. The aim was to optimize the lattice mismatch and the refractive index by gallium substitution and simultaneously to preserve excellent luminescent properties of Er^{3+} ions. The presence of gallium in our set of samples enhanced the infrared emission of Er^{3+} at 1530 nm (transition $^4I_{13/2}\rightarrow{}^4I_{15/2}$). There was no visible up-conversion emission even at the highest erbium doping level of 2% (x=0.06). All films exhibit one-exponential decay of the IR Er^{3+} emission with lifetimes between 5.1 and 5.8 ms indicating that there is no energy transfer from the Er^{3+} activators and the reduction of the lifetime due to gallium substitution is negligible. Due to the higher refractive index of the gallium containing films, the samples with y=1.1 of gallium were multi-mode planar waveguides at 1552 nm. More detailed structural and opto-geometrical study needs to be done in this system; however, the prepared films with the composition $Er_x:Yb_{3-x}Al_{3.9}Ga_{1.1}O_{12}$ seem to be very promising for the construction of a waveguide laser structure with IR emission in the third telecommunication window at 1.55 μm.

Acknowledgements

This work was financially supported from the specific university research (MSMT No. 20/2015) as well as by the Project P108/12/G108.

References

[1] P.K. Tien, R.J. Martin, S.L. Blank, S.H. Wemple, L.J. Varnerin, Appl. Phys. Lett. 21 (1972) 207.
[2] X.D. Xu, Z.W. Zhao, X.M. He, P.X. Song, G.Q. Zhou, J. Xu, P.Z. Deng, Mater. Lett. 58 (2004) 3153.
[3] H. Yagi, T. Yanagitani, K. Takaichi, K.-i Ueda, A.A. Kaminskii, Opt. Mater. 29 (2007) 1258.
[4] S. Murai, M.A. Verschuuren, G. Lozano, G. Pirruccio, A.F. Koenderink, J.G. Rivas, Opt. Mater. Express 2 (2012) 1111.
[5] D. Pelenc, B. Chambaz, I. Chartier, B. Ferrand, C. Wyon, D.P. Shepherd, D.C. Hanna, A.C. Large, A.C. Tropper, Opt. Commun. 115 (1995) 491.
[6] H.L. Xu, S. Kröll, J. Lumin. 111 (2005) 191.
[7] C. Xu, Q. Yang, G. Ren, Y. Liu, J. Alloy. Compd. 503 (2010) 82.
[8] K. Rubešová, T. Hlásek, V. Jakeš, P. Matějka, J. Oswald, P. Holzhauser, J. Sol–Gel Sci. Technol. 70 (2014) 142.
[9] Z.P. Li, B. Dong, Y.Y. He, B.S. Cao, Z.Q. Feng, J. Lumin. 132 (2012) 1646.
[10] D.K. Chatterjee, A.J. Rufaihah, Y. Zhang, Biomaterials 29 (2008) 937–943.
[11] F. Wang, X. Liu, J. Am. Chem. Soc. 130 (2008) 5642.
[12] Y. Mao, T. Tran, X. Guo, J.Y. Huang, C.K. Shih, K.L. Wang, J.P. Chang, Adv. Funct. Mater. 19 (2009) 748.
[13] M. Jelinek, J. Oswald, T. Kocourek, K. Rubesova, P. Nekvindova, D. Chvostova, A. Dejneka, V. Zelezny, V. Studnicka, K. Jurek, Laser Phys. 23 (2013).
[14] J.B. Shim, N. Yoshimoto, M. Yoshizawa, D.H. Yoon, Cryst. Res. Technol. 36 (2001) 1209.
[15] S. García-Revilla, R. Valiente, Y.E. Romanyuk, M. Pollnau, J. Lumin. 128 (2008) 934.
[16] X. Huang, G. Hu, Q. Xu, X. Li, Q. Yu, J. Alloy. Compd. 616 (2014) 652.
[17] E. Garskaite, M. Lindgren, M.-A. Einarsrud, T. Grande, J. Eur. Ceram. Soc. 30 (2010) 1707.
[18] J. Zhou, W. Zhang, T. Huang, L. Wang, J. Li, W. Liu, B. Jiang, Y. Pan, J. Guo, Ceram. Int. 37 (2011) 513.
[19] T. Hlásek, K. Rubešová, V. Jakeš, O. Jankovský, J. Oswald, J. Eur. Ceram. Soc. 34 (2014) 3779.
[20] H. Kimura, A. Miyazaki, Jpn. J. Appl. Phys. 41 (2002) 5334.
[21] H. Kimura, A. Miyazaki, J. Cryst. Growth 250 (2003) 251.
[22] M. Kučera, K. Nitsch, M. Nikl, M. Hanuš, S. Daniš, J. Cryst. Growth 312 (2010) 1538.
[23] M. Kucera, K. Nitsch, M. Kubova, N. Solovieva, M. Nikl, J.A. Mares, IEEE Trans. Nucl. Sci. 55 (2008) 1201.
[24] K.S. Chiang, J. Lightwave Technol. 3 (1985) 385.
[25] J. Gruber, J. Quagliano, M. Reid, F. Richardson, M. Hills, M. Seltzer, S. Stevens, C. Morrison, T. Allik, Phys. Rev. B 48 (1993) 15561.
[26] M. Kaczkan, M. Borowska, M. Malinowski, T. Lukasiewicz, K. Kolodziejak, Phys. Status Solidi B 246 (2009) 1677.
[27] F.D. Patel, E.C. Honea, J. Speth, S.A. Payne, R. Hutcheson, R. Equall, IEEE J. Quantum Electron. 37 (2001) 135.

Optical waveguides in Er:$LiNbO_3$ fabricated by different techniques – a comparison

Jakub Cajzl [a,b*], Pavla Nekvindová [a], Anna Macková [c,d], Petr Malinský [c,d], Jiří Oswald [e], Stanislav Staněk [a], Soňa Vytykáčová [a] and Jarmila Špirková [a]

[a] *Department of Inorganic Chemistry, Faculty of Chemical Technology, University of Chemistry and Technology, Technická 5, 166 28 Prague, Czech Republic*
[b] *Institute of Photonics and Electronics, Academy of Sciences of the Czech Republic, v.v.i., Chaberská 57, 182 51 Prague, Czech Republic*
[c] *Nuclear Physics Institute, Academy of Sciences of the Czech Republic, v.v.i., 250 68 Řež, Czech Republic*
[d] *Department of Physics, Faculty of Science, J. E. Purkinje University, České mládeže 8, 400 96 Ústí nad Labem, Czech Republic*
[e] *Institute of Physics, Academy of Sciences of the Czech Republic, v.v.i., Cukrovarnická 10, 162 53 Prague, Czech Republic*

[*]Corresponding author: cajzlj@vscht.cz

Keywords: Erbium, lithium niobate, optical waveguides, diffusion, ion implantation, luminescence.

Abstract

We report on the comparison of three techniques used for the fabrication of optical waveguides in erbium doped lithium niobate crystal substrates (Er:$LiNbO_3$). The techniques include ion in-diffusion from a titanium metal layer, annealed proton exchange (APE), and He^+ ion implantation. The main focus of the work was placed on the investigation of the influence of the used optical waveguides fabrication techniques on the structural and luminescence properties of Er:$LiNbO_3$ substrates. The results have shown that none of the used optical-waveguide-fabrication techniques significantly affect the position of erbium in the host crystal structure. It turned out, however, that the fabrication process affected luminescence intensities of the characteristic luminescence bands of erbium ions – the most significant decrease in the luminescence intensity was observed with the Ti-indiffused waveguides.

1. Introduction

Solid-state planar waveguide devices – doped with optically active ions – such as lasers, optical amplifiers and various optical modulators and switches are gaining growing attention nowadays along with the all-optics approach. Erbium-doped lithium niobate (Er:$LiNbO_3$, Er:LN) is one of the most widely studied erbium-doped crystal material in photonics and optoelectronics. This is thanks to its ability to amplify and especially modulate the optical signal transmitted. The modulation of an optical signal is enabled by the lithium niobate's unique combination of special effects: electrooptic, acoustooptic, piezoelectric, ferroelectric, optical nonlinearity, etc. [1].

In order to transmit a defined optical beam through the Er:$LiNbO_3$ structure, it is necessary to create an optical waveguide in this structure. Erbium-doped $LiNbO_3$ is mainly used as a bulk-doped or localized-doped material. None of these methods of erbium doping cause a sufficient refractive index change in the material to create optical waveguides. The most common techniques for the fabrication of the planar optical waveguides in $LiNbO_3$ substrates are high-temperature doping from the evaporated metal layer (Ti, Zn, …), ion implantation (H^+, He^+, Si^+, …) and APE (Annealed Proton Exchange) with adipic or benzoic acid [2-5]. Other technologies include various deposition techniques

(epitaxial growth, sol-gel, CVD = Chemical Vapour Deposition, etc.), dry and wet etching, and recently also direct optical UV writing [6-8]. It follows from a comparison of these methods in terms of waveguiding properties that the optical waveguides prepared by Ti in-diffusion and APE have the highest total refractive index change [2]. The thickness of the fabricated optical waveguides can be adjusted by the setting of the experimental conditions – i.e. the duration of the annealing process in the case of Ti in-diffusion and APE, and the energy and the fluence of ion implantation in the case of He^+ ion implantation. In the literature are works covering each of these waveguides-fabrication techniques (used for the $LiNbO_3$ crystalline material), but there is still a lack of a serious comparisons between different techniques in terms of waveguiding and spectroscopic properties (most preferably using same substrates and measurement setups for the characterization of the results). Many of these waveguides-fabrication techniques resulted in the production of various Er:$LiNbO_3$ photonic devices, mainly Ti:Er:$LiNbO_3$ waveguide lasers (Q-switched, mode-locked etc.) [9,11]. Since lithium niobate is a substrate material for the fabrication of various photonic devices such as acoustooptic switches, electrooptic devices, nonlinear optical devices, holographic memories, etc. [10] it gives an opportunity to fabricate quite complex, yet compact, photonic components and structures based on $LiNbO_3$ crystals.

The aim of this paper is to compare the three most widely used techniques for the fabrication of optical waveguides in erbium doped $LiNbO_3$ in terms of waveguiding, luminescence and structural properties, and to discuss the experimental results obtained. The main attention was focused on the investigation of the influence of the fabrication technique used on the structural and luminescence properties of the Er:$LiNbO_3$ substrate, as well as its influence on the position of erbium in the crystal structure. We have chosen to compare the optical waveguides in form of planar (slab) waveguides, not channel (or strip) waveguides, since we wanted to investigate the fundamental effects of fabrication of optical waveguides on optical and structural properties of the host material. Although channel waveguides are more close to the actual application in photonic systems and they also can be more precisely measured for e.g. optical attenuation (and optical amplification in Er:$LiNbO_3$ system), there are however many fabrication techniques for channel waveguides (e.g. litography methods or buried strip waveguides) and accordingly many more parameters of channel waveguides to design them (e.g. size, shape, etc.). These parameters can substantially change the behaviour of propagation of light in the fabricated channel optical waveguides and therefore make it hard to investigate the basic effects of fabrication process on the mentioned properties of optical waveguides. Also, channel waveguides are more difficult to make in terms of reproducibility as compared to planar waveguides, which make it harder to compare several techniques while having the same fabricated channel optical waveguides.

2. Experiments

2.1. The fabrication of optical waveguides in Er:$LiNbO_3$

The substrates used for the fabrication of optical waveguides were bulk-doped Er:$LiNbO_3$ single-crystalline wafers (erbium content was 0.5 at. % = 5000 ppm) synthesized by the Czochralski method in Crytur Turnov, Czech Republic. Two conventional crystallographic cuts were used – X <11-20> and Z <0001>. The dimensions of the samples were 25×25×0.7 mm. Optical waveguides were fabricated using three different technologies – high-temperature diffusion from an evaporated titanium metal layer, ion implantation of He^+, and APE.

The high-temperature diffusion from an evaporated titanium metal layer consisted of two basic parts – evaporation of a titanium metal layer and high-temperature annealing. The evaporation of the titanium metal layers with the thickness of 100 nm was done by magnetron sputtering on the crystal surface at Crytur Turnov, Czech Republic. High-temperature diffusions of titanium from the

evaporated metal layers were done under the following conditions: a temperature of 1060 °C, durations of 10 and 40 hours, a temperature ramp of 5 °C/min, atmosphere of dry O_2.

Ion implantation of He^+ was done using the ion implanter located at the department of the Nuclear physics ASCR, v.v.i. in Řež near Prague (Czech Republic). The crystal substrates were implanted with an energy of 2 MeV and ion fluences of 1.0×10^{14} and 1.0×10^{15} ions/cm^2.

APE was done in a melt with the composition of 99.5 mol. % of adipic acid and 0.5 mol. % of Li_2CO_3 at a temperature of 215 °C for 2 hours. Annealing was done under normal atmosphere with a temperature of 350 °C and duration of 1.5 hour. The experimental conditions were selected according to [12].

2.2. The characterization of the fabricated optical waveguides

Er:$LiNbO_3$ samples with prepared optical waveguides were characterized primarily in terms of waveguiding and luminescence properties. Structural changes connected with the fabrication of the optical waveguides – as well as the position of the erbium in the surface structure – were also studied.

Waveguiding properties were measured using m-line mode spectroscopy on a Metricon Prism Coupler at five different wavelenghts – 473 nm, 633 nm, 964 nm, 1311 nm and 1552 nm. The device works on the principle of the dark mode spectroscopy [13,14]. The measurements were done using the Metricon #200-P-2-60 rutile prism (n = 2.8654, n(measuring range) = 2.00–2.65). The measured and determined properties were following: the number of guided optical modes, the overall change of the refractive index of waveguides and the refractive index depth profiles. Since $LiNbO_3$ is an anisotropic crystal, it was necessary to use an optical polarizer for the measurements of the Z cuts of $LiNbO_3$ – i.e. to carry out the measurements in the TM (Transverse-Magnetic) polarization. The used optical polarizer transmitted wavelengths of 473 nm and 633 nm – the longer wavelengths were absorbed. Due to this fact, the waveguiding properties of the Z cuts of $LiNbO_3$ were measured for the wavelengths of 473 nm and 633 nm only. For the samples that guided three and more optical modes, it was possible to evaluate the dependence of the refractive index on the depth [15].

The photoluminescence spectra of the prepared samples were collected within the range of 1440–1640 nm at room temperature. A continuous-wave semiconductor laser POL 4300 emitting at 980 nm was used for sample excitation. Luminescence radiation was detected by a two-step-cooled Ge detector J16 (Teledyne Judson Technologies). For the scooping of specific wavelengths, the double monochromator SDL-1 (LOMO) was used. Luminescence spectra were measured in a reflection arrangement and normalized to the same base level using a reference sample. Therefore, it was able to compare the luminescence intensities of the samples. Regarding the measurements, it is worth noting that all the samples had same dimensions and the luminescence measurements were done in one set for all samples using the same measurement setup.

Structural changes caused by the optical waveguides fabrication technologies used were measured by the RBS/Channeling method. The properties investigated were the degree of structural disorder and the position of erbium in the structure. The analyses were performed on a Tandetron 4130 MC accelerator, using a 2.0 MeV He^+ ion beam. He^+ ions, backscattered at a laboratory angle of 170°, were detected. The collected data were evaluated and transformed into concentration depth profiles utilizing the GISA 3 computer code [16] using cross section data from IBANDL [17]. The erbium detection limit of this method is between 0.1 and 0.2 at. % – below this limit, erbium cannot be detected within the requested accuracy due to the statistical noise in the RBS spectrum recorded.

3. Results

A total of 12 samples of optical waveguides in Er:$LiNbO_3$ were prepared – 4 samples from each of the three fabrication techniques. An overview of the optical waveguide samples prepared specifying the conditions of preparation and the used crystallographic cuts of Er:$LiNbO_3$ is provided in Table 1.

Table 1 An overview of the optical waveguides samples prepared – specifying the conditions of preparation and the used crystallographic cuts of Er:$LiNbO_3$.

Waveguide type	Cut (sample no.)	Conditions of preparation
Ti diffusion	X (793) Z (794)	1060 °C, 10 h, atm. O_2
	X (797) Z (798)	1060 °C, 40 h, atm. O_2
APE	X (795) (1)* Z (796) (1)* X (799) (2)* Z (800) (2)*	215 °C, 2 h, adipic acid; annealing: 350 °C, 1.5 h
He^+	X (I-274) Z (I-276)	2 MeV, 1.0×10^{14} ions/cm^2
	X (I-275) Z (I-277)	2 MeV, 1.0×10^{15} ions/cm^2

** The roman numbers I and II of the APE waveguides denote the first and second experiment.*

3.1. Waveguiding properties (m-line mode spectroscopy)

The samples prepared were characterized in terms of the number of the guided optical modes, the maximum refractive index change, and the thickness of waveguiding layer. Table 2 and 3 summarize the evaluated waveguiding properties of the prepared samples with optical waveguides in X- and Z-cuts of the Er:$LiNbO_3$.

The results have shown that optical waveguides prepared by high-temperature diffusion of titanium have overall very good waveguiding properties – under the given conditions they guided from 2 to 8 optical modes (the number of guided optical modes was decreasing for longer wavelengths, as expected according to the theory) with the total refractive index change Δn_e in the range of 0.004–0.019 for the different measuring wavelengths. The thicknesses of the titanium diffused waveguides were up to about 13 μm in depth for the X-cut and about 15 μm for the Z-cut.

Using the APE method, it was possible to fabricate optical waveguides in both crystallographic cuts of Er:$LiNbO_3$. The fabricated waveguides had Δn_e of approximately 0.080 for the X-cut and 0.055 for the Z-cut (at 633 nm). The fabricated APE waveguides guided 2–6 optical modes and the overall values of waveguiding layer thicknesses were up to 7 μm.

The ion implantation beam energy for the optical waveguides prepared by He^+ ion implantation was set to such a value that the thicknesses of the waveguides had comparable depths of waveguides as the other two methods used. In the samples fabricated using the ion implantation fluence of 1.0×10^{14} cm^{-2} the optical waveguides with sufficient refractive index changes were not created. Using the ion implantation fluence of 1.0×10^{15} cm^{-2}, the optical waveguides were created, however very faint – the measured intensities of the mode spectra were of much lower values when compared to the

other two technologies used. The optical waveguides guided up to 5 optical modes with Δn_e in the range of 0.008–0.030 for the different wavelengths, and the depths of waveguides were up to about 4 μm for the X-cut and about 6 μm for the Z-cut. Interesting was that in the Z-cut the optical-beam-guiding was measured not only in the TM polarization, as expected, but also in the TE polarization (discussed in Part 4.3.).

Refractive index depth profiles were calculated according to [15] from the measured refractive index values of the respective modes for all the technologies used. Fig. 1 shows the refractive index depth profiles of the fabricated optical waveguides for the X-cuts and Z-cuts of Er:$LiNbO_3$ with optical waveguides fabricated by (a) APE, (b) Ti-indiffusion and (c) He^+ ion implantation (the data were evaluated for a wavelength of 633 nm with the measured mode-points indicated). The characters (shapes) of the refractive index depth profiles of APE and Ti waveguides were the same (i.e. the Gaussian-type profile) with the difference being that the APE waveguides had a higher Δn_e. The optical waveguides prepared by He^+ ion implantation had a distinctive profile character. In our experiments, step-index behaviour was measured in the X-cut sample, with a large difference in the refractive index (the extraordinary refractive index of the Er:$LiNbO_3$ substrate is 2.202 at 633 nm). In the Z-cut sample, the refractive index depth profile was of the Gaussian type, and the difference in the refractive index as compared to the substrate was lower than in the X-cut sample.

Table 2 The waveguiding properties of the prepared optical waveguide samples in the X-cut of the Er:$LiNbO_3$.

Waveguide type	Cut (sample no.)	Wavelength [nm]	No. of guided modes	Total refractive index change Δn_e [-]	Waveguide thickness [μm]
Ti diffusion	X (793) *Ti, 10 h*	473	7	0.0188	8.4
		633	5	0.0150	8.6
		964	3	0.0108	7.1
		1311	2	0.0073	-
		1552	2	0.0078	-
	X (797) *Ti, 40 h*	473	8	0.0100	13.2
		633	6	0.0084	13.2
		964	3	0.0052	10.2
		1311	2	0.0056	-
		1552	2	0.0038	-
APE*	X (795)	473	6	0.1028	4.4
		633	4	0.0794	3.6
		964	3	0.0599	3.4
		1311	2	0.0457	-
		1552	2	0.0418	-
He^+	X (I-275) *1.0 × 10^15 cm^-2*	473	6	0.0302	3.7
		633	4	0.0155	4.2
		964	2	0.0075	-
		1311	2	-	-
		1552	-	-	-

** The results of the waveguiding properties of samples with APE optical waveguides were practically the same. Therefore, the table lists the results of the first experiment.*

Table 3 The waveguiding properties of the prepared optical waveguides samples in the Z-cut of the $Er:LiNbO_3$.

Waveguide type	Cut (sample no.)	Wavelength [nm]	No. of guided modes	Total refractive index change Δn_e [-]	Waveguide thickness [μm]
Ti diffusion*	Z (798)	473	8	0.0070	14.1
	Ti, 40 h	633	6	0.0058	15.5
APE**	Z (796)	473	5	0.0761	3.2
		633	4	0.0552	6.9
He^+	Z (I-277) *1.0 × 10^15 cm^-2*	473	5	0.0173	5.0
		633	5	0.0207	7.3
		964	3	0.0141	6.8
		1311	2	0.0097	-
		1552	2	-	-

** In the Z-cut sample with the optical waveguide fabricated using Ti diffusion for 10 h, the attempt to make optical contact for the measurement of waveguiding properties was not successful and the sample is not listed in the results (the most probable cause of this was the high roughness of the sample surface).*

*** The results of the waveguiding properties of the samples with APE optical waveguides were of practically same values. Therefore, the table lists the results of the first experiment.*

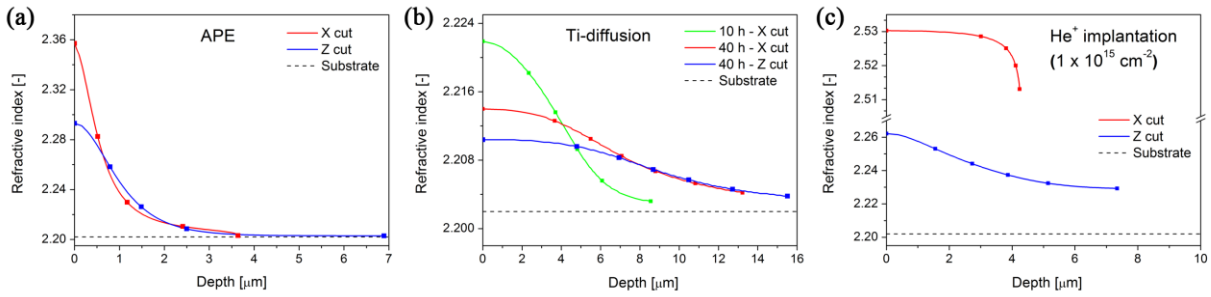

Fig. 1 The refractive index depth profiles with the measured mode-points for the X and Z-cuts of $Er:LiNbO_3$ with optical waveguides fabricated by (a) APE, (b) Ti-indiffusion and (c) He^+ ion implantation (spectra was measured at λ = 633 nm).

3.2. Luminescence properties (an analysis of the PL spectra)

In the measurement of luminescence properties, we focused mainly on the possible influence of the waveguide fabrication (in $Er:LiNbO_3$ substrates) on the luminescence of the optically active Er^{3+} ions. The luminescence spectra were collected in one measurement session for all the samples prepared; therefore, the measurement conditions were maintained and the luminescence intensities could be compared between samples (i.e. with different crystallographic cuts as well as different technologies used).

Fig. 2 shows the normalized measured luminescence spectra of all the X-cuts (a) and Z-cuts (b) of $Er:LiNbO_3$ samples with optical waveguides – in these spectra, the intensity was normalized from 0 to 1 in order to reveal the relative changes of the shapes between the spectra. From the spectra, it is evident that the fabrication of the optical waveguides does not change the shape of the main

luminescence bands of erbium for any of the technologies used (the same character of the spectra is always preserved for a given crystallographic cut – X and Z – of the Er:$LiNbO_3$).

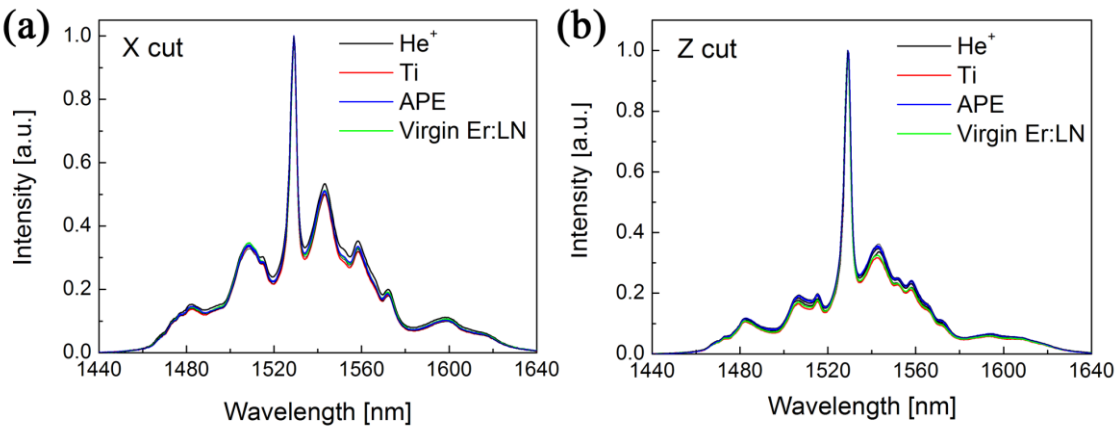

Fig. 2 The normalized measured luminescence spectra of all the X-cuts (a) and Z-cuts (b) of Er:$LiNbO_3$ samples with optical waveguides fabricated with the three technologies used.

Interestingly, small but significant changes of the absolute luminescence intensities of the samples were observed. In the Fig. 3 are depicted a comparisons of the absolute luminescence intensities of the prepared samples for the X-cuts of the Er:$LiNbO_3$. A comparison revealed that the optical waveguides prepared by He^+ ion implantation and the APE method had very similar luminescence intensities, which were comparable to the virgin Er:$LiNbO_3$ (X-cut and Z-cut) samples. On the contrary, the optical waveguides prepared by the Ti-diffusion technique exhibited significant decrease of the luminescence intensity of about 35% for the X-cut samples and 20% for the Z-cut samples. It was also confirmed known fact that the Z-cut samples had approximately 50% higher absolute luminescence intensities as compared to the X-cut samples – the luminescence intensity maximum was of about 3000 a.u. for the Z-cut and of about 2000 a.u. for the X-cut.

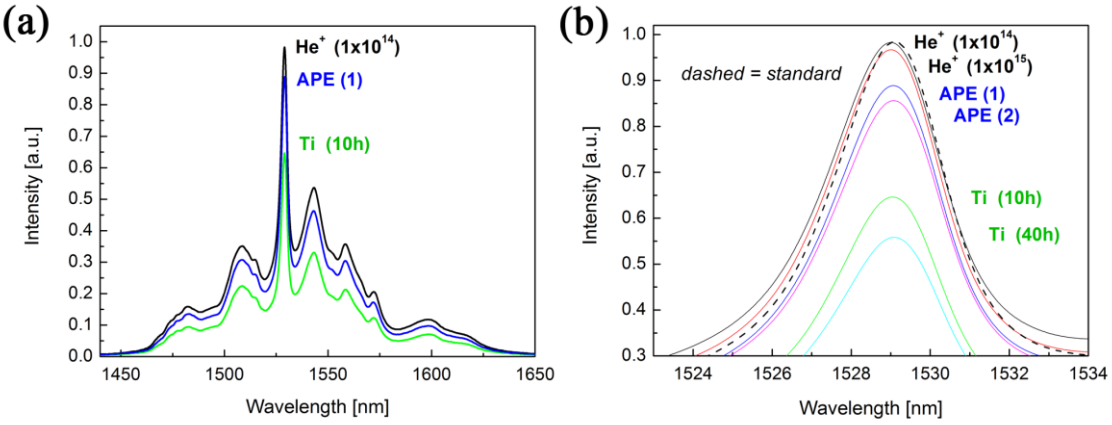

Fig. 3 A comparison of the absolute luminescence intensities of the prepared samples with the indication of the fabrication method used for the X-cuts of the Er:$LiNbO_3$. (a) The measured luminescence spectra of the prepared samples, (b) luminescence spectra of samples from all techniques in zoomed 1529 nm luminescence band.

3.3. The structural changes and positions of erbium (RBS/Channeling measurements, fine scans)

The structural changes induced by the fabrication of the optical waveguides were measured by the RBS/Channeling method. The results showed that the lowest structural disorder (practically zero) was

measured in the samples with optical waveguides fabricated by Ti diffusion, whereas the samples with APE waveguides had the highest values of the structural disorder – of about 12–14%. The samples with He^+ optical waveguides had for the lower ion implantation fluence practically zero structural disorder, whereas for the higher fluence the structural disorder raised up to 14% in the Z-cut.

It follows from the RBS/Channeling and fine scans results (see Fig. 4) that the erbium ions in all of the fabricated optical waveguides are in substitutional positions (i.e. substitution of lithium or niobium). The results are comparable to the virgin (unmodified) Er:$LiNbO_3$.

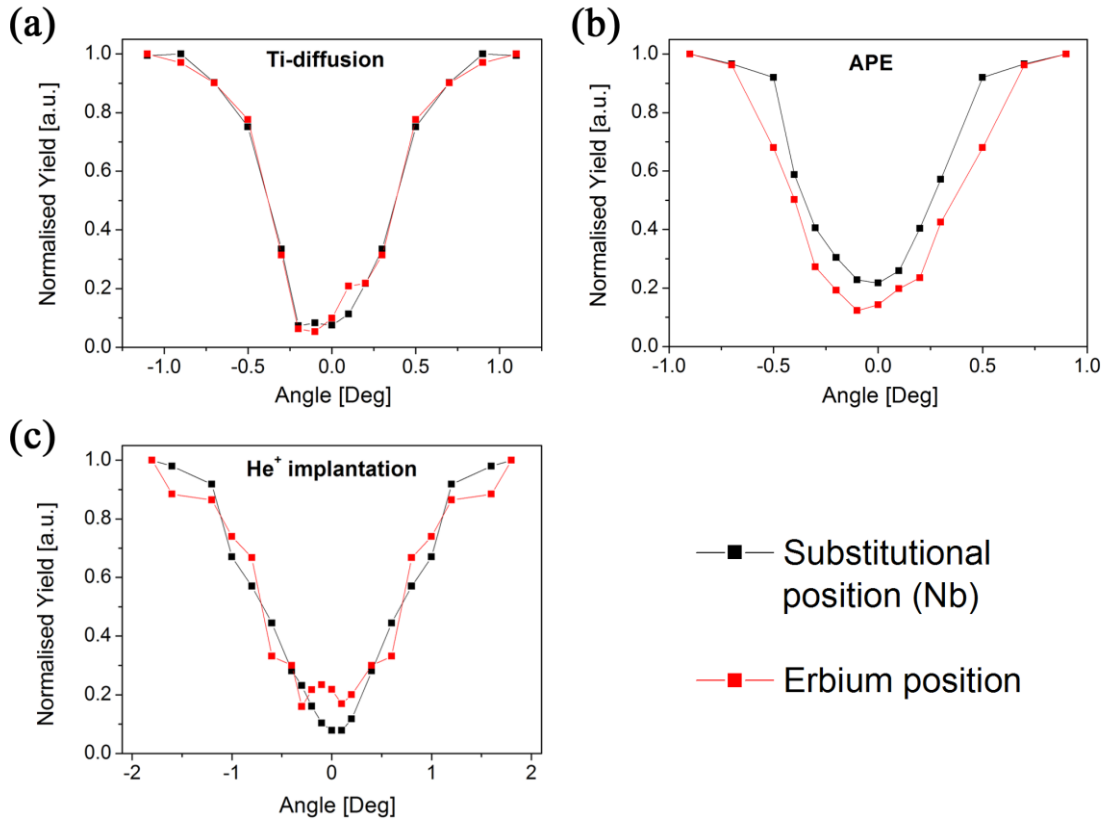

Fig. 4 The erbium position RBS/Channeling fine scans of the Z-cut samples for (a) Ti-diffusion, (b) APE and (c) He^+ ion implantation optical waveguides.
Samples: Ti-diffusion (10 h), APE (1), He^+ ion implantation (1.0×10^{15} cm^{-2})

4. Discussion – a comparison of the technologies used

A congruent crystal of lithium niobate can be easily doped with various elements and ions due to a large number of intrinsic defects caused by Li deficiency (approx. 6%). In the structure of the erbium bulk-doped $LiNbO_3$ (usually 0.5 at. % of Er), erbium is located in the substitutional positions of lithium, shifted along the c-axis of -0.02 nm [18,19] (a larger shift of -0.046 nm has also been published [20]). The refractive index value of Er:$LiNbO_3$ has practically the same value as the virgin $LiNbO_3$ crystal [21].

4.1. Diffusion from the Ti-metal layer

The diffusion of titanium into lithium niobate has been carried out at 1000 °C, i.e. above the temperature of recrystallization [22]. The process thus leads to the recrystallization of the whole structure of Er:$LiNbO_3$. The degree of structural disorder had an almost zero value, which indicates nearly recrystallized structure. Titanium, as well as erbium, occupy substitutional octahedral positions

of lithium [23] (lithium, niobium and substitutional positions of Ti and Er are aligned along the *c*-axis of $LiNbO_3$). It follows from the results that the position of erbium is not affected by the incorporation of Ti. The high degree of structural ordering is the presumable cause of the low attenuation of the optical signal of these waveguides. This has been confirmed by our m-line measurements of waveguide modes, since the the intensity of the mode spectra was very high. The total refractive index changes (Δn_e) of the waveguides prepared by this technique were the lowest among the three techniques. The Δn_e is most likely caused by the change of the polarizability of the structure resulting from the presence of Ti, which is a *d*-element. The positions of the luminescence bands of Er are not affected by the diffusion of Ti. The thicknesses of the titanium diffused waveguides were (using the specified preparation conditions) the highest of all three fabrication technologies and it reached up to 15 μm in depth. It follows from a comparison of both crystallographic cuts used that the titanium diffusion is faster in the Z-cut of Er:$LiNbO_3$ (i.e. in the Z-direction <0001>) than in the X-cut. This was determined by the fact that in the Z-cut a thicker waveguiding layer was created within the same amount of time.

4.2. Annealed Proton Exchange (APE)

During the process of proton exchange (PE), the lithium ions from the crystal surface are exchanged for the protons (H^+) from the acid melt. The lithium depletion in the surface of the crystal is dependent on the concentration of lithium in the acid melt and can be up to 100% [23]. Moreover, it has been published that there can be up to 7 different structural phases in the virgin crystal [25]. PE causes significant changes to the optical and physical properties of the crystal, which can be partially recovered by subsequent annealing at relatively low temperatures (~350 °C). The research results of the fabrication of the APE optical waveguides published previously by our group [26,18] revealed the important influence of the surface lithium depletion on the properties of the prepared optical waveguides. Furthermore, it has been found that during the process of APE, the Er ions are slightly shifted from their positions by 0.08 nm along the *c*-axis. The current results in this work show high degree of structural disorder in the APE waveguides which is caused by the significant change of the crystal-lattice parameters (probably the increase of lattice parameters values, which is referred to as 'swelling') caused by the depletion of lithium [27]. The change of the lattice parameters also lead to a substantial total refractive index change. The fabricated waveguides exhibited the highest refractive index change of all the three methods used – the Δn_e was approximately 0.080 for the X-cut and 0.055 for the Z-cut (at 633 nm); the Δn_e was thus about an order higher than in the case of Ti or He^+ waveguides. High intensity of the optical mode spectra indicates small optical attenuation of fabricated optical waveguides. The diffusion of hydrogen from proton exchange was faster in the X-cut, as expected – i.e. the thickness of the waveguide created in the X-cut sample was larger as compared to the Z-cut waveguide.

4.3. He^+ ion implantation

The optical waveguides fabricated by He^+ ion implantation technique are of diferent origin than the waveguides fabricated by two other techniques. The He^+ optical waveguides are created by local damage of the substrate crystal. The damaged layer depth and thickness are determined by the ion implantation energy and fluence, respectively. The ion implantation of the He^+ ions lead to a fluence-dependent helium and defect concentration in the damaged layers and therefore to a change of the refractive index [28]. The literature explains this change in two ways – as the creation of the so-called 'barrier waveguide' [29] and as the creation of the two layers, where one layer is created by the penetration of the implanted particle (close to the sample surface) and the other layer by the impact of the implanted particle (at a certain depth). The waveguide modes are confined between the buried

layer and the surface [30]. The ion implantated optical waveguides have similar refractive index change behaviour to step-index waveguides.

According to our results, it turned out that for Er:$LiNbO_3$ substrate the He^+ ion implantation fluence of 1.0×10^{14} cm^{-2} was insufficient to create optical waveguides; on the other hand, with the 1.0×10^{15} cm^{-2} ion implantation fluence, the optical waveguide was created (although it was not very pronounced). This implies that for the He^+ waveguides, higher ion implantation fluences or lower energies of ion implantation have to be used. However, one must consider the fact that higher ion implantation fluences or lower implantation energies also lead to a higher structural disorder (damage), which could not be recovered by the annealing process as usual, because it would cause the spread/diffusion of the optical waveguide.

The results further showed a substantial degree of structural disorder (2–14%), which is caused by the penetration of the implanted ions through the structure. This could lead to an increase of the lattice parameters, which would be an obvious reason for the considerably larger Δn_e. RBS/Channeling fine scans have not revealed any change of the position of erbium in the host structure. Regarding the fabricated Z-cut optical waveguides, it was interesting that the optical-beam-guiding was measured not only in the TM polarization as expected but also in the TE polarization. This indicates a different type of optical-beam guiding behaviour, which is presumably connected with the 'barrier' waveguide type of the He^+ ion implantation method. Moreover, it showed that the refractive index depth profiles of the waveguide samples prepared by He^+ ion implantation did not end at the value of the substrate refractive index (i.e. 2.202 at 633 nm) like samples prepared with other techniques. This is caused by the creation of the damaged layer by He^+ ion implantation in the certain depth in samples, which is responsible for the refractive index change in that depth – i.e. it is not a gradient Gaussian-type refractive index change profile, but rather a step-index profile, where the index change would be between the layer of He^+ penetration and the layer of He^+ impact (penetration causes intrinsic defects, while impact causes a He^+ incorporation defects).

It is also worth discussing the relatively large differences in the results between the two crystallographic cuts of the Er:$LiNbO_3$ (i.e. the X- and Z-cuts) in optical waveguides fabricated by He^+ ion implantation. The barrier-type (step-index-like) character of the refractive index was proven mainly in the X-cut, whereas the Z-cut has rather Gaussian-type of the refractive index profile. This could be explained by the fact that the degree of structural disorder (damage) was approximately 5-times higher in the surface layer of the Z-cut than in the X-cut; also the waveguide thicknesses were about 50% higher for the Z-cuts as compared to the X-cuts – i.e. the structural damage probably led to less 'sharp/step-index'-like behaviour of the waveguide in the Z-cut, and the waveguide was more diffused into the depth. The higher diffusion coefficient of the Z-cut could also play its role in the diffusion (or better incorporation) of the He^+ ions into the Z-cut samples during the ion implantation process. The more damaged structure of the Z-cut resulted in a higher Δn_e ($\geq$633 nm) and Gaussian-like refractive index profile.

4.4. The influence of the dopant on the luminescence properties

The elements in the structure of the Er:$LiNbO_3$ which are responsible for the desired luminescence properties around a wavelength of 1.5 μm are solely the erbium ions. The luminescence of erbium at around 1.5 μm is caused by the *f-f* transitions between the electron energy levels $^4I_{13/2} \rightarrow {}^4I_{15/2}$. Nevertheless, the *f*-orbitals of the erbium ions are (as opposed to e.g. *d*-elements) shielded by the outer *s* and *p* orbitals and thus are not so significantly affected by their surrounding ions. In our measurements, the previous assumptions proved to be right, because the luminescence properties of Er were not significantly affected by the structural changes but rather by the type of the codopant (i.e. Ti, H, He). According to Fig. 2, the positions of the luminescence bands were not affected; what was

affected, however, were the intensities of the luminescence bands (see Fig. 3b). The strongest influence on the luminescence intensities was observed with the Ti-waveguide samples. The reason for this phenomenon could be the energy-transfer processes that occur between the *d*- and *f*-orbitals of electrons in Ti and Er ions. The luminescence intensities were of the highest values in the He^+ and APE waveguide samples. Helium as a very small noble gas *s*-element hardly affects the Er luminescence properties. In the case of the hydrogen ions ('protons' as in annealed proton exchange), it is important to note that by incorporating hydrogen ions in the $LiNbO_3$ structure, there is a possibility of creation of -OH groups with stretch-vibration absorption overtones around a wavelength of 1.5 μm that couple non-radiatively to energy levels of Er^{3+} ions. However, the -OH groups influence was not observed or was of very low impact since the luminescence intensities of APE and He^+ waveguides were very similar.

5. Conclusions

In presented study the fabrication of optical waveguides in Er:$LiNbO_3$ using the the three different techniques (i.e. the diffusion of Ti from a metal layer, APE, and He^+ ion implantation) were carried out and results were discussed in detail. Comparing all three optical-waveguides-fabrication techniques in terms of the best waveguiding and luminescence properties, and in terms of the structure modification, the best technology appeared to be the APE method. The samples fabricated using APE method exhibited the highest refractive index change Δn_e, the highest overall quality of the waveguides (highest mode intensities in m-line spectroscopy measurements), and along with the He^+ waveguides they almost didn't affect the luminescence intensity of erbium. The measurements of luminescence spectra has revealed that the fabrication of the optical waveguides using the three techniques does not change the character (shape) of the luminescence spectra of the erbium ions in the structure, i.e. that there is no shift or relative attenuation of luminescence bands in the measured region around 1.5 μm. The fabrication of the optical waveguides has however influenced the intensity of the luminescence of erbium ions – the smallest decrease in luminescence intensity was observed in samples with optical waveguides fabricated by APE and He^+ ion implantation methods, whereas the Ti-waveguides exhibited a significant decrease in the luminescence intensity (which was substantially higher in the X-cut – of up to 35%). It can be therefore concluded that the luminescence intensity of Er ions is not influenced as much by the position of erbium in the surrounding matrix or by structural changes but rather by the type of the codopant used for the creation of optical waveguides. The highest influence on luminescence intensity was observed with the Ti-codopant. Regarding the choice of the crystallographic cut of Er:$LiNbO_3$, better cut for the fabrication of optical waveguides appeared to be the Z-cut, since the waveguides fabricated in the Z-cut had substantially higher luminescence intensities as compared to the X-cut; also the erbium luminescence in the Z-cut was not affected by the waveguide fabrication as much as in the X-cut. From the structural measurements it turned out that the erbium position in the crystal remains unchanged after the fabrication of the optical waveguides using each of the three techniques.

Acknowledgements

The research has been realised at the CANAM (Center of Accelerators and Nuclear Analytical Methods) infrastructure and has been supported by the Internal Grant Agency of the ICT Prague under the project A2_FCHT_2013_081. We also acknowledge the Czech Science Foundation project GA 14-05053S for the support of the research.

References

[1] K. K. Wong, *Properties of Lithium Niobate*, 1st ed.; INSPEC, IEE: London, 2002.

[2] L. Tsonev, Luminescent activation of planar optical waveguides in LiNbO3 with rare earth ions Ln3+ – a review, *Optical Materials* 30 (2008) 892–899.

[3] C. A Grivas, review – Optically pumped planar waveguide lasers, Part I – Fundamentals and fabrication techniques, *Progress in Quant. Electr*. 35 (2011) 159–239.

[4] F. Chen, X. L. Wang, K. M. Wang, Development of ion-implanted optical waveguides in optical materials: A review, *Optical Materials* 29 (2007) 1523–1542.

[5] M. Pollnau, Y. Romanyuk, Optical Waveguides in Laser Crystals, *C. R. Physique*, 8 (2007) 123–137.

[6] S.Mailis, C. Riziotis, I. T. Wellington, et al., Direct ultraviolet writing of channel waveguides in congruent lithium niobate single crystals, *Optics Letters* 28 (2003) 1433–1435.

[7] J. Burghoff, C. Grebing, S. Nolte, A. Tünnermann, Waveguides in lithium niobate fabricated by focused ultrashort laser pulses, *Applied Surface Science* 253 (2007) 7899–7902.

[8] E. Fazio, W. Ramandan, A. Petris, et al., Writing single-mode waveguides in lithium niobate by ultra-low intensity solitons, *Applied Surface Science* 248 (2005) 97–102.

[9] K. A. Winick, Rare-earth-doped waveguide lasers in glass and LiNbO3: a review, *SPIE Proceedings – Rare-Earth-Doped Devices II*, (1998) *3280*.

[10] L. Arizmendi, Photonic applications of lithium niobate crystals, *Phys. Status Solidi A* 201 (2004) 253–283.

[11] C. Becker, T. Oesselke, J. Pandavenes, et al., Advanced Ti:Er:LiNbO3 Waveguide Lasers, *IEEE Journal of Selected Topics in Quant. Electr*. 6 (2000) 101–113.

[12] P. Nekvindová, J. Špirková, J. Červená, et al., Annealed proton exchanged optical waveguides in lithium niobate: differences between the X- and Z-cuts, *Opt. Mat.* 19 (2002) 245–253.

[13] R. Ulrich, R. Torge, Measurement of thin film parameters with a prism coupler, *Appl. Opt.* 12 (1973) 2901–2908.

[14] M. J. Adams, *An Introduction to Optical Waveguides*, John Wiley and Sons, Ltd., 1981.

[15] K. S. Chiang, Construction of refractive-index profiles of planar dielectric waveguides from the distribution of effective indexes, *Journal of Lightwave Technology* 3 (1985) 385–391.

[16] J. Saarilahti, E. Rauhala, Interactive personal-computer data analysis of ion backscattering spectra, *Nucl. Instrum. Methods Phys. Res., Sect. B* 64 (1992) 734–738.

[17] IBANDL, http://www-nds.iaea.org/ibandl/.

[18] A. Macková, R. Groetzschel, F. Eichhorn, P. Nekvindová, J. Špirková, Characterization of Er:$LiNbO_3$ and APE:Er:$LiNbO_3$ by RBS–channeling and XRD techniques, *Surface and Interface Analysis* 36 (2004) 949–951.

[19] L. Rebouta, M. F. da Silva, J. C. Soares, et al., Nonaxial sites for Er in $LiNbO_3$, *Applied Physics Letters* 70 (1997) 1070–1072.

[20] T. Gog, M. Griebenow, G. Materlik, X-ray standing wave determination of the lattice location of Er diffused into $LiNbO_3$, *Physics Letters A* 181 (1993) 417–420.

[21] M. Jelínek, J. Oswald, T. Kocourek, et al. Optical properties of laser-prepared Er- and Er,Yb-doped $LiNbO_3$ waveguiding layers, *Laser. Phys.* 23 (2013) 105819.

[22] A. Meldrum, L. A. Boatner, W. J. Weber, R. C. Ewing, Amorphization and recrystallization of the ABO_3 oxides, *J. Nucl. Mater. 300* (2002) 242–254.

[23] T. Gog, et al., Location of Ti Atoms Diffused into Nearly Perfect Crystals of $LiNbO_3$: An X-Ray Standing-Wave Study, *Europhys. Lett.* 25 (1994) 253.

[24] J. Špirková-Hradilová, P. Nekvindová, J. Vacík, J. Červená, J. Schröfel, The possibility of tailoring the n_e vs c_{Li} relationship in lithium niobate optical waveguides, *Optical Materials* 15 (2001) 269–278.

[25] Y. N. Korkishko, V. A. Fedorov, S. M. Kostritskii, et al., Proton exchanged $LiNbO_3$ and $LiTaO_3$ optical waveguides and integrated optic devices, *Microelectronic engineering* 69 (2003) 228–236.

[26] P. Nekvindová, J. Červená, P. Čapek, et al., Features of APE waveguides in different Er: $LiNbO_3$ and (Er+ Yb): $LiNbO_3$ cuts: electrooptical coefficient r_{33}, *Optical Materials* 24 (2003) 527–535.

[27] F. Zhou, A. M. Matteo, R. M. De La Rue, C. N. Ironside, Swelling characteristics of proton-exchanged LiNbO3 waveguides, *Electronics Letters* 28 (1992) 87–89.

[28] E. Zolotoyabko, Y. Avrahami, W. Sauer, T. H. Metzger, J. Peisl, Strain profiles in He-implanted waveguide layers of LiNbO3 crystals, *Materials Letters* 27 (1996) 17–20.

[29] P. D. Townsend, P. J. Chandler, L. Zhang, *Optical Effects of Ion Implantation*, Cambridge University Press, 1994.

[30] V. V. Atuchin, Causes of refractive indices changes in He-implanted LiNbO3 and LiTaO3 waveguides, *Nuclear Inst. and Meth. in Phys. Res. Sect. B: Beam Inter. with Mat. and Atoms* 168 (2000) 498–502.